BNL 20550

PROCEEDINGS

of the

1975 ISABELLE SUMMER STUDY

July 14 - 25, 1975

Volume II

BROOKHAVEN NATIONAL LABORATORY
ASSOCIATED UNIVERSITIES, INC.
UPTON, NEW YORK 11973

BNL 20550

PROCEEDINGS

of the

1975 ISABELLE SUMMER STUDY

July 14 - 25, 1975

Volume II

Brookhaven National Laboratory
Associated Universities, Inc.
Upton, New York 11973

NOTICE

This report was prepared as an account of work sponsored by the United States Government. Neither the United States nor the Energy Research and Development Administration, nor any of their employees, nor any of their contractors, subcontractors, or their employees, makes any warranty, express or implied, or assumes any legal liability or responsibility for the accuracy, completeness or usefulness of any information, apparatus, product or process disclosed, or represents that its use would not infringe privately owned rights.

TABLE OF CONTENTS

Volume II

Page

A 4π Detector Experiment for ISABELLE 183

SUH-URK CHUNG, PAUL GRANNIS, DANIEL GREEN

Measuring Coulomb-Nuclear Interference as a First Round ISA Experiment 204

J.N. MARX, R.D. MAJKA

Elastic Scattering and Diffraction Dissociation in the Angular Range 1 - 50 mrad 234

R.M. EDELSTEIN, M. ZELLER

Small Angle Single Arm Spectrometer for ISABELLE 244

C-Y. CHANG, E. ENGELS, M. KRAMER, R. LANOU, L. PONDROM

A Single Arm Spectrometer to Study High $p_\perp$ Processes Near 90° at ISA 255

C.Y. CHIEN, H. GORDON, A. KANOFSKY, M.A. KRAMER, J. RUSS

A Brief Comment on Large $p_\perp$ Muons Near 90° 269

JANOS KIRZ

Experiments Using a Single Arm Spectrometer in the Intermediate Angle Region at ISABELLE 273

A. KANOFSKY

High $p_\perp$ π^0 Detector at ISABELLE 277

P. GRANNIS, D. GREEN

Single Particle Spectra at High Transverse Momentum as a Function of X 289

M.L. GOOD

Page

Search for Fractionally Charged Quarks at ISABELLE 292

K.J. FOLEY, B.T. MEADOWS

Monopole Searches at ISABELLE 301

G. GIACOMELLI, A. THORNDIKE

On the Possibility of Searches for Particles by Threshold Effects Using Precise Determination of the ISA Energy 316

A. KANOFSKY

A Versatile Central Spectrometer for ISABELLE 319

D. CHENG, K. GOULIANOS, B. KNAPP, J. ROSEN, P. SCHLEIN

Advantages of Asymmetric Operation of ISABELLE 327

RONALD F. PEIERLS

Jets in Large P_T Reactions at ISABELLE 333

FRANK E. PAIGE

$W^{\pm}$ Pairs and Neutral Currents at ISABELLE 340

K.O. MIKAELIAN

Downstream Calorimeters for ISABELLE 348

W. SELOVE

A Calorimeter Experiment for Jet Studies and Other Uses of Modular Calorimeters 351

A. KANOFSKY

Calculation of Rates for Heavy Lepton Search 356

C-Y. CHANG, N.P. SAMIOS

On the Possibility of Using ISABELLE with Gas Jets and Other Like Beams 363

A. KANOFSKY

Page

Channeling and Some of the Things You Might Do with It at ISABELLE 365

A. KANOFSKY

ISABELLE with One Low-β Insertion 372

A. GARREN

Closed Orbit Adjustment 382

D. EDWARDS

Some Effects of Random Errors in ISA Magnets 386

A.W. CHAO

Control of Betatron Tune and Resonances 395

J. GAREYTE, J.P. GOURBER

Betatron Tune Change Due to Direct Space-Charge Forces in the ISA 418

A.W. CHAO, J.C. HERRERA, M. MONTH

Sources and Characteristics of ISA Beam Loss 423

A. van STEENBERGEN, L.C. TENG

ISA Beam Dump Absorber 430

A. van STEENBERGEN

Injection-Ejection Protection Logic 442

H. BROWN

ISA Beam Scraper System 447

J. PETERSON, A. van STEENBERGEN, L.C. TENG

Caloric Deposition Downstream of the ISA Beam Scrapers 452

L. BLUMBERG, J. RANFT, A. STEVENS, A. van STEENBERGEN

Page

ISA Beam Scraper Criteria 463

A. van STEENBERGEN

Synchronization and Tolerances for Transfer of Beam from AGS to ISA 470

J. PETERSON, L.C. TENG

ISABELLE Kicker Magnets, Septa and Scrapers 476

A. FALTENS

An Estimate of Limits to the Longitudinal Coupling Impedance 486

A. FALTENS, L.J. LASLETT

Accelerating RF System 500

S. GIORDANO

Stacking RF System 508

S. GIORDANO

Shunt Impedance Correction 515

J. CLAUS

Phase Displacement Acceleration for the ISABELLE Stack 520

E. MESSERSCHMID, M. MONTH

Transverse Stability of Coasting Beams in ISABELLE 531

E. KEIL, A. G. RUGGIERO

Dependence of the Longitudinal Bunched Beam Stability on the Choice of the RF Harmonic Number in ISABELLE 539

A. G. RUGGIERO

Transverse Stability of the Bunched Beam During Acceleration in ISABELLE 545

A. G. RUGGIERO

Page

Longitudinal Coupling Effects Due to Beam-Beam Interaction 552

C. PELLEGRINI

Coasting Beam Theory Applied to Bunches 555

H.G. HEREWARD

Intrabeam Scattering in ISA 562

K. HÜBNER

Magnet Protection 565

D.A. BAYNHAM

Conductor Considerations for ISABELLE Dipoles 567

A.D. Mc INTURFF, B.P. STRAUSS,
R.H. REMSBOTTOM

ISABELLE Magnet Correction System 573

G. PARZEN

50 kG ISABELLE Dipole 583

P. DAHL, G. PARZEN

Some Remarks on Mechanical and Thermal Behavior of the Coil 585

J. PEROT

Some Three-Dimensional Magnetostatic Relaxation Programs 587

L.J. LASLETT

Shielding Criteria and Design Considerations 624

S.J. LINDENBAUM

Displacement Damage for 300 GeV Protons 626

PHILLIP SANGER

Page

Radiation Heating: Experience and Projections 631

G.T. DANBY

Thermal Desorption of Gases from Aluminum Alloy Al 6061, Their Rates and Activation Energies 640

H.J. HALAMA, J.C. HERRERA

Alternative Interpretation of the Measurements of Specific Outgassing Rates of Materials 652

J.P. HOBSON

Beam Clearing and Space-Charge Tune Depression 658

J.C. HERRERA

Clearing Requirements in ISABELLE Based on the Electron Proton Instability 661

O. GRÖBNER

η Measurements in Glow Discharged Chambers at the ISR 665

D. BLECHSCHMIDT

Ion Desorption Cross Section of Carbon Containing Molecules on Aluminum and Stainless Steel 672

M.L. YU

Pressure Measurements at ISABELLE 680

D. BLECHSCHMIDT

Experimental Insertions 688

H.J. HALAMA

Demountable Ultrahigh Vacuum Sections for ISABELLE 690

J.P. HOBSON

Outline of a Cold Bore Design for ISABELLE 694

R.C. WOLGAST

Page

Computer Control and Monitoring 701

D.G. DIMMLER

Organization and Design of an ISABELLE Control System 705

R.J. NAWROCKY

Some Guidelines for Control System Design 707

K.K. LI

Computer System Requirements 710

D. LOWENSTEIN

A New Approach to Control System Interfaces 712

K.B. MALLORY

$\bar{p}$-p Option 715

F. HALZEN, E. PASCHOS, R. PEIERLS, D.P. SIDHU, T.L. TRUEMAN

Heating Effects of an Unseparated $\bar{p}$ Beam in the ISA Ring 723

V. L. FITCH

On the Contamination during Antiproton Injection into ISABELLE 729

K. HÜBNER

Single Ring $\bar{p}$-p Colliding Beams as an Interim ISABELLE 739

D. BERLEY, A. CARROLL, A. MANN

Status of the ISABELLE e-p Option at Time of Summer Study 1975 751

R. CHASMAN

Review of e-p Collision Geometries 761

K. STEFFEN, J. MAIDMENT AND Y. CHO

Page

Comments on Injection into ISABELLE Electron Ring 774

J.R. MAIDMENT

Storing and Accelerating Electrons in One of the p-Rings of ISABELLE 778

M. TIGNER

Shielding the Cold Region of the ISA Magnets from Synchrotron Radiation 783

M. TIGNER

Does the Proton Beam in an e-p Colliding Device Deteriorate by Individual e-p Coulomb Interactions? 791

H. BRUCK

A Possible Alternative for the e-p Option 809

A. KANOFSKY

Vertical Dispersion Matching in the ISA Electron Option 814

A. GARREN

A 4π DETECTOR EXPERIMENT FOR ISABELLE

Suh-Urk Chung
Brookhaven National Laboratory
Paul Grannis
SUNY, Stony Brook
Daniel Green
Carnegie-Mellon University

I. Introduction

The design of the large solid-angle detector has been considered in several previous CRISP and ISA studies.[1-4] The present report revisits these problems with particular emphasis on several difficulties which have plagued the existing ISR experiments with large solid-angle coverage (Pisa-Stony Brook: counter hodoscopes only and Aachen, CERN, Heidelberg, Munich: streamer chamber). A reasonably detailed apparatus study is made with some attention given to expected errors, rate limitations, and running conditions.

It is our basic contention that, not only can we envision a good experiment measuring particle production over almost the full angular range, but that such an experiment will provide many physics results of great interest. The basic goal of the experiment is to measure the directions of all produced charged particles without reference to their identity or momentum. Such information, though obviously incomplete, gives a very important global picture of multiparticle production very early in the ISABELLE operation. The experience at the ISR has shown that such data, augmented by more detailed information in specific regions of phase space, can

---

1. A. Ramanauskas, BNL Informal Rept. CRISP 71-23 (1971).
2. A. S. Carroll, BNL Informal Rept. CRISP 71-53 (1971).
3. R. Arnold, G. Finocchiaro, P. Grannis, J. Kirz, C. Quigg, A. S. Carroll, BNL Informal Rept. CRISP 72-65 (1972)
4. A. M. Thorndike, BNL Informal Rept. ISA 75-2 (1975).

usefully address most of the important questions relating to ordinary (low $p_\perp$) p-p collisions.

The physics which motivates our study has been discussed before. We foresee five overlapping areas of experimental studies for which our apparatus is suitable. These are 1) total rate (hence, given a luminosity measurement, σ_{tot}); 2) charged multiplicity distributions and determination of the Mueller moments $< n >, f_2, \ldots$; 3) angular distributions for one, two, three particles both inclusive and semi-inclusive (fixed multiplicity); 4) topological studies of events (e.g. separation of diffractive and pionization components) and 5) combination with special purpose detectors or spectrometers for which global correlations are useful.

In these experiments, only angles of charged particles are measured. Consequently, no identification of particle type or momentum is available. Distributions can be presented in terms of the variables, $\sqrt{s}$ = c.m. energy, n = charged multiplicity, ϕ = azimuthal angle, and $\eta = -\ln \tan(\theta/2)$. [$\eta$ approximates the rapidity y in the limit $(m^2/p_\perp^2) \ll 1$.] With this type of measurement, there are a large number of interesting physics questions. We make a brief sampling of these below.

1) A 10% rise in σ_{tot} is observed over the ISR energy range. Estimates of the increase in σ_{tot} over ISABELLE energies vary between 0 and 50%. An accurate measurement (±1%) will severely constrain high energy models.

2) Measurement of the distribution of events as a function of charged multiplicities and the moments of that distribution gives global information on the degree of correlation within multiparticle events. Such information has not yet been obtained at the ISR, due primarily to the lack of a full 4π coverage and to the presence of secondary particle interactions in material surrounding the interaction region (hadronic showers, γ-conversions, δ-rays). While the information obtained through the multiplicity measurement is much less detailed than the rapidity distributions, it serves as a useful figure of merit for the experiment as a whole.

3) Single particle distributions, $(d\sigma/dy)$ are expected to show a central plateau of energy-independent height. At ISR energies, the plateau has barely emerged from the fragmentation cones surrounding the beam axes. The value of $(d\sigma/dy)$ at $y = 0$ is strongly suspected to be rising over the ISR range. It will be important to look for the emergence of a well-developed plateau at ISABELLE and the extent to which scaling is valid.

4) Two-particle correlation measurements at the ISR have identified important short-range collective effects. It will be important to examine this short-range component at higher energies where the central region is considerably larger. Present belief is that the intrinsic strength of the correlations will be nearly energy independent. A viable explanation for the observed correlations is the presence of substantial production of resonant states (often called clusters). It has been demonstrated that fixed-n studies (semi-inclusive correlations) greatly simplify the interpretation of clustering phenomena. At present no reliable study of three (or more) particle correlations has been made — largely due to the effects of missing solid angle and secondary particle production.

5) A variety of event-topology investigations have been suggested and to some extent attempted at the ISR. An interesting example is the separation of "diffractive" from "pionization" events based on the pattern of particle rapidities within the event. It has been shown qualitatively that such a separation can be made at $\sqrt{s} = 60$ GeV. At the highest ISABELLE energy with the increased available rapidity space, this type of study can be made much more quantitative. For example, present data indicates that for single diffractive excitation of a state of mass $\leqslant 30$ GeV, the decay products will be almost entirely contained within one hemisphere of the center-of-mass frame. Distinction of such an event (with an embedded rapidity gap of $\Delta y \geqslant 5$) from a pionization event seems easily feasible. It seems plausible that the majority of the diffractive cross section can be topologically isolated and that the

experiment can contribute usefully to the question of the energy-dependence of this component.

Various other topological studies have been suggested. Insight into cluster production can be gained through study of the rapidity gap. At ISABELLE, a reasonably bias-free isolation of double-diffraction events can be foreseen due to the large rapidity span and thus a direct test of factorization of diffractive and elastic scattering may be attempted.

6) The 4π apparatus, used in conjunction with a spectrometer, has many applications. For example, elastic scattering in the region $0.5 \leq |t| \leq 15\ (\mathrm{GeV/c})^2$ can be studied by momentum-analyzing one proton and requiring the second proton within a well defined angular region.

If the detector is used in conjunction with a small-angle (diffractive) proton spectrometer which measures the diffractive cluster mass, then the 4π detector provides valuable information on the angle and number distributions of the cluster decay. Such a study will allow a much improved measurement of the diffractive cross section over that of either spectrometer or 4π detector apparatuses alone.

With a 90° spectrometer capable of triggering on high $p_{\perp}$ particles, many interesting measurements are possible. The possible existence of jets may be inferred through a local excess in associated multiplicity. The event pattern associated with exotic high $p_{\perp}$ triggers (e's, μ's ...) will be of interest.

II. Constraints on the Experimental Design

In order to pursue the physics goals outlined above, there are several important design considerations. In general, one wants as complete solid angle measurement as possible, no contamination of the charged particle sample by secondary particles or converted neutrals, and good angular resolution.

The solid angle coverage can easily be made complete with the exception of the holes to allow beam entrance and exit. If we employ no detectors behind the quadrupoles at 20 meters, the stay-clear beam dump profile imposes the limit $\theta > 1$ mrad. It is imperative to know the number of particles which stay within this hole, as a function of s, and n. It is also critical for the measurement of σ_{tot} to know the trigger loss due to all charged particles in one hemisphere being contained in the hole. An adequate measurement of the hole loss then dictates two features of the experiment:

1) The detector at small angle should have sufficient angle and multiplicity resolution to allow extrapolation of rates to 0°, and

2) The experiment can profit from asymmetric operation of the two rings.

The latter point is illustrated by the observation that $\sqrt{s}$ = 155 GeV can be achieved both by $E_1 = E_2 = 77.5$ GeV and by $E_1 = 30$ GeV, $E_2 = 200$ GeV. Running in the symmetric mode gives rise to a 11% loss of single diffractive triggers [assuming $\theta_{min} = 2$ mrad and a diffractive slope of 5 $(GeV/c)^{-2}$]. In the asymmetric mode, the loss of single diffraction due to the undissociated proton being within the 2 mrad aperture is less than 2%. Operation in a few asymmetric beam energy modes allows direct verification of the extrapolation procedures.

The requirement of little neutral or vacuum pipe secondaries places severe restriction on the detectors. We consider separately δ-rays, hadronic showers, and γ-conversions.

The number of δ-rays produced varies as about q^{-2} where q is the δ-ray kinetic energy, with the emission angle given approximately by $\cos\theta = q/\sqrt{q(q+2)}$. Thus for an effective pipe thickness of 1 cm, the number of δ-rays per charged particle is $< 4 \times 10^{-3}$ and their angles relative to the charged particle are ≥ 200 mrad. Thus, even modest angular resolutions will allow the separation of the δ-ray track from the interaction diamond.

The hadronic interactions in the vacuum pipe are characterized by typical transverse momenta of 1/3 GeV/c. For 100 GeV/c primaries, we estimate the secondary pion shower to contain $\leq$ 30 GeV/c pions and hence $\geqslant$ 10 mrad divergence from the initial hadron direction. The number of interactions per hadron in an effective thickness of 5 mm $A\ell$ is about 2%. Angular resolution of better than 10 mrad will be required to cleanly isolate hadron showers — particularly in the forward directions.

Photon conversions pose a serious problem in these experiments. A converted pair has essentially zero opening angle and hence would give rise to an extra charged track. The conversion probability per γ will vary between 1% and 5% depending on the pipe thickness traversed. We would like to eliminate the greater part of this background. A possible means of identifying converted γ's is to separate spatially the e^+e^-. This becomes a real possibility if the e^- pair traverses a few percent of radiation lengths (almost unavoidable in view of the proposed vacuum pipe thickness) <u>and</u> very good spatial resolution detectors.

The above considerations lead us to contemplate the highest resolution detectors available — viz, drift chambers with resolution $\sim$ 0.1 mm. The problem which is then introduced is the rate sensitivity of the detector. We find below that presently achievable drift-chamber technology should allow such a detector to operate in the ISABELLE environment at luminosities approaching 10^{32} cm^{-2} sec^{-1}. In part, the performance at high luminosity employs the good resolution to reconstruct a vertex in the interaction region to within a small fraction of the beam-crossing volume.

Finally, one must provide a 4π trigger with good time resolution. Not surprisingly, we advocate a full coverage of scintillators of modest size. The total number of scintillators can, in fact, be kept quite small.

We envision the operation with this apparatus to proceed in several stages. The initial operation would be aimed at study of

the inclusive 4π trigger to obtain σ_{tot}, multiplicities and angular distributions. For this running period, the luminosity should be kept at moderate levels, ($< 10^{31}$ $cm^{-2}sec^{-1}$) so as to minimize accidental and dead-time problems. During this period several good statistics runs with asymmetric beam energies would be required in order to study systematic effects associated with trigger and particle losses in the holes in the apparatus. Substantial running time during this phase must be devoted to luminosity measurements in order to understand the systematic errors in the σ_{tot} measurement.

Subsequent running would be foreseen at higher luminosities in conjunction with various special triggers. For these runs, some regions of the drift chamber coverage may be removed to allow access by the special detectors. In these runs, less control of systematic errors in multiplicity and trigger loss will be demanded.

III. Experimental Arrangement

The vacuum pipe is shown in Figs. 1 and 2. Its shape is dictated by the stay clear profile (radius $\leq$ 2 cm), by the constraint of a smooth change of shape, by the desire for small detector diameter and by the criterion that any secondary particle traverse at most 5 times the perpendicular thickness of the pipe. A thickness of 1 mm of $A\ell$ is assumed.

These criteria are met in a cylindrical pipe at large angles which smoothly decreases to 2 cm radius at 1 m from the interaction region. Two further slow flares of the bicone then follow. The first, at moderate angles, also accommodates the entering beam. The second mates on to the main ring pipe at the location of the first quadrupoles.

The requirements discussed in II above incline one toward drift chambers with 2-D readout (current division or delay line). The intrinsic good angular resolution then compensates the longer

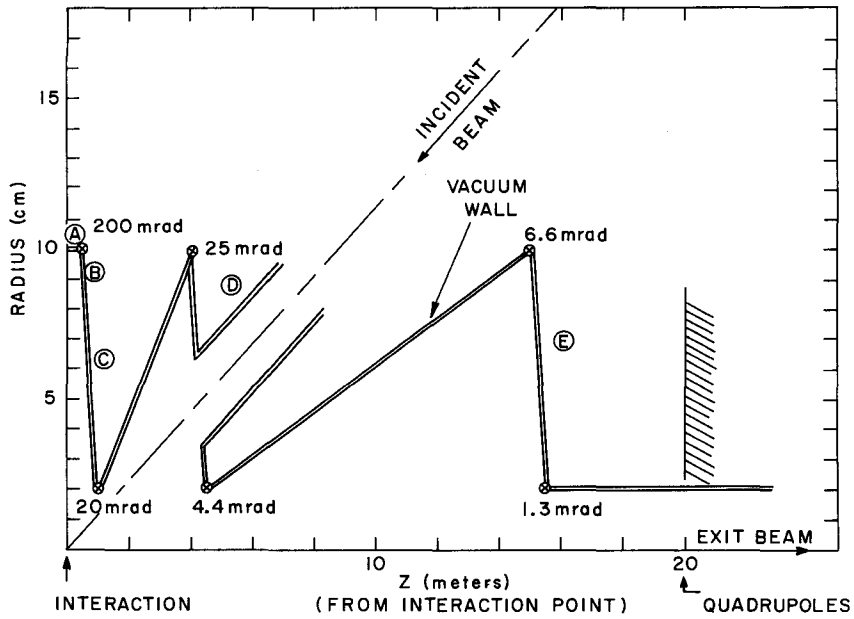

Fig. 1 - Vacuum chamber and detector regions.

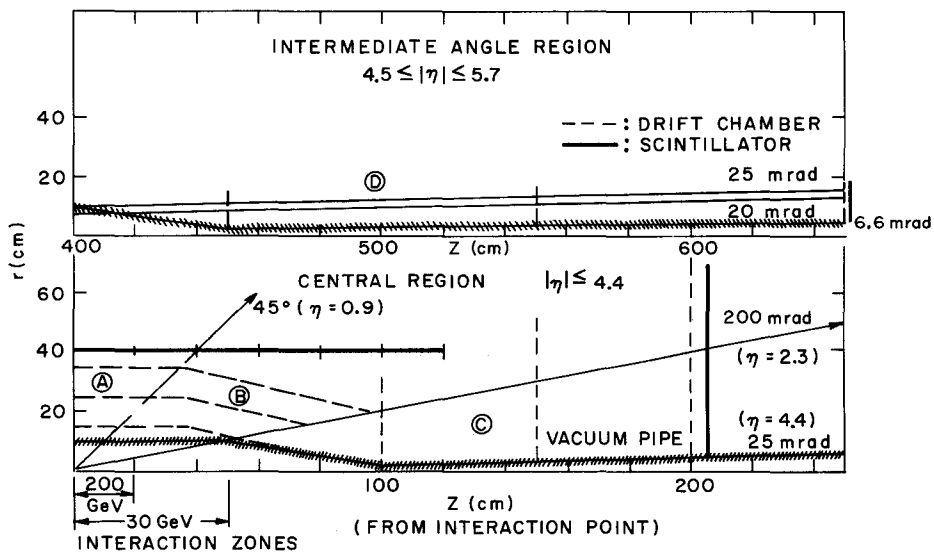

Fig. 2 - Detector arrangement showing drift chamber and scintillator positions relative to vacuum pipe.

memory time by providing vertex resolution sufficient to assign multiple events/trigger to distinct vertices. These chambers will be modular in units of π in azimuth for ease in dismounting for data taking in conjunction with other spectrometers.

A rough guide to the number of particles expected in various angular regions is given in Fig. 3. The chamber disposition is shown in Fig. 2. Angles up to 45°, Region A, are detected in cylinders surrounding the beam pipe. The remaining angles are detected in disks at locations B, C, D, and E. The drift directions are along the beams for Region A and radially for all other regions. This arrangement provides good θ and Z_c vertex information with cruder azimuthal information.

The angular ranges, pseudorapidity (η) ranges and number of wires for the various regions are shown in Table I.

Table I. Drift Chamber Specifications

$\Delta\eta$	Region	θ_{min} (mrad)	θ_{max} (mrad)	η_{min}	η_{max}	# Wires
1.8	A	785	1571	0.	0.9	420
1.4	B	200	785	0.9	2.3	480
2.1	C	25	200	2.3	4.4	660
1.3	D	6.6	25	4.4	5.7	180
1.6	E	1.3	6.6	5.7	7.3	180
7.3	Total	1.3	1571	0.	7.3	1920

The number of wires per unit η interval has been tailored to be roughly constant in the central region, $|\eta| \leqslant 4$, at ~ 60. For $|\eta| \geqslant 4$ where the rate/inelastic interaction falls off this falls to $\sim$ 20 wires/unit rapidity.

The apparatus will be triggered by crossed scintillators behind each triplet of chambers, this requires 40 counters, 24 of which are of a size 0.6 m $\times$ 0.3 m and 16 of which are of a size 0.6 m $\times$ 0.3 m. One will trigger with a loose left $\cdot$ right coincidence. Later time-of-flight cuts and vertex resolution will

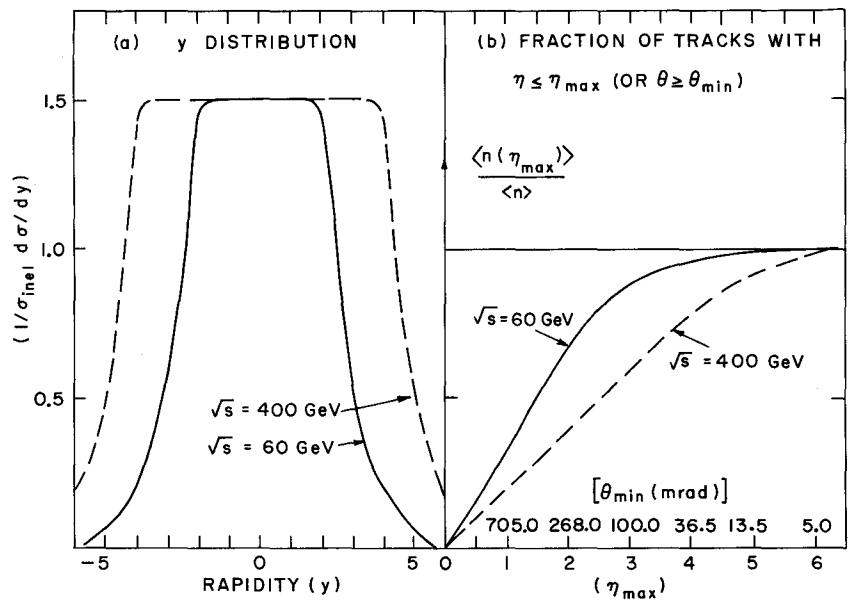

Fig. 3 - Angular distributions expressed in terms of rapidity, y, and pseudorapidity, η.

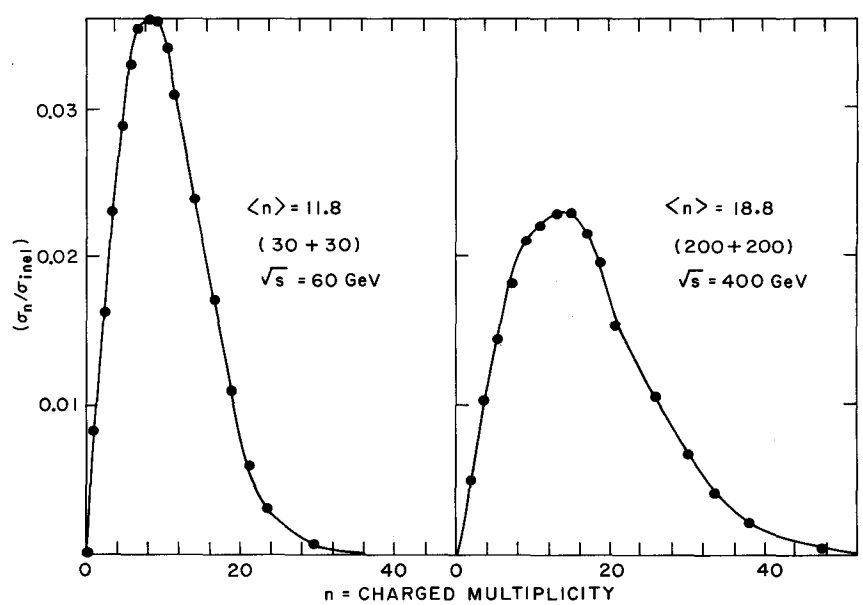

Fig. 4 - Multiplicity distributions assumed for 30 x 30 GeV and 200 x 200 GeV.

reduce the beam-gas background to a negligible level.

IV. Multiplicity Corrections

Corrections for both loss and gain of particles must be made. The elastic losses can be estimated assuming a slope of 10 $(GeV/c)^{-2}$ and a cross section of 8 mb out of a total of 40 mb. At 30 x 30 GeV/c, 0.13 mb is lost, and at 200 x 200, 4.1 mb is lost. Assuming the the relevant event sample is the 32 mb = σ_I of inelastic interactions, this is irrelevant, save to σ_T measurements.

Another class of events which is lost relatively copiously is that of single diffractive events. Assuming a 6 mb cross section and a slope of 5 $(GeV/c)^{-2}$ one loses 0.05 mb at 30 x 30 GeV/c, 0.52 mb at 100 x 100 GeV/c, and 1.8 mb at 200 x 200 GeV/c.

This class is corrected as follows. Those events with only a single track in one hemisphere are corrected in multiplicity for diffractive decay products escaping in the beam pipe. An extrapolated number of events with extrapolated charged multiplicity which have failed to trigger is then added to the inelastic event sample.

This procedure can be checked by asymmetric beam runs. For example, s = $(230\ GeV/c)^2$ for both 30 x 200 GeV/c and 78 x 78 GeV/c. These 2 runs with extrapolations of 0.025 mb + 0.9 mb vs 0.30 mb must yield the same multiplicity distribution.

Angular distributions for nondiffractive events at each multiplicity n will also be extrapolated into the beam pipe as $\Delta n_{lost} = (n/\sigma_n) \int_0^{\theta min} (d\sigma_n/d\Omega)\, d\Omega$. Experience with the ISR shows that this correction is of negligible importance.

Corrections for gain of particles must be made for hadronic showers, δ-rays, and γ conversions. Assuming a worst case of 5 mm of aluminum for vacuum pipe traversal, we have 1.7% of an interaction length and 5.5% of a radiation length.

The separations between triplets of drift chambers have been chosen to scale with the momentum of the secondaries. Assuming that all secondaries are pions with $< p_\perp >_\pi \sim 0.32$ GeV/c and that typical hadronic showers have $< p_\perp > = < p_\perp >_\pi$ and $< p_{||} > = < p >$ then, as in Table II, the minimum shower particle separation in any regular region is 2 cm. Assuming a drift chamber resolution of $\delta x = 0.1$ mm, this implies a shower probability of not being detected of $< 0.01\%$.

Table II. Hadron Shower Characteristics

Region	$< \theta >$ (mrad)	$< p >$ (GeV/c)	$< \theta >_{shower}$ (mrad)	Lever Arm (cm)	Separation (cm)
A	1178	0.35	910	20	18.2
B	493	0.68	470	20	9.4
C	112	2.9	112	100	11.2
D	15	21.3	15	200	3.
E	4	80.	4	500	2.

The δ-ray contribution to the background has already been discussed in Section II. It is a negligible problem over the whole angular range.

The probability of a photon conversion is 0.055 per photon, assuming a 5 mm pipe traversal length and $n_\gamma = n_{\pi^+} + n_{\pi^-} = 2n_{\pi^0}$. These extra tracks are reduced by using the electron multiple scattering in the beam pipe. Assuming $< p_\perp >_\gamma = 0.16$ GeV/c then the separations are shown in Table III.

Table III. Photon Conversion Characteristics

Region	$<\theta>$ (mrad)	$<p>_\gamma$ GeV/c	θ^{1-D}_{ms} (mrad)	Lever cm	Separation cm
A	1178	0.175	28.6	20	0.57
B	493	0.34	14.7	20	0.29
C	112	1.45	3.45	100	0.35
D	15	10.65	0.469	200	0.094
E	4	40	0.125	500	0.062

Since typically the separation is 2 mm and the drift chamber resolution is 0.1 mm one has of order 0.3% probability of the γ escaping identification.

The effect of these corrections to the multiplicity on the moments of the multiplicity distribution will be estimated in a later section. Losses of multiplicity have been minimized by use of the smallest hole consistent with the stay clear profile. Additions to multiplicity have been minimized by minimizing the beam pipe effective thickness for all angles and by using detectors with good angular resolution so as to detect secondary interaction vertices in the beam pipe.

V. Rate Considerations

The apparatus, as described, is capable of performing stand alone physics at a low luminosity for initial operation of ISABELLE. At a luminosity of $10^{30}/cm^2 sec$ the event rate is 40 kHz. Obtaining adequate statistics for global experiments is thus no problem. Given that an interaction vertex is reconstructed, requirements on initial beam quality are minimal.

We propose that the drift chamber wires should be spaced by 1 cm. This means a maximum drift time of 100 nsec. This rather modest memory time is compensated by the good vertex resolution.

The criterion is that for experiments in conjunction with spectrometers, which presumably will require high luminosity, the detectors should tolerate high rates.

At luminosity of $2.6 \times 10^{32}/cm^2 sec$, the event rate is $\sim$ 10 MHz. The particle rate is then $\sim$ 200 MHz. The apparatus is laid out so as to produce roughly constant rate on any triplet of chambers.

Table IV. Drift Chamber Rates

Region	Δn	Particle Rate (MHz)	Wires per Detector	Rate/Wire (MHz)
A	2.9	29	100	0.29
B	2.3	23	80	0.29
C	3.3	33	80	0.41
D	1.5	15	30	0.50
E	1.0	10	30	0.33
Total	19.1	191	540	0.35

The typical time spacing between tracks involving a single wire is then $\sim$ 3 μsec compared to a drift time of 100 nsec. This is clearly pushing the apparatus near its limits.

At the top luminosity for the standard insertion one will typically have 1 extra event/trigger. One beats this by finding a good vertex location within the $\Delta z \simeq 0.4$ m of the interaction diamond.

The resolution error in the vertex is dominated by multiple scattering in the vacuum pipe walls. Assuming all secondaries are pions with $< p_\perp > = 0.32$ GeV/c, their multiple scattering implies a vertex error of $\leqslant$ 1 cm in regions A, B and C, $\sim$ 5 cm in Region D and $\sim$ 17 cm in Region E. Clearly, tracks can be assigned to at least 2 distinct vertices/event for all angles covered by the detector.

Table V. Vertex Resolution

Region	$< \theta >$ (mrad)	$(\delta\theta)_{TOT}$ (mrad)	δz_{vertex} (cm)	δx_{vertex} (cm)
A	1178	10	0.16	0.15
B	493	5.2	0.38	0.18
C	112	1.2	1.07	0.12
D	15	0.17	5.07	0.08
E	4	0.05	16.75	0.07

Since the readout of the chambers is 2-dimensional, the pattern recognition load on computer time is minimal. For example, each wire hit (z position) in the cylinders has a unique ϕ coordinate corresponding to a azimuthal distance of $\sim$ 1 cm, or $\Delta\phi/2\pi \leqslant 1/80$. No track association of views is needed. One merely iterates over point combinations in different chambers in order to find a vertex. For chambers viewing the diamond at small angles this iteration can be reduced by defining narrow roads through the triplet of detector disks.

Each track has a minimum of 3 points plus a vertex. Hence the requirements on chamber efficiency are not terribly stringent. For 1% inefficiency of any wire, the fraction of tracks with fewer than 2 points/track is only 0.03%. The detectors themselves will give negligible contributions to multiplicity errors.

VI. Topological Studies

Topological classification of events becomes easier at ISABELLE than at the ISR with the extension of the available rapidity space. At 200 + 200 GeV/c one has $|y| \leqslant 6.05$. Appeal to ISR data shows that centered about the diffractive blob of mass M, rapidity y_M, the decay products have $\Delta y|_{fwhm} \sim \sinh^{-1} (M^2/2m^2)$ and

$\Delta y|_{total} \sim \Delta y|_{fwhm} + 1.$

Using this data and extrapolating to ISABELLE one can consider what range of single diffraction dissociation (SD) may be separated on topological grounds alone.

Table VI. Single Diffraction Properties

Mass^2 (GeV)^2	1 - x	y_M	$\Delta y\|_{fwhm}$	$y_{min}^{cluster}$	Rapidity Gap	$n_{cluster}$
4	2.4×10^{-5}	5.3	1.44	4.1	10.1	2
20	1.2×10^{-4}	4.5	3.0	2.5	8.5	4
100	6.2×10^{-4}	3.7	4.6	0.9	6.9	6
400	2.5×10^{-3}	3.0	6.0	-0.5	5.5	?
1000	6.25×10^{-3}	2.5	6.9	-1.5	4.5	?

These low multiplicity clusters occupy less than 1/6 of σ_{inel} or $\sim$ 5 mb. They, themselves, roughly saturate σ_n at low n, since σ_{sd} is $\sim$ 16 mb. Since pionization events are evenly distributed in rapidity, one achieves an additional separation by applying a large rapidity gap cut. Thus single diffractive clusters of mass up to $\sim$ 20 GeV/c^2 mass should be topologically identifiable.

Factorization implies a double diffraction dissociation section (DD) of $\sim$ 1 mb, about 1/30 of the inelastic cross section.

Table VII. Double Diffraction Properties

Mass^2 (GeV)^2	$y_{min}^{cluster}$	Rapidity Gap	$n_{cluster}$	n_{total}
4	4.1	8.2	2	4
20	2.5	5.0	4	8
50	1.6	3.2	5	10

Events with multiplicity $\leqslant 10$ at 200 + 200 GeV/c will account for only $\sim$ 10 mb of cross section. Roughly half is single diffraction. Assuming uniform density of pionization events a maximum rapidity gap cut of $\Delta y = 3.2$ will reduce the pionization contribution to 5 mb $e^{-4} \sim 0.1$ mb. Thus, a reasonable possibility exists of studying double diffraction disassociation at cluster masses $\leqslant 7$ GeV/c^2.

VII. Global Multiplicity Corrections

Of the two major problems facing the 4π measurements (loss of solid angle at the beam pipes and interactions) the more difficult to assess quantitatively is the effect of secondary particle interactions. A measure of this problem is the change induced in the multiplicity moments $< n >$, $< n >^2, \ldots$. In this section we attempt to calculate the systematic errors in these moments under some simplifying assumptions. We note that knowledge of these errors gives also a reasonable feeling for the systematic errors on the rapidity distributions due to the various sum rules; e.g.

$$\int \left(\frac{1}{\sigma} \frac{d\sigma}{dy} \right) dy = < n >$$

$$\iint \frac{1}{\sigma} \frac{d^2\sigma}{dy_1 dy_2} \, dy_1 \, dy_2 = < n(n-1) >$$

We have, to first approximation, made the detector arrangement have the property that corrections to multiplicity are independent of rapidity.

We use for the true multiplicity distribution, a scaled version of FNAL results (no reliable multiplicity distributions have been obtained at ISR).

$$\frac{\sigma_n}{\sigma_{inel}} = \frac{\pi n}{< n >^2} \, e^{-(n/<n>)^2}$$

at all energies and the ISR fit for $< n >$

$$< n > = -3.8 + 1.88 \, \ell n \, s + \frac{6.45}{\sqrt{s}}$$

Figure 4 shows this extrapolation for ISABELLE.

The most worrisome systematic effect is due to γ conversions which are not recognized by the system. If the fraction of all γ's thus contaminating the sample is α, then we find approximately (for small α)

$$< n >' \simeq < n > (1 + \alpha)$$
$$< n^2 >' \simeq < n^2 > (1 + 2\alpha) + \alpha < n >$$
$$< n^3 >' \simeq < n^3 > (1 + 3\alpha) + 3\alpha < n^2 > + \alpha < n >$$

Where the prime indicates moments of the distributions including the contaminating γ's.

A more explicit computer simulation of the γ-problem gives, for $\alpha = 0.005$, the results in Table VIII.

Table VIII. Effect of γ Conversion on Apparent Multiplicity Moments

Moment	30 + 30 GeV/c	100 + 100 GeV/c	200 + 200 GeV/c
$\Delta f_1/f_1$	0.005	0.005	0.005
$\Delta f_2/f_2$	0.013	0.012	0.012
$\Delta f_3/f_3$	0.021	0.019	0.019

here $f_1 = < n >, f_2 = < n(n-1) > - f_1^2, f_3 = < n(n-1)(n-2) > - 3f_1f_2 - f_1^3$. We believe the above estimates to be roughly correct, based on the estimates of the γ-tagging ability of the detector.

The estimated error in multiplicity moments due to the uncertainty in number of prongs running in the beam pipe has been calculated in the same computer simulation. Here the primary effect is seen in $< n >$ since the dispersion is to first order unaffected by particle loss. Table IX shows the effect on moments assuming a 0.1 particle uncertainty in pipe loss.

Table IX. Effect of Beam Pipe Loss on Apparent Multiplicity Moments

Moment	30 + 30 GeV/c	100 + 100 GeV/c	200 + 200 GeV/c
$\Delta f_1/f_1$	0.008	0.006	0.005
$\Delta f_2/f_2$	0.000	0.000	0.000
$\Delta f_3/f_3$	-0.010	-0.004	-0.003

Our conclusion is thus that the moments of the multiplicity distribution can be measured to within few percent accuracy up to the third moment. Similar systematic errors follow for inclusive distributions.

VIII. Total Cross Section and Luminosity Considerations

The measurement of σ_{tot} through a total rate measurement and knowledge of luminosity deserves some special comments. We assume that the luminosity will be measured by calibrating monitor telescopes with the VanderMeer method for each beam stack. The magnets for vertical displacements are presently programmed to reside between 13 and 20 meters from the crossing point. We must therefore comment on what the effect will be, due to shortening the detector.

A simple modification of the apparatus described above which will terminate at 13 m can be made. We find no inherent objection to scaling all dimensions on Figs. 1 and 2 by the ratio 13/20. Thus the angular ranges of detectors A through E remain the same. The vacuum pipe radius reduces to a smaller value but remains greater than the stay-clear profile (since the profile decreases as we go toward the crossing point). All chamber spacings are reduced by the same factor, but the relevant parameter for vertex reconstruction is the ratio of chamber spacing to extrapolation distance to the interaction point, and this is unchanged. (In fact, only the last flare of the vacuum pipe need be scaled down.)

We anticipate that errors in L will dominate the error on σ_{tot} (this is the experience of the ISR measurement and the trigger loss at ISABELLE is comparable or smaller than ISR). Thus special attention must be given to accurate and reproducible beam displacements. A rule of thumb is the relative vertical heights must be known to within a few percent of the beam heights (0.5 mm) in order to achieve a 1% error on L.

Measurements of anything besides σ_T do not depend on an absolute cross section calibration and for these the magnets may be removed to allow simpler access of additional spectrometers.

We note that the error on σ_{tot} due to incomplete trigger is expected to be small compared with the error in L. However, it is eminently reasonable to imagine that a very small angle hodoscope system be installed (before and after the quadrupoles as discussed in the Coulomb-Nuclear Interference proposals). Then the small-t elastic and diffractive trigger losses are drastically reduced.

Installation of the small-angle hodoscopes in the same region has a further strong advantage. Now σ_{tot} can be determined by

$$\sigma_{tot} = R_{tot}/L$$

and

$$\sigma_{tot} = \frac{4\pi}{p} \; \mathrm{Im} f(0) \simeq \frac{4\pi}{p} \left[\frac{d\sigma}{d\Omega} (\theta = 0) \right]^{\frac{1}{2}}$$

$$= \frac{4\pi}{p} \left(R_{E\ell} \; (\theta = 0)/L \right)^{\frac{1}{2}}$$

If both measurements are performed simultaneously, then σ_{tot} can be obtained independent of knowledge of L:

$$\sigma_{tot} = \left(\frac{R_{tot}}{R_{E\ell}} \right) \left(\frac{4\pi}{p} \right)^2$$

Estimate of the precision required for beam vertical displacements in order to know the luminosity can be made. Since

$$L = \frac{I_1 \; I_2}{ce^2 \tan(\alpha/z)} \times \frac{1}{h_{eff}}$$

where

$$h_{eff} \text{ (by VanderMeer method)} = \int \frac{R(\delta)d\delta}{R(0)}$$

and $R(\delta)$ = the measured (monitor) rate for beam separation $y_1 - y_2 = \delta$. If both beams are Gaussian (with $\sigma = 0.25$ mm as given in the June 1975 Yellow Book) then $h_{eff} = 2\sqrt{\pi}\,\sigma$. The component of error in L due to uncertainty in the displacement scale is thus

$$\frac{\delta L}{L} = \frac{\delta h_{eff}}{h_{eff}} = \frac{\delta\sigma}{\sigma} = \frac{\delta B}{B}$$

where B = the effective field in the vertical displacement magnets. Thus control of these magnets at the level of 1% in their absolute field integrals are required in order to know the luminosity to similar accuracy.

Some care must be taken in the beam displacements to keep the beam width from changing. A particular cause would be the spreading due to momentum dispersion in the beam and hence a dependence of displacement of momentum. The influence of dispersion on L should be at the level of $\delta p/p$ if no correction is made. Since the dispersion will be approximately known ($\delta p/p \simeq 0.7\%$) any correction for this effect should reduce the error on L to negligible proportions.

MEASURING COULOMB-NUCLEAR INTERFERENCE AS A FIRST ROUND ISA EXPERIMENT

J. N. Marx†

and

R. D. Majka

Yale University

Introduction

The ratio of real to imaginary parts of the forward scattering amplitude (ρ) is a quantity of fundamental interest which should, if possible, be measured through Coulomb-nuclear interference in an early experiment at ISABELLE. If small angle proton-proton elastic scattering is spin independent, then the optical theorem, crossing symmetry, and the basic tenets of quantum field theory allow ρ to be written as a dispersion integral of $\sigma_T(s)$ over s. The test of such dispersion relations at increasingly higher energies serves to confirm the validity of these assumptions over increasingly smaller distances. From the phenomenological point of view, these relations allow us a glance at the behavior of $\sigma_T(s)$ at values of s, the (total center-of-mass energy)^2, above those directly observable. This point is illustrated in Fig. 1 which depicts the behavior of ρ as a function of $E_{lab} \simeq \sqrt{s}/2$ for various models of the high energy behavior of the total cross section.[1]

The goal of the work reported here is to determine if such a measurement can be made in the first round of experiments at ISABELLE. We have not attempted to design the optimum experiment for ISABELLE; rather, we have investigated what could be done with the initial insertion (so-called "standard insertion"). As will be discussed below, we have defined "acceptable first round modifications

---

† Jr. Faculty Fellow; present address: Lawrence Berkeley Laboratory.

1. "A Proposal for Construction of a Proton-Proton Storage Accelerator Facility - ISABELLE", BNL 20161, June 1975, p. 20.

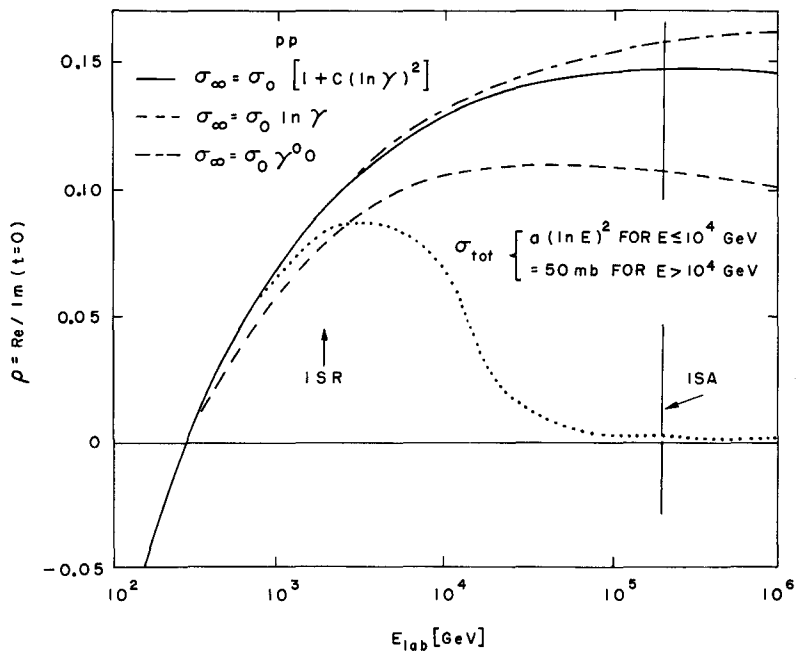

Fig. 1. Behavior of $\rho(s)$ for various models of the total cross section.

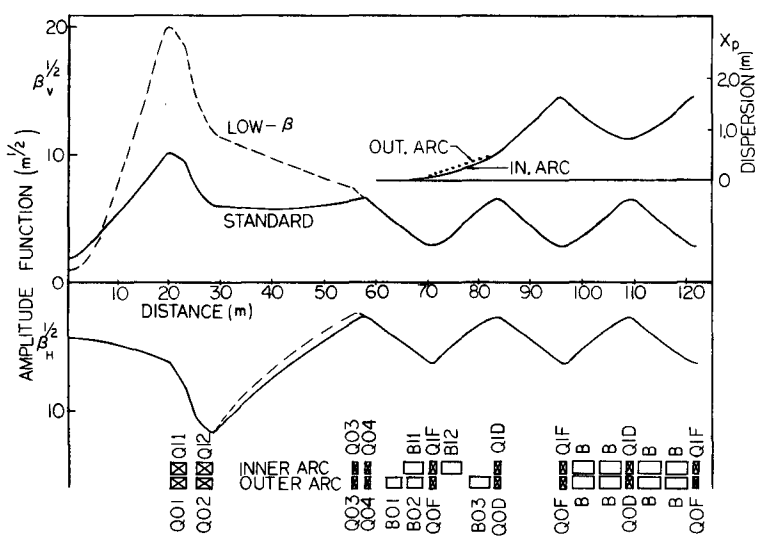

Fig. 2. Beta-functions for the standard insertion.

of the standard insertion" as meaning that no magnets can be moved from their initial positions in the lattice, but the currents of quadrupoles Q1 and Q2 can be changed to modify the β functions from the insertion to the regular machine lattice.

The experimental approach chosen is to measure the position of the elastically scattered protons at a place where the phase of the β function, Ψ, is close to 90° with respect to the beam crossing point. The advantage is easily seen from the transfer matrix relating position and angle at the crossing point (X_x, θ_x) to position and angle at another point in the lattice (X_d, θ_d),

$$X_d = X_x \cos\Psi + \theta_x \sqrt{\beta^* \beta_d} \sin\Psi$$

$$\theta_d = \frac{-X_x \sin\Psi}{\sqrt{\beta^* \beta_d}} + \theta_x \cos\Psi$$

where β^* and β_d are the values of the beta functions at the crossing point and the detector. If $\Psi = 90^{\circ}$ then one need only measure the position of the scattered proton, X_d, to determine the scattering angle θ_x.

The requirements placed on the beta functions come from the need to measure to very small t [the Coulomb-nuclear interference is maximal at $t \simeq 0.002$ $(\mathrm{GeV/c})^2$] with good resolution. Even with ideal detectors, the angular spread of the beams contributes significantly to the resolution. In addition, one wants to be able to place detectors at a safe distance from the beam and yet be able to detect very small scattering angles. Using the experience gained in measuring the Coulomb-nuclear interference at FNAL,[2] we have set as our goal a resolution in $p_\perp \simeq \sqrt{t}$ of $\leqslant 6$ MeV/c rms with a minimum t of 3×10^{-3} $(\mathrm{GeV/c})^2$. We limit our detectors to being 5 mm away from the beam center. If it should be required to increase this distance to 1 cm the experiment could still be done with somewhat reduced precision (see below).

---

2. FNAL Experiment E69 - Small Angle Scattering of $\pi^{\pm}$, $K^{\pm}$, $p^{\pm}$.

The experimental method consists of measuring the position of both scattered protons in order to provide an elastic constraint and using time-of-flight between the two scattered particle detectors to limit events to those originating in the crossing region. This method, its accuracy, and various detector schemes are discussed in detail below. We also discuss how the full range of s can be covered in the standard insertion by using asymmetric beam energies.

Standard Insertion with No Modifications

Using the formulas given in Appendix I of the note it is apparent that the experiment cannot be done without some modifications of the β functions. For the standard insertion, $\beta_v^* = 4$ m, $\beta_h^* = 20$ m so that the uncertainty in $p_\perp$ due to the beam spread is $\Delta p_\perp^{rms} = 13.7$ MeV/c at 200 GeV/c beam momentum. Even if we were to work within 5 mm of the beam centers, the minimum detectable t is $\simeq 0.01$ $(\mathrm{GeV/c})^2$. The values of β_{dv} and β_{dh} are obtained from Fig. 2.

Modification of the Standard Insertion - Retuning Q1 and Q2

Clearly as the values of β_v^* and β_h^* are increased, this experiment becomes easier. However, if one increases the beta functions at the crossing, the tune shift increases and at some point the beam currents must be decreased to keep $\Delta\nu \leqslant 5 \times 10^{-3}$. Any large decrease in the currents is not desirable since other intersection regions lose luminosity (which might be a dear commodity in the early days). Changing the crossing angle to restore the tune shift is not recommended in the early phase of ISA operation.

As a working value we have chosen[3] $\beta_v^* = 69.3$ m, $\beta_h^* = 61.7$ m. Figure 3 depicts the beta function throughout the insertion for this solution. The maximum betatron phase advance in the region

3. Detailed calculations of beam dynamics and matching from the insertion to the regular lattice were done by M. Month.

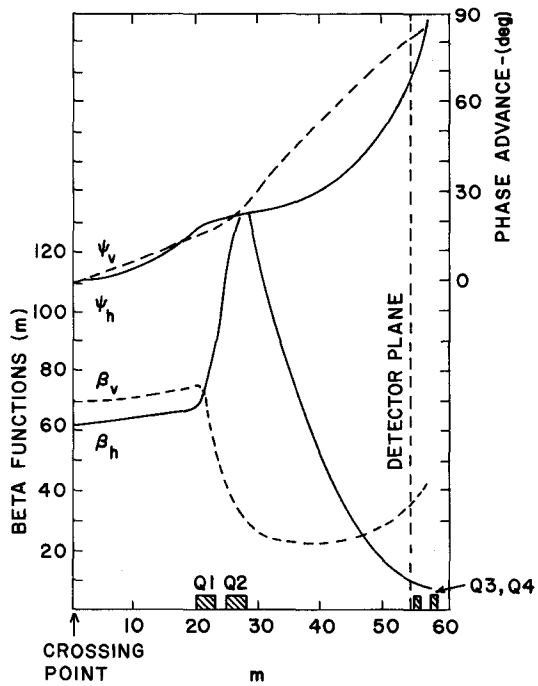

Fig. 3. Beta-functions and phase advance for the small angle scattering experiment.

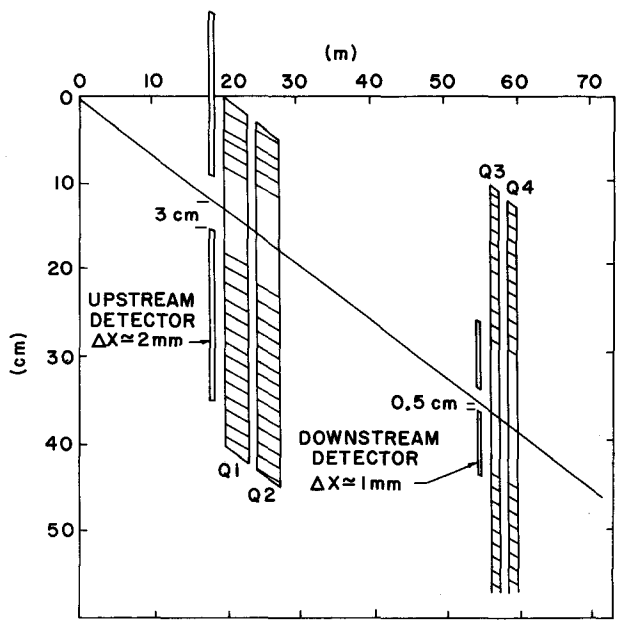

Fig. 4. Positions of the upstream and downstream detectors.

between Q2 and Q3 is 70.92 degrees in the horizontal and 82.40 degrees in the vertical at a point 55 m from the crossing point. This then is the detector position, which is 1 m away from Q3. The resulting beta functions at the detector and a summary of the properties of this solution are given in Table I. The rms uncertainty in $p_\perp$ due to beam divergence is 4.38 MeV/c. In addition, there is a contribution to $\Delta p_\perp$ from the angular measurement at the detector. Since the betatron phase advance is not quite 90°, one must "measure" an angle as well as a position to determine the scattering angle. If the detector consists of sensitive elements 1 mm wide (i.e. hodoscopes - see below) then two such hodoscopes separated by 10 m would contribute $\Delta p_\perp$ = 5 MeV/c due to the combined position and angle measurement (the error is almost split between position and angle). A superior approach from the point of view of cost, alignment and simplicity is to measure only a position and determine the angle from this position and the rms beam size at the crossing. For the values of the beta functions used here, the beam size at the crossing is $\simeq$ 1 mm $\times$ 1 mm rms and the resulting contribution to the error in $p_\perp$ due to measurement and beam size is 3.36 MeV/c. Thus we have $\Delta p_\perp^{rms}$ + 5.52 MeV/c from all sources. This approach is discussed in some detail in Appendix II.

We wish to point out the dangers of pushing this approach to the extreme and attempting to work with beta functions of several hundred meters at the crossing. First, for a fixed crossing angle the beam current must be reduced as $\sqrt{\beta}$ to keep the tune shift less than 5×10^{-3}. This of course affects other insertions in a potentially undesirable way. A more serious constraint is imposed by the machine itself. The larger the value of β at the crossing, the smaller advance in betatron phase in the length of insertion provided. Possibly, very high gradient quadrupoles for Q1 and Q2 might help alleviate this. Since for larger values of β at the crossing, the phase advance is further from 90° at the detector, the angle at the detector must be measured with higher precision. For larger beta functions at the crossing, the rms beam size at

TABLE I

SUMMARY OF MODIFIED STANDARD INSERTION - 200 GeV/c

Q_1 at 20 m as in Standard Insertion

$\Psi_h = 70.92^o$ $\psi_v = 82.40^o$ phase advance at detector

Detector at 55 m from crossing (Q_3 at 56 m)

$\beta_v^* = 69.256$ m $\beta_{dv} = 36.469$ m

$\beta_h^* = 61.693$ m $\beta_{dh} = 9.981$ m

$\Delta p_\perp^{rms}$ (beam) = 4.38 MeV/c

$\Delta p_\perp^{rms}$ (detector) = 3.36 MeV/c Measure position, no angle, use spot size at crossing.

$\Delta p_\perp^{rms}$ (all sources) = 5.52 MeV/c

$t_{min} = 3.3 \times 10^{-3}$ for all $\emptyset$, detector at 5 mm from beam center

$t_{min} = 3.2 \times 10^{-3}$ in horizontal plane, detector at 1 cm from beam center

Beam size at detector $\sigma^v = 0.40$ mm
$\sigma^h = 0.76$ mm

$I = 7$ A $\Delta\nu = 5 \times 10^{-3}$

$L/L_o = 0.118$

$L_o = 10^{29}$ cm^{-2}sec^{-1} → 60 events/sec all $\emptyset$

Dump profile: horizontal at detector: 0.8 cm
vertical at detector : 1.6 cm

the crossing is also larger, so the angle at the detector must be measured directly. It soon becomes evident, however, that the lever arm available puts a severe constraint on the resolution and alignment of the detectors. We have not completely optimized our solution for the beam dynamics, but we feel that values of β at crossing between 50 - 70 m are the best compromise between limiting beam divergence and the required accuracy of the angular measurement.

The range of t covered by the detector is limited on the high side by the 8 cm aperture of Q2 at 27 m from the crossing point. This corresponds to $t_{max} = 0.09\ (GeV/c)^2$ at 200 GeV. The minimum t is determined by how close to the beam center one can work (see Appendix I). With detectors at 5 mm from the beam center a minimum t of $t_{min} = 3.3 \times 10^{-3}\ (GeV/c)^2$ can be achieved for all azimuthal angles. If, however, we are limited to a distance of 1 cm, scatters in the horizontal plane can be detected down to $t = 3.2 \times 10^{-3}$ $(GeV/c)^2$ even though in the vertical $t_{min} = 13.2 \times 10^{-3}\ (GeV/c)^2$. Thus, if one is forced to go to relatively larger distances from the beam centers, there is a loss of useful azimuth. Should a value of $t_{min} \geq 5 \times 10^{-3}$ be the smallest t one can reach, the experiment can still be done, although with less sensitivity to ρ (see below).

We note here that Amaldi's experience in working close to the beam at the ISR is quite encouraging. He is working within 1 cm of the beam center with a beam size of 3 - 4 mm. At ISABELLE the values of β at the detector give an rms beam size of 0.40 mm X 0.76 mm and we hope to work at a distance of 5 mm, which is several beam widths further away than Amaldi's detectors. Amaldi finds singles rates of 10^4 - $10^5/cm^2$ in counters located 3 - 4 beam widths from beam center with a beam current equivalent to 10^{19} particle traversals per second.[4]

The chosen values of β^* result in a tune shift of $\Delta\nu = 7 \times 10^{-3}$ for 10 A of current, thus forcing a modest decrease in current

---

4. C. Rubbia, private communication.

to 7 A with a resulting tune shift of $\Delta\nu = 5 \times 10^{-3}$. If both beam currents are kept equal, the decrease in luminosity in this insertion is $L/L_o = 0.118$. If the value of L_o is the maximum predicted for the standard insertion ($L_o = 2.6 \times 10^{32}$ cm^{-2} sec^{-1}) the resulting luminosity is $L = 3.1 \times 10^{31}$ cm^{-2}sec^{-1}. For the early phase of ISA operation, a value of $L_o = 10^{29}$ cm^{-2}sec^{-1} may be more realistic. This results in a value of $L = 1.18 \times 10^{28}$ in this modified insertion.

With detectors placed at 55 m from the crossing point, the maximum value of t is determined by the aperture (8 cm) of Q2. In order to calculate event rates, we assume that events between $t_{min} = 2.5 \times 10^{-3}$ (GeV/c)^2 and $t_{max} = 0.09$ (GeV/c)^2 are detected. Assuming a total elastic cross section of 8 mb this gives about 5 mb of detected elastic cross section or 60 events/sec with $L = 1.2 \times 10^{28}$ cm^{-2}sec^{-1}. Even if we assume that the total acceptance is only 10% (solid angle loss, deadtime, packing fraction of detectors, etc.) one would still be able to collect 10^6 events in 40 hours of running. As will be shown below, this is more than an adequate sample to measure ρ to several per cent at one value of s. We summarize the parameters of the modified insertion in Table I.

Covering the Full Range of s

It is clearly desirable to determine the behavior of the real part of the nuclear elastic scattering amplitude over the full range of s covered by the ISA. In particular, it is important to be able to check one's experiment by making a measurement at s = 3600 GeV^2 which can be compared to the ISR experiments.

As the momentum of the ISA beams is decreased, the maximum t (t_{max}), which can be reached by the method described above, decreases. The limiting aperture of Q2 corresponds to $t_{max} = 2.3 \times 10^{-3}$ (GeV/c)^2 at 30 GeV/c. The minimum t (t_{min}), which can be

reached, decreases linearly with decreasing momentum:[5]

$$t_{min} \simeq kp^2 \sigma^2 = kp^2 \beta\epsilon \propto kp \beta$$

where:

k = a constant

p = the beam momentum

σ = the rms beam size at the detector

β = the beta function at the detector

ϵ = the beam emittance $(31.4/\gamma) \times 10^{-7}$ rad-meters.

Thus, for a 30 GeV/c beam, one can cover only the t range $4.5 \times 10^{-4} < t < 2.3 \times 10^{-3}$ $(GeV/c)^2$ by placing a detector downstream of Q2. A detector placed upstream of Q1 (20 m from the crossing point), however, will be able to cover a much wider range of t at 30 GeV/c. If one places the detector within 3 cm of the beam, then the coverage in t will overlap with that of the detector downstream of Q2 (Fig. 4). At 30 GeV/c the beam size just upstream of Q1 for the modified standard insertion is < 3 mm, so there should be no difficulty in working at a radius of 3 cm.

The situation is illustrated in Fig. 5 where the t region covered is shown as a function of beam momentum over the full ISA range. The lower right hand region is covered by a detector downstream of Q2; the upper left hand region is covered by a detector upstream of Q1. The t_{max} for the upstream detector is limited only by the size of the detector, but for measuring the Coulomb-nuclear interference, there is no need to measure events beyond $t \simeq 0.1$ $(GeV/c)^2$. We discuss the resolution of measurements upstream of Q1 below, considering explicitly the case of a 30 GeV/c beam with the same β functions used at 200 GeV/c.

At 30 GeV/c, the t_{min} of a detector placed 3 cm from the beam center and 20 m from the crossing region is 2.03×10^{-3} $(GeV/c)^2$. For a t_{max} of 0.1 $(GeV/c)^2$, the outer radius of the detector would

5. Many useful formulas can be found in "Formulas and Comments Concerning the Yellow Book Experimental Insertion Designs", J. Sandweiss, unpublished.

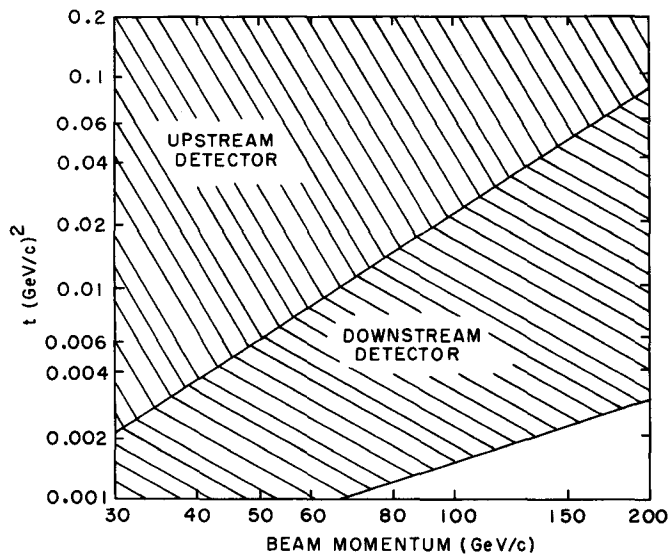

Fig. 5. Region in t covered by the upstream and downstream detectors as a function of beam momentum.

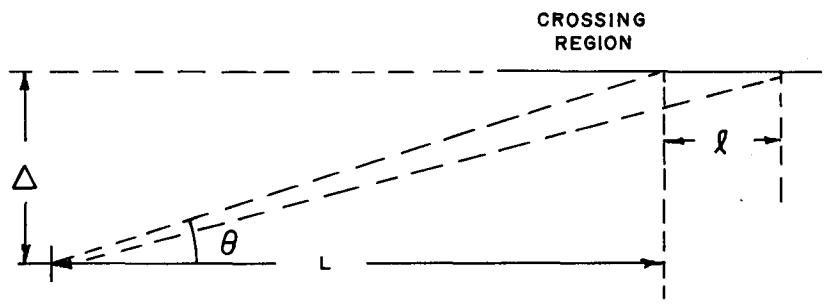

Fig. 6. Illustration of the error introduced in the measurement of the scattering angle due to the finite length of the crossing region.

have to be 21 cm (10.5 mrad). This is approximately the separation of the beam pipes at 20 m from the crossing, so one should be able to cover nearly the full azimuth. To achieve $\Delta p_\perp < 6$ MeV/c at 30 GeV/c, one must be able to measure the angle of the scattered proton to $\simeq 0.2$ mrad. This implies using a detector with resolution better than 4 mm. If one wishes to measure only a position, and not an angle, one must consider the error introduced by the finite beam size. At 30 GeV/c, for the beta functions given above, the beam size at the crossing region is:

$$\sigma_h = \sqrt{\beta_h \epsilon} = 2.5 \text{ mm}$$

$$\sigma_v = 2.7 \text{ mm}$$

In the vertical:

$$\Delta p_\perp = (2.7 \text{ mm} \times 30000 \text{ MeV/c})/20000 \text{ mm} = 4.04 \text{ MeV/c}.$$

One must also consider the error in angle due to the finite length of the crossing region. If one measures a displacement Δ at a distance L from the crossing region (Fig. 6), the scattering angle is $\theta = \Delta/L$. If the scatter really occurred at $L + \ell$, then $\theta = \Delta/L + \ell$, and the error in θ is:

$$d\theta = d\ell/(L + \ell).$$

At 30 GeV/c, the length of the crossing region for the modified standard insertion is $\simeq 1$ m, so $d\theta = 0.5$ mrad for $\theta = 10$ mrad and $\Delta p_\perp = 15$ MeV/c. If , however, one does a time-of-flight measurement between the two scattered protons, one should be able to localize the position of the scattering vertex along the beam direction to better than 30 cm (1 nsec $\simeq$ 30 cm). This means that the error in $p_\perp$ from this source will be less than 5 MeV/c in the worst case ($\theta = 10$ mrad). Since fraction of a nanosecond timing is achieved with today's electronics, we believe that it should be possible to reduce the error from this source to a negligible level.

One must also consider the contribution to the error in scattering angle from the uncertainty in the original beam direction.

At 30 GeV/c one has: (See Appendix I)

$$\Delta p_{\perp}^{rms} = 1.77 \sqrt{30(61.7 + 69.3)} = 1.7 \text{ MeV/c}$$

Thus, the error due to beam divergence is quite small. One can also build a detector with sufficiently small elements (compared to the 4 mm which is required) so that the contribution to measuring error from detector resolution is negligible.

Thus, we conclude that it is possible to have a detector upstream of Q1 which has acceptance and resolution for a 30 GeV/c beam comparable to the acceptance and resolution of the downstream detector for a 200 GeV/c beam. For beam momenta between 30 and 200 GeV/c, part of the t range will be covered by the upstream detector, and part will be covered by the downstream detector. Over the full ISA energy range, the combination of the two detectors will cover the range $0.003 < t < 0.1$ $(\text{GeV/c})^2$.

A point of concern here is the systematic errors which might be introduced by using two detectors to cover the t range. This problem can be studied, or even avoided entirely, by using asymmetric beam energies. Figure 7 shows lines of constant s as a function of the two beam momenta (p_1 and p_2). By keeping one beam momentum fixed at 200 GeV/c and varying the other beam momentum from 30 GeV/c to 200 GeV/c, one can cover the range $24000 < s < 160000$ GeV^2. One can use the downstream detector in the 200 GeV/c beam to measure the scattering angle, and both detectors in the other beam ($p_2 \neq 200$ GeV/c) merely to provide the elastic constraint. Thus, the resolution in $p_{\perp}$ will be identical for all measurements in the range $24000 < s < 160000$ GeV^2. To cover the range $3600 < s < 24000$ GeV^2, one can keep one beam momentum fixed at 30 GeV/c and vary the other beam momentum from 30 GeV/c to 200 GeV/c. One can use the upstream detector in the 30 GeV/c beam to measure the scattering angle and both detectors in the other beam to provide the elastic constraint. The upstream and downstream detectors can be cross checked by running at 30 + 200 GeV/c. This procedure involves extensive running with unequal beam energies. If this should not be

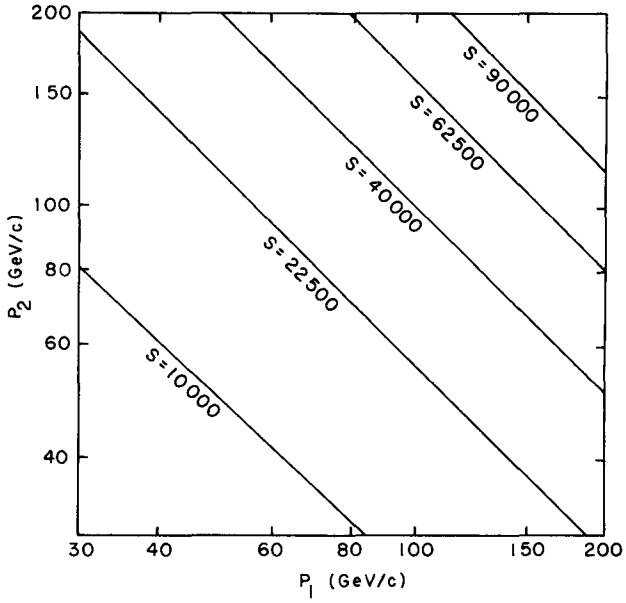

Fig. 7. Lines of constant s (c.m. energy squared) as a function of the momenta of the two ISA beams (P_1 and P_2).

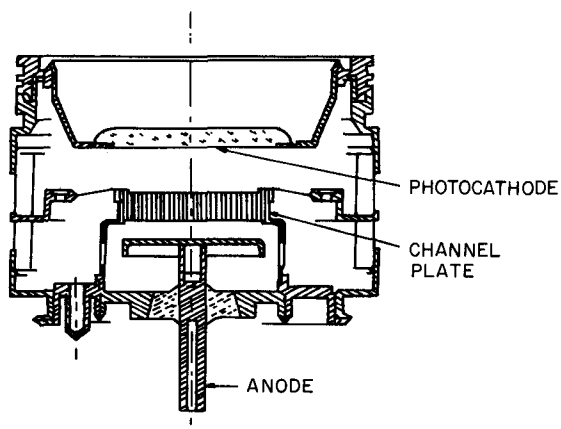

Fig. 8. Single anode phototube using channel plate multiplier with curved channels developed by L.E.P. This tube has operated with gains $> 2 \times 10^6$.

desirable due to compatibility with other experiments, one can probably take most of the data with equal beam energies and take a few runs with unequal energies to study the systematics and check the resolution of the detectors. We emphasize the importance of some running with unequal energies.

Detectors

The requirements for the upstream and downstream detectors are summarized below.

	Upstream Detector	Downstream Detector
Element size	$\simeq$ 2 mm	$\simeq$ 1 mm
Azimuthal range	$\simeq 2\pi$	$\simeq 2\pi$
Radial size	3 cm to 10 cm	0.5 cm to 4 cm
Rate capability	10^5 - $10^6/cm^2$-sec	10^5 - $10^6/cm^2$-sec
Time resolution	$\leqslant$ 1 ns for T.O.F.	$\simeq$ 1 ns for T.O.F.

A number of possibilities are available. Drift chambers can provide very high spatial resolution, but might have some problems with the rates encountered in working close to the beam. A drift chamber would have to be backed with a scintillator to provide the time resolution required for the time of flight measurement. The flexibility one has in configuring the drift region would be useful in developing a chamber that could be used with a "Roman pot" or similar bellows arrangement that would be necessary to get within 0.5 cm of the beam center.

Small PWC's can certainly provide the required spatial resolution and can handle higher rates than drift chambers. In the worst case, however, the wires nearest the beam may still be saturated. One may also have difficulty constructing a chamber of suitable shape for use with a Roman pot. A PWC would also have to be backed with a scintillation counter in order to have adequate time resolution for the T.O.F. measurement.

Scintillation counter hodoscopes can be built with adequate resolution ($\simeq$ 1 - 2 mm elements) and would have no problem in handling high rates. Such hodoscopes can also be tailored to fit Roman pots, and, of course, have good time resolution. The usual problem with such detectors is the packing problem for the large number of phototubes required. The cost of the phototubes is also a consideration for systems with large numbers of elements. A new type of phototube under development at a number of companies offers the possibility of avoiding these problems. The multiplication element is a flat, porous plate with each pore being a channel multiplier. The channel diameter is typically 10 - 40 μm with 2 μm walls between the channels. Gains as high as 10^7 have been achieved by using two plates with the channels in a "chevron" array, or a single plate with curved channels. The multiplier plate is placed in close proximity to a photocathode to make a photomultiplier (Fig. 8). Electrons emitted at the photocathode are accelerated toward the plate and multiply in the channels. An anode placed near the plate on the output side collects the burst of electrons to provide the output signal. The planar geometry of the tube and the high spatial resolution of the channel plate allow the image of photons striking the photocathode to be amplified and transmitted to the anode with excellent resolution. A segmented anode may be used to gain positional information about the light striking the photocathode.[6]

L.E.P. has developed a single anode tube and a 25 anode tube (5 $\times$ 5 square array) using channel multiplier plates. This company also has plans to build a 100 anode tube (10 $\times$ 10 square array).

---

6. The following are some companies which are involved in developing phototubes and image intensifiers using channel plate multipliers: Amperex Electronics Corp., Electro Optical Devices Division, Slatersville, R.I.; Galileo Electro-Optics Corp., Sturbridge, MA.; Laboratoirés d'Electronique et de Physique Appliquee, Paris, France; Varian / LSE, Palo Alto, CA.

Tubes of this type are ideal for hodoscopes since a single tube can accommodate all the elements in the hodoscope. The tubes developed at R.T.C. have time resolution which is far superior to standard phototubes. The total transit time is less than 2 ns and the output signal has a rise time less than 100 ps. The use of these tubes in an ISA experiment would allow one to make very precise time of flight measurements.

The gain of the channel plate is less than that of the dynode chain of a standard phototube. The signal size, however, is comparable to signals from proportional chambers, and vast experience exists in handling signals of this size from systems with large numbers of elements.

The flexibility in specifying the anode configuration allows a number of hodoscope configurations to be used. An obvious configuration for this experiment would be strips of scintillator covering the radial and azimuthal bites (Fig. 9a). If one uses a Roman pot, however, getting the light guides to the inner radial strips may be a problem. Figure 9b shows an alternate configuration which should be easy to construct and tailor to almost any bellows arrangement used. The channel multiplier phototube can now be connected to the scintillators at the outer edge. The disadvantage of this scheme is that each element now has a larger surface area and, therefore, is subject to a higher particle flux. Since one is using scintillator and very fast channel multiplier tubes, however, this should pose no problem. The azimuthal detectors can be strips of scintillator covering appropriate sections of azimuth (Fig. 9c).

We present below a cost estimate for the detectors needed for this experiment. At this early stage in the development of the channel multiplier phototubes, accurate cost estimates are not possible. It appears that one can obtain a tube with more than 100 outputs for $10 K - $30 K. If any of the companies involved in developing these tubes should begin to manufacture them on a

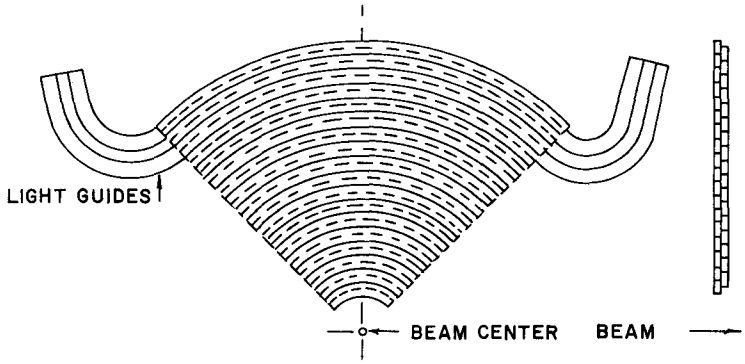

Fig. 9a. A possible configuration for the hodoscope to measure the radial position of the scattered proton. The detector consists of annular strips of scintillator. Only a few of the light guides are shown.

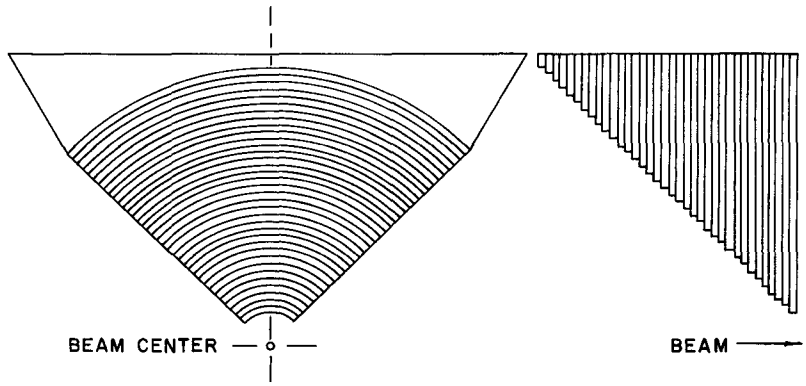

Fig. 9b. Alternate configuration for a hodoscope to measure the radial position of the scattered protons. Phototube views scintillators from the edge away from the beam.

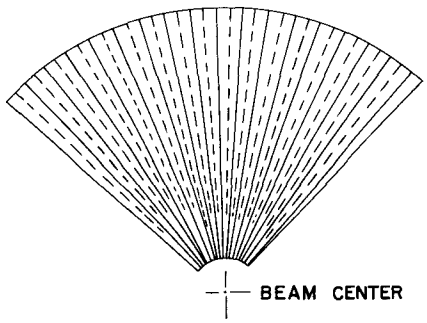

Fig. 9c. Hodoscope to measure the azimuthal angle of the scattered protons. Phototube views the scintillator from the outer edges.

production basis, the cost would, of course, be greatly reduced.

The upstream and downstream detectors would each need about 35 radial elements. Since it is impractical to have a single strip completely surrounding the vacuum chamber, we assume the detector would be segmented into 4 azimuthal sections. This gives 140 elements for the azimuthal measurement which gives 280 elements for a full detector. We assume that the 70 elements comprising a segment of ¼ of a detector (35 radial elements and 35 azimuthal elements) can be put onto one multianode channel multiplier tube. This means one needs 4 such tubes for each detector. We also assume that one will have 4 detectors (one upstream and one downstream in each of the beams). The cost of the readout electronics is estimated from a proportional chamber system we are currently using.

Estimated Cost of Detector

Number of elements per detector:	140 radial
	140 azimuthal
	280 total
Number of detectors:	4
Total number of elements:	1120
Total number of multianode tubes (4 per detector):	16
Cost:	
Purchase and assembly of hodoscopes:	$ 30 K
Multianode tubes:	160 K
Readout electronics:	70 K
Total	$260 K

Resolution and Errors

The error in measuring ρ from Coulomb-nuclear interference comes from several sources: resolution in t; normalization; uncertainties in σ_T and the nuclear slope; statistical error.

Ekelöf[7] of CERN has recently published a study of the error in determining ρ for π^+-p elastic scattering. The precision quoted below comes from his paper after the use of various scaling factors to relate his parameters (for π^+-p) to those appropriate for p-p elastic scattering at ISABELLE. Specifically, we have scaled t_{min} by the ratio of π^+-p to p-p total cross sections (the larger σ_T, the lower the value of t where the interference is maximal).

The error in the normalization comes from the assumption that the luminosity can be determined to 2% and from a 2.8% uncertainty in normalization due to the uncertainty in calculating the t bite of the experiment.[8] The error in normalization is then $\Delta K = 3.5\%$. We also assume a 2% error in σ_T ($\Delta\sigma_T \simeq 1$ mb) and a knowledge of the nuclear slope, b, to 0.5 $(\mathrm{GeV/c})^{-2}$. Figure 10 shows the error in ρ for $\Delta b = 0.5\ (\mathrm{GeV/c})^{-2}$, $\Delta\sigma_T \simeq 2\%$ (i.e. 0.5 mb for π^+-p) for $t_{min} = 0.002\ (\mathrm{GeV/c})^2$ and $t_{max} = 0.02\ (\mathrm{GeV/c})^2$. Table II is derived from Ekelöf's paper. Using this figure and table, we conclude that $\Delta\rho = 0.025$ if 10^6 events are accumulated. As mentioned above, this corresponds to about 40 hours of running. If other values of t_{min} are dictated by beam clearance, the corresponding $\Delta\rho$ can be obtained from Table II.

Backgrounds

We have considered two sources of background, first, the contamination of the elastic signal due to $p\pi^0$ decays of diffractively produced nucleon resonances, and second, particle fluxes through the detectors due to beam-beam and beam-gas collisions.

The excellent resolution in $p_\perp$ ($\Delta p_\perp \leq 6$ MeV/c) provides an elastic constraint which strongly biases against false events from resonance production. The fraction of resonance decays with a

---

7. T. Ekelöf, CERN, submitted to Nuclear Physics.
8. A discussion of luminosity measurement is included in J. Marx, BNL Informal Rept., CRISP 74-3 (1974).

TABLE II

$\Delta\rho \times 10^{-2}$ for Various t_{min} and t_{max}

For 1% Normalization, $\geq 10^6$ events

$p+p \rightarrow p+p$

$\lvert t\rvert_{min} \times 10^{-3}$	0.25	0.50	1.0	1.5	2.0	2.5	3.5	5.0	7.0	10.0	15.0	25.0
$\lvert t\rvert_{max} \times 10^{-3}$												
100.0	0.88	0.89	0.91	1.03	1.22	1.43	1.94	2.87	4.37	7.18	12.82	23.63
50.0	0.99	1.02	1.07	1.25	1.51	1.82	2.53	3.76	5.53	8.40	15.33	
30.0	1.01	1.05	1.11	1.30	1.57	1.88	2.61	3.92	6.36	12.81		
20.0	1.03	1.07	1.13	1.34	1.66	2.05	3.06	5.37	10.23			
14.0	1.11	1.16	1.25	1.54	2.00	2.60	4.31	7.83				
10.0	1.27	1.31	1.46	1.92	2.63	3.56	5.73					
7.0	1.49	1.53	1.80	2.50	3.44	4.36						
5.0	1.71	1.75	2.14	2.91	3.65							
4.0	1.82	1.86	2.28	2.94								
3.0	1.88	1.92	2.31									
2.0	1.90	1.94										
1.0	2.42											

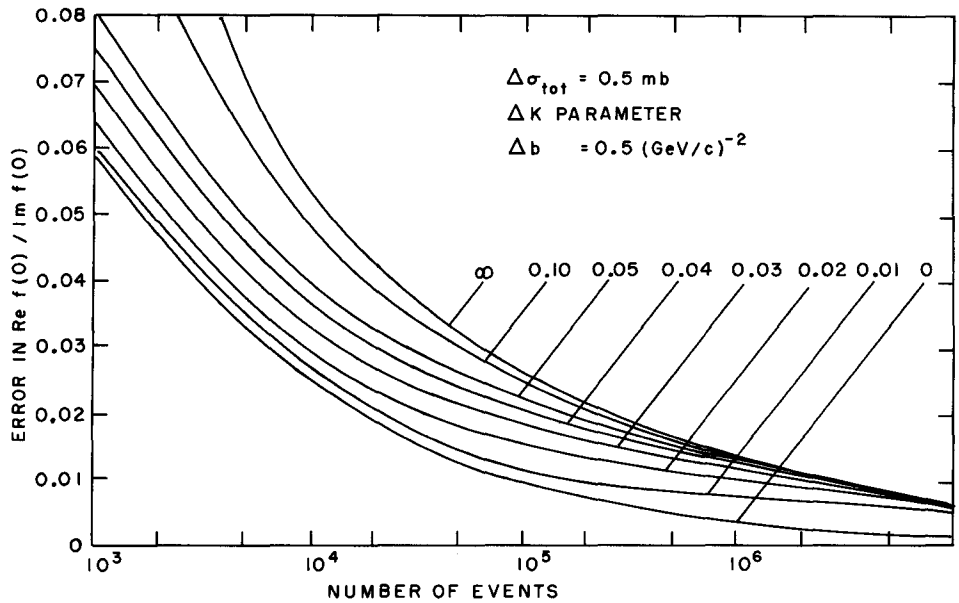

Fig. 10. Error in ρ as a function of the number of events for various errors in overall normalization (ΔK), and for t_{min} = 0.002 $(GeV/c)^2$ and t_{max} = 0.02 $(GeV/c)^2$. From Ref. 5.

$p_\perp$ imbalance compared to elastic scattering (when only the decay proton is observed) less than $< p_\perp >$ is

$$F = 1 - \frac{\sqrt{p_{cm}^2 - < p_\perp >^2}}{p_{cm}}$$

where p_{cm} is the momentum of the decay proton in the N^* center of mass. For safety we take $< p_\perp > = 36$ MeV/c, or six times the rms sensitivity. For the $N^*(1400)$, $p_{cm} = 365$ MeV/c, thus $F[N^*(1400)] = 4.9 \times 10^{-3}$. Furthermore, the N^* production cross section is considerably less than the elastic cross section and the slope is steeper. These factors result in a suppression of the $N^*(1400)$ background to $\leqslant 10^{-4}$ of the elastic signal. If further suppression should prove necessary, lead-scintillator π^o vetoes could be employed. The contamination by higher mass diffractive nucleon resonances is suppressed even further because of their larger p_{cm}. We conclude that the excellent resolution in $p_\perp$ results in an essentially pure elastic signal.

The total particle fluxes through the detectors bears on the question of deadtime and accidentals. The ISR experience of Amaldi gives rates through a small t detector of 10^4 - 10^5/cm^2-sec. We have calculated the flux due to beam-beam interactions. Such rates are $\sim 3 \times 10^6$/cm^2-sec for a luminosity of 10^{32} cm^{-2}sec^{-1}. Thus for the modified insertion at full luminosity, the flux is $\sim 3 \times 10^5$/cm^2-sec, and for the initial phase low luminosity ($L \sim 2 \times 10^{28}$ cm^{-2}sec^{-1}), which gives 10^6 events in 40 hours, the beam-beam flux is 600/cm^2-sec.

The flux of particles due to beam-gas collisions was calculated assuming a pressure of 10^{-11} Torr of hydrogen gas with 100 m of gas contributing. The resulting flux is 1.6×10^4/sec through the detector for 10 A of current.

The detector hodoscope elements subtend areas of ~ 1 cm^2 so that the expected singles rates per channel should be comparable

to the ISR experience. The 1 ns time resolution of the system results in these rates being of little concern.

Other Options

Were any of the purely hadronic options ($\bar{p}p$, pd, $\bar{p}d$, dd) implemented, one could proceed identically as with pp to measure ρ for the appropriate combinations of $\bar{p}$, p and n scattering. The luminosity is adequate. The ep option is of no relevance for very small t measurement unless one wants to search for fuzz on the proton.

Conclusions

We have shown that a measurement of the ratio of real to imaginary part of the forward nuclear scattering amplitude (ρ) can be done to 2 - 3% accuracy in the first phase of ISA operations. For a 200 GeV beam, the rms uncertainty in $p_\perp$ is $\Delta p_\perp \sim 6$ MeV/c with a t bite from 3×10^{-3} to 0.09 $(\mathrm{GeV/c})^2$. The measurement is done in the standard insertion with retuned quadrupoles to give values of $\beta \sim 60$ - 70 m at the crossing point. We point out the value of working at the point where the betatron phase is nearest 90° and the accompanying difficulties associated with very large values of β (> 100 m) at the crossing point.

The detector consists of 1 mm scintillators mounted as a radial hodoscope with azimuthal scintillator strips to determine ϕ. One would detect both scattered protons to give an elastic constraint. At 200 GeV beam energy we would hope to place detectors within 5 mm of the beam center even though the measurement could be done if 1 cm were the minimum working distance. The detector for 200 GeV is placed 1 m upstream of Q3.

We have also considered how to measure ρ below the highest value of s. For $24\,000 < s < 160\,000$ GeV^2, we would maintain one

beam at 200 GeV and reduce the energy in the other beam to reduce s. The detector in the 200 GeV beam would determine the scattering angle while the detector in the lower energy beam would provide the elastic constraint. For $3600 < s < 24\ 000\ \mathrm{GeV}^2$, both beams must be below 200 GeV. We discuss a detector of the sort described above which would operate at 30 GeV beam energy at the upstream end of Q1 covering the same t range with the same $\Delta p_\perp$. By placing two detectors, one of each kind (they differ only in distance from the beam center, size and distance from the crossing point) in each beam, the full range of s of ISABELLE can be covered. We emphasize the importance of running the machine with unequal energies to give the most precise coverage of the full range of s with a minimal change of systematic effects with changing s.

APPENDIX I

Useful Formulas

The rms emittance for a beam of energy E is $\mathcal{E} = 31.4/E(\text{GeV}) \times 10^{-7}$ rad-m. If β_v^* and β_h^* are the vertical and horizontal β functions at crossing measured in meters, the rms uncertainty in the scattering angle due to the angular divergence of the beam is

$$\Delta p_\perp^{rms} = 1.77 \sqrt{E(\text{GeV}) \left(\frac{1}{\beta_v^*} + \frac{1}{\beta_h^*}\right)} \quad \text{MeV/c}$$

The corresponding fractional resolution in t is $\Delta t/t = 2\Delta p_\perp/\sqrt{t}$. For a given t, the distance from the beam center to the point where the scatter must be detected when $\Psi = 90^\circ$ is:

$$X_{scat} = \sqrt{\frac{t}{2E^2} \beta^* \beta_d} \quad \text{meters} - \text{projection in vertical or horizontal.}$$

The beam size is:

$$\sigma_v^{rms} = \sqrt{\epsilon \beta_{dv}} \text{ meters}$$
$$\sigma_h^{rms} = \sqrt{\epsilon \beta_{dh}} \text{ meters}$$

where β_d is the beta function where the size is of interest. The tune shift for a fixed crossing angle is $\Delta\nu \propto \sqrt{\beta_v^*}$.

APPENDIX II

The effect of $\Psi \neq 90^{o}$

The transfer matrix from the crossing point to the detector results in the following relationship between scattering angle (θ_{sc}), measured angle (θ_d), and position (X_d) at the detector, and the advance of the betatron phase (Ψ) from crossing to the detector. The relationship holds for projections in either vertical or horizontal planes

$$\theta_{sc} = (\cos \Psi)\theta_d + \frac{\sin \Psi}{\sqrt{\beta^* \beta_d}} X_d$$

where β^* and β_d are the values of the beta functions at the crossing and at the detector respectively.

Using the parameters for the modified standard insertion given in Table I, we find

Vertical: $\theta_{sc} = 0.132\ \theta_d + 0.0197\ X_d$ (m)

Horizontal: $\theta_{sc} = 0.327\ \theta_d + 0.038\ X_d$ (m)

The coefficients of θ_d represent the extent to which $\Psi \neq 90^{o}$. If we choose to measure θ_d with two identical detectors separated by L meters with a resolution in position of ΔX_d then

$$\Delta\theta_d = \sqrt{2}\ \frac{\Delta X_d}{L}$$

so that:

Vertical:

$$\Delta\theta_{sc} = \left(\frac{0.187}{L} + 0.0197\right) \Delta X_d \qquad \Delta P_\perp^{(MeV/c)} = \left[\frac{37.4}{L(m)} + 3.94\right] \Delta X_d(mm)$$

Horizontal:

$$\Delta\theta_{sc} = \left(\frac{0.462}{L} + 0.038\right) \Delta X_d \qquad \Delta P_\perp^{(MeV/c)} = \left[\frac{92.4}{L(m)} + 7.80\right] \Delta X_d(mm)$$

With 1 mm hodoscopes, $\Delta X_d = \frac{1}{\sqrt{12}}$ mm so that

Vertical: $$\Delta P_\perp^{(MeV/c)} = \left[\frac{11.0}{L(m)} + 1.1\right]$$

Horizontal: $$\Delta P_\perp^{(MeV/c)} = \left[\frac{26.7}{L(m)} + 2.2\right]$$

Lever arms of $\simeq$ 10m are required to achieve $\Delta P_\perp < 6$ MeV/c.

A more attractive solution to measuring θ_d is to use a single position sensitive detector, and the rms beam size to determine the angle. The transfer matrix gives

$$\theta_d = \frac{X_*}{\sin \Psi \sqrt{\beta^* \beta_d}} + \frac{\cos \Psi \, X_d}{\sin \Psi \sqrt{\beta^* \beta_d}}$$

where X_* is the transverse interaction coordinate at the crossing

region.

Using the parameters from Table I the rms uncertainty in θ_d is:

Vertical: $$\Delta\theta_d = \left\{\left[\frac{\Delta X_* \text{ (m)}}{49.8}\right] + \left[\frac{\Delta X_d}{377}\right]\right\}^{\frac{1}{2}}$$

Horizontal: $$\Delta\theta_d = \left[\left(\frac{\Delta X_*}{23.3}\right) + \left(\frac{\Delta X_d}{71.4}\right)\right]^{\frac{1}{2}}$$

where $\Delta X_d = \frac{10^{-3}}{\sqrt{12}}$ m for 1 mm hodoscopes and ΔX_* is the rms beam size at the crossing region.

$$\Delta X_* = \sqrt{\epsilon\beta^*} \qquad \epsilon = \text{emittance} = \frac{31.4}{E} \times 10^{-7} \text{ m-rad.}$$

Thus at 200 GeV in the modified standard insertion:

$\Delta X_* = 1.04$ mm vertical

$\Delta X_* = 0.98$ horizontal.

Thus, θ_d is determined to an accuracy of

Vertical: $\Delta\theta_d = 20.8$ μrad

Horizontal: $\Delta\theta_d = 41.9$ μrad

This then yields an error in θ_{sc} of

Vertical: $\Delta\theta_{sc} = 9.45\ \mu rad$ or $\Delta P_{\perp} = 1.7$ MeV/c

Horizontal: $\Delta\theta_{sc} = 14.7\ \mu rad$ or $\Delta P_{\perp} = 2.9$ MeV/c

At 200 GeV/c we need only measure positions and then rely on the beam size at the crossing for angular determinations. The crucial point is that with the modified standard insertion, the betatron phase advance is so close to 90° that the angular measurement need not be made with undue precision. If Ψ were further from 90° the requirements on the angular precision would be correspondingly more severe.

ELASTIC SCATTERING AND DIFFRACTION DISSOCIATION IN THE ANGULAR RANGE 1 - 50 mrad

R. M. Edelstein
Carnegie-Mellon University
M. Zeller
Yale University

The goal of this study was to design a set of apparatus primarily to measure several related diffractive processes:

1) Elastic scattering at small and intermediate $|t|$.
2) Total cross sections through the optical theorem.
3) Diffractive and other low multiplicity systems near $x = 1$.

The apparatus is to be deployed in three upwards-compatible stages, the first of which is capable of running at turn-on of ISABELLE.

Stage 1 - Elastic Scattering by Colinear Angle-Angle Measurement (no magnets)

A vacuum tank for the intersection region is outlined in Fig. 1 which allows for the measurement of particles which exit normal to the bicone after scattering at 1 - 50 mrad from each beam. The criteria for establishing this range are: a) the minimum angle is set by the requirement to stay outside the 30 GeV beam dump envelope, and b) the maximum angle allows for measurements at the minimum energy, $\sqrt{s}$ = 60 GeV/c, out to $|t| = 2.25\ (\mathrm{GeV/c})^2$. The vacuum pipes follow roughly the contours of the 30 GeV beam dump envelope from 7 to 20 m from the intersection region and then join the standard 8 cm diameter pipe. The entire setup of vacuum tank and detectors can be fit into a ± 20 m free space region. The dump envelope presents the smallest vertical angle to the beam in the region 7 - 13 m where the first detector modules are placed. The rear detectors observe angles down to 1.3 mrad.

The detectors are modules of proportional chambers with 0.5 mm

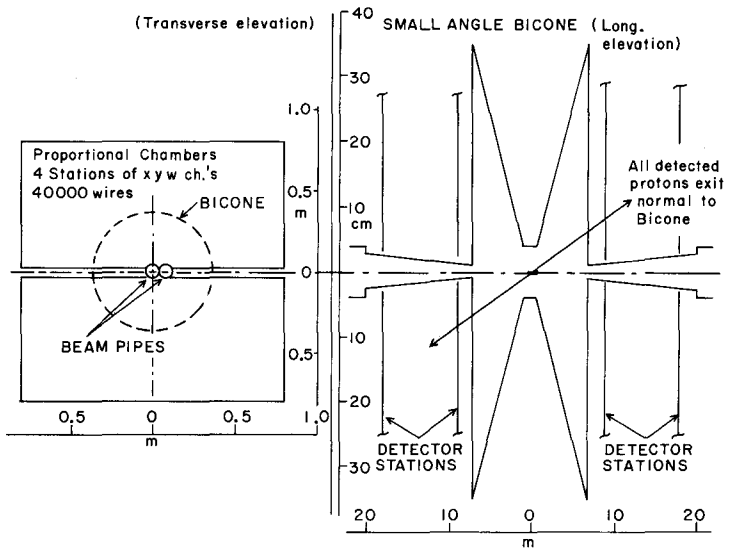

Fig. 1. Arrangement of vacuum tank and detectors for elastic scattering selection by angle-angle correlation.

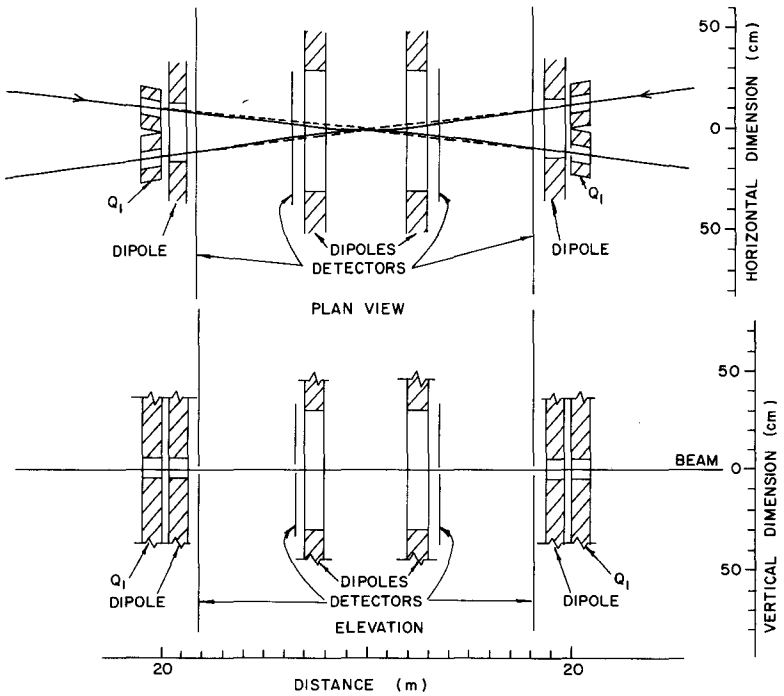

Fig. 2. Magnet and detector arrangement for stage 2 measurements with magnetic analysis.

spacing (two staggered planes with 1 mm spacing) to measure x, y, w. Each module covers an area 1.6 m square transverse to the beam, and there are a total of 4×10^4 wires. The detector system is augmented by veto counters surrounding the remaining solid angle to help suppress background from inelastic events. The following table gives the t ranges at several beam momenta and representative resolutions. (The latter are essentially due to angular dispersion in the beams which is 0.12 mrad at 30 GeV).

p(GeV/c)	t Range$(GeV/c)^2$	δt (full width) t = 0.1	t = 1
30 × 30	0.001 - 2.25	0.005	0.014
100 × 100	0.01 - 25	0.008	0.024
200 × 200	0.04 - 100	0.013	0.040

a representative counting rate is

30 events/hr for
$L = 10^{32}/cm^2/sec$
$d\sigma/dt = 10^{-33}\ cm^2/(GeV/c)^2$
$\Delta t = 0.1\ (GeV/c)^2$ (t bin width)

From the table it is apparent that in the range $60 < \sqrt{s} < 280$ GeV/c, t_{min} is less than 0.02 $(GeV/c)^2$, well within the t slope break seen at the ISR[1] in the region $|t| \sim 0.1\ (GeV/c)^2$. Even at $\sqrt{s} = 400$ GeV/c this structure will be well measured, assuming it remains similar to the lower energy data.

The accessible t_{max} is expected to be background limited since from the example above the elastic counting rates are ample. We anticipate that backgrounds from other reactions will limit the observable cross section to $\sim 10^{-32}\ cm^2/(GeV/c)^2$ judging from the

1. G. Barbiellini, M. Bozzo, P. Darriulat, G. Dambrini Palazzi, G. DeZorzi, A. Fainberg, M.I. Ferrero, M. Holder, A. McFarland, G. Maderni, S. Orito, J. Pilcher, C. Rubbia, A. Santroni, G. Sette, A. Staude, P. Strolin, and K. Tittel. Phys. Lett. 39B, 663 (1972).

experience of Böhm, et al,[2] who observed $\leqslant$ 25% background at 10^{-32} $cm^2/(GeV/c)^2$ using a similar technique. Judging from the data of the CHOV collaboration[3] this will allow observation of the dip bump structure at $|t| \sim 1.5$ $(GeV/c)^2$ given that the cross section holds up at higher energies.

Total cross sections will be measured by extrapolating the data for $|t| \leqslant 0.1$ $(GeV/c)^2$ to zero and using the optical theorem. Several factors which could limit the precision of the result have been considered: Angular resolution, setting error, uncertainty in acceptance near the small angle cut-off and the extrapolation procedure itself all are potentially significant sources of error but only for $\sqrt{s} > 200$ GeV/c where the extrapolation becomes significant. For example, at maximum energy, $\sqrt{s} = 400$ GeV/c, the extrapolation is about a factor of two assuming a t slope of ~ 15 $(GeV/c)^{-2}$. The first two sources mentioned are found to contribute < 1% to the error at all energies. The acceptance uncertainty while potentially $\sim$ 5% can be reduced through studies of spatial distributions of live data and by measurements at fixed $\sqrt{s}$ with unequal beam energies. The extrapolation procedure is something of an unknown at the highest energies, but will be based on methods which can be well studied at lower energies. The contribution from luminosity measurements is expected to be 2 - 3% based on current ISR experience. Finally if the ratio,

$$\frac{\mathrm{Re}\ f(0)}{\mathrm{Im}\ f(0)} < 0.1$$

its contribution is entirely negligible.

---

2. A. Böhm, M. Bozzo, R. Ellis, H. Foeth, M.I. Ferrero, G. Maderni, B. Naroska, C. Rubbia, G. Sette, A. Staude, P. Strolin, G. DeZorzi. Phys. Lett. 49B, 491 (1974).
3. E. Nagy, et al. 1974 SLAC Summer Institute on Particle Physics, paper 488 (unpublished), and G. Giacomelli, invited talk, SLAC Summer Institute, invited talk (unpublished).

Stage 2 - Elastic Scattering Using Magnetic Fields

The apparatus for this phase is similar to that used in Stage 1, but amplified by dipole magnets as shown in Fig. 2. The philosophy of the design was that the apparatus be useable over a large t range, to minimize systematic errors involved with matching different measurements, and be compatible with the "standard" intersection region. Incorporation of magnetic analysis of the final state particles provides an extra constraint and thus enhances signal to noise ratios.

The use of dipoles in the horizontal plane for magnetic analysis and compensation for the deflection of the circulating beam leaves the primary beam unaltered. The placing of detectors behind the first dipole minimizes the rates in those detectors and permits measurement of low momentum transfer events while remaining outside of the 30 GeV/c dump envelope. For the present design the detectors are proportional wire chambers with effective wire spacing of 0.5 mm, as for Stage 1.

In calculating the properties of the system, we have assumed 6.3 kG magnetic fields with 3 m effective lengths for the dipoles nearest the intersection regions, D1. The outer dipoles, D2 can be considerably smaller in field line integrals. These magnets reduce the angle of intersection of the primary beams from the nominal 11.4 mrad to 5.7 mrad. Increased luminosity is, of course, a useful by-product of the design.

With the detectors placed as shown in Fig. 2, the angular resolutions in both the vertical and horizontal planes is 0.0625 mrad. If one of the scattered particles is assumed to have the incident beam momentum, 200 GeV/c in this example, the projection of the track to the interaction region from the detectors has a cross section of 1.2 mm by 1.2 mm at the intersection region. Requiring that the other particle originate from this projected interaction point establishes an effective longitudinal momentum resolution

$\Delta P_L/P_L = \pm 2.2\%$ for the system.

The transverse momentum balance can be established to $\Delta P_\perp = \pm 10$ MeV/c from detector resolution; however with the standard insertion region, $\beta_h = 20$ m, $\beta_v = 4$ m, a factor of $\Delta P_\perp^h = \pm 5.6$ MeV/c and $\Delta P_\perp^v = \pm 12.5$ MeV/c has been added in quadrature. Thus, the transverse momentum balance uncertainty becomes $\Delta P_\perp^h = \pm 11.5$ MeV/c and $\Delta P_\perp^v = \pm 16$ MeV/c.

For an elastic scattering event, the momentum transfer is $t \simeq p^2\theta^2$. The uncertainty on this quantity has been taken as $\Delta t = 2t\sqrt{(\Delta P_L/P_L)^2 + (\overline{\Delta P}_\perp)^2/-t}$. In this expression, $\overline{\Delta P}_\perp$ is the weighted average uncertainty in transverse momentum as measured on each arm. We have used $\overline{\Delta P}_\perp = 20.7/\sqrt{2}$ MeV/c. We have also assumed $\Delta P_L/P_L = 1.7\%$. The above calculation yields an uncertainty in momentum transfer of 0.057 $(\text{GeV/c})^2$ for $t = -1.4$ $(\text{GeV/c})^2$ where the first minimum occurs in the ISR data. This uncertainty is dominated first by the uncertainty in longitudinal beam momentum, second by the vertical angular uncertainty of the beam, and third by the resolution of the apparatus. In theory one could minimize the first two factors and be left with $\Delta t = 0.011$ $(\text{GeV/c})^2$ at $t = -1.4$ $(\text{GeV/c})^2$ due to apparatus resolution.

We have assumed for low $|t|$ that the dominant background comes from isobar production in diffractive dissociation, and for convenience that these states decay isotropically in their own center of mass. The probability of such an occurrence being accepted within our transverse momentum balance restriction is

$$P(P_\perp < \Delta P) = 1 - \sqrt{P^{*2} - (\Delta P_\perp)^2}\ /P^* ,$$

where $\Delta P_\perp$ is 19.4 MeV/c, (we have added $\Delta P_\perp^h$ and $\Delta P_\perp^v$ in quadrature), and P^* is the center-of-mass decay momentum. For the N^* (1470) P^* is 420 MeV/c, thus the probability of acceptance is about 0.1%. Higher mass states have accordingly smaller probability, and greater than two body final states even smaller.

We thus assume a 0.1% acceptance probability for all states. If we use the ratios $R = \sigma(pp \to pX)/\sigma(pp \to pp)$ as measured at the ISR for $|t| \leq 0.48$[4] we can fit the data to a function

$$R = 3 \times 10^{-2} e^{(b_x - b_p)t},$$

where b_x is the single diffractive dissociation slope of 6 $(\mathrm{GeV}/c)^{-2}$ and b_p is the elastic slope of 10 $(\mathrm{GeV}/c)^2$. Using this information we obtain a signal to noise ratio of 10^3 at $t = -1$ $(\mathrm{GeV}/c)^2$ and 10^2 at $t = -1.5$ $(\mathrm{GeV}/c)^2$. Thus if the dip in the elastic cross section is one order of magnitude, we still expect 10:1 signal to background ratios.

For larger momentum transfers other processes become important, however our magnetic analysis of $\Delta P/P < 4\%$ will reduce such backgrounds. We can approximate the acceptance of our apparatus in $x_\perp$ vs x space by the shaded area shown in Fig. 3. We note that without the bending magnet, the acceptance would be all $x_\perp$ allowed by kinematics, i.e. $x_\perp \leq \sqrt{1-x^2}$.

We have approximated the pion background by the invariant cross section:

$$E \frac{d\sigma}{d^3p} \simeq \frac{x}{\pi} \frac{d\sigma}{dp_\perp^2 dx} = A(x) e^{-6p_\perp}$$

for $p_\perp < 2$ GeV/c, and

$$\frac{x}{\pi} \frac{d\sigma}{dp_\perp^2 dx} = A(x) e^{-12\left(\frac{p_\perp}{2}\right)^{-6}}$$

for $p_\perp > 2$ GeV/c. We have further assumed A(x) has little x dependence and can be taken as 10^{-26} $\mathrm{cm}^2/(\mathrm{GeV}/c)^2/\mathrm{sr}$.[4] Folding these distributions through the acceptance curve yields

4. G. Giacomelli, Recent Experimental Results from the CERN-ISR. Invited talk to the SLAC Summer Institute on Particle Physics, 1974 (unpublished).

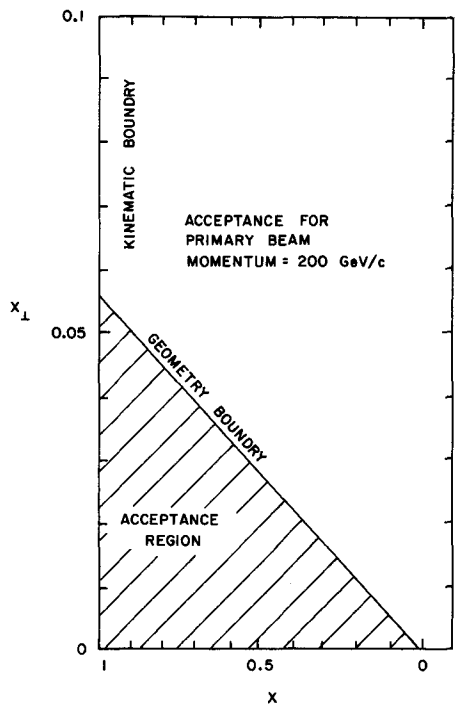

Fig. 3. Acceptance of apparatus for magnetic analysis.

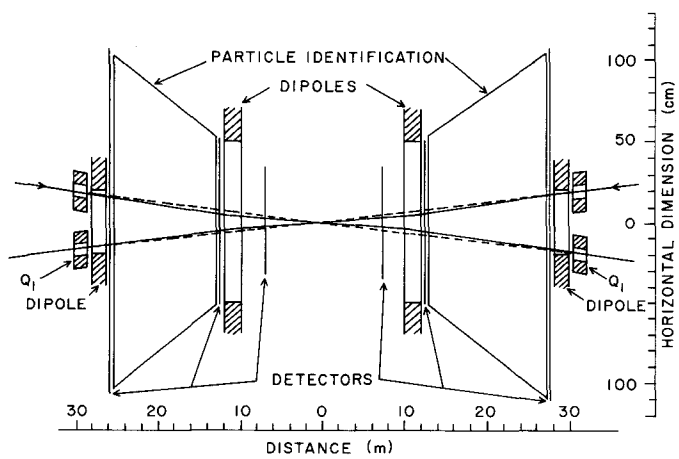

Fig. 4. Diffractive dissociation apparatus with magnetic analysis and particle identification.

$$\sigma \cong 10^{-25}\ cm^2 .$$

Protons accepted, due to leading particle effects, increase this number by a factor of ~ 1.5. For a luminosity of $10^{32}/cm^2/sec$ this would yield rates in the proportional chambers $\simeq 1.5 \times 10^7/sec$. This rate is in a 1 m^2 chamber leading to a rate of $\simeq 10^3$ particles/cm^2/sec, well within the capacities of proportional chambers. The rates in the low $|t|$ regions of the chambers would be higher, but the low $|t|$ measurements can be made at lower luminosities.

Stage 3 - Low Mass Diffractive Processes by the Effective Mass Technique

Recognizing that diffraction dissociation to low masses cannot be studied in colliding beam machines using the missing mass technique (the missing mass resolution is prohibitively large) we have augmented the schemes discussed for stages 1 and 2 by the addition of full magnetic spectrometers to measure the effective mass of low multiplicity systems near $x = 1$, see Fig. 4.

Here the magnet apertures are 1m × 1m × 2m long with maximum fields of 10 kG and bending power of $\Delta P_T = 600$ MeV/c. For low masses, hence small opening angles, the scattering angle range is similar to that for elastically scattered protons.

An order to provide adequate particle identification the insertion region has been increased from 40 to 60 m. Segmented gas Cerenkov counters are placed from 13 - 26 m from the intersection. With two counters in tandem one can obtain adequate discrimination for π/K up to 100 GeV/c and for π/p up to 200 GeV/c. Alternatively with one counter, π/K discrimination is good to 200 GeV/c.

Some representative resolutions are

P_T at 100 GeV/c - 15 MeV/c

Effective mass - 30 MeV

(M = 2 GeV, p = 200 GeV/c, 2 body decay)

The maximum P_T at 30 GeV/c is 1.5 GeV/c so that for most energies the "diffractive" systems can be traced well past the first diffraction minimum of elastic scattering.

Clearly, both single and double dissociation can be studied with this technique and with resolutions adequate to resolve low mass structures.

SMALL ANGLE SINGLE ARM SPECTROMETER FOR ISABELLE

C-Y. Chang
University of Maryland
E. Engels
University of Pittsburgh
M. Kramer
City University of New York
R. Lanou
Brown University
L. Pondrom
University of Wisconsin

I. Physics Interest

Inclusive production measurements of known secondary particles, as well as searches for new heavy stable particles (quarks, for example) are of great interest in the early experimental program at the ISA. Simple models of scaling predict that the invariant inclusive production cross section

$$E \frac{d^3\sigma}{dp^3} \quad (p + p \rightarrow \pi + \text{anything})$$

can be expressed as a function of $p_\perp = p \sin\theta$ and $x = (p \cos\theta)/p_{inc} \simeq 2(p \cos\theta)/\sqrt{s}$, and that such an expression is independent of s. Particles other than pions in the final state should obey similar rules. A variable essentially equivalent to x, the rapidity $y = \ln[(E + p\cos\theta)/(E - p\cos\theta)]$ is often used instead. The invariant cross sections are then written as

$$E \frac{d^3\sigma}{dp^3} = f\ (x,\ p_\perp)$$

or

$$E \frac{d^3\sigma}{dp^3} = g\ (y,\ p_\perp)$$

for any value of s. A further simplification is obtained if the cross sections factor into a product of two functions of a single

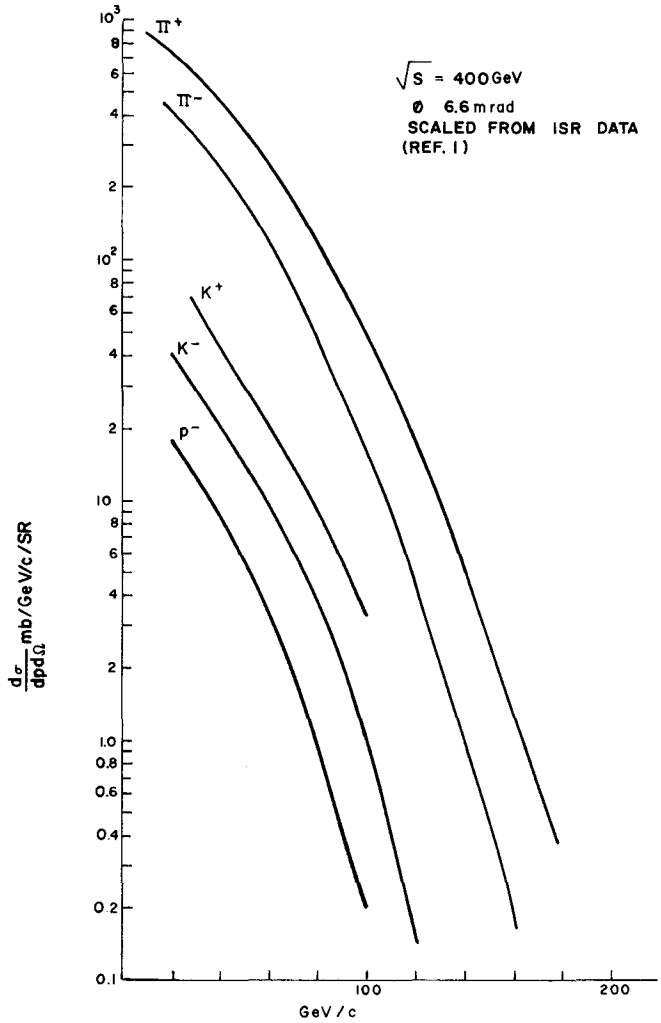

Fig. 1 Estimates of momentum spectra for $\pi^{\pm}$, $K^{\pm}$, and p^{-} scaled from ISR data.

variable. Since the ISA will offer values of $\sqrt{s}$ continuously variable from 60 GeV to 400 GeV, a broad range of energy will be available to test this behavior. Figure 1 shows a plot of ISR data[1] scaled to $\sqrt{s}$ = 400 GeV using these ideas. The plot is at a fixed angle of 6.6 mrad - rather large - but it serves as a guide to the various rates that can be expected.

Inclusive spectra of protons near x = 1 are of special interest in the study of missing mass states through the reaction

$$p + p \rightarrow p + m.m.$$

In the limit $x \rightarrow 1$ the triple-Regge model makes definite predictions for the shape of the proton spectrum in terms of the invariant missing mass squared, M^2, and the four momentum transfer squared $t = (p_1 - p_3)^2$. M^2 and x are approximately related by the formula

$$M^2 \cong s\ (1 - x).$$

Good resolution in the M^2 spectrum therefore requires a good resolution in (1 - x), which is a small number. Thus, stringent requirements are placed both on the knowledge of the incident proton momentum, and on the measurement of the outgoing proton momentum. For example for 10% resolution in M^2 near x = 0.99 (an interesting region), resolutions in momenta of the order of 0.1% are required.

II. Insertion Modifications

Inclusive studies at $\sqrt{s}$ = 400 GeV dictate the observation of secondary particles at forward angles near 1 mrad. In order to achieve a practical configuration, it is desirable to cover a wide range of angles and momenta without physically moving any apparatus. A wide acceptance spectrometer can be built at ISA, but requires certain modifications to the insertion region to accommodate small angle production.

---

1. J. C. Sens, "Topics in Particle Physics with Colliding Proton Beams" in Particle Interactions at Very High Energies, Speiser, Halzen, and Weyers, Editors, Plenum Press, New York, 1974.

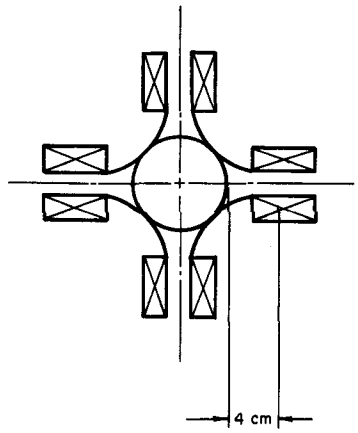

Fig. 2 Schematic of quadrupole magnet with slot for secondary particles.

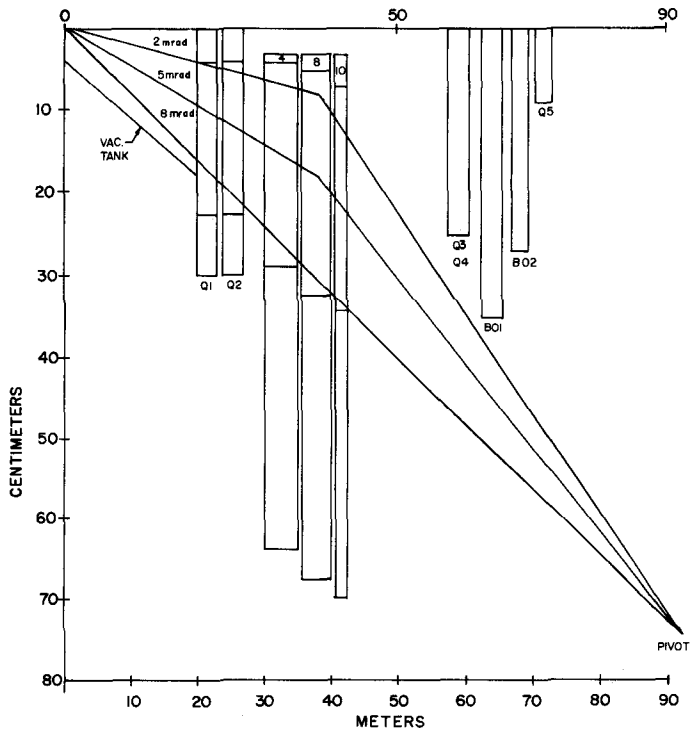

Fig. 3 Expanded view of intersection region showing location of septum magnets for spectrometer.

A normal insertion region is followed by a pair of superconducting quadrupoles (Q1 and Q2) 20 meters from the beam intersection. The dewar radius for these quads is 25 cm. Without any modifications or septum magnets, the minimum production angle is 12.5 mrad which is too large. The "stay clear" aperture for the beam is 1.5 cm horizontally (or 1 cm vertically) which restricts the distance of closest approach of a septum magnet coil to $\sim$ 2 cm. Assuming a conventional copper winding 1 cm thick, the entrance aperture for the secondary beam defined by the first septum magnet has a minimum distance of 3 cm from the beam. If placed at 10 meters, a minimum angle of 3 mrad could be achieved, but a bend of 50 mrad by the septum magnets would be required in order that the secondary particles miss the quadrupole. Such a bend would require an average magnetic field in the septum of 36 kG. Smaller angles are desirable and a septum field of 36 kG is uncomfortably large. The only alternative is to change the design configuration of Q1 and Q2.

The quadrupoles could be moved downstream. Placing Q1 at 40 meters and the septum entrance at 20 meters (1.5 mrad minimum angle) would require an average magnetic field of 11 kG over the next 10 meters to miss the dewar. The minimum angle could be decreased somewhat (to about 1 mrad by taking the secondary beam off vertically rather than horizontally. The septum field could be decreased by making the dimension of the dewar less than 25 cm. This might be a practical solution, but it would require a special tune of the machine because of the displacement of the quads, and it also might adversely effect the compatibility of the small angle spectrometer with other experiments sharing the same intersection region.

A second alternative would be to leave Q1 and Q2 at 20 meters, and to use either conventional or superconducting magnets, and to create a slot for secondary particles to escape by separating the quadrupole windings, as shown in Fig. 2. In the case of superconducting magnets, separate dewars for top and bottom windings may

be required. The quads in the two colliding rings could be staggered to make room for conventional magnet yokes. In this design the septum magnets would be placed downstream of the quads. The "stay-clear" envelope of the beam is larger behind Q1 and Q2 - 3 cm rather than 2 cm - but the minimum angle for positively charged particles remains the same since they are moving outward. For negative particles the minimum angle increases to 2 mrad because of the deflection resulting from the quadrupole fields. Again some improvement is gained by taking a vertical angle, although a horizontal configuration will be described here.

Figure 3 shows an expanded view of the intersection region. The vacuum tank has a simple flare to 18 cm from the beam just before Q1. Particles traversing the slot of Q1 and Q2 experience a dipole field which drops off linearly with distance across the coil, giving positive particles a net displacement outward of a few millimeters. The first septum magnet entrance is at 30 meters, and the inner current sheet is 3 cm from the beam center. Three septum magnets of 4, 8, and 10 kG are used, with a field integral of 80 kG meters and a total length of 12 meters. A vertical aperture of 2 cm is assumed, which serves to define the vertical angle of the beam (0.5 mrad).

In this design all trajectories between 1 and 8 mrad and all momenta up to 200 GeV/c can be made to intersect the pivot point, 92 meters downstream and 74 cm off the straight beam direction. Angles greater than 8 mrad would be possible, but the small spatial acceptance would lead to very low rates. A second magnet placed at the pivot point deflects this secondary beam through 11 mrad towards the spectrometer. The spectrometer measures the momentum and identifies the particles.

III. Spectrometer

The spectrometer is similar to the one described in the ISABELLE 1975 proposal.[2] Figure 4 shows the proposed floor plan in the small angle experimental hall. An extension of 140 meters is required to accommodate the apparatus. Depending on local ground level elevation, this extension could be a covered trench. A single spectrometer magnet 10 meters long with an aperture of 25 cm horizontally $\times$ 5 cm vertically is shown. The pivot magnet could also be of this type. It might be advantageous to use ferric superconductors for these magnets, to avoid power bus and cooling problems in the tunnel. In the figure two left bends of 11 mrad in the septum and the pivot magnet are followed by a 25 mrad right bend in the spectrometer to give momentum recombination. Space trajectories are measured by standard MWPC's of modest size. Two 10 meter and one 50 meter threshold Cerenkov counter are used to separate π, K, and p. C1 and C2 are set below proton threshold but above K threshold, to provide p-K separation, and C3 is set below K threshold to provide π-K separation. A chamber between C1 and C2 enables one to observe energetic knock-on electrons from protons that traverse both C1 and C2. Efficient operation at 200 GeV sets the scale of Cerenkov counter lengths. By using either helium at high momenta or nitrogen at low momenta a range of 20 GeV/c to 200 GeV/c could be covered at pressures less than 1 atmosphere absolute, avoiding the need for high pressure vessels. These counters are similar to several in use at FNAL, and are cheap and easy to build.

The characteristics of the spectrometer are summarized in Table I. The difference in space angle range is due to particle displacement in the split quadrupoles, as described earlier. The lower momentum cut-off is rather arbitrarily taken to be 20 GeV/c,

---

2. "A Proposal for Construction of a Proton-Proton Storage Accelerator Facility", BNL Report 20161, (1975).

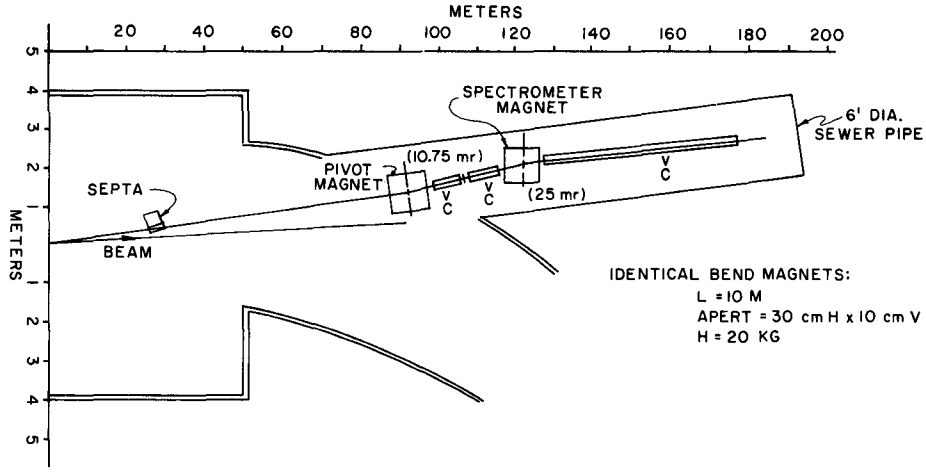

Fig. 4 Small angle spectrometer arrangement relative to ring tunnel and experimental hall.

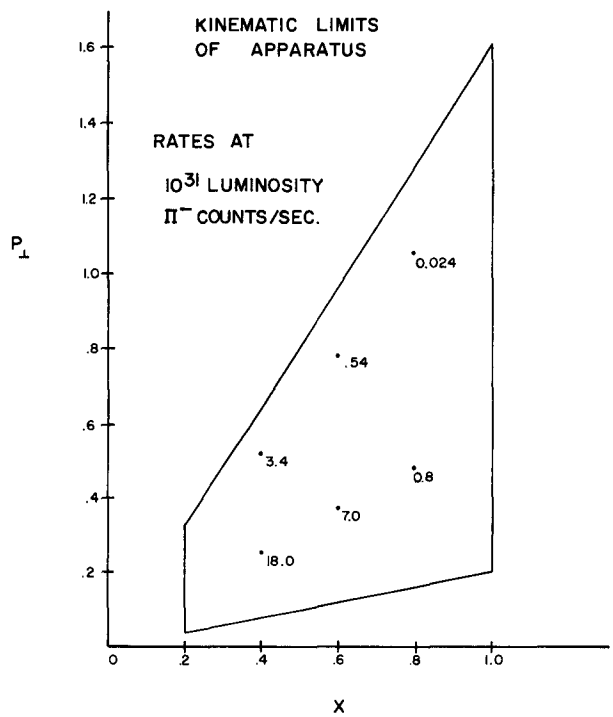

Fig. 5 Acceptance of spectrometer in X, $p_\perp$, space and typical pion counting rates.

where the loss of K mesons due to decay in flight is $\sim 1/e$. The spatial solid angle is set in the vertical dimension by the septum magnets and in the horizontal dimension by the spectrometer magnet. The momentum resolution quoted is based on an rms error of 0.75 mm over 20 meters, and a bending angle of 25 mrad.

TABLE I

Spectrometer Characteristics

Space angle range	$1 \leq \theta \leq 8$ mrad	positives
	$2 \leq \theta \leq 8$ mrad	negatives
Momentum range for particle identification	$20 \leq p \leq 200$ GeV/c	
Spatial solid angle	10^{-6} sr	
Momentum acceptance	10%	
Momentum resolution	$\Delta p/\Delta \sim 0.15\%$	

IV. Remarks

The capability of the spectrometer described seems adequate to measure inclusive particle production over a wide range of s. The acceptance of the spectrometer in $x - p_\perp$ space at $\sqrt{s} = 400$ GeV is shown in Fig. 5. Typical counting rate estimates for π^- per sec at a luminosity of 10^{31} cm^{-2} sec^{-1} are also shown. By lowering the energy of the "target" ring (asymmetric running) $\sqrt{s}$ can be lowered to 150 GeV without changing the characteristics of the spectrometer at all, thus allowing a very good test of the independence of $Ed^3\sigma/dp^3$ on s. To lower $\sqrt{s}$ to the ISR energy, both rings would have to go to 30 GeV, for which the spectrometer would be inconveniently long, but still workable. In this case the $p_\perp$ range would of course decrease. Data would normally be taken at a constant setting of the spectrometer momentum, which is very nearly constant

x, and $p_\perp$ would be varied by changing the angle tune, giving data along vertical lines in Fig. 5.

The quoted momentum $\Delta p/p = 0.15\%$ is adequate for a study of the missing mass distribution as discussed in Section I over a reasonable range of $x \approx 1$. The design momentum dispersion of the beams ($\sim 0.5\%$) should be improved for these measurements, or alternatively the beam momentum in a collision of interest must be measured. Momentum measurements could be made by dispersing the beam horizontally according to momentum, and constructing the spectrometer vertically - a possibility referred to earlier. Extrapolated precision of ~ 1 mm in the beam-beam intersection region would then suffice to determine $\Delta p/p$ of the beam to 0.1%, assuming that the momentum dispersion occurs over a 1 cm beam width.

The experiment could easily share an insertion with other large angle experiments. Various embellishments for the proposed experiment can be contemplated. A focussing spectrometer could be installed so that differential gas counters could be tuned to look for very low yield particles ($\bar{d}$, for instance), or to search for new long lived particles. Such a spectrometer would not have a solid angle much larger than 10^{-6} sr, however, because of the difficulty of getting quadrupoles closer than about 50 meters to the interaction point. A quark search could be made in such a spectrometer with the addition of dE/dX counters.

TABLE II

Estimated Cost of the Experiment

Item	Cost (thousands)
3 Septum magnets	100
2 Bending magnets	200
2 Special quadrupoles	60
6 MWPC's	60
3 Threshold Cerenkov counters	60
1 Tunnel miscellaneous	30
Total	$510

A SINGLE ARM SPECTROMETER TO STUDY HIGH $p_\perp$ PROCESSES NEAR 90° AT ISA

C.Y. Chien,
Johns Hopkins University

H. Gordon,
Brookhaven National Laboratory

A. Kanofsky,
Lehigh University

M.A. Kramer,
City College of New York
and
J. Russ,
Carnegie-Mellon University

I. INTRODUCTION

It has been demonstrated ever since Rutherford's days that large angle scattering of particles reveals their detailed structures and unexpected new phenomena. The most recent example is the large p_T inclusive π production from pp scattering data from ISR. The invariant cross section for π^0 production near 90° instead of falling off exponentially with increasing p_T as had been expected, falls off according to a power law p_T^{-n} where $n \simeq 8$ from the ISR data. At ISA, the maximum p_T is ten times higher than at ISR. Thus one can probe deeper into the proton, and it will be extremely important to see what new phenomena will happen in this new kinematic range.

This working group has taken as its charge the design of a device of moderate size to study large p_T production involving one or several particles in the region near $x = 0$. The emphasis is on a spectrometer to gather as much information as possible while remaining modest in size. The spectrometer should be modular so that more detectors can be added on later as guided by the new data obtained at ISA.

We propose to assemble a single arm spectrometer with medium acceptance in solid angle and rapidity ($\Delta\Omega = \frac{1}{2}$ sr, $\Delta y = 2$), good particle identification and good momentum resolution. We will describe the details of the spectrometer in Section II and the trigger logic in Section III. Cost estimate and physics capabilities are summarized in Sections IV and V. In Section VI we discuss possibilities of using other devices in conjunction with this spectrometer.

II. APPARATUS

The apparatus proposed (Fig. 1) is a magnetic spectrometer with a bending magnet and drift chambers (D1 to D7). Particle identification is provided by three gas C counters (C1, C2 and C3) and proportional chamber hodoscopes (P1 to P4) are used to provide fast signals for trigger logic for momentum selections. The details of each component are described in this section and the trigger logic is explained in Section III.

A. Magnet

The magnet is a conventional dipole with water-cooled copper coils and iron poles. The aperture furthest from the intersection region, 2m wide by 0.5 m high yields a solid angle of 0.5 sr and a large range in cos θ ($\theta = 90^{\circ} \pm 45^{\circ}$). The aperture closest to the intersection region, 1 m by 0.5 m, will have a magnetic shield to minimize the magnetic flux at the intersection region. If necessary a small compensating magnet (or symmetric spectrometer magnet) would be placed on the opposite side of the intersection region.

A vertical field of 15 kG provides a transverse kick of 450 MeV/c which sweeps most particles below 1 GeV/c (which account for more than 90% of all tracks produced at 90°) out of the spectrometer and allows analysis of faster tracks to a precision of $\Delta p/p = 3\%$ at 20 GeV/c. The vertical field was chosen so that all fast tracks point straight back to the intersecting region in the vertical plane. This characteristic simplifies the light collection problem in the C counters.

APPARATUS TO STUDY PARTICLES WITH LARGE P_T (2-20 GeV/c) AT I.S.A.

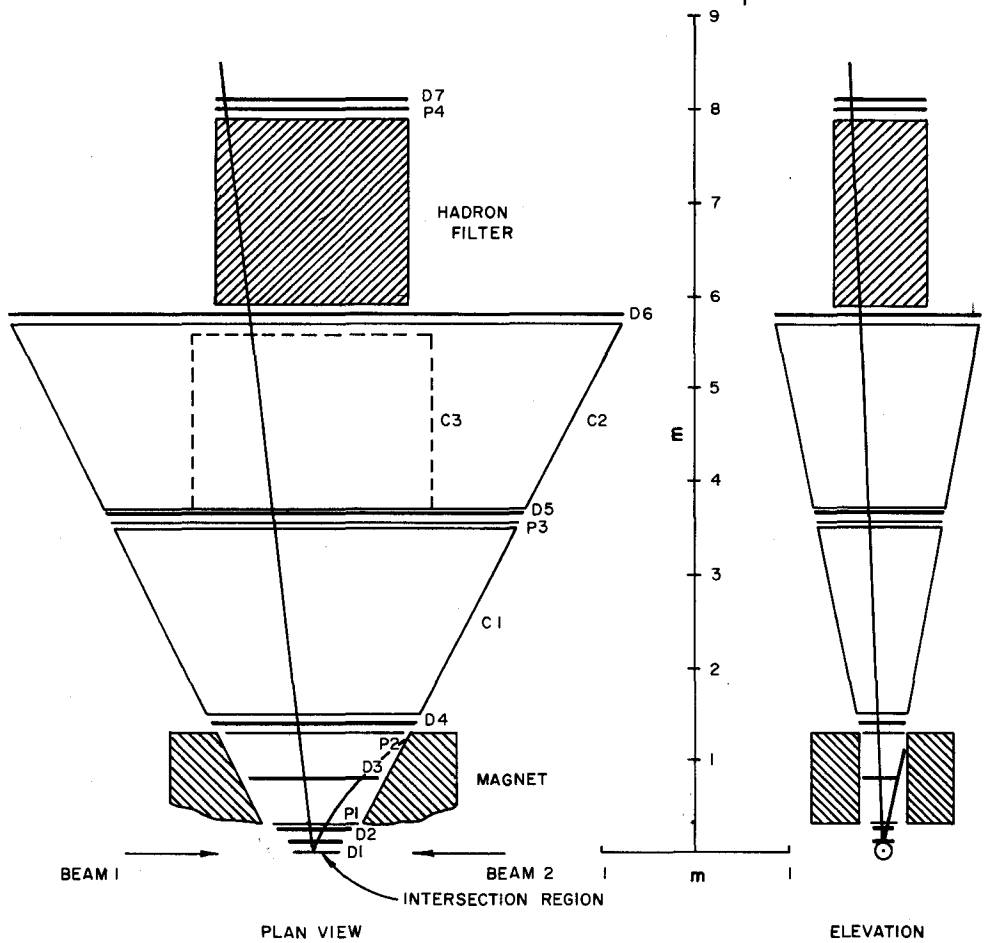

Fig. 1.

B. Drift Chambers

Drift chambers (D1 - 7) were chosen for their good spatial resolution and low cost. Their sizes and drift spaces (Table I) increase toward the end of the spectrometer to match the solid angle, counting rate and resolution needed.

The highest counting rate occurs in D1 and D2 where particles have not diverged and low momentum particles have not been swept out. Assuming $L = 2.5 \times 10^{32}$ and $dn/dy = 3$ (twice the ISR value near 90°), the counting rate in D1 is 400 kc/wire, which is manageable.

C. Proportional Wire Chambers

Since the cross section falls steeply as p_T increases, one needs a fast momentum trigger to select high p_T events. We chose a hodoscope system consisting of proportional wire chambers (P1 - 3) to cover large areas with fast response and good spatial resolution.

Their dimensions and wire spacing are shown in Table I. P1 has a counting rate of 40 kc/wire. P1, P2, P3 each have three crossed sense wire planes to provide unambiguous y, z coordinate pairs. The momentum trigger logic is described in Section III.

P4 is used to tag particles that penetrate the hadron shield. The function of the hadron shield is to detect μ's at the 1% level, just to monitor any unexpected increase in μ/π ratio. It is not aimed at direct μ production measurements.

D. Cerenkov Detectors

For charged particles, the intersection region represents a line source 38 cm $\times$ 0.05 cm high. Use of horizontal magnetic deflection and cylindrical C optics allows focusing of the C light onto a line image. Use of Winston-style adiabatic light collectors and 2-inch phototubes should permit light collection efficiencies exceeding 50% despite the large variation of horizontal projected angles.

Table I. Dimension of Wire Chambers

Detectors	$w \times hm^2$ Dimension	Effective Y.Z.U Wire Spacing cm	No. of Readout Channels
P1	1 × 0.25	0.2,0.2,0.2	1140
P2	2 × 1	0.2,0.2,0.2	2618
P3	4 × 1.5	0.5,0.5,0.5	1954
P4	2 × 1	1, -, -	100
D1	1 × 0.5	1, 1, -	150
D2	1 × 0.5	1, 1, -	150
D3	1.5 × 0.5	1, 1, -	200
D4	2 × 0.5	2, 2, -	125
D5	4 × 1.5	5, 5, -	110
D6	7 × 2	-, 5, -	40
D7	2 × 1	-, 5, -	20

We propose the use of two large, atmospheric pressure C counters covering the entire solid angles defined by the magnet aperture and the addition of modular high pressure ($\leqslant$ 5 atm) gas C counters to extend the lower limit of π/K separation at low p ($\sim$3 - 10 GeV/c). Use of Fr12 ($\eta = n - 1 = 1.08 \times 10^{-3}$) [Fr 114 ($\eta = 1.45 \times 10^{-3}$)] gives a π threshold of 3.0 [2.6] GeV/c, and a K threshold of 10.6 [8.9] GeV/c. Filling the second counter with CO_2 gives full efficiency for π's at 9.5 GeV/c and a K threshold of 17 GeV/c. Therefore, this pair of counters tags π, K, p from $\sim$10 - 20 GeV/c with complete identification. Presently, there are several 5 atmosphere C counters 1 m $\times$ 1 m $\times$ 2 m available at the AGS. Replacing C_2 by these counters gives $\pi/K/p$ identification over the span 5 - 10 GeV/c for most of the available solid angle. Finally, filling both C_1 and C_2 with nitrogen [$\eta = 3 \times 10^{-4}$] will give 5 photoelectrons for incident electrons while rejecting pions with a rejection ratio of $\sim 10^3$ per counter for $p_\pi < 6$ GeV/c. Using the two counters in coincidence should give rather a good measure of e/π ratios for $1\text{-}2 < p < 6$. Above 6 GeV/c, longer radiator lengths are required for adequate counter efficiency for electrons.

Construction of the counters is not complicated. Vertically, the divergence of the focused beam comes from C cone angle variations, which are at worst 3.5° in C_1 with Fr 114 fill. Placing the line focus near the magnet requires a 2.6 m mirror radius. The photomultipliers see restricted angular spreads ($\pm 3.5^\circ \times \pm 5^\circ$), so reasonable Winston-style lightpipes permit expansion of a 2-inch photocathode to a 5-6 inch circle. Using horizontal angular correlations, one can use some horizontal focusing, so that the coverage required is $\sim$ 3 m for C_1 and $\sim$ 5 m for C_2. Bisecting the cylindrical mirrors gives improved position definition, so that one must cover 16 m of focus, requiring $\sim$ 128 phototubes. Atmospheric counters scale roughly as phototubes cost, and we estimate the total cost to be $\sim$ 3 $\times$ 120 $\times$ (\$300/tube + base +

Table II. Momentum Coverage of Cerenkov Counters

Particle	Threshold			5 Photoelectrons	
	C_1	(Fr 114)	$C_2(CO_2)$	C_1	C_2
π	2.6		5	2.95	9.5
K	8.9		17	10.4	33.7
p	17.0		34	19.7	64
	C_1	(N_2)	$C_2(N_2)$	$C_1(N_2)$	C_2 (N_2)
e	0		0	0.25	0.25
π	6		6	∞	∞
	C_1	(FR 114)	C_3 (5 atm Fr 12)	C_1	C_3
π	2.6		1.35	2.95	1.42
K	8.9		4.75	10.4	5
p	17.0		9.0	19.7	9.5

Table III. Cerenkov and Particle Identification Modes

Particle Identifier	Mode	Momentum Range (GeV/c)
C_1(Fr 114), C_2 (CO_2)	π/K/p tag and π/Kp tag	10.5 - 18 3 - 9
C_1(Fr 114), C_3	π/K/p tag	5 - 9
C_3 and lower field	π/Kp tag	1.5 - 4.8
$C_1(N_2)$, $C_2(N_2)$ and lower field	e/hadron tag	1 - > 6
hadron filter, C_1 [a]	μ/π separation at 0.01 level	all

[a] Insertion of a uranium hadron filter near the beam pipe and in dipole (~ 1 m total) could improve the μ/π discrimination in this device for special runs.

lightpipe), or ~$100K. Each phototube should have an ADC channel to assist in multiparticle definition as well as improving mass identification. The summary of C performance is given in Table II.

The C counters can be used in various combinations for different kinds of particle identification as given in Table III.

III. TRIGGERING SCHEMES, RATES AND BACKGROUNDS

The high $p_\perp$ physics has inherently low background from sources like beam-gas collisions. The predominant trigger problem is the selection of single large $p_\perp$ tracks, given a very high flux of $x \sim 0$, small $p_\perp$ particles from the central region and an extended source. Here the plan is to develop a 2-dimensional matrix trigger scheme, using three PWC's as the hodoscope elements. High $p_\perp$ events from a given source point correspond to a set of allowed hit patterns in P_1, P_2, P_3. To accommodate full luminosity, it seems prudent to provide storage capability on each detector to "remember" events which occur while trigger calculations are being made on previous events.

To do anything at all, one must cope with a rate of ~10 MHz in the detector. The collision rate for $L = 2.5 \times 10^{32}$ $cm^{-2}sec^{-1}$ and $\sigma_{in} = 40$ mb is 10^7 sec^{-1}. This system has $\Delta\Phi/2\pi \sim 1/18$ and $\Delta y \sim 2$. Using 3 particles/rapidity unit near $x \sim 0$ (twice ISR), one expects a particle rate of 3 MHz, most of which is at low $p_\perp$ and therefore swept aside from the central portion of the apparatus. The trigger PWC's have resolving times of ~100 ns, so accidental extra tracks will occur at the few percent level. Since correlations are among the things one wants to study, the detector system must be able to cope with modest multiplicity, e.g., n = 4. This immediately requires each PWC plane to have angle wires, e.g., (0°, 45°, 90°) or (0°, 60°, 120°) so that hardwired fast adders provide correlated pairs of coordinates (y^i_α, z^i_α) for each particle i in PWC number α. The triggering then proceeds to find any hit combination y^i_1 , y^j_2 , y^k_3 such that the track points back to the intersection region in the vertical plane, viz., ay^i_1

$+ by_2^j - cy_3^k = 0$ where $a = x_2x_3$, $b = x_1x_3$, $c = x_1x_2$. This requires $4^3 = 64$ parallel adders to process the worst case hit patterns. When such a combination is found, the z_1^i, z_2^j, z_3^k for each valid y track are fed to the $p_\perp$ selector. This can be done by 4 parallel processors for maximum speed, but that is not necessary since each calculation should require < 50 ns with I^2L logic. New developments are sure to reduce that.

The $p_\perp$ calculation for a given track is done by calculating the slope after the field region (from $z_2 - z_3$) and the displacement in the field region ($z_1 - z_2$). These two numbers will be correlated for any $p_\perp$ independent of production point. Therefore, the numbers $z_1 - z_2$ and $z_3 - z_2$ can be used to address a 2 - d matrix which defines allowed bit patterns for $p_\perp > p_{\perp_{min}}$ and for the range of θ transmitted by the spectrometer. This pattern of allowed bits must be determined by computer ray tracing through the system and will have to be reprogrammed for every $p_{\perp_{min}}$ used in the experiment. The bit size of this 2 - d matrix depends largely on the sharpness of the $p_\perp$ cut required in the trigger. Exploiting full resolution of the PWC's proposed will require $\sim 10^6$ bits. Reduction by an order of magnitude in bit size is unlikely to raise the trigger rate to unacceptable levels.

Background due to several real low $p_\perp$ tracks simulating a high $p_\perp$ event in the trigger is drastically reduced by the (y,z) correlation method described above. Therefore, we do not foresee any real background limitations to this apparatus. The major problem in triggering will be checkout of the matrix to ensure the proper paths are enabled.

The real data rates are estimated using the CCR fit to the ISR data:

$$E\frac{d\sigma}{dp^3} = \frac{1.54 \times 10^{-26}}{(p_\perp)^{8.24}} \quad e^{-26.1\, p_\perp/\sqrt{s}} \quad cm^2\ GeV^{-2} sr^{-1}$$

This approximation will not necessarily describe ISA data, but it sets a scale. Using $\Delta\Omega = 1/2$ sr and $\Delta p = 1$ GeV/c, one finds the following rates for π's:

$p_\perp$	$\Delta\sigma$ (cm^2)	Rate ($L = 2.5 \times 10^{32}$)
5	2.5×10^{-32}	6 sec^{-1}
10	1.5×10^{-34}	2 min^{-1}
15	4.5×10^{-36}	4 h^{-1}
20	10^{-36}	1/h
25	1.4×10^{-37}	2/day

Use of the 90° spectrometer to search for W Bosons

In the "yellow book" discussion of W boson production at ISA, parton model predictions, assuming an antiparton distribution within the proton going as $(1 - x)^{7/2}$, are given for W boson masses $M_W < 160$ GeV/c^2, the cross section $\sigma_W > 10^{-34}$ cm^2. If the branching ratio $\Gamma(W \to \mu + \nu)/\Gamma_W$ is appreciable, e.g., 25%, then this simple spectrometer with an augmented hadron filter has a good chance to detect W boson decays. This is surely among the cheapest W boson detectors proposed. In the layout shown in Fig. 1, the μ detector subtends 1/64 sterad. Setting the $p_\perp$ threshold at 20 GeV/c, ~1% of pions decay to muons before they reach the hadron filter. Therefore μ decays of pions will not be a major background source for the W production experiment.

For W searches, the Cerenkov counters are not significant, so the μ filter can be moved behind C_1, just after the last momentum-measuring plane P3. By spending an additional $10K, one can increase the hadron filter coverage to a solid angle $\Delta\Omega \sim 1/3$ sterad. In the yellow book, Fig. 5 shows that the 90° cross section for a W boson of mass 90 GeV/c^2 is $d\sigma/d\Omega \sim 5 \times 10^{-35}$ cm^{2}sr^{-1}, integrating over a Gaussian in $p_\perp$. With a branching ratio $\Gamma(W \to \mu + \nu)/\Gamma_W(\text{all}) = 0.3$ and a luminosity of 2.5×10^{32} cm^{2}sec^{-1}, the detected W rate is 4 events/hour. The μ from W decay would be 45 GeV/c. Hence, tuning the spectrometer to accept 30 GeV/c and above, the background due to μ's from π decay would be less than 1 event/month. The point of this observation is to note that the 90° spectrometer is designed to study low rate processes. The two-body decay of the W boson, if it is produced at rates calcu-

lated by present models, is readily detected by this simple apparatus in a clean way. This by no means undermines the utility of special, large acceptance detectors. It does, however, suggest some relatively inexpensive, first round equipment may be able to set the mass and cross section scale for W bosons. Expensive, large-scale apparatus design might be enhanced by such input data.

IV. COST ESTIMATE

We estimate the total cost of the spectrometer as $570K, as itemized in Table IV. We note that the cost of electronics has been steadily decreasing while mechanical construction cost (materials and labor) has been increasing in recent years.

V. SUMMARY OF SPECTROMETER CAPABILITIES

In "normal" (15 kG) running the spectrometer has momentum resolution (σ) of $\sim$ (.15 $\times$ P)% for particles above 2 GeV/c. The field can be lowered for work with particles of 3 GeV/c. It accepts particles within the angular range of $90 \pm 45^{\circ}$ corresponding to rapidity $|y| < 0.9$. There are a number of modes of operation for particle identification which will separate π/K/p from 3 - 17 GeV/c, π/Kp down to 1 GeV/c and electrons from 1 - 6 GeV/c. An optional hadron filter will enhance the μ-π discrimination.

The acceptance ($\frac{1}{2}$ sr) is large enough to allow the investigations of the correlations of particles in the central region with large p_T events on the same side of the beam. As will be discussed in the next section, addition of other devices presently proposed and/or duplicating this one on the opposite side of the beam greatly augments the physics potential.

VI. DESIRABLE LINKAGE WITH OTHER APPARATUS

This spectrometer gives as much information as available in $\Delta\Omega = \frac{1}{2}$ sr near 90°. When a particle(s) with large p_T is produced, it is very interesting to have other information about the event:

a) Are there high p_T particles on the other side?

Table IV. Cost Estimate

(Dollars in Thousands)

Magnet (2 m × ½ m × 1 m, 15 kG, conventional)	$160
Proportional Wire Chambers	
4 Chambers	24
Electronics 5000 channels @ 20	100
Drift Chambers	
7 Chambers	40
Electronics 800 channels @ 50	40
Cerenkov Counters	
2 1 atm Counters	60
120 Phototubes + bases @ 300	36
120 ADC @ 80	10
Trigger Electronics	100
TOTAL	$570

b) Is the p_T balanced by particles with small $p_{||}$ or large $p_{||}$, by many particles or a single particle?

c) Are there photons or π^o's produced?

It will be useful to run the spectrometer in conjunction with other apparatus. Since this spectrometer has no special requirement on experimental insertions and occupies only the 90° area on one side of the beam, there are many possibilities for linkage with other apparatus. We shall discuss a few of them.

(1) With a 4π Detector System. As presently designed it is essentially compatible with the 4π system designed by Green and Grannis which uses drift chambers to measure angles of charged particles over 4π solid angle. In this case D1 and D2 would be replaced by the cylindrical drift chambers of the 4π setup and the magnet might have to be moved back $\geqslant$ 10 cm. (If desired, a collaborative design of the two detectors could probably eliminate the necessity of any movement.)

(2) A similar detector on the opposite side of the beam could be used to study correlations at large $p_\perp$. The acceptance would probably be large enough to be useful in studying reactions involving <u>one</u> large $p_\perp$ particle near 90° on one side and a few particles in the central region on the other.

(3) With a γ/π^o detector on the opposite side. A γ spectrometer with a magnet, wire chambers and Pb glass arrays similar to that in the CCR experiment at the ISR can easily fit into the opposite side of the beam <u>or under</u> the intersection region to study π^o correlations.

(4) A γ/π^o detector above or below the beam to study π^o distributions and multiplicities. [These π^o's presumably would not be involved in balancing $p_\perp$ as in (3).]

(5) A small angle spectrometer. A small angle spectrometer setup on the opposite side of the beam could be used to study how large $p_\perp$ at large x is balanced. If there are large angle detectors on both sides of the intersection region, the present design of the LAS would allow a SAS on the <u>same</u> side covering $\theta \leqslant 11^o$.

A BRIEF COMMENT ON LARGE $p_\perp$ MUONS NEAR 90°

Janos Kirz, SUNY, Stony Brook

Let us assume the same luminosity and acceptance as in Ref. 1. They expect 7 events/sec for π, K, p; $p_\perp > 5$ GeV/c. If $\mu/\pi \sim 10^{-4}$, then one may expect 2.5 events/hour for $p_\perp > 5$ GeV/c. The range of interest, then is $\sim$ 2-10(?) GeV/c.

The usual problem in μ identification is the background due to hadron decay: One wants to absorb hadrons as close to the production point as possible. One must design the absorber for K^+'s, because they are numerous, and nasty: decay length $\ell = \eta \times 3.7$ m, about 7 times shorter than for π's. Moreover K^+ total cross sections are low so the absorber is less effective for them (clearly, μ^- is easier to measure than μ^+). Too thick an absorber stops the desired μ's by range, so a compromise is suggested (which has been used in other inclusive μ measurements[2]) in which the absorber is in pieces: A segmented upstream part cuts hadron fluxes by $\sim$ 200X, then the momentum is measured in a magnetic spectrometer, and finally the muon is positively identified by a second absorber.

To increase solid angle or decrease size, combining absorber and magnet (e.g. using magnetized iron) might seem attractive, but multiple scattering makes the momentum resolution poor.

---

1. C.Y. Chien, H. Gordon, A. Kanofsky, M.A. Kramer, and J. Russ, "A Single Arm Spectrometer to Study High $P_\perp$ Processes Near 90° at ISABELLE", these Proc.

2. See R.C. Lamb, R.A. Lundy, T.B. Novey, D.D. Yovanovitch, M.L. Good, R. Hartung, M.W. Peters, and A. Subramanian, Phys. Rev. Lett. 15, 800 (1965); J.P. Boymond, R. Mermod, P.A. Piroué, R.L. Sumner, J.W. Cronin, H.J. Frisch, and M.J. Sochet, Phys. Rev. Lett. 33, 112 (1974).

One possible layout for the apparatus is shown on Fig. 1, PWC 1, 2 assure that the charged particle originates in the intersection region, before multiple scattering destroys that information. The absorber between these would be varied to calibrate the rest of the system by admitting larger numbers of decay muons.

The larger absorber following PWC 2 could be (1000) g/cm^2 ($\approx$ 52 cm) of tungsten.[3] This is followed by a short large angle spectrometer to give $\Delta p/p \approx 5\%$ at 5 GeV/c. The magnet described by Chien et al. would be about the right size, although ours is a bit shorter to regain the solid angle lost in providing space for the upstream absorber. (Note: The measured momentum is about 1.2 GeV/c lower, due to energy loss in the absorber.) Finally a range chamber completes the apparatus, and provides positive identification for the muon. Here, for $p_\mu < 4$ GeV/c the range is measured and compared to that expected from the momentum measurement; for $p_\mu > 4$ GeV/c reemergence should suffice as a positive μ signature, if no "scattering" is seen in the range chamber.

The trigger may be simply a threefold coincidence of hodoscopes H_1, H_2, and H_3 in the range chamber, the position of which would set the minimum p_μ accepted.

The apparatus will detect muon pairs. For low pair masses the acceptance is good, but for higher masses it depends strongly on the $p_\perp$ distribution of the pair.

---

3. Depleted uranium should probably be used to reduce cost. In this case, however, detectors near absorber must be protected from the radiation. The material in the range chamber is $\sim$ 200 tons!

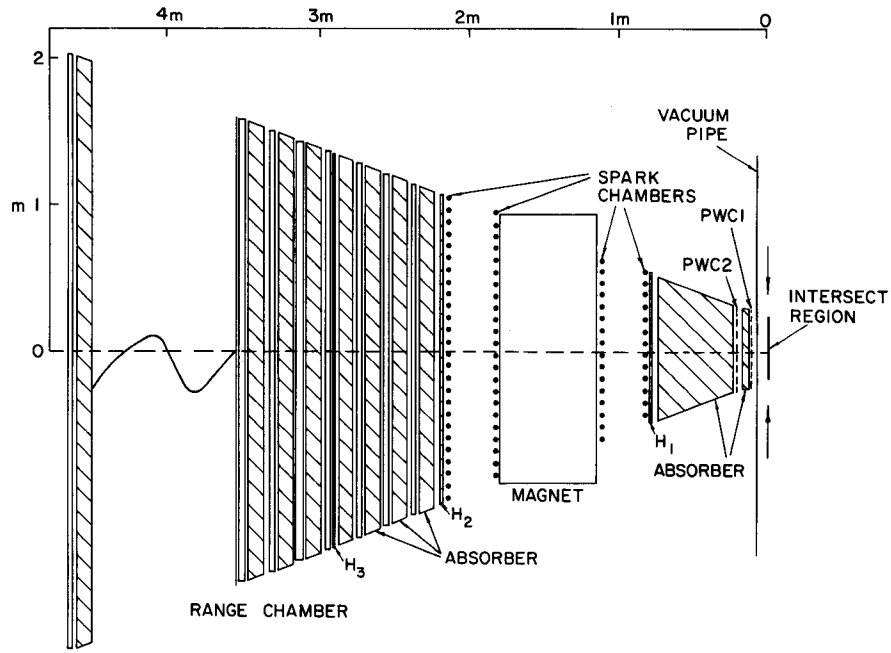

Fig. 1. Apparatus to observe muon production near 90°.

The ratio of direct muons to decay muons can be roughly estimated as follows: At 5 GeV/c the decay length of K^+'s is 37 m. With a mean path before absorption of 28 cm, 0.75% will decay, and 2/3 of these will give μ^+. Taking parent/daughter relation into account, the ratio (μ^+ from K^+ decay)/K^+ will be $\sim 5 \times 10^{-4}$ (depending on the $p_\perp$ spectrum used). If direct $\mu^+/K^+ \sim 2 \times 10^{-4}$, then direct μ^+/decay $\mu^+ \sim 0.4$. This ratio will vary roughly as $p_\perp^{-1}$. Clearly this is not an easy, elegant experiment. It may be better to try with beams of unequal energies to increase the K^+ decay length (as suggested by M.L. Good).

EXPERIMENTS USING A SINGLE ARM PARTICLE SPECTROMETER IN THE INTERMEDIATE ANGLE REGION AT ISABELLE

A. Kanofsky
Lehigh University

I discuss an apparatus that can be used to look at particle spectra in the intermediate angle region of 60° - 5° at ISABELLE.

Experiments using a similar apparatus have been run at the ISR to look at single particle inclusive reactions.[1] In these proceedings, Chien, Gordon, Kanofsky, Kramer, and Russ have discussed a 90° spectrometer for high momentum particles which would do particle identification up to 20 GeV (Ref. 2). This spectrometer covered an angle of $\pm 30^{\circ}$ about 90°. No discussion of particle identification below 2 GeV was included. Also particles above 20 GeV weren't discussed, especially since the rate at 90° should be very low.

I believe the 90° detector, suitably modified, could be used for the intermediate angle region. I now discuss the spectrometer and some of its modifications, needed by virtue of the larger number of particles and particles of high momentum. A rough drawing,with modifications needed for intermediate angles, is shown here in Fig. 1.

The apparatus consists of a bending magnet capable of going to 15 kG with wire planes before, in, and after the magnet. Momentum resolution is $\sim$ 2% at 200 GeV. Two Cerenkov counters after the magnet provide particle identification from 2 - 20 GeV. Below 2 GeV, timing on the scintillator planes in front and back can discriminate particle types. The length of the apparatus is $\sim$ 9 meters. Also, above 5 GeV, dE/dx measurements can discriminate particles.

---

1. British Scandinavian collaboration, ISR.
2. C. Y. Chien, H. Gordon, A. Kanofsky, M. A. Kramer, and J. Russ, "A Single Arm Spectrometer to Study High $p_{\perp}$ Processes Near 90° at ISABELLE", these Proc.

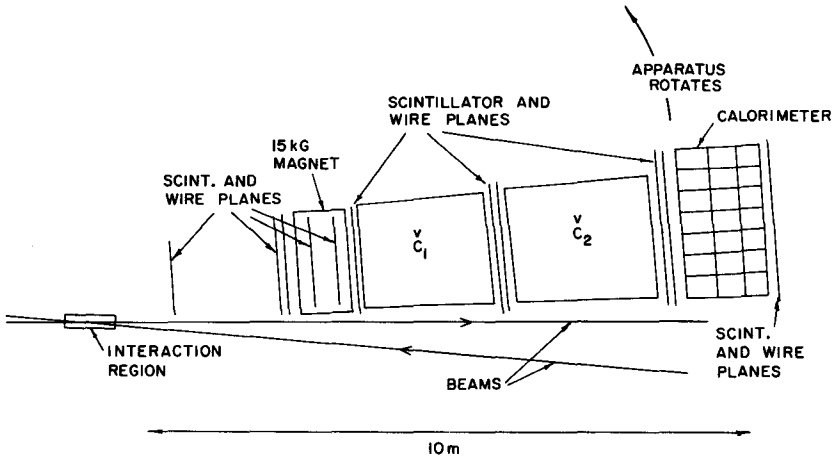

Fig. 1. Schematic arrangement of 90° spectrometer modified for use at intermediate angles.

A series of P.W.C. chambers[3] or a large drift chamber[4] could be used to determine the relativistic rise in dE/dx. Chambers 10 meters deep would have to be used to get an unambiguous measurement between π's, K's and p's. The longer the sampling region of dE/dx and the more samples taken, the better the ionization resolution. A value of 6.2% FWHM can be obtained from the 5 meter drift chamber described in Ref. 4. This would enable separation of π's and p's from 5 GeV to 100 GeV/c, where the plateau sets in. A 5 meter chamber gives a 5% overlap between p's and K's at 10 GeV/c momentum, an overlap of 1/2% between π's and K's, and essentially no overlap between π's and p's.

Now, if the distance of the chamber is increased to 10 meters, this would give a value of 4.5 FWHM for the ionization resolution and would result in about a 1% overlap between p's and K's and no overlap between π's and K's at 10 GeV/c momentum. There should be essentially no overlap between π's and p's all the way up to 100 GeV/c. Possibly a Cerenkov counter could be used above 20 GeV, but this would greatly reduce the rates because of the very low angular acceptance.

One of the properties of more forward spectrometer is that it should be able to discriminate between high and low momentum particles so as to record events discriminately and not have a lot of dead time reading in unwanted events. For example, the event rate at a luminosity of 10^{32} is 4 MC. If there is an average multiplicity of 20 particles/event, just on the basis of the 1/2 steradian solid angle subtended by the 90° detector without folding particles

---

3. D. Jeanne, P. Lazeyras, I. Lehraus, R. Matthewson, W. Tejessy, and M. Aderholz, Nucl. Inst. and Methods III, 28, 7-300 (1973); M. Aderholz, P. Lazeyras, I. Lehraus, R. Matthewson, and W. Tejessy, Nucl. Inst. and Methods, 123, 237-254 (1975).

4. W. M. Allison, C. B. Brooks, J. N. Bunch, J. H. Cobb, J. L. Lloyd, R. W. Pleming, Nucl. Inst. and Methods, 119, 499-507, (1974).

forward, we would expect about one particle into the spectrometer per event and hence a very high trigger rate. It could take about 1 millisecond to read the P.W.C.'s, etc., and hence the effective "live time" is considerably reduced from the actual time. However, if there is some preselection of the particle energy so as to only read in desired events, "live time" for the selected events can be increased considerably. Such a preselection can be made quickly with calorimeters of the type discussed for detection of jets.[5] These, since they absorb the particles, must be at the end of the spectrometer. They could be used for electron, hadron, and μ discrimination on the basis of pulse height. They should be segmented to accommodate several particles as well. Momentum discrimination could also be made on the basis of the wire coincidence matrix trigger, described in Ref. 2.

Finally, it should be possible to rotate the entire apparatus on tracks about the center of the intersection region. It will be necessary to move the magnet of the spectrometer further back from the intersection region so as to not interfere with the beam for the small angle particle detection.

Such an apparatus could be used to look for narrow jets, decay of neutral and charged resonances, and single particle inclusive cross sections in the region $.1 < x < .95$. It could be used in conjunction with the 4π detector, jet calorimeter array, or another single arm spectrometer to study particle correlations.

The costs would be that of the 90° spectrometer ($570 K) plus the additional cost of the calorimeters and P.W.C.'s for dE/dx measurements. We estimate an additional $200 K for the calorimeters and an additional $200 K for the P.W.C.'s.

---

5. A. Kanofsky, "A Calorimeter Experiment for Jet Studies", these Proc.

HIGH $p_\perp$ π^o DETECTOR AT ISABELLE

P. Grannis
SUNY, Stony Brook
D. Green
Carnegie-Mellon University

1. Introduction

The increased luminosity of ISABELLE over that of the ISR implies the possibility of extending the range of coverage of high $p_\perp$ events up to $p_\perp \simeq 20$ GeV/c. The simplest hadron to measure is the π^o; nonmagnetic analysis using Pb glass arrays is relatively cheap and straightforward for π^o energies $\lesssim 50$ GeV/c.

Initially one will measure the inclusive invariant cross section for $p + p \rightarrow \pi^o + x$ as a function of $x_\perp = 2p_\perp/\sqrt{s}$, $x_\parallel = 2p_\parallel^*/\sqrt{s}$, and s. At the ISR, measurements are limited to $\leqslant 10$ GeV/c and no substantial range of $x_\parallel$ outside of $x_\parallel = 0$ has been measured. The data has been fit to:

$$E\frac{d^3\sigma}{dp^3} \simeq \left[15\ (p_\perp)^{-8.24}\ e^{-13.1x_\perp}\right] \text{mb/(GeV/c)}^2 \qquad (1)$$

Since the simplest parton-quark pictures imply a $p_\perp$ exponent of - 4, it is clearly of interest to measure this exponent at the highest c.m. energies.

It is also of great interest to measure the $x_\parallel$ dependence over some substantial range of $x_\parallel$. Typical parton models predict a factor of $(1-x_\parallel)^m$ in the invariant cross section with $3 \leqslant m \leqslant 9$. For coverage in the range $0 < x_\parallel < 0.5$, one then expects a variation in cross section at fixed $p_\perp$ of a factor 8 or greater. One also wishes to see if this cross section factorizes as $E(d^3\sigma/dp^3) = F(x_\perp)g(x_\parallel)$ or if perhaps $E(d^3\sigma/dp^3) = f(x)$ where $x = \sqrt{x_\perp^2 + x_\parallel^2}$.

If the Pb glass array is mounted along with a 4π detector, then semi-inclusive data can be taken simultaneously with the inclusive data. ISR data at moderate $p_\perp$, $\leqslant 4$ GeV/c, showed that the π^o momentum was balanced by ~ 1 extra charged track/GeV in $p_\perp$. This balance was achieved in a region of ϕ opposite to the π^o with $\Delta\phi \sim 120^o$ FWHM, and a region of η with $\Delta\eta \sim 4$ FWHM where $\eta = - \log [\tan (\theta/2)]$. These spatial regions were roughly $p_\perp$ and s independent for $2 < p_\perp < 5$ GeV/c.

A typical parton jet picture would suggest, for events containing a $p_\perp = 20$ GeV/c π^o, jet multiplicities between 8 and 20. It is expected that a large fraction of these jet particles will be emitted within a rather narrow cone (half-angle in the vicinity of 10°). The existence of such a jet seems so compelling within parton models that it would be a major failure for them if it were not observed. If present, a highly desirable study of its properties could be undertaken with a large aperture spectrometer system around $\theta_{cm} = 90^o$. In this way the distributions of jet particles in angle and momentum could be measured.

The extent to which the jet particles balance the $p_\parallel$ of the high $p_\perp$ trigger particle is also of great interest. At the ISR, the observation has been made that the jet tends to balance $p_\parallel$ to some degree. However, it has been difficult to separate kinematic and dynamic effects. At ISABELLE, kinematic effects are somewhat reduced due to the increased rapidity space available.

Finally, one may contemplate $e^\pm$ detection at very high $p_\perp$. For reasonable assumptions about $W^\pm$ production and decay, $W^\pm$ bosons with mass ~ 100 GeV/c^2 would yield $\geqslant 200$ events/day. The intrinsic width in $p_\perp$ of the events from W decay at $\theta_{cm} = 90^o$ is less than the Pb glass resolution.

The background expected from hadron cascades is not clear. We investigate some plausible extrapolations of present data which suggest that such backgrounds should be small, particularly if

modest hadron rejection is obtained through the use of a transition radiation detector.

2. Apparatus

The apparatus as shown in Fig. 1 is arranged to run in conjunction with the 4 π detector.[1] It consists of a 10 $\times$ 10 array of Pb glass blocks 15 $\times$ 15 $\times$ 50 cm^3 ($\sim$ 21 radiation lengths deep). The energy resolution is assumed to be $\Delta E/E \sim 0.14/\sqrt{E}$ with E in GeV/c and ΔE the FWHM. This result ignores leakage of the shower out of the array. At a depth of 10 radiation lengths, a 50 GeV photon initiated shower contains one electron with $E > 0.5$ GeV on average. Hence, the leakage problem should be minimal.

The 2 photons from the π^o pass through a veto scintillator hodoscope, convert in a $\sim$ 2 radiation length Pb sheet, and are counted in a 2nd scintillator hodoscope. The shower conversion point is registered in a proportional wire chamber and the energy is measured in the Pb glass array. The π^o angle (and hence $P_\perp$) would be poorly known if no interaction vertex were measured. Given that the spectrum is steeply falling in $p_\perp$, the π^o angle must be well measured. The interaction vertex is obtained by charged track reconstruction in the drift chambers of the 4π detector. This vertex and the γ conversion point give a sufficiently accurate π^o angle measurement.

The trigger scintillators cover lab angles of $24^o \leqslant \theta \leqslant 69^o$ and $\Delta\phi/2\pi \sim 0.15$. The size of the interaction diamond at 200 $\times$ 200 GeV/c contributes an additional angular spread of $21^o \leqslant \theta \leqslant 75^o$. As we mentioned above, one wishes to cover as large a range of $x_{\parallel}$ as possible. The kinematic range of the apparatus is shown in

---

1. The 4π detector system is here assumed to be that proposed by S. U. Chung, P. Grannis and D. Green "A 4π Detector Experiment for ISABELLE", these Proc.

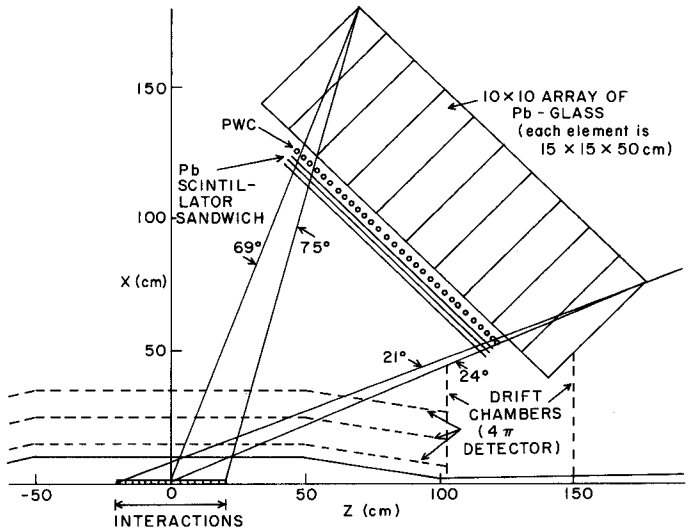

Fig. 1. Array of lead glass blocks to detect high $p_\perp$ photons.

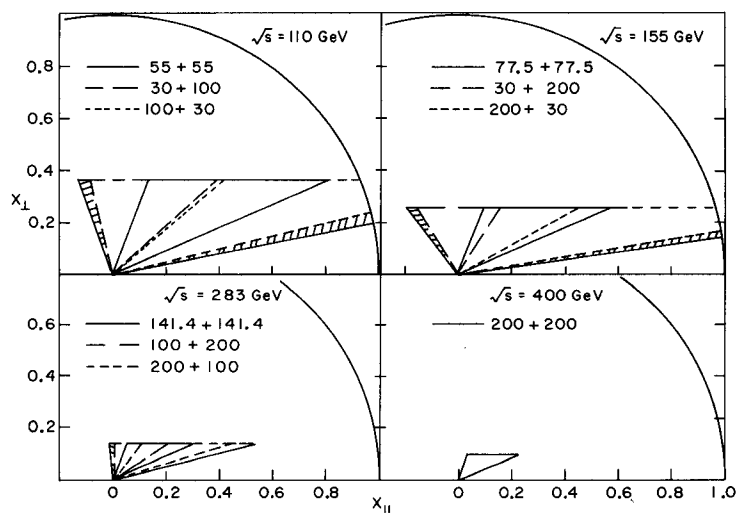

Fig. 2. Kinematic regions covered by photon detector.

Fig. 2. We assume $p_\perp < 20$ GeV/c due to rate limitations. The energy deposited in the Pb glass array is then $p \lesssim 50$ GeV/c.

Data taken with symmetric beam runs has an inadequate span of $x_\parallel$ at the higher ISABELLE energies. To increase this range to $0.0 \leqslant |x_\parallel| \leqslant 0.5$ for $s \leq 80\ 000\ (\mathrm{GeV}/c^2)^2$, one uses asymmetric beam energies for a fixed detector position. The kinematic limits of Fig. 2 are given in Table I. One sees the adequate coverage of the desired kinematic region is obtained for all c.m. energies, $\sqrt{s}$, less than half of the maximum ISA $\sqrt{s}$ value. Keeping the detector fixed and varying the beam energies has the important advantage of minimizing the systematic error in the measurement of the $x_\parallel$ dependence.

The cost for this array would be ~ \$100K. In view of the range of kinematic variables covered, it seems that $\pi^{o'}$s are perhaps the cheapest and simplest high $p_\perp$ hadrons to measure.

3. π^o Rates, Errors

The apparatus subtends $\Delta\eta \simeq 1.0$ and $\Delta\phi/2_\pi \simeq 0.15$. The CCR parameterization of the π^o cross section then yields $d\sigma/dp \simeq 2\pi(\Delta\eta)(\Delta\phi/2\pi)(15)\ p_\perp^{-7.24} e^{-13.1x_\perp}$ mb/(GeV/c). No dependence on $x_\parallel$ has been assumed. For the full luminosity of a standard initial insertion, $L \simeq 2.6 \times 10^5/(\mathrm{mb})(\mathrm{sec})$, the rates/(day)(GeV/c) shown in Fig. 3 are obtained. Note that the ISR, with over 10 times lower luminosity, yields only ~ 10 events/(day)(GeV/c) at $p_\perp$ = 10 GeV/c. With this apparatus at $s = 80\ 000\ (\mathrm{GeV}^2)$ one obtains ~ 250 events/day with $p_\perp > 16$ GeV/c. This rate assumes no $(1 - x_\parallel)^m$ factor. This factor should give a falloff of a factor ≥ 8 as $x_\parallel$ goes from 0.0 to 0.5.

These rates are sufficient to map out the cross sections for $p_\perp < 20$ GeV/c to good accuracy in ~ 1 week runs at each energy. We wish to find $E(d^3\sigma/dp^3) = F(x_\parallel, x_\perp, s)$. The error on s is negligible. At this luminosity the event rate is ~ 10 MHz. Given a

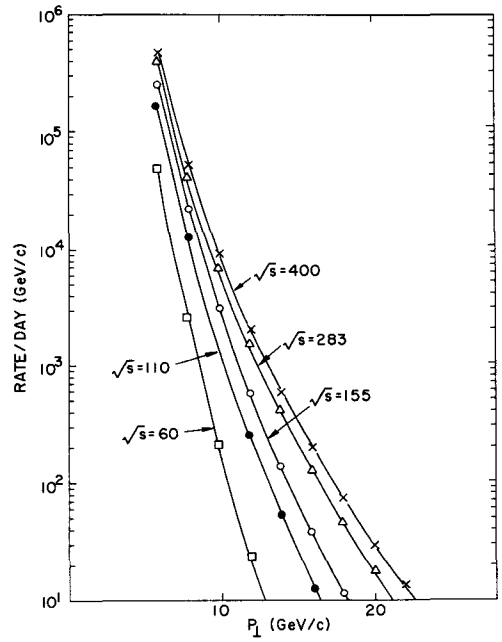

Fig. 3. Expected detection rates for high $p_\perp$ π^0's.

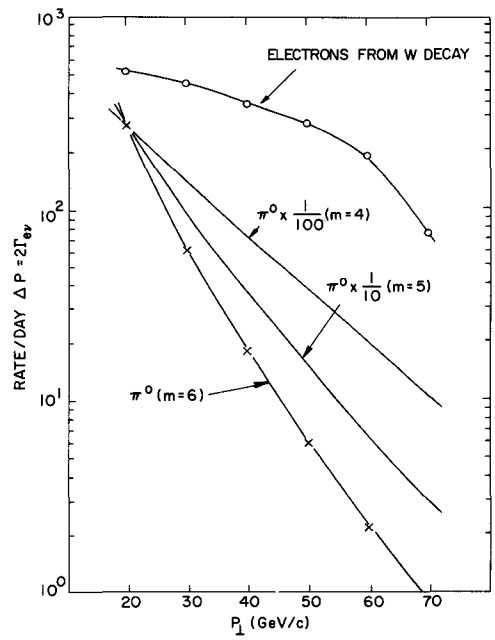

Fig. 4. Expected detection rates for electrons from W decay.

TABLE I. Kinematic Regions Covered for

$24^{\circ} \leq \theta_{lab} \leq 69^{\circ}$, $p_{\perp} = 20$ GeV/C

$\sqrt{s}$ (GeV)	E_1 (GeV)	E_2 (GeV)	$x_{\perp}$(max)	$x_{\parallel}$(min)	$x_{\parallel}$(max)
110	55	55	0.358	0.140	0.187
	30	100		-0.084	0.400
	100	30		0.416	1.0
155	77.5	77.5	0.258	0.099	0.580
	30	200		-0.156	0.164
	200	30		0.451	1.0
283	141.4	141.4	0.141	0.054	0.318
	100	200		0.004	0.214
	200	100		0.111	0.460
400	200	200	0.100	0.038	0.225

live time of $\sim$ 100 nsec for the 4π detector, as well as for the Pb glass pulse height analysis time, one typically has a second event along with the event containing the high $p_\perp$ π^o. The 4π apparatus can distinguish events with multiple vertices. For these events with extra vertices seen the π^o vertex is not known. Rejection of multiple vertex events will lead to a deadtime event rate loss of $\sim$ 50%.

Triggers with a single event vertex will be assigned a π^o energy equal to the total energy deposited in the four Pb glass blocks nearest the γ conversion points as given by the PWC information. Extra energy deposited on these blocks will make this assignment an overestimate.

At the ISR the total charged particle rate is $(d\sigma/dy)_{y=0} \sim$ 45 mb with $< p_\perp > \sim 0.32$ GeV/c. The π^o rate is $(d\sigma/dy)_{\pi^o} \sim 23$ mb with the same $< p_\perp >$. For the standard luminosity this means a rate in the Pb glass array $R = R_c + R_{\pi^o} \sim 2.8$ MHz (28 kHz per Pb glass block). This rate is not impossible to live with.

A typical event has 0.01 charged tracks and 0.005 π^o within the 4 blocks containing the high $p_\perp$ π^o. The typical charged particle gives Cerenkov light equivalent of $\leq$ 0.75 GeV energy deposit. The mean π^o energy deposit is about $< p_\perp >/< \tan\theta > \simeq 0.72$ GeV. Thus the average energy deposit from low $p_\perp$ particles aimed at the detector zone around the high $p_\perp$ impact is about 11 MeV per event. Their effect may be partially compensated since the charged tracks are seen in the drift chambers and extra π^o's which convert are observed in the PWC plane.

The main error in the π^o energy is just the intrinsic resolution of the Pb glass. For E = 5 GeV/c, $\Delta E \sim 0.14\sqrt{E}$ is 0.31 GeV. For E = 50 GeV/c, ΔE is $\simeq$ 1.0 GeV. One assumes the interaction vertex

is known well by use of the 4π detector. We assume the π^o conversion point is known to 1 cm FWHM. For $p_\perp$ = 10 GeV/c, $\delta p_\perp$ is $\sim$ 0.6 GeV/c. The error in $p_\perp$ is dominated by the energy resolution of the Pb glass array. Similar error estimates obtain for $\delta p_{\parallel}$. These errors are sufficiently small so that the expected structure in the cross section as a function of $x_\perp$ and $x_{\parallel}$ can be adequately measured.

The luminosity monitoring required for this experiment is not stringent. A 5% monitor will be sufficient to cross-normalize different runs. The number of π^o will be in error due to the triggering requirements. Runs taken without the veto requirement and using the drift chambers to track to the PWC will be made to measure this correction factor.

The 4π detector will supply good angular coverage, good multiplicity determination and good $(\theta,\emptyset)$ measurements for all charged tracks. This apparatus is of sufficient accuracy to supply detailed semi-inclusive information as to possible jet structure accompanying a high $p_\perp$ π^o.

4. Search for $W^\pm, Z^o$

The apparatus proposed could make a useful search for the intermediate bosons $(W^\pm, Z^o)$ through observation of a single electron at very large $p_\perp$. We rely here on the observation of a sharp peak in the $p_\perp$ dependence of electrons near $M_W/2$, due to decays $W^\pm \rightarrow e^\pm \nu$ (or $Z^o \rightarrow e^+e^-$). For this study we envision the Pb glass array centered at θ=90°. We focus attention on the rates expected for $W^\pm$ detection, assuming top ISABELLE energy, L = 2.6 x 10^{32} cm $^{-2}$ sec^{-1}, and $(W \rightarrow e\nu/\text{all}) = 1/3$. The Pb glass array discussed in Section 2 would subtend about 1 sr. Table II gives the expected rates of electrons as function of the mass of $W^\pm$ within a $p_\perp$ bin of width $2\Gamma_{e\nu}$. Here we assume $p_\perp$(electron) = $M_W/2$.

TABLE II. Expected Electron Rates from Intermediate Boson Decay

M_w(Gev)	$d\sigma/dp_\perp$ (cm^2/GeV/c)	$\Gamma_{e\nu}$ (Gev)	Rate/day
40	5×10^{-34}	0.024	520
60	1.5×10^{-34}	0.08	450
80	5×10^{-35}	0.19	350
100	2×10^{-35}	0.37	280
120	8×10^{-36}	0.64	190
140	2×10^{-36}	1.02	75

Clearly a one week run at full luminosity gives sufficient events <u>in the absence of backgrounds</u> to detect the sharp spike in the $p_\perp$ distribution which would characterize vector boson production.

The width of the characteristic peak in $p_\perp$ is largely determined by the detector resolution. For $p_\perp = 20$ GeV/c, $\delta p_\perp$ is .76 GeV/c and for $p_\perp = 70$ GeV/c, $\delta p_\perp = 1.2$ GeV/c. Typically $\delta p_\perp$ is large compared to $\Gamma_{e\nu}$. However, a sharp spike in $p_\perp$ with $\delta p_\perp / p_\perp \lesssim .025$ will still occur at the rate of $\gtrsim 50$ events/day for W masses with $M_W < 140$ GeV/c.

It is extremely unclear what background levels to expect at the very high $p_\perp$ anticipated here. We assume the dominant source of background to come from high $p_\perp$ γ's from π^o decay ("direct" electron production is lower by 10^4 at present energies). If the π^o cross-section follows the functional dependence given by Eq'n (1), above, then the background levels are negligible for $p_\perp >$ 20 GeV/c. In order to simulate an electron, the photons must be accompanied by a nearby charged particle, reducing the effect of photon backgrounds by an order of magnitude or more. However, ISR experiments searching for anomolous electrons were swamped by an unexpectedly large flux of γ's. We therefore ask by what factor could one tolerate an increase in π^o yields and still expect to observe the spike in electron yield at $M_W/2$.

We estimate background rates by the following simplified method. We hypothesize that the form of the π invariant cross-section for $p_\perp \geq 20$ GeV/c at ISABELLE be given by

$$E \frac{d^3\sigma}{dp^3} = A\, p_\perp^{-m}\, f(x_\perp).$$

We take $f(x_\perp)$ to be the same as that determined at the ISR ($e^{-13.1\, x_\perp}$) since our $x_\perp$ range is identical to that of the ISR. The scaling power m is allowed to vary down to m = 4 as hypothesized by constituent scattering models. The normalization is fixed

to that observed at the ISR at $p_\perp = 2$ GeV/c. The expected number of events due to background (with no suppression due to neutral particle veto included) is shown in Figure 4 for several values of m. Also shown are the expected electron rates from W decays from Table II. All rates are for a $p_\perp$ bin of $2\Gamma_{e\nu}$ at the indicated $p_\perp$ value.

We observe from Figure 4 that even if the π^o spectrum has a characteristic $p_\perp$ dependence $(p_\perp)^{-4}$ the trigger background is never more than 100 times the anticipated electron yield from W decay. This will be reduced by requiring the energy in the lead glass to be associated with an incident charged particle (we anticipate a factor of 10 rejection here). Further hadron rejection could be achieved by a transition radiation detector before the Pb glass to tag electrons.

Charged hadrons pose considerably less problem since they typically deposit a very small amount of energy (750 MeV on average) in the Pb glass detector. Thus, unless totally new mechanisms for electron or hadron production arise in this high $p_\perp$ region at ISABELLE, we expect to be able to find the electrons from W decay in the Pb glass detector array.

SINGLE PARTICLE SPECTRA AT HIGH TRANSVERSE MOMENTUM AS A FUNCTION OF X

M. L. Good, SUNY, Stony Brook

We consider a single arm spectrometer set at a fairly small laboratory angle ($\sim 3^{\circ}$) measuring the angle and momentum of hadrons by hodoscopes and MWPC's, with magnetic deflection (Fig. 1). The magnet, which is set on edge, has $\int Bdl = 32$ kg-m and the aperture is 8 X 51 cm. (The 51 cm dimension is the gap.)

The hadrons are identified as to π, K, or p by two atmospheric pressure Cerenkov counters: C1, filled with He, and C2, filled with a N_2 - Ne mixture. Complete particle identification is possible with these counters in the range 32 - 58 GeV/c,* and the spectrometer is set to cover this range. It is a direct copy of the Columbia-FNAL spectrometer at Fermilab, with hadron identifying Cerenkov counters as presently being designed by a Stony Brook group.

The deflection is vertical, thus decoupling the momentum determination from the production angle, and all detectors are downstream of the magnet, out of the neutral beam and out of the high flux of low momentum charged particles. The solid angle subtended is ~ 0.32 millisteradian, constant over the above momentum range.

---

* The Counter specifications are

	C1	C2
Length	12 m	4 m
Gas	He	N_2 - Ne
Aperture	104 cm wide X 33 cm high	130 X 52 cm
Tubes	Three 2" quantacons isolated from He by a quartz window	Three 5" 58 DVP's with wave length shifter
No. Photoelectrons	8	8

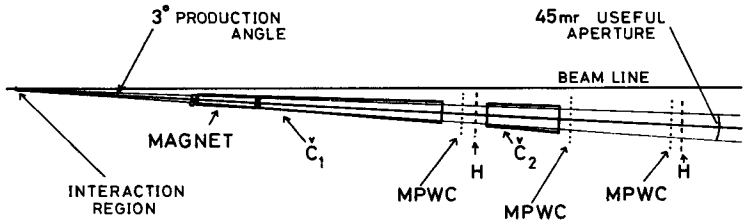

Fig. 1. Intermediate angle single-arm spectrometer. Deflection is vertical by $\sim 1^{\circ}$. Counter C1 starts inside the magnet.

Such a spectrometer should have no difficulty measuring, in one setting, the particle spectra at $p_\perp \sim 2$ to 3 GeV/c in the range $0.5 < x \leqslant 1$, with the ISA set at an asymmetric condition such that the beam coming toward the spectrometer is of energy $E_1 =$ 60 GeV/c, and the other beam is at full energy: $E_2 = 200$ GeV/c. ($E_{secondary} \leqslant E_1$ corresponds to $x \leqslant 1$).

Now consider what happens if the beam energies are varied, keeping E_1E_2 constant: $s \leqslant 4E_1E_2$ remains constant; for fixed spectrometer settings, the lab momentum, lab angle, and $p_\perp$ also remain constant. All that changes is the x range covered. At the opposite extreme ($E_1 = 200$, $E_2 = 60$) the x range for the same 32 - 58 GeV/c lab momentum range, is $0.16 < X < 0.29$. Thus the entire range of x, except for $x \leqslant 0$, is covered.

The counting rates, for the CCR parameterization (x=0) are ~16 counts/sec in a $\Delta p_\perp = 0.5$ GeV/c at $p_\perp = 3$ GeV/c, times whatever loss factor is entailed by working at nonzero x.

SEARCH FOR FRACTIONALLY CHARGED QUARKS AT ISABELLE

K.J. Foley
Brookhaven National Laboratory
and
B.T. Meadows*
University of Cincinnati

I. INTRODUCTION

Since first suggested 12 years ago by Gell-Mann and Zweig[1] to be the basic hadronic building blocks which would explain the SU(3) symmetry of the hadrons, quarks remain today as merely literary entities[2] - though probably four in number rather than three. Attempts have been made to find free quarks with masses $\leq$ 5 GeV using "conventional" 30 GeV accelerators,[3] $\lesssim$ 25 GeV using the ISR,[4,5] and, also without success, even more massive quarks

*Work supported by the National Science Foundation.

1. M. Gell-Mann, Phys. Lett. 8, 214 (1964); G. Zweig, CERN Reports TH401, 402.
2. James Joyce - "Finnegan's Wake".
3. Yu.M. Antipov, I.I. Karpov, V.P. Khromov, L.G. Landsberg, V.G. Lapshin, A.A. Lebedev, A.G. Morosov, Yu.D. Prokoshkin, Yu.V. Rodnov, V.A. Rybakov, V.A. Rykalin, V.A. Senko, B.A. Utochkin, N.K. Vishnevsky, F.A. Yetch, and A.M. Zajtzev, Phys. Lett. 29B, 245 (1969); J.V. Allaby, G. Bianchini, A.N. Diddens, R.W. Dobinson, R.W. Hartung, E. Gygi, A. Klovning, D.H. Miller, E.J. Sacharidis, K. Schlupmann, F. Schneider, C.A. Stahlbrandt, and A.M. Wetherell, Nuovo Cimento No. 10, 64A, 75 (1969).
4. M. Bott-Bodenhausen, D.O. Caldwell, C.W. Fabjan, C.R. Gruhn, L.S. Peak, L.S. Rochester, F. Sauli, U. Stierlin, R. Tirler, B. Winstein, and D. Zahniser, Phys. Lett 40B, 693 (1972).
5. B. Alper, H. Boggild, P. Booth, F. Bulos, L.J. Carroll, G. vonDardel, G. Damgaard, B. Duff, F. Heymann, J.N. Jackson, G. Jarlskog, L. Jonsson, A. Klovning, L. Leistam, E. Lillethun, G. Lynch, G. Manning, M. Prentice, D. Quarrie, and J.M. Weiss, Phys. Lett. 46B, 265 (1973).

were sought in cosmic ray experiments.[6] Upper limits for production cross sections for quarks are mass and model dependent. The best published results are generally about 10^{-34} cm^2 for isotropic production. Reasons for the failure to find these particles include the possibilities that they are too massive to have been found using existing accelerators, that they are confined quantum mechanically within the hadrons, or that they do not exist.

In the former two cases, there is the possibility that the availability of a new range of s from ISABELLE might lead to their discovery, and a search for free quarks should certainly be made. Such a search should place as low an upper limit on free quark production as possible or, alternatively, yield unambiguous evidence for their existence.

We propose a relatively simple experiment which will be sensitive to "conventional" quarks of charge 1/3e or 2/3e, and mass less than 200 GeV. The experiment uses a modest amount of conventional equipment, no magnetic momentum analysis and, in a period of one week will achieve a sensitivity of $10^{-36}cm^2$ to isotropic quark production ($m < 200$ GeV) - several orders of magnitude less than that obtained from cosmic ray data ($m < 20$ GeV), and from the ISR ($m < 25$ GeV) and comparable to cross sections for

---

6. A.F. Clark, R.D. Ernst, H.F. Finn, G.G. Griffin, N.E. Hansen, D.E. Smith, and W.M. Powell, Phys. Rev. Lett. 27, 51 (1971); Y. Fukushima, T. Kifune, T. Kondo, M. Koshiba, Y. Naruse, T. Nishikawa, S. Orito, T. Suda, K. Tsunemoto, and Y. Kimura, Phys. Rev. 178, 2058 (1969).

m < 5 GeV using the CERN PS. Despite the simplicity of this experiment, the signature provided by a fractionally charged quark should be unambiguous, since a certain amount of redundant information is provided by the apparatus.

We first describe the method, and then our apparatus. In sections IV and V we discuss background and counting rates and finally in section VI we give a cost estimate for this experiment.

II. EXPERIMENTAL METHOD

We plan to search for fractionally charged particles using a method similar to that employed by a CERN-Munich collaboration[4] at the ISR. Three telescopes (See Fig. 1) each consisting of 9 scintillation counters and 5 x-y pairs of proportional wire chambers (PWC's) will be used: the scintillators will measure dE/dx while the PWC's will permit the determination of the particle trajectory. In this way, a fiducial volume may be defined in a way which will make it possible to eliminate experimental background from particles traversing photomultiplier tubes, gamma showers, edge effects in scintillators, etc. Our search will concentrate on particles produced near 90° in the laboratory ($\sim 90^{\circ}$ in cms). If it is true that quarks have not yet been observed because they are confined within a quantum mechanical "bag" which may be burst at ISA energies, then they are just as likely to be produced at 90° as at any other angle, and the quark to pion ratio in this region will thus be greater than nearer to 0°. If, on the contrary, the quarks are merely too massive (< 25 GeV) to have been produced in the ISR experiments, then their angular distribution should not be too dissimilar to ordinary hadrons, and looking at 90° will simply result in a smaller sensitivity to

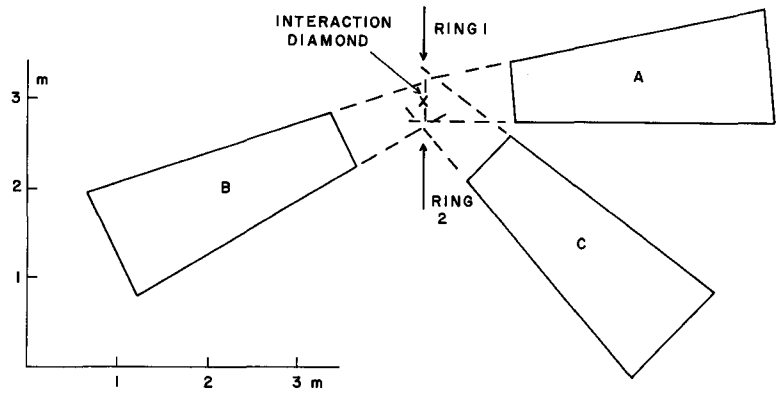

Fig. 1 Arrangement of three telescopes relative to intersection diamond.

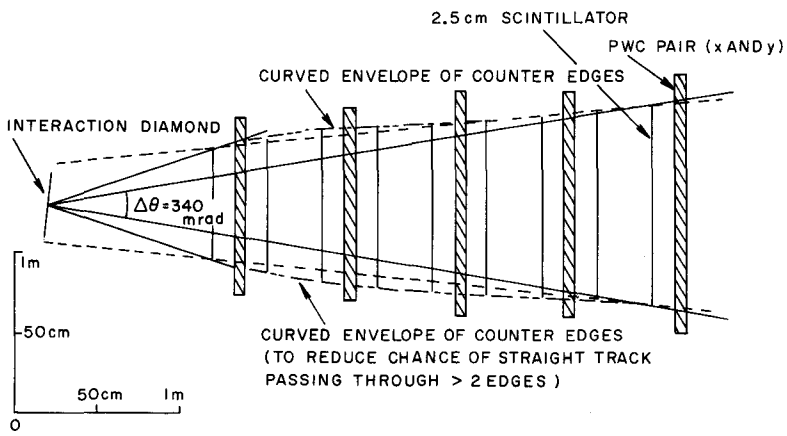

Fig. 2. Arrangement of counters and proportional wire chambers in each telescope.

their detection.[7]

Our trigger, which will be applied independently to each telescope, will require that a certain number (say 4) of the 9 scintillators produce a pulse height ≤ 0.9 I, and that at least 8 produce a signal of ≥ 0.05 I, where I is the height of a pulse generated by a minimum ionizing singly charged hadron. In addition, we shall require that at least 4x (or 4y) PWC's contain a single cluster within the same ($\leqslant 100$ nsec) gate. The ISA diamond will be constantly monitored by triggers requiring singly charged, minimum ionizing particles in the telescopes. Offline processing of such triggers will include the requirement that a single track be seen in the PWC's within a certain fiducial region. Time of flight information from each scintillator may also be used to provide redundant information in the event a "quark" event is observed.

III. APPARATUS

The three telescopes A, B and C are almost identical. Their arrangement around the interaction region is illustrated in Fig. 1. Each covers a θ range of approximately 1/3 radian, and the combined coverage is about 940 mrad from 90°. The coverages in $\eta (= -\log \tan \theta/2)$ and other parameters for each telescope are summarized in Table I.

---

7. In spite of these arguments, the measurements must eventually be extended to small production angles; these measurements will require very clean machine operation and will probably be carried out in a later stage of the experimental program.

TABLE I

Telescope	Range of $(\theta-\pi/2)$ (mrad)	Range of η ($\approx y$)	Counting Rate/sec.	Sensitivity counts $10^{-34}cm^2$/week
A	-56 to +270	-0.06 to +0.27	4×10^5	~ 180
B	270 to 610	0.27 to 0.65	5×10^5	~ 180
C	610 to 940	0.65 to 0.12	6×10^5	~ 180

Factors influencing the design of the telescopes are that

a. as large a $\Delta\theta$ as possible be covered by each;

b. the whole interaction diamond should be viewed;

c. the largest scintillator should be no larger than 4 ft $\times$ 4 ft so that good dE/dx information could be obtained;

d. the counter closest to the ISA should receive no more than an average of 1 particle/600 nsec at the design luminosity (2.6×10^{32} cm^{-2} sec^{-1}) so that the efficiency is high;

e. a single track cannot cross more than 2 scintillator edges;

f. the time of flight uncertainty for $\Delta\tau = 0.5$ nsec should be about 5% at $\beta \sim 1$.

The scintillator thickness (2.5 cms) is chosen to give an estimated 50 photoelectrons from a 1/9 minimum ionizing particle. The effect of the Landau tail in the dE/dx distribution of each counter will not only reduce the probability that π's fake fractionally charged particles, but also reduce the efficiency for finding real ones. The presence of 9 counters should, however, somewhat neutralize the effect of these tails as well as enhance, statistically, the results of the dE/dx measurements.

The detailed design of the PWC's will require that they operate if crossed by a 1/9 minimum ionizing particle with reasonable efficiency. The existence of 5 x-y pairs of chambers is to improve the chances of finding such tracks.

Our electronic equipment, in addition to that required for measuring pulse heights from scintillators, reading out PWC's and performing cluster tests on them, will include timing electronics for the scintillator signals relative to that from the first counter (closest to ISABELLE). As a refinement, we may also make crude measurements of pulse heights from the PWC's (!).

IV. BACKGROUND

The chief sources of background will be from

a. photon showers;

b. particles traversing a number of photomultiplier tubes;

c. particles traversing scintillator edges.

Experience by the CERN-Munich collaboration shows that (a) is the most potentially serious. The greater luminosity of the ISA over the ISR is sure to aggravate this, and is the reason for our choice of a more substantial PWC coverage of our telescopes, since photon showers are unlikely to fake single tracks. The high luminosity of ISA will also enhance the nuisance value of the other background sources, and we shall probably need to mask our photomultipliers with vetoes. The design of our telescopes is such that edge effects should be minimal.

V. SENSITIVITY AND ESTIMATED RATES

Various assumptions must be made to estimate counting rates in our apparatus.

a. the design luminosity for a standard insertion is achieved (2.6×10^{32} cm^{-2} sec^{-1})

b. the total cross section for pp collisions is 62 mb at $\sqrt{s}$ = 400 Gev. (This is the number obtained from a $(\log s)^2$ extrapolation from ISR, and nearly agrees with a log s extrapolation.)

c. the mean number of particles produced per interaction in the central plateau region in rapidity (y) is 1.5 per unit y. This is the same number as produced at the ISR[8]. Assum-

---

8. G. Giacomelli, SLAC Summer Institute on Particle Physics, (1974), Fig. 7.3 from Stony Brook - Pisa Collaboration.

ing that the range of the plateau region expands like log s as does the particle multiplicity, this is a reasonable assumption.

1. Counting Rate

The mean number of background counts in one of our telescopes per second is given by

$$< n > \approx \sigma_{pp}^{TOT} \times L \times (1.5\ \Delta\eta) \times \frac{\Delta\phi}{2\pi}$$

where $\Delta\eta$, $\Delta\phi$ are the acceptances in η and azimuthal angle ϕ. Our telescopes have square cross sections (i.e. $\Delta\phi = \Delta \approx \Delta\eta$). Inserting values for these, we obtain the figures in the penultimate column of Table I.

2. Sensitivity

Our sensitivity to quark detection will be model dependent. To compare with other experiments, we assume that the produced quarks are isotropic in the center-of-mass system, and are all minimum ionizing ($\beta \sim 1$). In this case, a simple calculation shows that, if $L = 2.6 \times 10^{32}$ cm^{-2} sec^{-1} our sensitivity is approximately 5 events/10^{-36} cm^{2}/week (7 days at 24 hours).

VI. COST

The cost of the apparatus is dominated by the PWC's. With ten planes per telescope, the cost for 2mm wire spacing is about $100 000 per telescope. The cost of scintillation counters is about $10 000 per telescope.

MONOPOLE SEARCHES AT ISABELLE

G. Giacomelli
Fermi National Accelerator Laboratory
and
University of Bologna
and
A. Thorndike
Brookhaven National Laboratory

I. GENERAL STATUS

There are a number of particles that might be found at ISABELLE, among which intermediate bosons, quarks or partons, and magnetic monopoles are the most obvious. A demonstration of the existence of any one of them would be a very important result for physics. Many physicists consider such a demonstration probable for intermediate bosons, and such experiments will receive a major effort. Quark or partons are more speculative, and few physicists would bet heavily on monopoles.

The reasons are mainly that monopoles were proposed long ago, by Dirac in 1931,[1] that various quite sensitive searches have given

---

1. P.A.M. Dirac, Proc. R. Soc. London, 133, 60 (1931).

negative results,[2-10] and that there are no experimental observations that are considered to require their existence by indirect arguments. Nevertheless, there are current monopole searches in cosmic rays, at Fermilab, and at the CERN ISR, and the topic retains a certain interest.

If such experiments should yield a reasonably convincing positive result before the completion of ISABELLE, it is clear that monopole experiments at ISABELLE would advance to a high priority. If we assume that results will continue to be negative, it still seems worthwhile to continue the search at ISABELLE, provided it can be done in a meaningful way without great expense and effort. The following discussion will show that such appears to be the case. This discussion is then based on the following assumptions: (1) by 1982 monopoles have not been found, (2) this indicates that, if they exist, they are very massive, (3) other monopole properties are as they are usually assumed to be.

---

2. E.M. Purcell, G.B. Collins, T. Fujii, J. Hornbostel and F. Turkot, Phys, Rev. 129, 2326 (1963).
3. E. Amaldi, G. Baroni, A. Manfredini, H. Bradner, L. Hoffman and G. Vanderhaeghe, Nuovo Cimento, 28, 773 (1963).
4. E. Goto, H.H. Kolm and K.W. Ford, Phys. Rev. 132, 387 (1963).
5. W.C. Carithers, R. Stefanski and R.K. Adair, Phys. Rev. 149, 1070 (1966).
6. R.L. Fleischer, H.R. Hart, I.S. Jacobs, P.B. Price, W.M. Schwarz and F. Aumento, Phys. Rev. 184, 1393 (1969).
7. R.L. Fleischer, P.B. Price and R.T. Woods, Phys. Rev. 184, 1398 (1969).
8. W.Z. Osborne, Phys. Rev. Lett. 24, 1441 (1970).
9. P.H. Eberhard, R.R. Ross, L.W. Alvarez and R.D. Watt, Phys. Rev. D, 4, 3260 (1971).
10. P.H. Eberhard, R.R. Ross, J.D. Taylor, L.W. Alvarez and H. Oberlack, LBL 3680, February, 1975.

There are three general ways to look for monopoles: (1) Since they would have very strong electromagnetic interactions, a search can be made for dense tracks in an appropriate detector, (2) monopoles would be trapped in solid matter and moving such matter through a conducting loop would induce an electric current in it,[11] and (3) produced in pairs monopoles might annihilate so quickly that they could be observed only as the production of a large number of γ-rays.[12]

If monopoles are so massive as to be impossible to produce at present accelerators, they should occur once in a while in cosmic rays. Perhaps they do. [The controversial event of Price et al. was reported some weeks after the summer study in Phys. Rev. Lett. 35, 487 (1975).] A number of peculiar interactions have been reported, that seem to have a lot of γ-rays.[13-15] They are hard to explain as statistical fluctuations, and do not have a generally accepted explanation at the present time. Experiments are in progress at FNAL and ISR to look for such multigamma phenomena, but if results of these experiments are negative or inconclusive, what might be found at ISABELLE remains an open question.

In the following an experiment to search for dense tracks is described by Giacomelli, an outline is given by Thorndike of a monopole collector for induced current detection, and, finally, some discussion is given of the multigamma approach.

---

11. L.W. Alvarez, M. Antuna, R.A. Byrns, P.H. Eberhard, R.E. Gilmer, E.H. Hoyer, R.R. Ross, H.H. Stellrecht, J.D. Taylor and R.D. Watt, Rev. Sci, Instrum., 42, 326 (1971).
12. M.A. Ruderman and D. Zwanziger, Phys. Rev. Lett. 22, 146 (1969).
13. M. Schein, D.M. Haskin and R.G. Glasser, Phys. Rev. 95, 855 (1954).
14. A. Debenedetti, C.M. Garelli, L. Tallone, M. Vigone, and G. Wataghin, Nuovo Cimento 12, 954 (1954) and 2, 220 (1955).
15. M. Koshiba and M.F. Kaplon, Phys. Rev. 100, 327 (1955).

II. SEARCHES FOR FREE MAGNETIC MONOPOLES AT ISABELLE

1. Introduction

Since the first proposal by Dirac in 1931,[1] many searches for magnetic monopoles have been performed, employing a variety of direct and indirect searches, all of which have yielded negative results.

The searches for free poles are based on the hypothesis that they should have a large magnetic charge g, according to the following relationship:

$$g = ng_o = \frac{1}{2}\frac{hc}{e}n \simeq n\frac{137}{2}e \qquad (1)$$

where e is the elementary electric charge and n is an integer, which in the original Dirac proposal could assume the values $n = 1, 2, 3, \ldots$; according to other authors n should be a multiple of 4.[16] If the elementary charge is that of fractionally charged quarks, then g_o in Eq. (1) would be three times larger. There is thus some uncertainty in the minimum allowed value of g; but even $n = 1$ implies a large magnetic charge and thus large effects. Because of the uncertainty in n, it is clear that searches for magnetic monopoles have to be designed in order to be sensitive to as large a range in n as possible, even for noninteger values and $n < 1$.

Because of the large g-value, magnetic poles are expected to have large masses. Theoretical estimates of the cross section for monopole production are difficult to make because of the large value of g, and thus of the coupling constant of poles to the electromagnetic field, $g^2/hc \simeq 34.2$; this prevents the use of any perturbation

---

16. J. Schwinger, Phys. Rev. 144, 1087 (1966); 151, 1048 (1966)

calculation.

The methods employed for searches for free magnetic poles may be classified into two groups:

(i) Direct detection of monopoles immediately after their production in high energy collisions.

(ii) Indirect searches, where monopoles are searched for long after their production.

Experiments of the second kind yield considerably better upper limits, since one may integrate the production over a long time; but one is forced to make a number of assumptions about the behaviour of monopoles in matter.

This note discusses the possibility of performing a search of type (i) and of type (ii) at ISABELLE.

2. Direct Search with Plastic Detectors

This search would use the same method as that used recently at the CERN-ISR by the Bologna-CERN-Roma Collaboration.[17] Magnetic monopoles, assumed to be produced in high energy proton-proton collisions, should have been detected with plastic detectors immediately after their production.

Figure 1 illustrates the setup employed at the CERN-ISR. Twelve stacks of plastic detectors were placed around the intersection region I1 of the ISR. Each stack consisted of 10 plastic sheets, each 300 μm thick, with a surface of 9×10 cm^2. The third and fifth sheets of each stack were of Makrofol-E, and the eight others of Nitrocellulose. The solid angle covered by the detectors was about 1/3 4π and the accepted azimuthal range was $30 \leqslant \theta \leqslant 90^\circ$.

---

17. G. Giacomelli, A.M. Rossi, G. Vannini, A. Bussiere, G. Baroni, S. di Liberto, S. Petrera and G. Romano,"Search for Magnetic Monopoles at the CERN-ISR with Plastic Detectors", Nuovo Cimento, to be published.

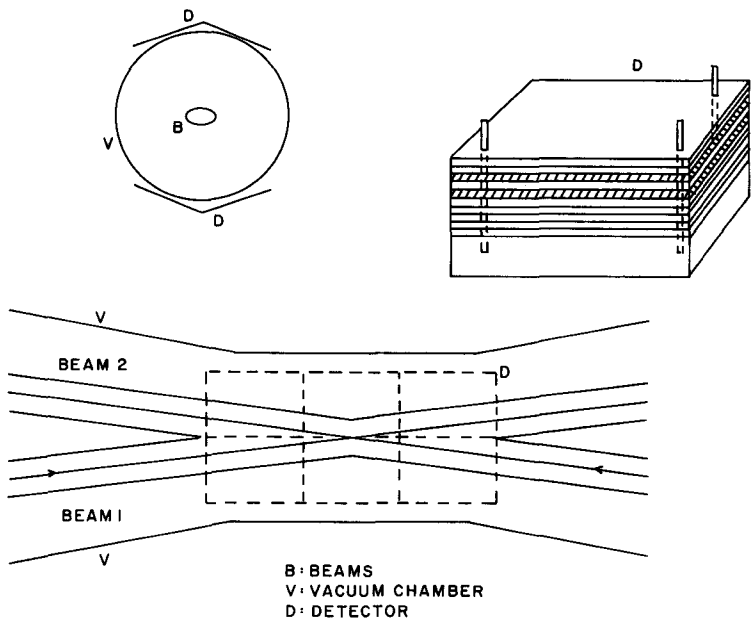

Fig. 1 Illustration of the experimental layout of the exposures at ISR and of the structure of each stack.

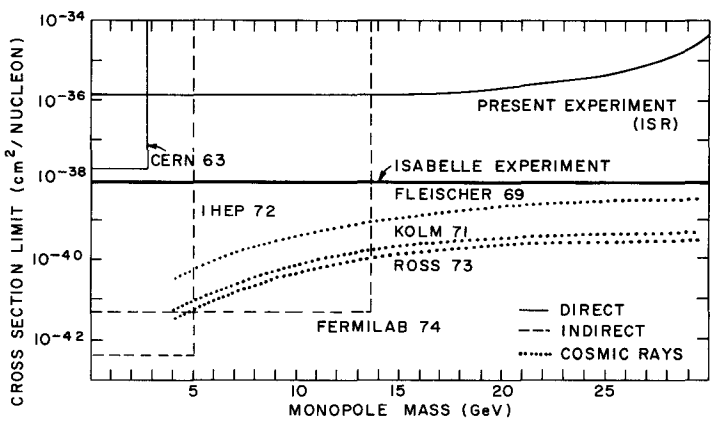

Fig. 2 Compilation of the recent upper limits for monopole production. Solid and dashed lines refer to direct and indirect measurements respectively at high energy accelerators; dotted lines refer to indirect cosmic ray experiments; large line refers to the limit expected from an experiment at ISABELLE.

Each plastic detector has its typical detection threshold: particles which ionize less than the threshold value are not detected at all. Nitrocellulose sheets are sensitive to particles which ionize more than 0.8 GeV/g cm^{-2}. The ionization energy loss of a monopole should be

$$\frac{dE}{dx}_{Pole} = \beta^2 n^2 \frac{g_o^2}{e^2} \left(\frac{dE}{dx}\right)_p \qquad (2)$$

where $(dE/dx)_p$ is the ionization energy loss of a proton with the same velocity β. For $\beta \simeq 1$, $(dE/dx)_{Pole} \simeq 9\ n^2$ GeV/g $cm^{-2} \simeq$ 4700 n^2 times the ionization of minimum ionizing particles. Nitrocellulose sheets are thus sensitive to relativistic monopoles with $n \geqslant 0.3$, while Makrofol-E is sensitive to $n \geqslant 0.7$. Nonrelativistic monopoles ionize less because of the factor β^2 in Eq. (2). The tracks are developed by means of chemical etching that proceeds preferentially along the particle trajectory.

A monopole candidate corresponds to a track which crosses at least the first Nitrocellulose sheet.

Because of the high dE/dx threshold values, plastic detectors may be used in a large background of minimum ionizing particles. After development the background tracks appear only at the two surfaces of each sheet. Consequently one may perform a quick scan by focusing the microscope in the middle of the sheets, where no background track is present.

In the ISR experiment two series of stacks were exposed each for about four months, when the ISR luminosity averaged 2×10^{30} $cm^{-2}sec^{-1}$. Since no monopole was observed the experiment yielded the following limits:

mass sensitivity $m_g \leqslant 20$ GeV

magnetic charge sensitivity $0.4\ g_o < g < 2.5\ g_o$

cross section upper limit (95% confidence level) $\sigma < 2 \times 10^{-36}$ cm^2.

A similar experiment could be performed at ISABELLE using the low-β region, with the obvious advantages of: (i) energy, which, in principle allows the search for monopoles up to 200 GeV mass; (ii) higher luminosity (10^{33} instead of 10^{30}-10^{31}). The smaller production angles may be a problem, but one should still be able to surround the intersecting region with plastic detectors, even at forward angle. This may require designing a special vacuum chamber with thin walls. If this is possible and if one can leave the detectors in place for about 6 months one should be able to reach the following limits (there should not be any problem of background in Makrofol-E, while there will be in Nitrocellulose):

$$m_g < 200 \text{ GeV}$$
$$0.5\ g_o < g < 4\ g_o$$
$$\sigma < 10^{-38}\ cm^2$$

This cross section limit compares very favorably with other types of searches made until now (see Fig. 2).

3. Indirect Search

This search would use the same method employed at the ISR by the Bologna-Fermilab collaboration.[18] An intersection region would be surrounded with iron pieces 2-4 cm thick. Magnetic monopoles produced in pp collisions would stop in the iron collectors where they would be trapped. After an exposure of about one year, the iron collectors could be removed and placed in front of the detecting equipment. That used at Fermilab consists of a half-meter long

---

18. R.A. Carrigan, Jr., G. Giacomelli and F. Nezrick, Search for Magnetic Monopoles at the ISR, CERN/ISRC/74-33.

superconducting solenoid, capable of reaching fields of 80 kG, and by a series of thin scintillator detectors. The solenoid field is used to extract the monopoles from the collector and accelerate them to energies in excess of 3 GeV. The monopoles would then be identified in the scintillators by their unique differential energy loss and range.

For an exposure of about one year one would expect the following limits (there is no problem with background):

ISR	ISABELLE
$m_g < 25$ GeV	$m_g < 200$ GeV
$0.5\ g_o < g < 24$	$0.8\ g_o < g < 30$
$\sigma < 2 \times 10^{-37}\ cm^2$	$\sigma < 5 \times 10^{-39}\ cm^2$

These measurements may not set cross section upper limits smaller than the existing cosmic ray limits, but would be established on much more controlled conditions.

III SEARCH BY ELECTRIC INDUCTION

Any monopoles that are produced at ISABELLE in an intersection without a magnetic field will lose energy very rapidly in material that they traverse. The range for a monopole of unit magnetic charge is about 25 grams/cm^2 for mass 50 m_p and energy 100 GeV. It is expected that individual monopoles stopping in the material surrounding the intersection would be trapped there, as in the "indirect search" described by Giacomelli. A very direct and sensitive form of monopole detector using electric induction has been built by Alvarez et al.[11] to search in lunar samples for monopoles that might have been produced by cosmic rays.

The principle of this detector is the following. Any piece of material containing a monopole has a net magnetic charge, and

moving such material through a coil would induce an electromotive force due to the change of flux. If the coil is a closed superconducting circuit, the result is a change in current. By carrying the sample through the coil a hundred or more times, a sensitivity of a fraction of one monopole is achieved. The most recent version uses a superconducting quantum interference device (SQUID) to measure changes in coil current.[19] This improves sensitivity to achieve a limit of about $g_o/100$, where g_o is the minimum monopole charge predicted by Dirac, $g_o = e/2\alpha = 68.5e$.

Applied to lunar material, this method has shown that the upper limit (95% confidence limit on the flux of the cosmic monopoles) is less than 10^{-18} ($m^{-2}sec^{-1}sr^{-1}$).[9] At the Fermi National Accelerator Laboratory aluminum targets were irradiated by about 4×10^{18} protons with no monopoles detected.[10]

To perform an experiment at ISABELLE, an initial phase could involve a low luminosity, but high luminosities would be the eventual requirement, with absorbing material covering a large solid angle. An integrated luminosity of 10^{39} would seem to be a reasonable goal, about 300 hours at luminosity 10^{33}. To search for monopoles emitted at low momentum, the vacuum tank for the high luminosity insertion used for weak interaction experiments could be removed at an appropriate shutdown, cut up to pieces of appropriate size and assayed for monopoles with this detector. To search for more energetic monopoles, the initial 20 grams of muon absorber could be removable in strips of about 2 g/cm^2 radial thickness. If monopoles were found, a rough measurement of their energy spectrum would be obtained.

Such an experiment could be planned to be carried out as a byproduct of the weak interaction program during the period when muon

---

19. P.H. Eberhard, R.R. Ross, and J.D. Taylor, Rev. Sci. Instrum. (to be published).

detector alone was in use. No additional running time would be required, and the expense of fabricating absorbers in pieces of useful size would not be great. The sensitivity would be about two orders of magnitude better than the cosmic ray limit for 200 GeV mass, and the conditions more clearly established. Figure 3 shows a cross section through the intersection with monopole absorber layers of iron 1/8" thick, which would extend for the length of the wide-angle muon detector, about two meters.

IV STUDY OF MULTIGAMMA EVENTS

The suggestion that various anomalous high energy photon showers seen in cosmic-ray emulsions might be due to the production and subsequent annihilation of bound monopole-antimonopole pairs was made by Ruderman and Zwanziger in 1969.[12] In such a process large numbers of "soft" photons are expected to result from the creation and acceleration of the monopoles, transitions of the bound system, and eventual annihilation. Exact predictions are not given, but the photon multiplicity might typically be ~ 100, and a large fraction of the energy carried away by photons.

A number of unusual cosmic-ray events have been observed.[13-15] These events have a very energetic narrow shower which indicates a corresponding cone of some tens of γ-rays which appear to have been produced with low energy in a rapidly-moving center-of-mass system. There are few, if any, charged particles accompanying them. Attempts to explain the events as conventional electromagnetic showers require the assumption of very large fluctuations which do not seem reasonable. The number of such events is not large, however, and there is no recent work that either confirms or refutes their anomalous properties.

At Fermilab Experiment #22 involves a search for multigamma events from monopole pairs using a lead converter sandwiched between proportional wire chambers covering the forward direction for

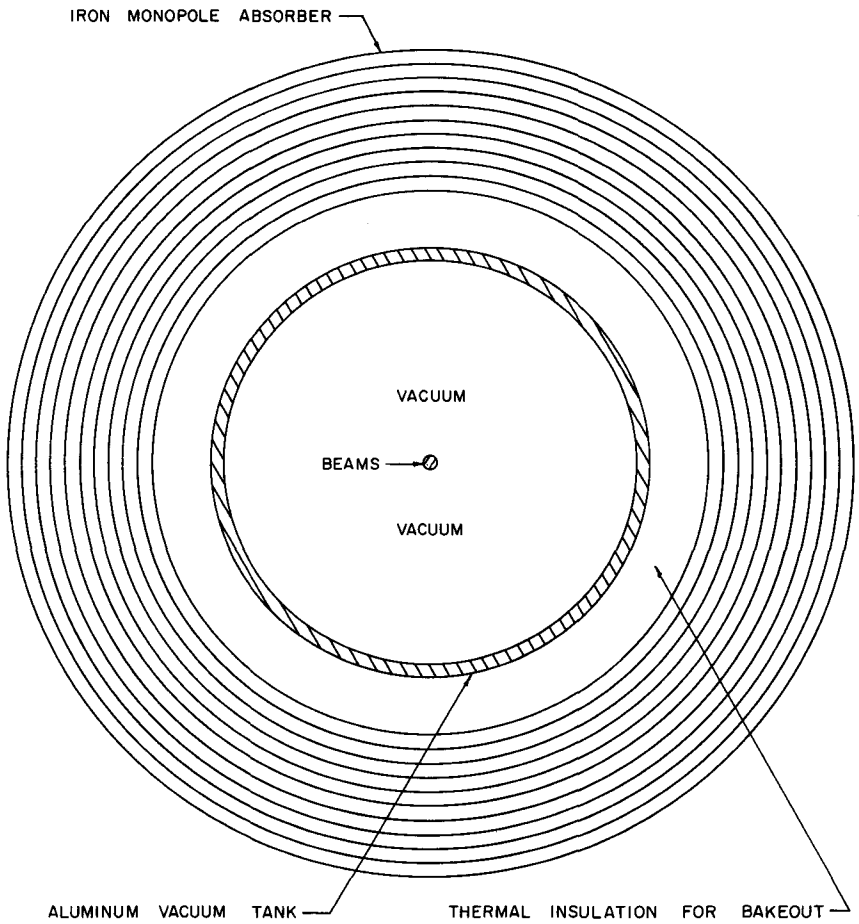

Fig. 3 Monopole absorber of concentric iron cylinders.

p-nucleus collisions.[20] Data collection has been in progress for several months, but no evidence for monopoles reported. At the ISR Experiment R-107 is in a similar condition. Some preliminary results were reported as evidence for high γ multiplicities, but the evidence seems inconclusive. The ISR experiment involves a more elaborate array of lead glass counters and proportional wire chambers covering a substantial solid angle.[21]

In the absence of positive results, it would be unreasonable to build an extensive detection system exclusively for a monopole search through multigamma events. Studies of weak and electromagnetic phenomena, however, also require detectors with the capability of detecting γ-rays that could be used. The qualitative properties that are desirable are:

1) Fairly large solid angle coverage. It need not approximate 4π, but at least 2π would be desirable. It can be centered at 90°, since monopoles are assumed to be very massive, and not moving with high longitudinal rapidity.

2) Fairly good resolution so that many showers can be resolved. If a lead-glass hodoscope is used, it should have at least 200 elements.

3) Some measurement of γ-ray energies, but not necessarily precise.

4) Ability to trigger on a large total energy deposition due to γ-rays to achieve a reasonable event rate.

---

20. G.B. Collins, J.R. Ficenec, W.P. Trower, J. Fischer and S. Shibata, NAL Proposal No. 22 "Experimental Proposal to the National Accelerator Laboratory for a Search for Multigamma Events from Magnetic Monopole Pairs", June 12, 1970.

21. J. Dooher, L.C.L. Yuan, G.F. Dell, H. Uto, E. Amaldi, Beneventano, Borgia, Dore, de Notaristefani, Pistilli, and Sestili, "Search for Multigamma Events," CERN/ISRC/73-7.

5) Ability to operate at luminosities of 10^{32} - 10^{33}.

These criteria are all given in purely qualitative terms. Several large-angle detectors are being designed in the course of the summer study.

Probably the most appropriate is the system designed to observe electron production due to weak interactions, in which the hadron calorimeter is also an electromagnetic shower detector. The initial layers of this detector have a thickness appropriate to identifying showers from electrons and γ-rays. The most common contribution will presumably be γ-ray secondaries of π^o's which account for something like 1/3 of the hadronic energy flux. Most of these γ-rays, however, will be at small angles to the beams while those from the hypothetical annihilation of massive monopoles would be distributed approximately isotropically.

An initial calorimeter with 16 uranium plates each 1/4 radiation length thick (0.8mm) with 2.0 mm of liquid argon would be appropriate as a photon sensor. With 8 azimuthal segments and 16 polar (or lengthwise) segments, there would be adequate resolution to identify events with high γ-ray multiplicity, a total of 128 (θ,φ) segments. In each segment currents from the 16 plates would be summed with weights determined by the photon shower distribution using the optimum signal processing technique of Gatti, Radeka and Rosenblum.[22] For the trigger signal the eight azimuthal segments would be summed to give 16 polar segment outputs. The polar segments would be summed with weights chosen to enhance the isotropic monopole signal in the presence of photons from hadronic interactions peaked at small angles.

---

22. E. Gatti, V. Radeka and M. Rosenblum, "Particle Identification by Processing of Signals from Multiple Detectors", BNL 20212, May, 1975 (presented at 2nd ISPRA Nuclear Electronics Symposium, Stresa, Italy, 20-23 May, 1975).

The trigger would require a total γ-ray energy of perhaps 20 GeV or more. The 16 individual polar signals would be displayed by oscilloscope and events of interest photographed for subsequent study to enhance background discrimination.

The luminosity which such a large angle detector could handle would be less than 10^{33} when operating in a counting mode which requires a small accidental rate. If, however, one considers it to be a multichannel ionization chamber, proper analog signal processing might present a useful signal even with several background interactions during the detector's sensitive time. If so, operation at 10^{33} luminosity might be a possibility using such generalized detector logic.

V SOURCES OF INFORMATION

We would like to thank R. A. Carrigan, Jr., G. B. Collins, P. Eberhard, R. L. Fleischer and L. C. L. Yuan for correspondence and other information concerning monopole detectors and monopole search experiments.

ON THE POSSIBILITY OF SEARCHES FOR PARTICLES BY THRESHOLD EFFECTS USING PRECISE DETERMINATION OF THE ISA ENERGY

A. Kanofsky, Lehigh University

I note that it might be possible at ISABELLE to search for new heavy particles and other phenomena (such as onset of new multiparticle inelastic production channels) in the same manner that the SLAC-Berkeley group found the φ/J - i.e. to increase the c.m.energy in very small steps and look for unusual behavior in the scattering. The occurence of threshold would be indicated by a slow moving lab proton which would be heavily ionizing. As the threshold energy is exceeded, the baryon energies would increase even more, and presumably the production cross section would drop as the energy increased.

We can ask the question what sort of energy resolution can we expect with ISABELLE. If we operate the beams in a dispersive mode, then the momentum changes uniformly along the horizontal dimension when the beam is bunched. This momentum spread could be only 0.1 -0 .2%. The colliding beam situation is shown in Figure 1. This spread within the beam would correspond to as little as $10^{-3} \times 200 = 0.2$ GeV or as much as 0.4 GeV. If the beam is spread 1 cm in the dispersive mode, and a position resolution of 1 mm is possible, then the minimum position determined momentum resolution is 20 MeV within a single beam or 40 MeV for the two colliding beams.

This could be improved on if the beam is spread more (with resultant loss in luminosity) or if the track resolution is better (which could be improved on to 0.1 mm with high resolution PWC's or drift chambers). The mean energy of the beam is determined by magnetic field measurement and could be as accurate as 1 ppm. A detector for the threshold processes could be a 4π proportional wire chamber with pulse height information incorporated as well as good position resolution. This could be similar to the 4π detector reported in these proceedings of Grannis et al. used

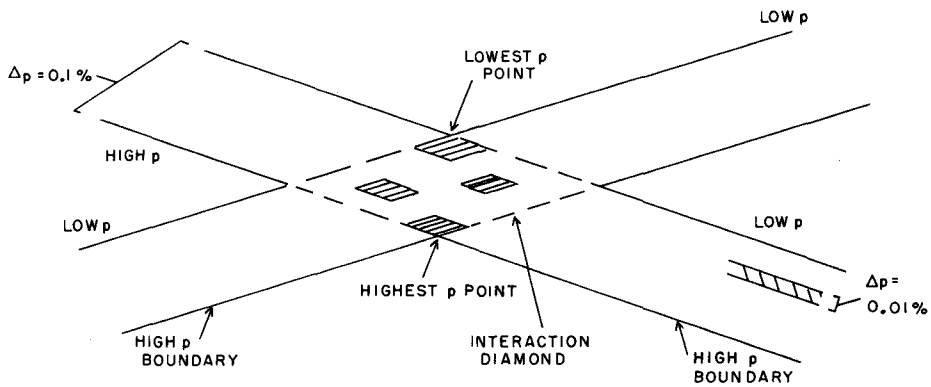

Fig. 1. Interaction diamond showing variation of momentum with position.

for the multiplicity and σ_T measurements. Very thin mylar windows could be used near the beam to allow entrance of low energy protons. This detector could be in turn surrounded by the calorimeter - μ detector of the weak interaction group. The total trigger would be the presence of a low energy proton in the 4π detector and a good signature in the μ detector.

An interesting aspect of this method is that at energies about threshold it would be possible to see the threshold events start abruptly to occur in one spatial region of the beam diamond, and an absence of the same events in the other regions.

Such sweeps in energy could be done in 0.4 GeV steps. Many experiments are insensitive to changes in c.m. energy of as much as 10 GeV. The choice and range of the energies of the threshold search experiment would have to be compatible with other experiments around the ring. Changes in energy over the entire range of the machine could be made in less than 10 minutes.

A VERSATILE CENTRAL SPECTROMETER FOR ISABELLE

D. Cheng, University of California, Santa Cruz
K. Goulianos, Rockefeller University
B. Knapp, Nevis Cyclotron Laboratory, Columbia University
J. Rosen, Northwestern University
P. Schlein, University of California, Los Angeles

I. INTRODUCTION

We propose a large aperture magnetic spectrometer to study hadrons and leptons produced in the central region at ISABELLE. The essential element of the spectrometer is a large double-dipole magnet system with common flux return straddling the intersection region as shown in Fig 1. The air gaps provide magnetic analysis of charged particles for up to 50% of the azimuthal angular range. Drift chambers, Cerenkov counters and shower detectors positioned on both sides of the beam lines comprise two spectrometers for analysis of hadrons and electrons. Muons can be momentum analyzed over a large fraction of the azimuthal angle by utilizing the upper and lower sections of the magnet yoke to provide hadron filtering and magnetic deflection. Cylindrical chambers around the vacuum pipe provide multiplicity information for events of interest. The proposed magnet configuration allows unobscured coverage of smaller angle particles with the addition of septum magnet spectrometers downstream of the central magnet in both arms.

The spectrometer is well suited for the following physics program.

(1) Survey of single and multiparticle large P_t phenomena including resonance structure and V^o detection.

(2) Study of lepton production. (a) single lepton (μ or e) high P_t and associated hadronic systems. (b) lepton pair ($\mu\mu$, ee, or μe) high P_t, invariant mass distributions and associated hadronic systems.

(3) Search for long-lived higher-mass particles using time-

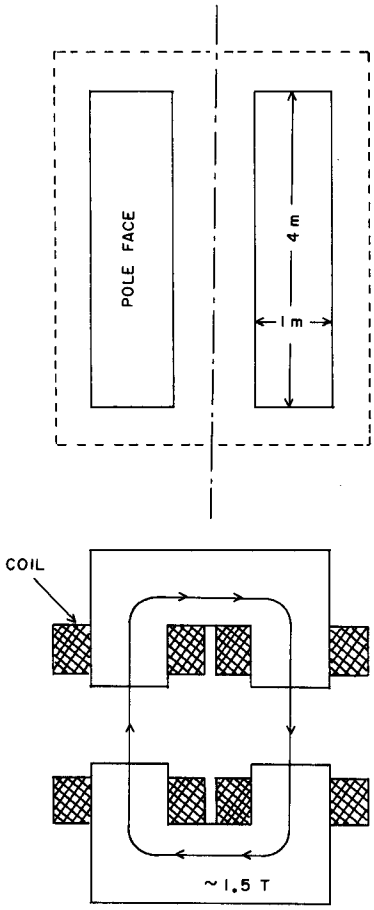

Fig. 1. Central region magnet.

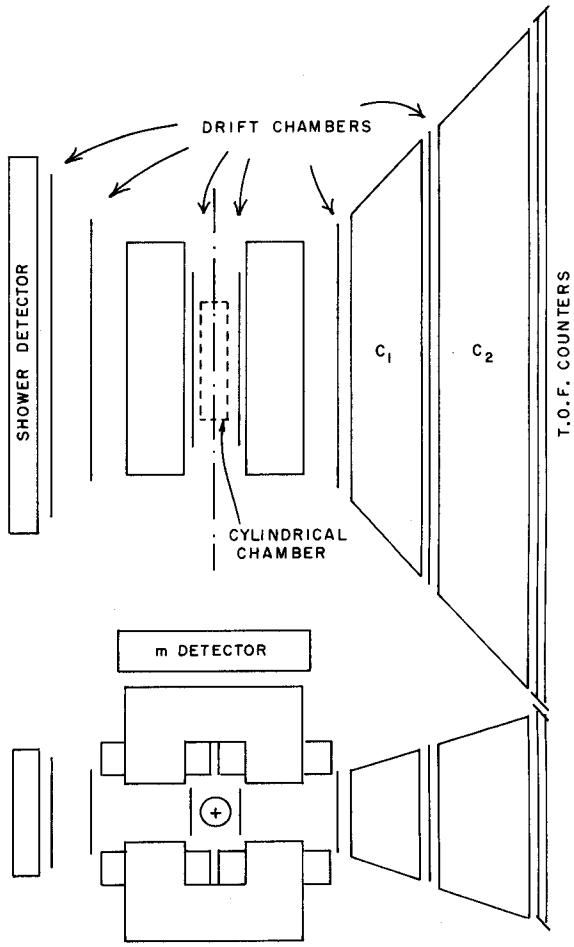

Fig. 2. Schematic layout of detection systems.

of-flight for stable charged particles. V^o's and very narrow resonances.

(4) Search for s-dependent threshold effects in all of the above. Search for $W^{\pm}$, Z^o, etc. production.

II. CENTRAL MAGNET

One important advantage of the double dipole magnet configuration is that the fringe fields tend to cancel in the vicinity of the vacuum pipe. Small higher order components can easily be corrected for.

There are several other advantages in our choice of the common flux return over the use of two conventional dipole magnets with opposing fields. These are:

(a) The forward direction is clear and accessible except for some structural posts which support the upper magnet section. Forward angle detection magnets and other equipment (e.g. calorimeters) can be accommodated.

(b) The magnet can be constructed with pancake coils. The fabrication of superconducting coils would then be materially simplified.

(c) The magnetic field lines in the crossover yoke are distributed in a relatively simple way and can be utilized for the magnetic analysis of promptly-produced high P_t muons.

Cost

The magnet incorporates ~ 300 tons of iron (cost less than $200 000). Detailed cost estimates have not been made, but extrapolating from several existing magnets, we estimate a total cost of ≤ $1 000 000, presumably including power supply (or refrigerator).

III. CHARGED HADRON DETECTION

For multiparticle hadron detection, the magnet will be equipped with drift chambers and Cerenkov counters as shown in

Fig. 2. Four sets of drift chamber planes in each of the two magnet gaps will measure particle trajectories and momenta to within about one per cent at 10 GeV/c; specifically we estimate that $\delta p/p \approx (0.1\%)\ p(\mathrm{GeV/C})$. The solid angle subtended by a single arm is sufficient to observe multihadron resonances of several GeV mass. The angular spread of the decay products is determined by the γ of the parent resonance, so that in the roughly one steradian of a single arm, one expects large acceptance for a resonance with a laboratory energy typically four times its mass. The 1 m transverse decay path available between the interaction and the second drift chamber plane will permit observation of K_s and Λ^o.

For luminosities below 10^{32}/sec cm^2, a cylindrical particle detector, either drift chamber or standard multiwire proportional chamber, will surround the vacuum pipe and provide accurate azimuthal and crude polar angle measurement over more than 90% of 4π solid angle.

A complete pattern recognition of the tracks in the interior system may not be essential. It may suffice to simply establish, by extrapolation of a few projected line segments, the common z coordinate of the event vertex. Given accurate line segments in the exterior chamber and an accurate field map, the particle trajectories can be completely specified.

A pair of segmented atmospheric pressure Cerenkov counters in series, one filled with neopentane, one with carbon dioxide, can uniquely identify pions with momentum 2.5 to 16.5 GeV/c, kaons of 8.8 to 16.5 GeV/c and protons of 8.8 to 34 GeV/c. For charged hadron separation at lower values of momentum, pressurized Cerenkov counters will be required. Angular coverage can be sacrificed to accommodate the structural demands on the detector vessels.

IV. SHOWER DETECTION

Consider first, the problem of electron identification. For this purpose a shower detector with relatively crude segmentation

($\sim 10^2$ strips) is needed to avoid pile up and rate problems. Given the momentum analysis provided by the drift chamber system, a hadronic rejection ratio of 10^{-4} to 10^{-5} with an electron identification efficiency of $\sim$ 90% can be achieved.

It is necessary to reject the e^+e^- pairs that are provided at the few % level by π^o and η^o decays. These electrons are of greatest concern at low $P_\perp$, but still constitute a problem at the 10^{-3} -10^{-4} level for high $P_\perp$. Since the second drift chamber module extends into the magnet fringe field, it should be possible to reject this source of background by observing the separation of the e^+e^- pair produced by magnetic deflection.

The shower detection configuration required for neutral detection (γ, π^o, η^o) is somewhat different. For quantitative spectroscopy, the γ-ray direction cosines must be well measured. The shower detection must be finely segmented, $\geq 10^3$ elements. We will not attempt to provide an extended discussion of this problem. We note that very promising results have been reported with the liquid Argon ionization chamber. Such a detector suitably sectorized may ultimately prove to be superior to the lead glass arrays (plus external γ-ray converters) which have been extensively used in recent years.

V. MUON DETECTION

As noted in the introduction, the yoke of the central spectrometer magnet provides a region of azimuth well suited to the detection of prompt muons. An absorber of nonmagnetic material can be inserted between the vacuum pipe and the coils so as to increase the absorption of π's and K's. The hevimet, brass and magnet Fe constitute $\sim$ 3 GeV of ionization energy loss. The absorption length for π's is $\sim$ 0.2 and the mean free path for decay of a 4 GeV π is 220 m. Consequently, hadron rejection at the 10^{-3} level is practical. Significant improvement in this factor is achieved for higher momentum μ's.

The transverse deflection provided by the magnetized Fe is $\sim$ 0.5 GeV/c. Multiple Coulomb scattering leads to an rms value of $\sim$ 0.125 GeV/c. Hence the muon momentum will be measured to $\sim$ ($\pm$25)%.

Muon detectors each subtending $\sim$ 1.0 steradian will be installed on top of the magnet. A set of large drift chambers will be used to detect muons and measure their direction cosines. A slab $\sim$ 1 ft of Fe will be sandwiched between chamber layers.

It will be very interesting to study the correlations between the particles recorded in other regions of the spectrometer system and the recorded prompt muon. For example, $\mu^{\pm}e^{\mp}$ correlations are particularly interesting. They can provide good circumstantial evidence for the associated production of new particles which subsequently decay semileptonically. It will be interesting to examine multihadron mass plots from data accumulated on the basis of the muon trigger. The observation of a sharp mass peak together with a detected muon could be interpreted as an associated production event in which one particle decayed leptonically (or semileptonically) and the second decayed hadronically.

VI. SEARCH FOR LONG-LIVED HIGH-MASS PARTICLES USING TIME-OF-FLIGHT

The time-of-flight system is installed to search for new long-lived particles. Such new particles might be produced in ISABELLE because of the large c.m. energy available. For example, there might be sufficient energy at ISABELLE to liberate the quarks from the proton.

The system uses the magnetic momentum determination together with time-of-flight information to determine the mass of the new particle. For a 5 m flight path, the time-of-flight (minus TOF of β = 1 particle) for particles of mass M and momentum p is shown in Fig. 3a. For new particles 1 GeV or more massive than the proton, the TOF differs from that of the proton with 4 GeV momen-

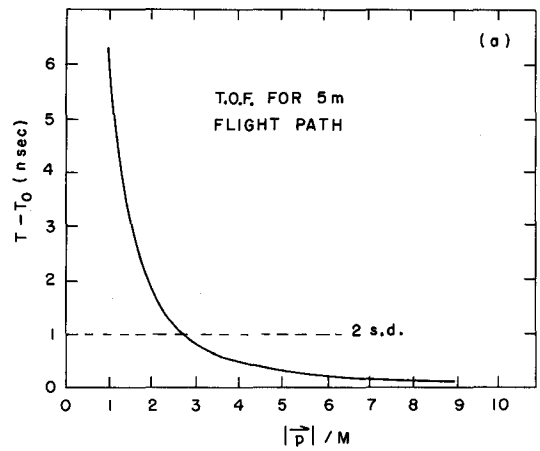

Fig. 3a. Difference in time-of-flight for a 5 m flight path.

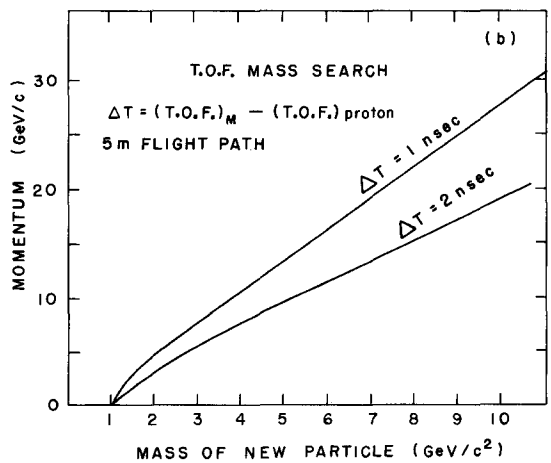

Fig. 3b. Maximum momentum at which particles can be distinguished by time-of-flight as a function of mass.

tum by more than 1 nsec. Assuming normal production mechanisms, this momentum range should include most of the new particles produced. That is, we expect to separate almost all particles entering the TOF region which are heavier than the proton. This is illustrated in Fig. 3b.

In addition to searching for new particles, the TOF system allows (2 standard deviation) π/K separation up to about 1 GeV/c and K/p separation up to 1.8 GeV/c. Particle identification in this region is important since it is difficult to apply the Cerenkov technique in this low momentum region.

ADVANTAGES OF ASYMMETRIC OPERATION OF ISABELLE

Ronald F. Peierls
Brookhaven National Laboratory

In a conventional accelerator, varying the beam energy changes the kinematics of the process being studied. In an ISA, however, by simultaneously varying the two beam energies, the same collision process can be observed but giving different distributions in the lab.

If E1, E2 are the energies of the two beams, then the total invariant squared energy is

$$S = 4E_1E_2 \cos^2 \tfrac{1}{2}\beta \tag{1}$$

where β is the crossing angle which we shall take to be neglibible for the purpose of this discussion (we have also neglected the mass of the beam particle).

Kinematics

Let E_{max}, E_{min} be the maximum and minimum beam energies accessible in the machine. The symmetric configuration has:

$$E_1 = E_2 = \tfrac{1}{2}\,(S)^{\frac{1}{2}} \tag{2}$$

The most asymmetric configuration is (for $E_1 > E_2$)

$$E_1 = E_{max} \quad E_2 = \frac{S}{4E_{max}} \quad (S < 4\,E_{min}\,E_{max})$$

$$E_1 = \frac{S}{4E_{min}} \quad E_2 = E_{min} \quad (S < 4\,E_{min}\,E_{max}) \tag{3}$$

The closer S is to the maximum, $S_{max} = 4E^2_{max}$, the less the available asymmetry.

The main effect of the asymmetry is to impart a velocity to the center-of-mass

$$|\beta_{cm}| = \left[1-S/(E_1 + E_2)^2\right]^{\frac{1}{2}}$$

$$= \frac{4E_1^2 - S}{4E_1^2 + S} \tag{4}$$

Hence the maximum obtainable value of β is

$$|\beta_{cm}^{max}| = \frac{S_{max} - S}{S_{max} + S}, \quad S > 4\, E_{min} E_{max}$$

$$= \frac{S - S_{min}}{S_{min} + S}, \quad S < 4\, E_{min} E_{max} \tag{5}$$

where $S_{min} = 4E_{min}^2$ is the smallest S achievable. Table I gives values for $|\beta_{cm}^{max}|$.

Applications

There are three regions where this flexibility can be useful.

(1) Very small angles: The smallest angle which can be observed is limited by the geometry of the vacuum system and magnets. For a fixed momentum in the center-of-mass, the asymmetric running allows the corresponding lab angle to be increased or decreased from the symmetric value by a factor $[(1+\beta_{cm})/(1-\beta_{cm})]^{\frac{1}{2}}$, assuming the particle to be relativistic. Hence it is possible to reduce the minimum observable center-of-mass angle by a factor $(S_{max}/S)^{\frac{1}{2}}$, [or $(S/S_{min})^{\frac{1}{2}}$, depending on the value of S] relative to that observable in the symmetric case. Numbers are also given in Table I.

(2) Central region: By varying the beam asymmetry, a fixed detector sitting at 90° can be made to sweep through a region of rapidity surrounding the central region. The shift in rapidity

Table I: Parameters associated with asymmetric beams. E1 is the higher beam energy in the maximally asymmetric situation. E2 the other beam energy. $|\beta_{cm}|/c$ is the velocity of the center-of-mass, θ_L/θ_{cm} the angular amplification available and Δy the resulting shift in rapidity.

These figures assume

$$E_{max} = 200 \ , \ E_{min} = 30.$$

$(S)^{\frac{1}{2}}$	E1	E2	$\lvert\beta_{cm}\rvert/c$	θ_L/θ_{cm}	Δy
100	83.33	30	0.47	1.67	± 0.125
150	187.5	30	0.72	2.5	± 0.37
200	200	50	0.6	2.0	± 0.22
250	200	78.125	0.438	1.6	± 0.11
300	200	112.5	0.28	1.33	± 0.04
350	200	153.125	0.13	1.14	± 0.008

is given by

$$\Delta y = \ln\left[\frac{E_1+E_2}{(S)^{\frac{1}{2}}}\right] = \ln\left[\frac{4E_1^{\,2}+S}{4E_1(S)^{\frac{1}{2}}}\right] \tag{6}$$

$$\Delta y_{max} = \begin{cases} \ln\left\{\frac{1}{2}\left[\left(\frac{S}{S_{max}}\right)^{\frac{1}{2}} + \left(\frac{S_{max}}{S}\right)^{\frac{1}{2}}\right]\right\} & S > 4\,E_{min}E_{max} \\ \ln\left\{\frac{1}{2}\left[\left(\frac{S}{S_{min}}\right)^{\frac{1}{2}} + \left(\frac{S_{min}}{S}\right)^{\frac{1}{2}}\right]\right\} & S < 4\,E_{min}E_{max} \end{cases} \tag{7}$$

the total resulting rapidity range is $2\Delta y_{max}$ and is indicated in the Table.

(3) Large X: In a similar fashion, a fixed detector can be made to scan a relatively wide region of x. Here the expressions for the range of x are more complicated and are best presented in the form of a graph, giving some typical ranges of values. This is done in Fig. 1.

Conclusions

The possibility of asymmetric running allows both the exploration of otherwise inaccessible kinematic regions and also allows a relatively simple detector to acquire effectively a much larger solid angle without sacrificing resolution and without introducing point to point bias from the detector. Obviously there will be some bias introduced by the varying beam characteristics at the different energies but that will tend to affect overall normalizations only.

Nothing is gained without some sacrifice: what is given up in asymmetric running is the ability to achieve the maximum S. However, it is clear that already effects at $(S)^{\frac{1}{2}} = 200$ are quite significant, and for many processes this will be high enough.

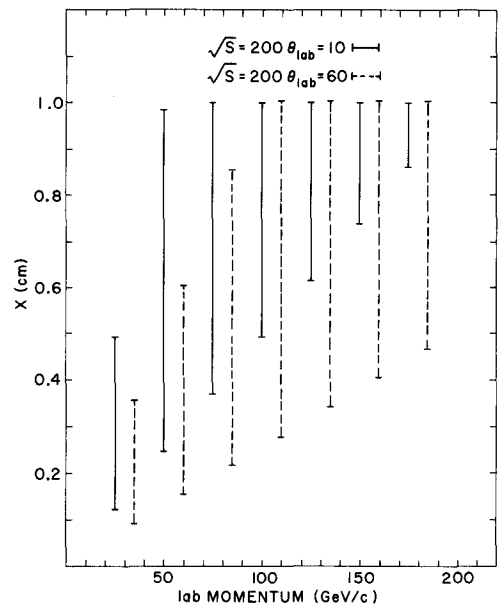

Fig. 1a. Range of X for fixed detector setting.

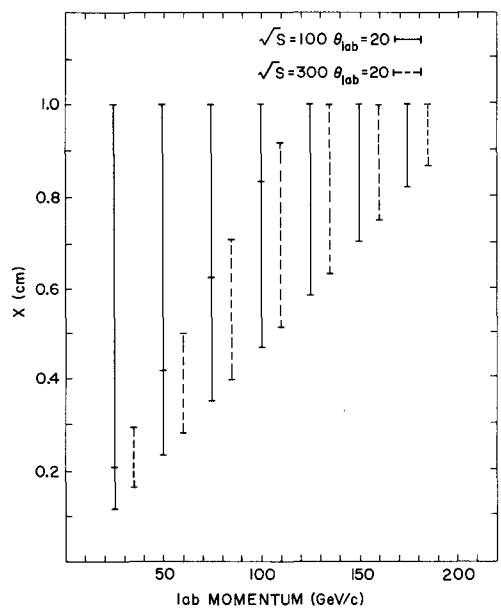

Fig. 1b. X range - change with energy.

Another use of asymmetric running is to keep E_1 fixed, and the detector fixed, but vary E_2 to study S-dependence, but this is more conventional and does not really need discussion.

It remains to be seen how severe the problem will be of scheduling the energy variations of two beams to satisfy multiple interaction regions.

JETS IN LARGE p_T REACTIONS AT ISABELLE

Frank E. Paige
Brookhaven National Laboratory

We consider the reaction $A + B \to C + X$, where C has a large transverse momentum. The parton model[1] for such reactions suggests that X should contain jets of hadrons with large transverse momenta. In this paper we discuss the possibility of observing such jets at ISABELLE.

In the parton model it is assumed that the process $A + B \to C + X$ proceeds through a subprocess

$$a + b \to c + d$$

in which constituents of the incident hadrons scatter at a large angle. See Fig. 1. With certain additional assumptions this leads to a cross section for $A + B \to C + X$

$$E \frac{d\sigma}{d^3p} \sim \frac{1}{(p_T^2)^N} f(x_T, x_L) \quad , \tag{1}$$

where

$$x_T = \frac{2p_T}{\sqrt{s}} \quad , \quad x_L = \frac{2p_L}{\sqrt{s}} \quad , \tag{2}$$

and p_T and p_L are the transverse and longitudinal components of the momentum of C in the center-of-mass. Various choices of a, b, c and d give various values for the power N. For example,

Subprocess	N
$q + q \to q + q$	2
$q + M \to q + M$	4
$q + \bar{q} \to M + M$	4
$q + q \to B + \bar{q}$	4

Here q, M, and B denote respectively a quark, a meson, and a baryon.

It is further assumed that quarks cannot appear in the final state, but instead that they fragment into hadrons with a scaling distribution.

---

1. D. Sivers, S.J. Brodsky, and R. Blankenbecler, SLAC-PUB-1595 (June, 1975). This paper contains a review of the model and references to the original papers.

That is, the distribution from a quark of energy E depends only on

$$x = \frac{p_{||}}{E} \text{ and } p_\perp^2 \quad .$$

(Here and in what follows, $p_{||}$ and $p_\perp$ denote components of momentum parallel and transverse to the quark direction, while p_L and p_T denote components with respect to the beam direction.) The value of $p_\perp^2$ is assumed to be limited, so that as E becomes large the number of hadrons grows like log E. Thus, there is a jet of hadrons around the direction of the quark.

In the constituent interchange model[1] the quark-quark-scattering subprocess is assumed to be absent. Thus, the leading graphs are those with N = 4. Some of these graphs are shown in Fig. 2. Note that (a) gives no jets, (b) and (c) give one jet balanced by a single high-p_T particle, and (d) gives two jets. Thus, observing the number of jets in each event would give information on the relative importance of the various graphs.

To discuss jets more quantitatively, we must make a model for the distribution of hadrons from a parton. We consider the simplest possible model, namely

$$\begin{aligned} \frac{dn}{dy_{||}} &= c \quad , \quad y_{||} < y_o \\ &= 0 \quad , \quad y_{||} > y_o \end{aligned} \tag{3}$$

where $y_{||}$ is the rapidity variable along the direction of the parton,

$$p_{||} = (p_\perp^2 + m^2)^{\frac{1}{2}} \sinh y_{||} \quad . \tag{4}$$

Then the average multiplicity $< n >$ is given by

$$\begin{aligned} < n > &= \int dy_{||} \frac{dn}{dy_{||}} \\ &= cy_o \end{aligned} \tag{5}$$

The total energy of the jet is

$$\begin{aligned} E &= \int dy_{||} < (p_\perp^2 + m^2)^{\frac{1}{2}} > \cosh dy_{||} \frac{dn}{dy_{||}} \\ &= c < (p_\perp^2 + m^2)^{\frac{1}{2}} > \sinh y_o \quad . \end{aligned} \tag{6}$$

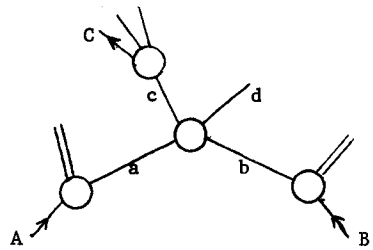

Fig. 1. The Structure of A + B → C + X in the Parton Model.

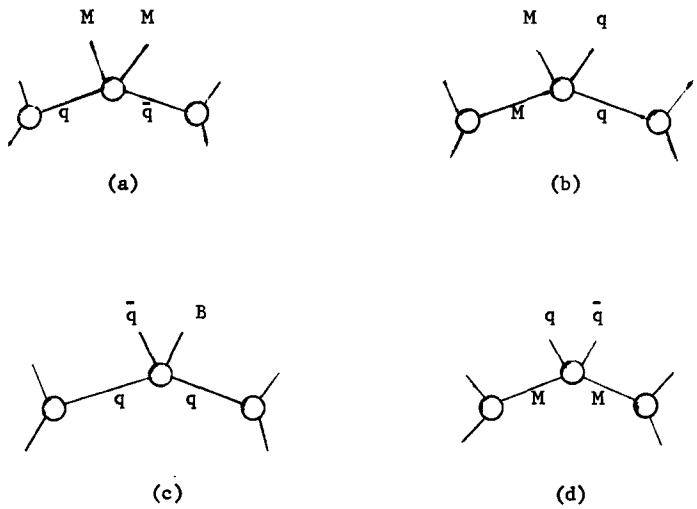

Fig. 2. Some Graphs of the Constituent Interchange Model.

We can also define a measure of the angular spread of the jet. The average $p_{||}$ carried by each particle in the jet is

$$< p_{||} > = \frac{1}{< n >} \int dy_{||} < (p_\perp^2 + m^2)^{\frac{1}{2}} > \sinh y_{||} \frac{dn}{dy_{||}}$$

$$= < (p_\perp^2 + m^2)^{\frac{1}{2}} > \frac{\cosh y_o - 1}{y_o} \quad . \tag{7}$$

We therefore define an (energy-weighted) average opening angle $< \varphi >$ by

$$\tan < \varphi > = \frac{< p_\perp >}{< p_{||} >}$$

$$= \frac{< p_\perp >}{< (p_\perp^2 + m^2)^{\frac{1}{2}} >} \frac{y_o}{\cosh y_o - 1} \quad . \tag{8}$$

If we ignore m^2 compared to $p_\perp^2$, then the above formulas simplify to

$$< n > = c y_o$$

$$E = c < p_\perp > \sinh y_o \tag{9}$$

$$< \varphi > = \tan^{-1} \left(\frac{y_o}{\cosh y_o - 1} \right) \quad .$$

Since the model is intended only as a rough guide, we will make this approximation.

We can estimate c and $< p_\perp >$ from the ISR data on correlations in large p_T reactions.[2] For p_T = 3 GeV an excess charged particle multiplicity of

$$< n_c > \approx 1.5$$

is found in the opposite hemisphere. The extra particles are spread over about $\pm 60^o$ both in the azimuthal and in the polar angles. We attribute these extra particles to a jet, albeit a very wide one. We take

$$E = 3 \text{ GeV} \quad ,$$

although this, of course, is only a lower limit,

$$< n > = 3/2 < n_c > = 2.25 \quad ,$$

and

$$< \varphi > = 45^o \quad .$$

---

2. For a review see L. DiLella, Proc. XVII Intern. Conf. London, 1974 p. V-13.

Then from Eq. (9),[3]

$$c = 1.41 \quad , \qquad (10)$$
$$< p_\perp > \; = 0.9 \text{ GeV} \quad .$$

For comparison we also consider jets with c and $< p_\perp >$ equal to their values in low p_T reactions,

$$c = 2.25 \quad , \qquad (11)$$
$$< p_\perp > \; = 0.35 \text{ GeV} \quad .$$

These were the values expected a priori.

In Fig. 3 we plot $< n >$ and $< \varphi >$ vs E. At ISABELLE we expect to reach p_T of at least 20 GeV,[4] and p_T is only a lower bound for E. Thus, over the ISABELLE range jets should become clearly visible if the model is correct.

We can construct "typical" events by noting that the average spacing of particles in $y_{||}$ is

$$\Delta y_{||} = \frac{1}{c} \quad . \qquad (12)$$

The angle φ of a particle with respect to the parton direction is given by

$$y = - \log \tan \frac{\varphi}{2} \quad . \qquad (13)$$

Consider E = 20 GeV. For c = 1.41 and $< p_\perp > = 0.9$ GeV,

$$< n > = 4.87$$
$$< \varphi > = 13.1^\circ \quad .$$

A typical event has

$y_{\|\|}$	φ (deg)	$\|p\|$ (GeV)
3.10	5.18	9.97
2.39	10.51	4.93
1.68	21.18	2.49
0.97	41.65	1.35
0.26	75.45	0.93

For c = 2.25 and $< p_\perp > = 0.35$ GeV,

$$< n > = 8.84$$
$$< \varphi > = 9.14^\circ$$

3. See also Ref. 1, Section II C.

4. A Proposal for Construction of a Proton-Proton Storage Accelerator Facility ISABELLE, BNL Informal Report BNL 20161 (June 1975), p. 25 ff.

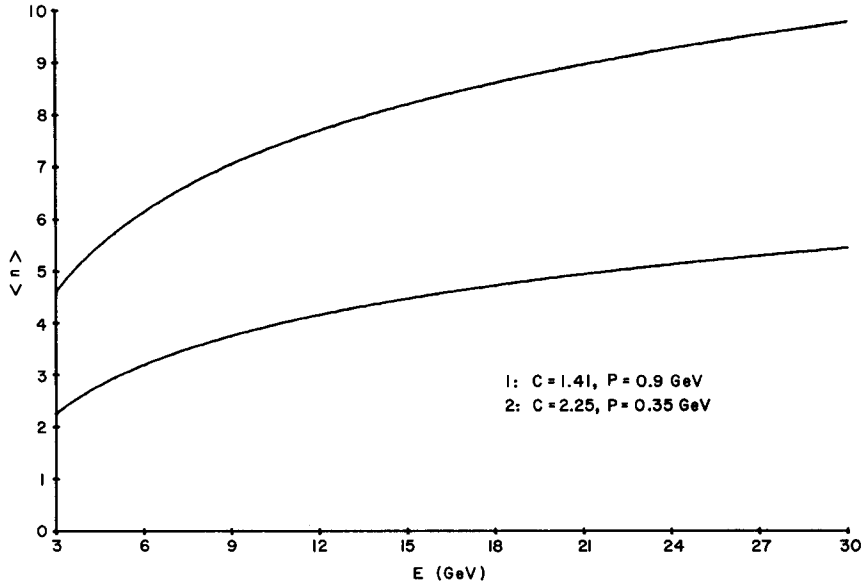

Fig. 3. (a) Average Multiplicity < n > vs Energy of Jet E.

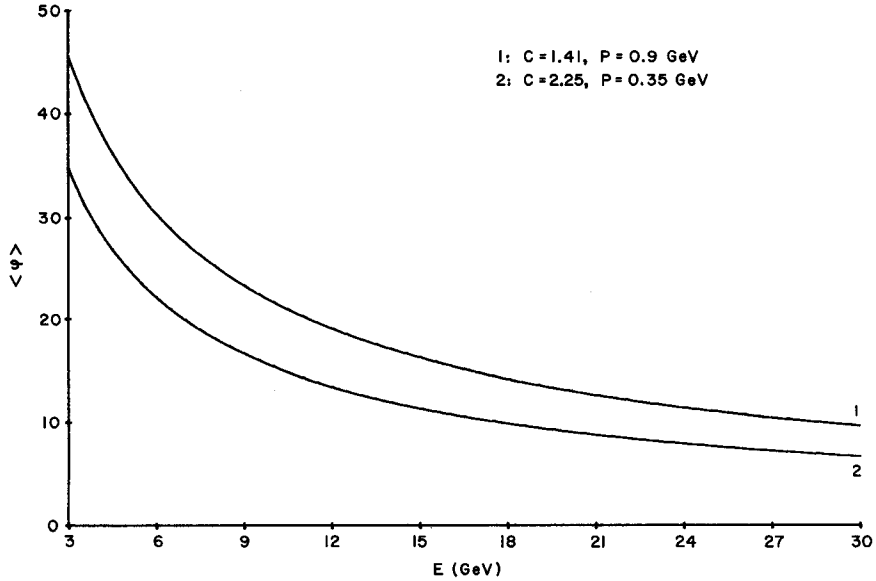

Fig. 3. (b) Opening Angle < φ > vs Energy of Jet E.

A typical event has

y	φ (deg)	|p| (GeV)
3.71	2.81	7.14
3.27	4.36	4.60
2.83	6.77	2.97
2.39	10.49	1.92
1.95	16.22	1.25
1.57	24.96	0.83
1.07	37.93	0.57
0.63	56.17	0.42
0.19	79.28	0.36

Obviously, particles in the jet with small momenta and large angles cannot be distinguished from particles produced by pionization.

The ideal apparatus for looking for jets is probably a calorimeter which can detect all hadrons and which has good angular resolution. Such a device is likely to be large and expensive. It is worth noting, therefore, that pions dominate other particles by a factor of three at large p_T. It is not clear that the measured particle ratios are directly related to the composition of the jets. For example, the graphs in Fig. 2 a, b would give extra mesons. However, it seems likely that a charged particle spectrometer combined with a lead glass π^0 detector would observe a large fraction of the particles in a jet.

I would like to thank Francis Halzen for a useful discussion.

$W^{\pm}$ PAIRS AND NEUTRAL CURRENTS AT ISABELLE

K.O. Mikaelian,
Pennsylvania State University

Introduction

This is a report on two different types of processes which may form part of the weak interactions program at ISABELLE. The first is the production of pairs of charged weak bosons; the second involves searching for neutral current effects in the rate for ordinary lepton production, without measuring any charge asymmetry or helicities.

Common sense and many models predict copious production of single intermediate bosons, charged or neutral, provided their masses are within range of ISABELLE energies. If they are not, virtual effects of the type discussed here become important. On the other hand, the charged bosons may be light enough to be produced in pairs: this may be the only process where we can learn something about their electromagnetic properties. Experimentally, the signal may be more accessible than singly produced W's. We refer to the "Yellow Book" and Ref. 1 for estimates of single boson yields, and proceed to calculate pair production.

Production of $W^{\pm}$ Pairs

One motivation to study the process

$$pp \rightarrow W^{+}W^{-}X \qquad (i)$$

is the possibility that pairs may be more easily identified than single W's. An interesting situation is when one W decays into a muon and the other into an electron

$$pp \rightarrow W^{+}\,W^{-}\,X, \quad W^{-} \rightarrow e\bar{\nu}, \quad W^{+} \rightarrow \mu\nu$$

1. R.L. Jaffe and J.R. Primack, Nucl. Phys. B61, 317 (1973).

which will appear as a "μ-e event". μ-e universality implies $\Gamma_{W \to \mu\nu} = \Gamma_{W \to e\nu}$ (ordinary lepton masses can and will always be dropped in this report).

If the branching ratio of W's into hadrons is big, a possibility which worries the experimentalist, the pair production may again be useful as hadronic jets of opposite sign appear back to back.

Reaction (i) is also interesting since the pairs may be produced electromagnetically and (unless very high energy photon beams become available to photoproduce them) it becomes our only handle on their electromagnetic properties.

Before turning to dynamics, it is worth noting that the high energies at ISABELLE allow a kinematical limit of about 200 GeV/c^2 for the maximum mass of each pair-produced particle. This being a respectable limit, we conclude that dynamics will be the major factor to determine the viability of (i).

Consider the case when the W pairs are produced electromagnetically, as in Fig. 1(a). Rather than compute this amplitude, we shall relate the resulting cross section to that of ordinary lepton pair production, Fig. 2(a). The result is

$$\left(\frac{d\sigma_{W^+W^-}}{d\sigma_{\ell^+\ell^-}}\right)^{1\gamma} = \frac{3Q^2}{8m^2}\left(1 - \frac{4m^2}{Q^2}\right)\left\{ (1+\varkappa)^2 - \frac{1}{3}\left[\left(1 - \frac{2m^2}{Q^2}\right)\left(1 - \varkappa^2 \frac{Q^2}{2m^2}\right) - \frac{4m^2}{Q^2}\right]\right\} . \qquad (1)$$

Here Q^2 = (invariant mass)^2 of $W^\pm$ and $\ell^\pm$ pairs, and $m = m_{W^\pm}$. $\varkappa$ is an "anomalous" magnetic moment of W which is equal to 1 in gauge theories. The above function is plotted in Fig. 3 for different values of $\varkappa$. From (1) we obtain:

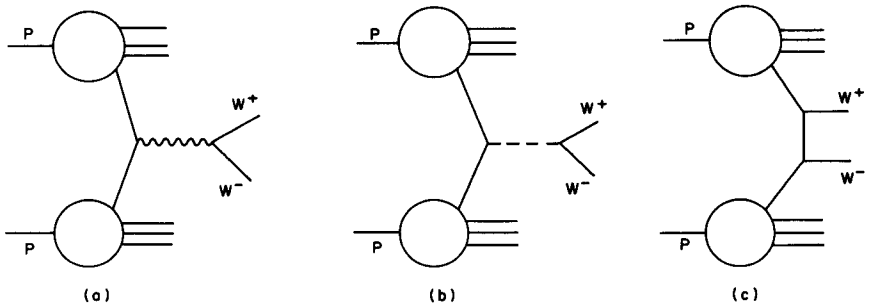

Fig. 1. The process $pp \to W^+W^-X$.

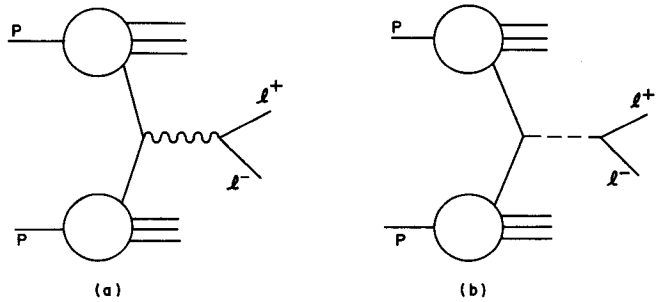

Fig. 2. The process $pp \to \ell^+\ell^-X$.

$$\left(\frac{d\sigma_{W^+W^-}}{d\sigma_{\ell^+\ell^-}}\right)^{1\gamma} \xrightarrow[Q^2/m^2 \gg 1]{} \frac{Q^2}{4m^2}\left(1 + \varkappa^2 \frac{Q^2}{4m^2}\right). \qquad (2)$$

The electromagnetic properties mentioned earlier refer to the value of $\varkappa$. This is an important quantity to know, as all gauge theories starting with Yang-Mills fields have $\varkappa = 1$.

Absolute rates are model dependent and for that reason we quote only the ratio, as in Eq. (1), of W to lepton pairs. This is independent of whatever mechanism one assumes for lepton pair production, as long as it is a single-photon annihilation. In other words, no matter how the massive photon is produced, its "branching ratio" into $(W^+ + W^-)$ vs $(\ell^+ + \ell^-)$ is given by Eq. (1).

This equation applies to production of any spin-one charged particles through single-photon annihilation. Whenever appropriate, a form factor (squared) multiplies this equation. As the weak bosons are supposed to be "structureless", this form factor has been put equal to one. However, the very high energy behavior [see Eq. (2)] must not be taken seriously, as any renormalizable theory would prohibit such linear or quadratic growth with Q^2. For weak bosons, Fig. 1(b) and (c), added coherently with Fig. 1(a), should yield $d\sigma_{W^+W^-}/d\sigma_{e^+e^-} \sim$ constant for $Q^2 \gg m^2$. The argument here is patterned after Weinberg's discussion[2] of $e^+e^- \to W^+W^-$. Exactly where this behavior sets in depends on the particular model, as does the value of the constant. The expected value is of order 1.

Neutral Current Effects

Neutral current effects arise in the reaction

$$pp \to \ell^+\ell^- X \qquad \text{(ii)}$$

where ℓ = e or μ. A previous study[3] dealt with the charge

2. S. Weinberg, Phys. Rev. Lett. 28, 1688 (1971).
3. R.W. Brown, K.O. Mikaelian, M.K. Gaillard, Nucl. Phys. B75, 112 (1974).

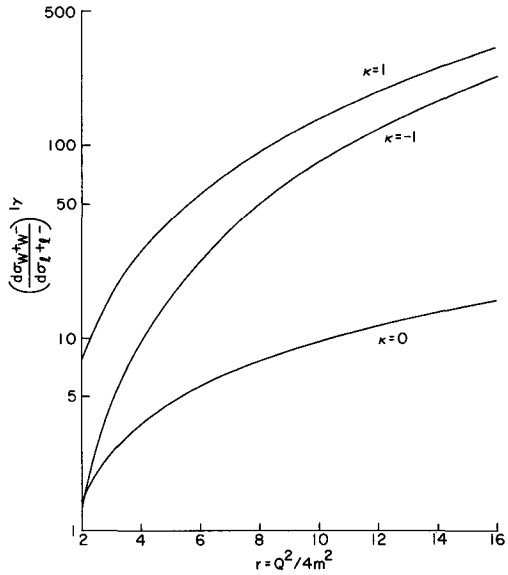

Fig. 3. Ratio of cross section for electromagnetic production of weak boson pairs to that for lepton pairs.

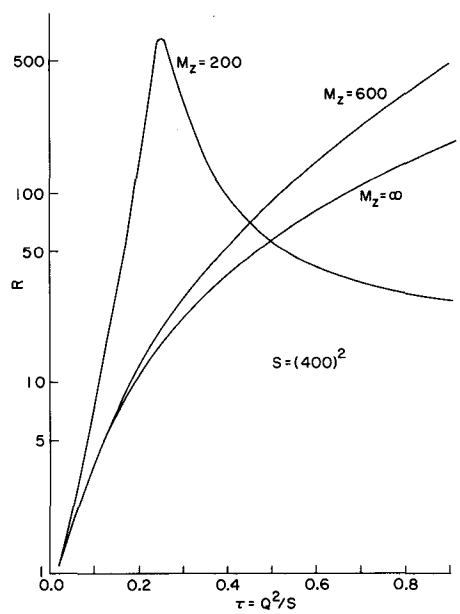

Fig. 4. Ratio of weak + electromagnetic production of lepton pairs to electromagnetic production.

asymmetry and helicity of $\ell^{\pm}$. Our purpose here is to see if other signals, more easily accessible than these two, are present. Identification of the charge of the leptons and especially measuring their helicities appear to be experimentally nontrivial problems. As mentioned above, virtual effects become relevant for the case of a neutral boson too heavy to be produced even at ISABELLE.

The idea here is to exploit the large range of values $1 \times 10^{-11} \leqslant GQ^2 \leqslant 1.8$ available at ISABELLE. This range (characteristic of the strength of weak interactions) and in particular the higher values of GQ^2 suggest substantial "interference with lower order" electromagnetic processes. In fact, at large Q^2 the weak terms alone dominate in the rate. The two amplitudes for (ii) are illustrated in Fig. 2.

The differential cross section is (we follow Ref. 3, using a Drell-Yan[4] type of process):

$$\frac{d\sigma^{\text{Weak + EM}}}{d\tau} = \frac{8}{3}\pi\frac{\alpha^2}{Q^2}\sum_i < Q_i^2 + 2aa_iQ_i\text{Re}g(Q^2)$$

$$+ (a^2 + b^2)(a_i^2 + b_i^2)|g(Q^2)|^2>. \qquad (3)$$

Here $\tau = Q^2/s$, $g(Q^2) = \dfrac{GQ^2}{4\sqrt{2}\,\pi\alpha\ (1 - Q^2/M_z^2 - i\,\Gamma/M_z)}$, Γ = total width of Z^o, the sum i goes over the quarks of charge Q_i in the proton, and the average is taken according to

$$<O_i> = \int_{\sqrt{\tau}}^{1} \frac{dx}{x}\, O_i[P_i(x)\ P_{\bar{i}}(\tau/x) + P_{\bar{i}}(x)\ P_i(\tau/x)]. \quad (4)$$

The P_i are quark distribution functions. It remains to define a, b, etc. They occur in

$$\mathcal{H}^{\text{Weak}} = M_z\left(\frac{G}{\sqrt{2}}\right)^{\frac{1}{2}}[\bar{\ell}\gamma_\mu(a + b\gamma_5)\ell + \sum_i \bar{q}_i\gamma_\mu(a_i + b_i\gamma_5)q_i]Z^\mu\ . \qquad (5)$$

4. S.D. Drell and T.M. Yan, Phys. Rev. Lett. 25, 316 (1970).

Both charge asymmetry and lepton helicities are seen to be proportional to b and are treated in detail in Ref. 3. Here, however, we concentrate on the rate as given in (3) and plot in Fig. 4 the quantity

$$R = \left(\frac{d\sigma^{\text{Weak + EM}}}{d\sigma^{\text{EM}}}\right)_{pp \to \ell^+\ell^- X} \tag{6}$$

For finite M_z, we have arbitrarily put $\Gamma/M_z = 15\%$, a large width corresponding to rather large ($\sim$ 100%) branching ratio into hadrons. The curve with $M_z = 200$ GeV/c^2 shows how such a broad resonance appears in the lepton pair distribution.

R is seen to deviate greatly from 1, obviously suggesting that a study of the rate for (ii) should reveal neutral current effects. The specific mechanism of quark-antiquark annihilation[4] was used together with the Weinberg model (with $\sin^2\theta_W = 0.4$) for a_i and b_i in constructing these curves. Other models, experimental cuts, etc. will alter the individual contributions (not shown) of $d\sigma^{\text{Weak + EM}}$ and $d\sigma^{\text{EM}}$, but the ratio is expected to be sensitive only to the values of M_z, a_i, etc. and should be fairly independent of detector acceptance and other imposed kinematical constraints.

Besides the advantage of being experimentally more accessible, this effect does not hinge on the presence of axial couplings b, b_i. It appears also in the case of purely vector particles, an example of which is the Lee-Wick[5] heavy photon.

Conclusion

This was an attempt to exploit the high energies available at ISABELLE by going beyond production of single weak bosons. Pair production may be more easily identifiable, and will certainly tell us more about the interactions of W's. A search for large Q^2 lepton pairs may not only reveal a neutral vector boson, but also indicate how neutral currents, associated with an extremely heavy Z^o,

5. T.D. Lee and G.C. Wick, Phys. Rev. Lett. D2, 1033 (1970).

overwhelm the electromagnetic current and induce gross violations of scaling. ISABELLE could put a tight constraint on gauge theories with neutral currents; the associated particle is either light enough to be produced, or too heavy, in which case the virtual effects are substantial.

DOWNSTREAM CALORIMETERS FOR ISABELLE

W. Selove

University of Pennsylvania

In most interactions at ISABELLE, one can expect several particles to be produced at quite small angles. Figure 1 shows a typical expected event if 150 GeV goes more or less along the beam direction and if the particles comprising that energy have a rapidity plateau distribution with $dN/dy = 2$. We thus consider the prospects of detecting particles of energies ~ 20 - 100 GeV, at angles of 1 - 20 mrad. These angles could be changed for charged particles by the use of magnets, but not for neutrals.

A particle emitted at 1 mrad is very difficult to get out of the beam pipe in a reasonable distance. In the present note we do not aim at detecting such neutrals. Instead we take a slightly weaker goal: we would like to measure separately the energies of two particles which might have energies of order 50 - 100 GeV each, and which might have a relative transverse momentum of $\sim 1/3$ - $\frac{1}{2}$ GeV/c. Such a pair of particles will separate with relative angle 5 - 10 mrad. We therefore consider a calorimeter array whose segments

a) are 5 - 10 mrad apart, and

b) are each large enough in area to give reasonable containment of a shower.

For the high energies we are dealing with, segment size could be as small as $\sim$ 4" x 4", to satisfy condition (b) -- then condition (a) suggests putting the calorimeter at least 20 m away from the intersection. A suitable arrangement with 24 elements 4" x 4" and 8 outer elements 10" x 10" is shown in Fig. 2. The calorimeter also has to be $2\frac{1}{2}$ - 3 m thick, and it therefore seems desirable to have straight sections with at least 30 m between intersection point and the first quadrupoles.

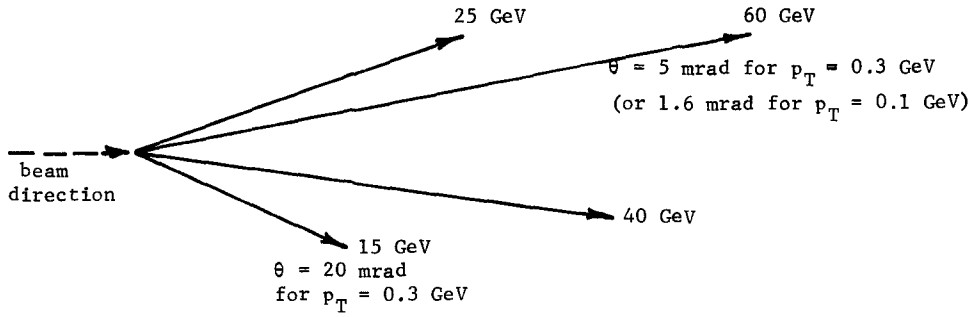

Fig. 1. Typical event with 150 GeV carried by four secondary particles near the beam direction.

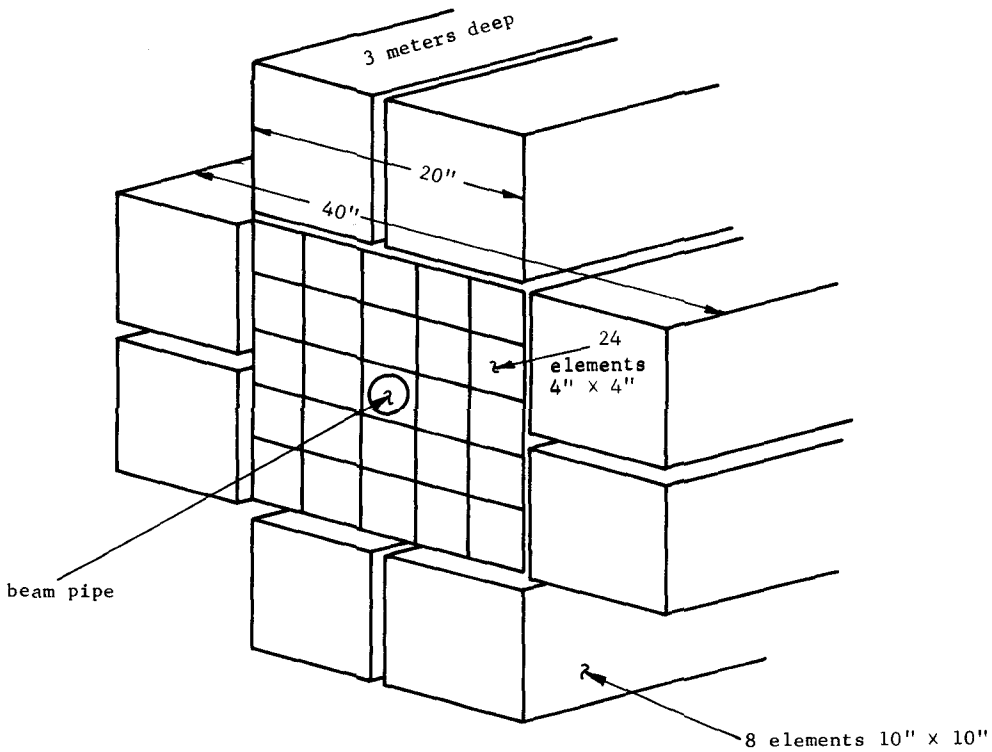

Fig. 2. Arrangement of calorimeter segments about the beam pipe.

Time resolution:

Pulse response

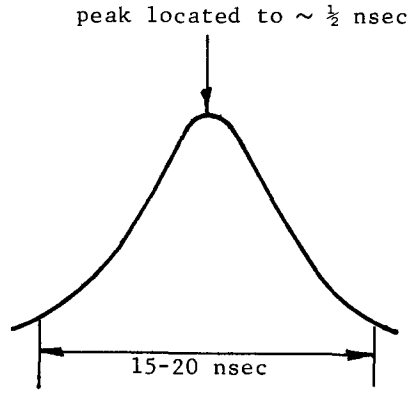

Use ADC gates of 20-30 nsec width.

Rates usable:

With 30 segments, and 3 - 5 particles/event, could work near full luminosity ($L = 10^{33}$, ~ 1 event/20 nsec).

Cost:

Central 24 elements: 150 phototubes
50 layers of plastic scintillator plus U or Fe
Cost, apart from electronics $ 75 000

Outer 8 elements: Cost, apart from electronics $ 50 000

[This is for one arm]

(Cost can be cut ~ ¼ by use of liquid scintillator)

A CALORIMETER EXPERIMENT FOR JET STUDIES AND OTHER USES OF MODULAR CALORIMETERS

A. Kanofsky
Lehigh University

I. Jet Studies

I describe here a modular calorimeter system to look for jets at ISABELLE. Part of the problem in any jet experiment is that you're not sure exactly what you're looking for,— i.e. at what values and over what range of angle, rapidity, or other kinematic variables jets occur. One solution, of course, is to cover the entire 4π solid angle with detector, but since one prediction for jet particles is that they have large $p_\perp$ values and also have small cross sections, one needs large momentum discriminating detectors, which are extremely costly. Such equipment could be expected to become operational after the first few years of ISABELLE, and it has been discussed in some detail by the large spectrometer group, and the weak interaction group. Even with such arrays, there is a possibility that a special augmenting detector necessary to discriminate between jets and other particles has been left out and will prove to be very difficult to incorporate into a massive 4π array.

Therefore, the approach taken here is that of starting small and building up. This is what has been done in a jet experiment at FNAL (Experiments 246 and 395) in which the author is a collaborator.

At Fermilab we have used a segmented modular calorimeter for detection of neutral and charged hadrons and photons and electrons. The segmenting is done optically with reflecting aluminum box inserts within the calorimeter modular boxes. Each calorimeter module box has four regions that are separately optically coupled to photomultipliers. Each region is 12" x 12" x 30" in volume, and is filled with liquid scintillator - iron sandwiches. A diagram of the module is shown in Fig. 1. For the experiment at FNAL the steel plates were 1 inch thick with 1 inch liquid scintillator gaps. With this arrangement, resolution of 15% FWHM has been determined for electrons, and

37% (without corrections) FWHM for pions. Uranium plates can improve these numbers by a factor of 2. The modules can be stacked so as to form larger arrays. Each box has about 2 interaction lengths of Fe plates in it.

We show in Fig. 2 such an array of calorimeter boxes arranged for a possible jet experiment. We have a wire chamber hodoscope placed in front of the boxes to determine the trajectory of the charged particles. The electrons and photons are detected by a large signal in the front of the first calorimeter, or 20" of Pb glass could be used. Of course, the Pb glass is much more expensive than the iron plate - liquid scintillator sandwich. Hadron showers penetrate further into the calorimeter boxes and are located by the segmented regions and by drift chambers sandwiched between the calorimeter boxes. The total length of the calorimeter is 8 interaction lengths. The optical segmenting is chosen to be 6" × 6" for a grid of 16 optically separated segments per module.

It is necessary to place the calorimeter boxes a sufficient distance away to separate the energies deposited in various regions.

The most difficult case will be detection of jets near the forward direction. One quarter of the particles in a 200 + 200 GeV high multiplicity event will be contained in a 5° forward cone. Average charged multiplicity at 400 GeV is 19 which gives about a total multiplicity of 30. Thus, there are approximately seven hadrons into each 5° forward cone. If the calorimeter module is placed to one side of the beam, as shown in Fig. 2, a distance 3 m away, a 6" segment subtends an angle of 3° per segment for an average of ~ 0.5 particles/segment. The solid angle subtended by a modest array of $(3 \times 3 \times 4)$ calorimeter boxes is ~ 0.5 steradians. The entire array should be expandable and moveable so as to allow for all possibilities. Additional modules are indicated in Fig. 2 by dotted outlines. It should be possible to rotate the apparatus out to 90° and swivel about an axis centered on the array so that the array can be pointed back to the intersection when not placed along the beam line. It would be best to use at least two such arrays, to look for correlations of

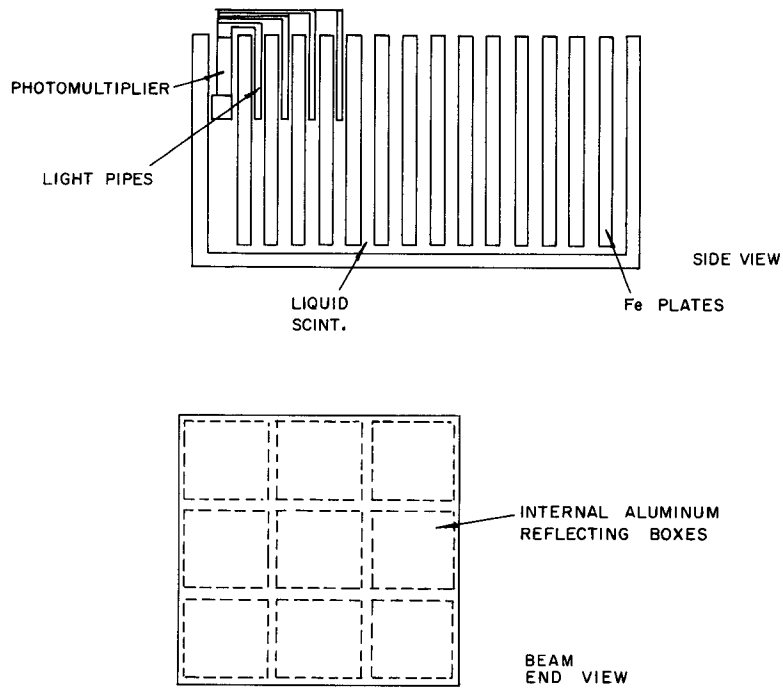

Fig. 1. Schematic arrangement of one module of modular segmented calorimeter.

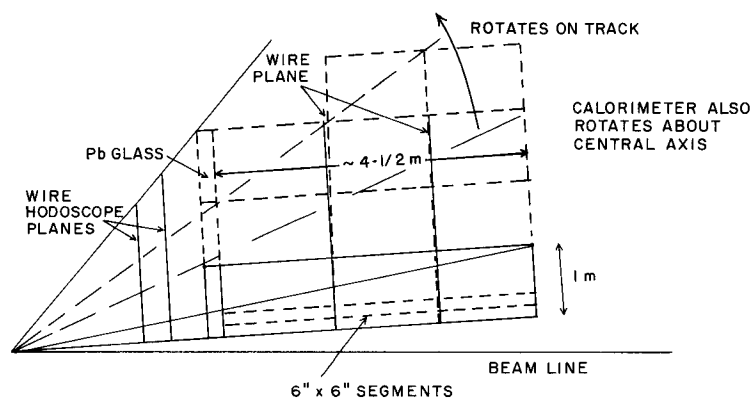

Fig. 2. Detector array made up of calorimeter modules.

particle-jet and jet-jet. It could also be used in conjunction with one or more magnetic spectrometers of the type described in other reports.[1,2] A large aperture low momentum resolution spectrometer placed before the array would certainly enhance the particle angle and energy resolving ability of the apparatus.

To give some idea of the costs, for an array of modules used for Experiment #395 with 27 segments, 40" x 32" and 130" deep, the cost is $25K for photomultipliers, $40K for construction, and $15K for electronics for a total of $80K.

II. Use in Conjunction with Other Apparatus

Calorimeter modules of the type described above may be used in conjunction with many other experimental setups at ISABELLE. They may be used as an integral part of the apparatus or as separate units enhancing the physics obtained from a separate apparatus.

The modules have the advantages (1) that they are segmented and thus offer angular resolution, (2) that they may be arranged in any array desired with very little dead space between, and (3) if such mass modules were produced in a couple of standard units, they could become very cheap and economical. These modules could be stocked in large numbers at HEEP much the same as logic circuits are. They could be constructed by Brookhaven people or by an outside manufacturer. The cost of materials and construction labor is not expensive compared to the cost of labor for design and jig fabrication.

We now briefly mention some of the experiments where such modules would be useful:

1. The high $p_\perp$ 90° experiment[1] would benefit greatly from such calorimeter modules.

---

1. C.Y. Chien, H. Gordon, A. Kanofsky, M.A. Kramer, and J. Russ, "A Single Arm Spectrometer to Study High $P_\perp$ Processes Near 90° at ISA", these Proc.

2. A. Kanofsky, "Experiments Using a Single Arm Spectrometer in the Intermediate Angle Region at ISABELLE", these Proc.

2. The large facility spectrometer envisions having spectrometers for downstream along the beam line.[3]

3. The 4π solid angle detector could be triggered on high $p_\perp$ events from either hadrons e's or μ's.[4] (See the report of P. Grannis and D. Green, these proceedings.)

4. The single arm spectrometer in the intermediate angle region needs these as an integral part of the unit.[2]

5. Stacks of these could be incorporated into the W search apparatus as the "end plugs" or as "end plugs" on an impactometer.[5]

---

3. L. Rosenson, S. Ting, J. Russell, W. Selove, S. Lindenbaum, W. Love, R. Louttit, S. Ozaki, F. Paige, E. Platner, and S. Protopopescu, "Large Equipment and Facilities", these Proc. Vol. I, p. 52.

4. S.U. Chung, P. Grannis, and D. Green, "A 4π Detector Experiment for ISABELLE", these Proc.

5. R. Burnstein, W.C. Carithers, M. Duong-van, R. Imlay, M. Kreisler, U. Nauenberg, C. Rubbia, L. Sulak, G. Snow, H.H. Williams, E. Paschos, M. Sakitt, C.L. Wang, and L.L. Wang, "Design of a Lepton Detector for ISABELLE", these Proc. Vol. I, p. 9.

CALCULATION OF RATES FOR HEAVY LEPTON SEARCH

C-Y. Chang
University of Maryland

N.P. Samios,
Brookhaven National Laboratory

The following expressions were used to calculate heavy lepton event rates and the background muon fluxes for planning the search for heavy leptons via a K_L^o-type experiment at ISABELLE. This search was described in Ref. 1.

A. Estimate of Event Rate:

1. Solid angle of decay region

$$\langle\Delta\Omega\rangle = 2\pi \int_1^{\cos\theta} -d\cos\theta = 2\pi\,(1 - \cos\theta)$$

$$= 2\pi\left(1 - \frac{15m}{\sqrt{15^2+1.5^2}\ m}\right) = 2\pi\,(1 - 0.995) = 0.031 \text{ sterad.}$$

2. Decay efficiency

$$\text{proper time of flight} = \frac{d}{\gamma v} = \frac{d}{c}\,\frac{M}{p}\,\frac{(\text{GeV})}{(\text{GeV/c})}$$

d_1 = crossing point to decay region $\simeq$ 12 meters

d_2 = decay region $\simeq$ 5 meters

$$\therefore\ t_1 = \frac{120}{3} \times \frac{M}{p}\ \text{nsec} = \frac{M}{p} \times 40\ \text{nsec}$$

$$t_2 = \frac{50}{3} \times \frac{M}{p}\ \text{nsec} = \frac{M}{p} \times 16.7\ \text{nsec}$$

Let $\tau' = \frac{p}{M}\,\tau \simeq \gamma\tau$ = laboratory life time

1. L. Lederman, "New and Unthinkable Ideas," these Proc., Vol. I, p. 84.

$$\varepsilon(\tau') = \int_{t_1}^{t_1+t_2} \frac{e^{-t/\tau}}{\tau} dt$$

$$= (e^{-t_1/\tau} - e^{-(t_1+t_2)/\tau})$$

$$= (e^{-40/\tau'} - e^{-56.7/\tau'})$$

$$\frac{d\varepsilon}{d\tau'} = 0 = \frac{40}{\tau'^2} e^{-40/\tau'} - \frac{56.7}{\tau'^2} e^{-56.7/\tau'}$$

i.e. $\frac{56.7}{40} = e^{16.7/\tau'} = 1.4175$

$$\tau' = 16.7/\ln 1.4175 = \frac{16.7}{0.34889} = 47.86 \text{ nsec}$$

$$\overline{e(\tau')} = e^{-40/47.85} - e^{-56.7/47.86}$$

$$= 0.43354 - 0.30584 = 0.1277$$

$$\therefore \varepsilon(\tau')_{\text{max efficiency}} = 0.1277$$

3. Most sensitive life time: $\tau = 47.86$ M/p

TABLE I

Most Sensitive Life Times

	M = 5	10	50 GeV/c^2
p = 10 GeV/c	24 nsec	47.9 nsec	239 nsec
20 GeV/c	12 nsec	23.9 nsec	119 nsec
50 GeV/c	4.8 nsec	9.6 nsec	47.9 nsec

4. Event rate at $L = 10^{32}$ $cm^{-2}sec^{-1}$

$$\Delta\Omega \times \varepsilon(\tau') = 0.0314 \times 0.1277 = 4 \times 10^{-3}$$

$$\therefore 10^{+32} \times 4 \times 10^{-3} \times 10^{-33} \text{ evt./nb-sec}$$

$= 4 \times 10^{-4}$ evt./nb-sec

$\simeq 400$ evt./nb-300 hr.

B. Estimate of the muon background flux:

1. The energy spectrum in the laboratory system of a μ-meson from a decaying primary meson of energy E' is rectangular between kE' and E' and zero outside these limits ($k = 0.57$ for π primaries, $k = 0.04$ for $K^{\pm}$ primaries).

2. The mean free path for decay of the primary is $\infty\ \lambda E$, where $\lambda = 55$ m - GeV/c^{-1} for π and $\lambda = 7.4$ m - GeV/c^{-1} for K-mesons.

3. Luminosity of ISABELLE is $L = 10^{32}\ cm^{-2}sec^{-1}$.

4. $\sigma_{inv.}\ (pp \rightarrow \pi^{+} + X) \simeq \sigma_{inv.}\ (pp \rightarrow \pi^{-} + X)$

$$\simeq (10 \text{ to } 20) \times \sigma_{inv.}\ (pp \rightarrow K^{\pm} + X)$$

and only $\simeq 60\%\ K^{\pm} \rightarrow \mu^{\pm}\upsilon$.

$\therefore$ We ignore $K^{\pm} \rightarrow \mu^{\pm}\upsilon$, and assuming $N_{\mu} \simeq 3\ N_{\mu^{+}}$ from π^{+} decay.

5. Contours of constant $\sigma_{inv.}$ at ISA for $pp \rightarrow \pi^{+} + X$ are shown in Fig. 1. (This was compiled by M. Albrow, et al., on ISR data.)

The acceptance of the apparatus is shown by the unshaded region. The limits are defined by

a. The beam pipe

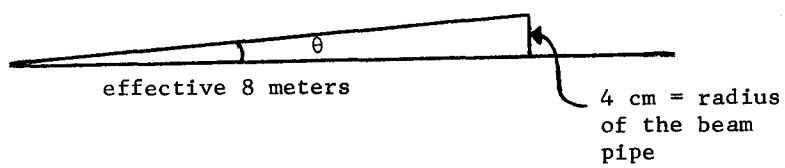

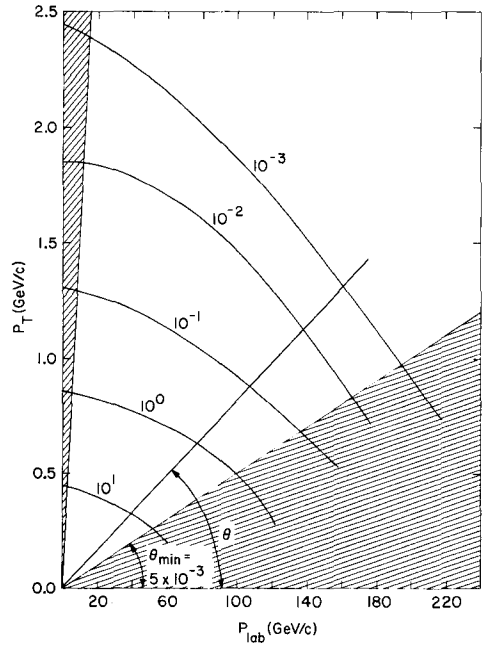

Fig. 1. Contours of constant $\sigma_{inv.}$ at ISABELLE, for $p + p \rightarrow \pi^+ + X$, based on ISR data of Albrow et al. The curves are for $E \frac{d^3\sigma}{dp^3}$ in mb/GeV^2.

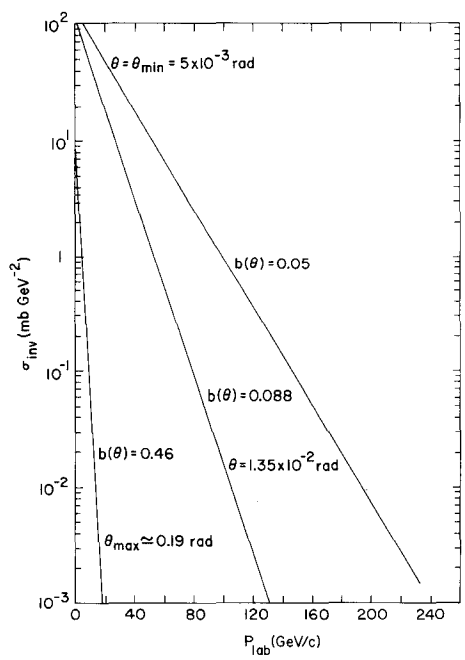

Fig. 2. Muon spectra at different angles.

$$\therefore\ \theta \simeq \frac{4}{800} = 5 \times 10^{-3}$$

$$P_t \text{ min} = 5\ P_L \times 10^{-3}$$

b. The dimension of the detector.

6. The $\mu^{\pm}$ spectrum

$$\frac{N_\mu(E_\mu)}{\Delta E_\mu} \cdot d\Omega = 3 \times L \times \int_{E_\mu}^{E_\mu/K} \frac{1}{E_\pi}\left(E_\pi \cdot \frac{d^3\sigma}{dp_\pi{}^3}\right) p_\pi{}^2 dp_\pi d\Omega$$

$$\times \frac{1 - e^{-x/\lambda E_\pi}}{(1-k)E_\pi}$$

where $k = 0.57$, $\lambda = 55$ m GeV^{-1}, $L = 10^{32}$ cm^{-2}sec^{-1}

$X \simeq 8$ meters, $E_\pi \simeq P_L \geq 7$ GeV/c

$$E\frac{d^3\sigma}{dp^3} = \sigma_{inv.} \times 10^{-27}\ \text{cm}^2 - \text{GeV}^{-2}$$

where $\sigma_{inv.}$ (in unit of mb-GeV^{-2}) can be represented approximately by $\sigma_o e^{-b(\theta)P_L}$. The parameter $b(\theta)$, given in Table II, can be obtained numerically from Fig. 1. This expression can be integrated as follows:

$$\therefore\ \frac{N_\mu(E_\mu)}{\Delta E_\mu} d\Omega \simeq \frac{3 \times 10^5}{0.43} \times \frac{8}{55} d\Omega \int_{E_\mu}^{1.75E_\mu} \sigma_{inv.} \frac{dp_L}{p_L}$$

$$= 10^5\ d\Omega \int_{E_\mu}^{1.75E_\mu} \sigma_{inv.}(P_L,\theta) \frac{dp_L}{p_L}$$

$$= 10^5\ d\Omega \int_{E_\mu}^{1.75E_\mu} \sigma_o e^{-b(\theta)P_L} \frac{dP_L}{P_L}$$

$$= 10^5 \sigma_o \, d\Omega \int_{b(\theta)E_\mu}^{1.75b(\theta)E_\mu} \frac{e^{-x}}{x} dx \text{ Sec}^{-1} - \text{GeV}_\mu^{-1}$$

Now: $El(x) \equiv - \int_{-\infty}^{-x} \frac{e^t}{t} dt = \int_x^{\infty} \frac{e^{-t}}{t} dt$

for $0 < X < \infty$

is the exponential integral.

$$\sigma_o \simeq 100 \text{ mb} - \text{GeV}^2\left(x \, e^{-6P_t}\right)$$

$d\Omega \simeq 10^{-3}$ str. (the total $\Delta\Omega$ is 31 m str.)

$$\therefore \frac{N_\mu}{\Delta E} \simeq 10^4\left(\int_{b(\theta)E_\mu}^{\infty} \frac{e^{-t}}{t} dt - \int_{1.75b(\theta)E_\mu}^{\infty} \frac{e^{-t}}{t} dt\right)$$

$$= 10^4 \times [El(b(\theta)E_\mu) - El\ (1.75b(\theta)E_\mu)]\text{sec}^{-1} - \text{m str.}^{-1}$$
$$- \text{GeV/c}^{-1}$$

where $b(\theta)$ is given in the table below:

TABLE II

Pion Spectrum Parameter

	θ	$b(\theta)$
θ min. =	$5 \times 10^{-3} = 0.29^o$	$\ln 10^4/185 = \frac{9.21}{185} = 5 \times 10^{-2}$ GeV^{-1}
	$1.35 \times 10^{-2} = 0.77^o$	$\ln 10^4/105 = 8.8 \times 10^{-2}$ GeV^{-1}
θ max. =	$0.19 = 10.9^o$	$\ln 10^4/20 = 4.6 \times 10^{-1}$ GeV^{-1}

TABLE III

Muon Spectrum Results

$\theta = \theta$ min. $= 5 \times 10^{-3}$		$b(\theta) = 5 \times 10^{-2}$		
E_μ	$x = b(\theta)E_\mu$	$E1(x)$	$E1(1.75\ x)$	$N_\mu/\Delta E_\mu$
10	0.5	0.56	0.27	3×10^{3}
50	2.5	2.5×10^{-2}	3×10^{-3}	2.2×10^{2}
100	5.0	1.3×10^{-3}	10^{-5}	13
150	7.5	10^{-4}	10^{-7}	1
200	10	4×10^{-6}	0	4×10^{-2}
$\theta = 1.35 \times 10^{-2}$		$b(\theta) = 8.8 \times 10^{-2}$		
E_μ	$x = b(\theta)E_\mu$	$E1(x)$	$E1(1.75\ x)$	$N_\mu/\Delta E_\mu$
10	.88	0.27	0.10	1700
50	4.4	2.3×10^{-3}	4×10^{-5}	23
100	8.8	10^{-5}	------	0.1
150	13.2	1.6×10^{-7}	------	10^{-3}
200	17.6	10^{-9}	------	10^{-5}
$\theta = \theta$ max. $= 0.19$		$b(\theta) = 0.46$		
E_μ	$x = b(\theta)E_\mu$	$E1(x)$	$E1(1.75\ x)$	$N_\mu/\Delta E_\mu$
10	4.6	1.8×10^{-3}	3.7×10^{-5}	18
20	9.2	1.2×10^{-5}	-------	1.2×10^{-2}
30	13.8	5×10^{-8}	-------	5×10^{-4}

ON THE POSSIBILITY OF USING ISABELLE WITH GAS JETS AND OTHER LIKE BEAMS

A. Kanofsky
Lehigh University

In this note I point out that the internal beams in ISABELLE are an effective factor of 200 higher in intensity than those available at the internal target area at FNAL. It should be possible to run the same types of experiments at an insertion area at ISABELLE. The FNAL internal target area has proved to be extremely productive for small angle elastic and inelastic scattering experiments. A representative list of experiments executed and proposed is given at the end of this note.[1] Larger angle scattering experiments will be run in the near future with the addition of a single arm spectrometer and with the addition of a superconducting spectrometer later.

At FNAL the beam intensity is given by[1] the product of the number circulating protons times beam traversals: $1 \times 10^{13} \times 5 \times 10^{4} = 5 \times 10^{17}$ with a pulse every tenth second for an average of 5×10^{16}. At ISABELLE, the same numbers are 6×10^{14} beam $\times 10^{5}$ traversals $= 6 \times 10^{19}$ with a continuous beam, for a number of 6×10^{19}, a factor of about 10^{3} higher. This should enable high beam intensity experiments to be performed with more ease. Such low rate experiments as elastic p-p scattering at large angles and rare particle decays might be possible. The gas jet provides particles that are essentially stationary and thus provides an extension of asymmetric beam operation to 200×0. This could be useful in checking normalization of results, comparison with FNAL and SPS, etc.

A gas jet target or possibly an atomic beam could be positioned at the beginning of the insertion with apparatus downstream. The 20 m to the intersection region should be more than adequate for the placement of spectrometer, etc. By comparison the room size at FNAL for housing the spectrometer is 40' $\times$ 50' in area. Shielding blocks could be placed about the beam line downstream of the

1. "Internal Target Area Expanded", D. Jovanovic, NALREP, June 1975.

apparatus, so that experiments might even be run in the same intersection region without undue background.

Beam Degradation

The typical jet target densities at the internal target area at FNAL are 1×10^{-7} g/cm^3 which corresponds to a particle density of $6 \times 10^{23} \times 10^{-7}/\text{cm}^3 = 6 \times 10^{16}/\text{cm}^3$. This would result in an interaction rate of (assuming 40 mb cross section) $6 \times 10^{16} \times 4 \times 10^{-26} \times 6 \times 10^{19} = 144 \times 10^9$ events/sec which corresponds to removal of a beam fraction $144 \times 10^9/6 \times 10^{14}$/sec $= 2.4 \times 10^{-4}$/sec. Thus the beam could run for 4000 sec before a significant reduction in luminosity occurred for the same jet density as at FNAL. This would of course, represent a rather short beam lifetime, and a lower jet density would probably be necessary for compatibility with other scheduled experiments. Also as we mentioned, polarized atomic beam targets could be used as described recently by Jovanovic.[1]

Any use of a gas jet assumes that it is possible to provide high enough pumping speed in the vicinity of the jet that the vacuum in the remainder of the machine does not deteriorate. This is a stringent requirement, which has not been evaluated quantitatively.

Representative list of Internal Target Experiments at FNAL:

#36 - "A Proposal to Study Small Angle p-p Scattering at Very High Energies", R.L. Cool et al., 1971.

#63 - "Survey of Particle Production in Proton Collisions at FNAL", J.K. Walker et al., 1970.

#184 - "Search for a New Class of Penetrating Massive Particles at C-O", A.K. Mann et al. , 1972.

#186 - "A Proposal to Study Small Angle Proton-Deuteron Scattering", A.C. Melissinos et al., 1972.

#221 - "P-P Inelastic Scattering in the Diffractive Region", P. Franzini et al. , 1973.

#317 - Proton-Nucleon Inelastic, S. Mukhin et al., 1974.

#386 - Particle Search, Jery Lord et al. (1975).

CHANNELING AND SOME OF THE THINGS YOU MIGHT DO WITH IT AT ISABELLE

A. Kanofsky
Lehigh University

I discuss here the phenomena of channeling of particles through crystals and how it may be used at ISABELLE. Channeling of particles is the phenomenon where particles are steered between the lattice planes in a crystal by the atoms of the lattice. If there is one direction in which many of these lattice planes lie, then this direction is the principal channel axis direction. The phenomenon is shown schematically in Fig. 1. Channeling was discovered in the mid-nineteen sixties and has been investigated principally at energies of a few MeV. It has been used to study crystal structure and as a means to determine lifetimes of excited nuclear states in the range of 10^{-18} sec.

Recently, this author initiated the first studies of high energy channeling in the GeV range. The author and his collaborators have observed dechanneling of negative pions of 4 GeV/c momentum (where they are scattered out of the channel) through a 1 cm thick Ge crystal.[1] Also an Aarhus-CERN group has observed channeling of protons of 1 GeV.[2]

The author and colleagues have an experiment scheduled at the FNAL to study channeling at energies up to 200 GeV. If the particles enter the crystal such as to make an angle with the principal axis direction greater than the so-called "critical angle" they will not be steered in the channel successfully through the crystal, but will instead leave the channel and undergo collisions with the crystal nuclei. The critical angle varies inversely as the square root of the energy and is $\sim$ 1 mrad at 1 GeV as measured by the author's group and at CERN.

---

1. D. Allen, W. Gibson, D. Gockley, A. Kanofsky, G. Lazo, and H. Wegner, to be published.
2. O. Fich, J.A. Golovchenko, K.O. Nielsen, E. Uggerhad, G. Charpak, F. Sauli, Phys. Lett. 57B, 90 (1975).

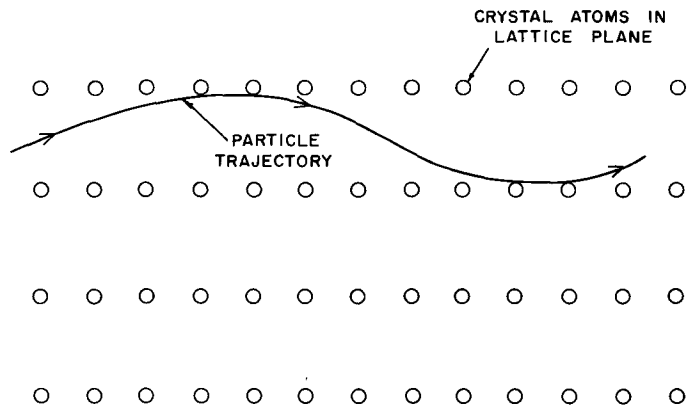

Fig. 1. Schematic of channeling in an aligned crystal.

Thus, at 200 GeV the critical angle would be about 1 mrad/$\sqrt{200}$ = 0.07 mrad or 70 μrad. The FNAL experiment will be able to provide such angular resolution. The angular spread of the proposed proton beams in the ISA storage rings will be less than 40 μrad, well within the critical angle. At low energies, if particles have an angle less than the critical angle most are transmitted through the crystal. Some, however, are still deflected out of the channel. A measure of how many are deflected out is the "dechanneling length" which is the thickness of the crystal at which half of the particles going along the channel direction are scattered out (i.e. have angle greater than the critical angle). The dechanneling length is proportional to energy. At MeV energies the dechanneling length is on the order of 10 microns. At 200 GeV, the length could be as high as 2×10^5 times larger — that is 2 m.[3] Thus, crystals of 1 cm thickness should appear "transparent" to the circulating proton beam. Such a possibility is intriguing. It offers several potential applications:

1. Measurement of beam profiles with a solid state counter attached to the crystal.

2. Measurement of energy and intensity of particles - possibility of reduction in relativistic rise shielding (i.e. density effect).

3. It can provide a variable density target where the density can be varied according to the rotation angle of the crystal. This could be used in place of a jet target for experiments similar to the internal target experiments at FNAL.

4. It can provide a means to do production target experiments where short lived particles produced at one nuclear site can then be targeted onto the following nucleus by aligning the crystal so that the beam is along the channel direction.

5. It can provide rapid reduction of beam energy without appreciable loss of intensity.

---

3. Experiments to be performed in the near future at FNAL will determine the exact values.

We now comment and elaborate on each of the above.

1. An experiment to measure ionization current in the channeling beam crystal was performed in the Aarhus-CERN experiments. The channeling crystal was also a solid state detector. When the crystal channeling axis was aligned along the beam direction, the pulse height from each of the particles was reduced to ½ the value when the crystal was oriented randomly. It would be possible to make a segmented solid state detector with at least 0.1 mm resolution so as to determine the exact beam profile. Such a microdetector is shown in Fig. 2. The probes would have to have overlaid insulator of the same structure as the channeling material so as not to dechannel the particles. Such a detector could provide direct measurements of beam profile and luminosity which are essential for many precision experiments, e.g. σ_T, assuming that it could function in the high intensity beam. This problem is discussed later.

2. The observation of the Aarhus-CERN group indicates a shielding of distant atoms by closest-to-channeling-particle nuclei. This means on-channel nuclei are the principal contributors to the ionization. Thus, one would expect no neighbor atom shielding which is responsible for the reduction of the relativistic rise — i.e., the density effect. Thus, one could expect very precise measurement of the energy and intensity (based on the integrated current from many beam particles).

3. I have already mentioned that the crystal would be "transparent" to the beam. One can make use of this fact to insert the crystal in the beam without loss of beam particles, the only effect being the ionization dE/dx energy losses. Now, if one rotated the crystal so as to give some of the particles an angle with the channeling axis greater than the critical angle, there would be interactions of the particles with the nuclei in the crystal. Thus, we could have a variable density target whose density, in effect, is determined by the crystal rotation angle. The goniometer at the AGS used in the dechanneling experiment had an angular reading of 1/1000 of a degree. The angular setting is at least as good as

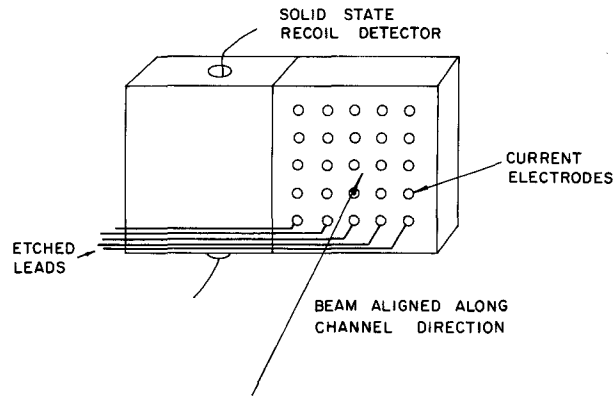

Fig. 2. Segmented solid state detector utilizing channeling.

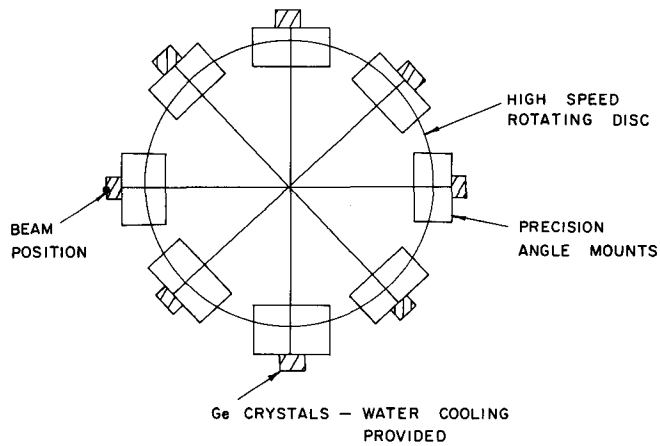

Fig. 3. Rotating crystal mount for short dwell time in beam.

ten times greater or

$$1/100 \times 1/57 = 1.75 \times 10^{-4} \text{ rad}$$
$$= 0.175 \text{ mrad} \quad .$$

If the setting were good to 1/1000 of a degree, this would be 17 μrad. This would be more than adequate to do precise alignment and rotation of the crystal. The crystal could serve as well as a solid state detector to measure recoil particle energies. The sensitive recoil particle region could be separated from the beam region. As mentioned before, it could serve the same function as a low density jet of particles at the internal target at FNAL.

4. Carrigan has proposed the use of an aligned crystal with the nuclei lined up along the incoming particle beam direction to measure interactions of short lived particles such as the φ/J with matter.[4] The process he envisions is that the φ would be produced at one nuclear site and would interact with the nucleus at the next site before it decayed. The probability for interaction would be enhanced by the fact that the nuclei are directly in line. However, thermal vibration of the nucleus prevents this from being strictly the case. Such experiments could certainly be performed at ISABELLE.

5. Rapid reduction of beam energy without appreciable loss of intensity is discussed below.

Mechanical Implementation

The channeling crystal must be cooled to keep it from reaching extreme high temperatures due to dE/dx losses which can be computed to be 10^4 kW/cm for Germanium and for 10 A beam intensity. This is a serious problem which can hopefully be solved by advanced engineering. Possibly the crystal could be rotated rapidly in and out of the beam with total dwell time being only 0.1 msec or so. A possible crystal mount is shown in Fig. 3. Possibly an internal magnetic accelerating system could be used instead of the rotating mount. Of course, the beam can be reduced by any factor desired.

---

4. R.A. Carrigan, W.M. Gibson, and A. Kanofsky, et al., Proposal submitted to Fermilab.

Also, one could steer the beam into the crystal for a short period. Finally, the crystal could be thinner and self-supporting, and crystals on the order of 10^{-3} cm thickness have been used for channeling studies and detectors of 10^{-3} cm have been constructed. Radiation damage might be another serious problem. It is not clear what happens in this case since presumably there are few displaced nuclei.

Also beam energy degradation would argue for thin crystals and short dwell times since the energy loss/particle - sec would be $5.36 \times 10^5 \times 1 \times 10^{-3} = 536$ MeV/sec for a 10^{-3} cm thick crystal that was in the beam for 1 second.

Now, if the dwell time is only 0.1 msec the energy loss is 0.053 MeV = 53 keV, an energy loss which could be made up by accelerating stations — or the beam could be allowed to degrade in some programmed way with the device. In fact, it would be possible in this way to rapidly lower the beam energy without reducing the intensity.

In conclusion, I foresee many useful machine and experimental applications for channeling at ISABELLE.

ISABELLE WITH ONE LOW - β INSERTION

A. Garren

Lawrence Berkeley Laboratory

1. Introduction

The standard ISABELLE configuration has eight identical insertions with $\beta_h = 20$ m, $\beta_v = 4$ m at the crossing points. It is possible to tune the betas by adjusting the four quadrupoles on each side of any crossing. During operation, it may be experimentally desirable to run with some crossings different than others in regard to their β values.

Such operation lowers the machine periodicity so that structure resonances from ring quadrupoles and chromaticity sextupoles will occur closer to the working point and may be larger compared to those in the standard configuration. Moreover, the momentum dependence of the tunes and betas at each crossing will be altered. The β-variations between crossings and their momentum dependence will cause beam-beam resonances to occur closer to the working point and to have a momentum dependence.

In order to investigate the feasibility of operating with unequal crossings, a study was made of the case where 7 insertions are standard and one is tuned to produce a lower β_v. To this end it was necessary to recalculate the quadrupole and sextupole strengths to restore the correct tunes, preserve matching of the insertions to the cells and bring the chromaticities to zero. Having done that, the momentum dependence of the tunes and of the β-values at the crossings were computed and the third order resonances from the sextupoles were calculated analytically.

2. Recalculating the Lattice

A run had previously been made by M. Month with TRANSPORT to obtain the strengths of the 4 quadrupoles on either side of the low-β crossing. This low-β insertion was combined with 7 standard ones in a SYNCH run of the complete ring. The tune values given

by this run were incorrect, due to the new insertion. Therefore, cell quadrupole strengths were changed in a way desired to produce the proper tunes. Since the cell β-values were thereby altered, the standard and low-beta insertions were rematched to the altered cells. This was done using a new fitting facility in SYNCH, that utilizes the CERN optimizing program MINUIT. The procedure was then iterated to improve the tune values.

Having obtained a well matched ring with the desired tunes $\nu_h = \nu_v = 25.63$, strengths of the sextupole windings located in the F and D quadrupoles of the 7 normal cells of each octant were calculated so that the chromaticities would be zero. For this calculation, the chromaticities produced by the quadrupoles are needed. These are calculated by SYNCH, using a modification introduced by E. Courant in the program. We will discuss the distribution of sextupoles in greater detail later on.

3. Calculation of Momentum Dependences and Results

The complete ring, including the chromaticity correcting sextupoles, was input to the routine FXPT of SYNCH. This routine calculates a closed orbit corresponding to a specified momentum deviation, and then calculates tunes and β-values by linearizing the nonlinear transformations in the neighborhood of the closed orbit. The calculation was done for $-0.018 \leq \Delta p/p \leq 0.018$ in steps of 0.001. The required momentum spread at 200 GeV is only 1/8 as large.

a) Variation of the Tunes

The resulting momentum dependence of the tunes is shown in Fig. 1. It will be recalled that the sextupoles strengths were calculated for zero chromaticities. In fact, small positive values will be required. When these are introduced the effect is roughly to tilt the curves, but not change their shape. It will be noted that the vertical chromaticity is not quite zero, but has a value $\xi_v = d\,\nu_v/d(\Delta p/p) = -0.07$ at $\Delta p/p = 0$. This small value could be removed by a slight change in sextupole strengths.

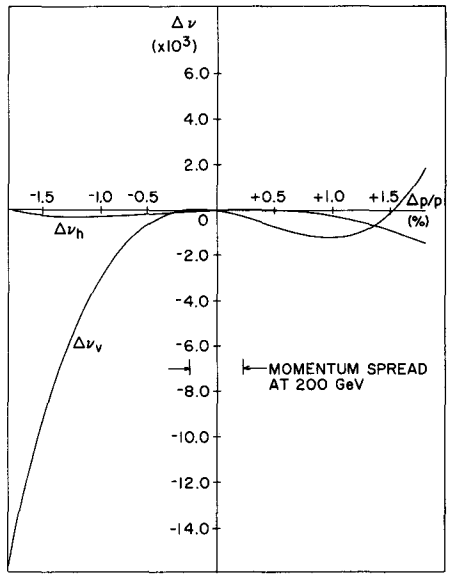

Fig. 1 - Dependence of tunes on momentum after chromaticity correction with sextupoles. $\Delta\nu = \nu(p) - \nu_o$. The central tunes are $\nu_{ho} = \nu_{vo} = 25.63$.

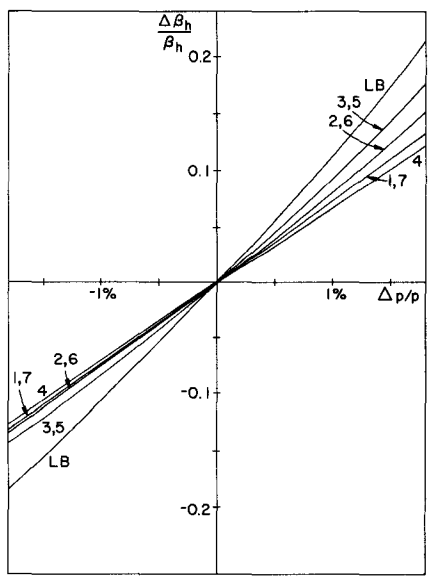

Fig. 2 - Relative variation of β_h with momentum at the crossing points, with 1 low-β crossing and 7 normal crossings. Curves show $(\beta_h - \beta_{ho})/\beta_{ho}$, where β_{ho} - 20.38 m at low-β crossing, β_{ho} = 20.44 m at crossings 1 - 7. Chromaticity has been corrected.

Figure 1 may be compared with Fig. 9 of a report by Month.[1] The horizontal tune is not changed very much - in fact it deviates less with the low-β insertion than without. However, the vertical tune behaves quite differently. In the case of 8 equal insertions $\Delta\nu_v$ is positive for both positive and negative $\Delta p/p$, but with the low-β insertion present the ν_v curve is S-shaped. There is appreciably more curvature within the momentum spread of the beam (0.45%), however, deviation of of $\Delta p/p = -1.5\%$ is about the same in magnitude but opposite in sign. The curvature within the stack is probably not too great to live with. It can be reduced with ocutpoles, and also by altering the distribution of sextupoles.

b) Variation of the β-functions

The momentum dependence of the horizontal beta function, β_h, at the low beta (LB) crossing and at the 7 standard crossings (1-7) are shown in Fig. 2. The corresponding curve for the ring with 8 standard insertions is shown in Fig. 9 of the report by Month.[1] The 7 standard insertions now show differences among themselves, but the average is similar to the symmetric case. The low-β crossing shows a somewhat stronger momentum than do the standard insertions. At each crossing β_h varies almost linearly with momentum.

The situation is very different for the vertical beta function, β_v, shown in Fig. 3. In contrast to the symmetric case, the β_v curves at all the crossings show on the average about five times as much total variation, they have considerable curvature, and the slopes vary in sign between crossings.

Over the beam stack width β_v varies by at most 10%. This may have implications on the beam-beam effects, but the largest such effect is the introduction of additional beam-beam resonances due to the one-fold periodicity, with one $\beta_v = 1$ m crossing and seven $\beta_v = 4$ m crossings. Compared to this gross effect the additional

---

1. M. Month, BNL Rept., ISA 75-10 (1975).

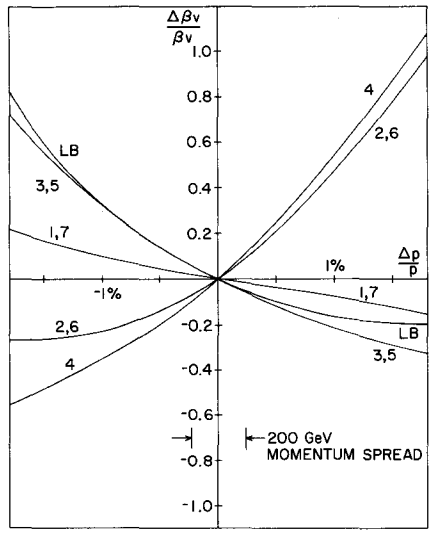

Fig. 3 - Relative variation of β_v with momentum at the crossing points, with one low-β crossing. Curves show $(\beta_v - \beta_{vo})/\beta_{vo}$, where β_{vo} = 1.00 m at the low-β crossing. β_{vo} = 4.00 m at crossings 1 - 7. Chromaticity has been corrected. The required momentum spread at 200 GeV is 0.46%.

10% momentum variations seem trivial. These variations probably do not affect the strong-beam density distribution seen by the weak beam very much, because the dispersion is zero at the crossings and the β_v curves are fairly linear over the stack width. The response of the weak beam to multipole components in the strong beam depends on the β-values of the former, and so will reflect the 10% β variations.

4. Sextupole Distributions and Resonances

It is the intent of the present exercise to get an idea whether one can live with one low-β insertion without resorting to heroic measures. Therefore, the calculations were done with only two families of sextupoles of the 7 normal cells of each octant. The distribution (called A) is shown in Fig. 5. The two sextupoles at the ends of the 7 cells are run at half-strength, to preserve symmetric distribution with equal strengths in 7 successive QF quadrupoles will give comparable values of the second and third order resonance widths.

The principal resonances induced by the sextupoles at tune values for which $\omega = \ell\nu_h + m\nu_v$ is an integer (p) occur for orders $n = \ell + m = 2,3$. Their widths are proportional to the magnitude of the integral[2]

$$I_n = \oint K^{(n-2)} \beta_h^{\ell/2} \beta_v^{m/2} e^{i(\ell\Psi_h + m\Psi_v)} ds$$

$$K^{(0)} = \frac{B''}{Bp} \eta \frac{\Delta p}{p} \quad , \quad K^{(1)} = \frac{B''}{Bp} \quad ,$$

Ψ_h and Ψ_v are the betatron phases and η is the dispersion function.* The resonance half-widths are given by

$$\Delta\omega = (1/2^n \ell!\, m!)\, |I|\, \epsilon_h^{\ell/2} \epsilon_v^{m/2} (\ell^2/\epsilon_h + m^2/\epsilon_v).$$

---

* Strictly speaking the phase factor in the integral for resonance $\omega = p$ is $\phi = \ell\Psi_h + m\Psi_v - (\ell\nu_h + m\nu_v - p)\,\theta$.

2. See for example "Chromaticity Corrections for Large Proton Storage Rings at CERN", by B. Autin and A. Garren, ISR report (1975), to be issued shortly.

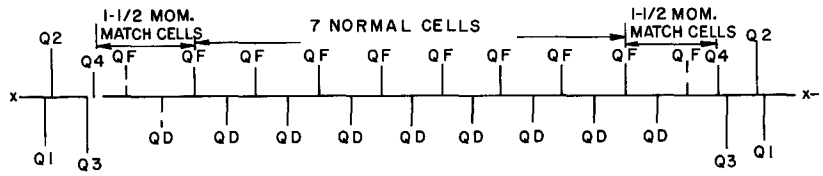

Fig. 4 - Schematic of the focusing structure of one octant. Windings for chromaticity sextupoles are included in the QF and QD quadrupoles. Two sextupole distributions discussed in the text are shown in Figs. 5 and 6.

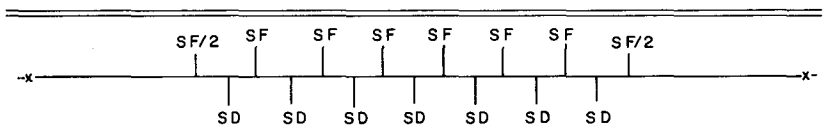

Fig. 5 - Sextupole distribution (A) used in numerical calculations with SYNCH that produces Figs. 1 - 3.

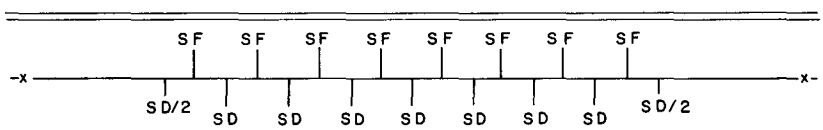

Fig. 6 - Alternative sextupole distribution (B). Sextupoles with strength SD/2 are placed in quadrupoles of the momentum match cells. $\ell B''(SF) = 886.2$ kG-m^{-1}, $\ell B''(SD) = -1905.2$ kG-m^{-1}.

For the distribution A of Fig. 5 we find

$$|I_n| = \frac{\sin(N_s\ \Delta_s/2)}{\sin(\Delta_s/2)} \quad \frac{\sin(N\Delta/2)}{\sin(\Delta/2)} \left[(S\ U_n \beta^{n/2})_F \cos(\Delta/2) + (S\ U_n \beta^{n/2})_D \right]$$

where

N_s = number of superperiods (8)

N = number of cells with sextupoles (7)

$\Delta_s = \ell\mu_{hs} + m\mu_{vs}$; μ_{hs} , μ_{vs} = phase advance per standard octant.

$\Delta = \ell\mu_h + \ell\mu_v$; μ_h , μ_v = phase advance per cell.

$S = \ell B''/Bp$

$U_2 = \eta\ \Delta p/p$, $U_3 = 1$

$\beta^{n/2} \equiv \beta_h^{\ell/2}\ \beta_v^{m/2}$, ϵ = beam emittance $/\pi$

The numerical values used, obtained from the fitting calculations with SYNCH are:

$$\frac{\mu_{hs}}{2\pi} = 3.19213, \quad \frac{\mu_{vs}}{2\pi} = 3.21982, \quad \frac{\mu_h}{2\pi} = 0.25129, \quad \frac{\mu_v}{2\pi} = 0.24824$$

$(\ell B'')_F = 1012.8$, $(\ell B'')_D = -2178.8$ (kG-m^{-1})

$\beta_{hF} = 42.76$, $\beta_{vF} = 7.60$, $\beta_{hD} = 7.48$, $\beta_{vD} = 42.86$ (m)

$\eta_F = 1.645$ m, $\eta_D = 0.797$ m

We evaluate the integrals and resonance widths corresponding to the 200 GeV beam emittances $\epsilon_h = \epsilon_v = 5.7 \times 10^{-8}$ rad·m and momentum half width $\Delta p/p = 0.0025$, and obtain the values shown in Table I:

TABLE I

Resonance Integrals and Half-Widths for Distribution A, Fig. 5. This Distribution was used to produce Figs. 1-3.

n	ℓ	m	$\lvert I_n \rvert$	$\Delta\omega/n$
2	2	0	0.501 $\Delta p/p$	0.10×10^{-3}
	0	2	11.29 $\Delta p/p$	2.25×10^{-3}
3	3	0	39.5	1.88×10^{-4}
	1	2	5.62	0.44×10^{-4}

The small widths of the 3rd order resonances suggest it may be possible to move the working line quite close to the resonance $\ell\nu_h + m\nu_v = 3 \times (25-2/3)$. The relative sizes of the 2nd order resonances is associated with the comparatively bad behavior of the vertical tune and β-values with momentum.

It is of interest to compare distribution A with distribution B of Fig. 6. The latter may be expected to give better results because of the cancellations that occur in sets of four cells with 90° phase advance,[3] at least for the 3rd order terms. For these terms the two sextupoles in the D-quadrupoles of the momentum match cell see the same $K^{(n-2)}$ as those in the normal cells. However, this is not so for the 2nd order terms, because the dispersion function is different. Specifically we find:

$$|I_3| = \frac{\sin N_s\Delta_s/2}{\sin \Delta_s/2} \; \frac{\sin N\Delta/2}{\sin \Delta/2} \left[(S\,\beta^{3/2})_F + (S\,\beta^{3/2})_D \cos \Delta/2 \right]$$

$$|I_2| = \frac{\Delta p}{p} \frac{\sin N_s\Delta_s/2}{\sin \Delta_s/2} \left| (S\,\beta^{2/2}\,\eta)_F \frac{\sin N\Delta/2}{\sin \Delta/2} + (S\,\beta^{2/2})_D\, e^{i\Delta/2} \times \left(\eta_D \frac{\sin(N-1)\Delta/2}{\sin \Delta/2} + \bar{\eta}_D \cos N\Delta/2)\right)\right|$$

where $N_s = N = 8$, $\bar{\eta}_D$ is the dispersion in the end sextupoles, $\bar{\eta}_D = 0.4811$ m, and the other quantities have been defined previously. The strengths of the sextupoles are less by 7/8:

$$(\ell B'')_F = 886.2 \text{ kG-m}^{-1}, \quad (\ell B'')_D = -1905.2 \text{ kG-m}^{-1}$$

The numerical values for the integrals and widths for case B are given in Table II.

TABLE II

Resonance Integrals and Half-Widths for Distribution B, Fig. 6

n	ℓ	m	$\lvert I_n \rvert$	$\Delta\omega/n$
2	2	0	0.294 Δp/p	0.058×10^{-3}
	0	2	5.90 Δp/p	1.17×10^{-3}
3	3	0	4.44	0.21×10^{-4}
	1	2	0.44	0.0035×10^{-4}

3. D. Edwards and L. Teng; Appendix 8 of the Insertions Working Group's Report. CERN/ISR-AS/74-64.

As predicted the 3rd order resonances are suppressed much better, and happily there is also substantial improvement in the off-momentum stopbands. This should be reflected in the momentum dependence of the tunes and β-functions.

The above discussion is not quite complete in that the quadrupole contribution of the 2nd order resonances was ignored in Tables I and II. It may be desireable to modify the sextupole distributions to cancel these, if this can be done in a way to avoid increasing the 3rd order terms. The behavior of the tunes and beta functions however show that 2nd order effects from both quadrupoles and sextupoles are not too serious.

5. Conclusions

Operation of ISABELLE with a single low-β insertion appears feasible from a single particle standpoint, even if only two families of chromaticity sextupoles are used in the normal cells. Improvements are available if two sextupoles are added in momentum-matching cells. Further confirmation of feasibility could be obtained by orbit tracking computations.

Implications of the one-fold periodicity of the beam-beam multipole effects should be investigated further. However, these are probably not much affected by mismatch of the insertions for off-momentum orbits.

CLOSED ORBIT ADJUSTMENT

D. Edwards

Fermi National Accelerator Laboratory

1. Estimate of Closed Orbit Distortions

Quadrupole placement errors are likely to be the dominant source of closed orbit distortions. The mean square orbit displacement at a point where the amplitude function is β (and $\alpha = 0$) is

$$\langle x^2 \rangle = \frac{1}{4 \sin^2 \pi \nu} \frac{\beta}{2} \sum_i \beta_i q_i^2 \langle \delta_i^2 \rangle$$

$\langle \delta_i^2 \rangle$ = mean square position error of ith quadrupole

$q_i = B'_i \ell_i / B\rho$; ℓ_i = length of ith quadrupole

β_i = amplitude function at midpoint of ith quadrupole

For this estimate, parameters were obtained from a SYNCH printout provided during the study. In the tabulation below, Q4 is the quadrupole nearest to the intersection point.

Quad	B' (kG/m)	$\lvert q_i \rvert$ (m^{-1})	$\beta_i q_i^2$ (m^{-1}) (H)	(V)
Q4	-317.6	0.143	1.10	1.97
Q3	297.7	0.134	2.21	0.86
Q2	-459.8	0.069	0.04	0.20
Q1	0	0	0	0
normal F	660.0	0.115	0.56	0.10
normal D	-660.0	0.115	0.10	0.56

Note that if $\langle \delta_i^2 \rangle$ is the same for all quadrupoles, the contribution to $\langle x^2 \rangle$ from the intersection region quadrupoles is essentially the same as that of all the other quadrupoles combined.

The rms placement error has been estimated to be 0.35 mm.[1] at a point where β = 100 m, one would then have

1. G. Parzen, "ISABELLE Magnet Correction System", these Proc.

$x_{rms} = 13.7$ mm, $y_{rms} = 13.3$ mm

and in the normal cells, these displacements drop to about 9 mm at the focusing quad in each plane. At the crossing points, the rms displacements are 5 mm horizontally (at $\beta_H = 20$ m) and 2.7 mm vertically (at $\beta_V = 4$ m).

2. Correction System

Currently, it is proposed[1] that dipole windings be included in the main quadrupoles to permit steering of the beam. Here, it will be assumed that horizontal deflections are made at horizontally focusing quads, vertical deflections at vertically focusing quads. It will also be assumed that each such dipole can be powered individually.

The present plan calls for a maximum field of 1 kG in the normal cell quadrupoles. Taking an effective length of 1.3 m, at 30 GeV a dipole can then achieve a bend angle of 1.2 mrad. The phase advance in a normal cell is $\sim 90^{\circ}$; two dipoles 180° apart in phase will produce a 50 mm deflection at the quadrupole midway between them. This deflection is a factor of 5 larger than the rms displacement of the preceding section, thus the correction dipole strength is comfortably large at injection.

At 200 GeV, the same pair of dipoles could produce a deflection of $\sim$ 8 mm. This is still a comfortable correction capability, for based on observations at low energy, large closed orbit excursions will have been removed by quadrupole realignment.

The intersection regions present special requirements. Here vertical position control to a fraction of the beam height is needed. During stacking and acceleration, it will be desirable to have the capability of separating the two beams vertically. Horizontal displacement of the orbit may be used to shift the crossing point in azimuth. Correction dipole windings on the quadrupoles near the intersection region can be used for these purposes.

If three dipoles are employed to make a local orbit distortion, then the ratios of their deflection angles are

$$\frac{\theta_2}{\theta_1} = -\left(\frac{\beta_1}{\beta_2}\right)^{\frac{1}{2}} \frac{\sin \Psi_{13}}{\sin \Psi_{23}} \; ; \; \frac{\theta_3}{\theta_1} = \left(\frac{\beta_1}{\beta_3}\right)^{\frac{1}{2}} \frac{\sin \Psi_{12}}{\sin \Psi_{23}}$$

where Ψ_{ij} is the phase advance between the ith and j^{th} dipole. A vertical bump using Q2 and Q4 on one side of the insertion and Q4 in the other can be used to center the beam in the first Q4. Assigning θ_1 to Q2, then

$$\frac{\theta_2}{\theta_1} = 1.0; \; \frac{\theta_3}{\theta_4} = 1.5.$$

If the dipole winding on Q3 is capable of the same angular deflection as the windings on the normal cell quadrupoles, then at 200 GeV, a displacement of 7 mm will be produced at Q4. This would appear to be more than adequate.

Vertical position and angle control at the crossing point can then be effected by combining the two orbit distortions used for adjusting the position at both Q4's as illustrated below:

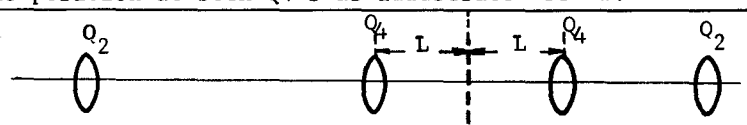

far left Q4 far right Q4	θ1	$\theta_2 = 1.0\ \theta_1$ $\theta_3 = 1.5\ \theta_1$	$\theta_3 = 1.5\ \theta_1$ $\theta_2 = 1.0\ \theta_1$	 θ_1
position angle	θ θ	2.5 θ (y = 5θL) -0.5 θ (|y′| = 0.5 θ)	2.5 θ 0.5 θ	θ -θ

With the dipole strengths assumed above, excitation of maximum deflections in both rings would provide a vertical separation of up to 14 mm at 200 GeV, which is large compared with the rms beam height of $\sim \frac{1}{4}$ mm at that energy. The angular control on a single beam would be 0.09 mrad, a 1% adjustment.

In the horizontal plane, position adjustment in Q3 can be performed by using the nearest standard quad on the same side of the intersection, and both Q3's. For this arrangement (assigning θ_1 to the normal quad)

$$\frac{\theta_2}{\theta_1} = 0.37 \; ; \; \frac{\theta_3}{\theta_1} = 0.53 \; .$$

The displacement at Q3 can then be 11.6 mm at 200 GeV. Under this circumstance, the displacement at the intersection point is $\sim$ 7 mm, so if the three dipole bumps are combined, a horizontal displacement of $\sim$ 14 mm can be obtained. The crossing center could thereby be displaced by 1 m in either direction. When combined as an angle control, the direction of a single beam could be altered by up to 0.15 mrad.

SOME EFFECTS OF RANDOM ERRORS IN ISA MAGNETS

A. W. Chao
Stanford Linear Accelerator Center

I. Introduction

Because of the relatively large random errors in the construction and installation of superconducting magnets, we have looked into the following effects:

1. Due to multipole field components in dipole and quadrupole magnets, the tune of a particle depends on its momentum. This tune variation will be evaluated in Section II. For dipoles, sagitta effect can be included if necessary.

2. Skew quadrupole components in dipole and quadrupole magnets or a solenoid can introduce a $\nu_x = \nu_y$ coupling. We have estimated the corresponding coupling constant $\langle C \rangle$ in Section III. To avoid coupling, we must have $|\nu_x - \nu_y| > \langle C \rangle$.

3. Skew quadrupole components can also introduce a finite vertical dispersion Y_p. Since the designed vertical beam size is very small for ISA a finite Y_p^* at the intersection point is undesirable. An estimate of (Y_p^*) can be found in Section IV.

4. An additional skew quadrupole component is introduced if the beam is vertically displaced relative to the center of a sextupole.† Implications of this effect on coupling and vertical dispersion are examined in Section V.

Calculation of resonance widths of various orders due to magnet multipole errors is not included in this report.

---

†The author is obliged to M. Lee and P. Morton who brought this effect to his attention.

II. Tune Shift of an Off-Momentum Particle

Tune shifts due to a magnetic field error $\Delta B_y(x)$ can be written as

$$\Delta \nu_x = \frac{1}{4\pi B\rho} \oint ds\ \beta_x(s) \left. \frac{\partial \Delta B_y(x)}{\partial x} \right|_{x = x_e}$$

$$\Delta \nu_y = \frac{-1}{4\pi B\rho} \oint ds\ \beta_y(s) \left. \frac{\partial \Delta B_y(x)}{\partial x} \right|_{x = x_e} ,$$

where $x_e = X_p\delta$ for quadrupoles and $X_p\delta + \Delta(s)$ for dipoles, where $\delta = \Delta p/p$ and X_p is the horizontal dispersion function. The quantity $\Delta(s)$ is the deviation of trajectory from the dipole magnet center due to sagitta effect. It is given by

$$\Delta_i(s) = \Delta_i(s_i) - \frac{(s-s_i)^2}{2\rho_i} , \quad |s-s_i| < \frac{\ell_i}{2} ,$$

where ρ_i and ℓ_i are the bending radius and length of the i-th dipole, s_i is the azimuthal position of the center of the dipole.

For quadrupoles, the magnetic field error can be written as

$$(\Delta B_y)_i = G_i \sum_j \Delta b_j\ x^j \quad .$$

Because of the random nature of Δb_j from magnet to magnet, we can only find the rms tune shift:

$$\langle \Delta \nu_x \rangle = \pm A_0 \pm A_1\delta \pm A_2\delta^2 \pm \ldots\ldots \quad ,$$

where coefficients A_0, A_1, ... can be found to be

$$A_{j-1} = \frac{j\langle \Delta b_j \rangle}{4\pi B\rho} \left[\sum_i \ell_i^2\ \beta_{xi}^2\ G_i^2\ X_{pi}^{2(j-1)} \right]^{\frac{1}{2}} \quad .$$

Similar expression can be obtained for $\langle \Delta \nu_y \rangle$.

For dipoles, it is natural to minimize the sagitta contribution[1] by choosing $\Delta_i(s_i) = \ell_i^2/24\rho_i$. When this is satisfied, sagitta contributions can be neglected and the rms tune shift is determined approximately by

$$A_{j-1} = \frac{j\langle\Delta b_j\rangle}{4\pi B\rho} \left[\sum_i \ell_i^2 \beta_{xi}^2 B_i^2 X_{pi}^{2(j-1)}\right]^{\frac{1}{2}}$$

where we have used

$$(\Delta B_y)_i = B_i' \sum_j \Delta b_j x^j \quad .$$

Relevant quadrupole and dipole quantities for a typical configuration can be found in Tables I and II. Values of $\langle\Delta b_j\rangle$ obtained from Ref. 2 and computed coefficients A_{j-1} are tabulated in Tables III and IV.

TABLE I. Quadrupole Quantities

Name	Number/Quad	β_x(m)	β_y(m)	X_p(m)	ℓ(m)	G(kG/m)
QF	64	42.7	7.68	1.635	1.16	663
	16	42.2	7.75	0.077	1.16	663
QD	56	7.45	42.9	0.79	1.16	-654
	16	7.45	42.9	0.48	1.16	-654
Q3	16	7.7	42.0	0	1	-460
Q2	16	123	48	0	3	298
Q1	16	54	96	0	3	-318

1. L. Smith, private communication.

2. G. Parzen, "Random Errors in the Magnetic Field of Superconducting Dipoles and Quadrupoles", Particle Accelerators, 6, 237 (1975).

TABLE II. Dipole Quantities

Name	Number/Dipole	β_x(m)	β_y(m)	X_p(m)	ℓ(m)	B(kG)
B	112	28.3	13.7	1.33	4.11	39.3
B′	112	13.4	28.6	0.97	4.11	39.3
BT	8	29.7	13.3	0.02	3.73	39.3
	8	29.7	13.3	0.02	6.27	39.3
BS	8	28.9	14.1	0.16	4.38	39.3
	8	28.9	14.1	0.16	3.77	39.3

TABLE III. $< \Delta b_j >$ and A_{j-1} for Quadrupoles

j	$< \Delta b_j >$	A_{j-1} for $<\Delta \nu_x>$	A_{j-1} for $<\Delta \nu_y>$
1.	4.0×10^{-4}	2.7×10^{-3}	2.4×10^{-3}
2.	$7.0 \times 10^{-5}\text{cm}^{-1}$	7.2×10^{-2}	3.6×10^{-2}
3.	$1.3 \times 10^{-5}\text{cm}^{-2}$	3.3	0.93
4.	$2.3 \times 10^{-6}\text{cm}^{-3}$	126	26

TABLE IV. $< \Delta b_j >$ and A_{j-1} for Dipoles

j	$< \Delta b_j >$	A_{j-1} for $<\Delta \nu_x>$	A_{j-1} for $<\Delta \nu_y>$
1.	$3.9 \times 10^{-5}\text{cm}^{-1}$	2.9×10^{-3}	2.6×10^{-3}
2.	$8.1 \times 10^{-6}\text{cm}^{-2}$	0.13	0.11
3.	$1.5 \times 10^{-6}\text{cm}^{-3}$	4.7	3.3
4.	$2.7 \times 10^{-7}\text{cm}^{-4}$	149	91

III. Coupling Coefficient due to Random Dipole and Quadrupole Errors

The coupling constant along $\nu_x \approx \nu_y$ due to skew quadrupole components in magnets can be written as[3]

$$C = \frac{1}{2\pi B\rho} \oint ds\ \beta_x^{\frac{1}{2}}\ \beta_y^{\frac{1}{2}} \frac{\partial B_y}{\partial y} \exp\left[i\int_o^s\left(\frac{1}{\beta_x} - \frac{\nu_x}{R}\right)ds' - i\int_o^s\left(\frac{1}{\beta_y} - \frac{\nu_y}{R}\right)ds'\right]$$

Due to random errors, we find

$$< C > = \frac{1}{2\pi B\rho}\left[\sum_i \beta_{xi}\ \beta_{yi}\ \ell_i^2\left(\frac{\partial B_y}{\partial y}\right)_i^2\right]^{\frac{1}{2}} \qquad (1)$$

A number of random skew components contribute to the coupling. Among them are:

(1) Tilting errors of ideal quadrupoles. The skewness is:

$$\left(\frac{\partial B_y}{\partial y}\right) = 2\ G_i\ \theta_i$$

which, for ISA, yields

$$< C > = 20.3 < \theta > \ .$$

If $< \theta > = 0.5 \times 10^{-3}$, we have $< C > = 1.0 \times 10^{-2}$.

(2) Random design errors of quadrupoles:

From Ref. 2, we find

$$\left(\frac{\partial B_y}{\partial y}\right)_i = G_i\ \left(\Delta a_1\right)_i$$

with $\langle \Delta a_1 \rangle = 4.0 \times 10^{-4}$. By changing $2\langle\theta\rangle$ to $\langle \Delta a_1 \rangle$ in the previous calculation, we obtain $\langle C \rangle = 0.4 \times 10^{-2}$.

---

3. G. Guignard, CERN/ISR-MA/75-23.

(3) Random design errors of dipoles:

The skewness is given by

$$\left(\frac{\partial B_y}{\partial y}\right)_i = B_i \ (\Delta a_1)_i$$

with $\langle \Delta a_1 \rangle = 3.9 \times 10^{-3}\ m^{-1}$ from Ref. 2. We thus obtain $\langle C \rangle = 0.5 \times 10^{-2}$.

(4) Vertical dipole coil displacement errors:

A vertical displacement error of the order of 0.05 mm yields[2] $\langle \Delta a_1 \rangle = 6.7 \times 10^{-3}\ m^{-1}$, which implies $\langle C \rangle = 0.8 \times 10^{-2}$.

Another possible contribution to coupling is a solenoid at the interaction region. Assuming $\alpha_x^* = \alpha_y^* = 0$, we find[3]

$$C = \frac{B_s \ell_s}{4\pi B\rho} \ (\beta_x^* + \beta_y^*) \Big/ \sqrt{\beta_x^* \ \beta_y^*}$$

when B_s and ℓ_s are the field strength and length of the solenoid. If $B_s = 10$ kG, $\ell_s = 3$ m, $\beta_x^* = 20$ m and $\beta_y^* = 4$ m, we find $C = 1.0 \times 10^{-3}$.

For low-β insertion with $\beta_y^* = 1$ m, we obtain $C = 1.7 \times 10^{-3}$.

IV. Vertical Dispersion due to Random Dipole and Quadrupole Errors

When a skew quadrupole is present at a position s_i, a finite horizontal dispersion X_{pi} can be coupled into vertical direction by the following equation:

$$\frac{d^2 Y_p}{ds^2} + K_y(s) \ Y_p = - \frac{X_{pi} \ell_i}{B\rho} \left(\frac{\partial B_x}{\partial x}\right)_i \ \delta(s-s_i)$$

The closed orbit solution is[4]

$$Y_p(s) = -\frac{\beta_y^{\frac{1}{2}}(s)\ \beta_y^{\frac{1}{2}}(s_i)}{2\sin\pi\nu_y}\ \frac{X_{pi}\ell_i}{B\rho}\left(\frac{\partial B_x}{\partial x_i}\right)\cos\left[\pi\nu_y + \int_{s_i}^{s}\frac{ds'}{\beta_y}\right].$$

For random skewness, we have at the intersection point

$$\langle Y_p^*\rangle = \frac{\beta_y^{*\frac{1}{2}}}{2B\rho\,|\sin\pi\nu_y|}\left[\sum_i \frac{\beta_{yi}}{2}\,X_{pi}^2\,\ell_i^2\left(\frac{\partial B_x}{\partial x}\right)_i^2\right]^{\frac{1}{2}} \qquad (2)$$

We have estimated the $\langle Y_p^*\rangle$ contributions due to the same type of random errors as in Section III. The method is similar and we only give the results for a standard configuration of $\beta_y^* = 4$ m.

(1) Tilting errors of ideal quadrupoles:

$$\langle Y_p^*\rangle = 9.6\ \langle\theta\rangle\ \text{m}$$

If $\langle\theta\rangle = 0.5 \times 10^{-3}$, it gives $\langle Y_p^*\rangle = 4.8$ mm.

(2) Random design errors of quadrupoles:

$$\langle Y_p^*\rangle = 1.9\ \text{mm.}$$

(3) Random design errors of dipoles:

$$\langle Y_p^*\rangle = 5.5\ \text{mm}$$

(4) Vertical dipole coil displacement errors:

$$\langle Y_p^*\rangle = 9.4\ \text{mm}$$

(5) A solenoid in the insertion region does not contribute because $X_p = 0$.

---

4. E. D. Courant and H. S. Snyder, Ann. of Phys. 3, 1. (1958).

V. Skew Quadrupole Contribution from Sextupoles

When the beam is displaced vertically from the center of the i-th sextupole with strength λ_i by a distance Δy_i, the beam will experience a skew quadrupole of strength

$$\left(\frac{\partial B_x}{\partial x}\right)_i = 2\lambda_i \, \Delta y_i \quad .$$

Substituting into Eqs. (1) and (2) gives

$$\langle C \rangle = \frac{\langle \Delta y \rangle}{\pi B\rho} \left[\sum_i \beta_{xi} \, \beta_{yi} \, \ell_1^2 \, \lambda_i^2\right]^{\frac{1}{2}}$$

$$\langle Y_p^* \rangle = \frac{\beta_y^{*\frac{1}{2}} \, \langle \Delta y \rangle}{B\rho \, |\sin \pi\nu_y|} \left[\sum_i \frac{\beta_{yi}}{2} \, X_{pi}^2 \, \ell_i^2 \, \lambda_i^2\right]^{\frac{1}{2}} .$$

Properties of ISA sextupoles are listed in Table V. If $\langle \Delta y \rangle$ = 1 mm, we find

$$\langle C \rangle = 7.2 \times 10^{-3}$$

$$\langle Y_p^* \rangle = 9.9 \text{ mm},$$

which are comparable to those found in Sections III and IV due to dipole and quadrupole random errors. A larger value of $\langle \Delta y \rangle$ has to be avoided.

TABLE V. Sextupole Quantities

Name	Number/Sextupole	β_x(m)	β_y(m)	X_p(m)	$\lambda\ell$ (kG/m)
SF	56	42.7	7.68	1.635	503
SD	56	7.45	42.9	0.79	-1005

VI. Conclusions

Effects mentioned in Section I are summarized below. Use of skew quadrupoles to control coupling and vertical dispersion is suggested.

(1) Tune shift due to random magnet multipoles comes mainly from random quadrupole components. Adding contributions from quadrupole and dipole magnets in a rms manner gives for $\Delta p/p = 0$:

$$\langle \Delta \nu_x \rangle = \pm 4.0 \times 10^{-3}$$

$$\langle \Delta \nu_y \rangle = \pm 3.5 \times 10^{-3}$$

The momentum dependence is weak. For example, chromaticities are roughly

$$\langle \xi_x \rangle = \pm 0.15$$

$$\langle \xi_y \rangle = \pm 0.12 \quad .$$

(2)(3) Effects due to random skewness in quadrupole and dipole magnets are perhaps tolerable. The coupling constant of $\langle C \rangle \sim 0.014$ seems strong but should impose little problem for ISA. The total rms vertical dispersion was found to be $\langle Y_p^* \rangle \sim 12$ mm, increasing the beam size of $\sigma_y^* = 0.24$ mm by about 10% at 200 GeV.

(4) Vertical displacements of the order of 1 mm from the sextupole centers can cause skew quadrupole effects comparable to the random field errors in dipole and quadrupole magnets. If however, a good orbit is not easily accessible, a set of skew quadrupole magnets may prove to be useful.

Acknowledgments

Helpful discussions with M. Lee, M. Month, P. Morton and L. Smith are appreciated.

CONTROL OF NONLINEAR RESONANCES AND OF THE TUNING OF THE ISA

J. Gareyte and J.P. Gourber
CERN

1. INTRODUCTION

Chromaticity and space-charge effects lead to a certain dispersion in the tune values. The representative points Q_x, Q_y for all $\Delta p/p$'s occupy a certain domain in the tune diagram which inevitably contains nonlinear resonances. The purpose of this paper is to study the influence of these resonances as well as the detuning produced by space-charge effects. A proposition is made for the tune of the machine at the various stages of operation. Although not absolutely necessary at this stage of the study, a compensation scheme for 3rd and 4th order resonances is proposed.

2. RESONANCE STOPBANDS

From a resonance point of view, the most critical periods are;

- the early part of the acceleration cycle when the working domain in the tune diagram is large and resonances are crossed periodically at the synchrotron frequency;
- the final stage with the coasting beam at 200 GeV/c where the implications for background are quite severe; as experienced in the ISR.

The resonance excitation results from the errors in the magnet and from single beam or beam-beam space-charge effects.

2.1 Stopbands due to errors in magnets

Table I gives the stopbands $\Delta Q_e = \Delta e/sN$ resulting from the random multipole errors in the magnets; these multipoles have

been calculated by Parzen[1] assuming an error of 0.05 mm rms in the position of the blocks of superconductor of the cosine dipoles or quadrupoles. ΔQ_e's have been calculated for twice the rms values of these multipoles for an emittance of $E_{2\sigma} = 0.4 \times 10^{-6}$ rad.m at 28.5 GeV/c. The 5th order resonance $5\ Q_h = 128$ is a structure resonance which is excited by the systematic b_4 in the dipoles ($b_4 = 2 \times 10^{-6}\ cm^{-4}$). This value is ten times larger than the random multipole, but fortunately due to the phase advance of $\pi/2$ in the cell, the effect cancels out for 6 cells over 7 in each octant and the resulting excitation is no larger than if this error were random. This systematic excitation can be suppressed by using the two b_4 correction windings with which the dipoles are equipped. This compensation can be made on the basis of the magnetic measurements or later when running the machine. At least two methods could be used:

a) a value of $2 \times 10^{-6}\ cm^{-4}$ for b_4 produces a Q-shift of 1.7×10^{-2} in both planes on the injection orbit. By measuring Q to within $\Delta Q = \pm 10^{-3}$, a reduction by a factor 10 of b_4 could be obtained;

b) The losses incurred when crossing the 5th order resonances can be monitored and used to minimize b_4.

In the same table, a limit (ΔQ_e^{limit}) is given, which is the value that would give an emittance blow-up of 20% during the acceleration period. The calculation assumes, pessimistically, that the beam sits on the resonance during the whole acceleration cycle. Due to chromaticity and space-charge detuning, the particles cross the resonance at the synchrotron frequency. According to the

---

1. G. Parzen, "Random Errors in the Magnetic Field of Superconducting Dipoles and Quadrupoles", Particle Accelerators, 6, 237 (1975).

Guignard-Schoch theory,[2] the emittance growth for repeated fast crossings is:

$$\left[\frac{1 - \left(\frac{r_o}{r}\right)^{n-2}}{n-2}\right]^2 = \frac{\pi^2 \, \Delta Q_e^2 \times f_{rev} \times t}{n \, \Delta Q}$$

where:

r_o and r = initial and final amplitudes

ΔQ = Q-oscillation amplitude of the particle

t = time

Results of Table I indicate that it is imperative to compensate 3rd and 4th order resonances if the beam is in their vicinity during acceleration. The 5th order resonances are not dangerous even if the systematic excitation is not compensated.

The stopbands of some 3rd and 4th order resonances have been measured in the CERN-PS and ISR. The corresponding random multipole errors in the magnets have been deduced from these measurements and are given for comparison in Table II.

2.2 Excitation of $5\,Q_h = 128$ by the Single Beam Space-Charge Force

In a machine with a horizontal median plane, the vertical force exerted by a stack on any of its particle at a position (x, y) is an odd function of the vertical coordinate y. This means that only

---

2. A. Schoch, Theory of Linear and Nonlinear Perturbations of Betatron Oscillations in Alternating Gradient Synchrotrons, CERN Report 57-23 (1957).

   G. Guignard, Effets des Champs Magnetiques Perturbateurs d'un Synchrotron sur L'Orbite Fermee et les Oscillations Betatroniques, Ainsi que Leur Compensation, CERN Report 70-24 (1970).

TABLE I. Resonance Stopbands

Order of the resonance n =	3	4	5
ΔQ_e^{limit}	1.2×10^{-6}	1.7×10^{-6}	2×10^{-6}
ΔQ_e	2.7×10^{-4}	7×10^{-6}	2×10^{-7} (1.7×10^{-6})

The ΔQe's are calculated from the random multipole errors in the magnets. For the 5th order resonance, the value in parenthesis is that which would result from the uncorrected systematic b_4 terms in the dipoles.

TABLE II.

Comparison of the Random Multipole Errors in the Magnets

Order of the resonance n =	3	4
ISA	$b_2 = 8.3 \times 10^{-6}$ cm^{-2}	$b_3 = 1.6 \times 10^{-6}$ cm^{-3}
CERN PS	$b_2 = 7 \times 10^{-6}$ cm^{-2} at 10 GeV/c	
CERN ISR	$b_2 = 2.2 \times 10^{-6}$ cm^{-2} at 11 GeV/c	$b_3 = 0.4 \times 10^{-6}$ cm^{-3} at 15 GeV/c $b_3 = 0.17 \times 10^{-6}$ cm^{-3} at 22 GeV/c

(For the CERN machines, the values have been deduced from measurements made with the beams).

resonances $n_1Q_h + n_2Q_v = p$ with even n_2 are excited. Among the 5th order resonances, for instance, $5\ Q_h = 128$ can be excited by the 4th derivative of the horizontal single beam space-charge force. Azimuthally, this force has the symmetry of the machine and produces a systematic excitation which has been calculated for a 10 A coasting beam having a uniform density distribution versus $\Delta p/p$ (Appendix 2). The stopband is maximum at the edges of the stack and is ten times larger than those quoted in Table I. However, this value is quite sensitive to the shape of the density curve and can be reduced by a factor 10 by smoothing a little the ends of the distribution with $\Delta p/p$ which will occur in any case in a practical machine.

For the bunched 28.5 GeV/c beam, an even smaller stopband is expected because of the elliptical shape of the density distribution with $\Delta p/p$. This value would probably be acceptable for the acceleration period, but it appears prudent to tune the machine in order to avoid crossing this resonance for particles of extreme $\Delta p/p$.

2.3 Beam-Beam Excitation of Nonlinear Resonances

In a large horizontal crossing angle machine, it is known that practically only the pure vertical resonances $NQ_v = p$ are excited by the beam-beam forces. A one-dimensional approach gives simple expressions for the linear tune shift ΔQ_{vo} and for the stopband $\Delta Q_e = \Delta e/2N$.

$$\Delta Q_e = \frac{\Delta e}{2N} = \frac{1}{2^{\frac{N}{2}-1}\,(N-1)\left(\frac{N}{2}-1\right)!}\,\Delta Q_o \qquad \text{for even } N$$

$$\Delta Q_e = \frac{\Delta e}{2N} = \frac{1}{2^{(N+1)/2}\left(\frac{N-1}{2}\right)!}\,\frac{z}{\sigma}\,\Delta Q_o \qquad \text{for odd } N$$

$$\Delta Q_o = 0.24 \times 10^{-7} \frac{I \beta_v^{int}}{\sigma p \sin \alpha}$$

where:

p = momentum (GeV/c)

I = beam current (A)

β_v^{int} = betatron amplitude at the intersection (m)

α = crossing angle

σ = vertical rms beam amplitude (m) .

This supposes beams with uniform horizontal and Gaussian vertical density distributions and a small beam separation $z/\sigma \ll 1$. The stopbands are calculated for one intersection and for twice the rms amplitude σ. For larger beam separations, the stopbands are proportional to

$$\frac{z}{\sigma} \exp\left(-\frac{z^2}{2\sigma^2}\right) \qquad \text{for 3rd order resonances}$$

and

$$\frac{z}{3\sigma} \left(\frac{z^2}{\sigma^2} - 3\right) \exp\left(-\frac{z^2}{2\sigma^2}\right) \qquad \text{for 5th order resonances}$$

At 28.5 GeV/c one has:

σ = 0.63 mm

$\Delta Q_{v_o} = 4.65 \times 10^{-3}$

The excitation of $3\ Q_h = 77$ is maximum for $z = 0.63$ mm; if this value is randomly distributed over the eight intersections, it gives $\Delta Q_e = 2.0 \times 10^{-3}$; for $5\ Q_h = 128$, the excitation is maximum for $z = 0.47$ mm and gives under the same conditions $\Delta Q_e = 0.86 \times 10^{-3}$. These values are much larger than those given by

the magnet defects and are the main reason for a complete decoupling of the two beams, at least during the acceleration period. To reduce these stopbands to the admissible limits in Table I requires a beam separation z of at least

$$z \geq 3 \text{ mm} + |\text{closed orbit distortion}| \quad .$$

The total beam-beam tune shifts of 3.72×10^{-2} at 28.5 GeV/c and 1.4×10^{-2} at 200 GeV/c are quite large values compared to the working domain in the Q-diagram (Fig. 2) and might create problems when coupling or decoupling the beams. In this respect, a system for measuring the vertical position of coasting beams in the intersections would be quite useful.

At 200 GeV/c, a random distribution of z of 0.05 mm gives stopbands ($\Delta Q_e^{3Qh} = 2.8 \times 10^{-4}$; $\Delta Q_e^{5Qh} = 1.1 \times 10^{-4}$) which are still larger than those due to magnet errors; they are, in principle, not harmful as the working line could be shifted far away from these resonances, but they emphasize the need for a precise control of z.

3. SPACE-CHARGE DETUNING

The beam-beam tune shift has already been discussed in the previous section. It is worth mentioning here that the tune shift is proportional to β_v^{int} which is not uniform with $\Delta p/p$. This means that the working line will be translated but also deformed during beam recoupling.

The single beam space-charge detuning has been calculated for a coasting and a bunched beam. A calculation made by A.W. Chao from SLAC indicated that in the case of ISA with a quasi-round and centered beam in a circular vacuum chamber, the contribution of the image space-charge forces is negligible and one remains with only

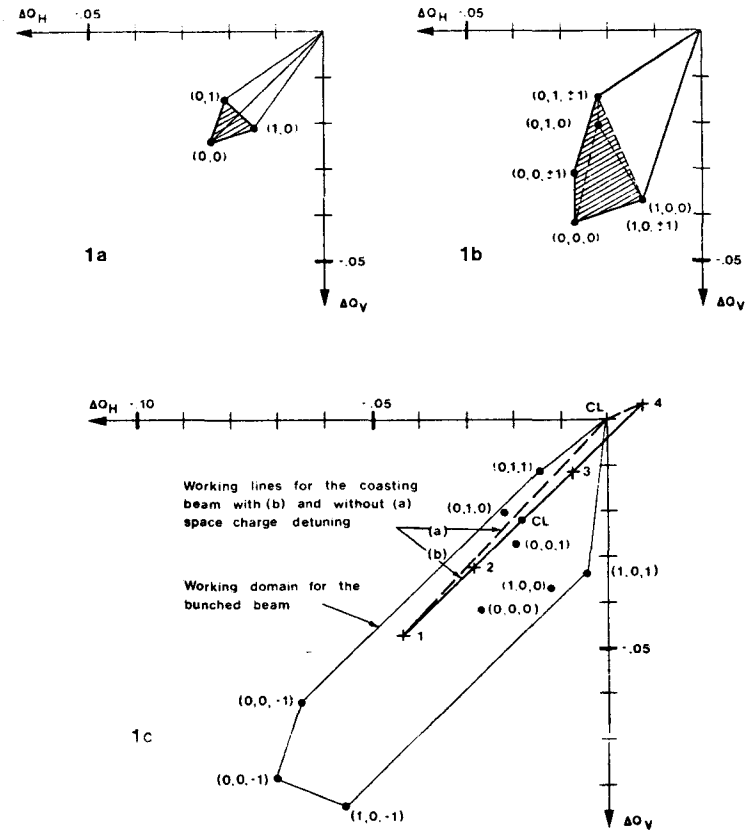

Fig. 1. Space-charge detuning at 28.5 GeV/c

a Effect arising only from the intersecting regions for the bunched beam

b Global effect for the bunched beam

c Relative positions of working lines and working domain for the coasting and the bunched beams with a chromaticity $\partial Q/\partial(\Delta p/p) = 3$.

(For the working lines, the points 1, 2, 3, 4 correspond to $\Delta p/p$'s of -0.0085, -0.0035, +0.0035, +0.0085. For working domains, the points are referenced X, Y for Fig. 1.a and X, Y, $\Delta p/p$ for Figs. 1.b and 1.c where X and Y are the maximum values of the betatron amplitudes.)

the direct space-charge effect.* This effect has been calculated carefully taking into account the beam shape variations along the machine (Appendix 1). The tune shifts are:

$\Delta Q_h = -0.018$
$\Delta Q_v = -0.022$ for the 10 A coasting beam at 28 GeV/c

and

$\Delta Q_h = -0.027$ for the central particle of the bunch
$\Delta Q_v = -0.042$ after rf capture at 28 GeV/c.

This is for equal transverse emittances of $E_{2\sigma} = 0.4 \times 10^{-6}$ rad.m. In Appendix 3, we give our estimation of plausible emittances for the injector (AGS) at two different intensities.

For the bunched beam, nonlinear space-charge effects must be taken into account to draw the region in the tune diagram spanned by particles while they perform synchrotron motion. The amplitude and momentum dependence of the tune shifts have also been derived in Appendix 1 giving for the global space-charge detuning of the 10 A, 28 GeV/c bunched beam the results summarized in Figure 1.b.

4. TUNING OF ISA AT THE VARIOUS STAGES OF OPERATION

For injection and stacking at 28.5 GeV/c, a total Q-spread of 0.066 is needed between injection and the top of the stack ($\frac{\partial Q}{\partial(\Delta p/p)} = 3$ and $\Delta p/p = 2.2\%$ according to Fig. 28 of the yellow book[3]). In the tune diagram, the working line could be placed across 5th and 8th

---

* The maximum image Q-shifts are $\Delta Q_h = 2 \times 10^{-3}$ and $\Delta Q_v = 1 \times 10^{-3}$ for the centered 28.5 GeV/c bunched beam. However, these Q-shifts increase for off-centered beams and may play a role during injection and stacking or in case of large closed orbit distortions.

order resonances and maintained in a fixed position by dynamically correcting the single beam space-charge detuning (the two beams are supposed to be decoupled for stacking and acceleration). After recentering the stack in the aperture, the final working line must be placed in position 1 in Fig. 2 in order to satisfy the next requirement.

For a short period of time during rebunching - typically a few synchrotron periods - the Q' necessary for the stability of the coasting beam will be superposed to the direct space-charge effect of the bunched beam. The domain containing the Q-values of the different particles in the bunch is represented in Figure 1.c.

It is clear that this phase of operation is the most critical although this domain 2 could still be placed between 2nd and 3rd order resonances (Fig. 2).

After rebunching, the space-charge tune spread is probably large enough (see remark in Appendix 4) to damp possible oscillations which will allow the suppression of the initial Q' and a substantial reduction of the working domain 3 in the tune diagram. This domain will be reduced proportionately to γ^2 during acceleration.

Prior to debunching, a Q' = 3 which is necessary for the stability of the final coasting beam has to be applied. After debunching, a further correction must be made to obtain the final working line 4 . This line is small enough ($\Delta Q_{h,v} = 0.014$ given by $\Delta p/p = 0.46\%$) to avoid all resonances up to the 8th order and the vertical resonance $8\ Q_v = 205$ excited by the beam-beam interaction.

---

3. A Proposal for Construction of a Proton-Proton Storage Accelerator Facility ISABELLE, Brookhaven National Laboratory, BNL 20161, revised: June 1975.

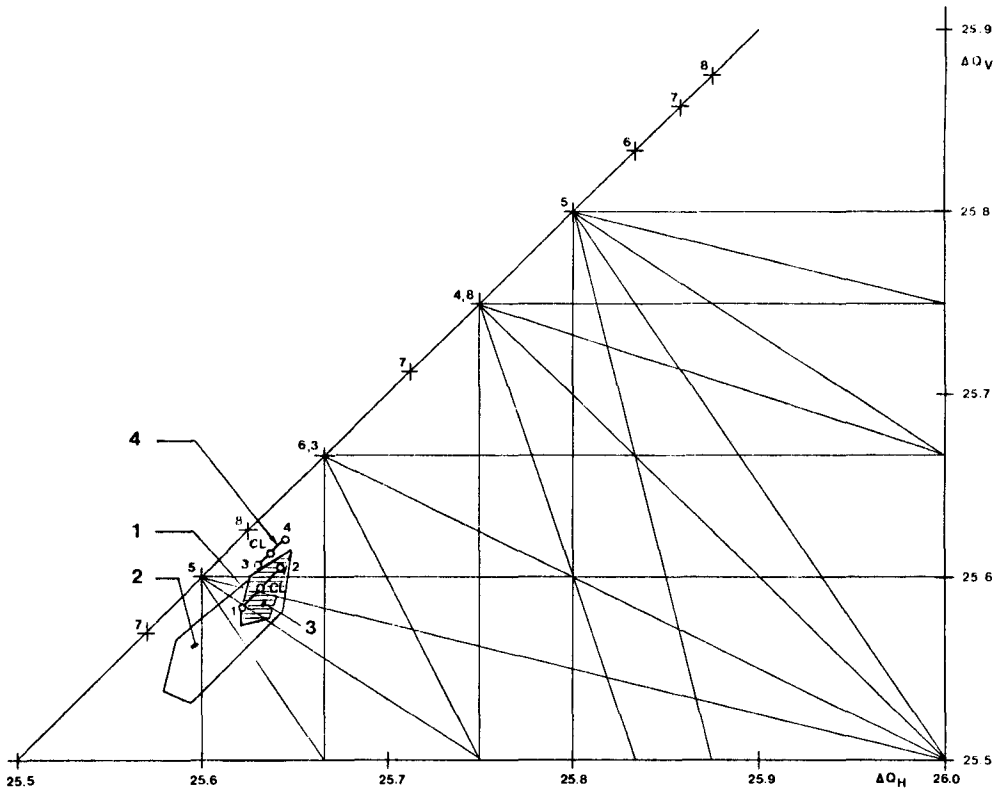

Fig. 2. A possible tuning for ISA. The points 1,2,3,4 correspond to $\Delta p/p$'s of -0.0035, +0.0035, -0.0023, +0.0023. 1 is for the centered coasting beam at 28.5 GeV/c; 2 and 3 relate to the bunched beam before and after the suppression of the chromaticity; 4 is the working line of the final 200 GeV/c coasting beam.

5. COMPENSATION OF THIRD AND FOURTH ORDER RESONANCES

The extension of the possible working region in the tune diagram requires the compensation of 3rd order resonances. If, like in the ISR, the Q-values are moved towards the integers $Q_h = Q_v = 26$ for special requirements in the future, a compensation of 4th order resonances would be helpful. The scheme which is proposed here will permit the simultaneous compensation of two strong ($n_1 Q_h + n_2 Q_v = p$ with n_2 even) and two weak (n_2 odd) resonances of each order. A more ambitious system which will allow, for instance, the compensation of five 4th order resonances or all of the 5th order resonances would be much more complicated but probably too difficult to operate. It is assumed that this system will be used with the 8-fold periodicity of the machine, i.e. that the reduction of periodicity due to the use of low- or high-β intersections will occur only with the final coasting beam when the compensation scheme will be switched off.

To compensate $3\ Q_h = 77$, a minimum of two normal sextupoles ($\partial^2 B_z/\partial z^2$) are needed; they must be placed in regions with $\beta_h \gg \beta_v$ and separated by 90° for the 77th harmonic, i.e. with a phase shift of $\Delta\mu_x = \pi/2(2k+1)$. For the other resonances, the requirements are:

$2\ Q_h + Q_v = 77$:

2 skew sextupoles $\beta_h \gg \beta_v$ $\quad 2\Delta\mu_x + \Delta\mu_y = \frac{\pi}{2}(2k+1)$

$Q_h + 2\ Q_v = 77$:

q 2 normal sextupoles $\beta_v \gg \beta_h$ $\quad \Delta\mu_x + 2\Delta\mu_y = \frac{\pi}{2}(sk+1)$

$3\ Q_v = 77$:

2 skew sextupoles $\beta_v \gg \beta_h$ $\quad 3\Delta\mu_y = \frac{\pi}{2}(2k+1)$

The same reasoning can be applied with octupoles for 4th order resonances.

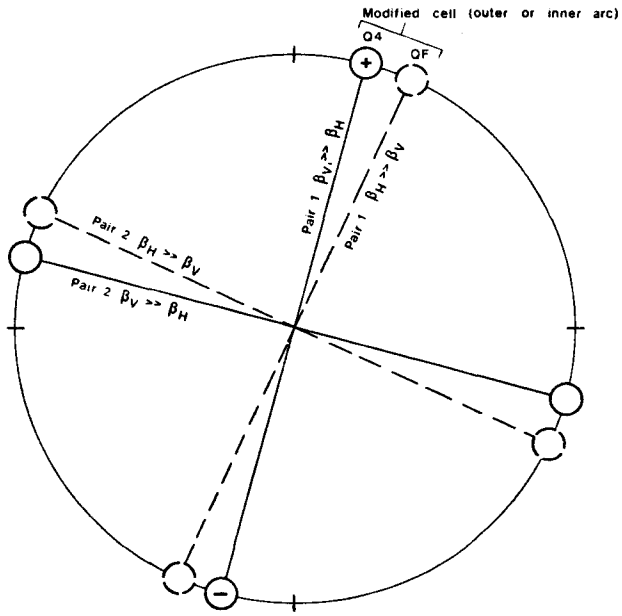

Fig.3. Compensation of third and fourth order resonances. The quadrupoles Q4 and QF in the ISABELLE yellow book notation are equipped with four windings (normal and skew sextupole and octupole).

The proposed scheme is shown in Fig. 3. The normal and skew sextupole and octupole windings are placed in some quadrupoles of the modified cells adjacent to the intersections. The momentum compaction function α_p is zero in these quadrupoles which gives the following advantages:

- no orbit and β-distortions when compensating resonances;
- complete decoupling of the 3rd and 4th order resonance corrections for off-momentum particles;
- The compensation windings take the place of the tuning windings which are normally mounted in the quadrupoles of the ring and which cannot be used for this purpose where $\alpha_p = 0$.

For a better repartition of the correction around the ring, the correctors are used in pairs: the two correctors of a pair being diametrically opposed and excited with opposite sign.

To compensate the errors in the magnet with a safety factor of 2.5, the strengths of these windings must be:

$$\frac{\partial^2 B_z}{\partial x^2} L = \frac{\partial^2 B_x}{\partial x^2} L = 13 \text{ Tm}^{-1} \quad \text{and} \quad \frac{\partial^3 B_z}{\partial x^3} L = \frac{\partial^3 B_x}{\partial x^3} L = 335 \text{ Tm}^{-2}$$

at 28.5 GeV/c. A more powerful system would be illusive because of the precision of compensation that it would require (the admissible $\Delta Q_e^{3Q_h=77}$ in Table I corresponds already to a precision of $\Delta I/I_{max} = 2^o/oo$ for the settings of the sextupole correctors).

These strengths are smaller than those used in the normal cell quadrupoles for tuning (14.25 Tm^{-1} are needed at 28.5 GeV/c in the Q_F quadrupoles for the chromaticity correction).

Obviously, this scheme must be reconsidered if one breaks the periodicity of the machine. The solution would then consist of:

- equipping more quadrupoles of the same type and admitting a certain loss of efficiency due to a poor phase relationship;
- including the quadrupole Q_D (with small α_p) of the modified cells in the scheme.

APPENDIX 1

Detuning Produced by the Direct Single-Beam Space Charge Forces

The intersecting regions, where only transverse emittances matter because $\alpha_p = 0$, and the normal cells, where on the contrary the momentum distribution plays the important role, are treated separately both for the coasting and the bunched beam, at 28.5 GeV/c.

Detuning for the central ($\Delta p/p = 0$) particle

For the intersecting regions, the usual formulae are used:

$$\Delta Q_h = - \frac{N r_p k}{\pi \gamma^3 B_F} \frac{1}{E_h \left[1 + \left(\frac{E_v}{E_h} \frac{\beta_v}{\beta_h} \right)^{\frac{1}{2}} \right]}$$

$$\Delta Q_v = - \frac{N r_p k}{\pi \gamma^3 B_F} \frac{1}{E_v \left[1 + \left(\frac{E_h}{E_v} \frac{\beta_h}{\beta_v} \right)^{\frac{1}{2}} \right]}$$

where:

N = number of circulating protons
r_p = classical proton radius
B_F = bunching factor (≤ 1)
k = coefficient depending on the distribution

The longitudinal distribution in the bunch is assumed to be parabolic and the bunch extension to be 0.66 of the rf wavelength, then $B_F = 0.5$. The coefficient k depends on the distribution of the betatron amplitudes. If one takes, in the above formulae, the emittances defined for 95% of the particles (as they are usually measured), one has:

$k = 3$ for a Gaussian distribution

$k = 1.55$ for a parabolic distribution.

Here, we will take the pessimistic case of a gaussian distribution with $E_{2\sigma} = 0.4 \times 10^6$ mrad. $E_h = E_v$ and $1/[1+(\beta_v/\beta_h)^{\frac{1}{2}}]$ averages to 0.5 which gives for the contribution of the intersections:

$$\Delta Q_h = \Delta Q_v = -0.012 \text{ for the coasting beam}$$

$$\Delta Q_h = \Delta Q_v = -0.024 \text{ for the bunched beam}$$

The contribution of the cells has been calculated using the Zotter formulae.[4] For the bunched beam with $\Delta p/p = 1.6\%$ the beam width given by the horizontal emittance is always small compared to the width due to the momentum spread and we can use an asymptotic development of these formulae:

$$\Delta Q_h = \frac{b^2}{2a^2} \Delta Q_o$$

$$\Delta Q_v = \left(\frac{b}{a}\frac{\sqrt{\pi}}{2} - \frac{b^2}{2a^2}\right) \Delta Q_o$$

$$\Delta Q_o = \frac{-Nr_p k}{\pi\gamma^3 B_F E_v} .$$

In Zotter's paper, the density distribution is uniform in $\Delta p/p$ (beam width 2a) and Gaussian vertically (rms amplitude b). If the coasting 28 GeV/c beam has a uniform distribution and if the capture is perfect (no dilution), the bunch momentum distribution is elliptic and 'a' must be taken as the momentum half-width divided by $4/\pi$. As things will probably not be so perfect, a parabolic bunch distribution will be considered, and then 'a' will be the half-width divided by 3/2. For the contribution of the cell structure,

---

4. B.W. Zotter, Q-shift due to the direct space-charge field of stacked particle beams, Divisional Report CERN ISR-TH/75-5 (1975).

the above formulae give:

$$\Delta Q_h = -0.003$$
$$\Delta Q_v = -0.018$$
for the bunched beam .

For the coasting beam, the simplifications used above are less valid and the complete formulae have to be used which give:

$$\Delta Q_h = -0.006$$
$$\Delta Q_v = -0.01$$

Therefore, the total Q-shifts are:

$$\Delta Q_h = -0.027$$
$$\Delta Q_v = -0.042$$
for the bunched beam

and

$$\Delta Q_h = -0.018$$
$$\Delta Q_v = -0.022$$
for the coasting beam .

Space-charge tune spread in the bunched beam

In the intersecting regions, the ΔQ's of a particle having a horizontal amplitude x and a vertical amplitude y in a beam of half-width 'a' and half-height 'b' are[5]:

$$\Delta Q_h = \Delta Q_{h_o} \left[1 - \frac{2a+b}{4a^2(a+b)} X^2 + \frac{1}{4b(a+b)} Y^2\right]$$

$$\Delta Q_v = \Delta Q_{v_o} \left[1 - \frac{2b+a}{4b^2(a+b)} Y^2 + \frac{1}{4a(a+b)} X^2\right]$$

---

5. B.W. Montague, Fourth order coupling resonance excited by space charge forces in a synchrotron, CERN Report 68-38 (1968).

where:

ΔQ_{h_o} and ΔQ_{v_o} are Q-shifts for the zero amplitude aprticle.

These formulae are rigorous for a parabolic distribution in real two-dimensional transverse space. In this case, the space charge results in a pure quadrupole and a pure octupole field. Then, the particle having extreme amplitude in one plane experiences for a round beam 5/8 of the Q-shift of the zero amplitude particle. For such a clear cut distribution, there are no particles with both vertical and horizontal maximum amplitudes, and all particles lie in a triangle, as sketched in Fig. 1.a (shaded area). This is for the slice of beam at the center of the bunch longitudinally; as the extreme particles experience no Q-shift, the complete kite of Fig. 1.a is spanned by particles as they perform synchrotron motion.

For a Gaussian distribution, the above formulae are valid only for small amplitudes (typically X and Y $\leq \sigma$), but one guesses that for the "95% emittance" particles, the result should not be very different. In fact, Month[6] has calculated the Q-shifts for a particle of arbitrary amplitude in a Gaussian beam: for a round beam, the "95% emittance" particle has a Q-shift of 0.42 times the zero amplitude particle Q-shift (instead of 5/8 for the parabolic distribution).

In the cells, the ΔQ_h is small and its dependence on amplitude and momentum is neglected. The ΔQ_v dependence on amplitude is again given by Month[6] for a flat beam. The Q-shift of the "95% emittance" particle is 0.58 the one of the zero amplitude particle. The momentum dependence can be evaluated as follows: the ΔQ_v at the edge of

---

6. M. Month, Beam-beam resonances in head-on collisions of electrons and positrons, Report BNL 19583, CRISP 75-1 (1975).

a rectangular beam is 0.5 that at the center according to Zotter; Herrera[7] calculated the case of a trapezoidal distribution which fits better our parabolic distribution and from his curves one gets a ratio of 0.4.

From these numbers one gets, for the global space-charge detuning of the 28.5 GeV/c, 10 A bunched beam, the results of Fig. 1.b.

---

7. J.C. Herrera, Fields and forces for rectangular beams in an AGS, BNL Internal Report, ISA 75-7 (1975).

APPENDIX 2

Excitation of 5 Q_h = 128 by the Single Beam Space Charge

The unidimensional case of a stack of many AGS pulses stacked between x = -a and x = +a is considered. The density distribution of each pulse is Gaussian with an rms amplitude σ. The density distribution of the stack, as derived from Zotter's formulae, is:

$$\rho(x) = \frac{\lambda}{4a}\left(\operatorname{erf}\frac{x+a}{\sigma} - \operatorname{erf}\frac{x-a}{\sigma}\right)$$

λ being the line density.

From Poisson's equation, one can deduce immediately the derivative of the electric field $\partial E_x/\partial x$ and then the focusing strength exerted on a particle at the abscissa x:

$$K(x) = \frac{Nr_p}{2R\gamma a}\left(\operatorname{erf}\frac{x+a}{\sigma} - \operatorname{erf}\frac{x-a}{\sigma}\right)$$

with the notation of Appendix 1 and R the average radius of ISA.

The third derivative of K(x) which excites the 5th order resonance can be calculated; it is maximum at the edge of the stack and arises to:

$$\left[\frac{\partial^3 K(x)}{\partial x^3}\right]_{x=\pm a} = \frac{1}{\sqrt{\pi}}\,\frac{Nr_p}{R\gamma a\sigma^3}$$

This value varies with the azimuth because of a and σ:

$$a = \alpha_p \frac{\Delta p}{p}$$

$$\sigma^2 = \frac{\beta_h E_h}{4}$$

Then, the stopband $\Delta Q_e^{5Q_h=128}$ can be calculated using the Schoch-Guignard theory. For the 10 A, 28.5 GeV/c coasting beam and for

a particle of twice the rms amplitude one finds:

$$\Delta Q_e = 2.8 \times 10^{-5}$$

For the bunched beam, the increase of 'a' by (1.6/0.7) in momentum roughly compensates the increase of N due to the bunching factor. In addition, the distribution in momentum is no longer uniform but more or less elliptic or parabolic which will probably reduce ΔQ_e.

APPENDIX 3

Some Remarks about AGS Emittances at 28 GeV/c

The emittance of the AGS beam quoted in the Gray Book[8] for twice the rms betatron amplitude is 0.4×10^{-6} rad.m for an intensity of 2.5×10^{12} proton/pulse. This gives a normalized (to $\beta\gamma = 1$) emittance E^* enclosing 95% of the particles of $18\ \pi\ 10^{-6}$ rad.m which is the value measured in the CERN-PS but at a somewhat lower intensity of 1.8×10^{12} p/p with 50 MeV injection. At injection in the AGS, at 200 MeV, a beam of 2.5×10^{12} p with $E^*_v = E^*_h = 18$ would suffer a Q-depression of 0.38 which seems very reasonable.

Now, if for longitudinal stability reasons, one wants to inject 5.5×10^{12} p/p, the situation is quite different. With $E^* = 18$, the Q-depression would be 0.83 which is impossible to accommodate with the AGS tune of 8.7. What will happen immediately after trapping is that the central density will decrease giving rise to a more parabolic-like distribution, for which the central Q-shift is only 0.42. Then, during acceleration, the particles will cross repeatedly 2nd and 3rd order resonances, which, even if they are compensated, will give some blow-up. Therefore, it seems reasonable to assume an emittance of 36 rather than 18 at 28 GeV/c. This is obtained in the CERN-PS for intensities of 5×10^{12} p/p and it corresponds to an emittance $E_{2\sigma}$ of 0.8×10^{-6} rad.m at 28 GeV/c.

---

8. "A Proposal for Construction of a Proton-Proton Storage Accelerator Facility ISABELLE, Brookhaven National Laboratory, BNL 18891, May, 1974.

APPENDIX 4

What Octupoles Are Needed to Ensure Stability of the Bunched Beam?

Chromaticity does not participate in stabilizing bunched beam modes. However, for the ISA parameters and for a chromaticity of 3, the wall resistance excites internal bunch modes (head tail modes) of very high order m, which have a slow growth rate and which can easily be stabilized by a small octupole Q-spread (a factor 1/m+1 comes in[9]). The worst case arises if the chromaticity is suppressed for other reasons (e.g. to avoid resonance crossings as was supposed in Section 4). Then, the mode 0 would grow and would have to be stabilized by an octupole Q-spread of the order of $\Delta Q = 0.015$ at 28.5 GeV/c according to Fig. 1.b. The Q-spread requirements vary as γ^{-2} which means that the octupole term $\partial^3 B_z/\partial x^3$ calculated for 28.5 GeV/c is large enough for the whole acceleration period.

If these octupole windings are placed in all F and D quadrupoles of the normal cells, their strength must be in the Parzen notation[1]:

$$b_3 = \frac{1}{6} \frac{\frac{\partial^3 B_z}{\partial x^3}}{G_{F,D}} = 6\ m^{-2}$$

$G_{F,D}$ being the gradients in the quadrupoles.

---

9. F. Sacherer, Bunched beam instabilities, Proc. IX Int. Conf. on High Energy Accelerators, SLAC, p. 347 (1974).

BETATRON TUNE CHANGE DUE TO DIRECT SPACE-CHARGE FORCES IN THE ISA

A. W. Chao
Stanford Linear Accelerator Center
J. C. Herrera and M. Month
Brookhaven National Laboratory

I. Introduction

The betatron tune in the ISABELLE storage ring will depend on the space-charge forces within the beam. For a given beam intensity these forces will in turn depend on the charge density and physical size of the beam. Since in the ISA the variations in beam dimensions are significant for different azimuthal positions in the ring, it is important that these changes be taken into account in estimating the ν depressions due to space charge. In this note we present a summary of a computer program in which the beam size due to the variation in the betatron functions and dispersion function is initially calculated. The ν changes are then obtained by summing the effect of the direct space-charge forces on a particle of given momentum within the beam.

II. Theory

In a previous report[1] we have considered the fields and forces within a proton beam of rectangular cross section. The ν changes due to these direct space-charge forces were calculated for a beam of uniform charge density and constant cross section. In the ISA storage ring the cross section changes significantly for different positions along the circumference. Thus designating the horizontal width of the beam at an intersection point by ($2a^*$) and the associated vertical height by ($2b^*$), we can express the corresponding dimensions at any azimuthal position (s) as

1. J. C. Herrera, BNL Informal Report, ISA 75-7, (1975).

$$a = a(s) = a^*\left[\frac{\beta_H(s)}{\beta_H^*}\right]^{\frac{1}{2}} + \left(\frac{\Delta p}{p}\right)_{HW} x_p(s) \tag{1}$$

and

$$b = b(s) = b^*\left[\frac{\beta_V(s)}{\beta_V^*}\right]. \tag{2}$$

We see that the horizontal extent (2a) of the beam depends not only on the variation in the beta function, $\beta_H(s)$, but also on the lattice dispersion, $x_p(s)$, and the half width of the momentum spread, $(\Delta p/p)_{HW}$, in the beam. Instead, the vertical size (2b) is only governed by the variation in the beta function, $\beta_V(s)$.

To derive the tune shifts, we proceed in a manner analogous to that used in Ref. 1. We use first order perturbation theory, and sum the effect of the perturbing gradient due to space charge. The result is

$$\Delta\nu_H = \frac{-\lambda_L r_p(1-\eta\gamma^2)}{4\pi e\gamma^3\beta^2} \sum_n (\Delta s)_n \frac{\beta_H(s)}{ab} X\left(\frac{a}{b}, \frac{x_p}{a}\frac{\Delta p}{p}\right) \tag{3}$$

and

$$\Delta\nu_V = \frac{-\lambda_L r_p(1-\eta\gamma^2)}{4\pi e\gamma^3\beta^2} \sum_n (\Delta s)_n \frac{\beta_V(s)}{ab} Y\left(\frac{a}{b}, \frac{x_p}{a}\frac{\Delta p}{p}\right), \tag{4}$$

where the tune-change functions X and Y are given by

$$X(\rho,\alpha) = \arctan\left[\frac{1}{\rho(1+\alpha)}\right] + \arctan\left[\frac{1}{\rho(1-\alpha)}\right], \tag{5}$$

and

$$Y(\rho,\alpha) = \arctan\left[\rho(1+\alpha)\right] + \arctan\left[\rho(1-\alpha)\right]. \tag{6}$$

The notation used in these equations is essentially that of Ref. 1 which, for the sake of completeness, we list:

e	-	proton charge, Coulomb
λ_L	-	charge per unit length, Coulomb/meter
r_p	-	classical radius of the proton, meter
γ,β	-	proton relativistic factors
η	-	degree of beam neutralization (Ne/Np)
$\Delta p/p$	-	momentum offset of particle
s	-	distance along circumference (from intersection point, $s = 0$)
(Δs)	-	increment in s
(2a)(2b)	-	cross section of beam at point s.

III. Application and Results

In applying Eqs. (1-4) in the computer program we have considered the ISA with the standard insertions. The appropriate beta and dispersion functions were derived from the SYNCH program. In performing the indicated summations, we have evaluated these lattice functions at 35 points along the length of the standard insertion itself, 20 points along the modified bending section, and 15 points within each lattice cell. For the horizontal and vertical dimensions, a^* and b^*, of the beam at the insertion point we have used $\sqrt{2}$ times the values given in Ref. 2. In this way the charge density in the center of the rectangular model of the beam is the same as that of the actual beam with a Gaussian distribution.

In Table I we present the beam parameters and the results of our calculation. We note that the vertical ν depression for a bunched beam at injection energy is the largest, about 0.03 ν units. This value may be significant since it represents a modulation in betatron tune which the particle will undergo while executing synchrotron oscillations. It is also interesting that, though we have only considered a beam model with a sharp cutoff in the horizontal

2. M. Month, BNL Informal Report, ISA 75-10, (1975).

TABLE I. Betatron Tune Changes for Bunched and Unbunched Beams in the ISA

GAMMA	Bunched or Unbunched	Charge per Meter	Momentum Spread Full-Width*	Horizontal Gaussian Half-Width	Vertical Gaussian Half-Height	Beam Neutralization	ν Depression		~ ν Spread	
γ		λ_L	$\left(\frac{\Delta p}{p}\right)_{FW}$	$\frac{a^*}{\sqrt{2}}$, mm	$\frac{b^*}{\sqrt{2}}$, mm	$\eta = \frac{Ne}{Np}$	$\Delta\nu_H(0)$	$\Delta\nu_V(0)$	$\delta(\Delta\nu_H)$	$\delta(\Delta\nu_V)$
30	Unbunched	3.35×10^{-8}	0.7×10^{-2}	1.414	0.632	1.5×10^{-4}	-0.012	-0.015	~ 0.001	~ 0.002
30	Bunched	6.7×10^{-8}	1.6×10^{-2}	1.414	0.632	0.	-0.024	-0.030	~ 0.002	~ 0.001
200	Unbunched	3.35×10^{-8}	0.46×10^{-2}	0.543	0.243	1.5×10^{-4}	$+1.4\times10^{-3}$	$+1.8\times10^{-3}$	~ 10^{-4}	~ 0.
200	Bunched	6.7×10^{-8}	0.46×10^{-2}	0.543	0.243	0.	-6×10^{-4}	-7×10^{-4}	~ 1×10^{-4}	~ 0.

charge density distribution, the calculated betatron spread within the beam is small. This is due to the fact that it is primarily the insertion regions of the ring, where the dispersion is zero and the beam is small, that contribute the most to the total ν depressions.

SOURCES AND CHARACTERISTICS OF ISA BEAM LOSS

A. van Steenbergen
Brookhaven National Laboratory
and
L. C. Teng
Fermi National Accelerator Laboratory

Introduction

With the large stored energy in the ISA beam, particle loss in the superconducting magnet environment must be kept to a low value and, whatever unavoidable losses do occur must be absorbed in properly designed beam scraper-absorber combinations. The magnitude of the potential problem is illustrated by the following parameters; Maximum tolerable caloric deposition into the superconducting-copper matrix[1] of the magnets 3-30 mJ/cm^3; total stored energy in the beam at 200 GeV, 20 MJ; a 200 GeV beam dump of 7×10^{14} protons in a beam cross section of 1 mm^2 into an aluminum wall would result in a maximum caloric deposition density of 40 kJ/cm^3; with Cu as the absorbing mass this could be as high as 1 MJ/cm^3 (Ref. 2). For this reason a systematic evaluation has been made of the ISA anticipated beam loss both during normal operation and due to possible component malfunctions.

A. Sources and Characteristics of Beam Loss During Normal Operation

1. Injection

A low intensity pulse (or pulses) from the AGS will be used to ensure that the injection orbit, the injection septum and kicker magnets, the injection scraper, etc., are properly established, aligned and in good operating condition.

---

1. P. A. Sanger and G. T. Danby, "Radiation Effects", these Proc.
2. A. van Steenbergen, "ISA Beam Dump Absorber", these Proc.

The beam should be properly shaped longitudinally in the AGS and properly scraped transversely in the transfer line before entering the ISA. It is assumed that the beam is kicked out of the AGS only after the proper sine-wave excitation of the ISA injection septa has been sensed by sensors.

Thus, in normal operation there should be no beam loss during injection.

2. Stack Formation

a. While the beam is being accelerated to the stack, the rf voltage is reduced and the bucket size reduced to fit tightly around the beam. During this process it is likely that $\sim$ 5% of the beam will stray out of the bucket and be "left behind". However, this stray beam will likely remain inside the dump profile[3] between the injection and the stacking orbits.

b. Overstacking may have to be used to obtain a high density stack. Since stacking will be done "on top", this will cause a low density "tail" to be pushed toward the injection orbit on the low momentum side. Perhaps 50% of the total beam stack of 7×10^{14} protons is pushed into the unusable tail and has to be cleaned up after the stacking process is over, but only less than 5% total is likely to be pushed beyond the injection orbit and stray out of the dump profile on the low momentum side. With the stacking of a new pulse every 5 sec a small fraction of the 5% will stray out of the dump profile. This stray beam can be stopped on a scatterer-absorber combination with the scatterer target placed at a high x_p location just outside the dump profile on the low momentum side. This combination will be called the "low-p scraper".

c. After stacking is completed, the beam stack is moved to the horizontal center of the aperture. At this time the entire unusable

---

3. A. van Steenbergen, BNL Informal Rept. ISA 75-6, July 1975.

tail containing up to 50% of the beam will be cleaned up on the "low-p scraper". This clean-up process could be arbitrarily slow and the beam loss rate can be controlled by a loss rate feedback system.

d. At the same time when the stack is centered and the low momentum tail is cleaned up the stack should be scraped vertically to give an improved vertical beam profile. Because of precise collimation in the beam transfer line, it is estimated that no more than $\sim$ 10% needs to be scraped off vertically. The scatterer target of the "vertical scraper" should be located at a high β_y location and could be retracted out of the vertical dump profile after scraping. The vertical scraping can also be done during stacking on each injected pulse while it is being accelerated into the stack. In this case a wedge shaped target would extend the loss over the duration of the stack acceleration time.

3. Adiabatic Capture and Acceleration

a. No accelerator has succeeded in adiabatic capture with more than 90% of the beam. Thus, one should expect a 10% beam loss at 30 GeV during the adiabatic rebunching. This 10% beam will stray out of the dump profile on the low momentum side and should be absorbed on the "low-p scraper". Since the adiabatic capture process can be arbitrarily slow, this 10% beam loss can be made to proceed at an arbitrarily slow rate.

b. No beam loss is expected during the acceleration from 30 GeV to 200 GeV.

4. High Energy Colliding Beam Operation

a. The beam loss due to beam-gas scattering, intrabeam scattering, and beam-beam interaction at 200 GeV are all negligibly small (otherwise the colliding beams will not be useful for physics experiments).

b. A few times during a physics run the beam may have to be scraped vertically to restore a sharp vertical beam profile. A very small part (10^{-3}- 10^{-4}) of the beam is scraped off each time. The scraping rate can be arbitrarily slow and the "vertical scraper" is used for this operation. The first scraping may be immediately after acceleration before the beams are made to collide for physics experiments.

5. Ejection

At the end of a physics run the beam is ejected in one revolution ($\sim$ 10 μsec) by the ejection system to be stopped on an external beam absorber. Approximately 0.1% of the beam will strike the ejection septum. The absorber to stop this beam is an integral part of the design of the ejection system.[4] So also is the external absorber which must stop the more than 99% of the beam which is ejected.

B. Sources and Characteristics of Beam Loss Due to Possible Malfunctions

1. Injection

The beam is extracted from the AGS only after the proper sine-wave excitation of the septum magnets has been noted by the sensors. However, the kicker magnet may misfire. In this case the injected beam of 2.5×10^{12} protons will stray out of the "dump profile" 90 betatron phase degrees downstream of the kicker. A 30 GeV beam absorber should be located there just outside the dump profile to stop the stray beam. This is called the "injection stopper". In addition the dump profile sensors will trigger the protective ejection sequence removing from the ISA ring the previously established stack and that part of the injected beam which did not exceed the dump profile boundary and progressed 7/8 of an orbit to the ejection insertion.[5]

---

4. A. van Steenbergen,"ISA Ejection System, Components and Parameters", (to be published as an ISA Informal Rept.)

5. H. N. Brown, "ISA Injection-Ejection Trigger Logic", these Proc.

2. Stack Formation

If the stacking rf system fails, the injected beam will simply be left parked on an orbit between the injection and the stacking orbits. It is extremely unlikely that the malfunction of the stacking rf system will cause it to decelerate or to over-accelerate the beam out of the dump profile. Of course, a malfunction of the stacking rf system will inhibit further extraction of beam from the AGS.

3. Adiabatic Capture and Acceleration

The accelerating rf system should be interlocked with the beam ejection system. If the rf system fails during the acceleration cycle the beam stack should be ejected and dumped. The ejection system components will track the momentum of the beam so that the beam stack can be ejected at any time during acceleration.

4. High-Energy Colliding Beam Operation

In this regime there should be no detectable beam loss for normal operation (except for the controlled vertical beam scraping to restore the beam profile). Any beam straying out of the dump profile and above a specified minimum level is interpreted as caused by component failure. Instead of trying to scrape the stray beam on an internal absorber the entire beam stack is immediately ejected and dumped on an external absorber by the ejection system. For normal operation the beam is ejected in one revolution ($\sim$ 10 μsec). Approximately 0.1% of the stacked beam (7×10^{14} protons) will hit the septum and more than 99% of the beam will be ejected and stopped on the external absorber.

5. Failure of Ejection System

In case the ejection system equipment (kicker and septa) fails to operate, a back-up kicker will kick the beam on to an internal absorber. The full stacked beam of 7×10^{14} protons will be dumped on the internal absorber in one revolution. This is by far the fastest rate of beam stopping internal to the ring of all operations.

Since this is a redundant back-up operation and not expected to occur more than a few times during the useful life of the ISA, more serious consequences, in terms of local damage or even driving downstream superconducting magnets normal because of energy deposition from the nuclear cascade downstream of the absorber, is thought to be tolerable. Preliminary designs for scraper-cascade shield combinations have been worked out[6,7] however, which will prevent, even in this case, the superconducting magnet units from going normal due to cascade deposition.

---

6. J. Peterson, A. van Steenbergen, L. C. Teng, "ISA Beam Scraper System", these Proc.

7. L. Blumberg, J. Ranft, A. Stevens, A. van Steenbergen, "Caloric Deposition Downstream of the ISA Beam Scrapers", these Proc.

Stray Beam		Injection	Stack Formation	Adiabatic Capture	Acceleration	Colliding-Beam Operation	Ejection
Normal Operation	# of P on Absorber	0	5×10^{14}	7×10^{13}	0	0[a]	$< 10^{12}$ on septa 7×10^{14} on ext. absorber
	Cause		Bucket Fit Overstack V.Scraping	?	-		
Malfunction of Specific Component	# of P on Absorber	2.5×10^{12}	0	0	-	-	7×10^{14} on int. absorber
	Cause	Kicker Misfire					Ejection Component Misfire
Ejection Triggers		DUMP-LOGIC REGIME			SCRAPE-LOGIC REGIME		
					Same as Dump-Logic Regime except:		
		Dump Profile Triggers					
		Absorber Radiation Triggers			← Suppress		
		Rf Malfunction Trigger					
		$\dot{I}$ Toroid Trigger			← Suppress		
		$\int \dot{I}$ Toroid Trigger			← Suppress		
		Magnet Quench					
		Sector Valve Closing (Vac Interlock)					
		Access Door Interlock					

(a) Few vertical scraping operations during a physics run (24 hrs. period).

ISA BEAM DUMP ABSORBER

A. van Steenbergen
Brookhaven National Laboratory

Introduction

In order to avoid potential catastrophic damage to the ISA structure it is required to extract the stored beam (design maximum stored energy, 20 MJ) in a fast, single turn, mode and direct it to an external beam absorber, the major objective being the optical enlargement of the beam and, consequently, the reduction of the particle flux density, prior to impacting on the external absorber. The extent of the enlargement required depends on the tolerable caloric deposition density, which, typically for 200 GeV protons, occurs well inside the bulk of the absorber block. Here, some aspects of this problem will be presented. The parameters and extraction component arrangement are presented elsewhere.[1]

Energy Deposition in the Absorber Block

The energy deposition data associated with the nuclear cascade data were obtained indirectly from Monte Carlo calculations using the computer program FLUKA, i.e. by using the data computed by Schönbacher of energy deposition in Be, C, Ti, Cu and W for 10 GeV/c and 400 GeV/c protons.[3] These are presented in the form of two dimensional isodensity contours for a cylindrical absorber geometry, a typical example of which is shown in Fig. 1. Using

1. A. van Steenbergen, "ISA Ejection System, Components and Parameters", (to be published as an ISA Informal Rept).
2. J. Ranft and J.T. Routti, CERN Lab II-RA/PP/73-1.
3. H. Schönbacher, CERN Lab II-RA/Note 73-21.

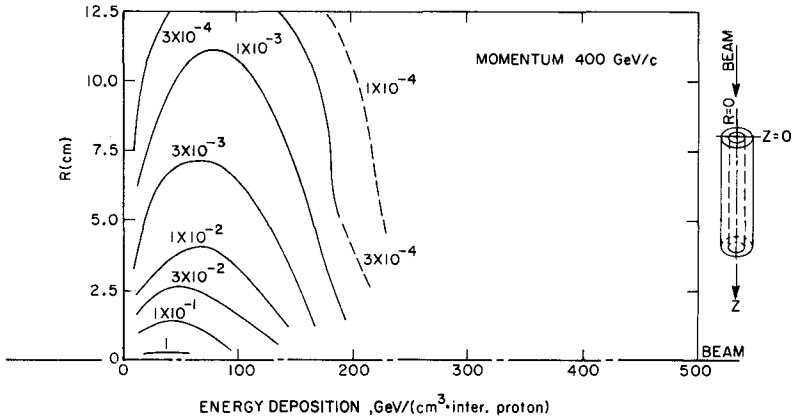

Fig. 1. Typical energy deposition isodensity contours.

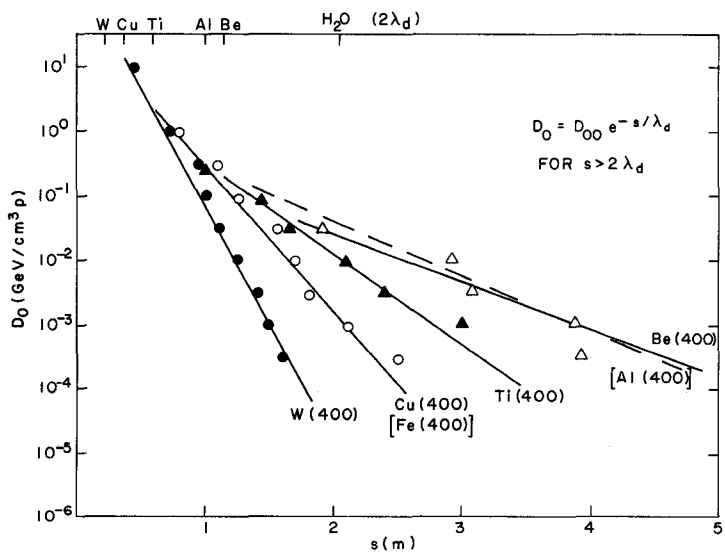

Fig. 2. D_o vs s (for $s > 2\lambda_d$).

now these graphical representations, an empirical expression for the maximum energy deposition has been developed which is readily applicable to materials of different density. Since, as will become evident, the maximum caloric deposition density is also dependent on the beam size for a fixed flux of primary protons (i.e. dependent on particle flux density), additional data have been used, as computed by Teutenberg[4] et al. of energy deposition densities in the nuclear cascade for various beam sizes of the primary proton beam impacting on an absorber.

Using the isodensity contours of Fig. 1 (and similar data) and extrapolations of the contours $r = 0$, the longitudinal energy deposition density attenuation can be obtained, as shown in Fig. 2. With this it is possible to define a characteristic caloric deposition density attenuation length λ_d, as also indicated in Fig. 2. Similarly, the radial fall-off can be obtained as shown in Fig. 3, yielding an approximate expression for the behavior near the axis of the cascade. For 400 GeV primary protons the maximum deposition density occurs for the various materials consistently at a distance from the front face of the absorber given by $s = 2\lambda_d$, i.e. for the various materials $1.8 \leq \rho \leq 19.3$ it is valid that $D_o(2\lambda_d) \cong \hat{D}(r = 0.1)$ for 400 GeV protons and for the beam geometrical parameters as used here. Consequently, the general behavior as given in Fig. 1 cannot be extrapolated to the front face of the absorber, i.e. $D_o = D_{oo} \exp(-s/\lambda_d)$ is valid for $s \geq 2\lambda_d$.*

*Note that the (dE/dx) contribution to the caloric deposition is only approximately 20% and the $\pi_o \rightarrow 2\gamma$ channel provides approximately 30% of the caloric deposition contribution for 400 GeV protons.

4. K. Teutenberg, P. Sievers, V.W. Middelkoop, CERN Lab II/BT/74-4.

The maximum deposition density $D_o(s = 2\lambda_d)$ and the intercept value $D(s = 0) \equiv D_{oo}$ have been plotted versus ρ, the specific density of the material, indicating a simple expontential behavior in ρ, i.e. $D_o(2\lambda_d) \cong 0.02\ \rho^{2.8}$ [GeV/cm^{2}pr] with ρ in g/cm^3 and $D_{oo} \cong 0.17\ \rho^{2.8}$, as shown in Fig. 4. Similarly, plotting the $\rho\lambda_d$ product versus ρ yields the relationship $\rho\lambda_d \cong 100\ \rho^{0.25}$(Fig. 5). Taking now also the information available (see above) regarding beam size dependence, as plotted in Fig. 6, it follows $D = D_o(2\lambda_d)$ $(A/12.5)^{-0.56}$ (with A in cm^2). In summary, the caloric deposition density data in the 400 GeV proton nuclear cascade is as given in Table I and the empirical conclusions to be drawn from this are as follows:

I. Dependence on s

$$D_o(s) = D_{oo} \exp(-s/\lambda_d) = 8.4\ D_o(2\lambda_d) \exp(-s/\lambda_d)$$

$$= 0.17\ \rho^{2.8} \exp[-s/(100\rho^{-0.75})]$$

$$\text{for } s \geq 2\lambda_d \quad \text{with} \quad \lambda_d \simeq 100\rho^{-0.75}$$

II. Dependence on r

$$\hat{D}_r = D_o\ (2\lambda_d)\ (0.1/r)^n \qquad \text{for } r \leq 18 \text{ cm}$$

$$\text{with } n = 0.9\ \rho^{0.32} \qquad \text{(400 GeV data)}$$

III. Dependence on beam size, limited data for Cu and Al combined with present evaluation of D_{oo} or $D_o(2\lambda_d)$ results in

$$D = D_o(2\lambda_d)\ A_b/12.5)^{-0.56}$$

TABLE I

Material	ρ g/cm^3	λ_d* cm	$\rho\lambda_d$ g/cm^2	D_{oo}* GeV/cm^{3}pr	$D_o(2\lambda_d)$** or $\hat{D}(r=0.1)$	[$\hat{D}$ from $\hat{D} \cong 7.2\rho^{2.8}A_b^{-0.56}10^{-3}$]
W	19.3	11.1	214	550	65	[92]
Cu (Fe)	8.9 (7.8)	18.8	167	78	10	[10.5]
Ti	4.8	30.4	146	10	1.5	[1.8]
Al	2.7	(50.0)	(135)	(2.5)	(0.3)	[0.37]
Be	1.8	57.2	106	1	0.1	[0.12]
			Fig. 5 $\rho\lambda_d \cong 100\rho^{1/4}$	Fig. 4a $D_{oo} \cong 0.17\rho^{2.8}$	Fig. 4b $D_o(2\lambda_d) \cong 0.02\rho^{2.8}$	

*From Fig. 2 D_o vs s $\rightarrow$ $D_o = D_{oo} \exp(-s/\lambda_d)$.

**From Fig. 1 , $D_o(s \cong 2\lambda_d) = \hat{D}_o[=\hat{D}(r=0.1)]$.

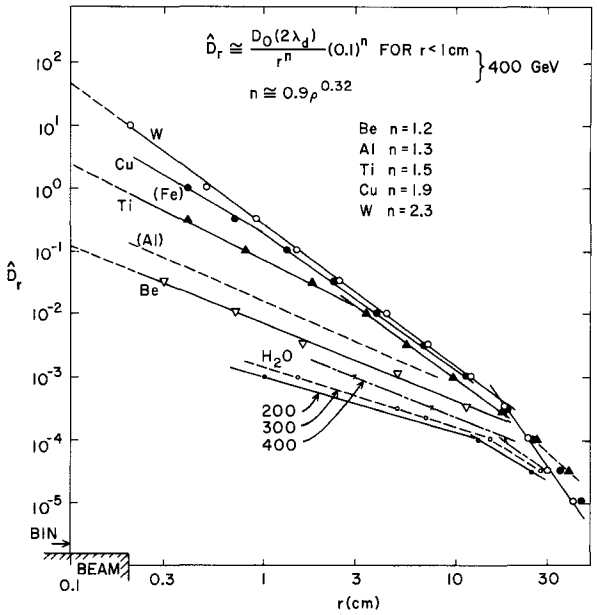

Fig. 3. $\hat{D}_r$ vs r.

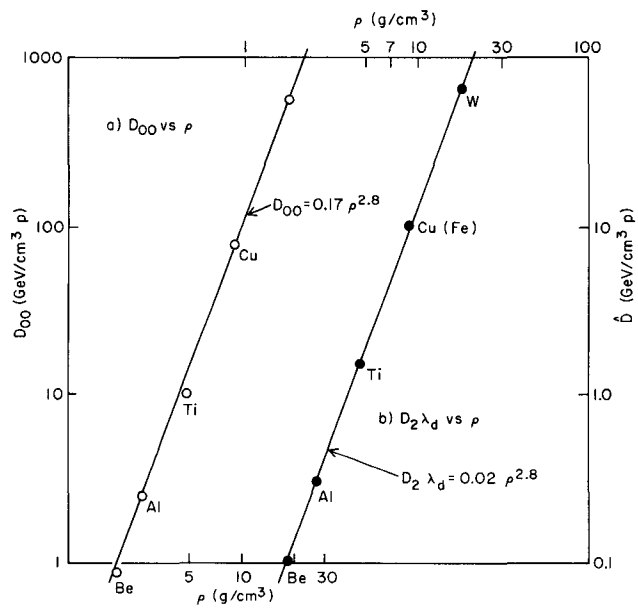

Fig. 4. D_{oo} vs ρ and $D_{2\lambda_d}$ vs ρ.

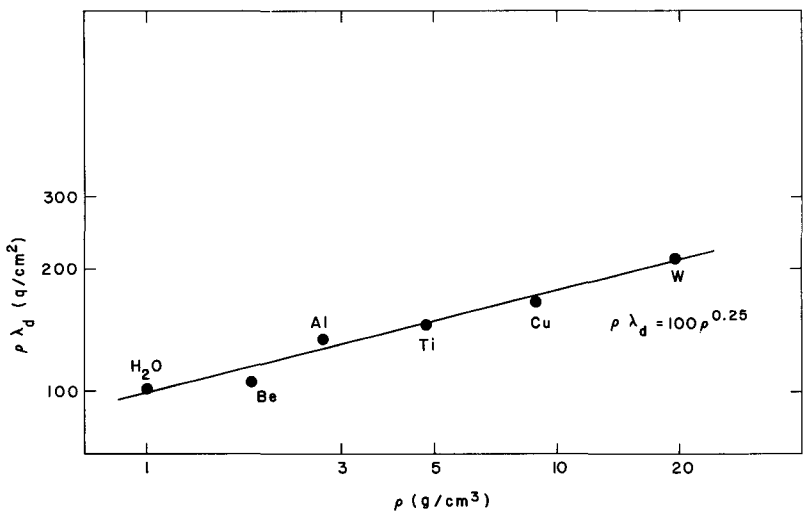

Fig. 5. $\lambda_d = f(\rho)$.

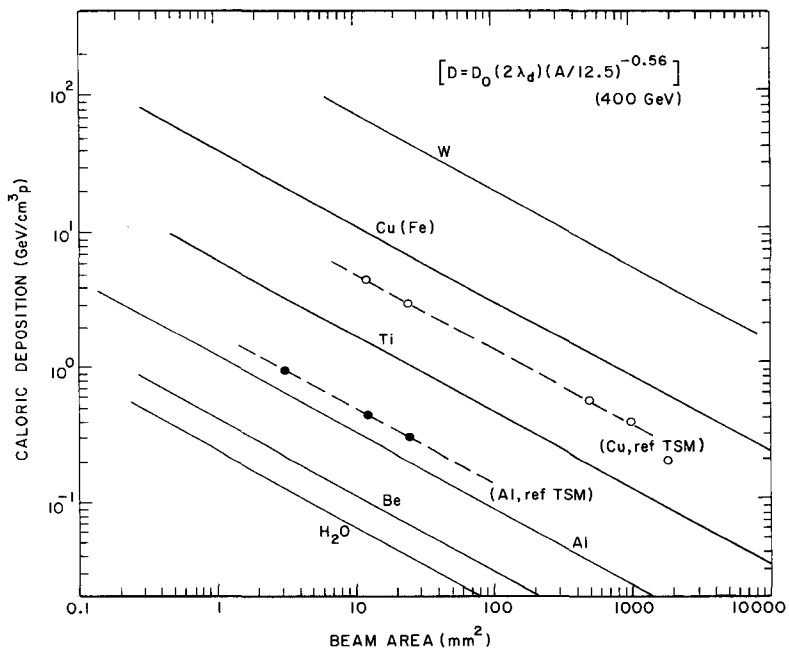

Fig. 6. D vs beam area.

Since the above data apply to 400 GeV protons, and the present interest is in the energy deposition for a 200 GeV proton or 30 GeV proton beam, a scaling with primary proton energy was required. This has been done using the standard CYLKA cascade program and the results* are shown in Fig. 7 indicating the validity of the maximum energy deposition for $s \cong 2\lambda_d$ for a 200 GeV and a 400 GeV primary beam, but also indicating, that the maximum for 30 GeV protons occurs at the front face of the absorber (since dE/dx dominates for 30 GeV protons). Using now the scaling factor for energy deposition as derived from these results, the empirical relationship for caloric deposition for 200 GeV protons is given by:

$$D \leqslant 3.5 \left(\frac{0.1}{r}\right)^n (8A_b)^{-0.56} D_o(2\lambda_d) \exp(-s/\lambda_d)$$

---

for $r \geq 0.1$ cm	r, s, λ_d [cm]
$s \geq 2\lambda_d$ cm	A_b [cm^2]
$A \leqslant 20$ cm^2	D [$GeV/cm^3 \cdot pr$]

with $n \simeq 1$ (or $n = 0.9\ \rho^{0.32}$)

$$D_o(2\lambda_d) \simeq 0.02\ \rho^{2.8} \quad \text{and} \quad \lambda_d \simeq 100\ \rho^{-0.75}$$

ρ [g/cm^3]

General expression $D = f(s,r)_{A_b,\rho}$

$$\hat{D}_{r=0.1}\ (s=2\lambda_d) = 3.5\ (8A_b)^{-0.56} \cdot e^{-2} \cdot (0.02\ \rho^{2.8})$$

$$= 3 \times 10^{-3}\ \rho^{2.8} A_b^{-0.56}\ GeV/cm^3 \cdot pr.$$

For 7×10^{14} protons

$$\hat{D}_{r=0.1}\ (s=2\lambda_d) \cong 3 \times 10^{-3} \times 7 \times 10^{14} \times 3.82 \times 10^{-11} (\rho^{2.8} A_b^{-0.56})\ cal/cm^3$$

$$\cong 80\ \rho^{2.8} A_b^{-0.56}\ cal/cm^3.$$

---

* Computer results obtained by A. Stevens

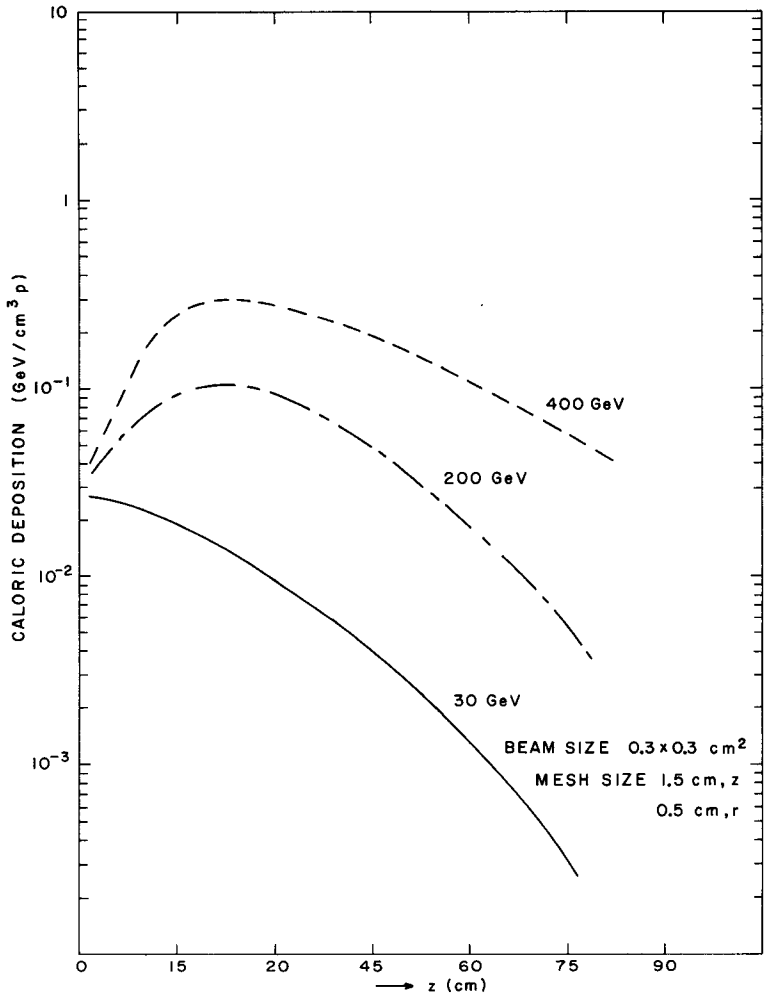

Fig. 7. Caloric deposition in a Cu absorber for 400 GeV, 200 GeV and 30 GeV protons.

Absorber Design

Using now in a first approach the melting point of the material as a design criterion for determining the maximum tolerable fast energy deposition, the above relationships provide for the determination of minimum beam size on impact of the external absorber for various materials, as given in Table II.

TABLE II

Material	ρ g/cm^3	c_p cal/g	mp ^oC	$\rho\, c_p(mp)$ [a] cal/cm^3	$A_b >$ [c] cm^2
W	19.3	0.03	3380	$2.1\ 10^3$	$8.6\ 10^3$
Cu	8.9	0.09	1080	$0.86\ 10^3$	$8.9\ 10^3$
Fe	7.8	0.11	1500	$1.3\ 10^3$	$2.2\ 10^2$
Ti	4.8	0.12	1660	$1.0\ 10^3$	$3.1\ 10^1$
Al (13)	2.7	0.21	660	$0.37\ 10^3$	$1.0\ 10^1$
B (5) [d]	1.7	0.30	2300	$1.2\ 10^3$	0.14
C (6) [b]	2.3	0.17	3500	$1.3\ 10^3$	0.5
Be (4)	1.8	0.44	1350	$1.1\ 10^3$	0.19

(a) Maximum instantaneous temperature rise. Relaxation time >> dump time. This quantity adopted as first order criterion [Excessive longitudinal stresses are avoided by using a sequence of disc absorbers rather than a continuous cylinder], for maximum value of $\hat{D}_{r=0.1}$ $(s=2\lambda_d)$. (Ambient temperature assumed to be 0^oC.)

(b) Graphite

(c) Using $[\rho\ c_p(mp)] \leq 80\ \rho^{2.8}\ A_b^{-0.56}$.

(d) Amorphous B.

On the basis of these data a beam size on impact area of 200 mm^2 has been adopted as a design value for a 7×10^{14} proton intensity impacting on a Be absorber. Since it is desirable to keep the total absorber to a reasonable length, the approach could be to increase sequentially the density of the absorber material. Assuming the tolerable instantaneous energy deposition to be approximately equal for the various materials, as suggested by the values of $\rho c_p(mp)$ given in Table II (reasonably valid except for Al) then, on the basis of the empirical expression for caloric deposition in various materials, the minimum length of each material of density ρ required, in a sequence of Be, Ti, Cu (Fe) and W is given by, neglecting also the further enlargement of the "beam" in the absorber:

$$\left(\frac{\rho_{Ti}}{\rho_{Be}}\right)^{2.8} \cdot \exp\left(-s_{Be}/\lambda_{Be}\right) < 1$$

$$\left(\frac{\rho_{Cu,Fe}}{\rho_{Ti}}\right)^{2.8} \cdot \exp\left(-s_{Ti}/\lambda_{Ti}\right) < 1$$

$$\left(\frac{\rho_{W}}{\rho_{Cu,Fe}}\right)^{2.8} \cdot \exp\left(-s_{Cu,Fe}/\lambda_{Cu,Fe}\right) < 1 \quad .$$

This results in minimum length values of sequential absorber material of $s_{Be} = 1.56$ m; $s_{Ti} = 0.53$ m, $s_{Cu} = 0.41$ m; with the length of W to be determined by considerations of adequate shielding. Assuming for the present a total equivalent absorber of 4 m of iron, it follows readily that a backstop of 1.62 m of W would be required. Alternatively, this could be substituted for 2.43 m of iron.

It is not expected that the above suggested sequence of materials would be used in the actual absorber construction. Since in the present ISA protective beam extraction design the beam is directed downwards and, associated with its location relative to the ISA structure, there is no restriction on the total absorber length (within practical limits) a more economical design is contemplated whereby a 2.5 m of Be front absorber, cast in an enclosing iron sleeve would be followed by an adequate length of iron as a backstop.

INJECTION-EJECTION PROTECTION LOGIC

H. Brown

Brookhaven National Laboratory

In the course of discussions centering on the questions of beam loss[1] and injection-ejection[2,3] at the ISA, it was useful to sketch out the beginnings of the protective logic which would be needed to guard against quenches or damage in the ISA rings. Two logic diagrams are presented here which illustrate the most obvious facets of the hard-wired protection system. Certainly, during the actual design, more careful thought will uncover omissions and may also point out that some of the interlocks shown are not necessary. In any event, this note can provide a starting point. One should make reference to the injection and ejection plans[2,3] in order to clearly see the meaning of some of the terms used here.

Figure 1 illustrates the injection protection sequence. Its intent is to ensure that no ISA magnets are quenched by an errant incoming pulse from the AGS. Various dc magnets in the transfer line are checked to be within tolerance. Then the pulsed injection septa and kicker magnets are checked about 7 μsec before the first bunch arrives at the kicker to allow for signal and proton transit times. After the AGS pulse is in transit, a final trajectory verification in the injection insertion region could be made by special detectors which are arranged to sense errors in the course of the first bunch in. An adverse result could cause an abort kicker to divert 9 or 10 of the following bunches. It is unlikely that the

---

1. A. van Steenbergen, L. C. Teng, "Sources and Characteristics of ISA Beam Loss", these Proc.
2. A. van Steenbergen, "ISA Injection", BNL Rept. ISA 75-6, July 1975.
3. A. van Steenbergen, "ISA Ejection System, Components and Parameters", (to be published as an ISA Informal Report).

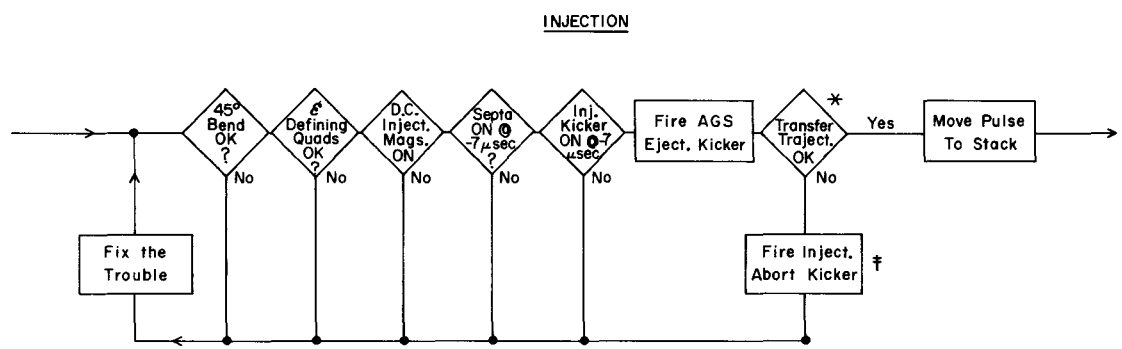

* Fast beam detectors (scintillators, probably) may be disposed near the injection trajectory, but outside the stack, which will signal if the incoming pulse is off course.

‡ A special kicker could be employed to divert all but the first few proton bunches.

Fig. 1. Injection protection sequence.

first 2 to 3 bad bunches could be rejected at this stage, due to the requirements of timing and placement of the abort kicker. One may, in the end, decide that this last minute abort is not really effective enough and decide to rely on the interlocks preceding AGS ejection.

Ejection protection logic is diagrammed in Fig. 2. There is a continuous monitoring of various trouble indicators from the time of the first injected pulse into the ISA. A negative test result on such items as mains voltages or magnets means that the quantity measured has just gone out of tolerance and is beginning to fail, but that the equipment will still perform its function long enough to dump the beam. The rf error is not really defined, but under various conditions one may wish to give the operator the option to continue or to dump. The same is true for the total loss (ΔI_{circ}).

Three tests, $\dot{I}$, Radiation Detectors, and Dump Profile Detectors, directly test the circulating beam condition. The action taken after a negative signal from one of these must be modified however, if the machine is in the (intentional) scraping mode, since this mode includes rubbing off up to 50% of the injected beam from the low energy tail after stacking is completed. Shown here is a simple bypass. However, this must be carefully thought out later. At least one vacuum chamber puncture occurred at the ISR when the usual $\dot{I}$ interlock was bypassed during a scraping operation.

A spurious firing of the ejection kicker, when the associated septum magnets have not been pulsed in advance, would probably lead to severe damage in some of the subsequent ejection magnets. Such a spurious firing might be annulled by means of a second, reversed polarity kicker in the same, dipole-free half-cell. (This cancellation kicker could also function as the emergency internal dump kicker.) The incomplete cancellation would no doubt trigger the normal dump sequence via a radiation or dump profile detector.

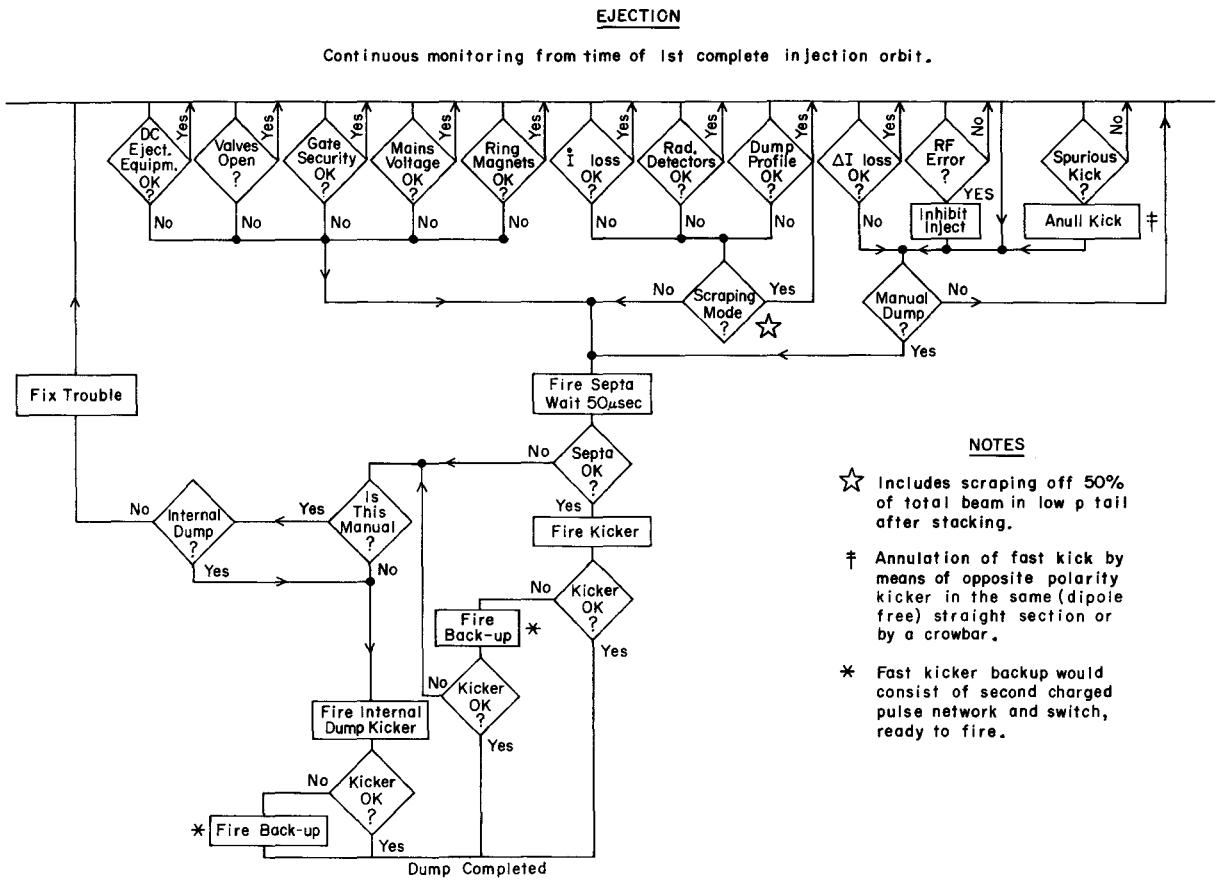

Fig. 2. Ejection protection logic.

In this event, the backup kicker power supply (consisting of a second charged pulse network and switch, ready to fire), would come into play. (To be consistent, one might decide to provide backup pulsers for the pulsed septum magnets as well.)

If the extraction system fails to operate, the last resort is to use the interanl beam dump. This would happen automatically when the dump request has been initiated automatically, but would be optional in the case of a manual dump, giving the operator a chance to fix the trouble.

Finally, an important property of the protective system must be that it is reliable enough to not only protect the ISA, but also to not paralyze it.

ISA BEAM SCRAPER SYSTEM

J. Peterson
Lawrence Berkeley Laboratory
A. van Steenbergen
Brookhaven National Laboratory
L. C. Teng
Fermi National Accelerator Laboratory

Introduction

Inherent in the goal of obtaining high beam-beam interaction luminosity is the objective of attaining the highest possible phase-space density of the beam stack at injection. This can be better achieved if the possibility of "overstacking" in the ISA exist, i.e. a lossy stacking mode whereby up to 50% of the injected beam may be discarded, predominantly during a time of recentering the beam stack after completion of the stacking process. This is only possible in a superconducting magnet system environment if a near 100% effective beam scraper-cascade shield system is incorporated in the ISA design. The basic concept of this is outlined here.

Scraper-Cascade Shields

Consider a beam scraping off an absorber which is thick enough to attenuate adequately the nuclear cascade. Then the beam coming out of the scraping edge will look like that shown in Fig. 1. Immediately following the absorber there is a "quiet" zone where a superconducting coil could be located. Assuming no magnetic field anywhere, the beam spray cone will enlarge as r^2. To locate another coil downstream, another quiet zone must be created by means of an additional shield. This shield should also be thick enough to attenuate sufficiently the cascade. A new spray cone is formed composed of all particles going through the opening

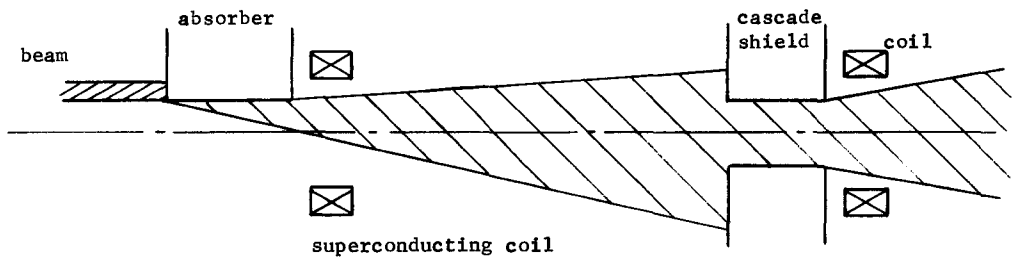

Fig. 1. Scraper-cascade shields.

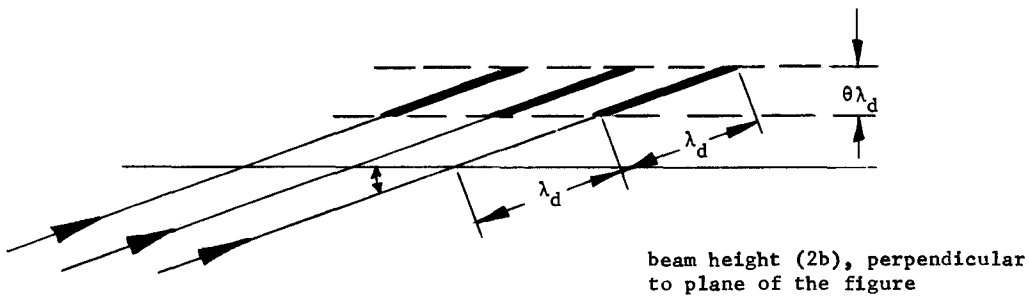

Fig. 2. Beam incident on superconducting coil.

in the shield and those coming out of the edges of the opening. It is assumed that a sequence of shield-coil sets is located downstream.

Neglecting the particles coming off the edges of all the shields, the amount of beam going through the opening of the last shield is given by the ratio of the solid angle subtended at the absorber by this last opening to the solid angle of the original cone from the absorber. The particles coming off the edges of the shields will add to this estimate. Thus shields must be placed in front of each successive downstream magnet at least to the location where the $(1/r^2)$ dependence reduces the particle flux to an acceptable value. [Again, particles coming off the edges of the shield will make the fall-off of the particle flux less rapidly than $(1/r^2)$. On the other hand, the presence of the dipole fields will make the charged particle fall-off faster, so that the $(1/r^2)$ law may be a reasonable approximation of reality.]

With a 30 GeV incident beam and a mean value of secondary particle energies of 15 GeV coming off the absorber edge, then the initial cone solid angle will be $(300\ \text{MeV}/15000\ \text{MeV})^2 = 4 \times 10^{-4}$. If the last shield has an opening of 20 cm^2 and is located 30 m downstream of the absorber, the solid angle subtended by the opening is $(20 \times 10^{-4}/900) \simeq 2 \times 10^{-6}$, and the particle flux is reduced by $(2 \times 10^{-6}/4 \times 10^{-4}) \simeq 5 \times 10^{-3}$. Note that this ratio is independent of the number of shields existing within the 30 m length. The number of shields depends only on the number of magnets one has to shield within the 30 m length following the absorber edge.

Tolerable Particle Flux from the Beam Scraper

In order to obtain now an estimate of the permissible particle flux downstream of the beam scraper, consider a beam of protons with a flux value of F (number/cm^2) incident on the superconducting coil at an impact angle of θ (see Fig. 2). The maximum energy

deposition is in a layer $\lambda_d\theta$ thick where λ_d is the caloric absorption length of the material. Thus the cross-sectional area of the beam contributing to the energy deposition is $\sigma = (\lambda_d\theta) \times (2b)$ where (2b) is the height of the beam (see Fig. 2). The energy deposition is therefore $J(\sigma).F.\sigma$, where $J(\sigma)$ is the energy deposition per proton, which is a function of the cross-sectional area of the beam, and $F\sigma$ is the total number of protons impacting on the wall. Because the superconducting coil is shielded by the Al vacuum chamber and stainless steel dewar inner wall the energy deposition in the coil is taken to be 0.1 times this, on the basis of the known character of radial fall-off of the nuclear cascade.

Limited guidance exists for the maximum tolerable caloric deposition into the superconducting matrix. On the basis of the conclusions of the Radiation Effects group of the ISA Summer Study the following numbers will be used:

Maximum acceptable caloric deposition into NbTi-Cu matrix:

3 mJ/cm^3, "fast" deposition

30 mJ/cm^3, "slow" deposition

(or $\sim$ 1 mJ/cm^3sec steady state) .

Consequently, for Cu, $\lambda_d \simeq 19$ cm; with $\theta \simeq 1$ mrad and 2b = 0.6 cm it follows $\sigma \simeq 1$ mm^2. For 30 GeV protons[1], with $\sigma = 1$ mm^2, $J \simeq 0.1$ GeV/cm^3. Therefore F is given by

$$(0.1F) \times (10^{-2}) \times (0.1) \times (1.6 \times 10^{-10}) = 3 \times 10^{-3} \text{ or,}$$

$F \simeq 10^{11}$ protons/cm^2. With an aperture in the "last" shield of $\simeq 20$ cm^2, the tolerable number of protons in the beam cone through this opening is 4×10^{12} particles. Using now the flux reduction factor arrived at in the foregoing of 5×10^{-3}, for the geometrical parameters as given, yields the tolerable particle flux from the absorber edge in case of a "fast" beam scraping occurrence as $(4 \times 10^{12}/5 \times 10^{-3}) \simeq 10^{15}$ particles. Since only approximately 3×10^{14}

1. A. van Steenbergen, "ISA Beam Dump Absorber," these Proc.

protons would be subjected to the scraper operation, the number of energetic particles coming from the absorber edge will be significantly less than the 10^{15} flux limit arrived at here, also the $J(\sigma)$ value used here was for 30 GeV protons only, consequently it is too large a value considering the realistic momentum spectrum.

Conclusion

On the basis of the foregoing model of energy deposition into the superconducting matrix, an order of magnitude estimate is provided for the permissible particle flux into the regular superconducting structure downstream of a beam absorber edge and the following sequence of cascade shields. Provided the superconducting elements over an extent of approximately 30 m downstream of the absorber edge are individually "pre-shadowed" by an Fe cascade shield, it is concluded that the beam scraping operations as required for high density beam stacking (low p scraper) can be carried out without exceeding the maximum caloric deposition tolerance of the superconducting magnets. Detailed cascade calculations are in progress (for preliminary results, see Ref. 2) to verify these conclusions.

---

2. L. Blumberg, J. Ranft, A. Stevens, A. van Steenbergen, "Caloric Deposition Downstream of the ISA Beam Scrapers," these Proc.

CALORIC DEPOSITION DOWNSTREAM OF THE ISA BEAM SCRAPERS

J. Ranft
Karl Marx Universität,

L. Blumberg, A. Stevens, A. van Steenbergen
Brookhaven National Laboratory

Introduction

Associated with the use of superconducting magnets in the ISA structure is the requirement to limit the caloric deposition from stray primary and secondary particles to a value, less than 3 mJ/cm^3 in the superconducting matrix.[1] This is an extremely small value compared with the total stored energy in the beam (20 MJ) or with the maximum caloric deposition value encountered when typically 0.1% of a 1 mm^2, 200 GeV, 7×10^{14} intensity, proton beam penetrates the copper matrix ($\simeq$ 1 kJ/cm^3).[2] Therefore, special design aspects must be incorporated to exclude "any" energetic particles from striking the vacuum wall. This is particularly difficult during the low momentum "tail" beam scraping mode following formation of the beam stack[3] and, to a lesser extent, during the protective beam extraction mode, during which, in one turn, the design beam of 7×10^{14} protons, at 200 GeV, must be extracted. In the first case up to 50% of the 30 GeV proton beam is "scraped" and in the latter case approximately 0.1% of the beam is targeted on a thin aluminum septum element of the extraction magnet. Because of nuclear cascade generation in either the

---

1. P.A. Sanger and G.T. Danby, Radiation Effects, these Proc.
2. A. van Steenbergen, "ISA Beam Dump Absorber", these Proc.
3. A. van Steenbergen, L.C. Teng, "Sources and Characteristics of ISA Beam Loss", these Proc.

absorber element of the scraper system[4,5] or the septum element of the extraction component sequence,[6] many energetic secondaries will exit from the absorber edge or from the thin septum and would tend to deposit in the downstream superconducting elements. Also, the multiple Coulomb scattered and elastically nuclear scattered primary protons in the above elements would contribute to an "uncontrolled" particle flux downsteam of the cited elements. Using the nuclear cascade programs developed by one of the authors* and in particular the CYLKAZ program,[7] with which the energy deposition (and star densities) can be calculated in a cylindrical block which can be subdivided radially and longitudinally in different materials; and the KASPRO program,[8] with which, in addition to energy deposition density and star density, the momentum spectrum and spatial spectrum of particles emerging from an absorber can be calculated, a first attempt has been made to determine the flux of secondary particles downstream of the absorber (septum) element and to determine if during a normal 30 GeV scraping mode, or alternatively, a normal protective extraction mode, the tolerable caloric deposition magnitude would be exceeded.

---

* J. Ranft [see for example J. Ranft, Part. Accel. 3, 129 (1972)].

4. J. Peterson, A. van Steenbergen, L.C. Teng, "ISA Beam Scraper System", these Proc.

5. A. van Steenbergen, "ISA Beam Scraper Criteria", these Proc.

6. A. van Steenbergen, "ISA Ejection System, Components and Parameters", Partial Draft Report, July 1975.

7. CERN, Lab II - RA/Note/74-12.

8. CERN, Lab II - RA/75-1.

(7. & 8. These and related cascade programs were made available to Brookhaven by the CERN, Lab II, Radiation Group, in particular with the assistance of H. Schonbacher and K. Goebel.)

Caloric Deposition Downstream of the Absorber of the Scraping System

The arrangement of relevant components in ISA Insertion VIII is shown in Fig. 1, where it is shown that a 3 m long Be absorber element and a 3 m long Fe cascade shield combination is located directly upstream of a superconducting dipole-quadrupole-dipole sequence. Further downstream, but benefiting from the $\left(r^{-2}\right)$ fall-off of the cascade cone, additional superconducting elements are located, which could conceivably receive too large a secondary particle flux during the beam scraping process. The CYLKAZ program was used to calculate the caloric deposition in the superconducting matrix of the dipole-quadrupole-dipole sequence. The appropriate element "mesh" is shown in Fig. 2. (The effect of the aluminum vacuum chamber wall and the stainless steel inner dewar wall of the superconducting elements has been neglected, although on the basis of the known radial fall-off of a 30 GeV cascade in various materials it is estimated that the caloric deposition density magnitude would be lowered by approximately one order of magnitude, if the details of the dipole inner structure would be fully taken into account.) The magnitude of the deposition density (GeV/cm^3pr) was calculated at the locations 1, 2, etc. shown in Fig. 2, referring to the maximum value in the first superconducting element following immediately the Be absorber-Fe cascade shield; similarly, in the superconducting element of the first unit of the two 1 m quadrupole elements, following a second Fe cascade shield; similarly, in the cascade shield immediately upstream of the "20 m" quadrupole doublet; similarly, in the cascade shield of the 20 m quadrupole doublet at the other side of the crossing point. The latter two values were approximated using the upstream deposition data and a $\left(r^{-2}\right)$ fall-off behavior. The results are as follows:

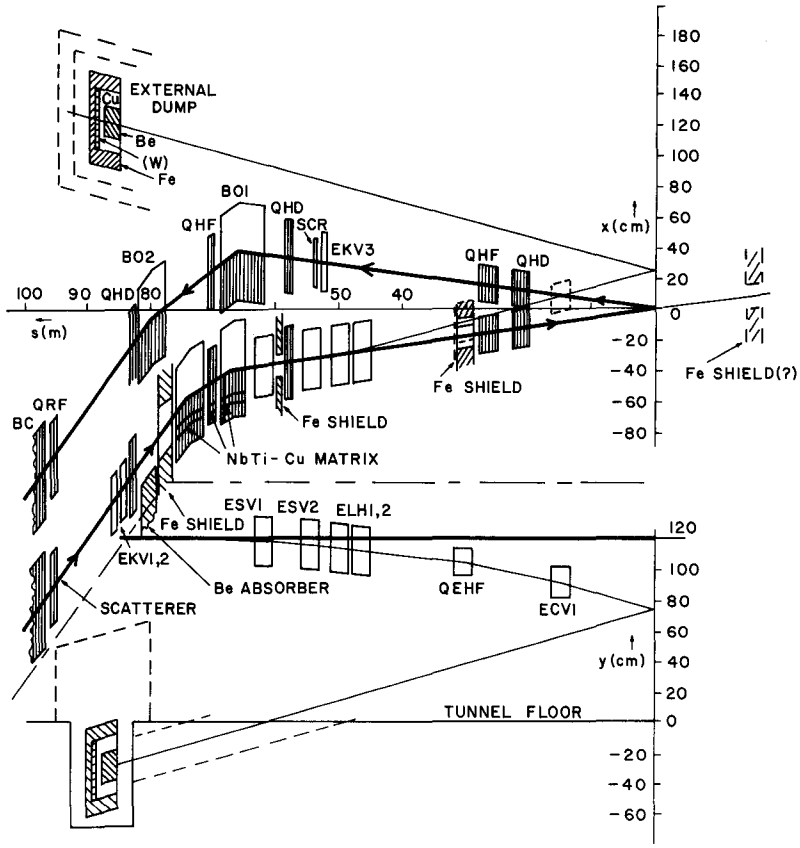

Fig. 1. Insertion VIII, Elements Downstream of the Be Absorber.

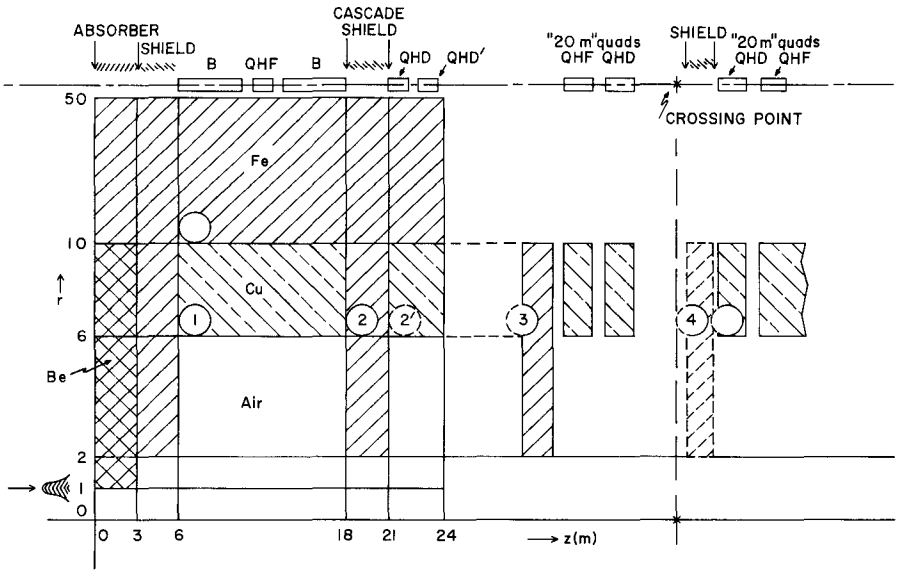

Fig. 2. Mesh Approximation for Caloric Deposition Computation Downstream of the Be Absorber.

Beam Scraping, 30 GeV, 3×10^{14} protons on absorber.

beam radius, $2\sigma = 3$ mm

divergence, $2\theta_{rms} = 0.5$ mrad

beam centered at the edge of the absorber.

Caloric deposition magnitudes:

Location 1 : 15 mJ/cm^3*

Location 2 : 30 mJ/cm^3

2′: 0.3 mJ/cm^3

Location 3 : $\sim$ 7 mJ/cm^3

Location 4 : $\sim$ 2 mJ/cm^3

Accepting now a maximum deposition rate of 1 mJ/cm^3 sec, these data permit the following preliminary conclusion to be drawn for the case of 30 GeV, 50% of the beam intensity scraping mode. (i) 3×10^{14} protons must be scraped on the absorber in a time of not less than approximately 1 min. (ii) With this rate of beam scraping the Fe cascade shield upstream of the 1 m quadrupole magnets may be superfluous. In any case, a 1 m long Fe cascade shield is more than adequate. (iii) No Fe cascade shield is needed upstream of the "20 m" quadrupole doublets (location 3). (iv) No cascade shield is required upstream of the quadrupole doublet at the 20 m location downstream of the crossing point.

(Note, that the case of a "fast" full intensity beam impact at 200 GeV, in case of failure of the protective extraction mode, i.e. the so-called redundant protection sequence, has not been considered here yet. Subsequent relevant cascade calculations could modify some of the above stated design aspects for the Insertion VIII components.)

---

* The values stated here are upper limit values, because of inadequate statistics associated with the relatively small number of protons (2000) used in the cascade calculation.

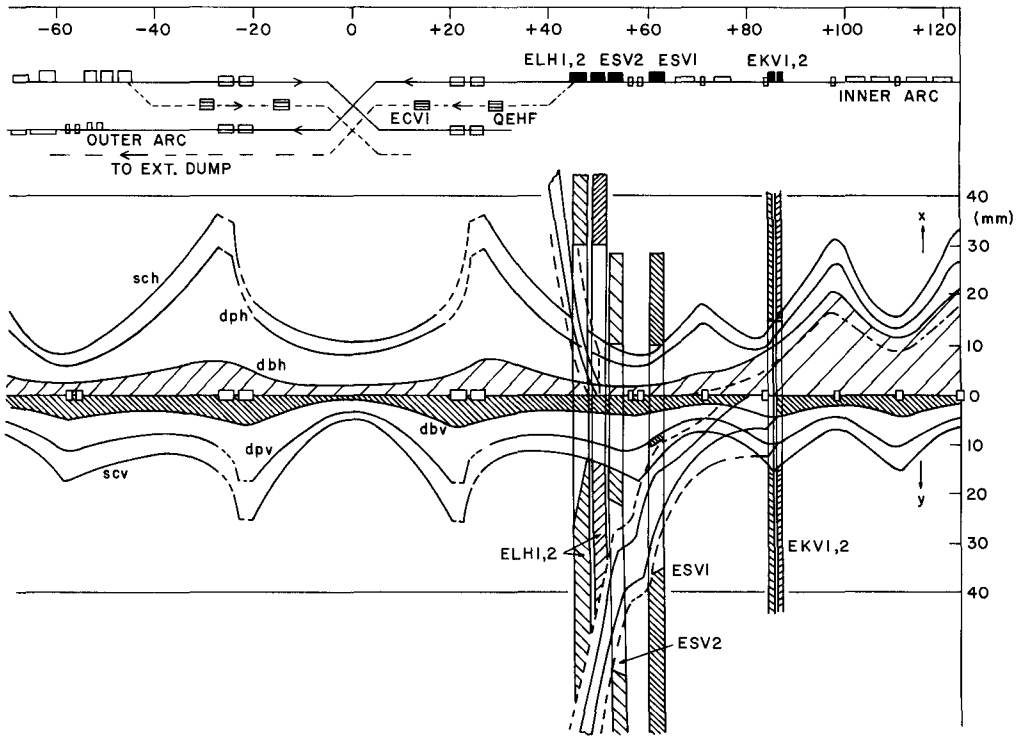

Fig. 3. ISA Ejection; Upstream end Ejection Trajectory.

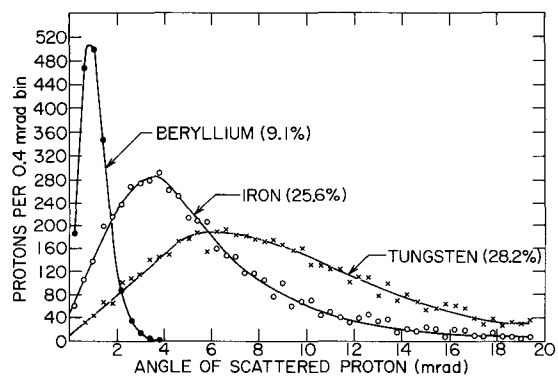

Fig. 4. Monte Carlo Calculation for Be, Fe, and W. Angle Distribution of 29 GeV/c Protons Scattered from 0.016". Boundary Layer of Absorber Element. Monte Carlo Code SCAT2. Sample = 20000 Incident Protons. Beam Absorber Length = 90 Inches.

Caloric Deposition Downstream of the Extraction Septum

The ISA upstream beam ejection trajectory and associated components is shown in Fig. 3. The calculated particle flux targeting on the 0.25 mm thick aluminum septum of ESV1 is $\sim 0.1\%$, i.e. approximately 7×10^{11}, 200 GeV protons could target on this element during a fast protective ejection sequence. Since the CYLKAZ program permits only five elements, again the actual element distribution has been approximated by a 12 m long, 2 mm radial extent (one radial mesh unit) Aℓ target located at 10.0 mm from the axis (representing together ESV1 and ESV2, see Fig. 3), followed by an Fe cylinder, 6 m in length, of inner radius of 12 mm, representing the iron septa of the Lambertson extraction magnets (ELH1,2) followed, after 15 m of free space, by the Fe cascade shield, Cu matrix combination of the "20 m" location quadrupole doublet. The maximum caloric deposition for 7×10^{11}, 200 GeV protons was calculated in the latter element as 4 mJ/cm^3 (fast, one turn, deposition) consequently, also during the fast extraction mode, with finite beam loss as calculated, the superconducting elements downstream will not receive such a caloric deposition that the danger would exist of driving these units normal.

Proton Scattering from the Surface of the ISA Absorber

So far only the cascade particles have been considered here. The results would be modified to a certain extent by also taking into account the protons directly scattered out of the absorber due to Coulomb and elastic nuclear scattering. The results of Monte Carlo calculations for the case of 30 GeV protons scattered out of a 90-in. long surface layer from three different materials, Be, Fe and W are shown in Fig. 4. The calculation includes multiple Coulomb scattering[9] and elastic nuclear scattering from

---

9. G. Moliere, Z. Naturforsch. 2a, 133 (1947); 3a, 78 (1948).

a diffraction model.[10] For tungsten 28.2% of the incident protons are scattered back into the machine aperture. A smaller fraction are outscattered for the case of beryllium (9.1%), moreover, for Be the scattered protons emerge at a small angle, $\sim$ 1 mrad, to the scraper surface and may therefore be more difficult to intercept with downstream absorbers. For tungsten, $\sim$ 96% of the outscattered protons are at angles $>$ 2 mrad. Thus, with absorbers located on the opposite side of the 8 cm beam pipe and ending $\sim$ 40 m downstream of the scraper it will be possible to intercept 99% of the scraped protons with the scraper-absorber combination.

Additional calculations are needed at 200 GeV where the scattering angles are smaller than above, and thus the problem of absorbing the scattered beam is more difficult.

Deflection of Cascade Particles in the Magnetic Elements

The foregoing results would be further modified when taking into account the realistic momentum spectrum of the secondaries coming out of the absorber face (surface approximately parallel to the beam axis). Considering the actual geometry downstream of the absorber element and an assumed substitution of a uniform, 12 m long dipole (3 segments) for the dipole-quadrupole-dipole configuration in Insertion VIII following the absorber edge, it can be shown that only charged secondaries with momentum values lower than 15 GeV/c (30 GeV/c primary protons) and emerging from the absorber face within an angle of approximately 5 mrad could additionally target on the "12 m" dipole chamber wall in the presence of the magnetic field and consequently create higher caloric deposition values than those obtained in the foregoing. The momentum and spatial spectrum has been obtained with the KASPRO program, cited before.

---

10. Fernbach, Serber and Taylor, Phys. Rev. 75, 1352 (1949).

For the case of a beam of rms radius = 1.5 mm and rms angle divergence = 0.25 mrad centered on the edge of the 3 m long Be absorber, the number of nucleon and pion secondaries emerging from the absorber edge back into the aperture of the ISA in an angle bin from 0 to 3 mrad is 0.3% incident proton; in the angle bin from 3 to 6 mrad, 0.21%/incident proton (0.13%/incident proton in the 6 to 9 mrad bin). The momentum distribution of the secondaries is illustrated in Fig. 5. Using these data it would be possible to follow quantitatively discrete ensembles of the < 5 mrad and < 15 GeV/c secondary spectrum through the dipole field and obtain the associated local increments of caloric deposition. This has not been done so far. The increment is expected to be small, however, since the most probable particle momentum for the first angular bin (0-3 mrad) is only 6 GeV/c.

Conclusion

A first quantitative examination has been made here of the maximum caloric deposition in the superconducting elements downstream of the scraper system absorber unit for conditions of extreme beam clean-up at 30 GeV/c. The results indicate that cascade shields would only be required for a limited number of superconducting elements immediately downstream of the absorber element and certainly can be limited to the spatial domain of Insertion VIII only, i.e. no cascade shields are required in the regular lattice downstream of the insertion. Further, the nuclear cascade associated with the particle loss of the normal fast protective extraction mode is mostly absorbed by the iron septa of the Lambertson type extraction magnets and will not create any unacceptable caloric deposition in the "20 m" quadrupole doublet downstream of it.

Since the cascade program used here can only approximate the various geometries under consideration, and also since the caloric deposition density tolerance for the ISA dipole (and quadrupole)

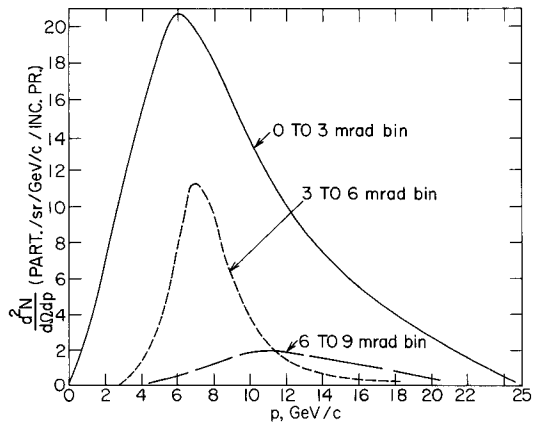

Fig. 5. Momentum Distribution of Secondaries. Monte Carlo Program KASPRO. Momentum Distribution of Secondary Protons, Neutrons and Pions Emerging from Surface of 3 m Long Be Absorber Irradiated with 30 GeV/c Proton Beam of rms Radius = 1.5 mm, rms Angle Spread of 0.25 mrad.

magnets is only presumed to be of the magnitude as used here, it is indeed desirable to experimentally pursue this matter for realistic geometries (effect of inner chambers, etc.) and to compare the results with further nuclear cascade computations using the relevant Monte Carlo programs.

ISA BEAM SCRAPER CRITERIA

A. van Steenbergen
Brookhaven National Laboratory

Introduction

A number of beam scraping operations are required during various phases of operation of the ISA. Shortly, these can be enumerated as: (i) Beam vertical scraping immediately following injection of the beam on the injection orbit and/or during the acceleration process of this beam into the stack. (ii) Beam vertical scraping of the stack, after its completion, and prior to the rebunching process, in order to eliminate unnecessary acceleration of a low density vertical phase space "periphery". This is partly brought about by unavoidable transverse phase space "filamentation" due to nonlinearities and partly due to the repetitive effect of the injection kicker stray field. (iii) Low momentum "tail" beam scraping to a minor degree during the repetitive stack built up process and to a major degree upon completion of the stack formation and movement thereof toward the center of the vacuum chamber. (iv) High momentum beam scraping for regular clean-up of the vertical phase space distribution in order to reduce background mainly associated with interactions outside the original well defined luminous domain in the beam-beam interaction region.

Beam Scraping Elements

The beam scraping operation will be performed by means of a sequence of a multiple traversal beam scattering target and a beam absorber edge located downstream of this. The purpose of the first scattering target is to effect a gradual growth of the betatron amplitudes, whereas the second unit, ideally, would completely absorb any protons impacting on its front (or side) face.

Regarding the location of the scattering target and absorber in the lattice structure, the phase separation of these units is not critical because of lack of phase coherence between scattering target traversals, i.e. scattering target traversals may be separated by many orbits. Even on the first turn the usually adopted phase advance ($\pi/2$) is not necessarily optimum as is illustrated in Fig. 1, where the beam scattering-beam "absorption" is schematically indicated in a normalized phase space diagram.

The location of the scattering target, inducing the betatron phase space blow-up, is associated with the particular beam scraping function to be performed, the following table indicates acceptable lattice locations:

TABLE I: Beam Scraper Element Locations

	Scatterer	Absorber
Vertical Phase Space Scraping	β_v max; x_p noncritical	Same
Low Momentum Tail Scraper	x_p max ($\neq 0$, required)	x_p non-critical
	β_h noncritical (preferably small)	($x_p = 0$ possible)

Because of cascade development in the absorber, it is further preferable to locate the absorber at such a location in the ISA lattice that azimuthal space is available for repetitive location of cascade shields upstream of the regular superconducting magnet structure. This is especially important for the low momentum tail scraper system (or "beam overstack" scraper) which may have to eliminate up to 50% of the 30 GeV/c injected beam.

Choice of Scatterer Material

Secondary particle production in the scattering target should

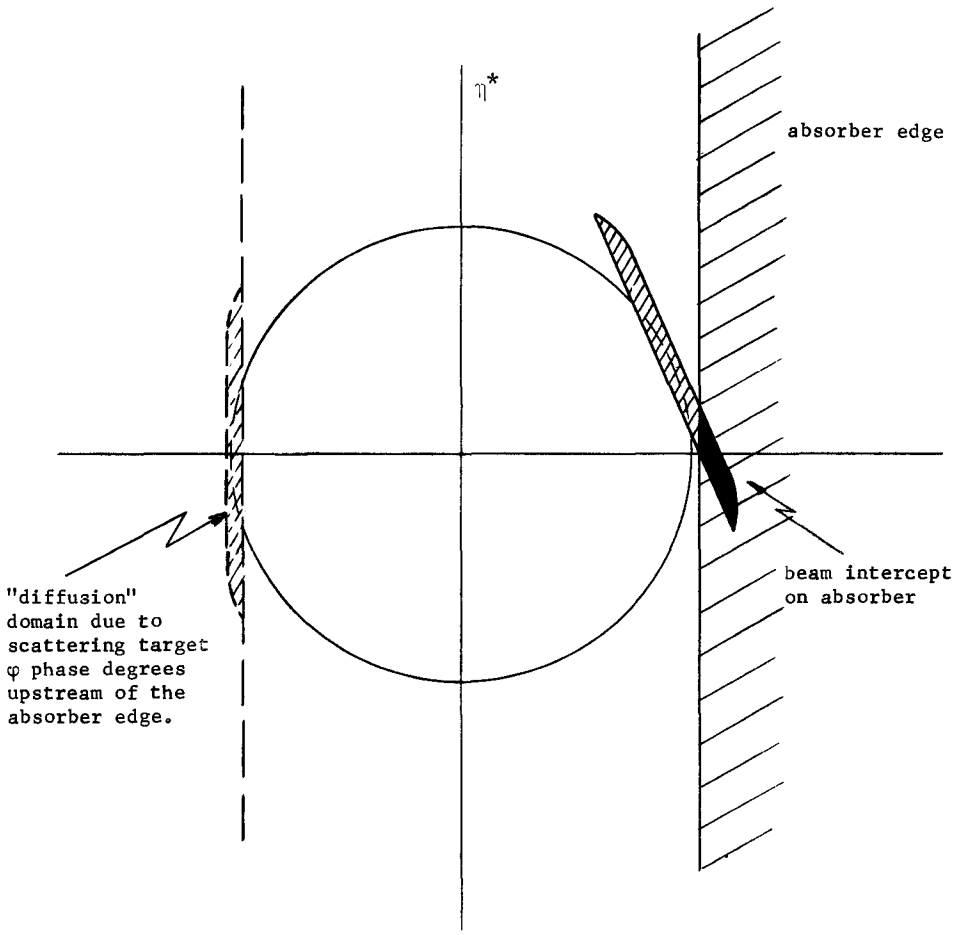

Fig. 1. Normalized phase-space representation at the location of the beam absorber.

be minimum in order to avoid "uncontrolled" particle fluxes into the downstream vacuum chamber. A favorable choice of material would be one whereby the protons are significantly deflected in angle as a result of multiple Coulomb scattering and elastic nuclear scattering before appreciable absorbtion (secondary particle production) would take place.

Considering the angular deflection due to Coulomb scattering only, the θ_{rms} value per interaction length ℓ_i, per single scattering target traversal is given by:[1]

$$\theta_{rms} = \sqrt{\frac{15}{p} \frac{\ell_i}{\ell_{rad}}} \quad .$$

[θ in mrad; p in GeV/c; ℓ_{rad}, radiation length].
Consequently, the scattering target material choice is guided by the maximum value of $(\ell_i/\ell_{rad})^{\frac{1}{2}}$. These values[2] are tabulated for various materials in Table II indicating the desirability of using a high Z material for the scattering target. Since Pb has a low melting point, W would seem to be the preferred choice.

Further, for multiple target traversal, the net rms scattering angle is given by

$$(n\theta)_{rms} = \frac{15}{p}\sqrt{\frac{n\ f\ \ell_i}{\ell_{rad}}} \quad , \text{ where}$$

$f = (th/\ell_i)$, th is the target thickness and n is the number of target traversals.

1. E. Segré. Experimental Nuclear Physics, Vol. I., Ch. II, p. 168.
2. Particle Properties, LBL Particle Data Group, April 1974.

TABLE II: Scattering Target Material

	ℓ_i(cm)	ℓ_{rad}(cm)	$(\ell_i/\ell_{rad})^{\frac{1}{2}}$	$(\ell_i^{3/2}/\ell_{rad}^{\frac{1}{2}})$(cm)
Be	37	36	1	37
C	50	67	0.86	43
Aℓ	37	9	2.0	74
Fe	17	1.8	3.1	53
Cu	15	1.5	3.1	47
W	10.3	0.35	5.4	57
Pb	18.5	0.6	5.5	102

The associated particle transverse deflection downstream in the lattice structure is given by

$$d_{rms} \cong \sqrt{n}\ \theta_{rms}\ \beta \quad .$$

Since only a small fraction of the protons traversing the scattering target (considering the first turn) may hit the absorber edge, the value of n, number of scattering target traversals, cannot be chosen too small. For the same reason, the d_{rms} value for n = 1 should not be too large, since then a larger fraction of protons would hit the vacuum chamber aperture. (For this reason locating the absorber edge close to the beam and having a large vacuum chamber aperture to beam size is favorable.) A competing objective is to avoid targeting a large number of protons close to the absorber edge in order to minimize outscattering of the protons. Disregarding here (see further below) the latter effect and taking $n \sim 20$,* $\beta \sim 40$ m, $3\ d_{rms} \leq 10$ mm it follows that $\theta_{rms} \simeq 0.02$ mrad. For W and p = 30 GeV/c a fractional (f) interaction length target thickness, given by

$$0.02 = 0.5\ \sqrt{f}\ (5.4) \text{ or } f = 5.5\ 10^{-5}$$

*This corresponds to a number of orbits >> 20 during the clean-up process.

would result; i.e. a target thickness of $\sim 5 \times 10^{-3}$ mm ($\sim 2 \times 10^{-4}$ in.). Since this is impracticably thin and, also, since the nuclear absorption would be negligible, even for 20 target traversals ($\sim$ 0.1%) a more suitable choice of scattering target material would be a lower Z material. The relevant numbers for Cu would be: $f' = 1.7\ 10^{-4}$; $th_{Cu} \sim 2.5\ 10^{-2}$ mm ($\sim 1\ 10^{-3}$ in.), nuclear absorption $\sim$ 0.3% which are a practicable set of parameters.

Since the rms value of the betatron amplitude after n scattering target traversals is given by[3]

$$(\langle a_n^2 \rangle - \langle a_o^2 \rangle)^{\frac{1}{2}} = \sqrt{n}\ d_{s,rms}$$

it follows that for these parameters and the original beam half size of $a_{o,rms} = 5$ mm a location of the absorber edge at an offset of 1 mm ($a_{n,rms} \simeq 6$ mm) is suitable.

The change in momentum for a 30 GeV proton after a single target traversal may be obtained by considering the ionization energy loss only in traversing the scattering target (for 30 GeV protons, $\sim$ 17.0 MeV/cm in Cu). The resultant orbit displacement at finite magnitude x_p values is negligible, moreover the absorber edge will be located at an $x_p = 0$ value in the insertion.

Choice of Absorber

Several considerations guide the choice of the absorber edge material (i) minimum outscattering of protons from the material per unit interaction length, (ii) maximum attenuation of the secondary particle cascade per unit length, (iii) acceptable caloric deposition density per "interacting" proton.

The latter two criteria are opposites, since minimum interaction length suggest a high density material, with as a consequence, a higher caloric deposition density per proton. (For

3. B. W. Montague, CERN ISR DI 71-51.

400 GeV protons the maximum caloric density is approximately proportional with $\rho^{2.8}$.)[4] The first criterion may be expressed as the objective that the displacement in the absorber material per interaction length should be minimum.[5] An additional criterion could be the requirement that the rms angle of protons emerging from the edge of the absorber be small, so that for a large fraction of the outscattered protons multiple orbits, with consequent multiple target-absorber traversals, are possible, or, alternatively, a very large value for the rms angle so that many of the outscattered protons could be trapped (absorbed) in auxiliary shields within approximately a one quarter betatron wavelength. Only a small rms angle is compatible with minimum displacement per interaction length, therefore, with

$$\theta_{rms} \propto (\ell_i/\ell_{rad})^{\frac{1}{2}} \quad \text{and}$$

$$\delta_{rms}, \text{ absorber, } s = \ell_i \cong \frac{15}{p} (\ell_i^{3/2}/\ell_{rad}^{\frac{1}{2}})$$

it follows that a minimum value for δ suggest a low Z material (see Table I). Beryllium would be the preferred choice, if this is unmanageable, aluminum should be adopted for the absorber edge, although its disadvantage is a lower melting point (about a factor of 2) and higher maximum caloric deposition density by a factor of $\simeq 3$.[4]

Using the elements discussed above a beam scraper system has been designed conceptually for the ISA.[6]

5. P. Sievers, CERN Lab II/BT/74-5.
6. J. Peterson, A. van Steenbergen, L.C. Teng, "ISA Beam Scraper System," these Proc.

SYNCHRONIZATION AND TOLERANCES FOR TRANSFER OF BEAM FROM AGS TO ISA

J. Peterson
Lawrence Berkeley Laboratory

L. C. Teng
Fermi National Accelerator Laboratory

The detailed procedure for matching during the transfer of beam from AGS to ISA has not yet been formulated. We shall assume here that both AGS and ISA are flat-topped for beam transfer and the rf voltages are properly adjusted to match beam-bunch shape. Specifically we shall take the AGS rf voltage to be 36 kV. This scheme may have to be modified when instability considerations are taken into account but will nevertheless serve to illustrate to first order the synchronization procedure required.

A. Beam-bunch dimensions in AGS

On the flat top $\phi_s = \pi$ and for the maximum dimensions of the bunch we have (for $\beta \simeq 1$)

$$\widehat{\frac{\Delta p}{p}} = \frac{A}{\gamma\eta}^{\frac{1}{2}} \qquad \widehat{\Delta\phi} = \left(\frac{A}{\frac{1}{2\pi h}\frac{eV}{mc^2}}\right)$$

where

$$A = \left(\frac{2}{\pi h}\frac{eV}{mc^2}\frac{\eta}{\gamma}\right)^{\frac{1}{2}} \frac{f\epsilon}{mc^2}$$

with

ϵ = longitudinal emittance = 0.36 eV sec

f = rf frequency of AGS or ISA = 4.45 MHz

V = rf voltage = 36 kV

$\eta = 1/\gamma_t^2 - 1/\gamma^2 = 0.0095$; ($\gamma = 31.4$, $\gamma_t = 9.75$)

h = harmonic number = 12

we get

$$A = 4.24 \times 10^{-8}$$

$$\widehat{\frac{\Delta p}{p}} = 3.8 \times 10^{-4}, \qquad \widehat{\Delta\phi} = 0.29 = 17^{\circ}$$

Thus, the full monentum and phase tolerances during transfer should be, say,

$$\frac{\delta p}{p} \simeq 7 \times 10^{-5}, \qquad \delta\phi \simeq 0.05 \simeq 3^{\circ} .$$

B. Bunch-shape matching

With ISA also on flat top, beam-bunch shape is matched if

$$\left(\frac{V}{h\eta}\right)_{ISA} = \left(\frac{V}{h\eta}\right)_{AGS}$$

with

$$\frac{h_{ISA}}{h_{AGS}} = \frac{11}{3} \qquad \text{and}$$

$$\eta_{ISA} = 0.00113 \quad (\gamma_t = 21.6)$$

we get

$$V_{ISA} = 0.436 \quad V_{AGS} = 15.7 \text{ kV}$$

A 1% tolerance on the rf voltage is good enough and should be rather easy to meet.

C. Momentum matching

Of the 3 quantities: magnetic field B, beam radial position x, and rf requency f, any two will fix the momentum. However, to get the same momentum definition, the accuracy requirements are

different for different sets of defining parameters.

1. B and f

In this case we have

$$\frac{\delta f}{f} = \frac{\delta \beta}{\beta} - \frac{\delta R}{R} = \frac{1}{\gamma^2}\frac{\delta p}{p} - \frac{1}{\gamma_t^2}\left(\frac{\delta p}{p} - \frac{\delta B}{B}\right) = -\eta\frac{\delta p}{p} + \frac{1}{\gamma_t^2}\frac{\delta B}{B}$$

or

$$\frac{\delta p}{p} = -\frac{1}{\eta}\frac{\delta f}{f} + \frac{1}{\eta\gamma^2}\frac{\delta B}{B} = -105\frac{\delta f}{f} + 1.11\frac{\delta B}{B}$$

If each term on the right-hand side has to be accurate to, say, 5×10^{-5} we get

$$\frac{\delta f}{f} \sim 4.8 \times 10^{-7} \qquad \frac{\delta B}{B} \sim 4.5 \times 10^{-5}$$

This accuracy in frequency is rather difficult to achieve in the AGS acceleration cycle.

2. B and x

$$\delta x = x_p\left(\frac{\delta p}{p} - \frac{\delta B}{B}\right)$$

or

$$\frac{\delta p}{p} = \frac{\delta x}{x_p} + \frac{\delta B}{B}$$

This same criterion gives

$$\frac{\delta x}{x_p} \sim 5 \times 10^{-5} \qquad \text{or} \qquad \delta x \sim 0.1 \text{ mm at } x_p = 2 \text{ m}$$

$$\frac{\delta B}{B} \sim 5 \times 10^{-5}$$

This, although difficult, is achievable. Of the 3 different

combinations this is the best. Also, momentum is defined by B and x more directly than by other combinations involving f. In principle, f defines only the synchronous momentum and any coherent phase oscillation will weaken the utility of f.

3. f and x

$$\frac{\delta f}{f} = \frac{1}{\gamma^2}\frac{\delta p}{p} - \frac{1}{\gamma_t^2}\frac{\delta p}{p} - \frac{\delta B}{B} = \frac{1}{\gamma^2}\frac{\delta p}{p} - \frac{1}{\gamma_t^2}\frac{\delta x}{x_p}$$

or

$$\frac{\delta p}{p} = \gamma^2 \frac{\delta f}{f} + \frac{\gamma^2}{\gamma_t^2}\frac{\delta x}{x_p} = 984\,\frac{\delta f}{f} + 10.4\,\frac{\delta x}{x_p}$$

The criterion leads to

$$\frac{\delta f}{f} \sim 5.1 \times 10^{-8} \qquad \frac{\delta x}{x_p} \sim 4.8 \times 10^{-6}$$

which is very much worse than either of the other two cases.

In summary, at 28.5 GeV the AGS should be flat topped (to give $\phi_s = \pi$) at a field strength accurate to $\delta B/B \sim 5 \times 10^{-5}$ and the rf should be adjusted so that the radial position of the beam is accurate to $\delta x \sim 0.1$ mm (at $x_p \sim 2$ m). The momentum of the beam is, then, accurate to $\delta p/p \sim 7 \times 10^{-5}$. The rf voltage is then reduced adiabatically to 36 kV. Both the momentum and the shape of the beam bunches are now properly matched and the injection sequence can start anytime. In practice the momentum defining tolerances $\delta B/B$ and $\delta x/x_p$ may be relaxed. Any excessive momentum error may be corrected in the ISA after injection (see Section E below).

D. Injection sequence

The firing sequence of the AGS extraction kicker, and the ISA injection kicker and septa is shown in Fig. 1. The first event in

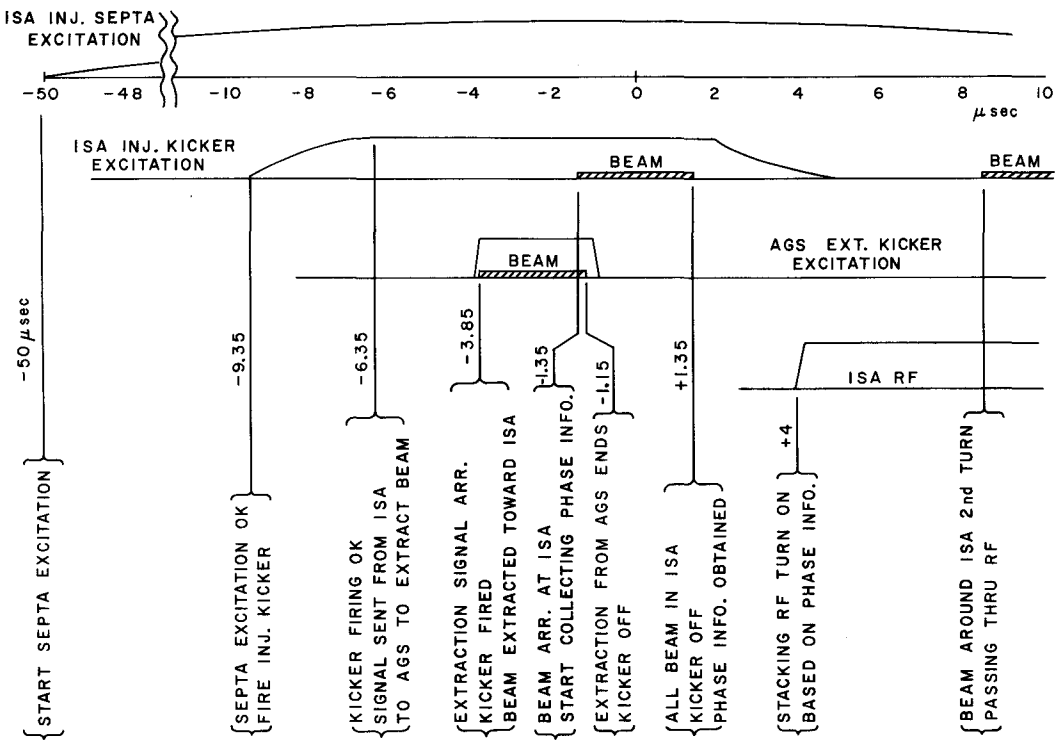

Fig. 1. Injection sequence. Assumed times - 1. ISA injection septa excitation - half sinewave half-period = 100 μsec. 2. ISA injection kicker rise and fall time = 3 μsec. (Can also be as long as 6 μsec.) 3. Transit time for beam or signal between AGS and ISA = 2.5 μsec. 5. AGS extraction kicker rise and fall time - negligible. 6. ISA stacking rf turn-on time = small. (Can be as long as 6 μsec.) 7. Beam revolution time in ISA = 10 μsec.

the sequence is the excitation of the injection septa shown at -50 μsec. The tolerances of the various times are rather loose and easy to attain, so that no special consideration of the timing tolerances is necessary.

The excitation of the pulsed injection magnets (two septa and a kicker) must be reproducible, pulse-to-pulse, and flat over the 2.7 μsec period of the 11-bunch train of beam bunches from the AGS. In order that the transverse phase space of the trapped beam not be diluted by more than 20%, the reproducibility and flatness must be good to ± 0.3% for the first septum magnet (KSV2), ± 0.6% for the second septum, and ± 1% for the kicker.

E. Synchronous capture by the ISA stacking rf system

After injection the beam-bunch phase in the ISA is picked up by a phase sensor during the first turn. The ISA rf is then turned on to a voltage of 15.7 kV and at the proper phase to synchronously capture the beam bunches on the second turn around. The phase oscillation frequency is $\sim$ 6.5 Hz, fast enough for correcting any excessive momentum error in a small fraction of a second. For example, a momentum error will turn into a phase error in ¼ of a phase oscillation (38.5 msec). The rf phase can then be shifted to center on the beam bunches. The time required for shifting depends on the magnitude of the shift, but should be no more than a few revolutions even in the extreme case of a 180° shift. However, if the required accuracy in B and x is attained, there should be no need for correction in the ISA.

ISABELLE KICKER MAGNETS, SEPTA AND SCRAPERS

A. Faltens

Lawrence Berkeley Laboratory

The injection and ejection kicker magnets have, in addition to their primary objective of providing specified deflections, the requirement that they do not perturb the stacked beam either by stray fields or by presenting any undesirably high impedances.

The transverse impedance is not considered specifically because, in the usual case, measures taken to provide a satisfactory current path for longitudinal currents also help transverse stability, and because feedback may be employed to damp transverse oscillations.

This note, therefore, is limited to briefly examining the principal characteristics of several designs and estimating their longitudinal coupling impedance. In every instance, a satisfactory geometry which contributes less than 1 Ω to Z_n/n appears possible. Minor design modifications were made in a few instances to lower the Z_n/n. All of the following are rough estimates which should be recalculated and measured if necessary for the final design.

Injection Kicker Magnets

The basic design requirements are: flat top, 3 μsec, fall time $\leq$ 7 μsec, rise time - not critical, length $\sim$ 1 m, $\langle B \rangle \sim$ 1 kG, stray field at beam location < 3.6 G. The cross-sectional view of the proposed[1] device is shown in Fig. 1. To decrease the stray field in the region of the stacked beam, magnetic shielding from the core, compensating windings external to the gap, eddy current shielding from additional conductors, or various combinations of these may be utilized. For the first two, it is desirable to have a high μ

1. A. van Steenbergen, "ISA Injection" ISA 75-6, July 1975.

magnetic yoke and on this basis laminated iron is preferred over ferrite. The diffusion time for magnetic fields, $T \simeq t^2 \mu\sigma$, for 1 mil thick laminations with $\mu = 10^4 \mu_o$ and $\sigma^{-1} = 80\ \mu\Omega$cm is about 1 μsec, and for the modest 1 kG field, the core will "work" for the required rise and fall times. The field in the narrow aperture decreases exponentially, while the field leaking all the way through to the region of the stacked beam will have chiefly a two dimensional dipole character, $B_x \propto \exp(-\pi x/g)$ in the gap and $B_x \propto 1/x^2$ in the aperture, with the expected magnitude of the dipole component about 1% of the kicker fields in the proximity of the beam stack. An external compensating current of $\sim$ 1% of the drive current will thus cancel the dominant component of the field.

The alternative shielding method (Fig. 2), an eddy current shield in the form of a tilted U, will exclude net flux from penetrating the aperture. The leakage field into that, because of the median plane symmetry, will have the appearance shown here and attenuate approximately as $\exp(-2\pi x/H)$ to provide very good shielding.

This latter geometry provides a conductor which may be smoothly joined to the beam pipe at either end. Except for a distance of about a beam pipe diameter into the pipe, and a gap width into the shielding box, the beam fields are compensated, i.e. the (γ^{-2}) cancellation between electric and magnetic forces holds. The "extra inductance" at the ends may be conservatively estimated as

$$\Delta L \simeq \frac{\mu_o}{2\pi} \ln\left(\frac{b}{a}\right) 2(b-a)$$

for a pipe radius "b" and aperture height 2"a", for which the low-frequency Z/n contribution is about $Z_n/n \simeq j$ 23 milliohms. Neither the flux exclusion function nor image current conductor function prevents the inclusion of some slots (preferably parallel to the beam direction) in the shield to facilitate vacuum pumping requirements.

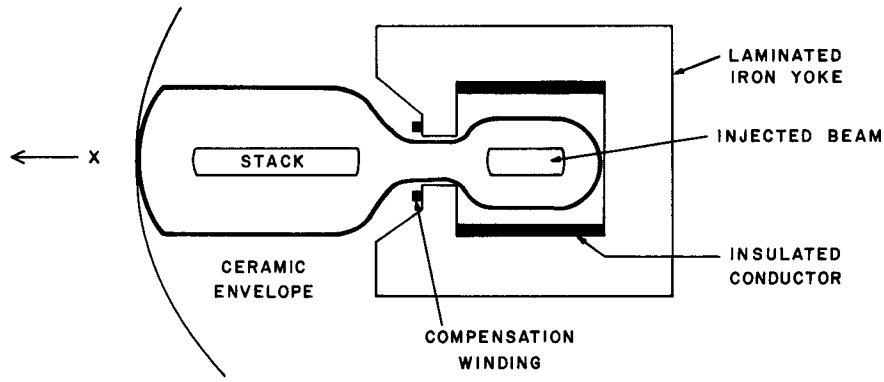

Fig. 1. Injection Kicker.

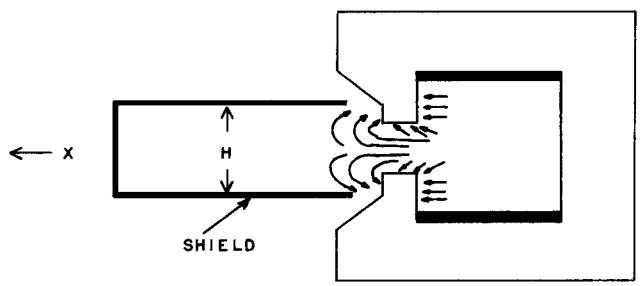

Fig. 2. Eddy Current Shield and Magnet.

At high frequencies, the constricted portion of the vacuum chamber, i.e. the shield, is able to radiate into the standard vacuum chamber pipe and into the lossy kicker magnet structure, so no resonances should occur.

In the event the eddy current shield conflicts with other requirements, a worst case estimate of the properties of the kicker may be made by assuming the geometry and properties as shown in Fig. 3. At low frequencies, the electric field distribution of the beam would appear as in the beam pipe, but the magnetic field would be distorted as shown, thereby approximately doubling the inductance. The extra inductance for this situation then is $\Delta L \simeq 0.2\ \mu H$ and $|Z_n/n| \simeq j\ 0.14\ \Omega$.

At low frequencies, the edges of the laminations are charged up by currents flowing transversely for a distance of the order of the beam pipe radius. At high frequencies, e.g. $n > 1000$ this process becomes lossy and the laminations could be considered as forming many lossy radial transmission lines or very low-Q resonators, in which the iron serves as the conductor and the interlaminar insulation as the dielectric. Over a broad band of frequencies then, Z takes the character of a real impedance of $R \simeq 100\ \Omega$, with $Z_n/n < 0.1\ \Omega$. If necessary, the high-frequency losses could be decreased by providing capacitively coupled conducting strips across the laminations (with care taken to avoid high-Q resonances), or by using a thin resistive coating on a ceramic (e.g. 1 Ω/square) which is transparent to fields with rise and fall times of the injector kicker.

Both ferrite and laminated iron are undesirable materials for high vacuum, and could be separated from it with a ceramic chamber or sleeve within the kicker. If the inside of this chamber is metallized over the region near the stacked beam, then the metallization provides a satisfactory image current path. If the ceramic is left unmetallized, then the dielectric adds a small amount of inductive impedance,

$$\frac{Z_n}{n} < \frac{j\omega_o\mu_o}{2\pi}\ \ell\ \frac{\Delta R}{R} \simeq j13\ m\Omega$$

for an assumed wall thickness, ΔR, of 4 mm, and radius, R, of 4 cm. High-Q dielectric resonances are unlikely here because of the nearby lossy magnetic materials.

Thus far, the discussion has centered on the effect of the injection kicker on the stack. The impedance seen by the injected beam is different, and may be estimated by the same methods as used for the ejection kicker, below, except that the inductance of the iron yoke surrounding the injected beam is determined by the gap through which the beam passes, $L \simeq \mu_o W\ell/g$, to give a $Z_n/n \simeq j1\Omega$. The tolerable impedance for the injected beam during the time it is within the kicker magnet poles is higher than for the coasting beam because at this time it is kept within a rf bucket.

Ejection Kicker Magnets[2]

Requirements:

Length	- 1 m
Aperture	- 3 cm x 3 cm
Risetime	- 300 nsec
Flat top	- 10 μsec
Fall time	- any
Field	- 2 kG

from which, $V = \frac{d\phi}{dt} = 20$ kV

$$I = \frac{B}{\mu_o} w = 5 \text{ kA}$$

The magnet would be used in a short-circuited configuration to avoid electrically stressing it for the relatively long period of a revolution. It would be driven in push-pull to permit placement of a conductor in the median plane to provide a low impedance image current path. The unit could be either ferrite loaded or air core as shown. An iron core was not considered.

2. A. van Steenbergen, "ISA Ejection System, Components and Parameters", (to be published as an ISA Informal Report).

The air core kicker would require perhaps 3 times the drive power of the ferrite kicker, because of the increased reluctance of the return path and the need for wider electrodes for field shaping.

To get orientation about the impedance of a full aperture kicker, a possible alternative, representative of how an acutal kicker might be constructed is considered in Fig. 4.

The period of the beam first harmonic is 10 μsec, which may be assumed to be much more than the travel time in the drive cables. If they are open circuited at the switches, as shown, then the drive plates carry little current and the beam "sees" the impedance of the ferrite yoke, with

$$L \simeq \frac{\mu \ell}{2\pi} \ell n(b/a) = \frac{(1000)(4\pi \times 10^{-7})}{2\pi} (1) \simeq 200 \ \mu H,$$

and $Z_n/n \simeq j\ 130\ \Omega$, for an assumed μ of 1000. Placing the median plane conductors through the ferrite breaks the magnetic circuit and lowers the inductance by about a factor of μ. The image currents will then run at the edges of the median plane conductors.

By back-terminating the drive lines at the switch tube, all line resonances are eliminated at the expense of a doubling of drive power, and the image currents are provided with additional conductors. The situation is further improved by replacing the terminating resistors with shorts and back terminating the PFN. Removing the ferrite also is beneficial at the expense of further drive power. The circuit chosen after this brief evolution is shown in Fig. 5. The Z_n/n for the ejection kickers at low n is therefore similar to the worst case example of the injection kicker, and also of the order of 0.14 Ω per magnet for the example with ferrite, and less than 0.1 Ω without ferrite.

The last point to consider is the possibility of transmission line type of resonances within the the kicker magnet chamber, because the drive line impedance required here is about 2 Ω, while the 1 meter or so length of the line inside the chamber will be approximately

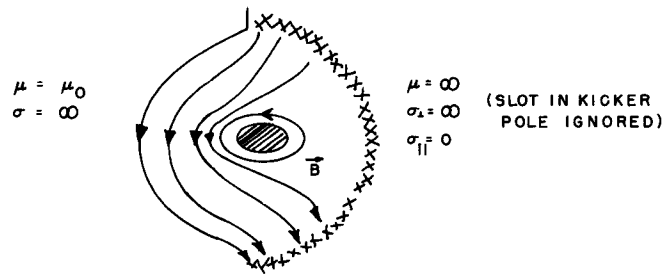

Fig. 3. Magnetic Field Distribution.

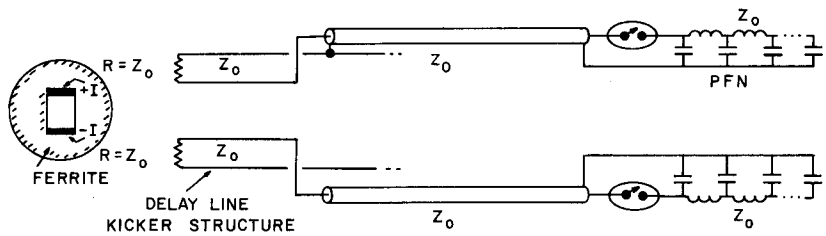

Fig. 4. Kicker Structure and PFN Drive.

50 Ω. The quarter line resonance will occur at 75 MHz, for the air core case, but it is overdamped by the drive cable impedance. The half wave resonance, at 150 MHz, will have a Q of about 25, and while not directly producing longitudinal fields, should be damped by placing a $\sim$ 50 Ω resistor near the middle of the chamber to "de-Q" it. If the placement of the resistor is made judiciously, several of such modes will be effectively damped.

The drive requirements for the ejection kickers can be met with thyratrons and lumped pulse forming networks. An increase in speed to $\sim$ 100 nsec switching time is within the state-of-the-art and will further decrease beam loss on the ejection septum. A delay line type of structure does not seem necessary for the ejection kicker and would complicate impedance question at the edges of the passbands of such a structure.

Septum Magnets

The various geometries shown[2] are all fairly innocuous with respect to impedances and their drive requirements are within the power capabilities of existing switches even when all the septa are made with one turn loops. The thickness of the pulsed septa could be reduced to about 1 mm (except for mechanical considerations) because of the limits on penetration depth of 100 μsec pulses. A half sine waveform obtained by discharging a capacitor, with a small peak-flattening circuit, is satisfactory. The impedances obtained for the kickers are a guide for the septum magnets, and from the similarity of the geometries will all contribute less than 1Ω. to Z_n/n, with practically zero in some geometries such as the coaxial septum magnet unit, as proposed.[2]

A more serious problem may arise with the connection of a septum magnet to the beam pipe in a manner which does not drive large currents into it. A possible solution is shown in Fig. 6. The intent is to make the impedance for external currents high, while allowing the image currents of the beam to flow without interruption

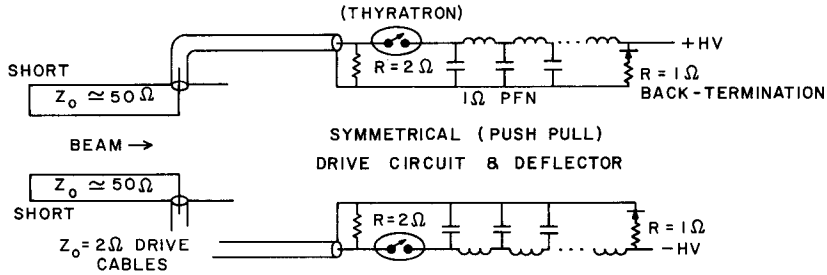

Fig. 5. Symmetrical (push pull) Drive Circuit and Deflector.

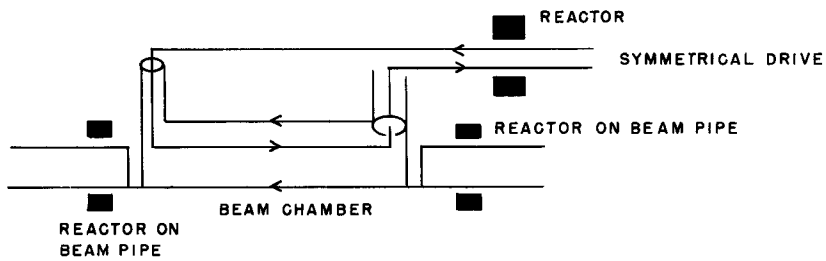

Fig. 6. Septum Magnet Connection.

on the inside of the pipe.

Beam Scrapers

The beam absorbers and shields also make a contribution to Z_n/n. The geometry for the shields is approximately as indicated in Fig 7. The electric field is shielded out of the corners of the discs for about a centimeter on each side, producing a $\Delta L \simeq \mu_o/2\pi[\ell n(4/3)](2 \times 10^{-2}) \cong 1$ nH and a $\Delta Z/n \simeq 1$ milliohm, which for an estimated total of 8 shields gives $\sim 8 \times 10^{-3}$ $j\Omega$.

The absorbers have a U-shaped geometry enclosing the stack so the relevant ΔL may be estimated as

$$\Delta L \simeq (2 \times 10^{-7})(8 \times 10^{-2})\ \ell n\left(\frac{8}{1}\right) \simeq 33 \text{ nH},$$

and a total (Z_n/n) for two vertical and two horizontal absorbers of ~ 40 j milliohms. These impedances are all quite small and they could be further lowered at low n by smoothing all the aperture transitions, but when added up systematically and combined with other equipment in the ring, they might affect the stability of the beam at injection, as the maximum permissible $|Z_n/n|$ is only $\sim 5\ \Omega$.

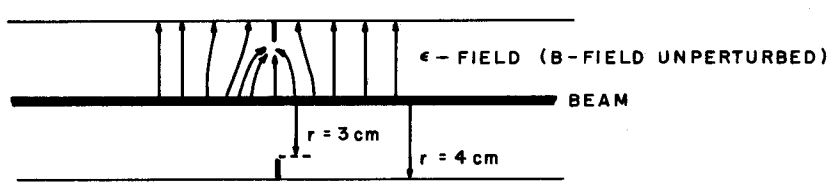

Fig. 7. Shield Geometry and Fields.

AN ESTIMATE OF LIMITS TO THE LONGITUDINAL COUPLING IMPEDANCE

A. Faltens and L.J. Laslett
Lawrence Berkeley Laboratory

Various simple models of structures in a storage ring and their contributions to the longitudinal coupling impedance are considered in an attempt to focus attention on possible problem areas and their solutions. In all cases emphasis is placed on the physical mechanism which is the source of the undesirable impedance. None of the mechanisms or structures considered prevent the attainment of a low $|Z_n/n|$, of the order of 1Ω, if sufficient care is taken over the frequency range from 0.1 MHz to about 10 GHz.

The various results and views in this note evolved mainly during the time of the Berkeley Electron Ring Accelerator project, in which a substantial effort was devoted to calculating, estimating, and measuring the properties of various beam-surrounding geometries which would simultaneously satisfy longitudinal and transverse stability requirements, and allow penetration of slowly increasing magnetic guide fields and fast inflection fields. Initially, interest centered on the low harmonic "inductive wall" effects, and later shifted to the microwave frequency region. It was shown that there are practical limits to attainable impedances, with the longitudinal impedance being the limiting one, with the limits manifesting themselves in the frequency region where free space wavelength and chamber dimensions are comparable. A value of $|Z_n/n|$ of about 30Ω was the lowest which might be attained in the geometries considered for electron ring accelerators.[1,2] The

---

1. A. Faltens, G.R. Lambertson, J.M. Peterson, J.B. Rechen Proc. IXth Int. Conf. on High Energy Accelerators, 1974, p. 226.
2. A. Faltens and L.J. Laslett, Particle Accelerators 4, 151, 1973.

corresponding limits for ISABELLE are less than 1Ω. Also, as in recent results from CERN, it was found that stability was determined by the instantaneous local energy spread in a beam filament. Multiturn injection of a beam with an instantaneous energy spread plus an energy ramp in time gave the same high-frequency thresholds as injection without the ramp, thereby imposing more stringent limits on allowable coupling impedances.

Before considering the effects of boxes and bends in the vacuum chamber, it may be appropriate to ask why a metallic vacuum chamber is necessary. The coupling impedance of a completely unshielded beam in free space may be obtained from synchrotron radiation results. The power radiated by an electron in a circular orbit, as derived by J. Schwinger,[3] is:

$$P\ (\omega,t) = \frac{3^{1/6}\Gamma\left(\frac{2}{3}\right)e^2}{\pi R}\ \left(\frac{\omega}{\omega_o}\right)^{1/3}\left[1 - \frac{\Gamma\left(\frac{2}{3}\right)}{2}\left(\frac{\omega}{2\omega_{crit}}\right)^{1/3} + \ldots\right]$$

for $\omega << \omega_{crit}$, independently of particle energy and therefore presumably the type of particle, and,

$$P\ (\omega,t) = \frac{3}{4}\ \left(\frac{3}{2\pi}\right)^{1/2}\frac{e^2}{R}\ \left(\frac{E}{mc^2}\right)^4\left(\frac{\omega_o}{\omega_{crit}}\right) \times$$

$$\left(\frac{\omega}{\omega_{crit}}\right)^{1/2} e^{-\omega/\omega_{crit}} \times \left[1 + \frac{55\omega_{crit}}{72\omega} + \ldots\right]$$

for $\omega >> \omega_o$ (2π times the revolution frequency), and $\omega_{crit} = (3/2)\ \omega_o\ (E/mc^2)^3$, or in our notation the harmonic number of the critical frequency is $n_{crit} \simeq (3/2)\ \gamma^3$.

---

3. J. Schwinger, Phys. Rev. 75, 1912 (1949).

The power raditated at any harmonic, n, may be related to the real part of the coupling impedance, R_n, and the nth harmonic current Fourier amplitude, I_n, of a δ-function charge traveling in a circle as $p_n = I_n^2 R_n/2$. Inclusion of the reactive terms leads to the result:[4]

$$\frac{Z_n}{n} = 354\ n^{-2/3}\left(\frac{\sqrt{3}}{2} + j\ \frac{1}{2}\right).$$

At very low harmonics, the more precise result is about 10% smaller, about 320Ω for n = 1, but very much larger than the "long wavelength limit",

$$\frac{Z_n}{n} \simeq -\left(jZ_o/\beta\gamma^2\right)\ \ln\frac{R}{na} \leq -\ j4\Omega$$

obtained by using the static inductance and capacity of a beam, and also greater than the tolerable impedance for ISABELLE.[5] The beam must, therefore, be shielded to suppress the low-harmonic radiation.

One shielding geometry of interest is a metallic pipe surrounding the beam. Such a pipe is an effective shield for wavelengths longer than its waveguide-cutoff wavelength, which for a circular pipe is given by

$$\lambda_{co} = \frac{2\pi a}{2.405} \quad \text{for TM or E-type waves.}$$

The harmonic number at which propagation begins for a 4 cm

---

4. A.G. Bonch-Osmolovsky, P9-6318, J.I.N.R., Dubna, 1972.
5. W. Schnell, "Stacking & Acceleration", Summary Report of Working Group, Vol. I, p. 126.

radius pipe of 2960 meter circumference is $n_{co} \simeq 2960/\lambda_{co} \simeq 28\ 325$, at which harmonic the $|Z_n/n|$ of free space has dropped to about 0.38Ω. Right at cutoff the impedance of the idealized smooth pipe is much less than this, but eventually, with increasing frequency many modes will propagate and the impedance should approach the free space values. The question regarding the beam pipe is: "At what frequency will it give behavior similar to free space, that is, for which wavelengths will the changes in pipe direction, wall losses, imperfections, clearing electrodes, etc. destroy the coherence of the radiated waves and scatter them randomly into the chamber until their energy is dissipated?" A reasonable estimate for this wavelength is about a centimeter, for which $|Z_n/n| \simeq 0.1\ \Omega$. Taking into account the local curvature of the particles only in the magnets, $n_{crit} \simeq 10^5$ at injection and $\simeq 3 \times 10^7$ at final energy, so we are interested in wavelengths down to centimeters and microns respectively.

In the nonphysical model of a perfectly smooth pipe bent into a circle, there will be resonances which for an aluminum wall could have high Q values, leading to higher coupling impedances than the free space values if the beam is able to excite them. Analogous problems using the eigenfunctions of a pill box cavity, coaxial cylinders, or a single cylinder showed that resonance that could be excited by a beam would occur at harmonic numbers n where

$$\frac{r_{beam}}{\beta R_{outer\ wall}} \simeq \frac{1}{1 + 0.80862n^{-2/3}} ,$$

where the required slowing of the phase velocity of the wave may be thought of as arising from the wave traveling at a slightly larger radius than the beam. In a straight, smooth pipe this synchronism does not occur because the phase velocity of any

mode is always greater than c, and the beam in vacuum will always travel at less than the velocity of light. The waves of course can be slowed down by loading of various types, and in ISABELLE this will undoubtedly be more important than the curvature effects, but the point is that even with smooth walls resonant effects may occur for $n \simeq 10^6$ at high γ.

One such "smooth wall" resonance is illustrated in the Appendix, where the properties of an 8 cm × 8 cm square cross sectioned aluminum chamber of 2960 meter circumference have been computed. The results of this computation are that a beam of $\gamma = 200$ will resonate at harmonic numbers of about 2.5×10^6 with modes having a $Q \sim 3 \times 10^5$. Fortunately, the $|Z_n/n|$ of these modes is only $\sim 0.2\Omega$, or about a factor of 10 above what radiation into space would give at that frequency, and no resonances at all are excited at the injection energy.

Returning to the real geometry of a beam pipe with bends, discontinuities, etc., resonances may be expected at the cutoff harmonic, n_{co} and even lower if resonant structures are introduced into the chamber. A rule of thumb for attainable cavity impedances is: $R \simeq \sqrt{f\ (\mathrm{MHz})}$ M Ω/meter. The maximum useful length for a cavity is $\ell \simeq \lambda/2$ before transit time effects start to decrease R; if the cavity length is much longer than $\lambda/2$, the net interaction with a beam is due to a length of $\lambda/2$ or less, with the remainder of the length acting as a load on the cavity. Combining the above yields an estimate for single, simple cavities of:

$$\frac{R_n}{n} \leq 4.7 \times 10^8 \left(\frac{\lambda}{2\ell}\right) n^{-3/2}$$

As an example of the sort of structure which should be avoided or modified, we consider a 30 cm long section of 12 cm

diameter pipe inserted in the standard 8 cm pipe in order to join beam pipes and provide a space for clearing electrodes and monitors (Fig. 1). The R_n/n for such an empty cavity could be as high as 50Ω. If this structure is complicated by insertion of clearing electrodes suspended at their midpoints, then this object is expected to resonate in a lower Q, half-wave TEM mode, coupling to the beam with the longitudinal fringing fields at its ends. Capacitive bypassing of such a clearing electrode is unattractive because a very large capacity, $C \sim 400\ \mu F$, is required for the $L \approx 12nH$ inductances which are to be bypassed. A well conducting clearing electrode at a 4 cm radius and $\sim$ 30 cm long will resonate near n = 4500 with a Q of $\sim$ 3000, and also produce an R_n/n of a few tens of ohms. By contrast, the contribution to Z_n/n from inductive wall effects is almost negligible. At low frequencies, the "inductance" of the empty box is due to the capacity of the fringing fields at the corners, which is effective over a distance comparable to the step size, $\Delta \simeq b - a$. The "inductance" of the box with clearing electrodes is approximately the inductance of the electrostatically shielded volume between the clearing electrode and the chamber outer wall. The impedances may be estimated as:

$$\frac{Z_n}{n} \simeq \frac{j\mu_o\omega_o}{2\pi}\left(\ell n\frac{b}{a}\right)\left(b-a\right) \simeq j\ 0.001\Omega, \text{and } \frac{j\omega_o\mu_o}{2\pi}\left(\ell n\frac{b}{a}\right)\left(\ell\right) \simeq j\ 0.0153\Omega$$

respectively. The impedance due to the use of bellows for the outer wall certainly is small compared to the latter value, but could be reduced by bridging the bellow convolutions with longitudinally conducting strips of metal. The precise value of the low-n (Z_n/n) may be measured.[6]

---

6. A. Faltens, E.C. Hartwig, D. Mohl, and A.M. Sessler, 8th Int. Conf. on High Energy Accelerators, 1971, p. 338

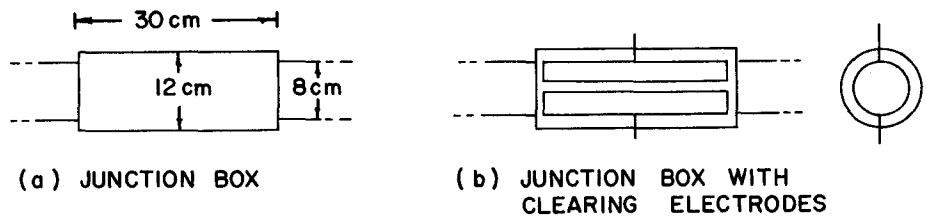

Fig. 1

After the obvious resonant structures are eliminated or otherwise made harmless, the beam pipe is still left with bends and other discontinuities. If no lossy materials are introduced at the discontinuities, then each junction simply transmits and reflects the incident waves, making each section of beam pipe no worse than an approximately 5 meter long cavity, for which a resonance at $n \approx n_{co}$ is expected with an $R_n/n \leq 1\Omega$. A long structure such as this poses questions which can only be answered statistically: will one of the cavity resonances fall exactly on some beam harmonic; what will be the transit time factor; and how many cavities will be resonant at the same frequency? Taking the worst case limit for each would make $Z_n/n \simeq 500$ for an estimated total of 500 beam pipe sections. The Z of an n = 28 000 resonance can be expected to be less than 30 000, so the probability of some harmonic hitting it is essentially 1. The transit time factor as used here oscillates as $\sin^2 (\pi\ell/\lambda)$ with increasing cavity length, giving an expected value of 1/2. Simultaneous resonance of many sections is more likely at the cutoff frequency than at higher frequencies, therefore the potential problem is serious. However, the problem is easily overcome as only a small amount of loss, attainable by numerous means, will lower the Q's sufficiently to make the impedance very low. If the de-Qing is very successful, then the coupling impedance will approach the free space limits again, as any radiated energy from the beam would be absorbed. As the problem area is right around the cut-

off frequency region, the $|Z_n/n|$ thus would tend towards 0.38Ω, perhaps enhanced by a small factor due to weak resonances remaining after de-Qing.

In the frequency region far above cutoff, that is, where modes are simultaneously propagating, the quality factors of individual resonances will be smaller than perhaps expected because any discontinuity, unless it is specially designed to counteract the effect, will scatter energy into other propagating modes. Likewise, the Q's of single resonators may be expected to be high only for frequencies below the cutoff frequency of the beam pipe. At these very high frequencies and at high γ the beam fields travel essentially as plane waves, parallel to the beam, with nearly identical fields to the fields of a TEM wave in a coaxial transmission line, and their scattering at obstacles may be estimated geometrically. Given a beam incident upon a number of obstacles, the reflection of the fields at the first obstacle will be higher than at subsequent ones because of the time required to re-establish the fields. In the rest frame of the particle the fields would be re-established with a transverse speed of c or less, which in the laboratory frame would be $v_t \leq c/\gamma$. The impedance of an isolated obstacle in the shape of a concentric disc with inner and outer radii a and b, respectively, based on the above considerations is:

$$Z = \frac{Z_o}{2\pi} \ln \frac{b}{a} .$$

As an example, for a = 3 cm, b = 4 cm.

$$Z \cong 17\Omega ,$$

and only one such obstacle would be effective per beam pipe junction. The total impedance for wavelengths of 1 cm or less, for which the above mechanism might apply is ~ 8.5 kΩ, and

$Z_n/n \leq 0.028\Omega$, and therefore no suprises or high impedances are expected for very high frequencies ($n > 10^5$).

The ordinary skin resistance contributes a term $Z_n/n = (1+j)\sqrt{\omega_o \mu \rho/2n}\ (\ell/2\pi a)$, which is important only at low harmonics, with a peak magnitude of 1.7Ω, and decreasing as $n^{-1/2}$. A small amount of wall impedance, of the order of $j1\Omega$, is desirable to offset the space charge term $Z_n/n \simeq jZ_o/\beta\gamma^2\ (\ell n\ b/a) \simeq -\ j1\Omega$ at the injection energy.

The preceding limits and the harmonic range over which they are important may be all combined on one graph (Fig. 2). Some specific items such as rf cavities and kicker magnets have been excluded here because they are treated separately elsewhere and because their impedances can be made small. The expected $|Z_n/n|$ curve, after elimination of low frequency resonances and diminution of wall inductances due to discontinuities, should follow the heavy line, and stay below 1Ω for all frequencies except the first two harmonics. On the other hand, any resonant object in a wide frequency band is potentially very harmful and should be avoided. The graph was constructed to show the large possible variation of coupling impedance. The single cavity approximation assumes only one cavity in the ring at any harmonic, and the presence of harmful low-harmonic resonances is unlikely in any event. The value of Z_n/n for vacuum chamber resonances is an estimate for the worst case of ~ 500 sections acting similarly.

The general recipe for obtaining low $|Z_n/n|$ for all n is therefore to shield the beam with a nearby good conductor to decrease the low harmonic free space impedance. The shielding geometry will in most practical cases introduce resonances at higher frequencies, and at that point it is beneficial to provide attenuation, which, in the limit of sufficient attenuation at high frequencies will make the impedance approach the free space values (see Ref. 2 for some computed examples). There is a trade-off between low-n and high-n $|Z_n/n|$'s, as measures taken to move the

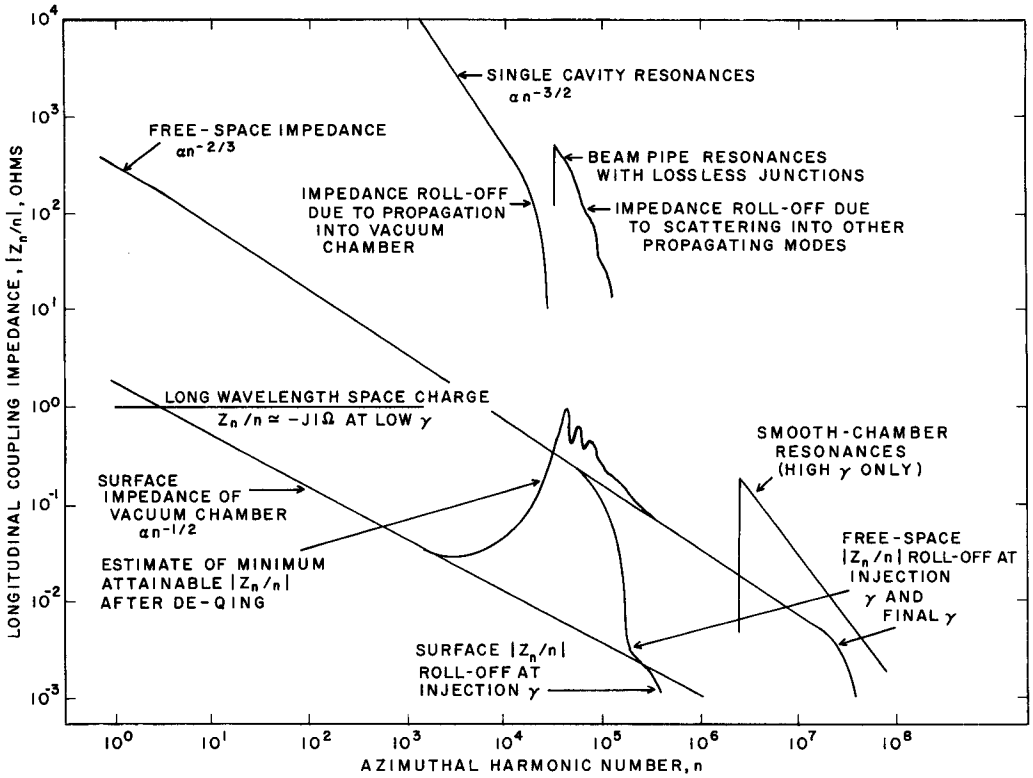

Fig. 2. Estimate of Coupling Impedance Limits

resonant behavior to higher frequencies by decreasing the shielding pipe diameter tend to increase the very low harmonic surface impedance. For the parameters of interest to ISABELLE, a maximum $|Z_n/n|$ of the order of 1Ω is estimated to be possible for all n.

APPENDIX

Coupling Impedance Contribution From the Electromagnetic Modes of a Toroidal Vacuum Chamber

The electromagnetic modes of a number of structures such as cylinders, pillbox cavities, and toroidal vacuum chambers may couple resonantly with an azimuthal current and produce a contribution to the longitudinal coupling impedance. The effect of such modes is computed for a toroidal aluminum vacuum chamber of square cross section of 8 cm × 8 cm and major radius of 471 meters such as might approximate the ISABELLE vacuum chamber if it were smoothly bent in a circle. Resonant behavior is exhibited only for $\gamma > \gamma_{inj}$, and a contribution to Z_n/n of 0.2Ω is computed for $\gamma = 200$.

The solution of the electromagnetic modes for the geometry:

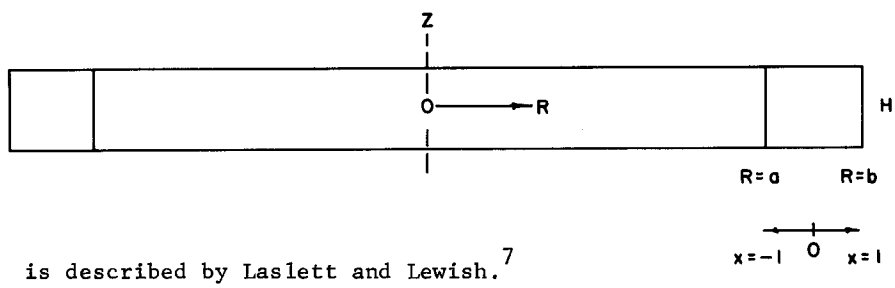

is described by Laslett and Lewish.[7]

The solution for the TE fields at high azimuthal harmonic numbers is depicted in Fig. A-1, where the functions Z and Z′, which are proportional to the B and E fields, are plotted across the normalized chamber radius, x. A beam located in the chamber midplane has a peak normalized coupling impedance on resonance of

---

7. L.J. Laslett and W. Lewish, Iowa State Report IS-189, 1960.

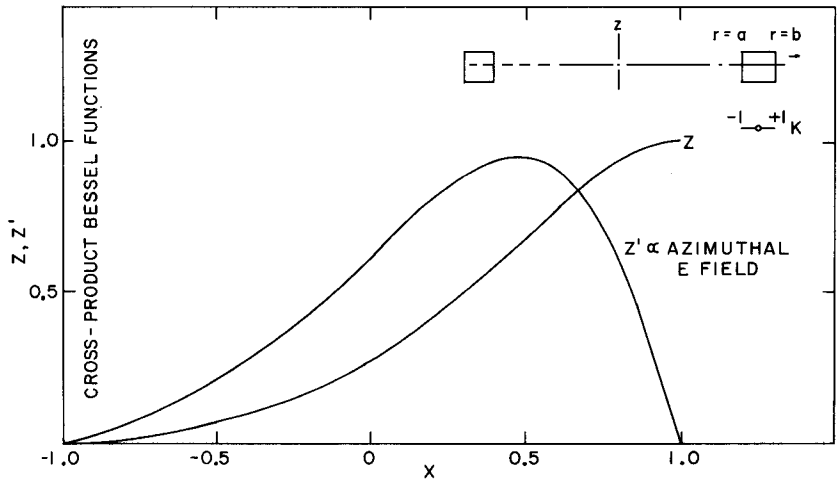

Fig. A1. Z & Z′ functions vs normalized chamber radius for $n = 2.47 \times 10^6$, $\eta = 8.49 \times 10^{-5}$, $\eta = (b-a)/(b+a)$, and square chamber cross section.

$$\frac{R_n}{n} = \frac{\pi Z_o^{\,2}}{\rho \lambda^2 K^2 n^2} \; \frac{\dfrac{1}{\eta^2} \left(\dfrac{dZ}{dx}\right)^2_{beam}}{\langle R\rangle^2 q^2 \eta \int (1+\eta x) Z^2 dx + \dfrac{H}{4}\left\{\dfrac{n^2}{\langle R\rangle}\left(\dfrac{Z^2_{outer}}{1+\eta x_o} + \dfrac{Z^2_{inner}}{1+\eta x_i}\right)\right.}$$

$$\left. + \frac{q^4}{K^2}\langle R\rangle \left((1+\eta x_o) Z^2_{outer} + (1+\eta x_i) Z^2_{inner}\right)\right\}$$

where $q^2 + K^2 = \left(\frac{\omega}{c}\right)$, $\langle R\rangle = \frac{b+a}{2}$, $K = \frac{\pi}{H}$, and $\eta = \frac{b-a}{b+a}$

A handier version of this formula, in terms of the chamber Q is:

$$\frac{R}{n} = \frac{4\pi Z_o Q}{n q^2} \; \frac{\lambda\!\!\!^{-}}{H \langle R\rangle^2 \eta^3} \; \frac{\left(\dfrac{dZ}{dx}\right)^2_{beam}}{\int_{-1}^{1} (1+\eta x) Z^2 dx}$$

Either formula, evaluated at the first resonance, which occurs for $n \cong 2.5 \times 10^6$ for a beam at the center with $\gamma \cong 200$, results in a value of $(R_n/n) \simeq 0.2\Omega$. The resonant radii for successive azimuthal resonances in this region are spaced by only 16 nanometers, which in combination with the high Q's of these resonances ($> 10^5$) may warrant reexamination of the usual relations between the peak value $|Z_n/n|$ and longitudinal stability.

ACCELERATING RF SYSTEM

S.T. Giordano
Brookhaven National Laboratory

Design Parameters

The present ISABELLE design calls for a 10 A average beam current, an energy gain of 12 kV/turn, a φ_s of 72° (measured from the peak of the rf voltage) and an operating frequency of 0.202 MHz (2nd harmonic). The total rf beam power, P_b, is 120 kW, while the maximum amplitude of the fundamental component of beam current, i_b, is 10 to 20 A.

The design to be presented is the result of practical engineering considerations regarding peak voltages, ferrite losses, stored energy requirements, efficient use of available power tubes, impedance requirements, etc. Each ring will have a total of four accelerating cavities, one of which is shown in Fig. 1. Table I lists the design and operating parameter for a cavity using a type 3B7 Ferroxcube low frequency ferrite.

Not shown in Fig. 1 are the copper water cooled discs that will be laminated in the ferrite. The overall cavity length, L_o, will probably be 1.5 to 2 m. Also not shown are the various ferrite damping devices to be used on the power amplifier feedlines, capacitor and filter, to damp spurious resonances.

Power Amplifier

In order to achieve a low driving point impedance over a wide frequency range a push-pull cathode follow amplifier circuit shown in Fig. 2 is being considered. Referred to the gap of the cavity the amplifier is capable of providing a peak voltage of 10 kV, a peak current of 20 A and a dynamic impedance of $< 50\ \Omega$. The maximum anode dissipation, is 55 kW per tube. In order to provide the low dynamic impedance over a wide frequency range (up to 20 MHz) neutralizing condensers, NC, are required. The leads coupling the

TABLE I

Accelerating Cavity Parameters

G gap length	~ 2 cm
L_f Ferrite length	110 cm
d_1 inner diameter	20 cm
d_2 outer diameter	50 cm
ℓ Ferrite gap	0.75 cm
C gap capacitance	0.02 μF
V Peak gap voltage	10 kV
φ_s stable phase angle	72 °
E energy gain per turn	3 kV
I_p peak cavity circulating current	20 A
J peak cavity stored energy	1 J
B_p peak field in ferrite	450 G
V_f volume of ferrite	0.18 m^3
W_f power density in ferrite	0.1 W/cm^3
W_t total power dissipated in ferrite	18 kW
RF effective shunt resistance of ferrite	2.8 kΩ
Q_f unloaded Q	77

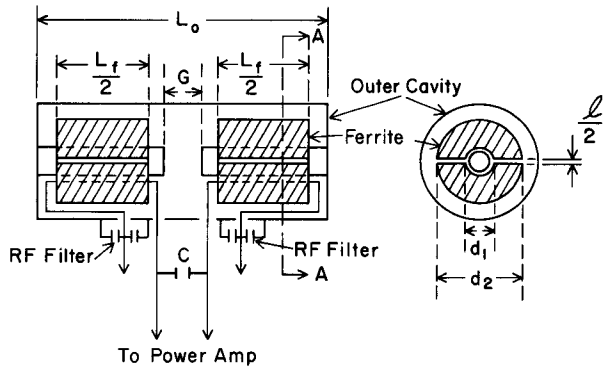

Fig. 1. Accelerating Cavity.

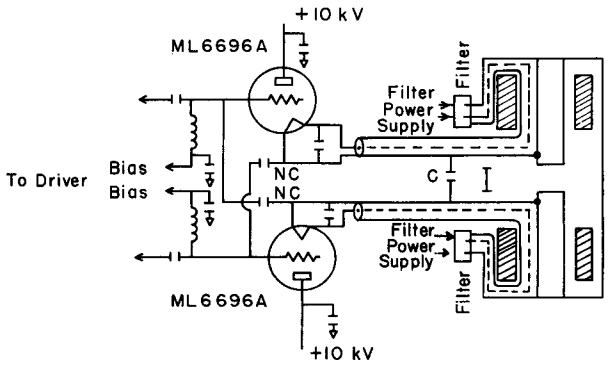

Fig. 2. Accelerating rf power amplifier.

cathode follower to the cavity will be either a coaxial line, strip line, or transposed pair of bus wire appropriately matched and damped with ferrite beads.

Equivalent Circuit Consideration

Considering the above cathode follower circuit and cavity, we can now make some calculations of the beam loading effect. Figure 3 shows the equivalent circuit from which we derive the following:

$$Y = G + j\left(\omega c - \frac{1}{\omega L}\right) = G\left[1 + j\frac{\omega_o C}{G}\left(\frac{\omega}{\omega_o} - \frac{\omega_o}{\omega}\right)\right] = G[1 + \tan\varphi_e] ,$$

and since

$$i_g - i_b e^{-j\varphi_s} = VY,$$

we get

$$i_g = VG + i_b \cos\varphi_s + j(VG \tan\varphi_e - i_b \sin\varphi_s) \quad .$$

To find reaction detuning of the beam we get

$$i_b \sin\varphi_s = VG \tan\varphi_e \quad .$$

For $\varphi_s = 72^o$ and $i_b = 20$ A we get $\tan\varphi_e = 0.0933$, and

$$\left|\frac{\delta\omega}{\omega_o}\right| \approx \frac{i_b \sin\varphi_s}{2V\,\omega_o C} = 0.034 \quad ,$$

and

$$|\delta f| \approx 8 \text{ kHz}$$

Acceleration

Let us first consider the case where the cavity is resonated to ω_o and the beam is bunched so that $i_b = 20$ A and $\varphi_s = 72^o$. (See case A Table II.) For the above case where $\omega = \omega_o$ we get

$$\tan\varphi_e = \frac{\omega_o C}{G}\left(\frac{\omega}{\omega_o} - \frac{\omega_o}{\omega}\right) = 0 \quad ;$$

therefore,

$$i_g = VG + i_b \cos\varphi_s - ji_b \sin\varphi_s = 209.6 - j19.$$

TABLE II

Beam Loading Parameters

Case	V(kV)	φ_s	i_b(A)	tan φ_e	V_g(kV)	i_{gV}(A)	Cavity Resonance
A	$10\underline{/0^\circ}$	72°	20	0	$10.5\underline{/-5^\circ}$	$21.3\underline{/-63^\circ}$	f_o
B	$10\underline{/0^\circ}$	72°	20	0.0933	$10.5\underline{/0^\circ}$	$9.6\underline{/0^\circ}$	f_o - 8 kHz
C	$1.25\underline{/0^\circ}$	90°	10	0.0933	$1.3\underline{/-16^\circ}$	$7.7\underline{/-86^\circ}$	f_o - 8 kHz
D	$1.25\underline{/0^\circ}$	90°	0	0.0933	$1.3\underline{/5.3^\circ}$	$2.46\underline{/+79^\circ}$	f_o - 8 kHz
E	$1.25\underline{/0^\circ}$	90°	10	0	$1.4\underline{/-20^\circ}$	$10\underline{/-87^\circ}$	f_o
F	$1.25\underline{/0^\circ}$	90°	0	0	$1.3\underline{/0^\circ}$	$0.45\underline{/0^\circ}$	f_o

We can now compute V_g and i_{gV} (see Fig. 3), which represent the operating conditions of the amplifier, and get $V_g = 10.5\underline{/-5^o}$ kV, and $i_{gV} = 21.3\underline{/-63^o}$ A. (Remembering that all phases are referenced to the gap voltage V which is at zero degrees.)

Let us now consider the case where the cavity is detuned by - 8 kc (see case B Table II), which results in $\tan \varphi_e = 0.0933$. We then get

$$i_g = VG + i_b \cos \varphi_s = 209.6\underline{/0^o} \quad ,$$

and when referenced to the equivalent voltage generator we get $V_g = 10.5\underline{/0^o}$ kV and $i_{gV} = 9.6\underline{/0^o}$ A

It is obvious that the best operating condition for acceleration is with the cavity detuned, as the peak rf current that the amplifier must supply is reduced from 21.3 A to 9.6 A. (See Table II.)

Capture

We have already established that the best operating conditions for the amplifier during acceleration is with the cavity detuned. If we elect to leave the cavity detuned, as above, we must now ascertain what the amplifier operating conditions are during the capture period. We We will consider the case when $V = 1.25$ kV, $\varphi_s = 90^o$, $\tan \varphi_e = 0.0933$ and for $i_b = 0$, which occurs at the beginning of the cycle, and for $i_b = 10$ A, which occurs at the end of the bunching cycle (Table II cases C and D). For the above two cases, we get that $i_{gV} = 7.7\underline{/-86^o}$ A and $2.45\underline{/+ 79^o}$ A respectively.

Conclusions

It should be pointed out that the particular cavity design selected using a gap in the ferrite results in two desirable features - a considerable reduction in the amount of ferrite needed, and a considerable reduction in the length of the cavity (an absolutely necessary requirement to fit the available space). A shortcoming of this design is that it is not possible to electrically tune the cavity with a biasing current.

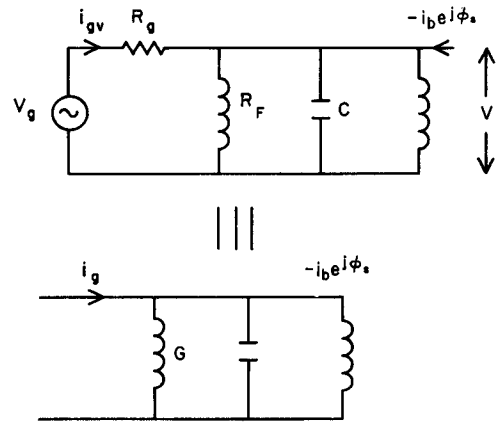

Fig. 3. Equivalent circuit; R_g = generator impedance = 50 Ω, R_F = ferrite losses = 2.8 KΩ, C = 0.02 μF, i_b = peak fundamental beam current = 10 A, i_g = peak current of an equivalent current generator, φ_s = stable phase angle = 72°, G = $1/R_g + 1/R_F$ = 0.02036, f_o = 0.202 MHz, V = peak voltage across cavity, i_{gv} = peak current of equivalent voltage generator.

As a consequence of not being able to tune the cavity during certain parts of the capture and acceleration cycle the cavity will present a reactive impedance to the power amplifiers. There is some concern about the stability of any feedback amplifiers when driving reactive loads. Table II lists the various operating parameter for different beam loading conditions. A reasonable compromise, related to minimizing the reactive load presented to the power amplifier, would be to tune the cavity to a frequency of f_o - 8 kc. Because of these reacting currents careful consideration of the feedback network is required. Some consideration is also being given to mechanical tuning of the cavity, and even if there is only a partial correction, the condition for an instability may be significantly reduced.

STACKING RF SYSTEM

S. Giordano
Brookhaven National Laboratory

System Parameters

It is planned to inject eleven AGS bunches into stationary buckets in the ISA. The rf frequency will be $\approx$ 4.45 MHz corresponding to h = 44 and the peak voltage at injection required for matching will be 12 kV. Acceleration toward the stack at this voltage and with $\Gamma = \sin \varphi_o = 0.63$ will proceed for a variable time t_a. Then the peak voltage will be reduced to 1.2 kV in $\approx$ 0.5 sec at which time suppressed bucket operation will be required as the bunches are moved the rest of the way into the stack. This means that the rf will be gated on for only one quarter of a revolution period during this final stacking phase (see Fig. 1).

At 12 kV the peak instantaneous beam current will be $\approx$ 2.8 A while the maximum amplitude of the rf component (@ 4.45 MHz) will be $\approx$ 0.6 A and $\varphi_s = 90^o$. At 1.2 kV the peak beam current will be $\approx$ 1.3 A while the rf component will still be $\approx$ 0.6 A but $\varphi_s \cong 51^o$.

Cavity Design

The circuit parameters selected, by necessity, will be a compromise between minimizing the beam loading effects for the above operating conditions and the capability of the circuit to switch the rf on and off with a minimum transient. In other words a large stored energy in the rf circuit is desirable to reduce beam loading effects, but a small stored energy will reduce the switching transient.

As a starting point in the design, a gap capacity of 200 pF was selected. At this time the 200 pF represents the minimum value to be considered for good cavity design. Because of the high dielectric

constant of ferrites, too small a gap capacitance will adversely effect the R/Q. Figure 2 shows a single ended cavity using Ferroxcube 4C4 type ferrite. The function of the lead labled "To Switch Tube" will be described later. Table I lists the design and operating parameters of the cavity.

TABLE I. Cavity Parameters

G	gap length	~ 2 cm
L_f	ferrite length	72 cm
d_1	inner diam	26 cm
d_2	outer diam	40 cm
ℓ	ferrite gap	1 cm
C	gap capacitance	200 pF
I_p	peak cavity circulating current	69 A @ 12 kV 6.8 A @ 1.2 kV
J	peak cavity stored cavity (joule)	0.144×10^{-1} @ 12 kV 0.144×10^{-3} @ 1.2 kV
B_p	peak field in ferrite	85 G @ 12 kV, 8.5 G
V_t	volume of ferrite	52×10^3 cm^3
W_f	power density in ferrite	0.2 kW/cm^3 @ 12 kV 0.002 kW/cm^3 @ 1.2 kV
W_t	total power dissipated in ferrite	10.4 kW @ 12 kV 0.104 kW @ 1.2 kV
R_t	effective shunt resistance and ferrite	6.9 kΩ @ 12 kV 6.9 kΩ @ 1.2 kV
Q_t	unloaded Q	40 @ 12 kV 40 @ 1.2 kV

RF Amplifier

At present no design exists for the rf amplifier, but a design, similar to that presently being used at CERN, using a single ended pentode operating as a class A amplifier with feedback is being con-

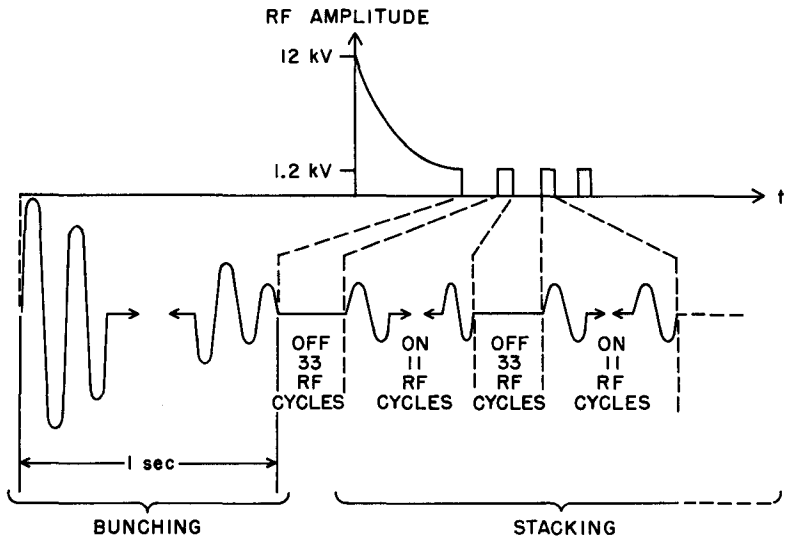

Fig. 1. RF cycle.

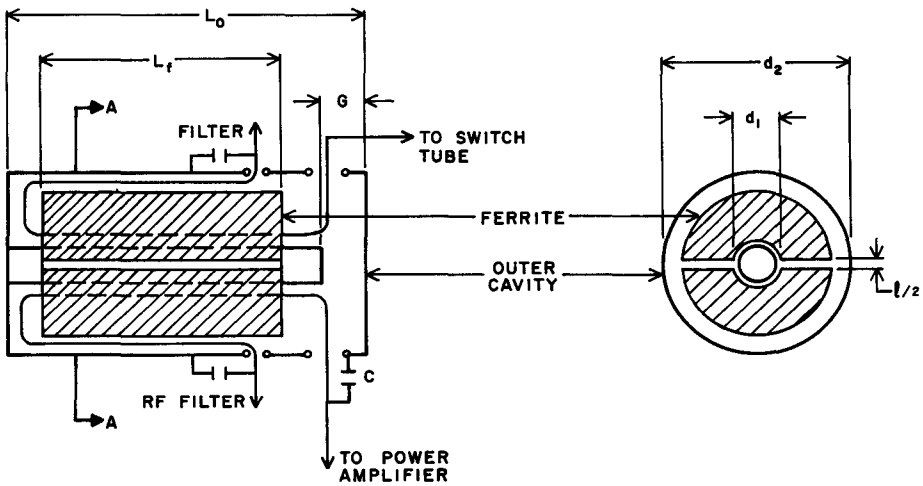

Fig. 2. Cavity.

TABLE II. Amplifier Operating Parameters

Case	V(kV)	φ_s	i_b(A)	tan φ_e	V_g(kV)	i_{gV}	Resonance
A	$12\underline{/0^\circ}$	90°	0.6	0	$12\underline{/0^\circ}$	$1.8\underline{/-19^\circ}$	f_o
B	$12\underline{/0^\circ}$	51°	0.6	0	$12\underline{/0^\circ}$	$2\underline{/-13^\circ}$	f_o
C	$1.2\underline{/0^\circ}$	51°	0.6	0	$1.2\underline{/-1^\circ}$	$0.72\underline{/-40^\circ}$	f_o
A'	$12\underline{/0^\circ}$	90°	0.6	0.00248	$12\underline{/0^\circ}$	$1.74\underline{/0^\circ}$	f_o-20 kHz
B'	$1.2\underline{/0^\circ}$	90°	0.6	0.0248	$1.2\underline{/0^\circ}$	$.174\underline{/0^\circ}$	f_o-200 kHz
C'	$1.2\underline{/0^\circ}$	51°	0.6	0.0193	$1.2\underline{/0^\circ}$	$0.55\underline{/0^\circ}$	f_o-155 kHz

sidered. An output impedance of 50 Ω has been achieved, and this number will be used in all subsequent calculations.

Capture and Initial Acceleration

The equivalent voltage generator requirements V_g and i_{gV}, for various operating conditions are tabulated in Table II. Case A and B represent the beginning and end of the capture and initial acceleration cycle respectively, and case C is the final stacking cycle. As seen in Table II, if the cavity is resonated to f_o then the amplifier must supply a reactive current. There is some concern about the stability of an amplifier using feedback during a reactive load. It would be a simple matter to tune the cavity to the resonant conditions as shown for cases A', B' and C'. The frequency change of 200 kHz would require a capacitance change of only 20 pF over a period of about 1 second. This can be easily accomplished with a mechanical system. The required phase difference between the gap voltage (V) and the beam phase will be controlled electrically by phase shifting the rf drive.

Suppressed Bucket Operation

Gating the rf during the final stacking process is accomplished by the circuit shown in Fig. 3A, which is a schematic representation of the cavity, rf amplifier and switch tube. Figure 3B shows the voltage across the cavity and the circulating inductor current for a steady state rf drive and with the switch tube cut off. Figure 3C shows what conditions must be satisfied to have a turn on and turn off of the rf voltage without a transient. The rf drive is turned on and off at T_{on} and T_{off} when V = 0, as shown in Fig. 3E. At T_{on} the voltage is zero and energy is stored in the magnetic circuit in the form of a current i_o flowing through the inductor; this energy is supplied by the switch tube current, i_o, as shown in Fig. 3D. At T_{on} the switch tube current, i_o, is cut off. At T_{off} the switch tube is turned on again when V = 0. It should be pointed

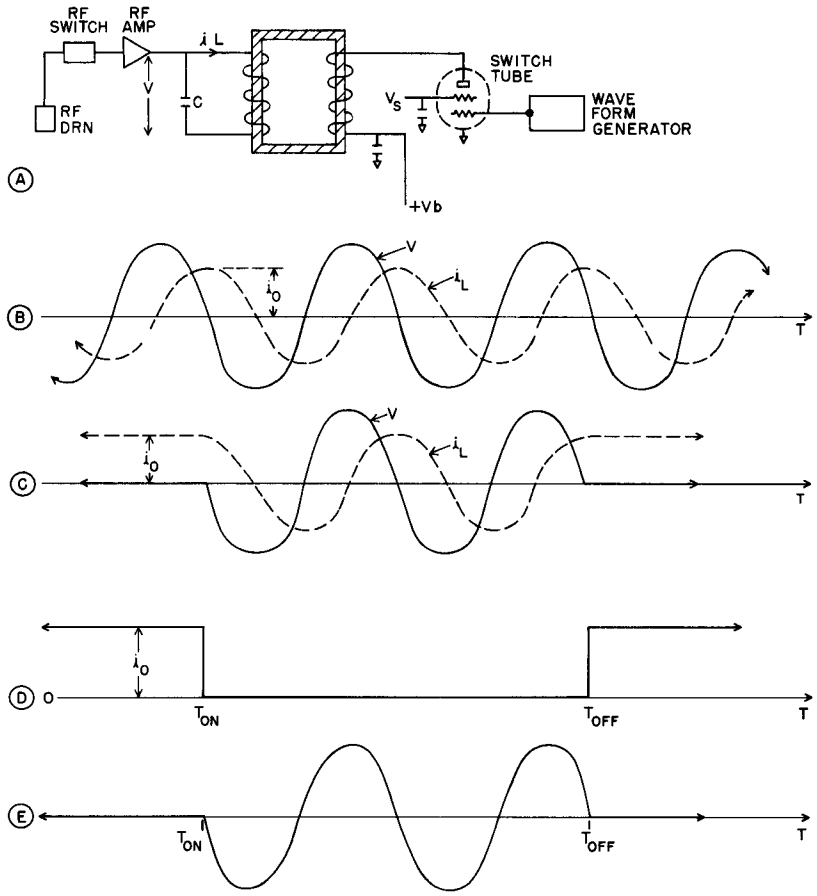

Fig. 3. RF pulsing cycle.

out that the switch tube does not see any voltage change when turning the current off and on, and as such its response can be made fast. The switch tube must be capable of holding off a peak voltage, when cut off, of $\pm(12\ dV + Vb)$, where Vb, the switch tube anode supply, is 2 to 4 kV, for the particular cavity previously described. The maximum switch tube current $i_o = 7$ A. Such tubes are readily available.

SHUNT IMPEDANCE CORRECTION

J. Claus

Brookhaven National Laboratory

The interaction of the beam with its environment may be described by means of coupling impedances. In order that it preserve stability these impedances may not exceed a lower limit which for any particular mode of oscillation is determined by beam current, frequency spread and form factor.

The shunt impedances across the accelerating gaps represent important contributors to the impedances that couple into the longitudinal motion. They should be as low as reasonably possible to provide some margin for other longitudinal impedances, e.g. those due to the vacuum chamber itself or to structures therein. The gap impedances can be made arbitrarily low at arbitrarily high expense in rf power by bridging them with resistors of small ohmic value. Other, more economic approaches make use of power amplifiers with very low internal impedances or of a compensation of the beam current with an equal but opposing electronic current. The three methods may be used in combination.

If the internal impedance of the final amplifier is low the output voltage becomes nearly independent of the load. The amplifier current may be split into two components: one practically equal to but opposing the beam current and one that develops the desired gap voltage across the gap shunt impedance. This implies that the amplifier should be capable of carrying at least the largest vector sum of these two components.

The amplifier impedance may be controlled over a wide range by means of negative feedback, a technique applied successfully in the ISR, and widely used at audiofrequencies. Qualitatively a voltage feedback tends to make the output voltage independent of the load, which is equivalent to saying that the impedance seen by the load is small. As is well known, the prime problem associated with feedback amplifiers concerns their stability. It is essential that up

to the highest frequency (and down to the lowest) the phase change around the feedback loop stay small; this requirement enforces small physical dimensions (a fraction of a wavelength) on amplifiers for high frequencies. If one assumes a net loop circumference of the order of 1 m (reasonable for amplifiers for the required frequencies and power levels) it follows that feedback looses its usefulness somewhere between 20 and 100 MHz, i.e. around mode number 200. Each amplifier is loaded by the gap shunt impedance as well as by the beam. To a first order approximation, the impedance may be represented by a simple LCR circuit with low impedances for frequencies outside a narrow band centered on the resonant frequency. Thus, the input signal must be a nearly pure sinusoid inside that band if amplifier saturation is to be avoided. Such saturation would open the feedback loop during part of the period of the wave form. The resonant circuit also makes the gap impedance nearly purely inductive at low frequencies and nearly purely capacitive at high frequencies; if amplifier stability is to be preserved under this reversal in sign of the imaginary component of the load, the phase lag in the feedback loop proper may not exceed $\pi/2$ inside the passband of the system. A cathode follower represents a suitable amplifier, and its use would yield a net gap shunt impedance of the order of 50 Ω or less. A slightly more elaborate circuit should reduce this number by an order of magnitude.

Another way of obtaining a low effective shunt impedance is to compensate the beam current through the gap impedance with a compensating current. Conceptually this method is not very different from the previous one, but it offers a number of advantages. Among them are: no restrictions on physical dimensions, lower shunt impedances and wide band response without saturation problems. Experiments with this approach at the ISR showed promising results.

If the compensating current i_e is related to the beam current i_b via $i_e/i_b = \alpha \exp(j\varphi)$ with α an amplitude factor and φ a phase factor, the effective shunt impedance becomes $Z_{seff} = Z_s[1-\alpha \exp(j\varphi)]$, with Z_s the uncompensated impedance, $Z_{seff} = 0$ is reached for $\alpha = 1$,

$\varphi = 0$, i.e. for exact compensation for all frequencies. $\alpha \neq 1$ introduces a damping or antidamping factor into the coherent motion, while $\varphi \neq 0$ affects the restoration constant. Logistically, one measures the instaneous intensity by means of a wide-band intensity pick-up and uses the information gathered to modulate a current source that forces the compensating current through the gap impedance. Measured beam samples and their matching compensating current samples must arrive simultaneously in the gap impedance. This can be achieved regardless of nonzero signal delay times because the longitudinal distribution of the beam changes very slowly in the ISA. The relative displacement of particles with $\Delta p/p = 0.01$ changes by 3.5 cm per revolution of 10 μsec at injection energy and by 6.3 cm per revolution at 200 GeV. This implies a bandwidth capability that reaches into the GHz range. Hardware limitations are likely to limit this to a lower value. Proper phasing of the compensating current relative to the beam can be done by choice of the location of the pick-up downstream of the accelerating stations and length adjustment of the interconnecting cables. A single pick-up, required for diagnostic purposes anyway, is sufficient to control the compensating currents in all accelerating stations.

At high frequencies an accelerating station may no longer be represented by a simple LCR circuit, the gap in particular is better described by a nonuniform transmission line of low characteristic impedance with a length that is small compared to the wavelength at the nominal frequency of resonance. Its transmission line character shows up at high frequencies introducing a gap shunt impedance as seen by the beam that is very difficult to eliminate by either feedback or compensation because beam and amplifiers are connected to opposite ends. Unless the gap is terminated properly at the amplifier side and/or contains lossy material it is likely to show a series of sharp resonances at high frequencies, which may well cause high order beam instabilities. It follows that the detailed physical design of the accelerating gaps and the way they merge with the vacuum chamber is a matter of considerable interest.

Once compensating currents can be generated they can be used to compensate for other impedance and impedance-like effects as well, e.g. longitudinal resistivity and inductivity of the vacuum chamber, longitudinal space charge. As an example we consider the compensation of a resistive vacuum chamber. One introduces somewhere in the circumference a resistive gap and drives through that gap, in addition to the beam current, a current such that for all particles the energy change in the gap is equal and opposite to the energy change/turn due to the wall resistivity. If the resistance of the gap is r_g and that of the chamber integrated around the circumference is r_c complete cancellation is obtained if $i_c/i_b = 1 + r_c/r_g$ where i_b is the beam current and i_c the compensating current. A truly resistive gap is physically impossible, but may be approximated with a conventional accelerating cavity-like structure of low gap capacitance with the gap capacitance shunted by resistors. For this application the resistors are acceptable with regard to cost (amplifier tube, power supply, power consumption) as long as the voltages required remain fairly low. More general compensation is obtained if the resistors are replaced by a more elaborate model of the impedance to be compensated. That model could contain components that would yield compensation for longitudinal space-charge effects. As suggested[1], one may also, or in addition, manipulate the wave shape of the compensating current such that adequate compensation is achieved even with an inaccurate model impedance.

It is perhaps superfluous to mention that the compensation scheme as described is <u>not</u> a beam feedback since the response is not controlled by the departure of a measured result from an externally supplied standard. Thus, there is no loop gain and the quality of the result depends upon accuracy of execution and adjustment. It becomes a beam feedback if the greatly amplified difference between the output of the intensity monitor and an externally imposed model is sent to the cavities instead of the compensating current. The difference between compensation and feedback may be summarized by the statement that while compensation aims at making the

1. E.C. Raka, private communication.

environment unresponsive to the beam regardless of its longitudinal distribution, feedback acts to make the beam conform to a specified model regardless of its environment. Feedback, in setting its aim higher than compensation, is the more complex of the two. Both methods require and deserve further study and experimentation.

We conclude that the longitudinal shunt impedance can be controlled by means of active electronic equipment at least up to mode number n = 1000.

PHASE-DISPLACEMENT ACCELERATION FOR THE ISABELLE STACK

E. Messerschmid*

M. Month

Brookhaven National Laboratory

1. INTRODUCTION

Applying a frequency modulated rf voltage to one or several accelerating gaps of an accelerator or storage ring, regions of phase stable oscillations (buckets) are created in which charged particles can be accelerated in synchronism with the rf frequency. This is the usual and well-known method of rf acceleration which necessitates a rebunching of a beam already stacked before acceleration. Particles initially not in synchronism with the rf voltage will experience an energy displacement associated with a dispersion, when they have been traversed by the buckets. Considering a proton beam as an incompressible fluid, on the average, the displacement equals the mean energy width of the moving bucket. Therefore, a beam can be accelerated by sweeping buckets from high energy through a stacked beam to low energy. This phase-displacement acceleration (PDA), applied many times, represents an alternative way to transport a beam up in energy. It has the advantage that no rebunching is required and that the energy spread of the accelerated beam can be smaller than the energy spread of a beam accelerated in the usual way.

In the ISR at CERN, PDA has been applied successfully[1] although the rf system was not designed especially for that purpose. In

---

1. K.N. Henrichsen and M.J. de Jonge, Proc. IX Int. Conf. on High Energy Acc., SLAC, 390 (1974).

* On leave from Freiburg University, West Germany.

ISABELLE, however, the rate of acceleration must be much larger than is available at the ISR. But since it is intended to have two rf systems for ISABELLE, one for stacking and one for acceleration, a special design of the latter could meet the requirements on acceleration rate and beam quality. In the following we shall attempt to develop a PDA scheme for ISABELLE and to decide in general terms whether or not it is feasible.

2. GENERAL CONSIDERATIONS

The increase ΔE_a of mean beam energy that a stack experiences when empty buckets are carried through can be derived from Liouville's theorem; it is found that after n passages

$$\Delta E_a = \frac{nA}{2\pi} = n\ \alpha(\Gamma)\delta E_{st} \tag{1}$$

A is the invariant bucket area in eV, $\alpha(\Gamma)$ the moving bucket factor depending on the quantity

$$\Gamma = \sin \phi_s,$$

where ϕ_s is the phase of a particle in synchronism with the rf frequency (stable phase angle). The averaged width δE_{st} of a stationary ($\Gamma = 0$) bucket is given by

$$\delta E_{st} = \frac{4\beta}{\pi} \sqrt{\frac{2eV_o E_o \gamma}{\pi\ |\eta|\ h}}$$

where β and γ have their usual relativistic meaning and

V_o = peak voltage

$h = f_{rf}/f_o$ ratio of rf frequency to particle revolution frequency

$E_o = 0.938256 \times 10^9$ eV: rest energy of a proton

$\eta = \frac{1}{\gamma_t^2} - \frac{1}{\gamma^2}$; γ_t: transition energy in units of E_o.

The energy dispersion δE_{rms}, introduced in an initially mono-energetic beam due to a single phase-displacement cycle, has been found to be[2]

$$\frac{\delta E_{rms}}{\delta E_{st}} = \Gamma \tag{2}$$

From the addition theorem for the convolution of a distribution of variance $\Gamma^2(\delta E_{st})^2$ into a distribution of initial variance $< \Delta E >_i^2$ it follows for the rms spread after n passages (convolutions):

$$\langle \Delta E \rangle_f = \sqrt{\langle \Delta E \rangle_i^2 + n(\Gamma \delta E_{st})^2}. \tag{3}$$

From the energy increase ΔE_s of a particle in synchronism with the rf voltage,

$$\Delta E_s = \text{number of turns} \times (\Gamma e V_o),$$

we can calculate the time Δt for n passages of the buckets through a corresponding energy range:

$$\Delta t = \frac{n\, \Delta E_s}{\Gamma e V_o f_o} \quad .$$

The total energy bite, ΔE_s, traversed by the buckets should always be considerably bigger than the width of the stack in order

---

2. E.W. Messerschmid, "Scattering of Particles by Phase-Displacement Acceleration in Storage Rings", CERN-ISR/TH/73-31 (1973).

to avoid additional dispersion due to switching transients at the beginning and the end of the empty bucket sweep. Consequently, to attain small Δt, the rf voltage has to be large. In some cases this means that the bucket size becomes comparable to the beam dimensions. In this case, it is convenient to rewrite the expression for Δt:

$$\Delta t = \frac{nm}{\Gamma e V_o f_o} \delta E_{st}, \tag{4}$$

where $m = \Delta E_s / \delta E_{st}$ is the energy sweep in units of the stationary bucket. From computer simulations on PDA[3] the choice m = 10 has been found to be a safe factor, which means large enough to avoid turn-on turn-off dispersion; i.e. large enough to avoid dispersion which is not intrinsic to the PDA process.

After suitable chosen small steps of acceleration, the magnetic field has to be readjusted in order to keep the center of the beam near to the center of the vacuum chamber. Equations (1) and (4) can be used to deduce the required program for the magnetic guide field.

When PDA is applied to a wide range of energy, then we find that a design can be chosen so that the increase of dispersion described by Eq. (3) is compensated by the natural damping of the relative energy spread, hence giving $\langle \Delta E/E \rangle_f \approx \langle \Delta E/E \rangle_i$. However, although the relative energy spread of the beam may not change very much, the final current is expected to be somewhat smaller than the initial one. This is due to random walks of particles into the tails. The loss rate due to aperture limitations at both sides of the particle distribution can easily be derived from random walk models with an energy step size given by Eq. (2).

---

3. E.W. Messerschmid, "Dispersion of Stacked Protons in Synchrotron Phase Space by a Modulated Radio Frequency Voltage", CERN-ISR/RF/72-28, (1972).

Assuming a sink at the distance $\pm \frac{1}{2} \Delta E_{ap}$ above and below the beam center, we find two different estimates for the loss rate, depending on the underlying loss mechanism:

(i) if particles outside the energy range ΔE_{ap} are allowed to return across the boundary in intermediate steps of the acceleration process and are only removed at the end of the PDA, the loss rate is given by

$$R_{cut\text{-}off} = 1 - \mathrm{erf}(x); \ \mathrm{erf}\ (x) = \frac{2}{\sqrt{\pi}} \int_0^x e^{-t^2}\, dt \qquad (5)$$

where

$$x = \frac{\Delta E_{ap}}{2\sqrt{2}\sqrt{\langle \Delta E \rangle_i^2 + n(\Gamma \delta E_{st})^2}}$$

(ii) if particles are lost instantaneously as they leave the energy range ΔE_{ap}, then from a random-walk-sink model[4] the loss rate is found to be

$$R_{sink} = 2R_{cut\text{-}off} \qquad (6)$$

Since particles are lost as they try to get outside of the available aperture and since other particles outside the smaller high density aperture will be scraped away at the end of the PDA, the loss rate inherent to PDA is expected to be larger than $R_{cut\text{-}off}$ but smaller than R_{sink}.

---

4. S. Chandrasekhar, Reviews of Modern Physics 15, 1 (1943).

3. OPTIMIZATION

In an optimization of the set of rf parameters we first must determine the voltage program. Possible approaches are to have the voltage program such that either δE_{st} or $\delta E_{st}/E$ is kept constant throughout the energy range. For ISABELLE parameters, however, this would lead to a decrease or increase of the voltage by a factor of 3.6 or 12.9, respectively. Since an unused peak voltage leads to an unnecessary prolongation of the PDA time, it is suggested to keep the voltage constant throughout the acceleration process. Taking into account the energy dependence of the parameter η, which relates an energy change to a frequency change, i.e. $\eta = (\Delta E/E)/(\beta^2 \Delta f/f)$, we find from Eqs. (1) and (2), assuming $\beta = 1$:

$$\gamma_f - \gamma_i = n\alpha(\Gamma)\sqrt{\frac{eV_o}{hE_o}}\,\frac{4}{\pi}\sqrt{\frac{2}{\pi}}\,\frac{\gamma_t}{\gamma_f - \gamma_i}\int_{\gamma_i}^{\gamma_f}\sqrt{\frac{\gamma^3}{\gamma^2 - \gamma_t^2}}\,d\gamma \qquad (7)$$

$$r = \frac{(\Delta\gamma/\gamma)_f}{(\Delta\gamma/\gamma)_i} = \frac{\gamma_i}{\gamma_f}\,\frac{1}{\gamma_f - \gamma_i}\int_{\gamma_i}^{\gamma_f}\sqrt{1 + a\,\frac{\gamma^3}{\gamma^2 - \gamma_t^2}}\,d\gamma, \qquad (8)$$

where

$$a = \frac{32\,n}{\pi^3}\left(\frac{\gamma_t \Gamma}{\gamma_i\,\langle\Delta E/E\rangle_i}\right)^2 \times \frac{eV_o}{E_o h} \quad .$$

Substituting n from (7) into (8), we find for ISABELLE ($\gamma_t = 21.6$, $\gamma_i = 31.4$, $\gamma_f = 214.2$, $\langle\Delta\gamma/\gamma\rangle_i = 2.3 \times 10^{-3}$) a condition for Γ and the ratio V_o/h:

$$\frac{\Gamma^2}{\alpha(\Gamma)}\sqrt{\frac{eV_o}{E_o h}} = 1.445 \times 10^{-5}\ a(r) \tag{9}$$

Figure 1 shows the results of the numerical evaluation of the intergrals. The quantity on the ℓ.h.s. of equation (9) is plotted as a function of $V_o h$ for different values of Γ and compared with the r.h.s. of the same equation which has been plotted as a function of the ratio r from equation (8). Thus, for example, Γ can be determined for given values of $V_o h$ and r.

It is interesting now to find the rf parameters for various values of r, the ratio of relative initial energy spread to relative final energy spread. The results of our computations are listed in Table I for different ratios $V_o h$ of peak rf voltage to harmonic number. The number n of phase-displacement cycles has been found from Eq. (7) which also can be used to compute the total time for the whole PDA process ($m = 10$, $f_o = 1.013 \times 10^5\ s^{-1}$)

$$\Delta t = \frac{nm}{\Gamma f_o}\sqrt{\frac{E_o}{eV_o h}}\,\frac{4}{\pi}\sqrt{\frac{2}{\pi}}\,\frac{\gamma_t}{\gamma_f - \gamma_i}\int_{\gamma_i}^{\gamma_f}\sqrt{\frac{\gamma^3}{\gamma^2 - \gamma_t^2}}\,d\gamma$$

$$= \frac{m(\gamma_f - \gamma_i)}{\Gamma\alpha(\Gamma)\ f_o h}\left(\frac{E_o h}{eV_o}\right) .$$

Assuming this time to be 20 minutes, we can find the harmonic number h and then the peak voltage V_o. Column 3 contains the estimates of the loss rate based on Eqs. (5) and (6) for an aperture of $\Delta E_{ap}/E$ of 1% and 1.2%, respectively. The rate of

TABLE I. Parameters of PDA for ISABELLE

$r = \frac{\langle \Delta E/E \rangle_f}{\langle \Delta E/E \rangle_i}$	V_o/h [V]	$R_{cut\text{-}off}$- R_{sink} [%]	Γ	n	$\Delta t \times h$ [min]	h_{20} (Δt = 20 min)	V_o [kV]	$\dot{f}_i/10^3$ [s^{-2}]	$\Delta f_i/10^3$ [s]	d_i [%]
0.8	2000	{0.7 -1.4	.04	566	3886	194	389	1.18	1.74	5.8
	1000	0.12-0.24}	.05	817	6350	318	318	1.98	2.02	8.2
	500		.06	1179	10803	540	270	3.42	2.43	11.6
	200		.08	1941	21085	1054	211	6.95	2.95	18.4
	100		.09	2800	38234	1912	191	12.84	3.84	26.0
1.0	2000		.06	590	2701	135	270	0.85	1.21	5.8
	1000	{3 -6	.07	851	4724	236	236	1.52	1.50	8.2
	500	0.9-1.8}	.08	1228	8434	422	211	2.78	1.90	11.6
	200		.10	2019	17547	877	175	6.00	2.49	18.4
	100		.12	2969	30411	1521	152	10.84	3.05	26.0
1.2	2000		.07	602	2362	118	236	0.76	1.06	5.8
	1000	{7.7-15.4	.08	868	4217	211	211	1.39	1.34	8.2
	500	3 - 6}	.10	1277	7019	351	175	2.40	1.57	11.6
	200		.12	2100	15206	760	152	5.42	2.16	18.4
	100		.13	3028	28624	1431	143	10.40	2.87	26.0

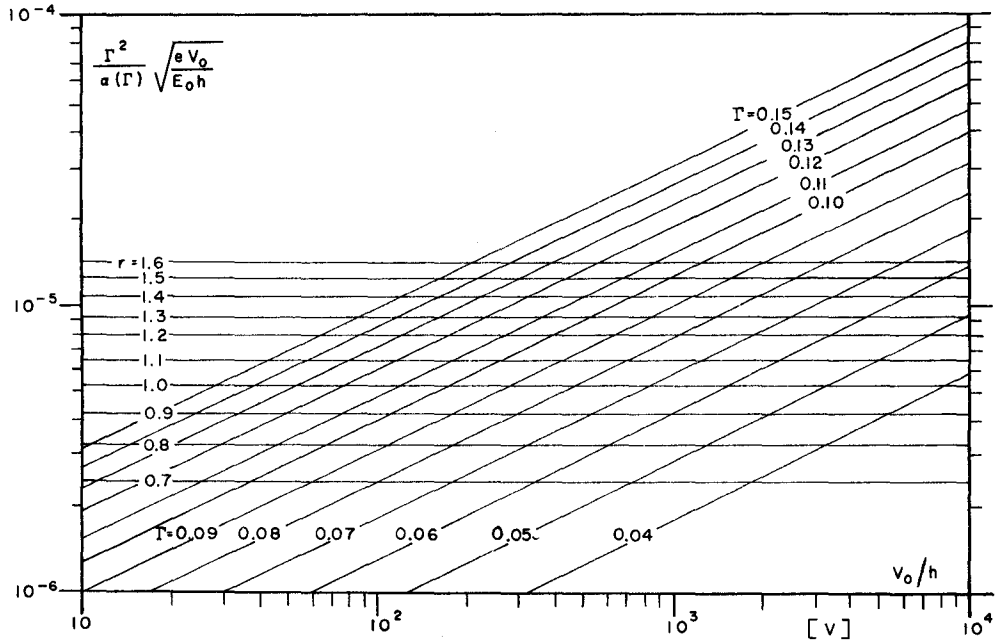

Fig. 1. Plot of Eqs. (8) and (9).

change of frequency and the frequency sweep are given by the formulas

$$\dot{f} = \frac{f_o^{\,2}}{E_o} (heV_o\Gamma) \left(\frac{\eta}{\gamma}\right)$$

$$\Delta f = mf_o h\eta \left(\frac{\delta E_{st}}{E}\right) ,$$

both of which are listed in Table I for γ_i. The corresponding values for γ_f are 3.6 and 1.9 times smaller. Defining the duty factor as the ratio of the frequency sweep over about 68% of the particle distribution to the total frequency sweep of a cycle,

$$d = \frac{2\langle\Delta E/E\rangle}{m\langle\delta E_{st}/E\rangle} ,$$

we find the numbers in the last column in the table, again given for γ_i. The corresponding value at the end of the PDA, γ_f, is, due to the reduction of the energy spread $\delta E_{st}/E$, about 3.6 r times larger. With the values of the voltage V_o and the duty factor d, and taking a current of about I = 10 A both the peak power ($\sim V_o I$) and the average power ($\sim V_o Id$) may be evaluated.

4. DISCUSSION OF THE RESULTS

By inspection of Table I we arrive at the following conclusions. Assuming a time of 20 minutes available for PDA, for ratios of the relative final spread to the relative initial spread between 0.8 and 1.2, a feasible range of values for the parameters Γ, peak voltage and harmonic number is obtained. A large range of values for the ratio $V_o h$ offers enough freedom

to find an appropriate rf system[5] (one or several ferrite-loaded cavities or TWT's).

If it becomes important to keep the ratio $V_o h$ low as well as to keep down the duty factor throughout the entire energy range of the PDA process, then a longer acceleration time would have to be accepted.

For reasonable apertures, the loss rates induced by the intrinsic PDA dispersion are within acceptable limits. There may be, however, other sources for beam loss, such as rf noise, excitations due to nonlinear resonances, and longitudinal instabilities due to the high bunching (small Γ, high voltage) of the beam during the passage of the empty buckets. These effects, however, require a more detailed investigation of the PDA process which is beyond the scope and intention of this report.

5. W. Schnell and S. Giordano, private communication.

TRANSVERSE STABILITY OF COASTING BEAMS IN ISABELLE

E. Keil

CERN

and

A. G. Ruggiero

Fermi National Accelerator Laboratory

1. Formulae

We define a transverse coupling impedance $Z_\perp$ as follows:[1]

$$Z_\perp = i \frac{\int_0^{2\pi R} (E + v \times B)_\perp \, ds}{\beta_\perp I \Delta} \tag{1}$$

Here E is the electric field and B the magnetic induction of the beam-induced field, $\beta_\perp$ is the amplitude function, I the circulating current and Δ the coherent amplitude. The transverse resistive wall instability is suppressed by Landau damping if the transverse impedance satisfies the following relation.[2]

$$|Z_\perp| < \left(\frac{E_o}{e}\right) \frac{\pi\nu\beta\gamma}{IR} \left|(n - \nu)\,\eta + \xi\right| \frac{\Delta p}{p} \tag{2}$$

Here, E_o is the proton rest energy, e the proton charge, ν the

---

1. F.J. Sacherer, Proc. IXth Int. Conf. High Energy Accel., SLAC 1974, 347 (1974).

2. K. Hübner and V.G. Vaccaro, CERN-ISR-TH/70-44 (1970).

tune, R the machine radius, β and γ are the usual relativistic factors, $n > \nu$ is the mode number, $\eta = |\gamma^{-2} - \gamma_t^{-2}|$, γ_t is the transition energy and $\xi = d\nu/dp/p$ is the chromaticity, and $\Delta p/p$ is approximately the full momentum spread at the base of the distribution function. When writing the stability criterion in the form (2), we exclude "unreasonable" distribution functions with long tails.

For a machine with a smooth resistive vacuum chamber of constant cross section all around the circumference, the transverse impedance becomes:[3]

$$Z_\perp = \frac{iRZ_o}{\beta^2\gamma^2} \left(\frac{1}{a^2} - \frac{1}{b^2}\right) + \frac{(1-i)R}{b^3} \left[\frac{2RZ_o}{\beta\sigma(n-\nu)}\right]^{1/2} \qquad (3)$$

Here, $Z_o = 120\ \pi\Omega$ is the impedance of free space, a is the average beam radius and $\sigma = 6.25 \times 10^7\ \Omega^{-1}m^{-1}$ is the conductivity of the vacuum chamber of radius b ($A\ell$). In the absence of Landau damping, the growth rate of the instability is given by[3]:

$$\frac{1}{\tau} = \frac{IRr_o}{eb^3\nu\gamma} \left[\frac{2\ R}{Z_o\beta\sigma(n-\nu)}\right]^{1/2} \qquad (4)$$

Here, r_o is the classical proton radius.

2. Stability Criteria for a Machine with a Smooth Vacuum Chamber

The machine parameters used and the stability criteria obtained by applying (2) and (3) are shown in Table I. We have

---

3. L. J. Laslett, V. K. Neil, A. M. Sessler, Rev. Sci. Instrum. 36, 436 (1965).

assumed that the momentum spread is adiabatically damped between 28.5 and 200 GeV, and have calculated the beam size accordingly. This leads to a smaller beam size than any other assumption, and therefore to tighter stability criteria at 200 GeV.

The chromaticity ξ and the tune spread $\Delta\nu$ are sufficient to provide Landau damping for all modes $n > \nu$. The stable number $(n - \nu)$ is the lowest mode number for which the revolution frequency spread alone provides enough Landau damping. The bandwidth Δf is calculated from $(n - \nu)$.

3. Stability Criteria for a Realistic Machine

The transverse impedance of a realistic machine will exceed that of a machine with a smooth vacuum chamber. We take this into account by assuming that the actual impedance will be a factor $(1 + A)$ bigger than that calculated above. It may be seen that in this case the figures for $|(n - \nu)\,\eta + \xi|$, ξ, $\Delta\nu$, $(n - \nu)$, Δf all have to be multiplied by the factor $(1 + A)$.

Some guidance concerning the actual value of A can be obtained from the following argument. For a smooth vacuum chamber and for cavity-like objects frequently found in a real machine, a relation between their longitudinal and transverse coupling impedances exists which can be written as follows:[2]

$$Z_{\perp} \approx \frac{2c}{b^2}\frac{Z_{\parallel}}{\omega} = \frac{2R}{b^2}\left(\frac{Z_{\parallel}}{n-\nu}\right) \tag{5}$$

Here, $\omega = (n - \nu)\omega_o$, and ω_o is the circular revolution frequency. Because of the requirement of longitudinal stability of the injected bunches at 28.5 GeV and of the coasting beam in the early

TABLE I. Machine Parameters and Stability Criteria

Machine Radius	R		471 m
Tune	ν		25.63
Circulating Current	I		10 A
Vacuum Chamber Radius	b		0.04 m
Energy	γ	31.4	214
	η	0.001	0.002
Momentum Spread	$\Delta p/p$	0.01	0.0015
Beam Radius	a	4.1	1.34 mm
Transverse Impedance	$Z_\perp$	$0.91 + 9.7i$	$0.91 + 1.24i$ MΩm
"Frequency Spread"	$\lvert(n - \nu)\eta + \xi\rvert$	1.95	0.30
Chromaticity	ξ	1.95	0.30
Tune Spread	$\Delta\nu = \xi\Delta p/p$	0.0195	0.00045
Stable Mode Number	$(n - \nu)$	1950	150
Bandwidth	Δf	195	15 MHz
Growth Rate	τ^{-1}	288	42.3 s^{-1}

phases of stacking a severe limitation on $Z_{||}$ exists,[4] where $|Z_{||}/n| \leq 5\ \Omega$. We now assume that this condition is satisfied and use (5) to estimate the transverse impedance. We find $Z_{\perp} \leqslant 3\ M\Omega/m$. Comparing this figure to the impedance shown in Table I would suggest that at 28.5 GeV, $A < 1$, while at 200 GeV, $A \approx 3$.

In order to stabilize the transverse instability by Landau damping alone, the tune spread needed is $\Delta\nu \leqslant 0.04$ at 28.5 and $\Delta\nu \leqslant 0.002$ at 200 GeV. The figure at 28.5 GeV appears to be somewhat on the high side for colliding beam operation at a current of 10 A,when compared with the space between nonlinear resonances, but acceptable for accumulation of that current before acceleration to a higher energy. The tune spread required at 200 GeV is quite small.

A more accurate estimate for the direct space charge tune shift was obtained by A. W. Chao, J. C. Herrera and M. Month,[5] taking into account the variation of the beam size and the amplitude and dispersion functions around the circumference of the machine. They arrive at even higher tune shifts than given in Table I.

4. Specifications of a Feedback System

If all or part of the damping of the transverse instability is to be done by a feedback system, that system must fulfill the following conditions:

i) Its damping rate must be higher than the growth rate

---

4. W. Schnell, Stacking & Acceleration, Summary Report of Working Group, these Proc.

5. A.W. Chao, J.C. Herrera and M. Month, "Betatron Tune Changes Due to Direct Space Charge in the ISA, these Proc.

by a certain safety factor.

ii) Its bandwidth must reach up to a frequency where there is enough damping from the spread in revolution frequency. The mode numbers $(n - \nu)$ for which this is the case, assuming that there is no damping from tune spread are shown in Table I. The bandwidth goes up by a factor A if the impedance in the real machine exceeds that of the smooth vacuum chamber wall by that factor A. The bandwidth is reduced by a factor B if feedback is expected to yield only a fraction B of the damping at low frequency, the rest being provided by tune spread.

iii) The noise in the feedback system causes a random increase of the beam sizé, and therefore has to be limited. In order to avoid getting into details of electronic engineering, we specify the limit of the noise in terms of the amplitude of random kicks recieved on every revolution.

Assume that an amplitude x_m is measured at a position where the amplitude function is β_m. This corresponds to an angle

$$\varphi_m = x_m/\beta_m \tag{6}$$

At the position of the kicker magnet where the amplitude function is β_k, the corresponding angle is

$$\varphi_k = x_m/(\beta_L\beta_m)^{\frac{1}{2}} \tag{7}$$

If the kicker is to damp the oscillation with an e-folding time of $\tau f/\alpha$ revolutions, τ is the growth time, f is the revolution frequency and $\alpha > 1$ is a safety factor, then the kicker must provide a kick Ψ_k given by

$$\Psi_k = \frac{\alpha \varphi_k}{2\tau f} \tag{8}$$

This corresponds to an amplitude

$$x_k = \Psi_k \beta_k = \frac{x_m \alpha}{2\tau f} \sqrt{\frac{\beta_k}{\beta_f}} \ . \tag{9}$$

If the beam recieves random kicks of amplitude Δ on each revolution, the mean square amplitude will grow according to

$$a^2 = a_o^2 + n\Delta^2 \tag{10}$$

if one assumes that the feedback loop is open. For a closed loop, the blow-up will be slower.[6] In the formula above, n is the number of revolutions. If we allow a doubling of a^2 in 10 hours, we obtain at 200 GeV, using $a_o = 1.41$ mm:

$$\Delta = 2.4 \times 10^{-8} \text{ m} \tag{11}$$

Here, Δ corresponds to x_k in (9). We transform it into a tolerance on the noise on x_m and find, using $\tau f = 2200$, $\alpha = 10$ and $\beta_m = \beta_k$:

$$x_m < 10^{-5} \text{ m} \tag{12}$$

---

6. L. Thorndahl and A. Vaughan, 1973 Particle Accelerator Conference, IEEE Trans. Nucl. Sci. NS-20, 807 (1973).

Converting this into a "dipole moment" Ix_m at I = 10 A yields

$$Ix_m < 100 \ \mu A \ m. \tag{13}$$

Noise figures of the above order of magnitude have been achieved.[6]

DEPENDENCE OF THE LONGITUDINAL BUNCHED BEAM STABILITY ON THE CHOICE OF THE RF HARMONIC NUMBER IN ISABELLE

A. G. Ruggiero

Fermi National Accelerator Laboratory

The strength of the bunched-beam instability is measured, in absence of Landau damping, by the complex shift of the synchrotron angular frequency $\Delta\omega_m$ which is given by[1]

$$\frac{\Delta\omega_m}{\omega_s} = - i\sqrt{m}\ \frac{IM^2}{2\pi h B^3 V \cos\phi_s}\ \frac{\omega_o \sum_p \frac{Z_{\parallel}(\omega_p)}{\omega_p} h_m(\omega_p)}{\sum_p h_m(\omega_p)} \qquad (1)$$

where ω_s is the unperturbed synchrotron angular frequency, I the average current in M bunches, h the harmonic number, B the bunching factor defined as the ratio of the bunch length to the bunch separation, ϕ_s the stable phase, ω_o the revolution angular frequency, $Z_{\parallel}(\omega_p)$ the longitudinal (complex) coupling impedance at $\omega = \omega_p$ and $h_m(\omega_p)$ the Sacherer's functions.[1]

The shift $\Delta\omega_m$ is a function of two indices: m, the internal bunch mode number, and n, the bunch-bunch mode number. If Q_s is the number of phase oscillations per revolution, $\omega_p = (p + mQ_s)\omega_o$ with $-\infty < p < +\infty$ for a single bunch or several bunches oscillating independently and $p = n + kM$, $-\infty < k < +\infty$ for coupled motion of the bunches.

The beam can be made stable by supplying enough Landau damping. The stability criterion is[2,3].

---

1. F.J. Sacherer, CERN/Si-BR/72-5 (1972).
2. F.J. Sacherer, IEEE Transactions on Nuclear Science, NS-20, No. 3, Page 825, June 1973.
3. F.J. Sacherer, CERN/MPS/BR, 73-1 (1973).

$$\left|\frac{\Delta\omega_m}{\omega_s}\right| < \frac{\sqrt{m}}{4}\frac{S}{\omega_s} \tag{2}$$

where S is the spread in ω_s between center and edge of the bunch (full spread) due to the nonlinearity of the synchrotron force.

It is customary by now to describe the design of a high-energy storage ring by assigning the upper limit for the longitudinal impedance that can be tolerated. We shall write this condition as

$$\left|\frac{Z_{\parallel}}{p}\right| = \left|\frac{Z_{\parallel}(\omega_p)}{\omega_p/\omega_o}\right| < Z_o \tag{3}$$

at any frequency ω_p. Z_o is for the moment an unspecified impedance of Z_o ohms.

By inserting (3) in (1) one has

$$\left|\frac{\Delta\omega_m}{\omega_s}\right| < \sqrt{m}\,\frac{IhZ_o}{2\pi B^3 V\cos\phi_s}$$

where we set M = h. The stability condition, then, becomes, from (2)

$$\frac{2IhZ_o}{\pi B^3 V\cos\phi_s} < \frac{S}{\omega_s} \tag{4}$$

which is not dependent on the mode numbers m and n.

The condition (4) is rather conservative, in the sense that if it is satisfied the beam is certainly stable, nevertheless, it is not necessary for beam stability.

We introduce another parameter, ε, which is the ratio of the

accelerating bucket area to the bunch area. This parameter is larger than 1 but not too large, say $1 < \epsilon < 1.5$, in order to enhance enough Landau damping. It can be either a constant or a slowly varying function of the time during the acceleration process. From the definition of ϵ one can derive the following expression for the rf peak voltage

$$\frac{V}{h} = \frac{2\pi|\eta|}{E}\left(\frac{\omega_o \ \epsilon A_t}{16 \ \beta\alpha}\right)^2 \tag{5}$$

where E is the total energy of a particle, $\eta = \gamma^{-2} - \gamma_T^{-2}$, γ = E/rest energy, γ_T = transition energy/rest energy, β = beam velocity/light velocity, A_t total beam area in the phase space in eV.s units and α is a function of ϕ_s (Symon and Sessler Function[4]).

If B_o denotes the ratio of the bucket length to the bucket separation[4], one has in good approximation $B = B_o/\sqrt{\epsilon}$. By inserting (5) in (4) one finally obtains the following limit for Z_o

$$Z_o < \frac{\pi^2\omega_o^2 \ A_t^2|\eta|\sqrt{\epsilon}}{256 \ I \ \beta^2 \ E} \ \frac{B_o^3 \ |\cos\phi_s|}{\alpha^2} \ \frac{S}{\omega_s}. \tag{6}$$

The spread S can be calculated by expanding the $(\sin\phi - \sin\phi_s)$ term in the phase equation and by retaining only the linear and cubic term, then one obtains in good approximation

$$\frac{S}{\omega_s} \simeq \frac{\pi^2 \ B_o^2}{12 \ \epsilon} \tag{7}$$

---

4. K. Symon and A. M. Sessler, CERN Symposium on Particle Accelerators, 1956, p. 46.

and the stability criterion finally becomes, after inserting (7) in (6)

$$\boxed{Z_o < \frac{\pi^4 \omega_o^2 A_t^2 |\eta|}{3072\ I\ \beta^2 E\sqrt{\epsilon}} \frac{B_o^5\ |\cos\phi_s|}{\alpha^2}\ .} \qquad (8)$$

The first factor is a machine parameter. The second factor depends on the choice of ϕ_s. The interesting result is that this formula does not depend on the choice of the harmonic number.

One has the following table which gives the second factor for some values of ϕ_s.

ϕ_s	$B_o^5\ \lvert\cos\phi_s\rvert/\alpha^2$
0°	1.00
10°	0.49
20°	0.39
30°	0.30
40°	0.26

As one can see from (8), the smallest value of Z_o occurs at high energy, E = 200 GeV. At this energy and by taking the following parameter values

$$\omega_o = 6.35 \times 10^5\ s^{-1}$$
$$A_t = 2 \times 10^3\ eV.s$$
$$\gamma_t = 21.6$$
$$I = 10\ A$$
$$\beta \simeq 1$$

$$\varepsilon = 1.25$$

$$\gamma = 214$$

we obtain

$$Z_o < 50 \frac{B_o^5 \, |\cos\phi_s|}{\alpha^2} \text{ ohm} .$$

If we let ϕ_s range between 0° and 20°, we can see from the table that Z_o can be at least 20 ohm. This value is larger than the new limitation (~ 5 ohm) which occurs for the beam debunching including the high frequency effects.[5]

In conclusion, there are three conditions that are to be satisfied during the acceleration:

(i) The ratio ε of the bucket area to the beam area must be kept fairly close to 1 and practically constant. The rf peak voltage is then given by (5) and clearly depends on the choice of the harmonic number.

(ii) The energy gain per turn is assigned.

$$\Delta E = V \sin\phi_s$$

ΔE is small and can be a slowly varying function of the time.

(iii) Finally, the impedance condition (8) has to be satisfied.

The combination of these three conditions should prescribe a reasonable choice for ϕ_s, V and ΔE once the harmonic number is assigned.

Leaving the details to be worked out by the rf parameter group people, we give here the following example.

At E = 200 GeV, with $\phi_s = 20^o$ and $\varepsilon = 1.25$ one obtains

---

5. A. Hofmann and E.C. Raka, private communication.

$V/h = 2.76$ kV. One can choose $h = 20$ and have $V = 55.2$ kV which corresponds to an energy gain of 18.9 keV/turn and an impedance limitation of 25 ohm.

The choice of the rf harmonic number for ISABELLE is weakly sensitive on the longitudinal stability of the bunched beam during the acceleration.

TRANSVERSE STABILITY OF THE BUNCHED BEAM
DURING ACCELERATION IN ISABELLE

A.G. Ruggiero
Fermi National Accelerator Laboratory

The complex shift of the betatron angular frequency is[1]

$$\Delta\omega_m = \frac{1}{1+m}\,\frac{i}{2\nu\omega_o}\,\frac{e\beta}{\gamma m_o}\,\frac{I_o}{L}\,\frac{\sum_p Z_\perp(\omega_p)\; h_m(\omega_p-\omega_\xi)}{\sum_p h_m(\omega_p-\omega_\xi)} \qquad (1)$$

where ν is the number of betatron oscillations per revolution, ω_o the revolution angular frequency, e the particle charge, β and γ the usual relativistic factors, m_o the mass at rest, I_o the average current in one bunch of length L, $h_m(\omega)$ the Sacherer's functions[1],

$$\omega_\xi = \xi\nu\omega_o/|\eta|$$

$\xi = (\Delta\nu/\nu)/(\Delta p/p)$ and $\eta = \gamma_T^{-2} - \gamma^{-2}$ and

$$\omega_p = (p+\nu)\omega_o$$

where $-\infty < p < +\infty$ for a single bunch or several bunches oscillating independently, and $p = n + kM$, $-\infty < k < +\infty$ for coupled motion of M bunches.

The shift (1) depends on the two mode numbers: m, the internal (or head-tail) bunch mode, and n, the bunch-bunch mode.

---

1. F. Sacherer, Proc. IXth Intern. Conf. on High- Energy Accelerators, Stanford 1974, p. 347.

Finally,

$$Z_{\perp} = -i \frac{RZ_o}{\beta^2\gamma^2}\left(\frac{1}{a^2} - \frac{1}{b^2}\right) + \frac{2c}{b^2}\frac{Z_{\parallel}}{\omega_p} \qquad (2)$$

= perfectly conductive wall impedance

+ any other impedance

where $2\pi R$ is the circumference of the equilibrium orbit, Z_o = 377 ohms, a the average beam radius, b the pipe radius, c the light velocity and $Z_{\parallel}$ is the longitudinal coupling impedance.

By using the same arguments used in the other paper which deals with the transverse instability of the ISABELLE coasting beam[2] we can set the condition that the second term in (2) does not exceed the first term by a factor ϵ, namely that

$$\frac{Z_{\parallel}}{\omega_p/\omega_o} < \frac{\epsilon Z_o}{2\beta\gamma^2}\left(\frac{b^2}{a^2} - 1\right) \qquad (3)$$

where ϵ does not depend on the frequency but may depend on γ.

For ISABELLE: b = 40 mm, a = 4.1 mm at 30 GeV, a = 1.2 mm at 200 GeV and

---

2. E. Keil and A.G. Ruggiero, "Transverse Stability of Coasting Beams in ISABELLE", these Proc.

$$\left|\frac{Z_{\parallel}}{\omega/\omega_o}\right| < 18\ \epsilon \text{ ohm} \quad , \quad \text{at 30 Gev}$$

$$\left|\frac{Z_{\parallel}}{\omega/\omega_o}\right| < 5\ \epsilon \text{ ohm} \quad , \quad \text{at 200 Gev.}$$

The new limitation[3] on the longitudinal coupling impedance is 5 ohm. Thus we can take $\epsilon = 1$ for the 200 GeV case and $\epsilon = 0.3$ for the 30 GeV case.

By inserting (3) in (1) we obtain

$$\left|\frac{\Delta\omega_m}{\omega_o}\right| < \frac{1+\epsilon}{1+m} \frac{eIZ_o}{4\pi\nu\beta^3\gamma^3 E_o B} \left(\frac{R^2}{a^2} - \frac{R^2}{b^2}\right)$$

where $E_o = 0.938$ GeV, B is the bunch length to the bunch separation ratio and I is the total average current. With ISABELLE numbers ($2\pi R = 2960$ m, $I = 10$A, $\nu = 25.63$) one has

$$|\Delta\omega_m/\omega_o| < \frac{7.1 \times 10^{-3}}{(1+m)\ B} \quad \text{at} \quad 30 \text{ GeV}$$

$$|\Delta\omega_m/\omega_o| < \frac{3.9 \times 10^{-4}}{(1+m)\ B} \quad \text{at} \quad 200 \text{ Gev} \quad .$$

The stability criterion is[1]

$$\Delta\nu > 4\left|\frac{\Delta\omega_o}{\omega_o}\right| \tag{4}$$

---

3. W.Schnell,Stacking and Acceleration, Summary Report of Working Group, these Proc., p. 126.

where $\Delta\nu$ is the full-spread at the base of ν due only to the amplitude of the betatron oscillation*. By simple insertion then one obtains

$$\Delta\nu > \frac{0.03}{(1+m)\ B} \quad \text{at} \quad 30\ \text{GeV}$$

and

$$\Delta\nu > \frac{0.0016}{(1+m)\ B} \quad \text{at} \quad 200\ \text{GeV}$$

and there is no dependence on the bunch-bunch mode number n.

According to calculations done by the Lattice Group people,[4] a tune shift is enhanced in the beam by the self-fields which is of the order of 0.04 at 30 GeV, mostly due to the dispersionless insertions where the beam might have roughly a Gaussian distribution. This would be equivalent to a tune spread of about 0.01. If one assumes that the tune-shift scales as the three-half power of the energy then it would be a factor 20 smaller at 200 GeV.

On the other hand, from the RF Group people,[3] we know that, with the choice of harmonic number h = 2, the bunching factor B will not be less than 0.6. Putting the numbers together we see, then, that there is enough tune spread for all the modes $m > 4$ at any energy, and that this tune spread comes from the beam itself and there is no need for addition of octupoles.

---

* A factor 4 has been added in (4) which does not appear in Ref. [1], in order to have consistency with the stability criterion for coasting beam[2].

4. L. Smith, Lattice, Summary Report of Working Group, these Proc., p. 111.

Let us look now in the range of small frequencies ($m \leq 4$). It is known[1] that, regardless of the type of the impedance, the mode $m = 0$ is stable when the phase advance across the bunch $X = \omega_\xi \tau_L$, τ_L being the bunch length in seconds, is positive and unstable for X negative. Above the transition energy (as in ISABELLE) X positive means positive chromaticity ξ. The choice of $\xi > 0$ is already determined by the stability condition for transverse coherent oscillations of the coasting beam.[2] Thus in our case the mode $m = 0$ is stable and this includes also the other two bunch-bunch modes ($n = 0$ and 1).

Actually many other modes $m = 1, 2, 3 \ldots$ will also be stable provided X is large enough. For ISABELLE

$$\begin{aligned} X &= \xi \, \nu \, \omega_o \, \tau_L / \eta \\ &= \pi \, \xi \, \nu \, B / \eta \\ &= 24{,}156 \, \xi \end{aligned}$$

at 200 GeV with $B = 0.6$. This is a large number!

By inspecting (1) one can see that the mode m (and again this includes the other two bunch-bunch modes $n = 0$ and 1) is stable when

$$R_\perp(\omega_p) \; h_m(\omega_p - \omega_\xi) \tag{5}$$

is positive for any ω_p. In Eq. (5) $R_\perp(\omega)$ is the resistance, namely the real part of the impedance $Z_\perp$. Regardless of the type of the impedance, $R_\perp$ is positive for positive frequencies and vice versa. Also in Eq. (5), $h_m(\omega_p - \omega_\xi)$ is the Sacherer's function[1] for the mode m and is always positive.

The product (5) is shown graphically in Fig. 1.

The function $h_m(\omega - \omega_\xi)$ is made of two humps which are separa-

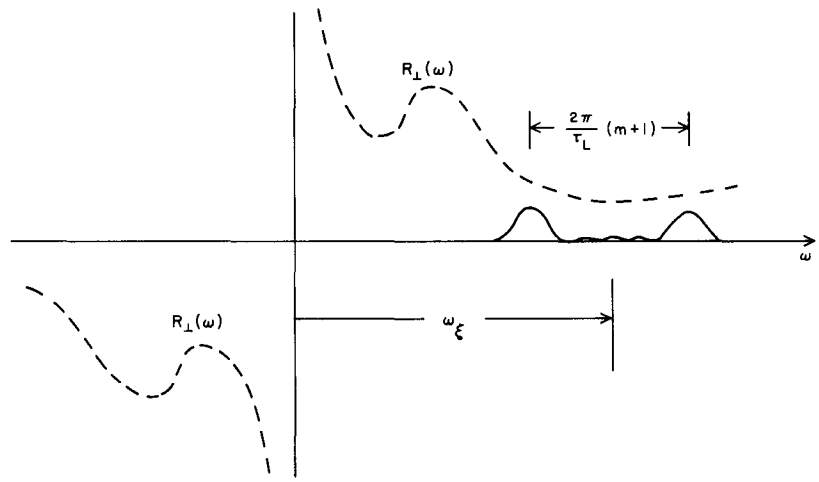

Fig. 1. Stability Function, Eq. (5).

ted by $\Delta\omega \sim 2\pi/\tau_L(m + 1)$. This is an extrapolation to any mode m from the available curves[1] for m = 0 to 3 included. The width of each bump is about $4\pi/\tau_L$, roughly independent of the mode number m.

The case shown in Fig. 1 corresponds to $X > 0$.

The product (5) is always positive and, henceforth the motion is stable, for all those modes m which satisfy

$$\omega_\xi - \frac{\pi}{\tau_L}(m+1) - \frac{2\pi}{\tau_L} > 0$$

namely

$$m < \frac{X}{\pi} - 3 \quad .$$

If we take for ISABELLE, $\xi = 0.001$, we have that all the modes $m \leqslant 20$ are stable. Of course this, in turn, means a much less stringent requirement for the tune spread to make the higher modes ($m \geqslant 20$) stable.

LONGITUDINAL COUPLING EFFECTS DUE TO BEAM-BEAM INTERACTION

C Pellegrini
Culham Laboratory

1. The beam-beam interaction, besides producing a shift of the betatron and synchrotron frequencies, produces also a coupling of the transverse and longitudinal coherent oscillation modes of the two beams. Wake fields in the interaction regions also introduce a similar effect Because of the coupling new modes of coherent oscillations appear which might be unstable, also when the single beam oscillation modes are stable Hence, in general, it might be desirable to operate the machine in a condition in which this coupling effect is avoided This can be achieved by separating the characteristic frequencies of the two beams by an amount larger than the beam-beam induced frequency shift.

The effect of beam-beam coupling on the transverse resistive wall instability has been studied by Pellegrini and Sessler.[1] In this note I want to make a few remarks on the effect of the coupling on the synchrotron motion.

2. During the acceleration period the coupling of synchrotron oscillations leads to a system of four coupled bunches which can be unstable with respect to dipole coherent oscillations even when the single beam, with two bunches only, is stable. Taking this into account the choice of a harmonic number two is no more sufficient to ensure the beam stability against coherent longitudinal dipole oscillations.

To avoid the coupling one needs to separate the synchrotron frequencies of the beams. The coupling can be induced by bunched beams beam-beam interaction, producing a focusing longitudinal

---

1. C. Pellegrini and A.M. Sessler, Proc. VI Intern. Conf. on High Energy Accelerators, Cambridge, Mass. 1967, p. 287.

force which gives rise to a frequency shift.

$$\Delta = \frac{\nu_S^2 - \nu_{S0}^2}{\nu_S^2} \tag{1}$$

To avoid this coupling the synchrotron frequency separation must be larger than Δ. The quantity Δ has been estimated by several authors and a review discussion can be found in a paper by Amman.[2] All these calculations are done for electron storage rings where the bunch length is much shorter than the crossing region. To apply these calculations to ISABELLE one must apply a correction factor, which we assume to be given by the ratio of the crossing region length ℓ_{int}, to the bunch length, ℓ_B. With this assumption the order of magnitude of Δ is given by

$$\Delta = \frac{2m}{\alpha}\left(\frac{I_b}{I_o}\right)\frac{1}{\gamma\sigma_p^2}\quad\frac{\ell_{int}}{\ell_B} \tag{2}$$

where m is the number of crossings, α is the momentum compaction I_b is the bunch current and $I_o = 3.12 \times 10^7$ A, γ is the energy in mass units, and σ_p the half-width relative energy spread. Assuming $m = 8$, $\alpha = 10^{-3}$, $I_b = 5$ A, $\gamma \approx 30$, $\sigma_p \approx 10^{-2}/2$, $\ell_{int} = 20$ m, $\ell_{bunch} \approx 1000$ m, one has

$$\Delta \approx 6 \times 10^{-2}$$

If the beams are vertically separated at the interaction region then the value of Δ can be reduced. A lower limit for Δ is

---

2. F. Amman, Proc. 1973 Particle Accelerator Conf., San Francisco 1973, p. 858.

obtained considering only the coupling due to the wakefields in the crossing region. In this case an order of magnitude estimate gives

$$\Delta \approx \frac{I\ Z}{V \cos \phi_s} \quad \frac{m\ \ell_{int}}{2\pi R} \tag{3}$$

where Z is the longitudinal impedance, R is the machine radius, V the peak rf voltage, ϕ_s the synchronous phase and I the total beam current. For I = 10 A, V cos $\phi_s \approx 20$ kV, $2\pi R = 3000$ m, $\ell_{int} = 15$ m, m = 8 we get

$$\Delta \approx 2 \times 10^{-5}\ Z$$

so that in this extreme case the frequency separation needed would be very small, for a reasonable value of the impedance.

3. The expressions for Δ in (2) and (3) are approximate and can be used only as an order of magnitude estimate. However, the values obtained for Δ, of the order of a few percent, are such that to separate the synchrotron frequencies of the two beams by this amount should be simple enough.

COASTING BEAM THEORY APPLIED TO BUNCHES

H. Hereward

CERN

INTRODUCTION

This has been done before in other connections, notably Sessler's 1973 PEP note on turbulence[1] and the transition-jump paper of Hardt.[2]

It is plausible to apply coasting beam criteria to bunches if one has:

- short wavelength disturbances of the bunch
- short memory wake fields

where short means short compared with a bunch length, for then one can argue that a piece of the bunch near the middle does not even know that the bunch has ends. We shall see that some other conditions are probably required to validate this approach.

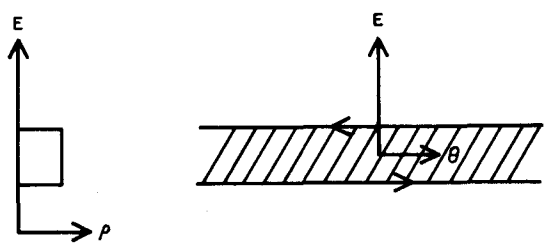

Fig. 1. Coasting Beam rectangular spectrum

INSTABILITY OF COASTING BEAM

I summarize the classical results in this field, for the

---

1. A. Sessler "Strongly Turbulent Collective Motion and the Anamolous Size of Stored Particle Beams", PEP Note 28, LBL 1973.

2. W. Hardt, Proc. IX Int. Conf. on High Energy Accelerators, Stanford, 1974, p. 434.

particular case of a rectangular energy spectrum. In 1959, Nielsen, Sessler and Symon[3] did the longitudinal space-charge case by the dynamics of the beam boundaries: it is easy to generalize their results to a general coupling impedance Z. Later work handled more general cases in terms of the interaction quantities U and V. To express U + jV in terms of Z one may use Keil and Schnell's paper.[4]

Using the Courant and Snyder[5] notation, but with $\theta = -\Phi$, and considering an exp $j(\omega t - k\theta)$ disturbance, all these methods give

$$\omega = \mp \sqrt{S^2 - 2jS\Delta}$$

$$\approx \mp S \pm j\Delta \ldots$$

where (1)

$$S = \tfrac{1}{2} \frac{\Delta E_{FWHM}}{E} \beta^{-2} \eta \, kh \, \omega_{rev}$$

$$\Delta = \frac{Ie}{\Delta E_{FWHM}} Z f_{rev}$$

This implies a growth rate

$$\alpha = - \mathrm{Im}\, \omega \approx \pm \mathrm{Re}\Delta \tag{2}$$

The phase velocity

$$R_e \left(\frac{\omega}{k}\right) \approx \mp \left(\frac{S}{k} + \frac{\mathrm{Im}\Delta}{k}\right) \tag{3}$$

---

3. C.E. Nielson, A.M. Sessler, and K.R. Symon, Proc. Intern. Conf. on High Energy Accelerators and Instrumentation, Geneva, 1959, p. 239.
4. E. Keil and W. Schnell, CERN ISR-TH-RF, 69/48 (1969).
5. E.D. Courant and H.S. Snyder, Ann. of Phys. 3, 1 (1958).

Notice that

- There are two solutions.
- The leading term in the phase velocity depends on ΔE, not on I or Z. In fact, the top and bottom signs correspond to waves running mainly along the top and mainly along the bottom of the stack, respectively, with velocity about the same as the velocity of the particles there.
- Bottom wave is antidamped by*

$$\propto \approx + \mathrm{Re}\Delta = \frac{Ie}{\Delta E_{FWHM}} R_c f_{rev} \qquad (4)$$

- Top wave is damped at the same rate.
- These rates are proportional to $I/\Delta E$, the phase space density, not to the current itself.

SAME METHOD ON BUNCH

Take a uniform phase space density inside. The Vlasov equation can be written down and manipulated into a wave equation for propagation of disturbances like exp ($j\omega t$).

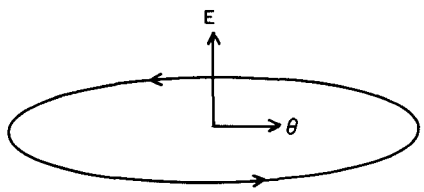

Fig. 2. Uniformly filled bunch.

---

* R_C is the real (resistive) part of Z. So it is positive.

Result:

Group velocity $\approx$ phase velocity = $\mathrm{Re}(\omega/k) \approx \mp S/k(\theta)$ ... (5)

$S/k(\theta)$ is just S/k (1) with $\Delta E_{FWHM}(\theta)$ put in.

Growth rate:

$$\approx \mp \mathrm{Re}\Delta(\theta) \ldots \tag{6}$$

$\Delta(\theta)$ is just Δ (1) with $I(\theta)$, $\Delta E_{FWHM}(\theta)$ put in. (Top signs for top of bunch, bottom for bottom.)

PROVISIONAL CONCLUSION

No instability for disturbances that run round a bunch. They are antidamped as they run along the bottom, but equally damped as they run back along the top.

This has been known for some time,* and is why most of the literature is about coupled-bunch modes and wakes that stretch at least from one bunch to the next.

SECOND LOOK - DANGEROUSLY FAST?

Ok, no instability if that growth rate is reasonably small. But suppose the random noise at the back of the bunch grows to be a <u>large</u> disturbance in traveling just once along the bottom to the front?

$$\frac{1}{\sqrt{N_\lambda}} \times \exp\left(\frac{\alpha T}{2}\right) > 1 \tag{7}$$

is the condition that the front of the bunch gets broken up by

---

* Sacherer has a method of proving it using the symmetry of $Z(\omega)$ and of his mode functions. The symmetry can be broken if one introduces some "longitudinal chromaticity", but this is a small effect. There are some EPIC Notes of mine that relate.

this mechanism. Here N_λ is the number of particles in one wavelength of the disturbance near the ends of the bunch. This can also be expressed as

$$\alpha > \frac{2}{\tau} \ln \sqrt{N_\lambda}. \tag{7a}$$

A smaller α will be enough for trouble if the bunch starts noisier than pure statistics, but it is not very sensitive because of the $\ln$ function.

Some imaginary part to Z, or a smoother distribution, will make the growth rate less than the α given by (4), (6); so one should regard (7) as a <u>necessary</u> condition for blow-up.

A tacit assumption in obtaining the local growth rate and local phase velocity (5) and (6) is that the perturbed current and resulting algebraic accelerating volts per turn are related by

$$V(\theta) = - ZI(\theta) \tag{8}$$

locally at each θ in the bunch. Strictly, this requires that Z be frequency independent; but if Z is not too frequency dependent we can just use its average value over the frequency band that the instability uses.

Note that the frequency seen by the hardware is not $\omega/2\pi$. It is approximately $kh\, f_{rev}$, and a disturbance of given ω has a k that varies with θ along the bunch. So the relevant frequency band is rather wide.

ISABELLE

For the long h = 2 bunches during acceleration, I supposed that N_λ might be like a few 10^9 for λ like 10 cm, so the logarithm is about 11. That makes $\alpha > 25\ \mathrm{sec}^{-1}$ and requires a ReZ of the order of 5000 Ω.

It is probably impossible to make a vacuum chamber that

stays below that: for example a Z/n that has 0.2 Ω real up to mode numbers like 25000 is dangerous.

THRESHOLD CONSIDERATION

If this bottom instability is fast enough to be dangerous, (7'), we must look whether we can stabilize it by Landau damping, and avoid crossing it's threshold.

[The above calculation of rate used a waterbag model, so had no Landau damping.]

We go back to the derivation of the wave solutions (5), (6) from the Vlasov equation and consider how it is affected by having a "reasonable" distribution rather than a waterbag. One gets a dispersion integral, formally the same as the coasting beam theory, but the width of the distribution and the currents are functions of θ.

I think it is obvious that in (3) anywhere where the shift $\mathrm{Im}\,\Delta(\theta)/k(\theta)$ is big enough compared with the particle velocity half spread $S(\theta)/k(\theta)$, there the Landau damping will not stabilize it. So maybe we can use a local Keil-Schnell criterion, in our notation

$$|\Delta(\theta)| > 0.3\ S(\theta) \tag{9}$$

as the condition for instability on the bottom of the bunch for "reasonable" distributions. The different numerical factors for other distributions can be obtained from Ruggiero and Vaccaro's 1968 ISR Report. It will be wise to trap a reasonable distribution in one's bunches and not a steep-edged one.

CONCLUSION

You can use coasting beam theory for short wavelength, short memory cases in a long bunch, in two steps:

1) Keil-Schnell criterion with local parameters to see

whether the bottom of the bunch is above or below threshold.

2) If bottom unstable use the $\alpha_T/2$ consideration (7) to see whether it is harmful.

To the two conditions mentioned on the first page one should add that Z must not be too frequency dependent.

DISCUSSION

Our derivation of a local Keil-Schnell criterion from the local dispersion integral at each θ is not rigorous and needs more study. It is probably best to consider ω as a single quantity which applies to the whole perturbation of the bunch, while k is local $k(\theta)$ and means $(j\partial\psi/\psi\partial\theta)$. The mapping technique of Ruggiero and Vaccaro (on which the Keil-Schnell criterion is based) is then used to calculate the value of Z at which the local energy spectrum is consistent with a real ω and a locally real $k(\theta)$. This I interpret as the condition for just no local growth rate.

INTRABEAM SCATTERING IN ISA

K. Hübner

CERN

The growth rates due to multiple interbeam scattering in an unbunched beam are given by [1]

$$\frac{1}{\tau_i} = \frac{1}{\sigma_i}\,\frac{d\sigma_i}{dt} = A\,G_i(\sigma_x,\ \sigma_z,\ \sigma_p,\gamma)\,, \qquad i = x,z,p.$$

This factorization reflects that intrabeam scattering is determined by two things

i) density in phase space

ii) the lack of balance between the momenta pertaining to the three degrees of freedom. These momenta are defined in the rest-system of a reference particle.

The former determines A which is given by

$$A = \frac{r_p^2}{\pi}\cdot\frac{I}{e}\cdot\frac{1}{\beta^2\gamma^2}\cdot\frac{1}{\frac{\epsilon_x}{\pi}\cdot\frac{\epsilon_z}{\pi}\cdot\frac{\Delta p}{p}}$$

where ϵ is the invariant emittance $E\beta\gamma$.

The latter is expressed by the functions G_i which contain also the machine parameters.

For the numerical computations the following machine parameters[2] were used

$$R = 2960\text{m},\ R/Q = 18\ \text{m},\ \alpha_p = R/\gamma_t^2 = 1\ \text{m}.$$

The beam parameters were evaluated from

$$\sigma_x = \sigma_z = \frac{1}{2}\sqrt{\frac{E}{\pi}\,\frac{R}{Q}} \qquad \text{at 30 GeV}$$

1. A. Piwinski, IX Intern. Conf. on High Energy Accelerators, Stanford (1974) 405.

2. "A Proposal for Construction of a Proton-Proton Storage Accelerator Facility, ISABELLE, BNL Rept. No. 20161 (1975).

$$\sigma_x = \sigma_z = \frac{h_{eff}}{2\sqrt{\pi}} \qquad \text{at 200 GeV}^*$$

$$\sigma_p = \frac{\Delta p/p}{2\sqrt{\pi}}$$

Table of Input Parameters

γ	$E_x = E_z$	$h_{eff}(\beta_z^* = 4\ m)$	$\Delta p/p$	$E\beta\gamma$
30.3	$0.4\pi \times 10^{-6}$ radm	-----	0.7%	$12\pi \times 10^{-6}$ radm
213	-----	0.88×10^{-3}	0.15%	$13\pi \times 10^{-6}$ radm

The growth rates given in the following table are computed for the nominal emittances, for emittances smaller by a factor 2 and for emittances blown up by a factor 2. The momentum spread is kept constant for a given energy. The beam current is assumed to be 10 A.

Table of Growth Rates

γ	$E_x = E_z$ radm	$\Delta p/p$	$1/\tau_p$	$1/\tau_x$	$1/\tau_z$
			percent per hour		
30.3	$0.4\pi \times 10^{-6}$	0.7%	6	5	-1
30.3	$0.2\pi \times 10^{-6}$	0.7%	10	20	-4
30.3	$0.8\pi \times 10^{-6}$	0.7%	3	1	-0.3
213	$0.062\pi \times 10^{-6}$ (a)	0.15%	30	8	-0.03
213	$0.031\pi \times 10^{-6}$	0.15%	60	40	-0.1
213	$0.120\pi \times 10^{-6}$	0.15%	10	2	-0.006

(a) nominal values

One learns from the table that mainly the longitudinal momentum spread will grow pretty fast at top energy. Thus, if the stack is bordered by nonlinear resonances, particles will be lost. The growth rates at injection energy are harmless since one does not

* h_{eff} was obtained from the luminosity assuming a Gaussian distribution in both beams.

dwell on this energy. The vertical growth is even negative initially. This is due to the fact that in ISA

$$p_{oz}/p_{op} > 1 \text{ and } p_{oz}/p_{ox} \cong 1$$

where p_{oi} are the average moments of the particles in the test system of some reference particle. Thus, the luminosity will not be influenced by a growing beam height as in the ISR where $p_{oz}/p_{ox} \simeq 0.3$, which leads to vertical beam growth and as a consequence to a gradual decay of luminosity.

MAGNET PROTECTION

D. A. Baynham
Rutherford High Energy Laboratory

The magnet protection scheme considered for the ISABELLE dipoles consists of a diode assembly connected across each pair of magnets. The diode circuit provides a bypass for ring magnet current should any dipole revert to the normal state. The system is extremely simple but requires that each dipole be capable of absorbing its own stored energy plus that of the linked dipole during quench conditions. The stored energy per dipole pair is 900 kJ and this must be dissipated without excessive temperature rise in the coil. In order to minimize local stress build-up in the windings, it is desirable that the temperature rise should not exceed 80 - 100 K.

Under test conditions the first 4.25 meter prototype magnet experienced a local temperature rise of approximately 400 K when the normal zone originated in the region of low current density. The coil system has been redesigned to give improved thermal transfer and computer studies indicate that the quench temperature should remain within the accepted range. However, before the diode protection system can be considered suitable for the ISABELLE ring, this magnet must demonstrate its stability under quench conditions. Temperature measurements must verify the computer studies when quenches are initiated in the low current density regions. Assuming that the single dipole performance is satisfactory then the system requires an extrapolation to include the energy associated with the linked dipole. A more appropriate solution would be to consider a system utilizing a diode assembly for each magnet. The small additional refrigerator load resulting from the increased number of current leads would be offset by the more effective protection. During quench conditions the protection circuit current leads must carry the ring current which is run down over a 120 sec period. The current rating requirements of these leads

must be established experimentally to avoid failure.

If an intermediate temperature heat shield is included in the dewar system then it may be possible to locate the diode assembly in this region. This would reduce the heat inleak to the system, but considerable development work is necessary to establish the reliability of diodes in a low temperature environment.

Should the diode protection scheme prove marginal in operation, then it may be necessary to apply a protection system which extracts stored energy from the magnet. Therefore early consideration of these more complex systems would be appropriate in order to assess relative merits.

In a superconducting magnet ring, main power supply failure could leave a circulating magnet current with a long time constant. Under these conditions the protection system current lead rating may be insufficient if a quench occurs. Protection could be obtained by including additional diode assemblies in parallel with the protection diodes, but with reverse polarity.

During the acceleration cycle magnet to ground voltages will be present. In certain regions the dielectric medium may be helium gas and voltage breakdown tests are advisable during the early magnet tests at 4.2 K as well as at room temperature.

CONDUCTOR CONSIDERATIONS FOR ISABELLE DIPOLES

A. D. McInturff
Brookhaven National Laboratory
B. P. Strauss and R. H. Remsbottom
Fermi National Accelerator Laboratory

I. Introduction

The conductor group worked under the overall conditions set down by the magnet working group chairman which set several time frames for the project. These are as follows:

1. Development in FY '76 and start of production in April 1977.
2. Two to three years of research and development before start of production.
3. Delay of production for more than four years.

We have concluded that the cost per pound of superconductor is essentially independent (± 10%) of the specific magnet design in the frequency range considered for the project (0.033 to 0.017 Hz). This conclusion then defines the present task as the possible reduction of per unit base cost within the following design parameters: overall winding current density; ac losses, or more specifically in ISA, induced harmonics; and mechanical properties such as strength, thermal expansion and ease of fabrication. We have also examined the question of the use of β-W superconductors such as Nb_3Sn.

II. Choice of Superconducting Unit (Alloy or Compound)

The group felt there were only two such superconductors whose technology had developed to the point to be feasible for consideration here.

Multifilamentary Nb_3Sn (and possibly other β-W conductors) have a very high current density, higher temperature and capability in the superconducting volume of the conductor. This high current density is offset by the following considerations:

If the Sn used to form the Nb_3Sn is leached from the material surrounding the Nb filament (a high Sn bronze matrix) one is limited for reasons of stoichiometry and workability to a matrix ratio of about 4:1. If the surface diffusion process is used then the basic unit (Cu-Nb) is limited to dimensions on the order of 0.0254 cm by the length of time in heat treatment to diffuse the Sn into the Cu and obtain uniform (small grain growth) filaments across the composite.

If the design of the coil requires that the magnet turns be under tension, then strengthening elements must be added to the turn resulting in a reduction of overall current density by 1.5 to 2 for most practical designs. One possible rule of thumb that could be applied is that the overall current density of the composite (CuSn; Nb_3Sn; Nb; Cu; strengthening element) should be 2 to 5 times that of the solid solution alloys at the design field to be competitive. Higher operating temperature (> 9 K) seems very attractive, but until magnets constructed from the β-W superconductors are available, the practical experience from which to base the operational advantages and savings are a bit speculative and should be so considered. This elevated temperature adds another option of either higher operating temperature or higher field that would have to be evaluated. Considering the present state of the art it was felt that this choice could not be made.

The working group felt the overall magnet machine production time schedules rule out β-W structures. If the construction of ISABELLE is more than 5 - 10 years away, then there is ample time to reverse this consideration given reasonable progress.

At this time the solid solution alloys provide the most immediate and attractive conductors because the current density is

derived from either cold work for the Nb rich side to a combination of cold work and precipitation heat treatment for the Ti rich side. Given production within 3 years, one is limited to the "alloy" now being used by the present commercial companies namely Nb (Ti 46.5 ± 1.5 wt%) a conductor whose Jc is normally obtained by cold work.

The conductor group felt that the only alternative that could be considered with any reliability and reality was the proven state of the art technology for the NbTi based alloys. It is our conclusion, given the overall funding in FY'77 or FY'79, that the NbTi is the only technical possibility at this time and the rest of the report will consider only this option.

Conductor Configuration

We confine ourselves to the two principal configurations presently used for multithousand A-turn conductor namely a) "Rutherford Cable" flat helical cable; b) BNL Flat Braid. Due to the requirement for greater than 1000 meter lengths of continuous conductor and present extrusion press capacity, a monolithic conductor will not be discussed here. First, let us discuss advantages and disadvantages of the various schemes:

a. Rutherford Cable - This configuration is a compacted flattened helical cable, two-dimensionally transposed, multithousand A-turn conductor.

The aspect ratio at the present time seems to be limited to about 12 to 1 or less, therefore requiring a multilayer coil structure for coils producing 4 T central field.

The electrical transposition rate for cables are limited to about 5 cm at present.

The compaction of cables are limited to the high 80 to low 90% region.

To date it is necessary to metal fill the cable to remove training effects in the magnets constructed.

The smallest unit strand used so far in a multi-thousand A-turn is 0.635 mm.

b. BNL Flat Braid - This is flat compacted braid, three dimensionally transposed multithousand A-turn conductor.

The aspect ratio at the present time seems to be limited to 22 to 1 or greater, therefore a single layer coil to 5 T can possibly be a one-layer structure.

The electrical transposition rate for braids is limited at present to 10 cm (5000 A at 4.0 T).

The compaction of braids is limited to the low 70 to low 80% region.

It has been necessary to fill the braid with metal to limit or eliminate training behavior in coils.

The largest unit strand used so far in a multi-thousand A-turn is 0.305 mm.

c. Electrical and Magnet Implications of the above Considerations

The aspect ratio has the following implications for the magnet operating and design limitations for a 12 cm aperture coil:

i) for a single layer coil the aspect ratio has to be greater than

a) 19:1 for 4.0 tesla
b) 23:1 for 5.0 "
c) 30:1 for 6.0 "

ii) for a double layer coil the aspect ratio has to be greater than

a) 9:1 for 4.0 tesla
b) 12:1 for 5.0 "
c) 15:1 for 6.0 "

The aspect ratio in the first approximation is directly linked to the possible transposition rate of the conductors, therefore the higher the aspect ratio the greater the magnetization of the conductor if it is metal filled. If not, then the magnetization is only inversely dependent on the strand size. Thus for metal filled multilayered structures the cable construction of low aspect yields a magnet that has less ramp rate dependent aberations. The metal filled single layer structure, using present technology can only be achieved by braid at the penalty of high ramp rate-dependent effects.

The above arguments are valid up to about 4.5 to 5.0 T, but the generalization can be drawn that a higher aspect ratio leads to fewer layers in the coil.

It should also be noted here that one of the methods by which one decreases the B sensitivity of the conductor is to introduce resistance between strands (up to the logical limit of insulating them). In the latest BNL design (ISA IV) this is done with Cu-Ni (90-10). If one wishes to reduce the cost/pound of the conductor using the Fermi Lab procedure one would have to replace the Cu-Ni with an η-phase bronze similar to that utilized in ISA I & II. This has the advantage of being able to use larger billets and we may use the Fermi Lab material estimates modified by the drawing cost for 8 more dies.

The percentage increase in the cost of the finished conductor, per pound at a given ampere-turn at 4 T is given for braid and cable in Tables II and II.

TABLE I: Cabling Costs (17 strand)

	Time (hours)	Rate/Hour	Total
Spool loading	8	$30	$240.00
Cabling and forming	14.25	30	427.50
Retinning	14.25	30	427.50
Total cost for 4890 A/turn 4 T cable (6000 ft)			$1095.00

Cost in $/A($10^{-12}$ Ω·cm at 4.0 T) per foot = 3.73×10^5

TABLE II: Braiding Costs

	a) 97 strand (hours)	b) 56 strand (hours)	Rate/ Hour	a)	b)
Spooling & loading	19	9	$30	$570	$270
Braiding 40 hours 2 machines/man	20	14	30	600	420
Tinning & forming	8	8	30	240	240
Total costs for 5820 A/turn 4 T braid (2500 ft) (1 pole)				$1410	$930

Cost in $/A(4.0 T)/foot = (a) 9.69×10^5 (b) 6.39×10^5, or it is from 3 to 2 times more expensive to produce the high aspect ratio braid to a lower aspect ratio cable.

If one uses a price of $35/lb of NbTi composite strands, the cabling represents approximately 10% of the raw material and braiding 20 to 30%.

The first shipment of BNL material was approximately $70/lb. The latest shipment was $79/lb.

ISABELLE MAGNET CORRECTION SYSTEM

G. Parzen

Brookhaven National Laboratory

I. Introduction

A number of suggestions for the ISABELLE Magnet Correction System came out of the 1975 ISABELLE Summer Study. Participants in these discussions included F. Arendt, P. F. Dahl, A. W. Chao, D. Edwards, J. Gareyte, A. Garren, J. P. Gourber, H. Hahn, M. Month, J. Perot, and L. Smith. Calculations which lie behind some of the suggestions are given in other papers of the Summer Study proceedings.

This paper is intended to be a summary of the suggestions made at the Summer Study, and to give a sketch of what the total Magnet Correction System now looks like. There still remain some unanswered questions, and some further calculations which need to be done and for which there was not enough time during the Summer Study. For this reason, the results presented here should be regarded as a first approximation which need to be studied more carefully.

It is convenient to break down the corrections needed for the ISABELLE magnets into three categories. These are the following:

1. The Equilibrium Orbit Correction System

A system of vertical dipoles and horizontal dipoles to correct the equilibrium orbit displacement caused primarily by misalignments of the quadrupoles, and of the current carrying coils in the magnets.

2. The Systematic Field Correction System

A system of field correction windings required for known effects which are the same in similar magnets around the ring. These include effects such as control of the working line shape, iron saturation effects at high field levels, eddy-current effects due to $\dot{B}$ at low field levels, and superconductor magnetization

effects at low field levels.

3. Imperfection Resonance Correction System

Imperfection resonances are generated by random errors in the magnetic field of the magnets, and in the beam-beam interaction. These resonances cause coupling between horizontal and vertical oscillations, vertical dispersion of the equilibrium orbit, and possible slow blow up of the beam.

The Equilibrium Orbit Correction System remained essentially unchanged. Detailed calculations of the orbit displacement to be expected because of the random errors in the position of the quadrupoles were done by D. Edwards. The Systematic Field Correction System was modified so as to keep the correction coils from introducing undesired effects. The Imperfection Resonance Correction Systems, which previous considerations had indicated could be omitted, was partially reinstated to correct for the linear coupling resonance, and the nonlinear 1/3 resonances, and possibly the nonlinear ¼ resonance. These changes are detailed below.

In the following where multipoles are given or mentioned they are defined by the following equations for the two components of the field in the median plane

$$B_y = B_o (b_o + b_1 x + b_2 x^2 + b_3 x^3 + \ldots)$$

$$B_x = B_o (a_o + a_1 x + a_2 x^2 + a_3 x^3 + \ldots)$$

where B_o is the unperturbed dipole field.

Table I lists the correction coils that are present, the maximum multipole strength provided, and indicates where they are located.

Table II shows the location of the correction coils, and the series electrical connections where this is possible.

In Table I, which shows the strengths of the correction coils

TABLE I

Correction Coil Parameters

	Multipole Correction Provided (cm^{-n})	Maximum Pole Tip Field/40 kG	Number of Independent Circuits/ring	Expected Multipole Correction (cm^{-n})
Equilibrium Orbit Correction System	b_o = 0.025 in F-Quads	0.025	108	$b_o = a_o$ = 5.8 E-3
	a_o = 0.025 in D-Quads	0.025	108	
Systematic Field Correction System	b_2 = 1 E-3 in Dipoles	0.036	1	b_2 = 3 E-4 Saturation effect
	b_4 = 6 E-6 in Dipoles	0.008	1	b_4 = 2 E-6 Saturation effect
	b_2 = 3.3 E-3 in Quads	0.12	2	b_2 = 2.2 E-3
	b_3 = 4.6 E-5 in Quads	0.01	2	———
	b_4 = 7.7 E-6 in Quads	0.01	2	———
	b_5 = 3.7 E-6 in Quads	0.028	2	b_5 = 1.2 E-6, Saturation effect
Imperfection Resonance Correction System	a_1 = 2 E-4 in Quads	0.001	112	
	a_2 = 3.4 E-4 in Q4	0.003	16	
	b_2 = 3.4 E-4 in QF	0.003	16	
			Total 370	

TABLE II

Location of the Correction Coils

	Crossing Point X		Q1	Q2		Q3	Q4		B1	QF	B2	QD		QF	B	B	QD	B	B	QF
									← Matching Cell →					← Normal Cell ←						
Equilibrium Orbit Correction System			a_o	b_o		a_o	a_o			b_o		a_o		b_o			a_o			b_o
Systematic Field Correction System									b_2		b_2				b_2	b_2		b_2	b_2	
									b_4		b_4				b_4	b_4		b_4	b_4	
														b_2			b_2			b_2
														b_3			b_3			b_3
														b_4			b_4			b_4
														b_5			b_5			b_5
Imperfection Resonance Correction System							a_2			b_2				a_1			a_1			a_1

provided, the sextupole coil in the quadrupoles can yield a chromaticity correction corresponding to $p\Delta\nu/\Delta p = 60$. At present, there is not sufficient information to determine the strengths of the b_3, b_4 and b_5 coils required for controlling the working line. The strengths of the b_3 and b_4 coils have been set arbitrarily so that the maximum pole tip field/40 kG is 0.01. It is not easy to make them too much stronger than this.

With the strengths shown in Table I, the b_3, b_4 and b_5 coils can produce a ν change, in going from the central orbit to an orbit momentum differing by 5×10^{-3}, of about $\Delta\nu = 0.015$, 0.003 and 0.001 respectively.

The Magnet Correction System now has a total of 370 circuits or independently excited coils per ring. This gives a heat loss of about 1 kW at 4.2 K in both rings (based on 1.5 W per 50 A lead pair).

II. The Equilibrium Orbit Correction System

The Equilibrium Orbit Correction System consists of a vertical dipole coil in each focusing quadrupole and a horizontal dipole coil in each defocusing quadrupole. Each of the dipoles is independently excited, and can produce a maximum field of 1000 gauss. There will be 112 dipoles in the 56 normal cells, 96 in the matching cells and experimental insertions, for a total of 208 correcting dipoles in each ring.

The largest source of equilibrium orbit displacement is the misalignment in the quadrupoles, which is assumed to be ± 0.35 mm rms. This misalignment of the quadrupoles can produce a displacement of the orbit whose rms value is about 1 cm at places in the normal cells where β has its maximum value.

Other sources of the field errors that affect the equilibrium orbit are the errors in the vertical alignment of the dipoles, about 0.4 mrad rms, and the errors in the position of the current

blocks of the main dipole coil, of about 0.005 cm rms. These two errors can produce rms field errors of 4×10^{-4} and 2×10^{-4} of the main field which can produce an rms orbit displacement of about 0.3 cm at β maximum locations in the normal cells.

III. The Systematic Field Correction System

The correction coils in the Systematic Field Correction System have been revised because of the following considerations. It seems best to correct nonlinear field terms introduced by effects like iron saturation at their source. This keeps the nonlinear correction coils from possibly exciting nonlinear resonances as, the nonlinearities introduced by the correction coils are exactly cancelled by the nonlinear systematic effects being corrected. In addition it was thought best not to put the rather large chromaticity sextupole coil in the dipoles because of the sagitta effect. The sagitta of the central orbit in the dipoles causes the particle to see a gradient due to this sextupole coil which upsets the matching of the long insertions, and introduces a further momentum dependence of the orbit parameters like the β-function.

Dipoles

The dipoles will have b_2 or b_4 coils. These coils will correct for iron saturation effects, $\dot{B}$ eddy current effects, end effects, and superconductor magnetization effects. The b_2 and b_4 coils will be in series in all dipoles and will not be used for chromaticity correction. There will be separate b_2 and b_4 coils in the quadrupoles for chromaticity correction as suggested by M. Month. The b_4 coils could be used for chromaticity correction also. This would require two independently excitable sets of the b_4 coils; one in the two dipoles adjacent to the focusing quadrupole and the other in the two dipoles adjacent to the defocusing quadrupole. It is believed that the sagitta effect for the b_4 coils may be small and can be neglected. However, in this paper

it is assumed that the b_4 coil is not used for working line control, and there is a separate b_4 coil in the quadrupoles for this purpose.

Quadrupoles

The quadrupoles will have b_2, b_3, b_4 and b_5 coils for systematic effects correction. The b_2, b_3 and b_4 coils are for controlling the working line shape. The b_5 coil will correct for iron saturation effects, and will also be used to control the working line shape. Experience at the ISR indicates that considerable flexibility is needed to control the working line shape and 5 knobs are available which can combine 5 different working line shapes as needed. The scheme proposed here will give ISABELLE 4 knobs, b_2, b_3, b_4 and b_5 coils, to control the working line shape. The b_2, b_3, b_4 and b_5 coils will have two independently excited circuits; one for those in the focusing quadrupole, and one for those in the defocusing quadrupoles.

The amount of b_3, b_4 and b_5 correction strength needed for controlling the working line is not well known at present and requires further study. The strengths indicated in Table I for the b_3 and b_4 coils were set by requiring that the pole tip field produced by each coil be less than 1% of 40 kG. The strength of the b_5 coil is that required by the iron saturation with a safety factor of 3.

IV. Imperfection Resonance Correction System

Imperfection resonances are generated by random errors in the magnetic fields of the magnets, and by random differences in the beam-beam interaction in the 8 intersecting regions. Experience at the ISR appears to indicate that for the most part one can avoid the harmful effects of these resonances by careful control of the working line shape. Thus, no correction coils will be provided for the most of the possible nonlinear resonances, but there is room to add such correction coils after the accelerator is

operating, if this proves desirable.

However, correction coils will be provided to control 3 imperfection resonances since it was felt these 3 might be damaging. The 3 resonance effects are

1. Coupling of horizontal and vertical betatron oscillations, $\nu_x = \nu_y$ resonance.
2. Vertical dispersion of the equilibrium orbit.
3. The 1/3 resonance, near injection.

Coupling Resonances and Vertical Dispersion

The vertical height of the beam is an important parameter in ISABELLE. The ISABELLE design assumes that the beam is round with equal vertical and betatron emittance. However, there is a fair possibility that circumstances may require that the horizontal emittance be larger than the vertical emittance by perhaps a factor of 2, and it would then be important to control the coupling resonance so that the vertical emittance is not blown up by coupling with the horizontal emittance. Control of the coupling resonance $\nu_x = \nu_y$ requires having skew quadrupoles, of a_1 correction coils, around the ring, since the $\nu_x = \nu_y$ resonance is excited by random a_1 quadrupole fields around the ring.

The existence of a random a_1 field also generates a vertical dispersion, that is, a dependence of the vertical position of the equilibrium orbit on momentum. This happens when a skew quadrupole a_1 field exists at a place where there is also a horizontal dispersion, $X_p \neq 0$.

Control of the coupling resonance and the vertical dispersion requires a distribution of skew quadrupoles, a_1 correction coils, around the ring as was suggested by L. Smith. One solution would be to put the a_1 coils in all the normal cell quadrupoles around the ring, 112 in all. One could reduce the number of coils, and put them in either the focusing quadrupoles or in the defocusing quadrupoles. The smallness of the maximum pole tip field of a_1 coils shown in Table I, indicate that fewer a_1 coils could be used.

Another approach is to control the vertical dispersion only locally near the intersection region by using only quadrupoles on either side of the intersection region as suggested by J. P. Gourber. The vertical dispersion that exists around the ring is small and only important in the beam intersection region. This approach requires further calculation to see if it is actually feasible.

The 1/3 Resonance Near Injection

Immediately after the beam is bunched to begin the acceleration stage, the size of the beam in ν-space increases due to space-charge effects and one may have a ν-spread of about $\Delta\nu = 0.06$ as calculated by J. Gareyte. There is a possibility that the space-charge effects which are difficult to compute exactly may be larger, and it may then not be possible to avoid having the beam sit on the 1/3 resonances during acceleration which is believed to be dangerous. In order to give one some freedom in positioning the beam in ν-space during acceleration, it is desirable to be able to correct out the 1/3 resonance; which consists of the 4 resonance lines

$$3\nu_x = 77,$$
$$2\nu_x + \nu_y = 77,$$
$$\nu_x + 2\nu_y = 77,$$
$$3\nu_y = 77.$$

The correction of the 1/3 resonance requires sextupole and skew sextupole, of b_2 and a_2 correction coils, distributed around the ring to generate the correct exciting harmonic in the field. One solution is to put these a_2 and b_2 coils in the Q_4 and Q_F quadrupoles of the matching cell near the experimental insertion (see Table II), as suggested by J. P. Gourber. These quadrupoles have $x_p = 0$, so that the b_2 and a_2 coils will produce no $\Delta\beta/\beta$ dependence on momentum. Also these quadrupoles have extra space as they have no b_2, b_3 chromaticity correction coils. The a_2 coils go in Q_4 which corresponds to a maximum in β_ν and the b_2

coils go in Q_F which corresponds to a maximum in β_H.

To correct a particular resonance, one needs to correct out the cosine part and the sine part of the driving harmonic. The correction coils which generate the cosine part need to be 0.25 ($2\pi/77$) in phase away from those that generate the sine part. Points around the ring that are an octant apart have a phase difference of $2\pi/4$ or 19.25 ($2\pi/77$). One sees that the sine coils and cosine coils can be placed 2 octants apart. Thus octants 1 and 5 can be used for the cosine coils, and octants 3 and 7 can be used for the sine coils to correct one resonance. Also, octants 2 and 6, and 4 and 8 can be used to correct a second resonance.

Altogether we have 16 b_2 coils in the 16 Q_F quads to correct the resonance $3\nu_x = 77$ and $\nu_x + 2\nu_y = 77$, and we have 16 a_2 coils in the 16 Q_D quads to correct the $2\nu_x \neq \nu_y = 77$ and the $3\nu_y = 77$ resonance; a total of 32 independently excited coils per ring. Since these coils are required only near injection, they will not have to be very strong.

The ¼ Resonance Near Injection

A working line for the ISR which has some desirable features lies close to the integer value of ν. The previous consideration about the 1/3 resonance would apply here if such a working line was desirable for ISABELLE, except that in this case it is ¼ resonance at $\nu = 26.75$ that would possibly need to be corrected near injection. The question of whether correction coils for the ¼ resonance should also be provided near injection needs further study.

50 kG ISABELLE DIPOLE

P. F. Dahl and G. Parzen
Brookhaven National Laboratory

Design computations have been carried out on a two-layer higher field (50 kG) version of the ISABELLE dipole, on request by the Summer Study magnet subgroup. A quadrant of the magnet is shown in Fig. 1. Each coil layer contains four blocks per quadrant, consisting of 27, 24, 18, and 9 turns respectively in the inner layer, and 35, 32, 24, and 13 turns in the outer layer. No spacer turns are interspersed between the current carrying turns. The same conductor is assumed as in the 4¼ m prototype dipole, i.e., a braid 0.076 cm in overall thickness and 1.7 cm wide. (Note, however, that in the case of a two-layer design it would appear desirable to narrow the conductor width somewhat compared to the present braid dimensions, in order to aid in the reduction of rate-dependent effects.) The iron thickness is approximately 17 cm.

At low field (infinite μ iron) the magnet produces 23.4 G/A at the center of the aperture. At 50 kG saturation of the iron shield raises the load line by 7% or $I/I(\mu = \infty) = 1.07$. At this central field the ribbon current is 2200 A, and the stored energy 230 kJ/m. The (two-dimensional) peak field is approximately 4.5% higher than B_o and is located in the third block of the inner coil layer, as indicated in Fig. 1.

Ideally, the magnet has a field homogeniety of $\Delta B/B_o = 1.14 \times 10^{-5}$ over 67% of the aperture (R = 4 cm), in the absence of iron saturation and errors in construction, because the conductor distribution eliminates the lowest undesired multipole coefficients. At 50 kG iron saturation gives rise to a sextupole term $b_2 = 2.4 \times 10^{-4}/cm^2$ and a decapole term $b_4 = -0.7 \times 10^{-6}/cm^4$.

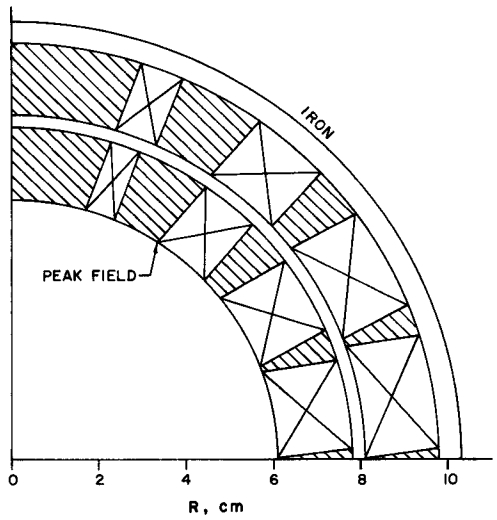

Fig. 1. Two Layer 50 kG Dipole.

SOME REMARKS ON MECHANICAL AND THERMAL BEHAVIOR OF THE COIL

J. Perot

C.E.N. Saclay, France

Introduction

The discussions during the Summer Study about the magnet design have led us to make some general remarks which could be applied to long magnet designs in the future.

I. About the "Law" Which States That the Coil Must Be in a State of Compressive Stress

This is generally true, but this scheme leads in the present design (LN_2-cooled coil mounted into the warm bore) to a very large amount of stress in the coil. When the magnet is brought to room temperature the structural materials included within the coil such as filled epoxy, fiberglass tape, and even metal-filled braid might possibly creep if the magnet should remain for a long period of time at room temperature. (Specifically, in the case of unsplit iron core.) This might result later in a poor fit of the coil into the iron and for subsequent runs to a degradation of the coils performance ("detraining" effect).

If, instead of that, the coil is considered as a "flexible" structure and designed so that it is not in a state of compressive load but fits very well within the iron when loaded by the electromagnetic forces, the magnet might train more during the first run but after that, the magnet would be very reliable.

II. Considerations Involving the Placement of a LN_2 Cooled Coil Into a Warm Iron Core

This process cannot be predicted from computation. Even the most sophisticated program available so far has not been able to take all parameters into account. It is not only a three-dimensional problem of stress, but it involves differential

displacements during the process as well.

After the LN_2 cooled coil has been placed into the warm iron core and the coil reaches room temperature, the radial compressive pressure prevents the coil from expanding axially. The bond between coil and iron is probably not uniform, therefore possibly causing large local stresses for a long coil, resulting in breaks, since the coil is very weak compared to the iron core.

III. Protection of a Coil during a Quench

It is generally said that the protection of the coil should be designed so that no point of the magnet goes up to a temperature which could damage it. A temperature of 300 - 350 K could be stated as safe because no damage would occur to most of the materials from melting. However, these temperatures are very dangerous if one considers them from a mechanical point of view. A coil, or even worse a part of a coil going up to 350 K while the rest of the coil, the bore tube and the iron core remain at LHe temperature, would result in compressive and shear stresses which would certainly damage the coil. Therefore, with the present design the maximum quench temperature must be reduced. A maximum temperature of 70 K seems to be reasonable because below this temperature most materials do not expand very much. For the present design, the protection scheme must guarantee a maximum temperature of less than 70 K, otherwise the magnet must be mechanically designed utilizing a different technique.

Conclusion

Most of the above problems might be eased by another approach of the mechanical design of the magnet. For the future and for magnets of higher sizes the philosophy of mechanically "flexible" coils should be regarded as an alternative to very rigid and compressed coils used here.

SOME THREE-DIMENSIONAL MAGNETOSTATIC RELAXATION PROGRAMS

L.J. Laslett

Lawrence Berkeley Laboratory

Introduction

During the 1975 ISABELLE Summer Study at BNL, Dr. Lloyd Smith discussed the dynamical effects of the end fields that arise from superconducting dipole magnets of typical design.[1] A detailed examination of these fields accordingly may be of interest and would require a magnetostatic analysis of the problem presented by a prescribed current distribution and a surrounding structure of ferromagnetic material. It is the purpose of this note to summarize a computational procedure that was found useful at LBL, in connection with the ESCAR Project, for pursuing this problem.

The LBL computations described here employed three-dimensional relaxation programs to determine the supplemental field provided by the magnetization of infinitely-permeable iron surrounding a prescribed current distribution. Results obtained under this assumption of infinite permeability for the ferromagnetic material may be expected to be less subject to error when obtained for a warm-iron configuration, since with a warm-iron configuration design the flux density in the iron will be substantially less than would be the case for a cold-iron design. [Attempts to perform three-dimensional relaxation computations for situations in which the iron was assigned a field-dependent permeability proved to be quite difficult and expensive. Some successful relaxation runs were made, however, in which the magnetic material was assigned a constant permeability (e.g., 100) but in these cases in which the relaxation process extended into the iron, a boundary condition of no flux leakage was imposed at the outer boundary of this material in order to prevent the core requirements from becoming excessive.]

The boundary surface formed by the inner surface of the iron was taken to be cylindrical, with a large change of radius at a

1. L. Smith, LBL Report No. 12, (January 2, 1975).

specified axial location (see Fig. 1). The prescribed current distribution was taken to be of a cos$\emptyset$ form, at a specified single radius, terminated in a manner advocated (for these purposes) by G. Lambertson. Specifically, this termination had a form (characterized by an angle α) that in side view has the appearance sketched. The details of the termination may be thought not to be critical with respect to fields produced as a result of magnetization developed in the iron — especially when the iron is as remote as it is in warm-iron designs. The "direct" contribution of this, or any other, terminated current, of course, can be calculated separately (through application of Ampere's Law), and in the computations performed at LBL such direct contributions were frequently evaluated for a current with the distribution and type of termination mentioned above.

The relaxation computations were designed to converge to give values (on a three-dimensional r,$\emptyset$,z cylindrical coordinate mesh, covering one quadrant in azimuth) of the magnetostatic potential function whose (positive) gradient gives the field arising from magnetization of the iron. Boundary conditions for this function were provided that were appropriate to meeting the correct boundary conditions for the total field (thus requiring, prior to initiating the relaxation, evaluation of "direct" contributions from the assumed current distribution), and (to be specific) it was presumed that the total field would have symmetry about the (somewhat remote) plane AA′ and about the (also remote) plane BB′.

After completion of the relaxation it was possible to examine the results in several ways. A useful option was one in which the values of the magnetostatic potential of the iron would be printed, as a function of the azimuthal angle $\emptyset$, at any specified r,z mesh values and in which the Fourier components (with respect to $\emptyset$) of these values also were tabulated. Similar output was simultaneously provided for the magnetostatic potential of the field arising "directly" from the current, <u>and</u> for the total field. Such Fourier components of the total field can be informative (especially if printed for moderately small values of the radial coordinate r) in consideration of the dynamical consequences of such a field.

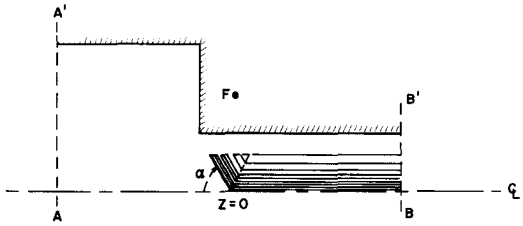

Fig. 1. Cylindrical Boundary Surface of Iron.

We attach to this note a listing of the program FIXED that performs the computations described above, together with an illustrative run (in which the ferromagnetic boundary is closer to the radius of the current sheet than would be typically the case in a warm-iron design). Surface-current densities and magnetic field strengths are given in this program in units of A/cm, and potentials in A. In some applications it was considered expedient to save the results of the relaxation computations in a form that could later be flexibly employed in other (e.g., dynamical) investigations. A second program (e.g., program FUBES) was available for this purpose, and undertook to make a development vs $(r,\emptyset)$ (in terms of coefficients of no more than two indices) of the magnetization potential on some particular radius, so that these coefficients (when stored on a physical tape) would permit the reconstruction of the magnetization potential (and hence of its associated field components) at any (preferably interior) radius by use of a Fourier-Bessel expression of Laplace's equation. With such data available, subsequent examination and analysis of the magnetostatic potential or of field components (polar or Cartesian components) of course can be subsequently undertaken in an economical manner.

It will be noted that the listings attached to this note are for an interactive (TTY) program that has, in practice, proven to be convenient for initiation of some of the ESCAR studies through use of the LBL Sesame interactive-computing facility for use with the CDC 6600. Batch-job adaptations of this program, for submittal to a CDC 7600 are, however, reasonably straightforward — and have, in fact, been made by Ms. Barbara Levine for some of the work at LBL. It is believed, however, that the main general interest that may be associated with the work summarized here may reside in the spirit (that we have attempted to indicate) in which we undertook to approach the problem presented by the end fields of superconducting magnets.

```
FIXED,12,20000,230000.453001,LASLETT
*6600,PSS
FLOOR(3)
LIBCOPY(JACKSON,LIB/RBR,EDGEV/RF,FATTY)
COPY(INPUT,1RM,LIB,1R,DECK/RBR)
RETURN,LGO.
RUN76(SCR,NL15000,I=DECK)
TTY.
LGO(TAPETTY,TAPETTY)
EXIT.
DMP.
DMP(214600)
TEXT,TAPETTY,[XEQ. ERROR].
CXIT.
TEXT,TAPETTY,[COMP. ERROR].
FIN.
SESAME.
EOR
      PROGRAM FIXED(INPUT,OUTPUT,TAPE5)
      COMMON/MESH/ICURT,IMAXR,IMAXE,JMAXS,JMAXW,KMAX
      COMMON/DIMS/ZLEFT,ZRITE,ZTRAN,RADTS,RADTW
      COMMON/PARM/A,TAL,AOT,SCALE,CUR0
      COMMON/CONS/MROM,F8,PHIFAC
      COMMON/IJKS/I,J,K
      COMMON/COOR/ZP,RP,PHIP
      COMMON/POTS/VI(90,18,18),VF(62,27,18)
      COMMON/EDGE/BE(90,18),BV(27,18),BL(45,18),BR(18,18)
      DIMENSION G(18,18), IRAY(7)
      DATA PI/3.14159265358979/
      ROD = PI/180.  $  DOR = 180./PI
      ILIMI=90 $ ILIMF=62 $ JLIMI=18 $ JLIMF=27 $ KLIM=18
      CALL OPNTTY  $  CALL DATE(L)  $  PRINT 8002, L
10    PRINT 8010   $  CALL DATA(ICURT,1)
      ICURT = MAX0(MIN0(ICURT,ILIMI),1)
      PRINT 8011   $  CALL DATA(IMAXR,1)
      IMAXR = MAX0(MIN0(IMAXR,ILIMI),ICURT)
      PRINT 8012   $  CALL DATA(IMAXE,1)
      IMAXE = MAX0(MIN0(IMAXE,ILIMF),1)
      PRINT 8013   $  CALL DATA(JMAXS,1)
      JMAXS = MAX0(MIN0(JMAXS,JLIMI),1)
      PRINT 8014   $  CALL DATA(JMAXW,1)
      IF (JMAXW .LE. 0) GO TO 10
      JMAXW = MIN0(JMAXW,JLIMF)
      PRINT 8015, KLIM  $  CALL DATA(KMAX,1)
      KMAX = MAX0(MIN0(KMAX,KLIM),1)
      PRINT 8017   $  CALL DATA(SCALE,1,A,1)
      A = ABS(A)   $  SCALE = ABS(SCALE)
      PRINT 8018   $  CALL DATA(CUR0,1,ALDEG,1)
      PRINT 8019   $  CALL DATA(MROM,1)
      ZLEFT = SCALE*(0.5 - ICURT)
      ZRITE = SCALE*(IMAXR - ICURT + 0.5)
      ZTRAN = SCALE*(IMAXE - ICURT + 1.0)
      RADTS = SCALE*(JMAXS + 1.0)
      RADTW = SCALE*(JMAXW + JMAXS + 1.0)
      ALDEG = ABS(ALDEG)
      IF (ALDEG .GT. 90.) ALDEG = 180. - ALDEG
      IF ((ALDEG .GE. 90.) .OR. (ALDEG .LE. 0.)) GO TO 10
      AL = ROD*ALDEG  $  TAL = TAN(AL)  $  AOT = ABS(A/TAL)
```

```
      IF (A .GE. RADTS) GO TO 10
      IF (ZRITE .LE. AOT) GO TO 10
      IF (ZLEFT .GE. -AOT) GO TO 10
      FKQOPS = (4.*KMAX/PI)**2
      F8 = CUR0*A*(0.125/PI)     $  PRINT 8000
      PRINT 8020, ICURT  $  PRINT 8021, IMAXR, IMAXE
      PRINT 8022, JMAXS, JMAXW  $  PRINT 8023, KMAX
      PRINT 8024, A, SCALE       $  PRINT 8025, CUR0, ALDEG

      PRINT 8026, MROM   $  PRINT 8031
      PRINT 8032, ZLEFT, ZRITE  $  PRINT 8033, ZTRAN
      PRINT 8034, RADTW, RADTS  $  PRINT 8039
      READ 9500, Q        $  IF (Q .EQ. 1HY) GO TO 10
      PRINT 8000  $ PRINT 8040  $  CALL DATA(NOPRINT,1)
*
      CALL EDGEV(NOPRINT)
*
      ITS = ITS2 = ITS1 = 0  $  EPS = EPSOLD = 0.
40    PRINT 8000  $  CALL STATUS(IRAY)
      AUSR = 0.001*FLOAT(IRAY(3))  $  PRINT 9000, AUSR
50    PRINT 8000  $  PRINT 8051  $  CALL DATA(JUMP,1)
      PRINT 8000
      GO TO (10,60,100,400,50,50,50,50,900) JUMP
60    PRINT 8052  $  CALL DATA(JUMP,1)
      GO TO (70,75,80,85,60,60,60,60,60) JUMP
70    PRINT 8000  $  PRINT 8053  $  CALL DATA(I,1,K,1)
      IF ((I .LE. 0) .OR. (K .LE. 0)) GO TO 50
      IF ((I .GT. IMAXR) .OR. (K .GT. KMAX)) GO TO 70
      ZP = SCALE*(I-ICURT)  $  RP = RADTS
      IF (I .LE. IMAXE) RP = RADTW
      DEG = DOR*((K-0.5)*PHIFAC)
      PRINT 8056, ZP, RP, DEG, I, K, BE(I,K)  $  GO TO 70
75    PRINT 8000  $  PRINT 8054  $  CALL DATA(J,1,K,1)
      IF ((J .LE. 0) .OR. (K .LE. 0)) GO TO 50
      IF ((J .GT. JMAXW) .OR. (K .GT. KMAX)) GO TO 75
      ZP = ZTRAN  $  RP = SCALE*(JMAXS+J)
      DEG = DOR*((K-0.5)*PHIFAC)
      PRINT 8057, ZP, RP, DEG, J, K, BV(J,K)  $  GO TO 75

80    PRINT 8000  $  PRINT 8055  $  CALL DATA(I,1,J,1,K,1)
      IF ((I.LE.0) .OR. (J.LE.0) .OR. (K.LE.0)) GO TO 50
      IF((I.GT.IMAXR).OR.(J.GT.JMAXS).OR.(K.GT.KMAX))GOTO80

      ZP = SCALE*(I-ICURT)  $  RP = SCALE*J
      DEG = DOR*((K-0.5)*PHIFAC)
      PRINT 8058, ZP,RP,DEG,I,J,K,VI(I,J,K)  $  GO TO 80
85    PRINT 8000  $  PRINT 8055  $  CALL DATA(I,1,J,1,K,1)
      IF ((I.LE.0) .OR. (J.LE.0) .OR. (K.LE.0)) GO TO 50
      IF((I.GT.IMAXE).OR.(J.GT.JMAXW).OR.(K.GT.KMAX))GOTO85

      ZP = SCALE*(I-ICURT)  $  RP = SCALE*(JMAXS+J)
      DEG = DOR*((K-0.5)*PHIFAC)
      PRINT 8059, ZP,RP,DEG,I,J,K,VF(I,J,K)  $  GO TO 85
```

```
*
100   PRINT 8000  $  PRINT 8101  $  CALL DATA(ITSADD,1)
      IF (ITSADD .LE. 0) GO TO 50
      ITS1 = ITS2 + 1    $    ITS2 = ITS2 + ITSADD
      PRINT 8102  $  CALL DATA(UNDER,1)  $ UNDER=ABS(UNDER)

      DO 300 ITS=ITS1,ITS2
      DO 290 II=1,IMAXR     $  I = IMAXR + 1 - II
      IF (I .GT. IMAXE) GO TO 200
      IFLAG = 0  $  IF (I .EQ. 1) IFLAG = -1
                    IF (I .EQ. IMAXE) IFLAG = 1
      DO 180 JJ=1,JMAXW     $  J = JMAXW + 1 - JJ
      HOJ = 0.5/(JMAXS+J)  $  FKQOPJS = HOJ*HOJ*FKQOPS
      RCOV = 0.5/(2. + FKQOPJS)
      JFLAG = 0  $  IF (J .EQ. 1) JFLAG = -1
                    IF (J .EQ. JMAXW) JFLAG = 1
      DO 170 KK=1,KMAX      $  K = KMAX + 1 - KK
      KM=K-1  $  IF (K .EQ. 1)  KM=1
      KP=K+1  $  IF (K.EQ.KMAX) KP=KMAX  $  VKP=VF(I,J,KP)

      VKM=VF(I,J,KM)  $  IF (K .EQ. 1) VKM = -VKM
      IF (JFLAG) 110,115,120
110   VDN=VI(I,JMAXS,K)  $  VUP=VF(I,J+1,K)  $  GO TO 125
115   VDN=VF(I,J-1,K)    $  VUP=VF(I,J+1,K)  $  GO TO 125
120   VDN=VF(I,J-1,K)    $  VUP=BE(I,K)
125   IF (IFLAG) 130,135,140
130   VLF=VF(I,J,K)+BL(JMAXS+J,K)  $  VRT=VF(I+1,J,K)
      GO TO 145
135   VLF=VF(I-1,J,K)    $  VRT=VF(I+1,J,K)  $  GO TO 145
140   VLF=VF(I-1,J,K)    $  VRT=BV(J,K)
145   VNEW = RCOV*(VLF + VRT + (1.-HOJ)*VDN
     $ + (1.+HOJ)*VUP + FKQOPJS*(VKM+VKP))
      IF (ITS .LT. ITS2) GO TO 160
      EPSTRY = ABS(VNEW - VF(I,J,K))
      IF (EPSTRY .GT. EPS) EPS=EPSTRY
160   VF(I,J,K) = (1.-UNDER)*VF(I,J,K) + UNDER*VNEW
170   CONTINUE
180   CONTINUE
```

```
144.      200   IFLAG = 0  $  IF (I .EQ. 1) IFLAG = -1
145.                          IF (I .EQ. IMAXR) IFLAG = 1
146.            DO 280 JJ=1,JMAXS     $  J = JMAXS + 1 - JJ
147.            HOJ = 0.5/J           $  FKQOPJS = HOJ*HOJ*FKQOPS
148.            RCOV = 0.5/(2. + FKQOPJS)
149.            JFLAG = 0  $  IF (J .EQ. 1) JFLAG = -1
150.                          IF (J .EQ. JMAXS) JFLAG = 1
151.            DO 270 KK=1,KMAX      $  K = KMAX + 1 - KK
152.            KM=K-1  $  IF (K .EQ. 1)  KM=1
153.            KP=K+1  $  IF (K.EQ.KMAX) KP=KMAX  $  VKP=VI(I,J,KP)

154.            VKM=VI(I,J,KM)  $  IF (K .EQ. 1) VKM = -VKM
155.            IF (JFLAG) 210,215,220
156.      210   VDN=0.            $  VUP=VI(I,J+1,K)  $  GO TO 225
157.      215   VDN=VI(I,J-1,K)  $  VUP=VI(I,J+1,K)  $  GO TO 225
158.      220   VDN=VI(I,J-1,K)
159.            IF (I .LE. IMAXE) VUP=VF(I,1,K)
160.            IF (I .GT. IMAXE) VUP=BE(I,K)
161.      225   IF (IFLAG) 230,235,240
162.      230   VLF=VI(I,J,K)+BL(J,K)  $  VRT=VI(I+1,J,K)
163.            GO TO 245
164.      235   VLF=VI(I-1,J,K)  $  VRT=VI(I+1,J,K)  $  GO TO 245
165.      240   VLF=VI(I-1,J,K)  $  VRT=VI(I,J,K)-BR(J,K)
166.      245   VNEW = RCOV*(VLF + VRT + (1.-HOJ)*VDN
167.           $ + (1.+HOJ)*VUP + FKQOPJS*(VKM+VKP))
168.            IF (ITS .LT. ITS2) GO TO 260
169.            EPSTRY = ABS(VNEW - VI(I,J,K))
170.            IF (EPSTRY .GT. EPS) EPS=EPSTRY
171.      260   VI(I,J,K) = (1.-UNDER)*VI(I,J,K) + UNDER*VNEW
172.      270   CONTINUE
173.      280   CONTINUE
174.      290   CONTINUE
```

```
300   CONTINUE       $  CALL STATUS(IRAY)
      AUSR = 0.001*FLOAT(IRAY(3))
      PRINT 8000     $  PRINT 8150, ITS, EPS, AUSR
      PRINT 8155, UNDER
      EPSOLD = EPS  $  EPS = 0.  $  GO TO 50
*
400   PRINT 8000  $  PRINT 8160  $  CALL DATA(I,1,J,1)
      IF ((I .LE. 0) .OR. (J .LE. 0)) GO TO 40
      IF ((I .GT. IMAXR) .OR. (J .GT. JMAXS)) GO TO 400
      ZP = SCALE*(I-ICURT)  $  RP = SCALE*J
*
      CALL FOUPOT(KMAX)      $  GO TO 400
*
900   PRINT 8000  $  PRINT 9600  $  READ 9500, Q
      IF (Q .NE. 1HY) GO TO 950
      DO 920 M=1,JMAXS
      DO 915 L=1,KMAX  $  NH = L + L - 1
      G(M,L) = 0.
      DO 910 K=1,KMAX
      G(M,L)=G(M,L)-(BL(M,K)+BR(M,K))*SIN(NH*(K-0.5)*PHIFAC)

910   CONTINUE
      G(M,L)=G(M,L)/FLOAT(M*KMAX)
915   CONTINUE
920   CONTINUE
      PRINT 8000  $  PRINT 9650  $  CALL DATA(NOPRINT,1)
      IF (NOPRINT .EQ. 0) GO TO 940  $  PRINT 8000
      DO 935 M=1,JMAXS
      DO 930 L=1,KMAX
      PRINT 9655, M, L, G(M,L)
930   CONTINUE     $  PRINT 8000
935   CONTINUE     $  PRINT 8000
940   CONTINUE
      JCOPY = INT(A/SCALE)  $  RCOPY = SCALE*JCOPY
      IF (RCOPY .GE. A) JCOPY = JCOPY - 1
      RCOPY = SCALE*JCOPY
      WRITE(5) PI,MROM,ROD,DOR,
     $ILIMI,JLIMI,KLIM,ICURT,IMAXR,IMAXE,JMAXS,JMAXW,KMAX,

     $ZLEFT,ZRITE,ZTRAN,RADTS,RADTW,A,AL,ALDEG,TAL,AOT,
     $SCALE,CUR0,PHIFAC,JCOPY,RCOPY,
     $(((VI(I,J,K),I=1,ILIMI),J=1,JLIMI),K=1,KLIM),
     $((G(M,L),M=1,JLIMI),L=1,KLIM)
      REWIND 5
      PRINT 8000  $  PRINT 8000  $  PRINT 9700
*
950   PRINT 8000  $  PRINT 9900  $  PRINT 8000
*
```

```
 8000  FORMAT(1H )
 8002  FORMAT(1H ,28X,A10,//)
 8010  FORMAT(* TYPE I-INDEX AT CENTER OF CURRENT TRANSITION*
)
 8011  FORMAT(* TYPE I-INDEX OF LAST POINT TO RIGHT*)
 8012  FORMAT(* TYPE I-INDEX ON LAST POINT WITHIN WIDE TUBE*)

 8013  FORMAT(* TYPE J-INDEX OF LAST POINT WITHIN NARROW TUBE
*)
 8014  FORMAT(* TYPE ADDITIONAL J-INDICES WITHIN WIDE TUBE*)

 8015  FORMAT(* TYPE KMAX [LE*I3,*]*)
 8017  FORMAT(* TYPE SCALE [CM/MESH] & CURRENT RADIUS [CM]*)

 8018  FORMAT(* TYPE CURRENT [AMP/CM] & ALPHA [DEG]*)
 8019  FORMAT(* TYPE M FOR ROMBERG INTEGRATION [E.G., 64]*)
 8020  FORMAT(* I-INDEX =*I3,* AT CENTER OF CURRENT TRANSITIO
N*)
 8021  FORMAT(*     IEND =*I3,* FOR SMALL TUBE*,6X,
      $*&*I4,* FOR LARGE TUBE*)
 8022  FORMAT(*     JMAX =*I3,* WITHIN SMALL TUBE,  &*,
      $I4,* ADDITIONAL WITHIN LARGE TUBE*)
 8023  FORMAT(*     KMAX =*I3,* FOR QUADRANT*,/)
 8024  FORMAT(* *,6X,*A =*F11.4,* CM*,18X,
      $*[SCALE =*F8.4,* CM/MESH]*)
 8025  FORMAT(* CURRENT =*F9.2,* AMP/CM  AT PHI = 0.,*,
      $3X,*ALPHA =*F8.4,* DEG.*)
 8026  FORMAT(* *,6X,*M =*I6,/)
 8031  FORMAT(* CURRENT TRANSITION CENTERED AT Z = 0.0*)
 8032  FORMAT(* MIRROR PLANES AT  Z =*F10.4,
      $*  &  Z =*F10.4,* CM.*)
 8033  FORMAT(* TUBE-RADIUS TRANSITION AT Z =*F10.4,*,*)
 8034  FORMAT(*  WITH TUBE RADII*F15.4,5X,*&*,F12.4,//)
 8039  FORMAT(* REVISE DATA?  TYPE Y OR N*)
 8040  FORMAT(* TO PRINT INIT. VALUES, TYPE 1 -- ELSE 0*)
 8051  FORMAT(* FOR NEW DATA, SEE VALUES, ITERATE,*,
      $* ANALYZE, OR TERMINATE*,/,
      $*     TYPE 1,*8X,*2,*8X,*3,*7X,*4,*4X,*OR*5X,*9*)
 8052  FORMAT(* FOR BE, BV, VI, OR VF*,
      $* -- TYPE 1, 2, 3, OR 4*)
 8053  FORMAT(* TYPE I,K -- OR 0,0 IF NONE*)
 8054  FORMAT(* TYPE J,K -- OR 0,0 IF NONE*)
 8055  FORMAT(* TYPE I,J,K  -- OR 0,0,0 IF NONE*)
 8056  FORMAT(* Z =*F8.2,*  R =*F6.2,*  PHI =*F6.2,
      $*     BE(*I2,*,*I2,*) =*G17.9)
 8057  FORMAT(* Z =*F8.2,*  R =*F6.2,*  PHI =*F6.2,
      $*     BV(*I2,*,*I2,*) =*G17.9)
 8058  FORMAT(* Z =*F8.2,*  R =*F6.2,*  PHI =*F6.2,
      $*  VI(*I2,*,*I2,*,*I2,*) =*G17.9)
 8059  FORMAT(* Z =*F8.2,*  R =*F6.2,*  PHI =*F6.2,
      $*  VF(*I2,*,*I2,*,*I2,*) =*G17.9)
 8101  FORMAT(* TYPE ITERATIONS TO PERFORM*)
 8102  FORMAT(* TYPE RELAXATION FACTOR*)
 8150  FORMAT(* *,I6,* ITERATIONS     EPS =*,
      $E11.4,F18.3,* CU'S REMAIN*)
 8155  FORMAT(* RELAX COEF*F7.4)
 8160  FORMAT(* TYPE I,J FOR VI-FOURIER*,
      $* -- OR 0,0 IF NONE*)
 9000  FORMAT(1H ,F11.3,* CU'S REMAIN*)
 9500  FORMAT(A1)
 9600  FORMAT(* SAVE RESULTS ON PSEUDO TAPE?  TYPE Y OR N*)
```

```
 9650  FORMAT(* TO PRINT G VALUES, TYPE 1 -- ELSE 0*)
 9655  FORMAT(*  G(*I2,*,*I2,*) =*G14.6)
 9700  FORMAT(1H ,19X,32H* PSEUDO TAPE HAS BEEN WRITTEN *,//)

 9900  FORMAT(1H ,27X,14H* END OF RUN *,/)
 ****
       STOP
       END
```

```
      SUBROUTINE EDGEV(NOPRINT)
      COMMON/MESH/ICURT,IMAXR,IMAXE,JMAXS,JMAXW,KMAX
      COMMON/DIMS/ZLEFT,ZRITE,ZTRAN,RADTS,RADTW
      COMMON/PARM/A,TAL,AOT,SCALE,CUR0
      COMMON/CONS/MROM,F8,PHIFAC
      COMMON/POTS/VI(90,18,18),VF(62,27,18)
      COMMON/EDGE/BE(90,18),BV(27,18),BL(45,18),BR(18,18)
      DIMENSION E(4)
      DATA(E(L),L=1,4)/-0.00035273368607,0.02962962962963,
     $-0.47407407407407,1.44479717813051/
      DATA TPI/6.28318530717959/
      PHIFAC = 0.25*TPI/FLOAT(KMAX)
*
C >>> BE&BV ARE THE NEGATIVE POTENTIALS OF CURRENT'S FIELD,
C  >  BL&BR ARE POT. DIFFS. (RIGHT-LEFT FOR EACH FUNCTION).
C  >  VI-FUNCTIONS SERVE AS TEMPORARY "SCRATCH" FUNCTIONS
C  >  IN THE EVALUATIONS OF BE, BV, BL & BR.
*
C >>> VI & VF ULTIMATELY REPRESENT MAGNETIZATION POTENTIAL,
C  >  AND ARE INITIALIZED BY LINEAR INTERPOLATION FROM BE
C  >  AT THE FINAL STAGE OF THIS SUB-ROUTINE.
*
      DO 102 K=1,KMAX
      DO 101 I=1,IMAXR  $  BE(I,K) = 0.
101   CONTINUE
102   CONTINUE  $  N = MROM
      IF (ABS(RADTS-A) .LE. 0.3750*A) N=MAX0(MROM,128)
      IF (ABS(RADTS-A) .LE. 0.1250*A) N=MAX0(MROM,256)
      IF (ABS(RADTS-A) .LE. 0.0625*A) N=MAX0(MROM,1024)
      DO 160 LR=1,4  $  F = TPI/FLOAT(N)  $  FF8 = -F*F8
      DO 111 K=1,KMAX
      DO 110 I=1,IMAXR  $  VI(I,1,K) = 0.
110   CONTINUE
111   CONTINUE
      DO 140 LX=1,N  $  X = (LX-0.5)*F  $  SI = SIN(X)
      ZL = AOT*ABS(SI)  $  ST = SIGN(TAL,SI)
      DO 130 K=1,KMAX  $  PHIP = (K-0.5)*PHIFAC
      CD = COS(PHIP - X)
      DO 120 I=1,IMAXR  $  ZP = SCALE*(I-ICURT)
      DZP = ZL + ZP  $  DZM = ZL - ZP
      RP = RADTS  $  IF (I .LE. IMAXE) RP=RADTW
      D1 = RP*RP - (A+A)*RP*CD + A*A
      TERM1 = SQRT(D1 + DZP*DZP)
      TERM2 = SQRT(D1 + DZM*DZM)
      B2 = ZL + ZL + TERM1 - TERM2
      Q = ((RP*CD - A)/D1)*B2
      VI(I,1,K) = VI(I,1,K) + Q*ST
120   CONTINUE
130   CONTINUE
140   CONTINUE
```

```
      DO 151 K=1,KMAX
      DO 150 I=1,IMAXR
      BE(I,K) = BE(I,K) - FF8*E(LR)*VI(I,1,K)
150   CONTINUE
151   CONTINUE  $  IF (LR .LT. 4) N=N+N
160   CONTINUE
*
      DO 202 K=1,KMAX
      DO 201 J=1,JMAXW  $  BV(J,K) = 0.
201   CONTINUE
202   CONTINUE  $  N = MROM
      IF (ABS(RADTS-A) .LE. 0.3750*A) N=MAX0(MROM,128)
      IF (ABS(RADTS-A) .LE. 0.1250*A) N=MAX0(MROM,256)
      IF (ABS(RADTS-A) .LE. 0.0625*A) N=MAX0(MROM,1024)
      DO 260 LR=1,4  $  F = TPI/FLOAT(N)  $  FF8 = -F*F8
      DO 211 K=1,KMAX
      DO 210 J=1,JMAXW  $  VI(J,2,K) = 0.
210   CONTINUE
211   CONTINUE        $  ZP = ZTRAN
      DO 240 LX=1,N  $  X = (LX-0.5)*F  $  SI = SIN(X)
      ZL = AOT*ABS(SI)  $  ST = SIGN(TAL,SI)
      DZP = ZL + ZP  $  DZM = ZL - ZP
      DO 230 K=1,KMAX   $  PHIP = (K-0.5)*PHIFAC
      CD = COS(PHIP - X)
      DO 220 J=1,JMAXW  $  RP = SCALE*(JMAXS+J)
      D1 = RP*RP - (A+A)*RP*CD + A*A
      TERM1 = SQRT(D1 + DZP*DZP)
      TERM2 = SQRT(D1 + DZM*DZM)
      B2 = ZL + ZL + TERM1 - TERM2
      Q = ((RP*CD - A)/D1)*B2
      VI(J,2,K) = VI(J,2,K) + Q*ST
220   CONTINUE
230   CONTINUE
240   CONTINUE
      DO 251 K=1,KMAX
      DO 250 J=1,JMAXW
      BV(J,K) = BV(J,K) - FF8*E(LR)*VI(J,2,K)
250   CONTINUE
251   CONTINUE  $  IF (LR .LT. 4) N=N+N
260   CONTINUE
*
      JLFTM = JMAXS + JMAXW
      Z1 = ZLEFT - 0.5*SCALE  $  Z2 = ZLEFT + 0.5*SCALE
      Z3 = ZRITE - 0.5*SCALE  $  Z4 = ZRITE + 0.5*SCALE
      DO 303 K=1,KMAX
      DO 301 J=1,JLFTM  $  BL(J,K) = 0.
301   CONTINUE
      DO 302 J=1,JMAXS  $  BR(J,K) = 0.
302   CONTINUE
303   CONTINUE        $  N = MAX0(MROM,64)
```

```
      DO 360 LR=1,4  $  F = TPI/FLOAT(N)  $  FF8 = -F*F8
      DO 312 K=1,KMAX
      DO 310 J=1,JLFTM  $  VI(J,3,K) = 0.
  310 CONTINUE
      DO 311 J=1,JMAXS  $  VI(J,4,K) = 0.
  311 CONTINUE
  312 CONTINUE
      DO 340 LX=1,N  $  X = (LX-0.5)*F  $  SI = SIN(X)
      ZL = AOT*ABS(SI)  $    ST = SIGN(TAL,SI)
      DZP1 = ZL + Z1    $  DZM1 = ZL - Z1
      DZP2 = ZL + Z2    $  DZM2 = ZL - Z2
      DZP3 = ZL + Z3    $  DZM3 = ZL - Z3
      DZP4 = ZL + Z4    $  DZM4 = ZL - Z4
      DO 330 K=1,KMAX   $  PHIP = (K-0.5)*PHIFAC
      CD = COS(PHIP - X)
      DO 320 J=1,JLFTM  $  RP = SCALE*J
      D1 = RP*RP - (A+A)*RP*CD + A*A
      IF (D1 .NE. 0.) GO TO 316
      DR = 0.1*SCALE  $  RP = RP - DR  $  Q = 0.
      DO 314 KOOK=1,2
      D1 = RP*RP - (A+A)*RP*CD + A*A
      TERM1 = SQRT(D1 + DZP2*DZP2)
      TERM2 = SQRT(D1 + DZM2*DZM2)
      B2 = TERM1 - TERM2
      TERM1 = SQRT(D1 + DZP1*DZP1)
      TERM2 = SQRT(D1 + DZM1*DZM1)
      B2 = B2 - (TERM1 - TERM2)
      Q = Q + ((RP*CD - A)/D1)*B2
      RP = DR + RP + DR
  314 CONTINUE  $  RP = RP - DR
      VI(J,3,K) = VI(J,3,K) + 0.5*Q*ST
      GO TO 318
  316 TERM1 = SQRT(D1 + DZP2*DZP2)
      TERM2 = SQRT(D1 + DZM2*DZM2)
      B2 = TERM1 - TERM2
      TERM1 = SQRT(D1 + DZP1*DZP1)
      TERM2 = SQRT(D1 + DZM1*DZM1)
      B2 = B2 - (TERM1 - TERM2)
      VI(J,3,K) = VI(J,3,K) + ((RP*CD - A)/D1)*B2*ST
  318 CONTINUE
  320 CONTINUE
```

```
      DO 325 J=1,JMAXS  $  RP = SCALE*J
      D1 = RP*RP - (A+A)*RP*CD + A*A
      IF (D1 .NE. 0.) GO TO 323
      DR = 0.1*SCALE  $  RP = RP - DR  $  Q = 0.
      DO 322 KOOK=1,2
      D1 = RP*RP - (A+A)*RP*CD + A*A
      TERM1 = SQRT(D1 + DZP4*DZP4)
      TERM2 = SQRT(D1 + DZM4*DZM4)
      B2 = TERM1 - TERM2
      TERM1 = SQRT(D1 + DZP3*DZP3)
      TERM2 = SQRT(D1 + DZM3*DZM3)
      B2 = B2 - (TERM1 - TERM2)
      Q = Q + ((RP*CD - A)/D1)*B2
      RP = DR + RP + DR
322   CONTINUE  $  RP = RP - DR
      VI(J,4,K) = VI(J,4,K) + 0.5*Q*ST
      GO TO 324
323   TERM1 = SQRT(D1 + DZP4*DZP4)
      TERM2 = SQRT(D1 + DZM4*DZM4)
      B2 = TERM1 - TERM2
      TERM1 = SQRT(D1 + DZP3*DZP3)
      TERM2 = SQRT(D1 + DZM3*DZM3)
      B2 = B2 - (TERM1 - TERM2)
      VI(J,4,K) = VI(J,4,K) + ((RP*CD - A)/D1)*B2*ST
324   CONTINUE
325   CONTINUE
330   CONTINUE
340   CONTINUE
      DO 352 K=1,KMAX
      DO 350 J=1,JLFTM
      BL(J,K) = BL(J,K) + FF8*E(LR)*VI(J,3,K)
350   CONTINUE
      DO 351 J=1,JMAXS
      BR(J,K) = BR(J,K) + FF8*E(LR)*VI(J,4,K)
351   CONTINUE
352   CONTINUE  $  IF (LR .LT. 4) N=N+N
360   CONTINUE
```

```
*
      IST = IMAXE + 1
      DO 460 K=1,KMAX
      DO 430 I=1,IMAXE
      SV = BE(I,K)/(JLFTM + 1.)
      DO 410 J=1,JMAXS
      VI(I,J,K) = J*SV
410   CONTINUE
      DO 420 J=1,JMAXW
      VF(I,J,K) = (J+JMAXS)*SV
420   CONTINUE
430   CONTINUE
      DO 450 I=IST,IMAXR
      SV = BE(I,K)/(JMAXS + 1.)
      DO 440 J=1,JMAXS
      VI(I,J,K) = J*SV
440   CONTINUE
450   CONTINUE
460   CONTINUE
*
      IF (NOPRINT .EQ. 0) RETURN
*
      PRINT 800
      DO 710 I=1,IMAXR
      ZP = SCALE*(I-ICURT)  $  RP = RADTS
      IF (I .LE. IMAXE) RP = RADTW
      PRINT 810, ZP, I, BE(I,1), I, KMAX, BE(I,KMAX)
710   CONTINUE   $  PRINT 800
      ZP = ZTRAN
      DO 720 J=1,JMAXW
      RP = SCALE*(JMAXS+J)
      PRINT 820, RP, J, BV(J,1), J, KMAX, BV(J,KMAX)
720   CONTINUE   $  PRINT 800
      DO 730 J=1,JLFTM
      RP = SCALE*J
      PRINT 830, RP, J, BL(J,1), J, KMAX, BL(J,KMAX)
730   CONTINUE   $  PRINT 800
      DO 735 J=1,JMAXS
      RP = SCALE*J
      PRINT 835, RP, J, BR(J,1), J, KMAX, BR(J,KMAX)
735   CONTINUE   $  PRINT 800
      J = MIN0(INT(A/(SCALE+SCALE)+0.5),INT(A/SCALE-0.5))
      RP = SCALE*J           $  PRINT 850, RP
      DO 740 I=1,IMAXR       $  ZP = SCALE*(I-ICURT)
      PRINT 840, ZP,I,J,VI(I,J,1),I,J,KMAX,VI(I,J,KMAX)
740   CONTINUE   $  PRINT 800
      J = MIN0(MAX0(INT(0.5*(JMAXW+1.)),1),JMAXW)
      RP = SCALE*(JMAXS+J)  $  PRINT 850, RP
      DO 745 I=1,IMAXE       $  ZP = SCALE*(I-ICURT)
      PRINT 845, ZP,I,J,VF(I,J,1),I,J,KMAX,VF(I,J,KMAX)
745   CONTINUE   $  PRINT 800
*
      RETURN
```

```
*
800   FORMAT(1H )
810   FORMAT(* Z =*F7.2,*  BE(*I2,*,1) =*G17.9,
     $* BE(*I2,*,*I2,*) =*G17.9)
820   FORMAT(* R =*F7.2,*  BV(*I2,*,1) =*G17.9,
     $* BV(*I2,*,*I2,*) =*G17.9)
830   FORMAT(* R =*F7.2,*  BL(*I2,*,1) =*G17.9,
     $* BL(*I2,*,*I2,*) =*G17.9)
835   FORMAT(* R =*F7.2,*  BR(*I2,*,1) =*G17.9,
     $* BR(*I2,*,*I2,*) =*G17.9)
840   FORMAT(* Z =*F7.2,*  VI(*I2,*,*I2,*,1) =*G14.6,
     $* VI(*I2,*,*I2,*,*I2,*) =*G14.6)
845   FORMAT(* Z =*F7.2,*  VF(*I2,*,*I2,*,1) =*G14.6,
     $* VF(*I2,*,*I2,*,*I2,*) =*G14.6)
850   FORMAT(* R =*F7.2)
*
      END SUBROUTINE "EDGEV"
```

```
      SUBROUTINE FOUPOT(KMAX)
C >>> TO BE STORED WITH "EDGEV" IN LIBRARY JACKSON,
C  >  FOR USE WITH PROGRAM "FIXED"
      COMMON/PARM/A,TAL,AOT,SCALE,CUR0
      COMMON/CONS/MROM,F8,PHIFAC
      COMMON/IJKS/I,J,K
      COMMON/COOR/ZP,RP,PHIP
      COMMON/POTS/VI(90,18,18),VF(62,27,18)
      DIMENSION E(4), P(18), CC(18), CV(18)
      DATA(E(L),L=1,4)/-0.00035273368607,0.02962962962963,
     $-0.47407407407407,1.44479717813051/
      DATA TPI/6.28318530717959/
*
      DO 501 K=1,KMAX  $  P(K) = 0.
501   CONTINUE         $  N = MROM
      IF (ABS(RP-A) .LE. 0.3750*A) N=MAX0(MROM,128)
      IF (ABS(RP-A) .LE. 0.1250*A) N=MAX0(MROM,256)
      IF (ABS(RP-A) .LE. 0.0625*A) N=MAX0(MROM,1024)
      DO 560 LR=1,4    $  F = TPI/FLOAT(N)  $  FF8 = -F*F8

      DO 510 K=1,KMAX  $  CC(K) = 0.
510   CONTINUE
      DO 540 LX=1,N    $  X = (LX-0.5)*F    $  SI = SIN(X)

      ZL = AOT*ABS(SI) $  ST = SIGN(TAL,SI)
      DO 530 K=1,KMAX  $  PHIP = (K-0.5)*PHIFAC
      CD = COS(PHIP - X)
      DZP = ZL + ZP    $  DZM = ZL - ZP
      D1 = RP*RP - (A+A)*RP*CD + A*A
      IF (D1 .NE. 0.) GO TO 516
      DR = 0.1*SCALE   $  RP = RP - DR      $  Q = 0.
      DO 514 KOOK=1,2
      D1 = RP*RP - (A+A)*RP*CD + A*A
      TERM1 = SQRT(D1 + DZP*DZP)
      TERM2 = SQRT(D1 + DZM*DZM)
      Q = Q + ((RP*CD - A)/D1)*(ZL + ZL + TERM1 - TERM2)
      RP = DR + RP + DR
514   CONTINUE         $  RP = RP - DR
      CC(K) = CC(K) + 0.5*Q*ST              $  GO TO 518
516   TERM1 = SQRT(D1 + DZP*DZP)
      TERM2 = SQRT(D1 + DZM*DZM)
      Q = ((RP*CD - A)/D1)*(ZL + ZL + TERM1 - TERM2)
      CC(K) = CC(K) + Q*ST
518   CONTINUE
530   CONTINUE
540   CONTINUE
      DO 550 K=1,KMAX
      P(K) = P(K) + FF8*E(LR)*CC(K)
550   CONTINUE   $  IF (LR .NE. 4) N=N+N
560   CONTINUE   $  DOR = 360./TPI
```

```
*
      PRINT 800  $  PRINT 810, ZP, RP  $  PRINT 820
      DO 610 K=1,KMAX    $  PHIP = (K-0.5)*PHIFAC
      DEG = DOR*PHIP     $  P1 = P(K) + VI(I,J,K)
      PRINT 830, K, DEG, P(K), VI(I,J,K), P1
610   CONTINUE   $  TOKM = 2./KMAX
      PRINT 800  $  PRINT 840
      DO 720 L=1,KMAX    $  NH = L+L-1
      CV(L) = CC(L) = 0.
      DO 710 K=1,KMAX    $  ARG = NH*((K-0.5)*PHIFAC)
      SARG = SIN(ARG)
      CC(L) = CC(L) + SARG*P(K)
      CV(L) = CV(L) + SARG*VI(I,J,K)
710   CONTINUE
      CC(L) = TOKM*CC(L)
      CV(L) = TOKM*CV(L)
      P1 = CC(L) + CV(L)
      PRINT 850, NH, CC(L), CV(L), P1
720   CONTINUE
*
      RETURN
*
800   FORMAT(1H )
810   FORMAT(* Z =*F8.2,6X,*R =*F6.2,/)
820   FORMAT(*  K  DEGREES   POT OF CURR*,
     $*    POT OF IRON     TOTAL POT*,/)
830   FORMAT(* *I2,F9.4,3(E15.6))
840   FORMAT(* SINE*,/,* COEFFS   NH*,
     $*   OF CURR POT    OF IRON POT   FOR TOTAL POT*,/)
850   FORMAT(*      *I6,3(E15.6))
*
      END SUBROUTINE "FOUPOT"
```

Addendum — Three-Dimensional Programs

The current distribution advocated by G. Lambertson as one which may be taken as representative of ESCAR magnets is one in which

$$\vec{J} = - J_o(\cos\phi)\ \delta(r-a)\hat{e}_z \quad \text{for} \quad z > \frac{a|\sin\phi|}{\tan\alpha} \quad ,$$

$$\vec{J} = \frac{J_o}{2}\ \{[\mathrm{Sign}(\sin\phi)]\ (\tan\alpha)\hat{e}_\phi - (\cos\phi)\hat{e}_z\}\ \delta(r-a)$$

$$\text{for } - \frac{a|\sin\phi|}{\tan\alpha} < z < \frac{a|\sin\phi|}{\tan\alpha} \quad ,$$

$$\vec{J} = 0 \quad \text{for } z < - \frac{a|\sin\phi|}{\tan\alpha} \quad .$$

The field produced directly by this current distribution itself exhibits Fourier components other than the fundamental component characteristic of a pure dipole field. Lloyd Smith has suggested that it would be of interest — especially in connection with an examination of dynamics shortly after injection — to examine the characteristics of the total field produced by this current distribution when contained (coaxially) within an iron tube that terminates (or assumes a much larger internal radius) somewhere in the neighborhood of the current termination and whose magnetic permeability may be regarded as infinite.

The problem as posed is basically a three-dimensional problem in magnetostatics. Because the fields arising directly from the current are calculable (by Ampere's Law), it may be convenient to characterize the remaining contribution to the field — namely that due to the induced magnetization of the iron — by a scalar potential function, and to solve for this potential function by a 3-dimensional relaxation procedure. The fields of the current itself may also be characterized by a scalar potential function, with a discontinuity ("cut") along the cylindrical surface where current is present. If we write

$$\vec{H} = + \text{grad } V$$

(with V given, for example, in units of ampere-turns and J_o in A/cm*), the potential function that describes the field arising directly from the current distribution is given by

$$V^{(c)} = -\frac{J_o a}{8\pi}\int_o^{2\pi} \frac{[\mathrm{Sign}(\sin\phi)]\,(\tan\alpha)[r_p\cos(\phi_p - \phi_I) - a]}{r_p^2 - 2ar_p\cos(\phi_p - \phi_I) - a^2} \times$$

$$\left[2Z_L + \sqrt{r_p^2 - 2ar_p\cos(\phi_p - \phi_z) + a^2 + (Z_L + Z_p)^2} - \right.$$

$$\left. \sqrt{r_p^2 - 2ar_p\cos(\phi_p - \phi_z) + a^2 + (Z_L + Z_p)^2} \right] d\phi_z \quad ,$$

where Z_L denotes the function

$$Z_L = \frac{a|\sin\phi_I|}{\tan\alpha} \quad .$$

The negative of this quantity $V^{(c)}$, evaluated at the inner surface of the iron cylinder, provides a boundary value for the potential function $V^{(I)}$ that characterizes the magnetization fields, so that the <u>total</u> potential will vanish on such surfaces. To complete the boundary value problem for the magnetization potential, we also consider that the axial derivative of the total potential will vanish on presumed (remote) planes of symmetry (Z = ZLEFT and Z = ZRITE), and that the potential vanish at r = 0.

Relaxation solutions for the problem posed with respect to the magnetization potential are found by the interactive (SESAME) program FIXED,† that then permits (i) examination of the magnetization

---

*The potential function expressed in ampere-turns can be converted to Oe-cm by multiplication by the factor $4\pi/10$ ($\cong 1.256637$), and this same factor will serve to convert field strengths from ampere-turns/cm to Oe.

† This program, stored in Library Jackson, makes use of a PSS call for EDGEV (from Library Jackson), that provides the subroutines EDGEV and FOUPOT used in this program. [It also employs FATTY, to implement the interactive execution of the program.]

potential function and (ii) Fourier analysis (at selected I,J values — i.e., at particular values of Z and r) of (a) the potential function for the current alone, (b) the potential function for the magnetization, and (c) the sum of these quantities. The values of the potential function that result (on a cylindrical polar-coordinate mesh) from the relaxation computations of Program FIXED can be saved — together with various parameters — on a physical tape (if desired), so that subsequent (and possibly more extensive) analysis may be performed by a subsequent program.

The program FUBES* (also interactive) can read the tape prepared by FIXED -- and also can perform the examination of individual values of the magnetization potential, or perform the Fourier analyses of FIXED. It moreover is available for additional analyses of the results of the relaxation computations performed by FIXED.

As an example, results for the first few Fourier coefficients of the total potential function may be given for a case in which:

The current termination, with $\alpha = 45^{\circ}$, is centered at r = 10.0 cm, Z = 0 between symmetry planes at Z = ±44.5 cm. The inner radius of the surrounding iron cylinder (with $\mu = \infty$) changes from 30.0 cm to 12.0 cm at Z = -26.0 cm. The relaxation mesh was formed with axial and radial intervals of 1 cm per mesh unit, and 18 points were employed to describe the azimuthal variation within a quadrant for each pair of Z,r values.

The first of the following major Tables gives values of the first 3 Fourier sine coefficients, of the total potential, evaluated at r = 7.0 cm. It may be remarked that the low values found for s_3 (e.g., at large values of Z) is due in large measure to a high degree of cancellation between the contributions to this quantity

* The program FUBES (also stored in Library JACKSON) makes use of a PSS call for FOUPOT (from Library JACKSON), that provides, in suitable form, the Sub-routines FOUPOT and BESSI. [This program, again, employs FATTY, to implement its interactive execution.]

TABLE I

Sine Coefficients in Fourier Development of Total Potential Function for J_0 = 10,000. Amp/cm and R = 7.0 cm.

Z (cm)	s_1	s_3	s_5
44.	5.930953×10^{4}	1.573235×10^{-4}	-2.334645×10^{-7}
43.	5.930952×10^{4}	1.708149×10^{-4}	-2.754904×10^{-7}
42.	5.930949×10^{4}	1.967829×10^{-4}	-3.545752×10^{-7}
41.	5.930945×10^{4}	2.363967×10^{-4}	-4.805107×10^{-7}
40.	5.930938×10^{4}	2.932294×10^{-4}	-6.586908×10^{-7}
35.	5.930839×10^{4}	1.311082×10^{-3}	-4.186321×10^{-6}
30.	5.930352×10^{4}	1.132122×10^{-2}	-4.611507×10^{-5}
25.	5.927956×10^{4}	1.378565×10^{-1}	-9.789970×10^{-4}
20.	5.916167×10^{4}	1.860068×10^{0}	-3.074020×10^{-2}
17.	5.892396×10^{4}	9.017885×10^{0}	-2.700913×10^{-1}
15.	5.857761×10^{4}	2.600592×10^{1}	-1.197129×10^{0}
13.	5.791519×10^{4}	7.548607×10^{1}	-5.392280×10^{0}
11.	5.664202×10^{4}	2.159989×10^{2}	-2.196950×10^{1}
10.	5.562927×10^{4}	3.513254×10^{2}	-3.782389×10^{1}
9.	5.428215×10^{4}	5.352552×10^{2}	-5.173194×10^{1}
7.	5.050469×10^{4}	9.344830×10^{2}	-1.990396×10^{1}
5.	4.545320×10^{4}	1.106382×10^{3}*	$+8.824809 \times 10^{1}$
3.	3.948955×10^{4}	8.863777×10^{2}	1.433898×10^{2}
1.	3.299151×10^{4}	3.370983×10^{2}	6.939050×10^{1}
0.	2.965485×10^{4}	$\lvert s_3 \rvert < 2.4 \times 10^{-9}$	s_5 is substantially 0.
- 1.	2.631820×10^{4}	-3.370983×10^{2}	-6.939050×10^{1}
- 3.	1.982016×10^{4}	-8.963777×10^{2}	-1.433898×10^{2}
- 5.	1.385650×10^{4}	-1.106382×10^{3}	-8.824809×10^{1}
- 7.	8.805025×10^{3}	-9.344830×10^{2}	$+1.990396 \times 10^{1}$
- 9.	5.027565×10^{3}	-5.352552×10^{2}	5.173194×10^{1}
-10.	3.680439×10^{3}	-3.513254×10^{2}	3.782389×10^{1}
-11.	2.667690×10^{3}	-2.159989×10^{2}	2.196950×10^{1}
-13.	1.394531×10^{3}	-7.548607×10^{1}	5.392280×10^{0}

* Note that at Z = 5.0 cm (and r = 7.0 cm), s_3 is more than 2.4% of s_1.

TABLE I (Cont'd)

Z (cm)	s_1	s_3	s_5
-15.	7.321267×10^{2}	-2.600593×10^{1}	1.197129×10^{0}
-17.	3.857928×10^{2}	-9.017902×10^{0}	2.700913×10^{-1}
-20.	1.481640×10^{2}	-1.860148×10^{0}	3.074035×10^{-2}
-23.	5.726002×10^{1}	-3.883572×10^{-1}	3.768133×10^{-3}
-25.	3.071406×10^{1}	-1.386200×10^{-1}	9.819893×10^{-4}
-26.	2.267248×10^{1}	-8.364741×10^{-2}	5.143867×10^{-4}
-27.	1.687651×10^{1}	-5.109261×10^{-2}	2.765339×10^{-4}
-28.	1.269063×10^{1}	-3.175610×10^{-2}	1.538245×10^{-4}
-29.	9.651007×10^{0}	-2.019000×10^{-2}	8.914055×10^{-5}
-30.	7.426527×10^{0}	-1.319151×10^{-2}	5.399878×10^{-5}
-32.	4.560593×10^{0}	-6.188531×10^{-3}	2.248107×10^{-5}
-33.	3.641190×10^{0}	-4.453523×10^{-3}	1.528462×10^{-5}
-35.	2.414021×10^{0}	-2.530474×10^{-3}	7.594744×10^{-6}
-37.	1.694138×10^{0}	-1.597098×10^{-3}	4.023995×10^{-6}
-39.	1.268885×10^{0}	-1.097887×10^{-3}	2.234190×10^{-6}
-40.	1.129105×10^{0}	-9.380695×10^{-4}	1.698276×10^{-6}
-41.	1.025656×10^{0}	-8.192855×10^{-4}	1.317040×10^{-6}
-42.	9.526045×10^{-1}	-7.339634×10^{-4}	1.053522×10^{-6}
-43.	9.059265×10^{-1}	-6.778754×10^{-4}	8.848702×10^{-7}
-44.	8.831525×10^{-1}	-6.494272×10^{-4}	8.000797×10^{-7}

from the direct field of the current and from the field due to the magnetization of the iron -- thus, forming $s_3^{(current)} + s_3^{(iron)} = s_3^{(total)}$ for a few values of Z we find (for r = 7.0) cm

Z(cm)	$s_3^{(current)}$	+	$s_3^{(iron)}$	=	$s_3^{(total)}$
35.	-0.1279526	+	0.1292637	=	0.0013111
30.	-0.3588976	+	0.3702188	=	0.0113212
-30.	+0.3588976	+	(-0.3720891)	=	-0.0131915
-35.	+0.1279526	+	(-0.1304831)	=	-0.0025305

The close approximation to symmetry about Z = 0, at least for points close to the transition region, will be evident (Table I).

The variation of the Fourier coefficients with respect to radius may also be of interest:

TABLE IIA

Fourier Coefficient s_1

Z	r = 5.	r = 7.	r = 9.
15.	4.163795×10^4	5.857761×10^4	7.572489×10^4
10.	3.912449×10^4	5.562927×10^4	7.321934×10^4
7.	3.546568×10^4	5.050469×10^4	6.653789×10^4
5.	3.200490×10^4	4.545320×10^4	5.958930×10^4
0.	2.118296×10^4	2.965485×10^4	3.812643×10^4
- 5.	1.036103×10^4	1.385650×10^4	1.666355×10^4
- 7.	6.900252×10^3	8.805025×10^3	9.714957×10^3
-10.	3.241444×10^3	3.680439×10^3	3.033516×10^3
-15.	7.280001×10^2	7.321267×10^2	5.279786×10^2

The proportionality of these coefficients to r is seen to be, at best, only approximate.

TABLE IIB

Fourier Coefficient s_3

Z	r = 5.	r = 7.	r = 9.
15.	1.475452×10^1	2.600592×10^1	2.562674×10^1
10.	1.454070×10^2	3.513254×10^2	4.947743×10^2
7.	3.131084×10^2	9.344830×10^2	2.260553×10^3
5.	3.560785×10^2	1.106382×10^3	2.799032×10^3
0.	----------	----------	----------
- 5.	-3.560785×10^2	-1.106382×10^3	-2.799032×10^3
- 7.	-3.131084×10^2	-9.344830×10^2	-2.260553×10^3
-10.	-1.454070×10^2	-3.513254×10^2	-4.947743×10^2
-15.	-1.475453×10^1	-2.600593×10^1	-2.562675×10^1

These coefficients clearly show a tendency to vary in proportion to r^3 only in the neighborhood of Z = 0.

TABLE IIC

Fourier Coefficient s_5

Z	r = 5.	r = 7.	r = 9.
15.	-0.3983267	-1.197129	-1.483127
10.	-6.249422	-37.82389	-117.6009
7.	-0.6754147	-19.90396	-196.7698
5.	+14.19947	+88.24809	+387.5946
0.	----------	---------	----------
- 5.	-14.19947	-88.24809	-387.5946
- 7.	+ 0.6754147	+19.90396	+196.7698
-10.	+ 6.249422	+37.82389	+117.6009
-15.	+ 0.3983267	+ 1.197129	+ 1.483127

It is evident that a proportionality to r^5 is not generally fulfilled by the coefficients shown in this table.

TYPE I,J FOR VI-FOURIER -- OR 0,0 IF NONE
50,7!

Z = 5.00 R = 7.00

K	DEGREES	POT OF CURR	POT OF IRON	TOTAL POT
1	2.5000	1.375933E+03	7.664437E+02	2.142377E+03
2	7.5000	4.108681E+03	2.291797E+03	6.400478E+03
3	12.5000	6.784397E+03	3.794752E+03	1.057915E+04
4	17.5000	9.366392E+03	5.261038E+03	1.462743E+04
5	22.5000	1.182085E+04	6.677327E+03	1.849817E+04
6	27.5000	1.411927E+04	8.031513E+03	2.215079E+04
7	32.5000	1.624116E+04	9.312896E+03	2.555406E+04
8	37.5000	1.817528E+04	1.051225E+04	2.868753E+04
9	42.5000	1.991865E+04	1.162180E+04	3.154045E+04
10	47.5000	2.147368E+04	1.263510E+04	3.410877E+04
11	52.5000	2.284507E+04	1.354684E+04	3.639191E+04
12	57.5000	2.403767E+04	1.435273E+04	3.839040E+04
13	62.5000	2.505541E+04	1.504928E+04	4.010468E+04
14	67.5000	2.590107E+04	1.563369E+04	4.153476E+04
15	72.5000	2.657642E+04	1.610374E+04	4.268016E+04
16	77.5000	2.708243E+04	1.645773E+04	4.354016E+04
17	82.5000	2.741962E+04	1.669440E+04	4.411402E+04
18	87.5000	2.758817E+04	1.681294E+04	4.440112E+04

SINE COEFFS	NH	OF CURR POT	OF IRON POT	FOR TOTAL POT
	1	2.845435E+04	1.699885E+04	4.545320E+04
	3	9.277435E+02	1.786384E+02	1.106382E+03
	5	8.060147E+01	7.646621E+00	8.824809E+01
	7	-5.740927E+00	4.721062E-02	-5.693717E+00
	9	-4.561360E+00	-4.902536E-02	-4.610385E+00
	11	-8.491406E-01	-6.953312E-03	-8.560939E-01
	13	6.504975E-02	-1.911884E-04	6.485857E-02
	15	8.177783E-02	1.427284E-04	8.192056E-02
	17	1.948522E-02	3.494673E-05	1.952017E-02
	19	-9.807210E-04	1.115149E-06	-9.796058E-04
	21	-2.083543E-03	-1.852181E-06	-2.085395E-03
	23	-5.855036E-04	-5.954967E-07	-5.860991E-04
	25	1.046087E-05	4.818301E-10	1.046136E-05
	27	6.254819E-05	7.310559E-08	6.262130E-05
	29	2.014045E-05	2.685637E-08	2.016731E-05
	31	3.312954E-07	-1.515016E-09	3.297804E-07
	33	-1.987740E-06	-5.815915E-09	-1.993556E-06
	35	-7.843814E-07	-2.010185E-09	-7.863916E-07

Z = -7.00 R = 9.00

K	DEGREES	POT OF CURR	POT OF IRON	TOTAL POT
1	2.5000	-5.664537E+01	2.526380E+02	1.959927E+02
2	7.5000	-1.668677E+02	7.588421E+02	5.919743E+02
3	12.5000	-2.675293E+02	1.267711E+03	1.000182E+03
4	17.5000	-3.509561E+02	1.780612E+03	1.429656E+03
5	22.5000	-4.070594E+02	2.298241E+03	1.891181E+03
6	27.5000	-4.211746E+02	2.820279E+03	2.399104E+03
7	32.5000	-3.699944E+02	3.345007E+03	2.975013E+03
8	37.5000	-2.146377E+02	3.868951E+03	3.654314E+03
9	42.5000	1.025299E+02	4.386670E+03	4.489200E+03
10	47.5000	6.204920E+02	4.890798E+03	5.511290E+03
11	52.5000	1.289348E+03	5.372411E+03	6.661759E+03
12	57.5000	2.008984E+03	5.821671E+03	7.830655E+03
13	62.5000	2.702698E+03	6.228568E+03	8.931267E+03
14	67.5000	3.324210E+03	6.583611E+03	9.907821E+03
15	72.5000	3.845555E+03	6.878351E+03	1.072391E+04
16	77.5000	4.249126E+03	7.105751E+03	1.135488E+04
17	82.5000	4.523717E+03	7.260401E+03	1.178412E+04
18	87.5000	4.662601E+03	7.338647E+03	1.200125E+04

SINE COEFFS	NH	OF CURR POT	OF IRON POT	FOR TOTAL POT
	1	2.756028E+03	6.958929E+03	9.714957E+03
	3	-1.866185E+03	-3.943678E+02	-2.260553E+03
	5	1.986270E+02	-1.857209E+00	1.967698E+02
	7	1.384870E+02	3.175497E+00	1.416625E+02
	9	-2.905171E+01	1.396617E-01	-2.891205E+01
	11	-2.732598E+01	-7.702060E-02	-2.740300E+01
	13	6.318222E+00	-7.144609E-03	6.311077E+00
	15	7.369370E+00	3.404545E-03	7.372775E+00
	17	-1.628493E+00	4.524149E-04	-1.628040E+00
	19	-2.319870E+00	-2.475529E-04	-2.320118E+00
	21	4.555563E-01	-3.682432E-05	4.555195E-01
	23	8.004513E-01	2.755759E-05	8.004789E-01
	25	-1.297952E-01	3.721138E-06	-1.297915E-01
	27	-2.933016E-01	-4.375667E-06	-2.933060E-01
	29	3.123780E-02	-4.599844E-07	3.123734E-02
	31	1.116536E-01	9.283014E-07	1.116546E-01
	33	7.152277E-03	1.336452E-07	7.152411E-03
	35	-4.158784E-02	-2.554364E-07	-4.158809E-02

Although, in this example, the potential functions VI for the magnetization extrapolate to give a field strength of approximately 3416.14 amp.T/cm on the axis at the right-hand symmetry plane (i.e. a strength some 98.4 percent of the theoretical value $\frac{10000}{2}\left(\frac{10}{12}\right)^2 = 3472.222\ldots$), the Fourier analyses of the <u>total</u> potential in that symmetry plane suggest a field strength $\sim$ 8472.8 that is within one part in 10^4 of the theoretical value (8472.222...) for the deep interior of a very long dipole magnet of this type.

For use in the dynamics program "FLITE" (to be stored in Library JACKSON), <u>field components</u> (evaluated by the Sub-routine BEECYL associated with that Program) will be required. Tests of field components, evaluated by that Sub-routine in the neighborhood of Z = 25.0, r = 5.0, and $\emptyset$ = 32.5 degrees, have been made (i) with respect to their agreement with numerical (finite-difference) derivatives of the potential function $V^{(T)} = V^{(Fe)}(I,J,K) + V^{(current)}(Z_p,r_p,\emptyset_p)$, (ii) by forming the components of the curl of the total field (by finite-difference approximations), and (iii) by evaluating the divergence (by finite-difference approximations) of the total field.

In all cases, the results appeared concordant to a relative accuracy of 3×10^{-4}, and in many cases to a considerably more precise accuracy.

For future work (e.g., in dynamical applications) it appears convenient to develop either V^{Iron} or V^{Total} in a Fourier-Bessel series, rather than rely on interpolated derivatives (with their attendant lack of smoothness) for the <u>fields</u>. Because the "<u>direct</u>" fields of the prescribed current distribution are explicitly calculable by integration, it may be most appropriate to employ a finite Fourier-Bessel series only for representation of the (smoother) potential function VI that characterizes the field (as + grad VI) arising from the induced magnetization of the iron.

Because the boundary conditions imposed on VI are such that

$\partial(VI)/\partial Z$ has values that are close to zero at the boundaries ZLEFT, ZRITE (corresponding, conceptually, to $I = \frac{1}{2}$ and $I = IMAXR + \frac{1}{2}$), one might infer that the Fourier-Bessel development of VI might just employ terms that include factors of the form $\cos\left(M \frac{Z-ZLEFT}{ZRITE-ZLEFT} \pi\right) = \cos\left(M \frac{I-0.5}{IMAXR} \pi\right)$. In attempting to take some recognition of the small values of $\partial V/\partial t$ that are imposed on VI during the relaxation process, however, it appears desirable to include in its Fourier-Bessel representation some recognition of the quantities BL and BR, by the inclusion of terms that depend only on the combination $\frac{1}{2}(BL + BR)$ -- evaluated at the radius at which the Fourier-Bessel development is undertaken -- and that contribute only to the fundamental Fourier component of the field. [It may be noted that the distinction between the values of BL and of BR will vanish in circumstances such that the transition point for the current (ICURT) is midway between the two assumed symmetry planes -- i.e., if $ICURT = \frac{1}{2}(IMAXR + 1)$.]

We thus undertake to develop the potential function VI, that characterizes the field arising from magnetization of the iron, in the form

$$VI = \sum_{L=1}^{KMAX} G(JL)\cdot(I-ICURT)\cdot J\cdot \sin(n_H \phi_K)$$

$$+\sum_{L=1}^{KMAX} \left[D_\phi(L) J^{n_H} + \sum_{m=1}^{MM1} D(M,L) I_{n_H}\left(M \frac{J}{IMAXR} \pi\right) \cos\left(M \frac{I-0.5}{IMAXR} \pi\right)\right] \sin(n_H \phi_K),$$

with the coefficients evaluated at some suitable value of J within the dynamical range of interest and in which

$$n_H = L + L - 1,$$
$$MM1 = IMAXR - 1,$$

and the coefficients G(J,L) are such as to give the proper average values of $\Delta(VI)$ imposed on the function VI at the left-hand and right-hand symmetry planes at the radius defined by the index J (that characterizes the radius at which the Fourier-Bessel expansion is to be undertaken). In order that the supplemental terms shall be

harmonic (i.e. satisfy $\nabla^2 V = 0$), we shall, in practice, employ only coefficients G(J,L) for which L = 1.

Since, at any particular selected J, BL and BR represent $-\left\langle \frac{\partial}{\partial I} (VI) \right\rangle$ for $\Delta I = +1$ at $I \simeq 0$ or $I \cong$ IMAXR, we have:

$$G(J,L) = -\frac{1}{[KMAX]\cdot J} \sum_{K=1}^{KMAX} [BL(J,K)+BR(J,K)] \cdot \sin(n_H \emptyset_K),$$

where $n_H = L + L-1$ and $\emptyset_K = (K-0.5)*PHIFAC \left[\text{with } PHIFAC = \frac{\pi}{2(KMAX)}\right]$.

To evaluate the coefficients DØ(L), we write:

$$\sum_{K=1}^{KMAX} VI(I,J,K)\sin n_H \emptyset_K = \frac{KMAX}{2}\left\{\left[D\emptyset\ (L)J^{n_H} + \sum_{m=1}^{MM1} D(M,L) I_{n_H}\left(\frac{J}{IMAXR}\pi\right) \times \cos\left(M\frac{I-0.5}{IMAXR}\pi\right)\right] + G(J,L)\cdot (I-ICURT)\cdot J\right\}$$

and so obtain

$$\sum_{I=1}^{IMAXR} \sum_{K=1}^{KMAX} VI(I,J,K)\sin n_H \emptyset_K = \frac{IMAXR\cdot KMAX}{2} D\emptyset(L)\cdot J^{n_H} + \frac{KMAX}{2} G(J,L) \times \left[\sum_{I=1}^{IMAXR} (I-ICURT)\right] J.$$

Since

$$\sum_{I=1}^{IMAXR} (I-ICURT) = \frac{IMAXR(IMAXR+1)}{2} - ICURT\cdot IMAXR = \tfrac{1}{2} IMAXR\ (IMAXR+1-2 \times ICURT),$$

we find

$$D\emptyset(L) = \frac{2}{IMAXR\cdot KMAX} \frac{1}{J^{n_H}} \left\{ \sum_{I=1}^{IMAXR} \sum_{K=1}^{KMAX} V(I,J,K)\sin(n_H \emptyset_K) - \tfrac{1}{4} G(J,L) IMAXR(IMAXR+1.-2. \times ICURT) \times J\cdot KMAX \right\}.$$

Similarly, to evaluate the ceofficients D(M,L), we obtain

$$\sum_{I=1}^{IMAXR} \sum_{K=1}^{KMAX} VI(I,J,K)\cos\left(M \frac{I-0.5}{IMAXR} \pi\right)\sin n_H \phi_K$$

$$= \frac{IMAXR \cdot KMAX}{4.} D(M,L) I_{n_H}\left(M \frac{J}{IMAXR} \pi\right) + \frac{KMAX}{2} G(J,L)\left[\sum_{I=1}^{KMAXR} (I-ICURT) \times \cos\left(M \frac{I-0.5}{IMAXR} \pi\right)\right] J$$

and thus find

$$D(M,L) = \frac{4}{IMAXR \cdot KMAX} \frac{1}{I_{n_H}\left(M \frac{J}{IMAXR} \pi\right)} \left\{ \sum_{I=1}^{IMAXR} \sum_{K=1}^{KMAX} VI(I,J,K) \times \cos\left(M \frac{I-0.5}{IMAXR} \pi\right) \cdot \sin n_H \phi_K - \tfrac{1}{2} G(J,L)\left[\sum_{I=1}^{IMAXR} (I-ICURT) \times \cos\left(M \frac{I-0.5}{IMAXR} \pi\right)\right] J \cdot KMAX \right\}$$

$$= \frac{2}{IMAXR \cdot KMAX} \frac{1}{I_{n_H}\left(M \frac{J}{IMAXR} \pi\right)} \left\{ \sum_{I=1}^{IMAXR} \sum_{K=1}^{KMAX} VI(I,J,K) \times \left[\sin\left(M \frac{I-0.5}{IMAXR} \pi + n_H \phi_K\right) - \sin\left(M \frac{I-0.5}{IMAXR} \pi - n_H \phi_K\right)\right] - G(J,L)\left[\sum_{I=1}^{IMAXR} (I-ICURT)\cos\left(M \frac{I-0.5}{IMAXR} \pi\right)\right] J \cdot KMAX \right\} .$$

The Fourier-Bessel series developed for the function VI gives, as it should, values that coincide exactly with those of the function itself, when summed for a radius-value corresponding to the index (J=JEVAL) at which the coefficients were evaluated. For other radii the values obtained from the series do not differ greatly from the original values of VI, the values of the series differ very little when all L-values are used in the G(J,L) or (alternately, as we shall adopt) when only G-values with L=1 are actually employed, and the series function appears to provide a smooth transition between mesh points.

The foregoing features may be illustrated by (and indeed were inferred from) tests made with a mesh in which

I-INDEX AT CENTER OF CURRENT TRANSITION = 45

IEND = 89 for SMALL TUBE and 18 for LARGE TUBE

JMAX = 11 within SMALL TUBE and 18 ADDITIONAL WITHIN LARGE TUBE

KMAX = 18 (for QUADRANT)

A = 10.0 cm [scale-factor = 1 cm/mesh unit]

J_0 = 10,000 A/cm α = 45 deg.

CURRENT TRANSITION CENTERED AT Z = 0.

"MIRROR PLANES" at Z = ±44.5

TUBE RADIUS TRANSITION AT Z = -26.0 cm.

TUBE RADII: 30.0 and 12.0 cm.

M (first sub-division factor for normal rumberg integration) = 64.

At Z = 44.0, R = 1.0, Ø = 87.5 deg (I = 89, J = 1, K = 18), the value of VI obtained by relaxation is VI(89, 1, 18) = 3412.35307. From series summation we find (for JEVAL = 7):

<u>No</u> introduction of G(J,L) ---------- 3405.08334

G(J,L) employed with <u>all</u> L (L = 1, 2, ... 18)----- 3410.20015

G(J,L) employed only with L = 1 ---------- 3410.17694

[For comparison, the total potential at this point (including the "direct" potential function of the current, and hence giving approximately the total radial derivative in A turns/cm) is of the order of 8.46 x 10^3 (at Φ = 87½ deg).]

The variation of the series-sum with radius also can be illustrated, by the Table below:

TABLE III

Sum of Fourier-Bessel Series for Z = 44.0 (I = 89) and Ø = 87.5 Deg. (K=18)

R	← JEVAL = 7 →			← JEVAL=6 →	VI
	No (G,JL)	All G(J,L)	G(J,1) only	G(J,1) only	(from relaxation)
1	3405.08334	3410.20015	3410.17694	3410.38169	3412.35307
2	6810.73276	6820.52203	6820.47842	6820.88514	6823.35980
3	10217.5598	10231.0851	10231.0267	10231.6296	10234.0021
4	13626.2894	13642.0041	13641.9395	13642.7289	13644.5950
5	17037.8969	17053.3862	17053.3270	17054.2883	17055.3405
6	20453.9661	20465.3270	20465.2880	20466.3980	20466.3980
7	23877.9041	23877.9041	23877.9041	23879.1204	23877.9041
8	27320.5555	27291.1600	27291.2238	27292.4397	27289.9811
9	30835.7782	30705.0363	30705.2061	30705.9549	30702.7405

It appears that the use of "G(J,1)ONLY" -- thus retaining the harmonic character of the development -- will be satisfactory, and that a development radius (specified by JEVAL) that is some 2/3 of the current-winding radius (i.e., JEVAL ≅ 7 in this example) should be suitable.

With respect to axial variations near the "symmetry plane" at Z = 44.5, we may record the following values from runs in which the series development employed G(J,1)ONLY, with JEVAL = 7. The values tabulated are for R = 5.0, Ø = 87.5 deg. and for R = 7.0, 87.5 deg.

R	Z	41.0	42.0	43.0	44.0
	V(SERIES)	17013.8773	17027.8592	17040.9948	17053.3270
5.	V(CURRENT)	25309.5938	25295.6312	25282.4781	25270.0781
	V(TOTAL)	42323.4711	42323.4904	42323.4729	42323.4051
	V(SERIES)	23823.1979	23842.5389	23860.7475	23877.9041
7.	V(CURRENT)	25429.8004	35410.5032	35392.3217	35375.1781
	V(TOTAL)	59252.9983	59253.0421	59253.0692	59253.0821 [a]

[a] Rounding

The values of V(TOTAL) are thus seen to maintain a reasonable constancy as Z approaches the boundary-plane value of 44.5 cm.

Finally, with respect to the limiting value of the field strength, we expect that deep within a dipole magnet, of the current-strength and dimensions employed in the present illustration,

$$H_y = \frac{10{,}000}{2}\left[1 + \left(\frac{10}{12}\right)^2\right] = 8472.222\ldots$$

and that at $\phi = 87\frac{1}{2}$ deg.

$$H_r = \frac{\partial V}{\partial r} = H_y \sin 87.5 = (8472.222\ldots)(0.9990482216^{-}) = 8464.15854_4$$

Using this fundamental component of G(J,L) only, with JEVAL = 7, when evaluating the series, we find (at Z = 44.0):

R = 7.	V(I,J,K) =	23877.9041	V(SERIES) =	23877.9041
	V(CURRENT) =	35375.1781		35375.1781
	V(TOTAL) =	59253.0821 [a]		59253.0822
R = 2.		6823.35980		6820.47842
		10108.7713		10108.7713
		16932.1311		16929.2497
R = 1.		3412.35307		3410.17694
		5054.43878		5054.43878
		8466.79185		8464.61572
Average H_r, from R = 7;			8464.7260	
Extrapolated H_r near R = 0;		8467.03		8464.61

[a] Rounded.

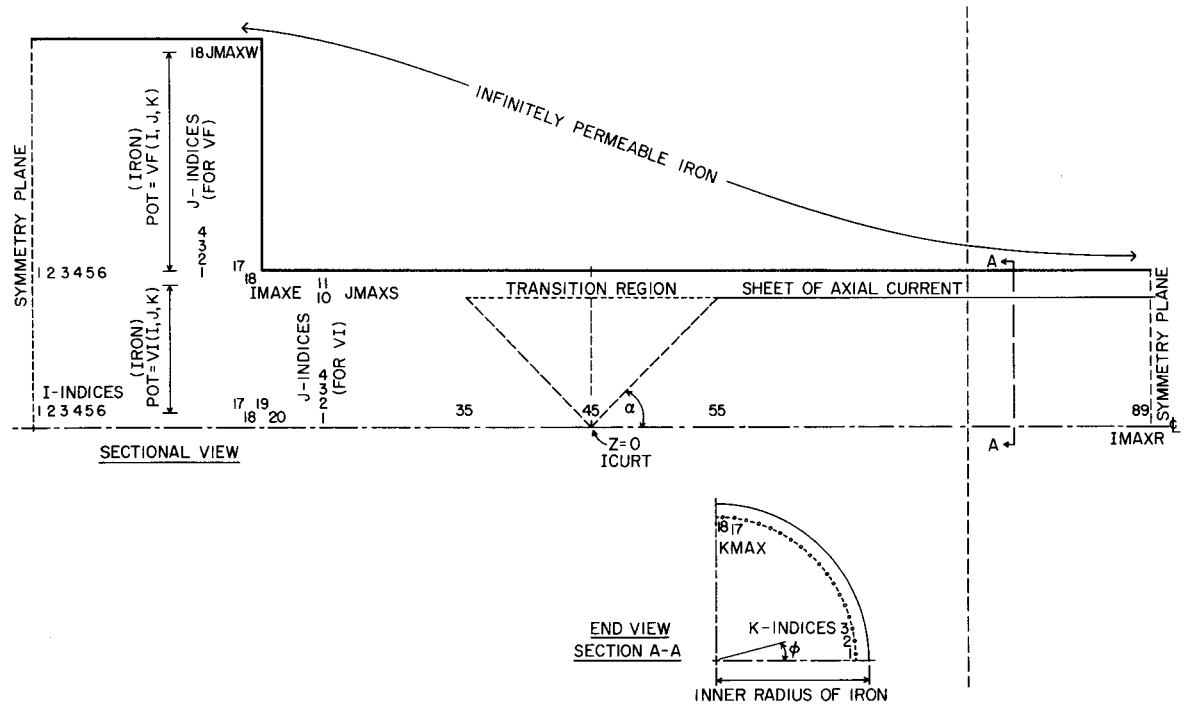

Fig. 2. Details for Cylindrical Boundary Computation.

The field-component strength H_r, so estimated, thus appears to differ from the theoretical deep-dipole value by an amount that, to an order of magnitude, is $\sim 1/10^4$.

SHIELDING CRITERIA AND DESIGN CONSIDERATIONS

S. J. Lindenbaum
Brookhaven National Laboratory
and
City University of New York

The general design criterion for design of the shield[1] was that in the worst case of a fault where all protons in a ring $\sim 10^{15}$ interacted within a small region (i.e. approximately a point source), the dose to an individual anywhere outside the shielding due to hadrons and muons should not exceed 100 mrem, which is the weekly dose limit for radiation workers. One would depend on radiation monitors to prevent subsequent operation of the accelerator (until reset) whenever a radiation spill of sizeable magnitude occurred.

The dose at the site boundary due to such a fault is expected to be < 0.1 mrem. The skyshine dose at the site boundary for such a fault is expected to be $< 10^{-3}$ mrem.

It should be noted that present radiation regulation standards* suggest that off site dose be made as small as practicable. This also applies for nonradiation workers. The order of 5 mrem per year is a suggested working goal. Even for workers on the BNL site if one expects that the integrated dose per year could exceed 500 mrem the present practice is to require that they carry radiation badges and be radiation monitored personnel. When one considers the full implications of the above, our basic criteria are considered reasonable, but not excessively cautious.

These criteria lead to about 6 m of earth cover over the accelerator and a lateral extension of earth cover sufficient to reduce the muons to the appropriate level.

---

* Consultations with the Health Physics and Safety Division Head in regard to the above radiation standards were most valuable.

1. BNL 16716 (ISABELLE, May 1972); BNL 18891 (ISABELLE, May 1974); BNL 20161 (ISABELLE, June 1975).

Designers of pipe inserts, access doors to experimental areas, etc., should be aware that, if done naively, they may have drastic impacts on shielding effectiveness. Final design should use methods that have proved to be satisfactory at existing accelerators.

DISPLACEMENT DAMAGE FOR 300 GeV PROTONS

Phillip Sanger*

Fermi National Accelerator Laboratory

The long term radiation effects for high energy particles is an area of investigation for the most part ignored in accelerator magnet design. This report intends to show that the damage can be substantial but at the same time can be dealt with easily by proper accelerator operation.

Since extensive data on the damaging effects of neutrons and low energy ($E < 10$ MeV) charged particles exists,[1] it would be helpful to determine which type of radiation most nearly represents the probable defect configuration created by GeV protons. It is believed that due to nonelastic events, the primary knock-on atom (PKA) will have sufficient energy to produce zones of high displacement density (the mean defect separation ~1 lattice spacing) called displacement spikes. This type of defect configuration is also produced by fast neutrons. Low energy charged particle irradiation results in predominantly single well-separated defects due to the forward peaked behavior of Rutherford scattering. For this reason fast neutron damage data has been chosen as most representative of GeV proton damage based on present knowledge.

---

*Work supported by Universities Research Association and the University of Wisconsin.

1. Comprehensive reviews of this work are given in J. A. Corbett, "Electron Radiation Damage in Semiconductors and Metals", Solid State Physics, Advances in Research and Applications, Vol. 7 (1966), W. Schilling, G. Burger, K. Isebeck, and H. Wenzl, "Annealing States in the Electrical Resistivity of Irradiated FCC Metals", Vacancies and Interstitials in Metals, edited by A. Seeger, D. Schumacher, W. Schilling, and J. Diehl (Wiley, New York, 1970), H. Ullmaier, "Irradiation Effect in BCC Type II Superconductors", Proc. Int. Conf. on Defects and Defect Clusters in BCC Metals and Their Alloys, Gaithersburg, Maryland, 1973.

However, the problem of establishing the amount of damage created by GeV protons relative to fast neutrons must be considered. This comparison will be made using the displacement cross section, i.e. the probability that an event will occur imparting sufficient energy to a lattice atom to dislodge it from its equilibrium lattice position. A nonelastic event from a proton on copper yields a broad spectrum of residual nuclei and energies.[2] An approximate displacement cross section can be readily obtained by assuming one particle as characteristic of this spectrum.

A nuclei of Z = 18, A = 38, and E = 10 MeV has been chosen as this particle and is treated by Lindhard theory,[3-5] as recommended by Doran, et al[6] to determine the displacements created. For a displacement energy of 42 eV, the displacement cross section would be 5600 barns which can be compared with 500, 1580, 1890, 2120, barns for 1, 5, 10, 15 MeV neutron respectively.

The question may be raised concerning the sensitivity of the above result to the choice of the energy and mass of the particle representative of the actual spectrum. The damage energy T_{dam} varies slowly with energy in the range 5 to 50 MeV. This effect is due to the dominance of the electronic energy loss which cannot

---

2. R. G. Alsmiller, unpublished data.

3. J. Lindhard, M. Scharff and H. E. Schiott, "Range Concepts and Heavy Ions Ranges", Mat. Fys. Medd. Dan. Vid. Selsk., 33(14), 1 (1963).

4. J. Lindhard, V. Nielsen, M. Scharff and P. V. Thompsen, "Integral Equations Governing Radiation Effects", Mat. Fys. Medd. Dan. Vid. Selsk., 33(10), 1 (1963).

5. M. T. Robinson, "The Energy Depdendence of Neutron Radiation Damage in Solids", B.N.E.S. Nucl. Fusion Reactor Conf., Culham England, p. 364 (Sept. 1969).

6. D. G. Doran, J. R. Beeler, N. D. Dudey, and M. J. Fluss, "Report of the Working Group on Displacement Models and Procedures for Damage Calculations", HEDL Rept. to be published.

contribute to lattice displacements. Nuclear energy loss is important in the low energy region at the end of the particle range. The damage energy is the integral of the nuclear energy loss and therefore remains insensitive to changes in energy. The mass dependence of T_{dam} at a constant initial energy is strong, increasing with increasing mass. The characteristic particle is in the middle of the particle spectrum and therefore represents some average mass.

The neutron data examining the change in electrical resistance[7] and critical current[8] of the NbTi composite superconductor can be approximately applied to 300 GeV protons through the ratio of the displacement cross sections. The displacements per atom were calculated from a typical reactor spectrum using 9×10^{-22} dpa/ncm^2. Figure 1 uses this correlation to plot both resistivity changes and critical current deterioration. The upper scale is given in terms of hadrons/cm^2, which should include the effects of hadronic cascade. Typical buildup factors are on the order of 10^2.

One would like to determine an order of magnitude time scale on which these property changes would occur. From the following section on radiation heating, an upper limit for the "fast" particle flux can be set equivalent to 3×10^9 protons/cm^2 sec (using 2 MeV·cm^2/gm), or roughly 1×10^{-3} joules/gm sec. An operational safety factor of 10% of the critical quenching heat load is now assumed. A buildup factor of 100 would be typical and accordingly reduces the primary proton flux to 3×10^6 protons/cm^2/sec. Let one further assume this "fast" proton loss occurs

---

7. J. A. Horak and T. H. Blewitt, "Fast Neutron Irradiation Induced Resistivity in Metals", Phys. Status Solidi, 9, 721 (1972).

8. M. Soell, Report IPP 4/104 of the Max-Planck Institut für Plasmaphysik, Garching, Germany, Oct. 1972.

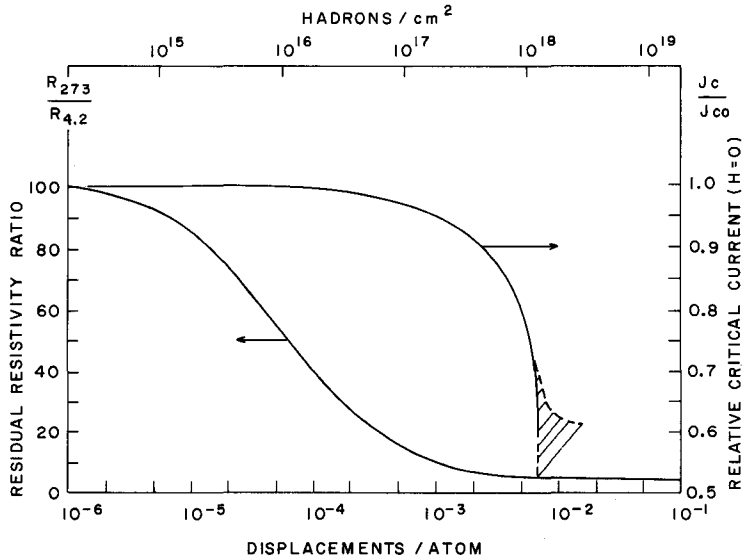

Fig. 1. Resistivity and critical current changes.

once per second for a year, i.e. 3×10^7 radiation pulses. These considerations lead to 10^{16} hadron/cm^2 in one year or a twofold increase of resistance with no appreciable loss in critical current. This increase in resistivity can affect the usable current of the conductor by reducing the stabilizing role of the copper. In fact, this effect has been experimentally seen but not fully analyzed in neutron irradiations at 77 K.[9]

Fortunately this resistivity increase can be partially annealed out at room temperature. Defects created at 4.2 K are "frozen" into the matrix. At higher temperatures the defects become mobile and tend to annihilate each other. This resistivity recovery can reach ~80% at room temperature.[10] The recovery of the critical current proceeds in a similar fashion.[11] Note that it is not presently known how the residual resistivity behaves with successive anneals.

The conclusion can be drawn from this extreme exercise that displacement damage occurs on a long time scale such that machine operation is not impaired. Furthermore, when damage does occur, it can in large part be removed provided periods of complete warmup are provided. This conclusion is only valid within the framework of the assumptions contained in this paper.

---

9. M. Couach, J. Doulat, E. Bonjour, "Effects of Fast Neutron Irradiation at Low Temperature on the Properties of NbTi Superconductor Wires", Supercond. Conf., Oakbrook, 1974.

10. J. Horak and T. Blewitt, "Isochronal Recovery of Fast Neutron Irradiated Metals,", J. Nucl. Mat. (to be published).

11. M. Soell, C. A. M. Van de Klein, H. Bauer and G. Vogl, "The Influence of Low Temperature Neutron Irradiation on Super-Conducting Magnet System for Fusion Reactors", Appl. Supercon. Conf., Oakbrook, 1974.

RADIATION HEATING: EXPERIENCE AND PROJECTIONS

G. Danby
Brookhaven National Laboratory

I. Introduction

One feature of high energy storage rings is that the energy stored in each beam is sufficient to produce considerable damage in the rare event of an accidental rapid beam dump into a concentrated area. Indeed this has happened at the ISR, resulting in a ruptured vacuum system. In ISABELLE 22 MJ of energy will be stored in each beam, assuming 7×10^{14} protons at 200 GeV. For perspective, this would be about equivalent to the energy required to melt 100 lbs of copper which is initially at room temperature. In ISABELLE great care will be taken to minimize beam loss in the machine and to efficiently extract the beam at the end of a running cycle or when a malfunction is indicated. In contrast to very high energy accelerators, storage ring operation provides the possibility of routinely deaccelerating the beam back down to low energy prior to extraction, if this proves desirable.

Superconductivity adds an additional element to the beam control problem. Relatively small imposed thermal energy can raise portions of superconducting coils to a temperature at which magnets go normal, or "quench". It is a basic property of superconductor that its current carrying capacity decreases as temperature rises. Furthermore, heat capacities are very small at the low temperatures required to sustain superconductivity.

Of necessity, in the design of high current density magnets a large fraction of the current carrying capability of the conductor must be utilized to reach peak field at the standard operating temperature. Thus, the thermal reserve of the superconducting magnets decreases rapidly as the magnetic field rises. Furthermore, typical radiation patterns due to lost protons in the machine will

result in fully developed cascades of secondaries which may in part impinge on the coils. Thus peak energy density deposition per lost proton will increase approximately proportional to the rising energy, or field.

What is the impact then of the superconducting magnets? In addition to designing the machine for very low levels of internal proton loss, which is good practice in any case, great care is being taken with extraction septum magnet and beam scraping systems to provide energy absorbers to screen and protect the magnet coils. However, at the present advanced state of superconducting magnet development and of the ISABELLE Program, it is generally agreed that it is necessary to have more detailed data on radiation heating effects.

II. Experience

There has been only very limited experience with superconducting magnet systems operating in primary proton beams, much of this at BNL. The experience to date was outlined by speakers from various laboratories, and is summarized below.

1. Saclay (Bronca and Perot)

A superconducting quadrupole doublet has been used extensively in a pion beam of 2 GeV/c at the Synchrotron "SATURNE". Details of the construction of this device have been published.[1] These are given in Table I.

---

1. G. Bronca, J. Hamelin, J. Neel, J. Parain, M. Renard, Proc. of 1972 Applied Superconductivity Conference, Annapolis, Maryland, p. 288.

TABLE I

Parameters	Unit 1	Unit 2
Warm bore diameter	20 cm	30 cm
Magnet length	68 cm	67 cm
Design gradient	35 T/m	23 T/m
Stored energy	0.67 MJ	0.77 MJ
Design current	1200 A	1200 A
B_{max} in coil	5 T	5 T
Conductor short sample	1940 to 2150 A at 5.7 T	

Operating experience with this magnet has been described.[2] After a prolonged secondary beam run an exposure to primary protons was made as a test of sensitivity to radiation heating. The 3 GeV proton beam with 1.5×10^{11} ppp was extracted every 3 seconds with a beam spill time of 100 to 200 ms. The proton beam cross section of 7 cm^2 was deflected on to the internal high field region of the coils. The first quadrupole current was raised, and quenched at 850 A, resulting in a coil short. The second quadrupole was then raised as high as 600 A without a quench. (The damaged magnet was then repaired and again used on a secondary beam line.)

2. Argonne (Cho and Wang)

A superconducting dipole magnet, designed for a ZGS Flat Top Stretcher Ring,[3] has been tested for radiation heat sensitivity in a 12 GeV external beam of several hundred milliseconds spill duration and 4.6 sec repetition rate. This dipole has a 10 cm winding bore, and a 7.6 cm useful aperture. Its length is 36 in. The potted coil has many turns and operates at 190 A at the design field of 30 kG. The short sample rating of the conductor was > 300 A at 40 kG.

---

2. J. Hamelin, Saclay Report, Department Saturne SEDAP/75 -31, (1975).

3. J. R. Purcell, S. T. Wang, R. C. Niemann, K. F. Mataya, H. Ludwig, J. A. Biggs, IEEE Trans. Mag., MAG-11, No.2,455(1975)

Beam intensities up to the maximum obtainable, 2.7×10^{11} protons per pulse at 12 GeV, when properly focussed could pass through the magnet with no evident effect on magnet performance or helium gas boil-off.

The magnet immediately quenched when a single pulse of 7×10^9 protons focussed to $\sim 1/2$ in diameter was shot through the coil. This occurred at 164 A.

Five successive pulses of 5×10^9 protons were sent through the coil at 40 A without quenching. Two or three minutes later the boiloff had increased by 0.4 ℓ/sec. Similar tests were performed at 75 A and 100 A* without quenching.

The beam was defocused to 6 in diameter and partially impinged on the superconducting coil. At 100 A, beams as high as 2.5×10^{11} were used without quenching. The magnet current was increased to 140 A and an attempt to repeat this test was made. It was found that the heating effect takes at least five to six minutes to reach equilibrium. At 2.7×10^{11} protons per pulse, the magnet quenched after running for quite a few minutes. The boil-off of helium was increased by about 2 ℓ/sec due to the beam heating during this time.

3. <u>FNAL (Edwards, Sanger, Strauss, Sutter)</u>

A pair of "Dual Dipoles",[4] each 74 cm long constructed on a 3.5 cm diameter bore tube, have been powered in series opposition and tested for radiation heat sensitivity[5] in the 300 GeV/c extracted primary beam. The short sample characteristic of the moderate performance conductor used in these magnets was defined as 1850 A at

---

* $5 \times 5 \times 10^9$ protons at 12 GeV/c contains an integrated beam energy of 48 joule. Helium boil-off of 0.4 ℓ/sec corresponds to 1.6 watts.

4. B. P. Strauss, D. F. Sutter, Fermilab Tech. Memo, TM-456-0248. Dec. 1973.

5. C. Rode, P. Garin, R. Norton, IEEE Trans. Nucl. Sc. Vol. <u>NS-22</u>, No. 3, June 1975, p. 1185.

27 kG. These early models are of the characteristic FNAL design with warm iron.

The radiation exposure was performed by moving a Cu wedge located 5 feet upstream of the first magnet into the proton beam. Both fast and slow spills were used, all with a 6 sec repetition rate and 300 GeV/c protons. The quench threshold was expressed in terms of the product of magnet current I (A), protons/pulse Q (in units of 10^{12}) and target thickness T (in mils).

For fast spill (20 μ sec to 1 rms)

$$IQT = 4 \times 10^4$$

For slow spill (1 sec)

$$IQT \leq 5 \times 10^5$$

As an illustrative example, consider I = 1000 A and Q = 1×10^{12} protons. Then T = 40 mils for fast spill or ≤ 500 mils for slow spill

4. BNL

The radiation heating experience which has been gained with the 8° magnet[6,7] was described by BNL personnel. This bending magnet operates as a part of the extracted fast proton beam to the North Experimental Area at the AGS. Quenching has on occasion occurred due to malfunction or error in normal beam operation. In addition, by inserting targets of different materials and thicknesses at two upstream locations, considerable information on beam heating and quench thresholds has been obtained.

The magnet consists of 2 units electrically connected in series. Each unit is ~ 2 m long with a 10 cm winding bore and a 7.3 cm i.d. warm beam pipe. The short sample rating of the conductor used was

---

6. J. Allinger, G. Danby, B. DeVito, H. Foelsche, S. Hsieh, J. Jackson, A. Prodell, IX Inter. Conf. on H.E. Accel., SLAC, (1974) p.198.

7. J. Allinger, G. Danby, B. DeVito, S. Hsieh, J. Jackson, and A. Prodell, IEEE Trans. Mag. 11, 467 (1975).

at 27 kG. These early models are of the characteristic FNAL design with a maximum field in the coil region of ~ 40 kG. At operating temperature this corresponds to about 45% of short sample. The enthalpy increase required to carry the coil temperature up to 100% of short sample, which should occur at slightly over 6 K, is 0.3 mJ/g of conductor or a total of 32 joules in each magnet unit.

This external beam has been operated periodically for the last 2 years. Intensities of up to 6×10^{12} protons at 28.5 GeV/c, or ~ 30 kJ of beam energy per pulse of 3 μsec duration, pass routinely through the magnet aperture. Because of sagitta, the beam center is less than 2 cm from the vacuum tube at either end and the center of each magnet unit. The magnet has operated without quenching during major malfunctions of other beam transport components. A tripout of the upstream string of quadrupoles resulted in losses of several hundred joules per pulse extending over a series of pulses. Operation also continued with several beam pulses striking one jaw of a collimator located ~ 6 m upstream. About one-half of the beam was intercepted on the collimator. The magnets can be quenched by a gross missteering of the beam which has occurred on the order of a dozen times over the lifetime of the beam.

During two different study periods, the magnet was exposed to radiation from Cu targets varying in thickness from 1/8 in. to 2 in. These targets were located about 2 m upstream from the magnets. It was found that 2 in.of Cu and 1×10^{12} protons per pulse was required to quench the magnet, or any equal product of protons per pulse (N) times target thickness (L). Furthermore, if the magnet survives a single heating pulse it can survive a prolonged series at the AGS repetition rate (i.e. ~ 1.5 to 2.5 sec). This indicates that the thermal time constant is quite short for heat exchange within the coil.

The magnet system is itself quite an accurate calorimeter. When a train of radiation pulses is initiated, the rate of pressure increase in the dewar is initially proportional to the product N L

of protons per second times target length. This held true over the large range of heat loads that were tested.

Only after the order of a minute delay does the refrigeration system respond to the large change in heat input. The calibration can be determined quite accurately by powering heaters within the magnet dewars. Identical pressure rise rate responses can be produced with known power inputs. It was found that the Cu target quench threshold produces approximately 1 kJ per pulse heat load into the dewar. Since the coils are about 5% of the total cold weight, for uniform heating of the entire system the coils would receive $\sim$ 50 watts, slightly below the enthalpy limit of 64 watts.

It is clear that the coils receive much more than this. They are located at very small angles with respect to target production, and cascades will be strongly peaked in the coils. This radiation exposure has been simulated using Monte Carlo calculations with computer programs MAGKA and CYLKA.[8,9] These calculations, which do not include the effect of magnetic fields sweeping charged secondaries or the effect of sagitta agree quite well on the total heat load. They show mean coil temperatures higher than can sustain superconductivity on an enthalpy basis, and peak energy deposition of $\sim$ 3 mJ/gram. This is ten times the enthalpy limit.

In a further series of experiments, graphite, copper, and lead targets were compared at the 2 m upstream location. The total heat load per interacting proton per second, normalized to Cu was:

C	1.8
Cu	1.0
Pb	1.0

---

8. H. Schonbacher and M. Van de Voorde, CERN Technical Note, ISR-MA, Sept. 1973.

9. H. Schonbacher and M. Van de Voorde, CERN Rept. ISR-MA-CR-HS MVV/cb, Sept. 24, 1974.

The quench thresholds were found per 1×10^{12} incident protons per pulse:

$C = 0.38\ L_{coll}$

$Cu = 0.43$ "

$Pb = 0.59$ "

It was clear that the quench threshold was considerably higher for Pb, and also corresponds to $\sim$ 1400 joule per pulse total heat load.

Finally, to illuminate the impact of small angle quasielastic versus large angle production, Pb was tested at 2 m and 4 m upstream of the first magnet. If exposure of the upstream end of the magnet dominated, an inverse square law should hold and the threshold should be $\sim$ 4 times larger. If very small angle quasielastic exposure of the downstream end dominated, moving further away could increase the sensitivity.

The thresholds were almost the same: 3.2×10^{12} protons on 1 in. of Pb at 2 m and 3.1×10^{12} on 1 inch of Pb at 4 m. This indication of a mixed effect was confirmed by electromagnetic observation. For the 2 m target case, the front magnet unit quenched. For the 4 m location, the back unit quenched.

III. Discussion

The preliminary experiments described, which were performed at various laboratories, provided limited information on a multiple parameter problem. The magnets vary widely in conductor used, in methods of construction and cooling of the coil structure, and in the presence or absence of cold iron. Spill times also widely varied. The results do however provide a semi-quantitative "first look" at this question. To attempt to draw any detailed conclusions from these experiments was beyond the scope of the presentations and would have required further information. For the case of deliberately missteered primary proton beams incident on coils, a detailed knowledge of proton beam density distributions and angle of incidence on the coils inside the aperture are required for good

energy density predictions. For the case of targets inserted upstream of superconducting magnets, Monte Carlo calculations are available which use known production data to develop the cascades. However, geometrical simplifications must be made and the absence of sweeping magnetic fields and of sagitta introduced errors, most likely, and particularly, into the critical question of peak energy density in the coils. Both these techniques can be developed further and, where practical, experimental simplification to aid computations should be used in the planning stage.

The transient thermal response of a given magnet will depend on the enthalpy of the magnet coil materials. Also, since the enthalpy of the cryogen is relatively very large, questions such as transient nucleate boiling, etc., can play a major role. Both the magnitude and the time response of a thermal impulse will depend very strongly on details of construction.

Steady state heat transfer will eventually be reached. It too will be subject to structural details. The present experiments demonstrate large variation in heat absorption. In addition, large variations in thermal time constants were obtained: steady state conditions were established after delays ranging from seconds to minutes.

Experimental knowledge of unsteady state as well as steady state heat transfer of superconducting magnets must be enlarged. This should include radiation exposures of and computer cascade predictions of ISABELLE magnets. This understanding can also be augmented by more easily performed electrical simulation experiments on magnet models. The information obtained will aid in detailed iteration of the machine design.

THERMAL DESORPTION OF GASES FROM ALUMINUM ALLOY Al 6061, THEIR RATES AND ACTIVATION ENERGIES

H.J. Halama and J.C. Herrera
Brookhaven National Laboratory

I. Introduction

In large intersecting proton storage rings, tubular vacuum chambers several kilometers long must be maintained at a pressure of less than 10^{-11} Torr. In addition the residual gas molecules should have a low ionization cross section, i.e. their atomic number should be low. The pressure, in such a long tube, depends on the distance between pumps, the gas conductance, and the outgassing rate. Since the lengths and apertures are, in general, governed by other requirements such as magnet construction and cost, the outgassing rate of the metal from which the chamber is fabricated is the principal vacuum parameter and should, therefore, be as low as possible. Furthermore, the surface of the chamber should be free of adsorbed gas which will desorb when ionized residual gas molecules formed by the circulating beam bombard the wall of the vacuum envelope.[1]

The above conditions were satisfied at the CERN ISR by using a special stainless steel vacuum chamber[2] pumped by a large number of sputter-ion and titanium sublimation pumps.[3] Because aluminum has several interesting properties such as a low outgassing rate[4,5] and good electrical and thermal conductivity, we have undertaken studies

---

1. E. Fischer, Proc. 3rd All Union Conf. Charged Particle Accelerators, Moscow, 1972, 1, p. 101.
2. R. Calder and G. Lewin, Br. J. Appl. Phys. 18, 1459 (1967).
3. E. Fisher, J. Vac. Sci. Technol., 9, 1208 (1972).
4. T.H. Batzer and J.F. Ryan, Trans. 10th AVS Symp., McMillan New York (1963), p. 166.
5. G. Moraw and R. Dobrozemsky, Proc. 6th Intern. Vac. Cong., 1974 Japan J. Appl. Phys., Suppl. 2, Pt. 1, 1974, p. 261.

on long pipes made of the common aluminum alloy Al 6061 to see whether this material could be used for the vacuum chamber of the proposed proton storage accelerator facility, ISABELLE, at Brookhaven.[6] In this case the high electrical conductivity of the wall is an asset as far as beam stability is concerned, while the good thermal conductivity and lower cost of the aluminum decrease the price of the vacuum envelope and associated equipment. The smaller atomic number also reduces the radiation background in the experimental straight sections.

The measurements reported were performed on commercially available 2.6 m long aluminum tubes such as might be used in storage rings rather than small carefully prepared samples. Effective outgassing rates of 1×10^{-14} Torr liters/sec cm^2 at room temperature were obtained in tubes with two transitions. Hydrogen which diffuses from the bulk of the metal constituted 99% of the residual gas present in the chamber.

Since all commercially available UHV equipment uses stainless steel flanges we have also investigated the behavior of stainless steel to aluminum transitions up to $350^{\circ}C$ and have found them reliable. On the basis of these measurements, we have concluded that aluminum is well suited for the construction of a UHV system for storage rings.

II. Experimental Considerations

The gas coverage of a metal surface depends not only on the previous history but also on the residual pressure and the sticking coefficient. It is, therefore, important that low outgassing measurements be carried out at the lowest pressures attainable. Opening and closing of valves should be avoided. If valves are used, a long time should be allowed to reach equilibrium. The pumping speed of various components such as gauges should be determined and their contribution taken into account. In the measurements to be described,

---

6. H. Hahn and M. Plotkin, Ed., "A Proposal for Construction of a Proton-Proton Accelerator Facility ISABELLE", BNL Report 18891 (1974).

the above guidelines were followed. Both the gauge pumping and/or outgassing were measured in separate experiments. Two experimental setups yielding comparable results were used to obtain the data. The lowest net outgassing rates were measured at an operating pressure of 10^{-11} Torr.

1. Pressure Gradient Method

This method is based on the solution of the equation

$$C \frac{d^2p}{dx^2} = - Q$$

and tha apparatus is shown in Fig. 1. The effective outgassing rate Q [Torr $\ell sec^{-1} cm^{-2}$] for a given gas conductance per unit length C [$\ell msec^{-1}$] is then calculated to be

$$Q = \frac{2C\ (P_1 - P_o - P_G)}{LA}$$

where A(cm^2) is the total area and L(m) is the length of the tube. Pressures P_1 and P_o are read directly on the calibrated gauges G_1 and G_0 as shown in Fig. 1. The pressure correction, P_G, is calculated from the outgassing of the Helmer gauge G_1. This outgassing was determined in a separate experiment to be $\leqslant 1 \times 10^{-11}$ Torr liters sec^{-1}. It is significant only in measurements where $Q < 3 \times 10^{-14}$ Torr $\ell sec^{-1} cm^{-2}$. The mass spectrometer, MS, in this setup indicates only the relative abundance of various residual gas species in the tube.

2. Calibrated Conductance Method

This method (Fig. 2) is used most commonly in thermal desorption studies.[7] The effective outgassing rate Q

$$Q = \frac{C_o\ (P_1 - P_2)}{A}$$

where C_o[ℓsec^{-1}], is the conductance of a calibrated orifice (diameter = 6.38 mm), P_1 and P_2 are the pressures read on the Helmer

7. Y.E. Strausser, Report VR-51 1968 Varian, Palo Alto, California.

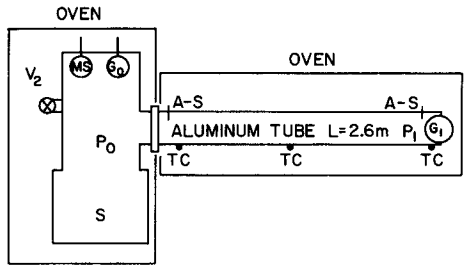

Fig. 1. Pressure gradient measuring setup. G_1 - Helmer gauge, G_o - modulated BA gauge; MS-mass spectrometer; S-pump, V_2-bakeable valve; TC-thermocouples; A-S-aluminum to stainless steel transitions.

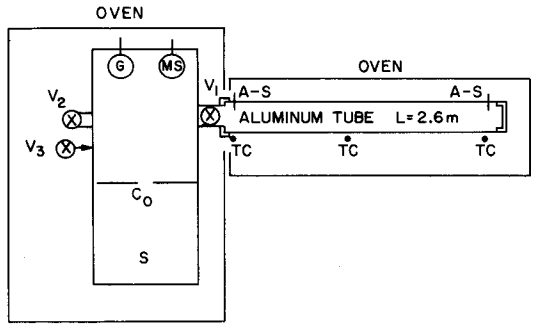

Fig. 2. Calibrated conductance setup. G-Helmer gauge; MS-mass spectrometer; Co-orifice; S-pump; V_1, V_2-bakeable valves; V_3-variable bleed valve.

gauge G with the valve V_1 open and closed respectively. The conductance C_o in these measurements was about 100 times smaller than the pumping speed S.

The pumps employed in both experimental setups were either an Ultec 400 ℓ/sec sputter-ion pump with a residual pressure of $\sim 1 \times 10^{-11}$ Torr or an 1000 ℓ/sec Excalibur liquid helium cryosorption pump capable of operating in 10^{-12} Torr range. Partial pressures were measured by 2 quadrupole mass spectrometers (Extranuclear and UTI). The apparatus was initially glow-discharged in argon and oxygen and baked-out to 300°C. Then after every exposure to atmospheric pressure it was rebaked to 250°C. The gauges and mass spectrometers were rigorously outgassed.

3. Calibration

The correctness of the data presented depends on the accuracy with which we can determine both total and partial pressures. The gauges and the mass spectrometers were therefore calibrated[8] using a leak with a known accuracy of ± 10% traceable to an NBS standard. During the measurements the gain of the multiplier in the UTI mass spectrometer was often checked and adjusted. The calibration of the UTI Quadrupole yielded the following sensitivities with the multiplier gain set to 10^5:

H_2	104 A $Torr^{-1}$,
N_2	73 A $Torr^{-1}$,
CO	70 A $Torr^{-1}$,
CO_2	49 A $Torr^{-1}$,

It must be stressed that most of the measurements were carried out in 10^{-11} Torr range where even with the greatest care and rigorous gauge outgassing the accuracy was estimated to be not better than ± 30%. Furthermore, since the accuracy decreases with the measured pressure, we quote a value of ± 50% on outgassing rates less

8. H.J. Halama and J.R. Aggus, J. Vac. Sci. Technol. 11, 333 (1974).

than 5×10^{-14} Torr ℓ/sec cm^2. The values, however, are likely to be too high rather than too low since the detection capability is around 5×10^{-15} Torr liters sec^{-1}cm^{-2}.

III. Measurements

The measurements were performed on 260 cm long tubes with a 7.2 cm diameter, manufactured from an aluminum alloy Al 6061-T4. These tubes were terminated on both ends by stainless steel to aluminum (Al 5038) transitions so that they could be attached to the stainless steel chamber and accept a vacuum gauge. The total area of $\sim$ 6000 cm^2 thus included about 150 cm^2 of stainless steel surface for which no correction was made. The tubes were subjected to the following surface treatments:

- A Degreasing in acetone with a methanol rinse,
- B Chemical polishing[9] in a solution of 805 ml water at 80°C. This solution was pumped through the tube for five minutes and followed by a water rinse and cleaning with a soft brush. Finally, it was rinsed with methanol.
- C Glow discharge[10] in pure argon at a pressure $2\text{-}3 \times 10^{-2}$ Torr for 30 minutes with a current density $5\text{-}10 \times 10^{-5}$ A/cm^2 and T = 20°C.
- C′ Same as C but T = 120°C.
- D Glow discharge in pure oxygen for 3 minutes, T = 20°C.
- D′ Same as D but T = 120°C.
- E Firing at 340°C for 4 hours in a vacuum furnace P = 5-10 P = $5\text{-}10 \times 10^{-4}$ Torr.

Both dc and ac glow discharge cleaning resulted in the same final outgassing. After each treatment the tubes were exposed to the lab atmosphere for a day before they were incorporated into the measuring apparatus in order to approximate the condition which will exist during the assembly of ISABELLE. After the tubes had reached

---

9. W.J. McG. Tegart, The Electrolytic and Chemical Polishing of Metals, Pergamon Press (1959)., p. 104.

10. R.P. Govier and G.M. McCracken, J. Vac. Sci. Technol. 7, 552 (1970).

room temperature and pressure equilibrium the outgassing rates were measured for three 24-hour bake-outs at 100°C, 150°C and 200°C. Total outgassing rates Q_t in nitrogen equivalent and the relative abundance of H_2, CO and CO_2 corrected for mass spectrometer sensitivity and pumping speeds are tabulated in Table I.

TABLE I

Outgassing rates Q_t in Torr liters $sec^{-1}cm^{-2}$ and residual gas composition in % at 20°C after 100, 150 and 200°C bake-outs.

Bake-out C	100	150				200			
Treatment	Q_t	Q_t	H_2		CO	Q_t	H_2	CO	CO_2
A	6×10^{-12}	1×10^{-12}				6×10^{-13}			
A,B	3×10^{-12}	7×10^{-13}	89	5	6	2×10^{-13}	92	4	4
A,B,C	5×10^{-13}	2×10^{-13}	97	1.5	1.5	6×10^{-14}	98	1	1
A,B,C,C′,	5×10^{-13}	6×10^{-14}	98	1	1	3×10^{-14}	99		
D′	4×10^{-13}	5×10^{-14}	99			1×10^{-14}	> 99		
	+ 8 hours	at 250 C				$< 1 \times 10^{-14}$	> 99		
B,E,C	8×10^{-13}	1×10^{-13}	97	1.5	1.5	5×10^{-14}	98	1	1
B,E,C,C′,	4×10^{-13}	7×10^{-14}	98	1	1	2×10^{-14}	> 99		
D′	4×10^{-13}	4×10^{-14}	99			$< 1 \times 10^{-14}$	> 99		

In addition to the outgassing rates at 20°C, the activation energies of the residual gases were obtained from their temperature dependence listed in Table II. When these values are plotted versus T^{-1} (T being absolute temperature) the activation energy E can be calculated from the slope of the curve according to

$$Q = Q_o \, e^{-E/RT}$$

where R is the gasconstant. In Fig. 3 a straight line fitted to

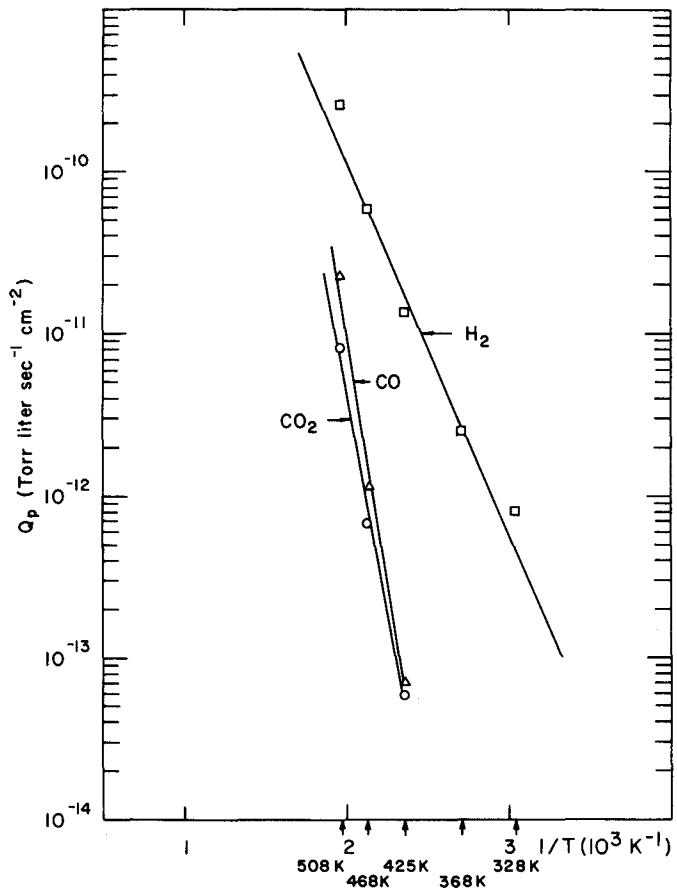

Fig. 3. Outgassing rate as a function of temperature.

experimental points by the least square method yields $E_{H_2} = 10.5 \pm 1.0$ k cal $mole^{-1}$ which is in good agreement with the heat of diffusion for H_2 in pure aluminum[11] (E_{H_2} = 9780 cal/mole).

TABLE II

Thermal desorption rate Q_p in Torr liters $sec^{-1} cm^{-2}$ corrected for individual gases at various temperatures. (Surface treatment: last entry in Table I)

Mass No.		55	95	150	195	235
2	H_2	8×10^{-13}	2.5×10^{-12}	1.3×10^{-11}	5.5×10^{-11}	2.7×10^{-10}
14					7×10^{-14}	8×10^{-13}
15					2×10^{-13}	2×10^{-12}
16					3×10^{-13}	5×10^{-12}
18	H_2O				1.1×10^{-13}	3.9×10^{-11}
28	CO			6.8×10^{-14}	1.1×10^{-12}	2.3×10^{-11}
40	Ar				4×10^{-13}	7×10^{-12}
44	CO_2			6×10^{-14}	6.5×10^{-13}	8×10^{-12}

Though only 3 points are available for CO and CO_2 the binding energy can also be obtained but with less accuracy. In these cases the least square fits yield

$$E_{CO} = 29 \pm 2 \text{ kcal mole}^{-1}$$

$$E_{CO_2} = 25 \pm 2 \text{ kcal mole}^{-1}$$

It should be pointed out that the tube had been baked-out at 200°C for approximately 30 hours before the data in Table II were taken. Inspection of Table II shows that as this temperature (200°C) is approached, gases adsorbed on the surface with activation energies larger than 25 kcal/mole begin to appear in appreciable quantities. Following the experiment detailed in Table II, the tube was heated

11. W. Eichenauer, K. Hattenbach and A. Pebler, Z. Metallkd, 52, 682 (1961).

to 320°C and the release of argon, implanted in the surface during the glow discharge cleaning, was monitored on the mass spectrometer. Maximum rate of release appeared at temperatures between 280 and 300°C. This can be compared with argon implanted in nickel.[12] Subsequent measurement at 235°C gave argon outgassing rate of 3×10^{-13} as compared with 7×10^{-12} Torr liters $cm^{-2}sec^{-1}$ at that temperature in Table II.

1. Transitions

The aluminum vacuum chamber in ISABELLE will be connected to stainless steel pumping stations through an aluminum to stainless steel transition. In addition to sputter ion and sublimation pumps the pumping stations will contain vacuum diagnostic equipment and valves. They will be bakeable to 300°C and the transitions must, therefore, withstand these temperatures. There are two types of transitions suitable for UHV applications, namely explosively bonded (DuPont) and friction welded (Japanese Oxygen Company). Because of the excellent performance they showed at SLAC[13] only the former was tested.

The transitions were subjected to the following tabulated tests:

Heat Cycle C	Times	Hours at High Temperature
20 - 200 - 20	10	100
20 - 250 - 20	3	10
20 - 300 - 20	4	24
20 - 350 - 20	1	2

12. D. Edwards, Jr., J. Vac. Technol. 12, 476 (1975).

13. SLAC Storage Ring Group, Proc. 8th Intern. Conf. on High Energy Accelerators, CERN, Geneva, 1971, p. 145.

Mass spectrometric measurements revealed no surprises and the transitions remained leak tight within the accuracy of our instrumentation which is better than $\sim 5 \times 10^{-13}$ Torr liter sec^{-1}. The aluminum alloy Al 5083 used in these transitions contains two high vapor pressure elements, i.e. 4 - 5% Mg and 0.25% Zn. A magnesium peak starts appearing in the spectrum at $T > 180^{\circ}C$ while zinc, M = 65, appears at $T > 270$. No aluminum peak was observed during this test. In the ISA the transitions will be made of the same alloy as the vacuum chamber, i.e. Al 6061 which contains only 1% of Mg.

IV. Conclusions

Based on the results of our investigation, we can draw the following conclusions:

1. Effective outgassing rates of 1×10^{-14} Torr liters sec^{-1} cm^{-2} can be achieved in vacuum systems using commercially available alloy 6061 with a rather simple surface treatment.

2. The most abundant residual gas in a baked-out Al system is hydrogen which difuses from the metal. This is consistent with the fact that H_2 is the only gas known to be appreciably soluble in either solid or molten aluminum.[14] Due to the insufficient sensitivity of the apparatus[15] which was 5×10^{-3} cm^3 (STP) g^{-1} for S/N = 1, no H_2 was detected in samples cut from the measured tubes. Because of the low permeation of H in Al,[16] outgassing rates below out measuring capability (5×10^{-15} Torr liters $sec^{-1}cm^{-2}$) can be achieved in Al vacuum systems using the surface treatment described.

3. Other gases such as H_2O, CO, CO_2 and hydrocarbons commonly found in vacuum systems seem to be adsorbed on the surface with a

---

14. K.R. van Horn, Ed. Aluminum, American Society for Metal, Metals Park, Ohio Vol. 1, p. 26 (1967).

15. Concentration of H_2 in Al was measured by Dr. R.W. Stoenner, Brookhaven National Laboratory.

continuous spectrum of binding energies. After a 200°C bake-out the binding energies of these gases are above 25 kcal/mol and their outgassing rates are negligible at room temperature.

4. Argon is implanted in the metal during glow discharge cleaning. Its release rate is negligible at room temperature and reaches a maximum between 280 and 300°C. The implanted argon can be rapidly depleted by heating to this temperature.

5. During the oxygen glow discharge the oxygen combines with aluminum to form aluminum oxides. Besides its cleaning effects, oxygen also probably removes carbon from the surface by forming CO and CO_2.

6. Aluminum to stainless steel transitions can be heated safely up to 300°C.

Acknowledgments

We would like to thank J.R. Aggus for his skillful handling of mechanical design problems and F. Timm for his able technical assistance throughout the experiments. We are grateful to Dr. Stoenner for measuring the hydrogen concentration in the aluminum samples.

ALTERNATIVE INTERPRETATION OF THE MEASUREMENTS OF SPECIFIC OUTGASSING RATES OF MATERIALS

J. P. Hobson

National Research Council
Ottawa, Canada

I. Introduction

In vacuum design it is often important to design for a particular value of the background pressure. The problem often presents itself in the form that it is found in ISABELLE, namely: If material X is used in a certain geometry what pumps are needed to give an upper limit of p_{max} at a certain point in the structure? The answer depends upon the properties of material X, in particular, upon a quantity called the specific outgassing rate q (Torr liters cm^{-2} sec^{-1}), which is the rate of desorption of gas per cm^2 of surface. Often assumed, as in the ISABELLE tests,[1] is that the rate of readsorption of gas onto the surface is zero. When this assumption is made the measured outgassing rate tends to be the net outgassing rate of the surface which is invariably lower than the true outgassing rate, and can lead to design errors. This general problem is illustrated in a simple example in which the calculations can all be made explicitly.

II. Simple Example of Outgassing Measurement

Consider a vessel of spherical form with surface area A made of the material X whose outgassing is to be measured so that a pump may later be added to the vessel to achieve p_{max} at its center. The test set-up contains a valve leading to a pump of known speed C_o liters sec^{-1}, small compared to the valve conductance and

1. H.J. Halama and J.C. Herrera, "Thermal Desorption of Gases from Aluminum Alloy Al 6061, Their Rates and Activation Energies," these Proc. p. 640.

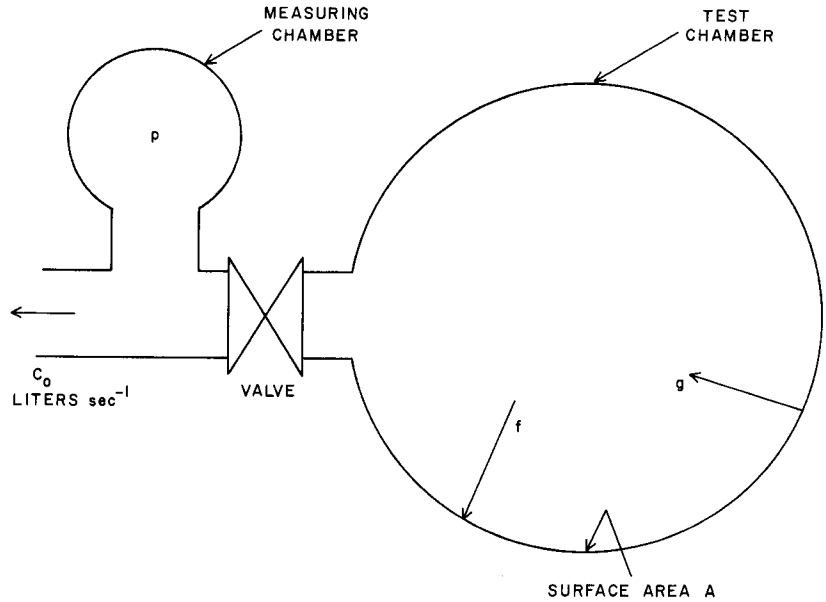

Fig. 1. Test chamber for measuring rate of gas flow from wall.

associated piping. A pressure gauge measures the pressure p as close to the vessel as possible. Two equilibrium measurements are made: p_1 with the valve open and p_2 with the valve closed.

$$p_2 = \frac{Q_M}{C_o} \text{ Torr} \tag{1}$$

where Q_M is the net outgassing load in the measuring chamber in Torr liters sec^{-1}

$$p_1 = \frac{Q_M + Q_T}{C_o} \text{ Torr} \tag{2}$$

Q_T is the gas passing from the test chamber through the valve to the measuring chamber and coming from the walls of the test chamber.

Elimination of Q_M from (1) and (2) yields

$$Q_T = C_o (p_1 - p_2) \text{ Torr liters sec}^{-1} \tag{3}$$

Equation (3) is used[1] to obtain the rate of gas flow coming from the walls of the test chamber and should be a valid measure. With the valve open the pressure in the test chamber is p_1 since it is measured. Thus there is a molecular flux striking the walls

$$f = \text{Molecular Flux} = \frac{10^3}{\sqrt{MT}} p_1 \text{ Torr liters sec}^{-1} \text{ cm}^{-2} \tag{4}$$

where M is the molecular weight of the gas (2 for ISABELLE since gas is H_2 and T = temperature in test chamber = 300 K for ISABELLE). Assume this flux has a sticking coefficient on the wall of s. Total number disappearing from the gas phase by this mechanism is

$$\text{Rate of Pumping} = fAs \text{ Torr liters sec}^{-1} \tag{5}$$

At equilibrium

$$Q_T = qA - fAs \text{ Torr liters sec}^{-1} \tag{6}$$

$$q = \frac{Q_T + fAs}{A} \text{ Torr liters sec}^{-1} \text{ cm}^{-2} \tag{7}$$

$$q = \frac{Q_T}{A} + \frac{10^3}{\sqrt{MT}} sp_1 \text{ Torr liters sec}^{-1} \text{ cm}^{-2} \tag{8}$$

This is the equation needed to calculate q from Q_T.

Consider various values of s.

(a) $s = 0$

$$q = \frac{Q_T}{A} \text{ Torr liters sec}^{-1} \text{ cm}^{-2} \tag{9}$$

This is the assumption made in Ref. 1 and the values of q so obtained (for a different geometry to be sure; discussed below) are quoted in Tables I and II of Ref. 1.

The values of q depend on surface treatment and fall as low as 3×10^{-14} Torr liters sec^{-1} cm^{-2} (for true H_2 quantities). The values of p_1 measured are not quoted because they are not used in Eq. (9). However they become of importance in Eq. (8) if $s \neq 0$. Actually $p_1 \doteq 3 \times 10^{-11}$ Torr (H_2).[2] Let us now look at this case

(b) $s = 1$

$$q = 3 \times 10^{-14} + \frac{10^3 \times 3 \times 10^{-11}}{24.5} \tag{10}$$

$$= 3 \times 10^{-14} + 1.2 \times 10^{-9} \text{ Torr liters sec}^{-1} \text{ cm}^{-2}$$

$$= 1.2 \times 10^{-9}$$

Note that the second term completely dominates and raises the specific outgassing rate by 5 orders of magnitude.

(c) $s = 10^{-5}$

$$q = 3 \times 10^{-14} + \frac{10^{-2} \times 3 \times 10^{-11}}{24.5}$$

$$= 4.2 \times 10^{-14} \text{ Torr liters sec}^{-1} \text{ cm}^{-2}$$

Hence the sticking probability must be as low as 10^{-5} to reduce the error in the specific outgassing rate to 30%.

2. Private communication.

Complete neglect of this term in Eq. (8) can therefore be a risky assumption.

III. Suggested Methods for Measuring s

It is clear that what is needed is a method for assessing the approximate magnitude of s. In Fig. 1 this is fairly easy to do by installing a gauge in the test chamber and recording its reading when the valve is open (it should be p_1) and when closed. If when the valve is closed the pressure does not change at all then the total

$$\text{Internal Pumping Speed} = 10^3\ sA/\sqrt{MT}\ \text{liters sec}^{-1} \tag{11}$$

completely dominates C_o and a lower bound can be placed on s.

Note that to lower the pressure significantly in the test chamber it needs an external pump large compared to Eq. (11). For s = 1 and A = 6000 cm^2, this is 250 000 liters sec^{-1} and is totally impractical.

If when the valve is closed the pressure rises quickly to a new equilibrium value p_{eq}, one can write from Eq. (8)

$$q = \frac{10^3\ s}{\sqrt{MT}}\ p_{eq} \tag{12}$$

Equations (8) and (11) then provide two simultaneous linear equations from which both q and s can be obtained.

In practice such a measurement does not usually lead to a clear equilibrium value p_{eq} but a quasiequilibrium value drifting up slowly with time. It is not known how to analyze this curve quantitatively.[3] One can only hope that the quick initial rise is sufficiently clearly defined to be identifiable. Further a quick drop of the same type should be seen when the valve is opened quickly and should be correlated in magnitude with the quick rise.

3. J.P. Hobson and J.W. Earnshaw, J. Vac. Sci. Technol. 4, 257, 1967.

Perhaps a more certain method is to add another pump of known speed quickly to the test chamber perhaps through another valve. In this case sharp pressure drops have been observed[3] which can be used to yield values of s.

IV. The ISABELLE Geometry

The ISABELLE geometry is complicated by being a long pipe rather than the sphere of Fig. 1. However it is possible to place gauges at both ends of the pipe[1] and to perform the tests suggested in Section III above. The results should indicate whether $s \neq 0$ has to be considered. In the event that this is so, then a complete computer analysis with outgassing and readsorption the full length of the pipe is advised, coupled with pressure measurements down the pipe to test the analysis.

Conclusion

It is possible to interpret the measurements on the specific outgassing rate of Al in terms of a sticking coefficient of H_2 on the walls. Semiquantitative tests are suggested to establish whether this is true or not. If it is true, then the calculation of pressures achievable in the bore are altered in a way which will require further detailed analysis. The conclusion that Al tubing is satisfactory for ISABELLE is not necessarily vitiated in this event. The practical situation could conceivably be either better or worse. Nor are the ISR results on outgassing completely[4] free from this change of interpretation.

4. R. Calder and G. Lewin, Br. J. Appl. Phys. 18, 1459, (1967).

BEAM CLEARING AND SPACE-CHARGE TUNE DEPRESSION

J. C. Herrera
Brookhaven National Laboratory

The residual gas in the ISA chamber will consist primarily of hydrogen at a pressure of approximately 10^{-11} Torr. High energy protons passing through this gas will ionize it and thereby produce positive ions and electrons. In contrast to the positive ions which will be repelled by the beam field, the electrons of low energy will tend to be trapped by the attracting field and result in the neutralization of the beam. For a 200 GeV/c proton beam of 10 A, the attractive potential is at most 2 kV and the production rate (R_p) is 11×10^{-3} electrons per second for each beam proton. If there were no means of clearing these electrons, the beam would therefore become neutralized in approximately 100 seconds. Instead, if the equilibrium ratio of trapped electrons to beam protons, that is, the degree of neutralization ($\eta = Ne/Np$), is to be $\sim 10^{-4}$, then the required electron clearing rate must be

$$R_c = \frac{R_p}{\eta} = 110/\text{sec}.$$

To achieve adequate clearing in the ISA it is planned to place clearing electrodes at the ends of the dipole magnets in the lattice cells and at intervals of approximately 30 meters in the straight sections. Each pair of such electrodes will be 10 to 20 cm long and operate at a voltage of up to ± 5 kV. With this physical arrangement the electrons which arrive at these electrodes will be readily swept from the beam. However, with such a discrete distribution of clearing electrodes, it becomes necessary that the electrons which are produced in regions away from the electrodes be driven longitudinally toward the location of the clearing fields. It is under these circumstances that the self-clearing mechanisms of the beam become important. Considering the straight sections, one can see that there are several mechanisms, in addition

to their thermal velocity, which give the electrons sufficient longitudinal velocity to achieve a high rate of clearing. These are:

a) Beam heating - This is the process whereby the electrons undergo successive collisions with the circulating protons and thereby gain longitudinal energy.

b) Longitudinal Electric Field - Changes in the size of the proton beam due to the betatron function modulation will produce a longitudinal field.

Though the energy contributions arising from these two causes are small, they are sufficient to give the electrons the requisite longitudinal velocity and thereby provide good self-clearing ($R_c \sim 10^4$/sec) in the straight sections. Such is not the case in the dipole magnets where the low energy electrons tend to travel in small circular paths normal to the magnetic field. Fortunately, however, the transverse electric field due to the proton beam itself remains sufficiently high over most of the cross section of the ISA beam. One can then take advantage of the longitudinal drift velocity arising in crossed electric and magnetic fields. Thus, at injection when the magnetic field is 0.59 tesla, a beam of 10 A (charge per unit length of 3.4×10^{-8} Coulomb/meter) having a cross section of 1.2×0.4 cm will have an electric field sufficient in magnitude to result in an average degree of neutralization of about 5×10^{-5}. At high energy when the guiding magnetic field has increased to 4 tesla, the longitudinal drift velocity will decrease and the calculated clearing in the dipoles is reduced to about 4×10^{-4}. Since the dipole magnets occupy only 1/3 of the distance around the ISA ring, the above estimate of local neutralization yields an upper limit on the overall average neutralization of about 1 to 2×10^{-4}.

Corresponding to this degree of neutralization and a beam cross section in the intersections of 1.4×0.6 mm^2 at low energy, we can now estimate the change in betatron tune characteristics of

an unbunched beam in the ISA. Thus at injection field one calculates[1,2] a vertical tune depression of 0.015, while at 200 GeV one obtains a value of 2×10^{-3}. The accompanying horizontal tune changes are respectively -0.012 and 1.4×10^{-3}.

It is important to emphasize that the above maximum betatron tune depression of 0.015 is based on an average neutralization of 1.5×10^{-4}. Local variations in this degree of neutralization due to changes in the ratio of chamber to beam sizes (longitudinal electron traps) are therefore to be avoided. Consistent with the experience at CERN, it may be necessary to provide additional clearing electrodes at special locations in the ISA, for example, in the experimental straight sections, where such longitudinal electron traps can exist.

1. J.C. Herrera, "Fields and Forces for Rectangular Beams in an AGS," BNL Report, ISA 75-7, (1975).
2. A.W. Chao, J.C. Herrera, and M. Month, "Betatron Tune Change Due to Direct Space Charge in the ISA," these Proc.

CLEARING REQUIREMENTS IN ISABELLE BASED ON THE ELECTRON-PROTON INSTABILITY

O. Gröbner

CERN

It is known from experience in the ISR that the concentration of electrons in the proton beam, N_e/N_p, must be reduced below the threshold for coupled electron-proton oscillations to obtain good beam conditions. The detrimental effect of the repeated occurrence of this instability manifests itself mainly as an increased beam blow-up rate and in drastically increased background counting rates for high energy experiments.

In the following we calculate the tolerable degree of neutralization in ISABELLE based on formulae derived in Ref. (1).

1. e-p instability threshold without Landau damping

The threshold value, $(N_e/N_p)_{th}$, above which the electron-proton oscillations become unstable, can be expressed in the following form

$$(N_e/N_p)_{th} = (r_e/r_p) \cdot \gamma \left[(n - \nu_e)^2 - \nu^2\right]^2 \Big/ \left[4 \cdot \nu_e^3 (n - \nu_e)\right]$$

where r_e is the classical electron radius,

r_p the classical proton radius

γ the relativistic factor

ν the tune of the protons, and

ν_e the number of electron oscillations inside the beam per proton revolution.

With a tune of 25.63 the number of the least stable mode will be $n = \nu_e + 26$. From the bounce frequency of the electrons inside the proton beam one obtains

$$\nu_e^2 = \frac{2\, N_p\, r_e\, R}{\pi\, b(a+b)} \qquad \text{where}$$

1. "Landau-Damping of coupled Electron-Proton Oscillations", E. Keil and B. Zotter, CERN-ISR-TH/71-58.

N_p is the total number of protons

R the average machine radius

2a and 2b the horizontal and vertical beam dimensions.

We take typical ISA parameters from the yellow book, $N_p = 6.2 \times 10^{14}$ protons, corresponding to 10 A circulating current,

$R = 471$ m

$\upsilon = 25.63$

$\gamma = 213$

$a = 6.10^{-3}$ m, $b = 2.10^{-3}$ m { valid at 28.5 GeV and giving an equivalent beam cross section for a uniform density distribution.

The beam cross section at 200 GeV is obtained approximately by scaling with γ^{-1}. With these figures one obtains $\upsilon_e = 1.4 \times 10^4$ and the threshold neutralization $(N_e/N_p)_{th} = 5.10^{-7}$.

2. e-p instability threshold with Landau damping

A more detailed theory of the e-p instability developed in Ref. 1 takes into account the spreads in the electron and proton frequencies. The resulting damping increases the threshold neutralization and this leads to reduced clearing requirements.

The instability threshold for this case can be written in the form

$$(N_e/N_p)th = 64/9\pi^2 (r_e/r_p) . \gamma (\upsilon/\upsilon_e)^2 (\Delta/\upsilon) (\Delta\upsilon_e/\upsilon_e)$$

where Δ is the proton tune spread and $\Delta\upsilon_e$ the electron spread. The latter may be estimated by considering the effect of the azimuthal beam dimension variations on υ_e. One obtains

$$\Delta\upsilon_e/\upsilon_e = 1 - \left[(\beta_{min}/\beta_{max})^{\frac{1}{2}} \frac{(\Delta p/p)\alpha p_{max} + 2\ (e\beta_{max}/\pi\beta\gamma)^{\frac{1}{2}}}{(\Delta p/p)\alpha p_{min} + 2\ (e\beta_{min}/\pi\beta\gamma)^{\frac{1}{2}}} \right]^{\frac{1}{2}}$$

The typical electron frequency spread in the normal lattice of ISABELLE is $\Delta\nu_e/\nu_e \sim 5 \times 10^{-2}$, which is obtained with the following numerical values:

$$\Delta p/p = 4.5\times10^{-3}$$
$$\gamma = 213$$
$$e = 11\,\pi \times 10^{-6} \text{ rad m}$$
$$\alpha p_{max} = 1.65 \text{ m}$$
$$\alpha p_{min} = 0.8 \text{ m}$$
$$\beta_{max} = 42.5 \text{ m}$$
$$\beta_{min} = 7.5 \text{ m}$$

The tolerable residual neutralization in ISA, taking into account the damping, will be $(N_e/N_p)_{th} = 3.6 \times 10^{-4}$.

3. Conclusions

The threshold neutralization with Landau damping is calculated to be about 3 orders of magnitude larger than the limit for undamped oscillations. However, one assumes that the neutralizing electrons are fairly regularly distributed around the circumference rather than being concentrated in a few localized neutralization pockets. The actual spreads could therefore be smaller than the calculated ones. However, this reduction of the threshold may be partly compensated by the increase of the electron frequency spreads due to the changing vacuum chamber geometries. Furthermore, when ISA is operated with low-β insertions, the beam parameters change much more drastically than previously assumed and the e-p instability threshold increases by about one order of magnitude.

It seems useful to make a comparison with ISR conditions where the calculated threshold is about 1.3% for a 20 A beam. Since the actual residual pressure is only about 10^{-11} Torr the clearing due to beam heating alone (clearing electrodes switched

off) should be almost adequate to reduce the average residual neutralization below the threshold. Nevertheless, e-p oscillations can occasionally be observed even when the clearing system is switched on and the neutralization reduced to a level below 10^{-3}.

In the light of the ISR experience it would seem necessary to achieve a residual neutralization well below the calculated figure for the e-p threshold. The quoted ISABELLE design value of 1×10^{-4} would therefore appear to be a reasonable choice.

η MEASUREMENTS IN GLOW DISCHARGED CHAMBERS AT THE ISR

D. Blechschmidt

CERN

Beam induced gas desorption is still one of a few phenomena that determine the upper limit of the beam current in the ISR. However, proton beams of intensities beyond the design value have been stacked to date, and even further increase of beam current - and therewith luminosity - is aimed for. Since the glow discharge cleaning procedure has been implemented together with the installation of additional sublimation pumps at the center of main magnets to reduce the distance of lumped pumps, the vacuum limit, i.e. the maximum beam current stacked with a stable pressure has improved almost by one order of magnitude. There is no obvious reason why the beam induced vacuum instability could not be eliminated entirely by a continued improvement program that reduces the beam induced net desorption coefficient η to almost zero or even less throughout the whole machine.[1]

In a good approximation, the critical current for vacuum breakdown is given by[2]

$$I_c = \frac{(\eta I)_{crit}}{\eta} \approx \frac{40}{3} \cdot \frac{1}{\eta} \cdot \frac{C}{(d + 4\,\frac{C}{S})^2} \qquad [A] \qquad (1)$$

where C is the conductance (ℓ.m/sec) of the beam pipe, d (m) the distance between pumps of pumping speed S (ℓ/sec) for mass 28 (N_2 or CO). This relation applies to a periodic vacuum structure, with lumped pumps of high speed. The exact relation that cannot be written in an an analytic closed form is given elsewhere also for

1. R. Calder, E. Fischer, O. Gröbner and E. Jones, 9th Intern. Conf. on High Energy Accelerators, Stanford, p. 70, 1974.
2. D. Blechschmidt, CERN-ISR-VA/73-52 (1973).

unequal pumps.[3] In the ISR, $C \approx 80$ ℓ.m/sec for the elliptical beam chamber the aperture of which is limited by the magnet gap size. The speed of the lumped pumps S is so high that $d \gg 4C/S$, since the interpump distance is reduced to $\simeq 3.3$ m on average. This has been achieved by the installation of additional sublimation pumps halfway between the existing ones, and even at the center of the long bending magnets ("midget pumps"). Hence with the above figures for the outer arcs of the machine and from Eq. (1):

$$(\eta I)_{crit} \approx 95 \text{ A} \tag{2}$$

Thus, at the present state it is only the reduction of η that yields an increase of the critical current without unreasonable effort. The main procedure is therefore to reduce the surface contamination of the vacuum walls seen by the beam. This is a difficult task, since almost 2 km of beam pipe would have to be demounted, glow discharged in a mixture of Ar and O_2, and baked in situ at 300 - 250° C in the short shutdown periods.

This improvement program is monitored by η measurements in the field, carried out during special machine development runs. It is also supported by a laboratory study program to improve this pre-installation surface treatment.[4] In the machine, however, the purpose of such in situ η measurements is not only to find out places with high η for subsequent performance improvement, but also to investigate the result of new methods in the field, to study the long term behavior and also special materials.[5]

In the ISR η is measured via the augmented equilibrium pressure after a beam has been stacked. If we denote the equilibrium pressures in the absence of beam by p_o and p_1 with a beam of

3. E. Fischer and K. Zankel, CERN-ISR-VA/73-52 (1973).
4. A. Mathewson, work in progress, to be published.
5. O. Gröbner and R. Calder, IEEE Trans. Nucl. Sci. 20, 760 (1973).

current I, an average η value in the vicinity of the respective total pressure gauge is given by[3]:

$$\eta = \frac{(\eta I)_{crit}}{I} \left(1 - \frac{p_o}{p_1}\right) \tag{3}$$

where $(\eta I)_{crit}$ is the corresponding value obtained as was Eq. (2) from Eq. (1), or Ref. 3 if more accuracy is required.

Equation 3 is, however, an approximation only. This is because the pressure gauges have, for technical reasons, to be installed in the space left between the magnets, and therefore next to the pump stations. There p_o/p_1 has its maximum value because the beam induced gas desorption increases with the gas pressure that has its minimum at the pumps. It is estimated[3] that the error arising from Eq. (3) is less than about 20%. Hence Eq. (3) is still a good approximation, taking into account other sources of error that will be discussed below. The η value obtained by this method is a lower limit estimation for an average value extending from the left midpump position to the right one with the respective gauge in the center.

Total pressure measurement provides only very little information on the pressure bump mechanism. The sudden rise of the pressure once a certain threshold current is achieved (about 29 A in Fig. 1) is not consistent with the picture on which Eq. (3) is based. This equation also does not take into account whether η is a function of the beam current via the ion energy provided by the positive beam potential. It has been observed that η from total pressure measurement is very small at low currents, and often rises rapidly beyond a threshold current, this making η measurements rather meaningless and pressure bump behavior unpredictable.

Very sensitive mass spectrometers[6] have therefore been

6. Instruments from Balzers AG, Liechtenstein, QMG 511.

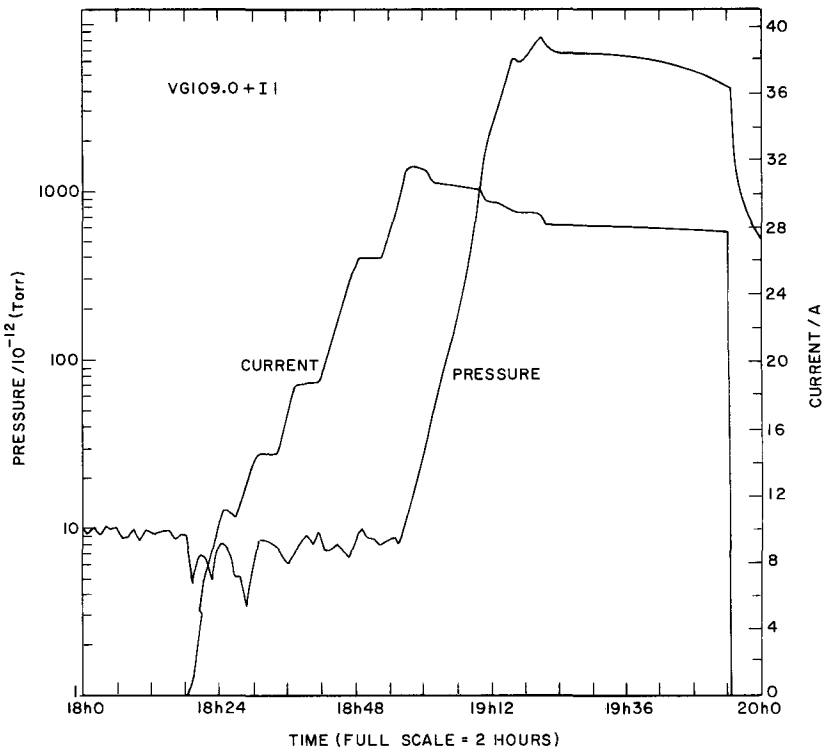

Fig. 1. Beam Induced Pressure Rise.

installed at strategic places to observe the changes of residual gas composition with increasing beam current. It was found that pressure bumps are triggered by CO mainly.[1] The critical current is independent of the total pressure but depends rather on η, beam pipe conductance, distance and speed of lumped pumps. Hence, any residual gas component with high partial η but still low partial pressure may be harmless at low currents and the increase of partial pressure is yet unnoticed by a total pressure measurement, even if the partial pressure has increased by more than an order of magnitude according to Eq. (3). Any further and even small rise of the beam intensity may then cause vacuum breakdown, even if the mutual desorption of molecules of different mass is not taken into account. This is particularly true for CO in a vacuum system as the ISR with over 95% hydrogen partial pressure, because CO was found to yield the largest partial η value for all the gas components released by N_2^+ - bombardment of stainless steel. These results were obtained in laboratory measurements.[7] In fact, inserting CO partial pressures, p_o, p_1 into Eq. (3), one comes out with η values that are by far more consistent with real pressure bump behavior.

According to those measurements, $\eta_{CO} \approx 2 - 3$ molecules/ion at bad places. This is consistent with an observed critical current which is at present around 30 to 33 A in the ISR, found from Eq. (3) as the current at which p_1 rises steeply and with increasing slope, i.e. for $p_1 \to \infty$, (see Fig. 1), whereas $\eta \approx 0$ is predicted for $I < 30$ A from total pressure measurement. Unfortunately, mass spectrometers for the pressure range in question are very expensive. Information about η is therefore limited to a few specific places only and to particular test sections. Vacuum improvement is thus very much based on finding the "tops of the icebergs" that show up during high intensity vacuum machine runs by logging the almost 350 total pressure gauges once every minute on magnetic tape. The

7. A. Mathewson, private communication on work in progress.

results of new or improved methods, like another composition of the discharge gas, new materials, like titanium alloy or surface coating by sputtered material are investigated via η measurements performed in special test sections in the machine equipped with spectrometers. Also, in order to improve the measurement accuracy of η, sublimation pumps are often not activated, to achieve low $(\eta I)_{crit}$ values and hence a high p_o/p_1 ratio, see Eq. (1) and (3).

As the result of today's knowledge of pressure bump behavior in the ISR we may conclude that H_2 is actually inoffensive. This is due to its high molecular speed, hence high $(\eta I)_{crit}$ and probably also because of its ineffectiveness in desorbing heavier molecules due to its low mass. Therefore, the main effort is concentrated in removing heavier residual gas molecules with high sticking probability from the surface, in particular CO. This might probably be a good reason in favor of Al as a chamber material, if it ever can be shown that it is less CO-contaminated than stainless steel after equal pretreatment.

We are confident that critical currents in the ISR of over 100 A may be achieved in the future by reducing the η_{CO} to below unity throughout the whole machine circumference. This would be more current than most likely can be achieved from the point of view of stacking space and transverse beam stability. Such improvement of the vacuum conditions seems to be possible, once all the beam chambers have been glow discharged in an Ar-O_2 mixture and are baked in situ at over 300° C. The beam gas desorption long term behavior of such chambers is encouraging, as η values remain low even after more than one year of operation.[8]

In situ glow discharges promise to be even better with regard to the achievement of lower η values, however, the constraints that the existing ISR would give to such an installation rule out its advantage. However, this method should be considered seriously for

8. O. Gröbner and R. Calder, private communication in the form of an ISR Performance Report, 12th June 1975.

a future machine design if η values have to be close to zero due to the requirement of a small aperture, which saves considerably on the construction cost.

Ion Desorption Cross Section of Carbon Containing Molecules on Aluminum and Stainless Steel

M. L. Yu

Brookhaven National Laboratory
Upton, New York 11973

It was proposed that the "pressure bump" phenomenon[1] observed in the CERN ISR proton machine is caused by ion induced desporption of gas molecules from the vacuum chamber wall.[2] Residual gas molecules ionized by the proton beam are accelerated by the beam to wall potential (order of kV), and bombard the chamber wall with near normal incidence sputtering off molecules. Mass spectrometric analysis of the residual gas content showed that gas molecules desorbed during the pressure bump are mostly carbon containing molecules, e.g. carbon monoxide and hydrocarbons. Such evidence seems to indicate that carbon containing contamination adsorbed on the vacuum chamber wall may be one of the major contributors to the pressure bump. The important parameter in the theory of the pressure bump is the ion desorption coefficient η which is the net number of molecules desorbed from the wall per incident ion. The desorption coefficient η_c for carbon containing contaminations can be defined as the number of carbon containing molecules desorbed per incident ion.

Both stainless steel and aluminum have been proposed or used as the vacuum wall material for the recent generation of accelerators, e.g. ISR at CERN uses stainless steel and aluminum is being proposed for ISABELLE at Brookhaven. Here we are going to compare the ion induced desorption rate of carbon containing molecules from the surfaces of these materials. η_c which depends on the surface coverage of the adsorbate does not characterize the material. At

1. E. Fisher, Proc. 3rd All-Union Conf. Charged Particle Accelerators, Moscow 1, 101 (1972).
2. O. Gröbner and R.S. Calder, IEEE Trans. NS-20, 760 (1973).

very high (>> monolayer) coverage, η_c is expected to be constant with coverage as it depends mainly on the interaction among the adsorbate molecules. At low coverage ($\leqslant$ monolayer), we can define the ion desportion cross section σ_c by

$$\sigma_c = \eta_c / n_c \tag{1}$$

where n_c is the number of adsorbate molecules per unit area. Assuming the collision cascade theory of sputtering,[3] σ_c is expected to depend on the energy and mass of the sputtering ions and the surface potential between the adsorbate molecules and the substrate. σ_c is hence a convenient parameter for the comparison of aluminum and stainless steel and for the comparison of the efficiencies of various species of sputtering ions.

Equation (1) can be rewritten in the following form

$$\eta_c = \frac{dn_c}{dN_i} = n_c \sigma_c \tag{2}$$

where N_i, the ion dosage, is the number of sputtering ions incident on unit area of the surface. Integrating,

$$n_c = n_c\ (0)\ e^{-\sigma_c N_i}\ . \tag{3}$$

In our experiment, n_c was measured with Auger electron spectroscopy. For low covarage close to a monolayer the size of the carbon Auger signal V_c is proportional to the surface density of carbon atoms. Assuming that the molecules contain one carbon atom per molecule (e.g. CO, CO_2, CH_4), V_c is proportional to n_c. A plot of log V_c versus ion dose N_i should give a straight line with slope $-\sigma_c$.

The samples used in the experiment were half-inch square flat pieces of 304 stainless steel and 6061 aluminum. They were subjected to the following three kinds of surface treatments:

---

3. P. Sigmund, Phys. Rev. 184, 383 (1969).

(I) chemical polishing,[4] (II) chemical polishing and argon discharge cleaning,[5] (III) chemical polishing, argon discharge and oxygen discharge cleaning.[6] The samples were exposed to air in the laboratory for time periods ranging from half a day to about a week in a closed container, a situation that may be encountered in the actual accelerator assembly procedure.[7] Then they were mounted on a sample manipulator inside a stainless steel, ion pumped, ultra-high vacuum system with a base pressure in the 10^{-9} Torr range. The final stage of sample preparation involved heat treatment to about 190°C for at least 8 hours.

The samples were examined with a Varian cylindrical mirror Auger electron analyzer unit. A 1.5 keV, 50 μA normal incidence electron beam was used to excite the Auger transitions. The diameter of the electron beam, which defined the area of the sample examined, was a few hundred microns. The beam was turned on only during measurements although desorption by the electron beam was not noticeable. During sputtering a continuous leak of sputtering gas raised the chamber pressure to about 1×10^{-4} Torr and a Physical Electronics ion gun was used to produce a 1 keV ion beam. The

---

4. The etching agent for aluminum is a mixture of 80.5% H_3PO_4, 3.5% HNO_3 and 16% H_2O. That for stainless steel contains 40% HNO_3, 5% HF and 55% H_2O. The samples were etched at 80°C for five minutes.
5. Discharge was done at 5×10^{-2} Torr Ar for 26 minutes. Current density was about 5×10^{-5} A/cm^2.
6. Discharge was done at 5×10^{-2} Torr O_2 for 3 minutes.
7. Samples were prepared for us by H. Halama and F. Timm of the Accelerator Department.

angle of incidence was about 70° to the sample normal. Oblique incidence is expected to give a slightly higher sputtering rate; however, since the sample surfaces were microscopically rough, the angular dependence is not expected to be significant. The ion beam was intentionally defocused to provide a uniform beam throughout the whole sample surface. The dose of ions intercepted by the sample was estimated by the ion current collected by the sample.[8]

All Auger measurements were taken after the sputtering gas was pumped out and the chamber pressure returned to the low 10^{-8} Torr range. The standard ac modulation technique for the derivative (dN/dE) of the energy distribution N(E) was used to recover the Auger electron spectrum. Curve (a) of Fig. 1 shows a typical Auger spectrum of an aluminum surface. Al, C, and O are the major peaks. Assuming a standard line shape, the peak to peak value of dN/dE of the carbon line is proportional to the surface density of carbon atoms on the surface at low coverage (~ monolayer). On stainless steel surfaces, Fe, Cr, C and O are the main peaks. Surfaces that were just chemically polished often showed small amounts of P and S, possibly from the etching agents. The amount of carbon containing contamination gathered once the surfaces were exposed to air did not show any obvious correlation to previous surface treatments. Curve (b) of Fig. 1 shows the Auger spectrum of the same surface after 80 μA-min/in.^{2} dose of 1 keV N_2^+ ions. The carbon signal is significantly reduced while the aluminum signal is much enhanced. We attribute these to the decrease of the carbon containing overlayer which attenuated the aluminum Auger electrons. There is no abrupt change in the size of the oxygen

---

8. There is a correction to the sample area arising from the roughness of the sample. This can be important since n_c for a rough surface can be much higher than that for a perfectly flat surface with the same coverage (e.g. monolayer), giving the rough surface a higher η_c. The area correction was not determined in this experiment.

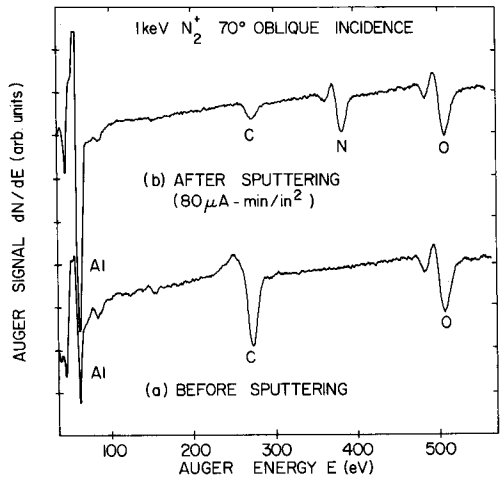

Fig. 1. Auger spectrum of an aluminum surface (a) before and (b) after sputtering by a dose of 80 μA-min/in.^{2} 1 keV N_2^+ ions with 70° angle of incidence.

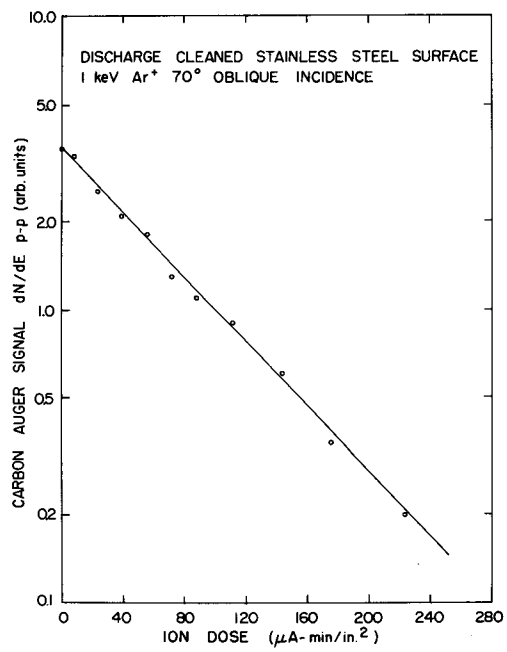

Fig. 2. Variation of carbon Auger signal on an argon and oxygen discharge cleaned stainless steel surface with Ar^+ ion dose.

signal, showing that the concentration of oxygen in the contamination layer was comparable to that in the top layer of the aluminum oxide. The strong nitrogen Auger signal shows an appreciable embedding of the bombarding ions. Stainless steel samples showed similar behavior.

The exponential behavior of Eq. (3) was actually observed in our samples except at high ion dose regions where the carbon Auger singal in general tended to level off. We suspect that this residual carbon signal was due to the carbon inclusions in the material and possibly a small amount of carbon contamination from the filament of the sputter gun. Ninety-five percent of this residual signal which usually amounts to less than 10% of the initial carbon Auger signal before sputtering is subtracted off from all the Auger readings. Figure 2 shows a log plot of V_c versus N_i after such a correction. The straight line obtained suggests that the coverage is close to the monolayer limit at which Eq. (3) applies. The resulting correction on the slope at the low ion dose end is not serious (~10%). The desorption cross section is deduced from the slope. Table I gives the desorption cross section σ_c of some tested samples determined in this way. Hydrogen ions which are probably less efficient in energy transfer during the collision cascade process because of its smaller mass, gave lower σ_c than N_2^+ and Ar^+. The desorption cross sections associated with N_2^+ and Ar^+ are very similar. The results showed no clear correlation between the variation of σ_c with the different surface treatments.

For the same material (aluminum or stainless steel) our results have about a factor of two variation in the desorption cross sections for the same kind of sputtering ion. We suspect that the composition of the contamination might vary from sample to sample and the distribution of contamination on the surface was nonuniform and possibly with patches of multilayer coverage. Aggregates of carbon containing molecules might have been desorbed and would thus have enhanced the local desoprtion rate. Scanning of the Auger electron beam across the sample indeed showed

TABLE I

Desorption cross sections of carbon containing molecules for various 1 keV sputtering ions with 70° angle of incidence. I, II and III refer to surface treatments described in the text.

Ion	Surface Treatment	Desorption Cross Section (10^{-16} cm^2)	
		Aluminum	Stainless Steel
H_2^+	I	0.32	0.87
	II	0.33	0.33
	III	0.40	0.83
N_2^+	I	3.3	3.6
	II	4.2	4.3
	III	3.6	3.6
Ar^+	I	1.5	4.5
	II	3.6	2.0
	III	2.0	2.2

nonuniform carbon concentration on the surfaces. Roughness of the sample surfaces might be another factor. Aside from such variations, the desorption cross sections for carbon containing contaminations on our stainless steel and aluminum samples are very similar in magnitude.

Acknowledgments

The author would like to thank M. Strongin, H. Hahn, H. Halama and L. Friedman for their stimulating discussions. Special thanks go to F. Timm for the preparation of the samples and the construction of the apparatus and G. Hrabak for his valuable technical assistance.

PRESSURE MEASUREMENTS AT ISABELLE

D. Blechschmidt
CERN

The low average pressure ($< 10^{-11}$ Torr N_2-equiv.) specified for ISABELLE makes it necessary to use pressure gauges of a low pressure limit $p < 10^{-12}$ Torr. This is, even with the present technology, hard to achieve.

In order to come to an appropriate selection of the type of gauge to be used, we shall briefly summarize the effects determining the low pressure limit of such an instrument, which is defined as its pressure indication, if the true pressure really would be zero. We will furthermore consider hot filament ionization gauges only, since cold discharge gauges tend to be nonlinear at the pressure range in question and they also need a magnetic field that makes them rather bulky or at least not particularly handsome.

Performance limitations

The ion current measured by a hot filament gauge is given by

$$I^+ = SI_e p \qquad (1)$$

where S is the gauge sensitivity (Torr^{-1}), I_e the electron emission current at which it is operated and p the pressure. The sensitivity for N_2 may be obtained from

$$S \approx 10 g\lambda \qquad \left[\text{Torr}^{-1}\right] \qquad (2)$$

where λ is the electron path length in the ionizing volume (cm) and g the probability that an ion produced therein, actually reaches the collector. At very low pressures, however, a residual current arising from various nonpressure dependent processes may be dominant. We will only give the most predominant ones:

(a) If the gauge operates at emission I_e, the residual current due to soft x-ray emission from the grid is

$$I_x = I_e Y_a G Y_c \tag{3}$$

where Y_a is the yield of x-rays at the anode, Y_c the photoelectric yield at the collector, and G the fraction of x-rays emitted by the grid that is intercepted by the collector. The equivalent pressure is

$$P_x = Y_a Y_c G/10g\lambda \qquad \left[\text{Torr}\right] \tag{4}$$

The reverse x-ray effect should be mentioned in this context. It arises from photoelectrons impinging at the collector; they are created at the walls of the vacuum system by x-rays originating from the anode. This effect is opposite to the normal x-ray effect and depends on the mounting of the gauge relative to the walls of the vacuum system.

(b) The electrons striking the anode release ions which in turn may reach the collector. The pressure equivalent reading is time dependent

$$P_d = \frac{w\theta_o\sigma}{10g\lambda} \quad \exp\left\{-\frac{eFt}{\sigma I_e}\right\} \qquad \left[\text{Torr}\right] \tag{5}$$

where w is the probability of a desorbed ion to reach the collector; θ_o (molec/cm^2) is the grid coverage at t = 0; σ ($\sim 10^{-18}$ cm^2) the electron induced molecular desorption cross section; e the elementary charge and F the anode surface area.

(c) Thermal effects may cause false pressure readings. They arise from the gauge operation, and are in fact real pressures. However, they will be considered as a residual pressure, as they would pertain at "real" zero pressure. First, if the cathode is too hot, the vapor pressure of the filament material is no longer negligible. Second, the heat radiated to the vacuum walls surrounding the gauge increases the thermal outgassing and in case of a poor conductance to the beam pipe, then measures its "own pressure".

In this latter case

$$P_t = AQ(T) \quad / \quad \left\{C + s\right\} \qquad \left[\text{Torr}\right] \tag{6}$$

where A is the area of the irradiated surface, Q its specific outgassing rate at equilibrium temperature and C the vacuum conductance to the beam pipe and

$$s \approx 0.2\ I_e\ .\ S \qquad \left[\ell/s\right] \tag{7}$$

the gauge's intrinsic pumping speed.

The total low pressure limit is thus $p_r = p_x + p_d + p_T$.

(d) Space-charge limits the maximum emission in a gauge. However, even if the filament potential is carefully selected the maximum electron emission current is [1]

$$I_e^{max} = 2 \times 10^{-3}\ U_{gf}^{3/2}\ A_f\ d^{-2} \qquad \left[\text{mA}\right] \tag{8}$$

where U_{gf} is the anode-to-filament potential ($\simeq$ 120 V for max ionization cross section), A_f the filament geometrical surface area (in cm^2) and d the anode-filament distance (in cm). In normal gauges, with $U_{gf} \simeq 120$ V, $I_e^{max} < 10$ mA, hence very low collector currents ($I^+ \leq 10^{-12}$ A) are the consequence at ISABELLE design pressures.

There are not many types of gauges that might be adopted for ISABELLE. We will hereafter discuss some of them, to find out whether their design principally offers the possibility to improve their parameters such that they really achieve a low pressure limitation below 10^{-12} Torr and qualify to measure ISABELLE pressures without problems. Some of their typical parameters relevant to this question are listed elsewhere.[2]

---

1. D. Blechschmidt, J. Vac. Sci. Technol. 11, 1160 (1974)
2. D. Blechschmidt, J. Vac. Sci. Technol. 10, 376 (1973)

A. Bayard-Alpert Gauge

This gauge has, for a reasonable anode grid diameter, < 4 cm, a sensitivity $S < 40$ Torr^{-1}, assuming $g = 1$, see Eq. (2). A geometrical factor of $G \simeq 2 \times 10^{-3}$ is about the minimum that might be achieved without reducing the collection efficiency g and also for mechanical reasons as for this figure the collector has a diameter of about 30 μ only and is several cm long. The product $Y_a Y_c$ is about 2×10^{-7} and cannot be further reduced. The resulting x-ray limit is $p_x \sim 10^{-11}$ Torr, and is even rather optimistic. A gauge of normal Bayard-Alpert design is therefore principally not suitable for ISABELLE.

B. Extractor Gauge

This type of gauge has been developed about 10 years ago.[3-5] The ions produced within the anode grid volume are extracted and focussed at a small and short collector that is almost completely protected from direct x-ray irradiation. This is, however, at some expense of sensitivity, since typically $0.5 < g < 1$ due to the reduced extraction efficiency and also because a smaller grid diameter at the same gauge size is usually required for this gauge for ion optics reasons. Hence $S_{Ex} < 25$ Torr^{-1}. However, a geometry factor of $G = 2 \times 10^{-5}$ is relatively easy to achieve. This yields $P_x \simeq 10^{-13}$ Torr theoretically, but this figure has so far not yet been experimentally proved. Existing extractor gauges have low pressure limits ranging from the upper 10^{-13} Torr range to about $2 - 3 \times 10^{12}$ Torr. Their contribution from electronic ion

3. P.A. Redhead, J. Vac. Sci. Technol. 3, 173 (1966)
4. F.P. Clay and L.T. Melfi, J. Vac. Sci. Technol. 3, 167 (1966)
5. J. Groszkowski, Le Vide, 142, 226 (1969)

desorption to the low pressure limit is lower than for a Bayard-Alpert gauge. This is because the ion optics used for extraction offers the possibility of suppressing a large fraction of desorbed ions that have typically a higher initial kinetic energy than residual gas ions.

C. Orbitron Gauge

This gauge is known for its extremely high sensitivity electron path lengths up to 10^4 cm have been observed.[6] However, $Y_a Y_c$ is about an order of magnitude higher than in a typical Bayard-Alpert gauge and so is its geometrical factor. Unfortunately, the orbitron gauge is limited in the low 10^{-11} Torr range[7] and not, as to be expected from Eq. (4) at some 10^{-13} Torr. This limitation is due to the considerable space-charge barrier built up by electrons placed at stable orbits with extremely long free path lengths for electron molecule impact ionization. This space charge barrier has the consequence that a few electrons only are placed at stable orbits of extremely long path lengths (creating the barrier) whereas most of the other for energetical reasons are injected at unstable trajectories and fall at the anode after only a few revolutions, thus giving rise to the increased x-ray limit.

D. Modulated Bayard-Alpert Gauge

An extension of the working range of a Bayard-Alpert gauge is possible by installing a modulator electrode [8,9], i.e. a small wire mounted in the ionizing volume parallel to the collector. With the

---

6. W.G. Mourad, T. Pauly and R.G. Herb, Rev. Sci. Instrum. 35, 661 (1964)
7. D. Blechschmidt, Proc., 6th Intern. Vacuum Congress, Kyoto (Jap. J. Appl. Phys., Supl. 2, p. 105), 1974
8. P.A. Redhead, Rev. Sci. Instrum., 31, 343 (1960).
9. J.P. Hobson, J. Vac. Sci. Technol. 1, 1 (1964)

modulator at high potential (usually the anode potential), the collector current is

$$I_1 = I^+ + I_r, \tag{9}$$

where I^+ is the true, i.e. gas pressure dependent signal and I_r the gauge's intrinsic residual current from x-rays, electron ion desorption,etc. Switching the modulator to low potential (usually the ground potential) we have

$$I_2 = (1 - k)\ I^+ + (1 - \epsilon)\ I_r\ ; \tag{10}$$

whereas k is determined at high pressures where $I_r \ll I^+$ from $k = (I_1 - I_2)/I_1$, the other modulation factor ϵ is usually neglected. Thus $I^+ = (I_2 - I_1)/k$ for $\epsilon = 0$.

In fact, however, pressure measurements far below the normal limit of the gauge tend to yield values that are systematically higher than the true pressure. This is the case if ϵ is not negligible. A simple calculation yields

$$\delta_1 = \left| \frac{\epsilon}{k}\ \frac{Pr}{P} \right| \tag{11}$$

for the systematic error, defined as in

$$\frac{I^+\ (\epsilon \neq 0)}{I^+\ (\epsilon = 0)} = 1 + \delta_1 \tag{12}$$

obviously, pressure readings are up to 100% too high for k = 1 (which is rather optimistic) and $\epsilon < 0.1$ (which is most likely too optimistic), once $I_r > 10.I^+$, i.e. if the gauge is used to measure pressures of less than one order of magnitude below its low pressure limit (defined for the unmodulated mode). At low emission currents, ϵ may be much higher than just 0.1 due to electron impact desorbed protons that are highly modulated.[10]

---

10. J.P. Hobson and J.W. Earnshaw, Proc., 4th Intern. Vac. Congr. Manchester (Inst. of Physics and Physical Society, London, p. 619) 1968.

Furthermore, the low currents (some 10^{-13} A) are subject to noise fluctuations. This in turn makes it very difficult to measure far below 10^{-11} Torr. If γ is the rms noise, the statistical error is

$$\delta_2 = \left[1 + \frac{K}{2\gamma(1 + \frac{Pr}{p} - \frac{K}{2})} \right]^{-1} \tag{13}$$

As an example with a gauge of sensitivity S = 25 $Torr^{-1}$, I_e = 4 mA, and p = 10^{-12} Torr : $I^+ = 10^{-13}$ A. Hence with an optimistic γ = 0.1, k = 1 and $P_r = 10^{-11}$ Torr, we get $\delta_2 \approx 0.7$.

In conclusion, we may say that pressure measurements with modulated Bayard-Alpert gauges are in principle possible down to 5×10^{-12} Torr (as the minimum low pressure limit is around 5×10^{-11} Torr), however difficult to perform and up to a factor of two too high. These same considerations also apply to extractor type gauges

E. Bent-Beam Gauges

The best known gauge of this type is the Helmer gauge.[11] Although its low pressure limit is originally claimed to be around 10^{-13} Torr, it is in fact limited at about 2×10^{-12} Torr by the evaporation of tungsten from the hot cathode.[12] Thoria-coating has been a remedy and pressures in the low 10^{-13} Torr range are presently believed to be the limit.[13] However, its low sensitivity of little less than 10 $Torr^{-1}$ makes it difficult to measure pressure below 10^{-12} Torr; another drawback is its relatively complex power supply and high costs. At the present state, it is certainly overqualified for ISABELLE compared with extractor type gauges. This

---

11. J.C. Helmer and W.H. Hayward, Rev. Sci. Instrum. 37, 1652 (1966)
12. B. Angerth and Z. Hulek, J. Vac. Sci. Technol. 11, 461 (1974)
13. C. Benvenuti and M. Hauer, private communication.

same argument holds for other even more sophisticated gauges designed for lower pressures that are equipped with secondary electron multipliers.[2,14] These instruments are considered to be useful only once the pressure is far below 10^{-12} Torr, as might be expected in particular straight sections.

Mounting of the Gauges

Correct pressure measurements depend critically on how the gauge is mounted. Unfortunately, the gauges can only be installed between magnets, i.e. next to the pumping stations, thus giving no information about the maximum pressure in the beam pipe but rather a control of the pressure equilibrium next to the pump unit. For this reason, some gauges should be mounted directly on the beam pipe and as far as possible from the pumping station in order to obtain meaningful information of the pressure in the pipe, in particular, at high beam currents or near the vacuum stability limit.

Provision has to be made that electrons from the cathode cannot be extracted into the proton beam using an electrostatic screen or by mounting the gauge into an elbow. Under any circumstances, however, care must be taken to reduce thermal desorption of the walls irradiated by the hot gauge cathode, eventually by using a thoriated filament, and also to provide high conductance between gauge and beam pipe to prevent it from measuring its "own" pressure, see Eq. (6).

---

14. D. Blechschmidt, J. Vac. Sci. Technol. 12, Sept/Oct. (1975)

EXPERIMENTAL INSERTIONS

H.J. Halama

Brookhaven National Laboratory

All proposed experiments discussed with various experimental groups seem to impose one or more of the following demands on vacuum equipment located in the insertions:

1. Small diameter vacuum chamber
2. Minimum mass between the beam and the detectors
3. Utilization of maximum solid angle
4. Complex vacuum chambers with movable parts in some cases
5. Restriction on temperature rise of the chamber during bake-out
6. Minimum amount of equipment (pumps, electrodes, etc.)

Low pressure, however, which is essential in the experimental straight sections dictates large gas conductance C ($C \propto d^3$, d being the diameter of the beam pipe), large pumps, small distance between pumps L and minimum effective outgassing Q. Thus,

$$P \propto \frac{L^2 Q}{d^3}$$

The vacuum system in the experimental insertions will therefore have to be very different from that of the lattice and will require additional study to achieve the above goals. In particular the use of local and distributed Titanium sublimation pumping could permit a beam pipe of smaller diameter as well as limit the number of large ISABELLE pumping units. Outgassing (Q) can possibly be lowered by either an in situ glow discharge cleaning or by the use of a Titanium chamber. Complex vacuum chambers could serve as sublimation pumps which would not be objectionable from the vacuum point of view. Unfortunately, the resulting discontinuity in the beam pipe introduces two undesirable effects, namely:

a) A reactive component of the wall impedance seen by the beam. This impedance has to be compensated to keep the total

impedance of the chamber acceptably low. Failure to do so could cause instabilities leading to an increased background.

b) A neutralization pocket where the electrons from the ionized gas molecules can be trapped by the beam potential wall. A clearing electrode which would remedy this situation might be objectionable as an additional mass between the detectors and the beam or as an impedance problem.

In addition a complex chamber will introduce some mechanical and structural difficulties.

Due to the higher thermal and electrical conductivity of aluminum ohmic heating could be used with minimum insulation between the chamber and detectors. Furthermore, a $150^{\circ}C$, or possibly even a lower temperature bake-out may be sufficient to achieve acceptable vacuum conditions if the in situ glow discharge cleaning methods are developed.

It is, therefore, suggested that a program aimed at designing an experimental straight section be initiated with due consideration of the experimental, beam impedance and vacuum problems. A prototype of such a section containing the features most desirable to the experiments should be constructed at an early date. A few topics to be investigated in the prototype are listed below.

1. Feasibility and mechanical properties of thin windows.
2. Double wall vacuum systems.
3. In situ glow discharge cleaning.
4. Titanium sublimation pumping.
5. Removable sections of beam tube while maintaining high vacuum.

DEMOUNTABLE ULTRAHIGH VACUUM SECTIONS FOR ISABELLE

J. P. Hobson
National Research Council
Ottawa, Canada

I. INTRODUCTION

A sketch of the proposed design as applied to an experimental section is shown in Fig. 1. The central idea is that the 4 arms coming out of an experimental intersection be terminated by ultra-high vacuum gate valves, with matching valves terminating the main ring. With all 8 valves closed, a break would be made between the valves and the whole experimental intersection removed, probably on wheels. While the necessary valves are not currently "on the shelf" items, versions meeting everything but the closed conductance requirements do exist commercially and valves which do meet these requirements are under development in several laboratories. The commercial nonavailability of the gate valves should not be grounds for rejection of this proposal if other advantages outweigh this element of risk. Sections which are not experimental sections may also be demountable. An estimate of $10 000 per valve might be reasonable at present.

II. VACUUM PREPARATION OF DEMOUNTABLE SECTIONS

It is visualized that the vacuum preparation of a demountable section be done prior to its introduction into the storage ring. At this time, pumps probably of the sputter ion type could be attached at 3 of the 4 ends while the 4th end could be used (Fig. 2) for insertion of various devices such as:

(a) a glow discharge electrode
(b) a titanium evaporator (or another metal)
(c) a small ion pump with its magnet outside the pipe
(d) any other device considered useful.

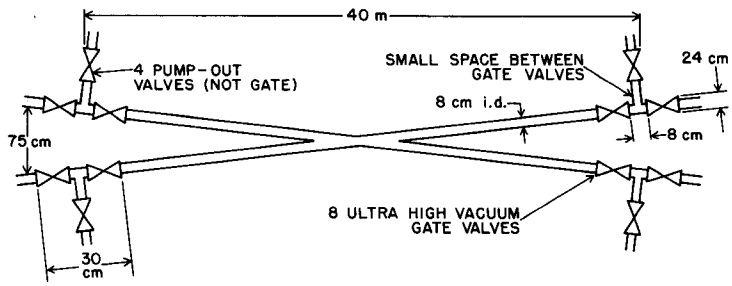

Fig. 1. Demountable ultrahigh vacuum sections.

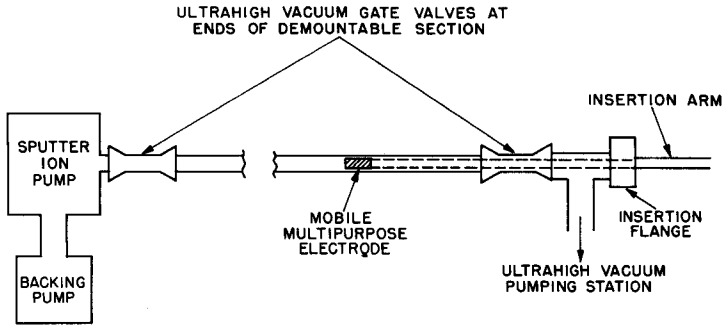

Fig. 2. Ultrahigh vacuum gate valves at ends of demountable section.

The insertion arm would be designed so that the item on the end could traverse the whole length of the section (40 m in Fig. 1) and also be withdrawn behind the gate valve. The temperature of the section could be any desired value during vacuum preparation. As a final step in vacuum preparation, a getter film could be deposited along the whole length of the pipe giving the walls a high internal pumping speed for active gases like H_2. Tests might reveal too high an outgassing rate of inert gases like CH_4 which would have to be pumped by small ion pumps, an undesirable addition, or by cooling the pipe walls (cold bore). After vacuum preparation to the desired pressure ($< 10^{-11}$ Torr), the section would be sealed by its gate valves whose outside could be pumped temporarily to reduce any possibility of leaks contaminating the interior surfaces of the section. After installation in the ring, only the space between the valves estimated to be 8 cm in length would be pumped and prepared until the pressure was below 10^{-11} Torr. At this time, the small pumping valves would be closed, the external pumps permanently removed and the gate valves opened. Normally, the pressure in such an internally pumped device can be held at very low values for long periods ($\geq$ 1 year) provided the vacuum design has been done carefully. The pressure might be well below 10^{-11} Torr, and hence be in the range where the beam itself pumps the residual gas by beam heating effect.

Without experimental tests, it is difficult to estimate how often it might be necessary to warm the cryopumps (cold bore) to remove physically adsorbed gas, which could be pumped through the small pump-out valves. Pressure gauges might be incorporated into the main gate valves, which could be constructed to present a completely smooth internal bore, when the gate was withdrawn. Similarly, the pump-out ports between valves could be covered when not in use to make the bore completely smooth. Thus, it is possible to visualize a vacuum design yielding a completely smooth bore the entire length of the storage rings. A cylinder surrounding the beam would be broken only by insertions required for purposes other than vacuum and by the intersection regions.

III. ADVANTAGES AND DISADVANTAGES

The main advantage is that the vacuum design does not contribute at all to breaks in the smooth cylindrical wall around the beam, hence does not contribute to the radiofrequency impedance of the ring. Other advantages may be logistic considerations in having demountable sections. Temporary replacements for sections are of course possible.

The major disadvantages are that the design is untested and that putting the ring back into service after a catastrophic vacuum failure might be slow, since much has been sacrificed to simplifying the internal vacuum system. Clearly, the latter problem would be reduced by fast-closing gate valves so that a catastrophic pressure could be localized. Also, the quality control against leaks in the demountable design needs to be extremely good since no nonsaturable pumps are available.

However, if other considerations of ISABELLE dictated a simplified internal vacuum design, then the type of design sketched in this note might be worth serious consideration.

OUTLINE OF A COLD-BORE DESIGN FOR ISABELLE

R. C. Wolgast
Lawrence Berkeley Laboratory

Some of the machine parameters that have a strong influence on the desirability of cold-bore cryopumping are listed below. ISABELLE (ISA), ESCAR (E), and the ISR are entered on the chart as they rate low, medium, or high in these paramters.

	Low	Med	High	Effect
1. Beam current	E(3A)	ISA (10A)	ISR (30A)	Press bumps
2. Bunch frequency	ISA ISR		E	Bore heating
3. Magnet rise rate	ISA ISR		E	
4. Ratio of bore diam.	ISA ISR		E	Low condition to lumped pumping

One might conclude from the chart that ESCAR should be warm bore and that ISA should be cold bore. In fact, ESCAR has a problem due to bore heating; but it will be made cold-bore because it is part of the ESCAR experimental mission to investigate the feasibility of cold bore. Cold bore for ISA is questionable due to possible pressure bumps; but this could be circumvented by the addition of a liner at low temperature to shield the cold bore from beam-gas produced ions. A liner for ESCAR is one way to circumvent the problem of bore heating, so ironically, a cold bore design for ESCAR and ISA could look very similar for different reasons. The point of this discussion is that the desirability of cold or warm bore needs to be based on the strengths and weaknesses of developed designs, rather than solely on general arguments.

Besides cold and warm, there are hot and cool bore possibilities. The table below lists a number of possible bore temperatures and salient advantages and disadvantages relative to room temperature:

III. ADVANTAGES AND DISADVANTAGES

The main advantage is that the vacuum design does not contribute at all to breaks in the smooth cylindrical wall around the beam, hence does not contribute to the radiofrequency impedance of the ring. Other advantages may be logistic considerations in having demountable sections. Temporary replacements for sections are of course possible.

The major disadvantages are that the design is untested and that putting the ring back into service after a catastrophic vacuum failure might be slow, since much has been sacrificed to simplifying the internal vacuum system. Clearly, the latter problem would be reduced by fast-closing gate valves so that a catastrophic pressure could be localized. Also, the quality control against leaks in the demountable design needs to be extremely good since no nonsaturable pumps are available.

However, if other considerations of ISABELLE dictated a simplified internal vacuum design, then the type of design sketched in this note might be worth serious consideration.

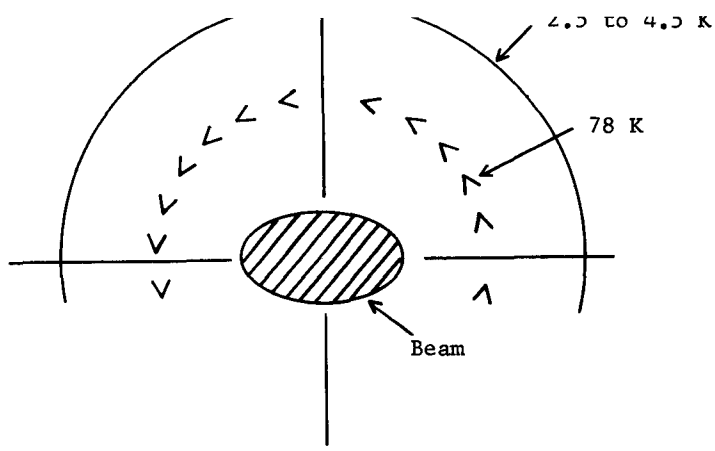

Fig. 1. Tubular cryopump

Cryopumping has been used successfully inside the Hilac linac cavities, in the Oak Ridge cyclotron, in the Bevatron, and in ISR intersections. An improved cryopump for the ISR intersections has been designed with tubular geometry:

Quotation:[1]

"Before one can plan on using a cold vacuum chamber, one should, therefore:

i) guarantee that the helium leaks are eliminated,

ii) decrease the surface coverage of H_2O and hydrocarbons by bakeout since these gases are broken up into free hydrogen by ion bombardment,

iii) provide the possibility for leak checking when the system is cold, and

iv) minimize the gas flow from the warm into the cold sections."

Responses:

i) Thousands of liquid helium dewars around the world are leak tight. No one in the vacuum study group has ever known of a leak in tubing, which indicates that leaks in magnet dewars could be repaired without junking the magnet.

ii) As the magnet is cooled, the liner will cool more slowly. This will transfer water and lighter hydrocarbons to the cold bore out of reach of beam produced ions. There will be some heating of the liner by eddy and image currents. If these effects are not sufficient to transfer these gases to the cold bore, induction heaters, shown on Fig. 4, (or other heating methods) can insure the result.

---

1. H. J. Halama and J. C. Herrera, Comparison of Cold and Warm Vacuum System for Intersecting Storage Rings, IEEE Trans. Nucl. Sci. NS-22, No. 3, 1492 (1975).

iii) Leak detector heads can be installed at intervals around the ring to indicate helium leaks and to leak check room temperature walls and leaks from the insulating vacuum.

iv) Vacuum requirement for the ISA experimental areas is 10^{-11} Torr H_2 max. If the gas flows through an 8 cm diam aperture onto the cold bore, it would saturate 70 cm^2 of bore surface with H_2 each month. Actual conductance to the cold bore is much less than the 8 cm aperture.

Warm to cold transitions: There are two warm to cold transitions per sector valve. Suppose there are 26 magnets per sector valve. This gives 40 transitions for ISA. Maximum radiant heat load per transition is 2.5 W or 100 W total. If we allow 50 W for thermal conduction and 50 W for the ion gauges, the total heat load is 200 W.

Finally, this design could be developed sufficiently to make a cost estimate.

What is being done to demonstrate feasibility of cold-bore vacuum systems:

BNL: Henry Halama plans to measure ion induced desorption from warm and cold bores in ISA geometry.

CERN: Diether Blechschmidt reported that Roger Calder, ISR Division, has planned a series of studies and measurement. A cold bore length may be installed in the ISR.

LBL: ESCAR is an experimental 4 GeV proton accelerating and storage ring which will use cold-bore cryopumping.[2] ESCAR will attack the problem of bore tube heating from the combination of eddy and image currents and demonstrate pumping capacity of the 4.5K cold bore for H_2, i.e. length of time between H_2 degas cycles. ESCAR will investigate the cold-bore pressure bump problem. Although average beam current is only 3 A, there may be sufficient

---

2. R. C. Wolgast, IEEE Trans. Nucl. Sci. NS-22, No. 3, 1496 (1975).

pressure rise due to beam to compare to present theory, and the pressure bump may be induced by:

1. Increased surface coverage of H_2 and He - thus increasing η.

2. Operation with bunched beam to peak current of 10 A - thus increasing ion energy and η.

3. Blocking off some of the pumping surface - thus decreasing pumping speed and $(\eta I)_{crit}$.

A small test program will:

1. Measure effect of low rates of temperature rise of the cryosurface upon the vacuum in the existing test chamber.

2. Measure electrical conductivity of $\sim$ 1000 Å metal films at cryogenic temperatures.

3. Measure pressure rise due to magnet pulsing on the existing prototype magnet.

4. Investigate usefulness of CO_2 and N_2 cryosorption of H_2.

ESCAR will demonstrate that magnetic measurement coordinates can be accurately transferred to external fiducials (an objection to cold-bore raised by CERN).

The schedule for ESCAR construction extends 2 - 3 years, limited by support.

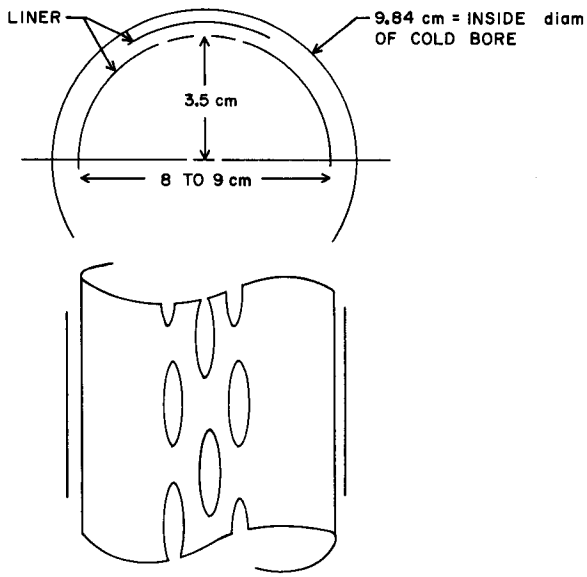

Fig. 2a. Magnet bore cross section with liner, vertical direction unspecified.

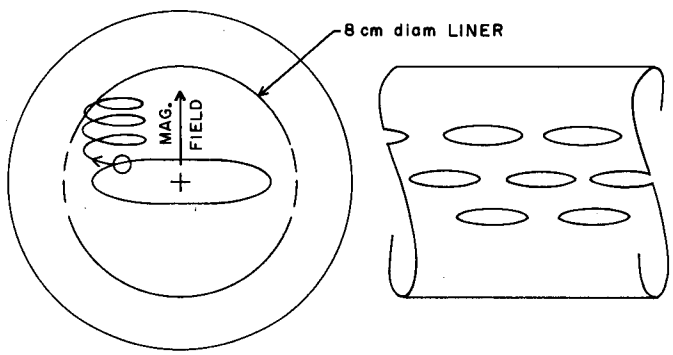

Fig. 2b. Simpler cross section which takes advantage of trapped orbit of the gas ion.

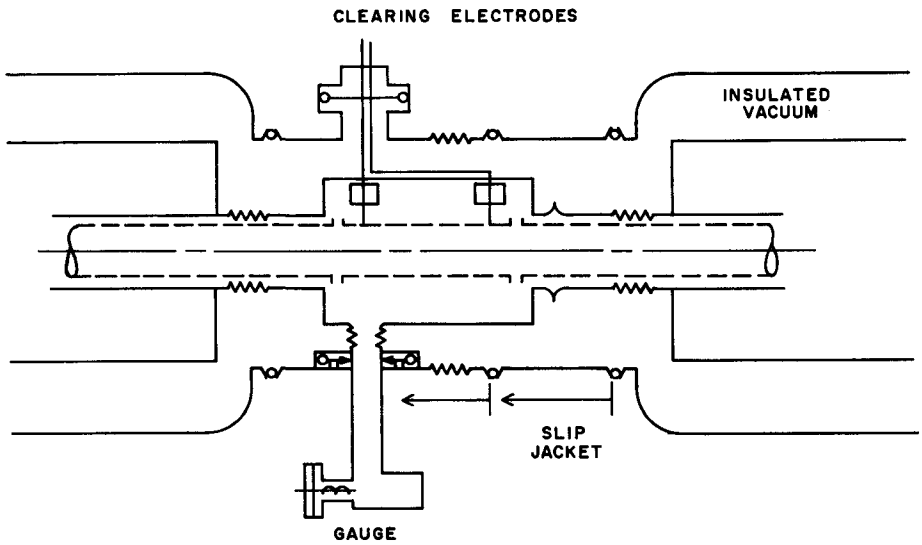

Fig. 3. Intermagnet section with clearing electrodes and gauge. No warm to cold transition except for the gauge.

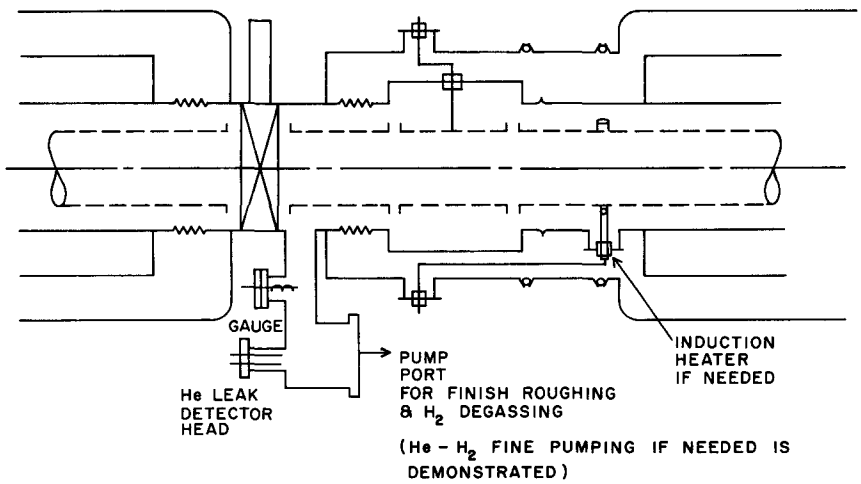

Fig. 4. Intermagnet section with sector valve and pump port.

COMPUTER CONTROL AND MONITORING

D. Gerd Dimmler
Brookhaven National Laboratory

It seems to be a common property of Control Systems that specifications for the system can be determined after the parameters of the machine to be controlled are known; yet it has to be completed and tested before the machine to be controlled is ready for test operations. The first portion of the statement is based on the assumption that control system specifications ought not to constrain but ought to be adapted to a machine design. The second portion of the statement takes into consideration.

a.) that a machine requires a major portion of the control system in order to be operational, and

b.) that modifications to initially established control philosophies, functional architectures as well as hardware and software structures of the control system create often unacceptable disturbances to the progress of the machine. They are, thus, to be avoided.

ISABELLE is a machine which is in the study phase. Key parameters are still to be determined. Thus, the above discussion suggests that the activities of the working group "Computer Control and Monitoring System" should be very loosely structured in order to allow adaptation to events and ideas created in other working groups. The following list of topics, therefore, should be considered as a possible guideline rather than as an agenda. Present suggestions for topics are:

Conceptual Considerations of Control System Architectures

There are considerations which are based on the state of the technology in the computer and control field and are not specific to the machine to be controlled and to specific hardware/software

structures. Considerations of distributed vs centralized architectures are in this class. Clear definitions of the various types of architecture are as important as considerations concerning suitability. Report,[1] CRISP 75-5, may serve as a contribution to the definition of a distributed function concept.

Collection of Machine Parameters with Significance to the Control System

A major activity may be to collect and classify information about significant machine parameters as they are discussed and developed in other working groups. An interesting suggestion has been made here to try to interest individuals from other working groups to present their views of the expected requirements to the control system.

Operational Aspects of Accelerator Control

It is hoped to gain information on past experience and new ideas on control room layouts, level and complexity of operator/system interaction, etc.

---

1. D.G. Dimmler BNL Report, CRISP 75-5 (1975).

ORGANIZATION AND DESIGN OF AN ISABELLE CONTROL SYSTEM

R. J. Nawrocky
Brookhaven National Laboratory

From the control point of view,* the ISABELLE machine may be considered as a set of complex systems (such as the main magnet and magnet correction system, the rf system, the refrigeration and vacuum systems, etc.) which must be operated simultaneously in a synchronized fashion.

Though the machine is still in the design stage, it is apparent that the number of variables (digital or analog) which will have to be independently controlled will be large. For example:

a. The magnet correction system (including equilibrium orbit corrections, chromaticity, $\dot{B}$, etc.) $\simeq$ 1500 variables

b. The vacuum system (gauges, pumps, valves, clearing electrodes, etc.) >2000 variables etc.

It is obvious that due to the large number of control functions, the control system for ISABELLE will require a computer or a network of computers to perform the necessary control and data logging operations.

A general organization of such a control system may of the following form:

---

*In this context, control includes the following:

i. monitoring
ii. open-loop control (setting)
iii. closed-loop control (sensing and automatic setting)
iv. triggering

I. The Control Centers

Alternatives: (a) A single control area vs (b) a number of control areas.

(a) Ideally, ISABELLE should be controlled via a computer control system from a central control area. The goal, which is reasonable in theory, should be to approach a one-man control of the machine. The operator should not be burdened with continuous routine logging and tuning. The accelerator should run well enough so that he can concentrate on

1. responding to experimenter requests and minimizing the interactions between the experimenters,
2. determining how to keep the machine running in case of equipment malfunction, and
3. observing and analyzing "unusual" behavior of the beam and optimizing machine performance.

(b) In practice, however, it is unreasonable to think that there will be a single control room. As at the AGS, or FNAL, there will be several control areas. These will be dedicated to particular systems and are essential for servicing, turn-on and system diagnostics away from the chaos of a central control room at turn-on. The subsystem control area can and should contain the specialized instruments and detailed displays necessary to operate a particular subsystem.

A key number of control and monitoring functions could be remoted from each subsystem control center to a central area, from which the whole machine could be operated. Logging of information, generation of displays from beam diagnostic apparatus could be performed in the central control area. Some of the functions of the human operator, such as learning what are the best configurations for operating the machine, could be aided by computer programs.

II. The Control Computer(s)

Alternatives: (a) A single computer vs (b) a system of computers.

(a) A single computer would have to handle an enormous amount of data transfers, would lack the necessary degrees of parallelism, etc., and would be, therefore, undesirable.

(b) It seems reasonable to consider a scheme where each system or subsystem (e.g. refrigeration, vacuum, etc.) provides its own control system (not necessarily computerized) as well as the facility to remote these controls to a central location.

Where the use of a computer is desirable, the control network may consist of a number of microprocessors linked with a minicomputer.

A central control computer (global node) could be used to communicate with the subsystem computers (local nodes) and/or control the communication between subsystem computers.

If the computer system is distributed, it should in general satisfy the following requirements:

1. A computer should be used in a given situation only if necessary.
2. The system should be flexible - must be able to grow.
3. The subsystem should be locally automatic rather than depend on control from a central "think tank".
4. Some uniformity should be imposed so that all subsystems obey and respond as to status, etc. in the same "language", i.e. word length, bit pattern, file structure, signal level, etc., although within each subsystem the designer should have a free hand in controlling his hardware.
5. The group responsible for the ISABELLE control system

should provide assistance (hardware and software) to the individual sections so as to more easily accomplish step (4)

6. Certain subsystem computers should be extremely reliable, such as that for the vacuum system, and must be available at all times (may require a stand-by unit).

The following are some of the many remaining questions:

1. Should there be standardization with respect to a given type of computer?
2. Should the program preparation for a subsystem computer be performed locally or compiled outside and loaded from a higher-level node of the system?

III. The Timing System (Clock)

The timing system necessary for the synchronization of the injection/ejection, stacking and acceleration phases, etc. could be either part of the control computer or a separate hardwired system.

IV. The Data Base

Alternatives: (a) A central data base vs (b) a distributed data base.

(a) With a central data base, information retrieval may be difficult (too much data to sort out)

(b) In a distributed system, data from different bases may be difficult to correlate.

SOME GUIDELINES FOR CONTROL SYSTEM DESIGN

K.K. Li

Brookhaven National Laboratory

It seems that the basic difficulty facing the control group is that the problem is not yet defined, at least not at a level that concrete steps or decisions can be made. The problem can only be defined by collecting a set of parameters and operating procedures, however tentative, from all other groups. Without such information, discussions can only be philosophical and may lead to unrealistic conclusions.

As ISABELLE is a machine of one of a kind, perhaps it is unrealistic to expect to have an ultimate control system in the beginning. The system is surely going to grow once the machine starts operating. It seems that the immediate goal will be to design a system to help to debug and control the individual machine systems, and to be used in the start-up and the early operating phase of the machine. Flexibility, however, has to be built in to allow for future expansion.

Even though ISABELLE is unique, some of the systems are not, e.g. vacuum system, security system, beam dynamics, general data storage, etc. It is unreasonable to assume that the control and monitor of them will have to be worked out from scratch. Experience should be drawn from other laboratories, and from the manufacturers of various systems. It is imperative to find out what their difficulties were and what they intend to do in the future. Some of this information may or may not be relevant to ISABELLE, but at least the same mistakes should and must be avoided.

The control of ISABELLE should be built so that it will be operated by a very small number of people, ultimately one, not only when it runs smoothly but also when small beam perturbation exists or is needed. When serious component failure occurs, people who are expert in that area have to be called in. It is important

then that all relevant information be made available to him and the system under investigation can be switched to local control until it is fixed. The control system would consist of a main control center and a number of subcenters distributed around the machine. Each subcenter is assigned a special task, e.g., for the vacuum system, for the security system, etc. These subcenters should normally be unmanned, and interact with one another only through the main control. All the raw data are generated and should be stored at these subcenters. They should be made available to the main control upon command. The main control then may generate and store a higher order data set. The operating parameters should be kept and simultaneously updated in both the main control and the subcenter so that each subcenter can operate in a self-sufficient manner, especially when it is desired to have local control, manual or otherwise. In addition to these centers, there should be data terminals in the user's areas so that the user can obtain data from the main control upon command from their own data gathering system.

The main control will have one or maybe even two computers. Computers will also be used at the subcenters if necessary. The system will be digital. There will have to be a universal and flexible interface between the subcenter computer and the outputs of machine data gathering devices, and between the main control computer and the user's data gathering system. It is important to limit the type of computers used to a smallest possible number, preferably one. It is also important not to do any in-house hardware development if at all possible. The same applies to software development, perhaps to a lesser degree. The number of languages used must be limited, preferably to two, e.g. FORTRAN and one assembly language and the same languages must be used throughout the whole system. All software packages must be made callable by programs of different language.

The control and monitoring concept or method for a particular

subsystem will grow and develop with the hardware development of that system and will only finalize, if at all, when the system is functioning. The control group should assign a person to work with the subsystem groups (or vice versa) and make sure the subsystem will operate as self-sufficiently as possible. If so, in the start-up phase of ISABELLE, the main control system could perhaps be rather rudimentary which will then develop as needs arise.

It should be emphasized again that in-house development must not be done for development sake. The system planning should not wait for newer and perhaps better devices to be developed commercially. Well proven devices should be considered so long as they are economically feasible. Self-contained and working software packages from other laboratories should be adapted and used.

Until a complete set of parameters is defined, perhaps the immediate task of the control group is to set guidelines or specifications for the system after some consultation with other groups. For example, what computer and languages are to be used, what type of interface, what kind of signal expected from various monitoring devices, etc. The idea is to have a firm control on hardware and software proliferation from the beginning.

COMPUTER SYSTEM REQUIREMENTS

D. Lowenstein

Brookhaven National Laboratory

ISABELLE is presently in the design stage where few parameters are decided, other than that it consists of 2 × 30/200 GeV proton rings. This then defines how much detail of the control system may be determined. One of the few criteria that may be presently placed on such a system is that it be modular, and as simple as possible. As to the modularity details, at this time, I feel that one or more processors be dedicated to perform a particular function in the machine, e.g., power supply control. These processors would then have the ability to communicate with the console computer as well as being able to be run locally. This console computer may have other processors connected to it that run displays, knobs, etc. The criteria that a particular function, i.e., devices, be connected to a computer should be determined by:

1. If it is to be controlled in or monitored in the main control room.
2. If the group responsible for the design and implementation of a device decides that a computer is required. This does not imply that this local computer be linked to the control room computer.

With this scheme the implementation of each local computer is the responsibility of the local group. A strong interaction between the "controls" group and the local users is mandatory and a series of rules must be made at the start. For example:

a. commmunications system structure, i.e. a definition of pulse specs, etc.;

b. communications data protocol, i.e. block format structure;

c. communications hardware, line impedance etc.;

d. the local section is responsible for both the hardware and software of their particular controls;

e. if one is very lucky, perhaps standard types of multiplexers, A/D, D/A etc., can be agreed upon to be used for most applications;

f. the users should be urged to standardize on a particular type of computer. At the bare minimum, at least a common word size. One instruction set may lead to nonduplication of some software and perhaps less confusion.

Global control systems, whether or not computers are used, cannot make up for equipment deficiencies. If a magnet, power supply, refrigerator, etc., cannot regulate to the required tolerances, one cannot expect a computer to constantly compensate for these design errors. This problem is of particular concern for the magnet corrections. An inordinate number of magnet corrections (time dependent, etc.) will make ISABELLE an uncontrollable machine.

A NEW APPROACH TO CONTROL SYSTEM INTERFACES

K. B. Mallory
Stanford Linear Accelerator Center

Each time a new accelerator is designed, the controls people make a new analysis of the control problem. Each time they tend to come up with the same kind of solution. Regulators and servo loops are considered part of the equipment they control and, as much as possible, left to the equipment designer. The controls group work with interactions between subsystems, collection and analysis of monitoring data, generation and transmission of set-point data to the equipment, and the entire man-machine interface.

There have been trends toward more reliance on computer systems for operations of a machine and toward more decentralization of the logical systems, but in general the interface between equipment designers and the "control system" has remained at the point where the signals first enter the general cable plant.

With the increased use of minicomputers within subsystems and particularly with the advent of the microprocessor, it is possible that a radical change should be made in the logical interface point between the equipment designer and the control system. A function generator no longer need look like fifty registers that must be addressed by separate wires or I/O addresses of a computer. It can be an intelligent terminal which converses with the central control system in the same "language" as might be used between the equipment designer and the control (or supervisory) system should be in software, not hardware: it should be made between his control programs in the (micro)processor and a standard program that handles the link interface. The interface can be made in the interaction between user programs and a "supervisor", an interaction that is generally well understood by programmers.

A number of other interface problems may also be changed, of course. In particular, signal multiplexers which typically have been part of the control group's data transmission system or of the I/O structure of a larger computer may now become part of the user logic in the micro-processor. Sets of data tables may be stored locally and be changed by selection instead of by rewritting the table from a higher level supervisor. Much more complicated control algorithms will be performed locally with minimal supervision.

To make this new division of effort work, the microprocessor usage must be standardized early and left fixed, at least through the end of construction of the machine. A type of microprocessor should be selected; its hardware and software interface to the rest of the control system must be designed; the method of communication between the link handler and user programs must be defined; the method of communication between the link handler and user programs must be defined; and all of this should be accomplished before the equipment designers are ready to connect microprocessors into their equipment.

The control algorithms and the hardware connections to the equipment being controlled remain strictly the responsibility of the equipment designer. The processor itself is physically part of his equipment, and physical responsibility for the signals is passed to the controls group where the signals enter the cable plant. But this shift of logical responsibility would make system design and maintenance much simpler by increasing the uniformity of all interfaces.

I do not know if a heterogeneous collection of design engineers can be persuaded to use such a redefined interface. It would require a major development effort early during the design phase of the accelerator. But it could save a great deal of multiple design for specialized interfaces. This relocation of the interface between equipment and the control system should be studied in

much more detail, and seriously considered for installation in new machines such as PEP and ISABELLE.

$\bar{p}$-p OPTION

F. Halzen
University of Wisconsin
E. Paschos, R. Peierls, D.P. Sidhu, T.L. Trueman
Brookhaven National Laboratory

It is generally accepted that the $\bar{p}$-p option adds great versatility to p-p colliding rings. There are, however, luminosity limitations in the $\bar{p}$-p option, which demand a detailed comparison of the physics capabilities to the capabilities of the p-p machine.

1. Weak Interactions

Parton models suggest that the cross section for the production of W's is larger for $\bar{p}$-p than p-p beams. This is a consequence of the fact that there are more antiquarks in the antiproton. Figure 1 shows the results of such a calculation using the quark distributions of Pakvasa, Parashar, and Tuan.[1] It is noted that for p-p collisions the W^+ production is greater than W^- as is evident from the fact that there are more u-quarks in the proton than d-quarks. The cross section for W^+ and W^- with $\bar{p}$-p beams are equal in the model. The cross section for $\bar{p}$-p beams is an order of magnitude larger than the average cross section

$$\tfrac{1}{2}[\sigma(pp \to W^+ + x) + \sigma(pp \to W^- + x)].$$

Figure 2 shows the differential cross section for the same processes in the absence of an intermediate vector boson, where the same qualitative features hold. For comparison, we have also included the differential cross section for the electromagnetic production of electron-pairs.

As is discussed in Section 2.2, the hadronic backgrounds for p-p and $\bar{p}$-p are expected to be equal. Consequently, the signal-to-background ratio is better by a factor of 10 for the $\bar{p}$-p option.

---

1. S. Pakvasa, D. Parashar, and S.F. Tuan, Phys.Rev. D10, 2124 (1974); ibid D11, 214 (1975).

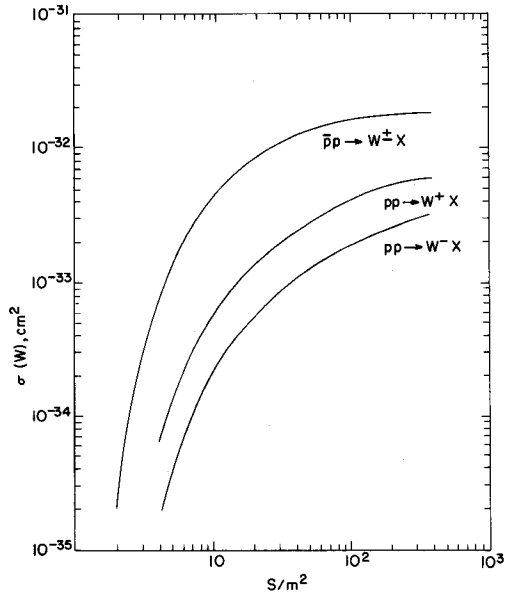

Fig. 1. Production Cross Sections for the Reactions (a) $\bar{p}p \rightarrow W^{\pm}X$, (b) $pp \rightarrow W^{+}X$, (c) $pp \rightarrow W^{-}X$.

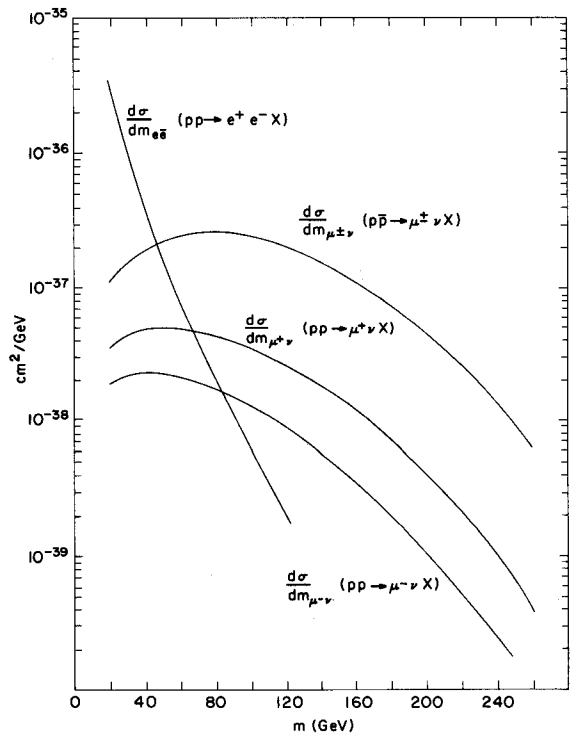

Fig. 2. Differential Cross Sections in the Absence of a W for the Reactions (a) $\bar{p}p \rightarrow \mu^{\pm}\nu X$, (b) $pp \rightarrow \mu^{+}\nu X$ (c) $pp \rightarrow \mu^{-}\bar{\nu}X$, (d) $pp \rightarrow e^{+}e^{-}X$.

2. Strong Interactions

2.1 Total Cross Sections and Elastic Scattering

The hadronic cross sections are so large that limited luminosity (even of 10^{29} $cm^{-2}sec^{-1}$) will yield substantial counting rates. The important questions in this case are whether the observed energy trends and asymptotic estimates persist throughout the ISA energy range. Available data for the total cross section and the ratio ρ = Ref/Imf are shown in Figs. 3 and 4. The total ($\bar{p}p$) cross section, at the highest available energy at this time, is still flat. The real part of the scattering amplitude seems to go through a zero at $p_{Lab} \approx 100$ (GeV/c). The curves in the figures show the result of dispersion relation calculations.[2] The extrapolation of the theoretical calculations for σ_{tot} and ρ are shown in Figs. 5 and 6. Figure 7 shows data on the slope parameter b(s) and its extrapolation to ISA energies. The theoretical curves for Figs. 5 through 7 are from Ref. 3.

2.2 Hadron Production at Large Transverse Momenta

The theoretical models in this case are based on the scattering of quark substructure within the hadrons. In fact, the dominant contribution is assumed to arise from quark-meson scattering and leads to the $(1/p_\perp^8)f(x_\perp)$ law, where $x_\perp = 2p_\perp/\sqrt{s}$, $\sqrt{s}$ is the total center-of-mass energy. The fundamental diagrams which contribute to p-p scattering also contribute to $\bar{p}$-p scattering. Thus the two cross sections are expected to be the same. The limitation in luminosity restricts the experimentally accessible region to smaller values of $p_\perp$. For instance, adopting the $1/p_\perp^8$ law and looking at Fig. 8 we note the maximum values of $p_\perp$ accessible to the two options are given in Table I.

---

2. R.E. Hendrick and B. Lautrup, Phys. Rev. D11, 529 (1975).
3. D.P. Sidhu and U.P. Sukhatme, Phys. Rev. D11, 1351 (1975); D.P. Sidhu, unpublished calculation.

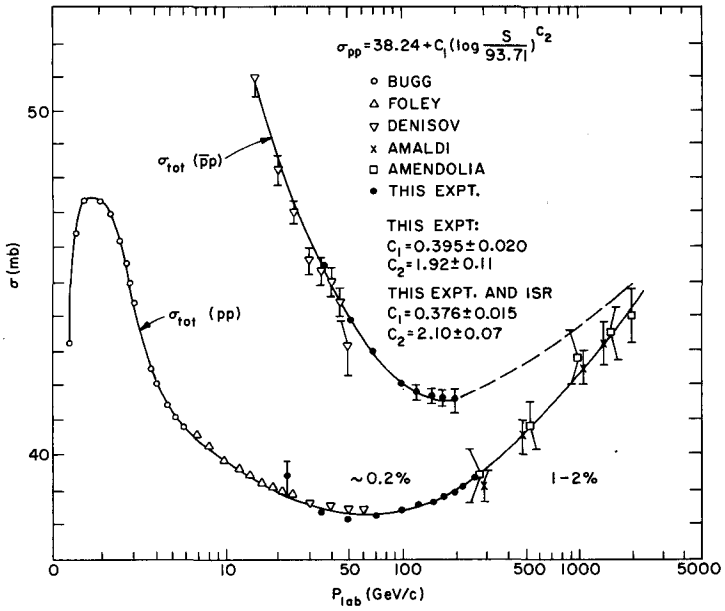

Fig. 3. Available Total Cross Section Data for Reactions pp and $\bar{p}p$. σ_{pp} fit: P. Mazur, APS Annaheim Meeting, 1975.

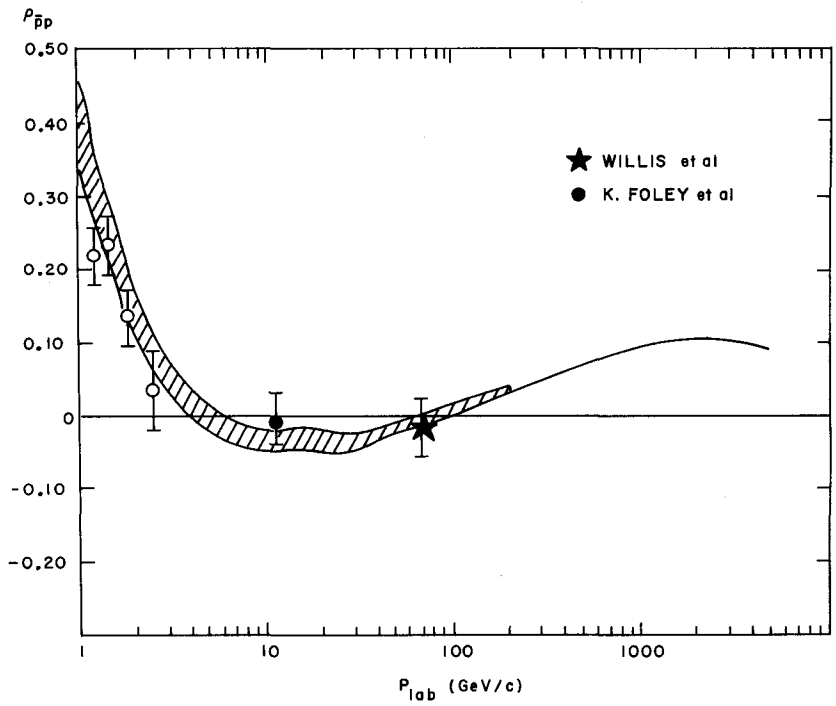

Fig. 4. Available Data for the Ratio $\rho_{\bar{p}p}$ = ReF/ImF.

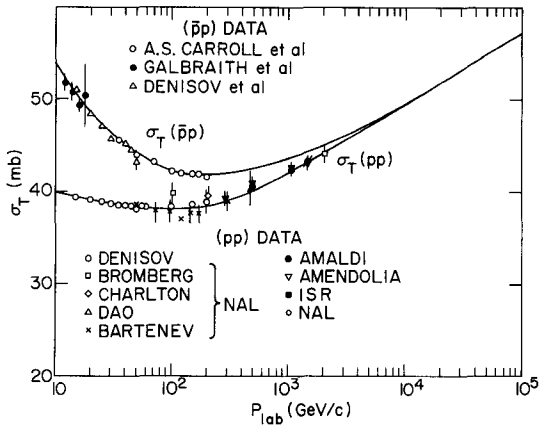

Fig. 5. Theoretical Predictions for the Total Cross Sections.

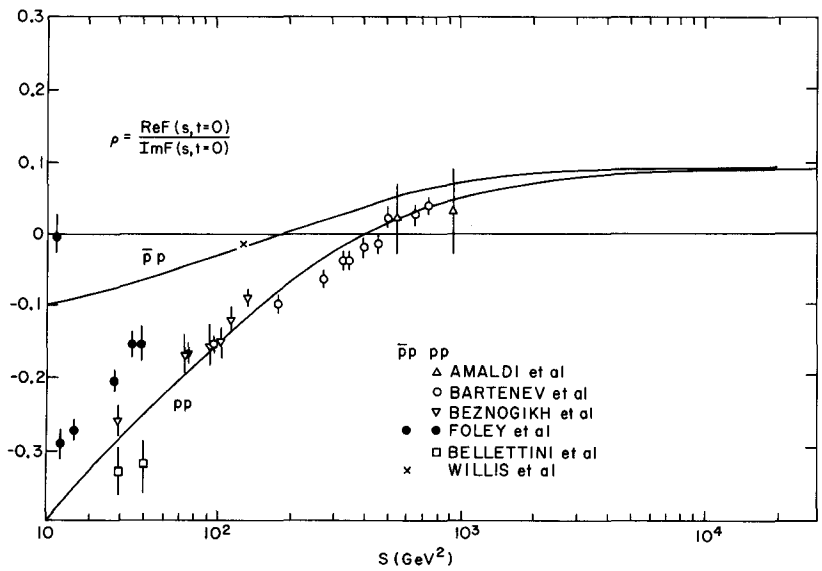

Fig. 6. Theoretical Predictions for the Ratio of the Real to the Imaginary Parts of the Forward Scattering Amplitude for pp and $\bar{p}p$, Ref. 3.

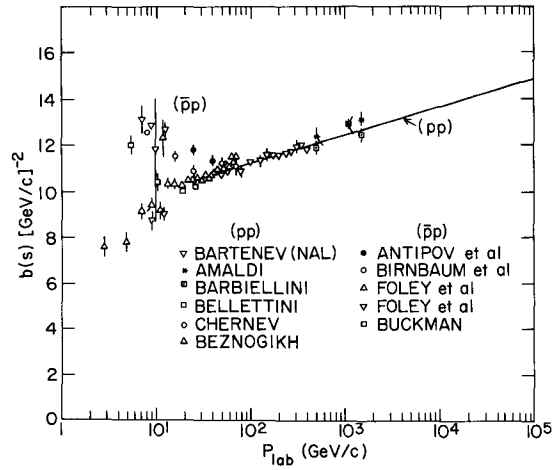

Fig. 7. Theoretical Prediction for the Slope Parameter, b(s). Theory from Ref. 3.

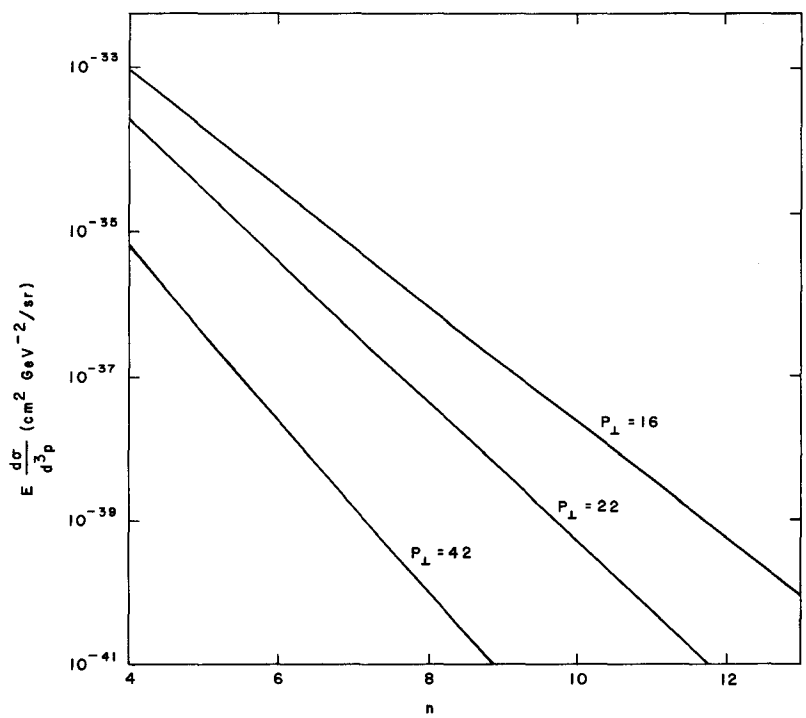

Fig. 8. Examples of Scaling Laws for High Transverse Momenta.

Table I.

p-p machine with $L = 10^{33} cm^{-2}/sec$ GeV/c	$\bar{p}$-p option[5] $L = 10^{31} cm^{-2}/sec$ GeV/c	
25	16	Maximum $p_\perp$ for n = 8
18	12	Maximum $p_\perp$ for n = 10

These values are obtained under the expectation[4] that cross sections at the level of 10^{-38} (cm^2 GeV^{-2}/sr) are measurable for a luminosity of 10^{33} cm^{-2}/sec.

3. New Aspects

3.1 Symmetry

The $\bar{p}$-p initial state is invariant under charge congugation. Thus it provides new tests of C-invariance for strong interactions. Consider the inclusive and charge-congugate reactions

$$\bar{p} + p \rightarrow h^+ + x \tag{3.1}$$

$$\bar{p} + p \rightarrow h^- + x \tag{3.2}$$

and define by θ the scattering angle of h^+. Then

$$w(\theta) = \bar{w}(\pi - \theta)$$

where w is the rate for reaction (3.1) and $\bar{w}$ is the corresponding rate for reaction (3.2).

For two body reactions there is a test of CP invariance. Consider

$$\bar{p} + p \rightarrow \bar{\Lambda} + \Lambda \tag{3.4}$$

If we denote by $\bar{q}(\Lambda,\theta)$ and $\bar{q}(\bar{\Lambda},\theta)$ respectively, the polarizations of Λ and $\bar{\Lambda}$, if any, where θ is the angle between the particle in question and the $\bar{p}$ direction, then CP implies

$$\bar{q}(\Lambda,\theta) = \bar{q}(\bar{\Lambda},\pi - \theta) \quad . \tag{3.5}$$

4. A Proposal for Construction of a Proton-Proton Storage Accelerator Facility ISABELLE, BNL Rept. 20161 (1975) p. 25-27.

5. D. Berley, A.S. Carroll, A.K. Mann, Single Ring $\bar{p}$-p Colliding Beams as an Interim ISABELLE, these Proc.

More tests can be found in Ref. 6. Similar tests can be devised for the production and decays of polarized W bosons.

3.2 Annihilation Channels

One may wish to define precise annihilation channels like

$$\bar{p} + p \rightarrow e^{+} + e^{-} \tag{3.6}$$

Cross sections where the $\bar{p}$-p system couples directly to a photon are very small because of the electromagnetic form factors of the proton. A single pole extrapolation for (3.6) proceeding through a Z^{o} gives

$$\sigma \approx 10^{-40}\ \mathrm{cm}^{2}$$

at $M_Z \approx 100\ \mathrm{GeV}/c^2$. Thus, one is forced to open the hadronic final states and look for

$$\bar{p} + p \rightarrow e^{+}e^{-} + \text{hadrons}$$

but now the discussion of the section on weak interactions applies.

---

6. A. Pais, Phys. Rev. Lett. 3, 242 (1959).

HEATING EFFECTS OF AN UNSEPARATED $\bar{p}$ BEAM IN THE ISA RING

V.L. Fitch
Princeton University

I. Assumptions and Caveats

1. Following the "Gray Book", we assume the $\bar{p}$'s are derived from 200 BeV proton beam target, 30 BeV negative particles are selected in the forward direction. We assume that the optical system defines the secondary beam appropriately – that there are no particles outside the $d\Omega$, dp/p acceptable by the ISA ring.

2. We consider the heating effects in the conductor from
a) pion, kaon, and muon decay,
b) antiprotons injected, but not captured in the ISA ring (30% of the beam).

3. In the case of pion or kaon decay we visualize the decay products, because of their lower momenta, spiralling into the inside edge of the vacuum chamber and thence into the magnet coil. The magnet coil is correspondingly exposed over a small fraction of its total volume. In the estimates below we restrict the exposure to the median plane ± 0.93 cm which is the magnitude of the vertical betatron oscillations. Decay kinematics increase this vertical band of exposure especially for kaon decay. However, we are interested in "worst case" effects and ignore, for the present, these other broadening effects. We also assume that all decay products originating in the straight sections stay in the beam and then spiral inward in the magnet sections.

II. The Conductor Coil

The braided conductors on which the particles impinge is constituted as shown in Table I. The coil is 1.7 cm thick.

III. Pions

For each proton bunch $N(\bar{p})/N(p) = 10^{-5}$; $N(\pi^-)/N(\bar{p}) = 40$; $N(p) = 10^{14} \times 2.5$; and $N(\pi^-) = 1 \times 10^{11}$. The mean decay length of the pions is 1650 m. If ISA magnets accept $\Delta p/p = \pm 1.2\%$, then 3% of the muons will be trapped in orbit. The other muons spiral inward and enter the magnet coil with a crossing angle given by

$$\theta_c = \sqrt{\frac{2\delta}{R_m}} \sqrt{\frac{30}{p} - 1} ,$$

$$\theta_c = 27.4 \times 10^{-3} \sqrt{30/p - 1} ,$$

where we have assumed a mean distance, orbit to coil, of 6 cm and a magnetic bending radius R_m of 160 m. The total coil thickness is 1.7 cm. As a function of momentum, the muons traverse ℓ cm of magnet coil (Table II).

From pion decay the muons are uniformly distributed in momentum from 30 down to 17.2 BeV. The average conductor length traversed in this interval is 131 cm. Of the 1.7 cm, 0.43 cm is NbTi with a density of 5.9. The average superconductor traversed by the muons is 182 g/cm^2, which leads to an average energy loss in the SC of 250 MeV per muon.

$$\text{Total energy loss} = 10^{11} \times 250 \times 1.6 \times 10^{-6} \text{ erg}$$
$$= 4 \text{ joule} = 1 \text{ calorie} .$$

The 1 cal will be distributed over $(1650/3000) \times 240 = 132$ magnets, each of which has 430 cm of SC along the beam. The amplitude of the betatron oscillations is 0.93 cm. Therefore we distribute the energy over 1.8 cm vertically. This results in the energy from the muons going into 2.9×10^5 grams of SC.

Heating from pion decay $= 1/(2.9 \times 10^5) = 0.34 \times 10^{-5}$ cal/g.

TABLE I.

Material	Fractional Volume	Weight g/cm^2	Density g/cm^3
Niobium	0.13	1.86	8.4
Titanium	0.12	0.92	4.5
Copper	0.33	5.03	8.96
Indium	0.22	2.72	7.28
Glass	0.10	0.44	2.6
Epoxy	0.05	0.08	2.6
Helium	0.05	0.02	

TABLE II.

p	$\theta_c (\times 10^3)$	ℓ (cm)
28	7.3	233
26	10.7	159
24	13.6	125
22	16.5	103
20	19.4	88
18	22.4	76
16	25.6	66
14	29.3	58
12	33.5	51
10	54.8	31
8	75.3	22

IV. Heating from Kaon Decay

Two-thirds of the decays are to muons. The calculation proceeds as for pions except that the muon spectrum extends from 30 down to $\sim$ 0 BeV.

$$\frac{N(K^-)}{N(\pi^-)} = 0.1$$

$$N(K^-) = 10^{10}$$

The average superconductor length traversed = 99 cm. Total energy loss of μ- = 0.05 calories. One decay length corresponds to $\sim$ 31 magnets, or 6.9×10^4 g of NbTi.

$$(\text{Heating from } K \rightarrow \mu + \nu) = \frac{0.05}{6.9 \times 10^4} = 0.07 \times 10^{-5} \text{ cal/g.}$$

The remainder ($\sim$ 1/3) of the K decays are to strongly interacting particles. We assume all of this energy is absorbed in the coil 25% of which is NbTi. This comes to 1 cal deposited in the NbTi.

The heating from kaons decaying to strongly interacting particles and photons = 1 cal/6.9×10^4 g = 1.5×10^{-5} cal/g.

V. Heating from Loss of $\bar{p}$

It is estimated that 30% of the $\bar{p}$'s (0.9 cal) will not be captured. These will end up in 240 magnets, i.e. $5.3 \times 10^{+5}$ g.

$$\text{Heat from lost } \bar{p}\text{'s} = \tfrac{1}{4}\,\frac{0.9}{5.3 \times 10^5} = 0.04 \times 10^{-5} \text{ cal/g.}$$

VI. Heating from Decay of Stored Muons

Three percent of the muons are in orbit and decay with 1/12 of their energy ending up in the SC in all 240 bending magnets.

$$\text{Heating from stored muon decay} = 0.06 \times 10^{-5} \text{ cal/g.}$$

VII. Total Heating

Pions	0.34×10^{-5} cal/g
kaon $\rightarrow \mu + \nu$	0.07×10^{-5}
kaon $\rightarrow \pi$'s	1.5×10^{-5}
lost $\bar{p}$'s	0.04×10^{-5}
Decay of stored muons	0.06×10^{-5}
Total	2.01×10^{-5} cal/g

VIII. Heat Capacities[1] at 4 K

$$\text{NbTi} = 7 \times 10^{-5} \text{ cal/g K}$$
$$\text{Cu} = 2.1 \times 10^{-5}$$
$$\text{In} = 23 \times 10^{-5}$$

IX. Conclusions

From the total heating and heat capacity figures, we deduce that the superconductor would be warmed by ~ 0.3 K. Since the superconductor is operating at 4 K and the critical temperature at 30 BeV is approximately 9 K the safety factor is about 15. The energy loss/gram in the Cu is approximately the same as in the NbTi. The temperature rise in the copper would be about 1 K, in the indium ~ 0.1 K. We note these are maximum heat loads, at the peak of the exponential decay.

In the above estimates we assume the heat load has been deposited instantaneously, i.e., in a time short compared to the characteristic cooling times of the various conductor components. This is probably not a valid assumption especially insofar as the superconductor and the copper in which it is enmeshed. The characteristic cooling time is

$$t = \alpha^2 a^2$$

where

$$\alpha^2 \sim \frac{\text{density} \times \text{specific heat}}{\text{thermal conductivity}}$$

$$a = \text{characteristic radius.}$$

1. W.B. Sampson, private communication.

If we take the thermal conductivity to be that of tin at 4 K, i.e., 10 cal $sec^{-1}cm^{-1}K^{-1}$ and a characteristic radius of the superconductor filament to be 5×10^{-4} cm, then

$$t \sim 10^{-11} \text{ seconds (for superconducting filament).}$$

For the 0.3 mm copper wire with SC imbedded, the time becomes (using same thermal conductivity)

$$t \sim 10^{-8} \text{ seconds.}$$

This latter time is much shorter than that characteristic of the duration of the bunch ($\sim 10^{-6}$ sec) of particles injected into the ISA ring. Therefore, to calculate the heating, one should use a specific heat which is an average between the copper and SC. Weighting with the relative mass of material present, the combined specific heat is calculated to be 3.84×10^{-5} cal/g K. The temperature rise in the combined conductor would then be ~ 0.6 K, and the safety factor is only 8.

X. Comment

We note the major heating effect comes from K decay to strongly interacting particles and electrons which are expected to deposit nearly all their energy in the coil. The problem is compounded by the relatively short decay length of the K's - 220 m. The above estimates do not take into account the attenuation of kaons through decay in going from the target to the ISA ring and are therefore conservative. It is not unreasonable to expect that more than half the kaons would be lost in this beam transport. The heat load due to kaons would be reduced accordingly.

We conclude that at the $\bar{p}$ fluxes proposed in the Gray Book, the heat load due to the decay of the π's and K's is acceptable. However, it would become a problem at ~ 2 times the proposed flux. Since most of the heat load comes from the kaons, it would then be desirable to lengthen the beam before injection into ISA magnets to attenuate this component of the beam.

ON THE CONTAMINATION DURING ANTIPROTON INJECTION INTO ISABELLE

K. Hübner

CERN, Geneva, Switzerland

INTRODUCTION

It is shown that up to 2.5×10^9 particles will be lost per m within 10 μs in ISA during each injection of an antiproton bunch. The energy lost by these particles in the superconducting magnets may drive them normal. The particles are mainly muons from the π^- decay. Various remedies are presented and discussed.

1. Number of Secondaries Produced Per ISA Pulse

The number of antiprotons injected per ISA burst is[1]

$$N_{\bar{p}}^{inj} = N_p \frac{N_{\bar{p}}}{N_p} \frac{1}{\eta_s 10} = 6 \times 10^{14} \times 8 \times 10^{-5} \frac{1}{0.7 \times 10} = 7 \times 10^9$$

1.1 Number of Particles Accepted by Channel after Target

Table I

Particle	$\partial^2 N/\partial p \partial \Omega$ [(a)] GeV/c^{-1}sr^{-1}	$N_x/N_{\bar{p}}$	N_x
$\bar{p}$	0.5	1	0.7×10^{10}
π^-	30	60 [(b)]	41×10^{10}
K^-	3	6	4.2×10^{10}
$\Sigma^- = \frac{1}{4}\Sigma$	0.07	0.14	0.1×10^{10}

(a) H. Grote, R. Hagedorn, and J. Ranft, Atlas of Particle Production Spectra, CERN (1970).

(b) Measurements at FNAL indicate a value smaller by ~ 20%, cf. W.F. Baker, A.S. Carroll, I. Chang, D. Eartly, O. Fackler, G. Giacommelli, P. Kohler, T. Kycia, K.K.Li, P. Mazur, P. Mockett, K. Pretzl, S. Pruss, D. Rahm, R. Rubinstein., A. Wehmann, NAL-PUB-74/13-EXP (1974).

1. C. Baltay, R. Chasman, H.W.J. Foelsche, H. Hahn, M. Month and A. van Steenbergen, Proc. IXth Int. Conf. on High Energy Accelerators, SLAC, 572 (1974).

The distance between target at injection point is one-eighth of the ISA circumference, hence ℓ = 370 m. The intensity of the unwanted particles will have decayed by a small amount on the way to the ring. Table II gives the numbers.

Table II

Particle	decay-length ℓ_d (m)	ℓ/ℓ_d	$e^{-\ell/\ell_d}$	N_x^{inj}
π^-	1780	0.21	0.8	33×10^{10}
K^-	240	1.5	0.22	0.9×10^{10}
Σ^-	130	2.8	0.06	0.006×10^{10}

N_x^{inj} is the number of particles injected.

2. Distribution of Particle Loss in ISA

2.1 Pions

The π^- are decaying exponentially into $\mu\nu$. The longitudinal momentum of the μ's is[2]

$$p_\mu/p_\pi = 0.79 + 0.21 \cos \Theta^*$$

where Θ^* is the decay angle in the rest system of the π^-. Thus, some of the μ decaying in the forward direction will be accepted in the ring. They will decay relatively slowly and get distributed uniformly around the ring. The μ's not accepted will be lost immediately and their azimuthal distribution is that of the π^- decay. How many μ's are accepted?

Since the decay is isotropic we get for the fraction $\bar{f}$ accepted

$$\bar{f} = \frac{1}{1.7} \left(\frac{\Delta p}{p} \right)_{max}$$

2. J. Bailey, W. Barth, G. von Bochmann, R. Brown, F. Farley, M. Gusch, H. Jöstlein, S. van der Meer, E. Picasso, R. Williams, Nuovo Cimento 9A, 4, 424 (1972).

where $(\Delta p/p)_{max}$ is the maximum acceptance of the machine. With

$$\left(\frac{\Delta p}{p}\right)_{max} = \frac{\Delta R_{max}}{\alpha_p} = \frac{80 \times 10^{-3}}{1} = 8 \times 10^{-2}$$

$$\bar{f} \cong 5\% \quad .$$

Since their decay-length corresponds to 59 turns, they are deposited uniformly around the ring. We get

$$dN_\mu/ds = \frac{33 \times 10^{10}}{2.96 \times 10^3} \times 0.05 = 0.05 \times 10^8 \ \mu's/m \quad .$$

The remaining 95% of the μ's which are not accepted are lost according to

$$dN_\mu/ds = \frac{0.95\ N_{\pi^-}^{inj}}{\ell_d}\ e^{-s/\ell_d}$$

$$dN_\mu/ds = 1.8 \times 10^8 \times e^{-s/1780}, \mu's/m \quad .$$

2.2 Kaons

In this case, a small fraction of the decay products will be accepted. However, the total amount is small so we neglect this fact. Their decay is more rapid than the decay of π's. One gets

$$dN_k/ds = \frac{0.9 \times 10^{10}}{240}\ e^{-s/240} = 0.38 \times 10^8\ e^{-s/240}, K^-\text{-decays/m.}$$

Adding up yields for the cumulative loss per meter:

Table III

Azimuth	Number of Particles Lost per m
right after injection point	2.5×10^8
opposite to injection point	0.95×10^8
right before injection point	0.46×10^8

If the energy deposition in the magnets associated with this loss were too high, one would have to think of remedies to avoid or reduce the amount of secondaries injected into the ring. In the next chapter some possible solutions are discussed in greater detail.

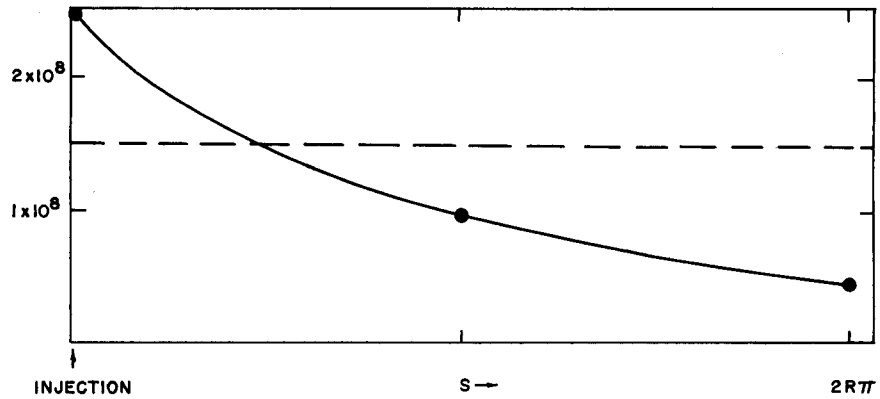

Fig. 1. Number of particles lost per meter vs azimuth.

3. Reduction of Contamination

To make the examples more illustrative, we assume that the pion contamination must be reduced by a factor 5 to 0.5×10^8 particles lost/m right after the injection point.

3.1 RF-Separator

A separator working at this momentum is being built for CERN at Karlsruhe.[3] It operates at 2.9 GHz. In our case, the distance between the two deflecting cavities has to be chosen such that the pions are fanned out by the second cavity and the net deflection of the antiproton is zero. (This is opposite to the usual operation where the wanted particles are fanned out and the unwanted particles hit a central stopper.)

However, two problems arise:

i) more than 50% of the pions are transmitted[4]

i) it is doubtful whether the acceptance of the separator can be made to match the acceptance of an ISA ring. As a matter of fact, the proposed separator has an acceptance of only $\Delta\Omega(\Delta p/p) = 3.5 \times 10^{-7}$, a factor 14 smaller than ISA.[3]

Problem i) may be overcome, in principle, by using a second separator in the other plane. The intercavity distance becomes for a frequency of f = 2.9 GHz,

$$s = \frac{c\gamma_p^2}{f}\left[1 - \left(\frac{m_\pi}{m_p}\right)^2\right]^{-1} = 130 \text{ m} \quad .$$

This can easily be accommodated between the target and injection point of the antiprotons.

---

3. W. Bauer, A. Citron, G. Dammertz, M. Grundner, H. Lengeler, and E. Rathgeber, Proc. Intern. Conf. on Instrum. for High Energy Physics, Frascati 1973, p. 716.

4. H. Hahn, Proc. Int. Conf. on Instrum. for High Energy Physics, (1966), p. 245.

3.2 Longer Distance Between Target and Injection

In order to attenuate the pions by a factor 5 a drift length of 2800 m is needed. Solution: Let the π's make 2 turns in the AGS before injecting them into ISA as shown in Fig. 2.

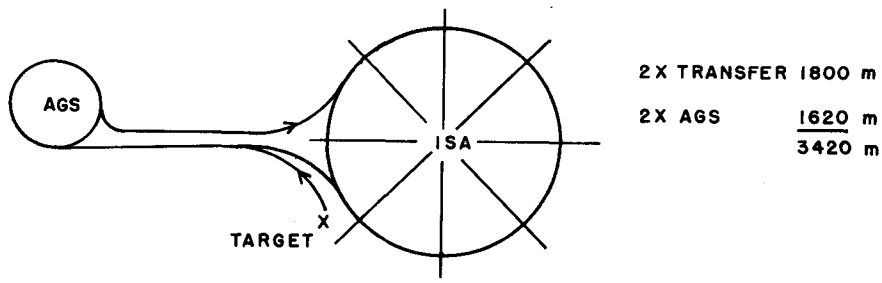

Fig. 2. Attenuation of Pions by Inection into the AGS.

This length is sufficient for an attenuation by a factor 6.5.

The acceptance of the AGS is large enough to avoid any clipping of the pulse. This is shown below. The antiproton beam has the following parameters[1]

$$E_h = 2\pi \times 10^{-6} \text{ rad m}$$
$$E_v = 8\pi \times 10^{-6} \text{ rad m}$$
$$\Delta p/p = 2.5\% \quad .$$

The AGS parameters are

$$\beta_h^{max} = \beta_v^{max} = 22 \text{ m}$$
$$\alpha_p = 1.8 \text{ m} \quad .$$

This yields for the total aperture occupied by the beam

$$\Delta x = 60 \text{ mm}$$
$$\Delta z = 30 \text{ mm}$$

which is well within the AGS aperture

$$\Delta x = 80 \text{ mm}$$
$$\Delta z = 40 \text{ mm} \quad .$$

A drawback of this scheme is the complicated transfer of this large

beam at 30 GeV/c. A complete second ejection system of the AGS is needed. The risetime of the kicker must be around 1.7 μsec.

3.3 Reduction of Primary, Longitudinal Bunch Area

The number of contaminating secondaries which got into the $\bar{p}$ ISA ring/ISA burst is proportional to the number of protons N_{pb} in the primary proton bunch whereas the final number of antiprotons $N_{\bar{p}}$ depends on the bunch length ℓ_b of the primary proton bunch as well.

$$N_{\bar{p}} \sim N_{pb}/\ell_b \quad .$$

Thus, we would like to keep this ratio large when N_{pb} is diminished. Call the longitudinal area of the primary bunch A. The relations:

$$N_\pi \sim N_{pb} \sim A$$
$$\ell_b \sim \sqrt{A}$$
$$N_{\bar{p}} \sim \sqrt{A} \ ,$$

suggest that a reduction of primary bunch area A reduces $L_{p\bar{p}}$ only $\sim \sqrt{A}$ while the contamination scales like A. Thus, for a reduction of a factor 5 in the contamination we pay with a factor 2.2 in $L_{p\bar{p}}$.

This scheme is very simple and does not require any additional equipment. Only the harmonic number and the voltage of the $\bar{p}$ rf system has to be increased accordingly since we accumulate more and shorter bunches.

The filling time does not increase though we need more ISA cycles n_c to fill the $\bar{p}$ ring. Since the time of an ISA cycle T is dominated by the initial stacking time T_{st} which will decrease like $\sqrt{A}$ as we get away with smaller stacks, the filling time T_f will be virtually unaffected.

$$T_f \sim n_c T \sim n_c (T_{st} + T_{acc}) \sim n_c T_{st} \left(1 + \frac{T_{acc}}{T_{st}} \right)$$
$$T_f \sim \frac{1}{\sqrt{A}} \sqrt{A} \left(1 + \frac{T_{acc}}{T_{st}} \right)$$

Since $T_{acc}/T_{st} \ll 1$ (Ref. 5) the filling time T_f will hardly increase. For

$$\ell_b \sim \frac{1}{\gamma_{tr}(Vh)^{\frac{1}{4}}}$$

one may try also a γ_{tr}-jump (of CERN PS) to increase the line density in the primary bunches. However, the concomitant increase in filling time may make the scheme impractical.

3.4 Cutting Secondary Bunch Length

Cutting out the middle part of the secondary bunch with a kicker in the antiproton transfer line reduces the unwanted secondaries.

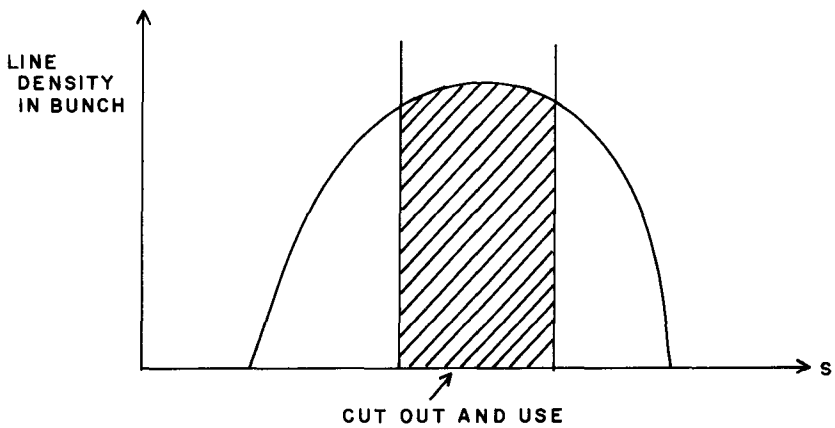

Fig. 3. Cut line density in bunch.

The luminosity will rise somewhat because we use the part with the high line density. Unfortunately, the filling time will be increased by the same factor as the number of unwanted secondaries is cut down. The harmonic number and the voltage of the $\bar{p}$ rf system must be adjusted to match the bunch length. A set of collimators removes the halo due to the finite risetime of the kicker.

---

5. E.C. Raka, private communication.

3.5 Expansion of Burst

One may argue that the superconducting magnets recover very quickly, say within a few seconds, from the heat deposited.[6] Thus, it would be sufficient to eject the protons in small quantities always waiting a few seconds before extracting the next batch.[7] In the meantime the target can be replaced.*

The simplest way to implement this is a higher harmonic rf system in the p ring. A fast kicker is used for a bunch-by-bunch transfer to the target. All the bunches are used, one after the other. A few seconds elapse between each transfer.

Since we assumed that a factor 5 has to be gained we need an rf system with h = 10 for acceleration. One may think to use this system also for the initial stacking. For acceleration a peak voltage of 200 kV is needed, 5 times more than with the h = 2 rf system. The bunch length is 60 m at 200 GeV/c. The line density in the bunch is the same as with h = 2, hence $L_{p\bar{p}}$ is not changed.

The risetime of the kicker magnet must be 0.8 μsec which is not unreasonable. Synchronization problems may lower the efficiency of the boxcar stacking in the $\bar{p}$ ring, if so many bunches have to be stacked.

4. Conclusions

It was shown that up to 2.5×10^9 particles/m, mainly muons, will be lost within 10 μsec in ISA during injection of the antiproton bunch. In order to reduce this by a factor F the following remedies were considered as shown in Table IV.

---

*In the same way one could use both ISA bunches in the original scheme and reduce the filling time by a factor 2.

6. G. Danby (private communication) 1975.

7. H.G. Hereward (private communication) 1975.

TABLE IV

Remedy	Reduction in $L_{p\bar{p}}$	Increase in filling time	Comments
rf separator	10(?) due to low acceptance of rf separator	--	normal separator has only 50% suppression. Hence the circular polarized type needed (Panofsky-type). Acceptance low.
Inject $\bar{p}$ in AGS before transfer to ISA	1	--	Needs a second ejection system in the AGS
Reduction of longitudinal area of primary bunch by F	$\sqrt{F}$	negligible	Cheapest way; no additional equipment. Harmonic number and voltage in $\bar{p}$ ring higher by $\sqrt{F}$.
Cutting secondary bunch length by about F	small increase	F	Needs a fast kicker in the transfer channel between target and $\bar{p}$ ring. Harmonic number and voltage in $\bar{p}$ ring higher by F.
Expansion of burst by using h = 2F in the p ring	1	negligible	Harmonic number and voltage in both rings increased by F. Fast kicker of 0.8 μsec risetime in the p ring at 200 GeV/c.

SINGLE RING $\bar{p}p$ COLLIDING BEAMS AS AN INTERIM ISABELLE

D. Berley
National Science Foundation
A. S. Carroll
Brookhaven National Laboratory
A. K. Mann
University of Pennsylvania

INTRODUCTION

Aim: To find a method whereby a single 200 GeV superconducting storage ring can be used in conjunction with the AGS to accelerate and store $\bar{p}$ and p with a luminosity of 10^{30} $cm^{-2}sec^{-1}$. We want primarily to keep within these constraints (AGS plus one 200 GeV ring) but in addition we will briefly consider other more complicated, more expensive possibilities later.

Purpose: Our principal motivation is that a single superconducting ring capable of storing and colliding $\bar{p}$ and p provides a good interim step toward a final two ring, higher luminosity, system.

It would be a good interim step because (a) there is a substantial amount of significant physics that can be done with $\bar{p}$ on p at $L = 10^{30}$ $cm^{-2}sec^{-1}$, and (b) there is a potential appreciable saving in initial cost of a single ring relative to two rings.

Physics: A more detailed comparison of $\bar{p}$ + p physics with p + p physics in the center of mass region 60 to 400 GeV will be found in Ref. (1). The main points, however, are the following:

(i) Basic similarity of $\bar{p}$ + p to $\bar{e}$ + e as the collisions of high energy fermion and antifermion. At sufficiently high energy Q_2 , does some fundamental annihilation process take place involving

1. F. Halzen, E. Paschos, R. Peierls, D.P. Sidhu, T.L. Trueman, $\bar{p}$ - p Option, these Proc.

primitive fermion and antifermion? Is the process largely independent of the dressing of the fermions and antifermions, e.g., of whether they are "dressed" with lepton number or baryon number?

Observe that if there is any validity to the above conjecture, 200 GeV $\bar{p}$ on 200 GeV p have considerable promise of producing the massive intermediate vector bosons ($M_W > 50$ GeV/c^2) that are now suggested both theoretically and experimentally. In this sense, 200 GeV $\bar{p}$ on 200 GeV p enables us to perform the same physics as 15 GeV e^+ or 15 GeV e^-, but extend it by more than an order of magnitude in center of mass energy to insure being above the now anticipated vital energy thresholds. In the parton picture, the presence of the "valence" antipartons are estimated, theoretically, to give an order of magnitude increase in W production for $\bar{p}$ + p over pp. Some confirmation of this increase comes from the recent experiment of Northeastern on the production of $\mu^+\mu^-$ pairs by pions at FNAL.

(ii) Strong interaction studies with $\bar{p}$ + p lead to similar type physics as studies of p + p and can be done with low luminosity. For example, total cross section, Coulomb interference effects, real <u>vs</u> imaginary amplitude studies, and all low $p_\perp$ studies can be done. (It should be noted that the average ISR luminosity has been $\sim 2 \times 10^{30} cm^{-2} sec^{-1}$). It is expected that the production of large $p_\perp$ hadrons by $\bar{p}$ + p collisions will be about the same as by p + p, so that there is an order of magnitude improvement in signal to noise in a $\bar{p}$ + p colliding rings for weak and E.M. processes.

<u>Cost</u>: We do not want to get involved in detailed estimates but an oversimplification can be made by leaving costs of magnet enclosure and beam injection tunnel as indicated in the ISABELLE proposal and halving all other costs. One obtains then about 70M$ as the reduced cost compared with the originally estimated cost without contingency or escalation of 130M$. It is probable that an initial saving of that magnitude cannot be accomplished, but there is enough room between 130M$ and 70M$ to allow a significant reduction in initial cost to be made if the initial scope is reduced

according to the outline described here.

SINGLE-RING $\bar{p}$-p COLLIDING BEAMS

Parameters and Constraints

In considering this single 200 GeV ring design we used the following parameters and constraints:

1. Luminosity $\geq 10^{30} cm^{-2} sec^{-1}$
2. Bunch length = 1 to 2 meters
3. Filling time $\leq$ 24 hours
4. Number of bunches = 4
5. Cooling time comparable to injection cycle
6. Consider one intermediate ring of $\leq$ 10 GeV with an aperture approximately equal to that of the AGS.

The luminosity is chosen for the physics reasons listed in the Introduction. A bunch length of 1 to 2 meters is about the maximum tolerable length for most experiments. Since the lifetime of the beam is probably a few days, a filling time of more than one day seems unreasonable. Given that there are eight insertion regions, 4 bunches provide collisions in each region. In order to be able repeatedly to inject $\bar{p}$'s created by 30 GeV protons from the AGS, we must be able to cool the previously injected $\bar{p}$'s in transverse phase space within the injection time cycle. (Note: this is a normal injection scheme in $e^+ e^-$ colliding rings where the synchrotron radiation cools the beam naturally.) Although the principal scheme discussed below does not include an $\sim$8 GeV "accumulator" storage ring, such a small ring was considered as being within the scope of this study. For the case without cooling the relative yields of antiprotons by 30 and 200 GeV protons are discussed in Appendix A. The conclusion is that it is not useful to consider production at 30 GeV unless cooling is possible.

Number and Emittance of $\bar{p}$'s Required

For a bunched beam with a bunch length comparable to the β

value at the intersection point, the maximum transverse brightness of the proton beam is given by [2-4]

$$\frac{N_p}{B\epsilon_p} = \frac{\pi^{3/2}}{\sqrt{2}} \frac{\gamma\Delta\nu}{r_p} = 2.6 \times 10^{18}\ m^{-1} \qquad (1)$$

for $\gamma = 200$, where N_p is the total number of protons stored and B is the number of bunches. ϵ_p is the rms emittance in meters and r_p is the classical proton radius of 1.54×10^{-18} meters. We use the standard value of the beam-beam tune shift limit of 5×10^{-3}.

Following Month's CRISP report,[3] we assume that we stack 4 bunches of 10^{12} protons which corresponds to 4 bunches directly from the AGS. Using Eq. (1) this leads to an emittance at 200 GeV of $\epsilon_p = 4 \times 10^{-7}$ mrad. Taking into account the γ factor in Eq. (1) this corresponds to a value of 10×10^{-6} at 8 GeV/c. This emittance at 8 GeV is now about 0.5 of the emittance of the $\bar{p}$'s as produced by the AGS.

When this limit is put into the expression for bunched beam, colliding head on, we have [2-4]

$$L = \frac{c}{4C} \frac{\pi}{2} \frac{N_{\bar{p}}}{r_p \beta_o} \gamma\Delta\nu \doteq 2.6 \times 10^{18}\ N_{\bar{p}}/cm^{-2}\ sec^{-1} \qquad (2)$$

for a 3×10^3 m circumference C of ISABELLE, a value of 3×10^8 m/sec

2. M. Sands SLAC-121/UC-28 (1970).
3. M. Month, CRISP 73-20 (1973).
4. J. Sandweiss, Notes for 1975 ISABELLE Summer Study. There were some small inconsistencies (less than a factor of 2) between references 1 - 3 due to different methods of calculating the overlap integrals involved in the luminosity and tune shift. The formulas given are in agreement with Sandweiss who uses rms values for the emittance, where rms beam size, $a = \sqrt{\epsilon\beta}$.

for the velocity of light c and the value of the β function at interaction of β_o = 1 meter. This equation implies that we require 2.7×10^{11} $\bar{p}$'s for a luminosity of 10^{30} $cm^{-2}sec^{-1}$.

Assuming that we can use ~ 6 cm vertical size and a 3 cm horizontal aperture for injection into ISABELLE, then using the equation of the 1974 "Gray Book",[5] the solid angle $\Delta\Omega$ for acceptance of $\bar{p}$'s by this aperture in ISABELLE is ~ 0.6 msr. Furthermore, the requirement that the rf voltage be less than ~ 10 MeV/turn limits us to a $\Delta p/p$ of ~ 1.2 %.[5] This leads to a number $\bar{p}$'s/AGS pulse of

$$N_{\bar{p}} = (1/3) N_p \frac{d^2 N_{\bar{p}}}{dp d\Omega} \Delta\Omega \Delta p = (1/3)(10^{13})(2\times10^{-2})(0.5)(10^{-3})(0.1) = 0.3 \times 10^7.$$

Thus the total time to produce 2.7×10^{11} $\bar{p}$'s is 25 hours. Note that the emittance of the produced $\bar{p}$'s for an 0.5 msr acceptance is only about twice that required for the 10^{30} luminosity at 200 GeV.

One possible cycle is with the ISABELLE ring operating at ~ 8 GeV, where we operate the AGS in a one bunch mode (ℓ_{bunch} = 13 m) at the highest intensity and repetition rate to produce $\bar{p}$'s. The cycle is as follows:

1. Operating the AGS in a one bunch mode, inject 8 GeV $\bar{p}$'s into 1 of 4 rf buckets in sequence into ISABELLE.
2. Cool injected $\bar{p}$'s before next bunch is loaded so that phase space is available for transverse stacking.
3. Stack until total number of $\bar{p}$'s $\approx 2.7 \times 10^{11}$ (~ 25 hours).

4a. Take $\bar{p}$'s through transition in ISABELLE at 20 GeV; or

---

5. A proposal for Construction of a Proton-Proton Storage Accelerator Facility, ISABELLE, BNL Rept. 18891, p. 305 (1974).

4b. Transfer $\bar{p}$'s back to AGS and accelerate $\bar{p}$'s to 30 GeV. Meanwhile raise ISABELLE to 30 GeV.

5. Inject 10^{12} protons of 30 GeV into each of 4 rf buckets in ISABELLE ring.

6. Accelerate to 200 GeV and bunch to 1 to 2 m.

7. Perform experiments for several days. (For a luminosity of 10^{30} and 2.7×10^{11} $\bar{p}$'s stored, the beam lifetime due to nuclear collisions is $\sim$ 50 days.)

As mentioned above, the AGS is operated in a one bunch mode so that the resulting $\bar{p}$'s occupy as little longitudinal phase space as possible.

The cooling and stacking stated in steps 2 and 3 are the most difficult and most uncertain of the steps. Basically the stacking depends on the

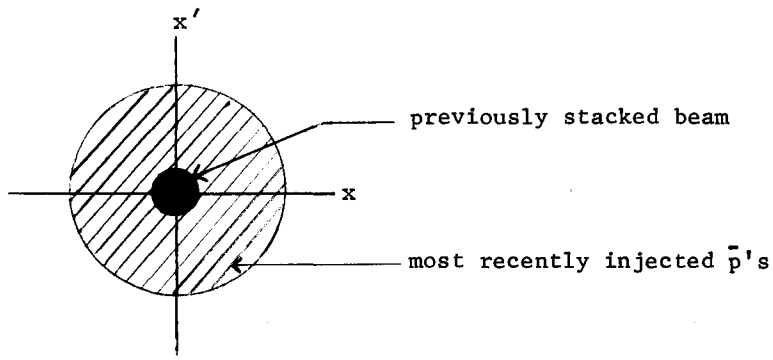

most recently injected $\bar{p}$'s being cooled sufficiently in transverse phase space so that more $\bar{p}$'s can be injected into the same area (as shown in the above figure). Possible methods for performing this cooling are discussed in a later section.

The choice between 4a and 4b represents a technical problem which we have not had the time to consider. 4a means that we must hold together a tightly bunched, but low current sample of $\bar{p}$'s through transition in a relatively slowly rising magnetic field.

4b avoids the transition problem at the expense of additional complications in beam transfer and in designing an rf system in the AGS to hold the $\bar{p}$'s from ISABELLE. Steps 5 and 6 are extensively discussed in the report by Month,[3] where he concludes that the rf voltages are not unreasonable. The principle uncertainty is in the long term ($\sim$ hours) stability of such highly bunched beams.[3]

There are two basic problems in the possible cycle described above. These arise principally because of the constraints set by having only a single ring in addition to the AGS.

(i) The cooling of the $\bar{p}$'s presents a serious difficulty because the cooling process must operate at very low values of $N_{\bar{p}}$ where the signal to noise ratio may well be less than unity.

If we take the theoretical signal to noise ratio $S/N = Q^2/kTC$, with Q the total charge sampled in the capacitor C and kT = 1/40 eV at room temperature, then roughly $S/N \approx 10^{-6}$ per particle for a possibly realistic capacitive pickup system. If 5×10^6 $\bar{p}$'s are introduced to ISA from each burst of the AGS and the sampling ratio ℓ/L is 10^{-2} (ℓ is length along the circumference of the sample and L is total bunch length), we must use the signal from $N_{\bar{p}} = 5 \times 10^4$ particles. Hence $S/N \approx 5 \times 10^{-2}$, and the noise limited cooling factor f is $(S/N)^2 \ (1/\bar{n}_{\bar{p}}) = 5 \times 10^{-8}$. The expressions for f are derived in, for example CRISP 73-19 by R.B. Palmer, which also contains reference to some earlier reports on stochastic cooling. Since it requires 10 microseconds to traverse the ISA, the cooling time is $T = 10^{-5}/f = 200$ sec. By the time we reach $N_{\bar{p}} = 10^8$ ($n_{\bar{p}} = 10^6$), $S/N \approx 1$, and $f = 1/n_{\bar{p}}$ thereafter. The cooling time is then $10^{-5}\ n_{\bar{p}}$, which becomes 5×10^3 sec at $N_{\bar{p}} = 5 \times 10^{10}$. With these cooling times, if we take 10^3 sec as a rough estimate of the average, we need $\sim 10^2$ days to cool 5×10^{10} $\bar{p}$ inserted in bursts of 5×10^6 particles.

There are several ways of shortening these cooling times, which we mention briefly here. (a) Work at a much lower value of

kT for the pick-up amplifier system to increase S/N at values of $N_{\bar{p}} < 10^8$. (b) Then cool each new bunch of 5×10^6 $\bar{p}$ independently of the total $N\bar{p}$ in the ISA at any time. It might be done by employing corrective signals proportional to $\langle \text{displacement}^3 \rangle$ rather than $\langle \text{displacement} \rangle$, i.e. with sextupole rather than dipole pick-up and correction. (c) Increase AGS intensity/pulse. (d) Decrease ℓ/L by increasing L or increasing bandwidth of amplifiers. (e) Reduce the ultimate value of $N_{\bar{p}}$. Roughly speaking, one needs to reduce the average cooling time by a factor of 10^2 to make the total cooling time calculated above about the same as the total time to inject 4 bunches of $5 \times 10^5 \bar{p}$.

(ii) The second basic problem arises from the need to limit the final $\bar{p}$ longitudinal bunch length in the ISA to 1-2 m for experiments. This places additional high voltage, high harmonic requirements on the rf system which would need additional study to determine their feasibility. There is, in addition, the serious concern about the long term instability of such short proton bunches.

Two-Ring System

(a) The use of a small diameter ($\sim$ 1/4 of AGS) "accumulator" storage ring for storage of $\bar{p}$'s produced by the AGS was considered at some length. The advantages of such a low cost ring would be that it could be built with a large acceptance and radiation hardened to accept a large number of $\bar{p}$'s. The smaller diameter would lead to a large reduction in the cooling time because of the factor of 10 shorter revolution time. However, if used in conjunction with a single ring, bunched beam arrangement, the low harmonic number of such a small ring leads to an impossibly high rf voltage ($\gtrsim$ 100 MeV) requirement.[6]

---

6. R. Chasman, private communication.

(b) We note that the principal difficulties in the way of achieving high $\bar{p}$-p luminosity in a single storage ring are largely eliminated in the two ring ISA system. One can expect $L = 10^{29}$ cm cm^{-2} sec^{-1} in a scheme which repetitively uses 200 GeV protons from one ring of ISA to make $\bar{p}$ which are stored in the second ISA ring.[5] Clearly the bunched length problem disappears. We wish to indicate that if stochastic antiproton cooling is utilized it may be possible to achieve a $\bar{p}$-p luminosity $\geq 10^{30}$ cm^{-2} sec^{-1}. For example, one can produce and collect about 4×10^{9} $\bar{p}$ per pulse of 5×10^{14} protons at 200 GeV, and store azimuthally 10 such bunches, each about 300 m long. This takes roughly 1 - 2 hours to accomplish, which is then the maximum time available for cooling. With $\ell/L \approx 1/500$ and $N_{\bar{p}} = 1.5 \times 10^{11}$/bunch, the cooling time is about 1 hour. This is a possibility which deserves additional attention since it has the potentiality of bringing the $\bar{p}$-p luminosity roughly within about two orders of magnitude of the p-p luminosity.

APPENDIX A

COMPARISON OF $\bar{p}$ PRODUCTION WITH 30 AND 200 GeV PROTONS

Antiprotons can be produced either by using 30 GeV protons from the AGS or 200 GeV protons from the ISA. Since the antiproton production yields at 200 GeV are many times higher when 30 GeV protons are used, considerably brighter antiproton beams can be stored if the antiproton source is a target bombarded with 200 GeV protons rather than 30 GeV protons. A comparison of the luminosities achievable by the two methods can be made by following the scheme described in the May 1974 ISABELLE proposal document (BNL 18891, page 303).

The number of antiprotons which can be stored in the ISA is

$$N_{\bar{p}} = N_p M \frac{\partial^2 N_{\bar{p}}}{\partial\Omega\partial p} \Delta\Omega\Delta p \eta_s \eta_t$$

N_p = number of protons in accelerated AGS or ISA per acceleration cycle

M = number of acceleration cycles used during the antiproton stacking process

$\partial^2 N_{\bar{p}}/\partial\Omega\partial p$ = number of $\bar{p}$ produced per unit solid angle per unit momentum acceptance

$\Delta\Omega$ = solid angle acceptance of ISA

Δp = momentum acceptance of ISA

η_t = target efficiency

η_s = stacking efficiency

Protons are extracted from either the AGS or the ISA with their bunch structure maintained. The particles in one bunch are mostly contained within 1/10 of the interbunch distance. The antiprotons

will have the same bunch structure. Therefore ten ISA acceleration cycles are required to fill the circumference of the second ISA ring with antiprotons. Similarly the number of AGS pulses required is greater by a factor of the ratio of the ISA and AGS circumferences.

For the purpose of this comparison it is assumed that the $\Delta p/p$ momentum acceptance, stacking efficiency and target efficiency are the same for both cases and as defined in BNL 18891. The useful vertical beam acceptance is inversely proportional to the square root of the injected antiproton momentum and the solid angle $\Delta\Omega$ reflects this difference.

	Protons from AGS	Protons from ISA
E_p - bombarding proton energy	30 GeV	200 GeV
$E_{\bar{p}}$ - antiproton energy	8 GeV	30 GeV
N_p	1×10^{13}	6×10^{14}
M	37.5	10
$\partial^2 N_{\bar{p}}/d\Omega dp$	0.02	0.5
$\Delta\Omega$	1.7×10^{-4}	1.0×10^{-4}
$\Delta p (\Delta p/p = 2.5\%)$	0.20 GeV	0.75 GeV
η_t	0.33	0.33
η_s	0.7	0.7
$N_{\bar{p}}$	5.8×10^{7}	6.3×10^{10}
Filling time	40 sec	3050 sec
Antiproton production 10^5 sec	1.5×10^{11}	2×10^{12}

The luminosity achievable is 8×10^{28} cm^{-2} sec^{-1}, $\Delta\nu$ =0.005; without cooling.

The acceleration in the AGS alone before making antiprotons is therefore far less interesting.

With cooling it may be possible to store 1×10^{11} antiprotons

per day with AGS protons and 2×10^{12} antiprotons per day with the ISA protons. Up to 5 times these numbers of stored antiprotons may be possible with cooling since one could inject into the entire ISA aperture and then cool to the required size. Then luminosities approaching a 10^{31} cm^{-2} sec^{-1} are, in principle, achievable.

STATUS OF THE ISABELLE e-p OPTION AT TIME OF SUMMER STUDY 1975

R. Chasman

Brookhaven National Laboratory

INTRODUCTION

The basic design of the ISABELLE e-p option including a 15 GeV electron ring, was started more than three years ago and a considerable effort was devoted to it during the 1972 Summer Study. Later that year, the existing design features were summarized in a paper[1] presented at the 1973 National Accelerator Conference and with only small modifications that e-p option was included in the ISABELLE proposal[2] submitted to the AEC in June of 1974.

Meanwhile, changes have been introduced into the basic ISABELLE design[3] and much thought is being given to ways that would reduce the cost of ISABELLE itself as well as of its options. As a result of this, modifications of the e-p options are required and these will constitute the focus of the present summer study e-p option working group.

The electron ring was originally assumed to be housed in a separate tunnel, either on the side or inside of the proton rings. At this time the possibility of placing the electron ring inside the proton ring tunnel is being considered and furthermore, storing electrons in one of the proton rings has not been ruled out.

One arrangement in which the electron ring would be placed ~ 0.5 m above one of the proton rings has been studied in some detail. A short description of this scheme will be given here.

---

1. R. Chasman and G.A. Voss, IEEE Trans. Nucl. Sci. NS-22, Vol. 3, 777 (1973).
2. "A Proposal for Construction of a Proton-Proton Storage Accelerator Facility ISABELLE", BNL 18891 (May 1974).
3. "A Proposal for Construction of a Proton-Proton Storage Accelerator Facility ISABELLE", BNL 20161 (June 1975).

Injection at 4 GeV is assumed, using the AGS as an electron booster.

GENERAL DESIGN FEATURES

In the most recent ISABELLE design[3] the two proton rings lie side by side similar to the ISR rings. They intersect 8 times at an angle of 11.4 mrad, this being made possible by the small separation of 0.75 m between the rings. The crossing points are surrounded by straight sections in which the horizontal dispersion function is brought to zero.

The electron ring is envisioned to follow one of the proton rings at a vertical distance of + 0.54 m. Because it is felt to be essential that the electron ring be operated independently and with minimum interference with the proton rings it bulges out horizontally around the p-p interaction areas to a maximum distance of 6 m *(see Fig. 1). e-p collisions take place in a few, say two, oppositely situated p-p crossing regions to which the electrons will be brought through a bypass including a vertical translation.

LATTICE

The electron ring itself, excluding the use of bypasses, has nearly 8-fold symmetry (some asymmetry is introduced by inner-outer arc considerations). The regular electron ring arcs are made up by cells identical to those of the proton rings. They are 25.4 m long and consist of 4 bending magnets and 2 quadrupoles. The bulges are made up of 8 shorter bending free cells (21.2 m long) and 2 normal cells. Lattice parameters are listed in Table I and a schematic of the magnet arrangement in one-half octant is shown in Fig. 2 together with β and x_p functions. Further study is necessary to determine if the free spaces in the bending free cells in the bulges is adequate for placement of rf cavities as well as for injection or if some rearrangement of the focusing elements is required that would leave longer free sections.

* The author is indebted to M. Month for proposing this idea and doing the related lattice computations.

TABLE I

Lattice Parameters of e Ring

Type of Lattice	Separated Function
Circumference	2960 m
Magnetic radius	170 m
Regular cells (FBDB):	
Number	64
Length	25.7 m
Magnetic field at 15 GeV	2.94 kG
Maximum quadrupole gradient at 15 GeV	0.46 kG/cm
Modified cells (without bending):	
Number	64
Length	21.20 m
Maximum quadrupole gradient at 15 GeV	0.62 kG/cm
ν_x	30.72
ν_y	30.72
Transition γ	18.8
Number of experimental insertions (in form of bypasses)	2

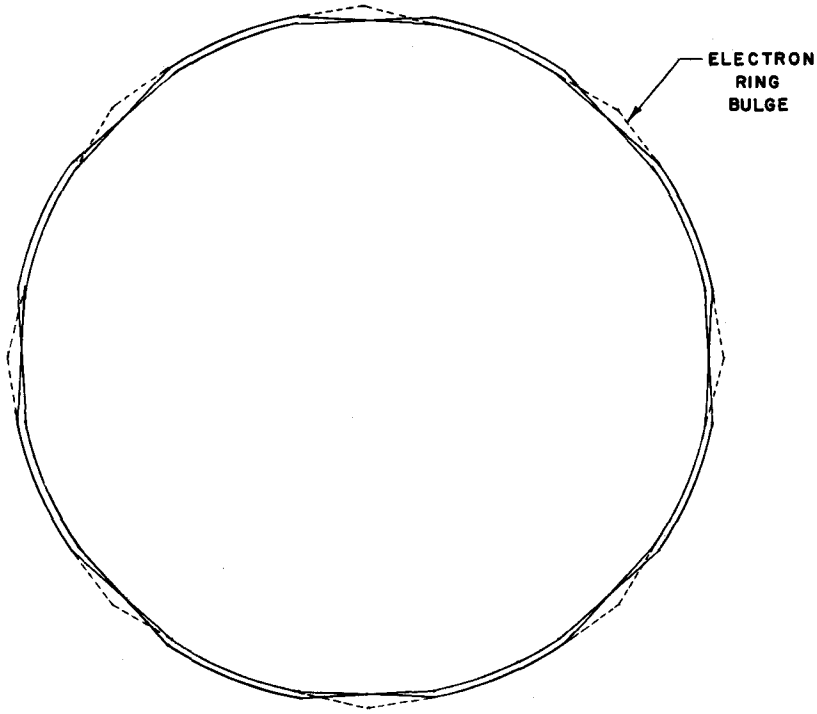

Fig. 1. Plan View of e-p rings.

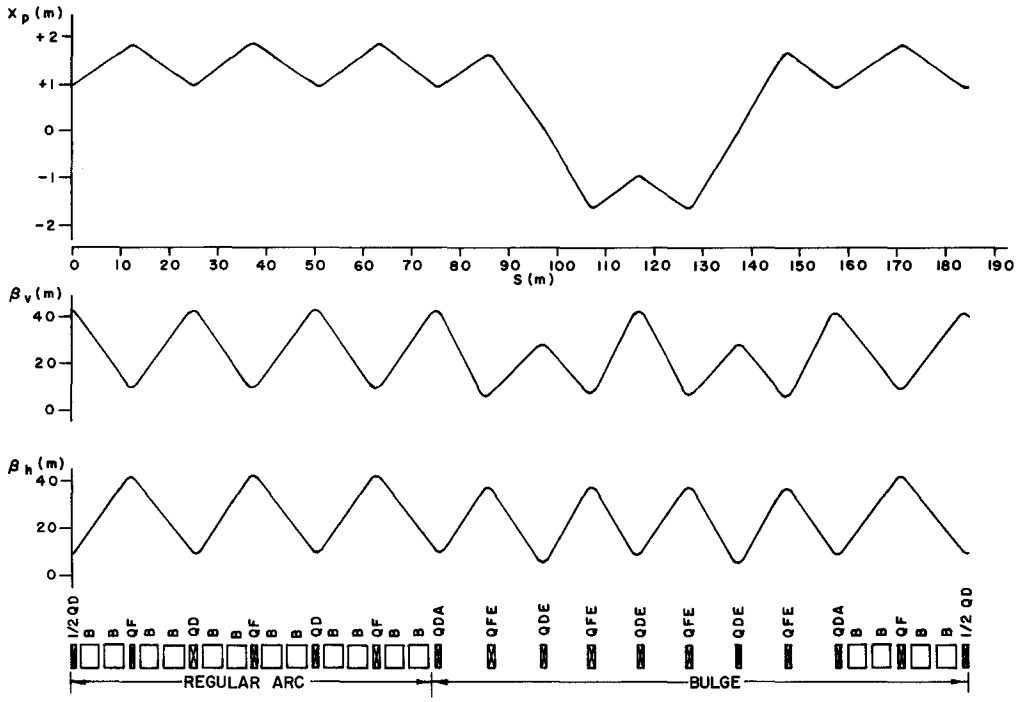

Fig. 2. Beta and dispersion functions in ½ octant of electron ring with bulge (other half is nearly mirror image).

e-p EXPERIMENTAL INSERTION

As mentioned earlier, the electrons will be brought down to the plane of the proton rings and enter the p-p interaction area for e-p collisions, whereafter they will go back up into the electron ring. One-half of the electron ring bypass is shown in Fig. 3 together with β and x_p functions. In the first part of the bypass the horizontal dispersion function is brought to zero in the same way as in the proton rings. The x_p matching section is followed by the vertical translation, shown in further detail in Fig. 4, at the end of which the p-p interaction area is reached. Quadrupoles Q1, Q2, Q3 and Q5 are adjusted to make $\alpha_h = 0$, $\alpha_v = 0$, $\beta_h = 20$ m, $\beta_v = 1$ m and $y_p' = 0$ at the crossing point, resulting in $y_p = -0.25$ m there. It should be pointed out that the nonzero value of the vertical dispersion function does affect the luminosity when horizontal crossing is employed. (A different bypass with an achromatic vertical translation leading to $y_p = 0$, $y_p' = 0$, at the crossing point has been designed but found to lead to excessively high chromaticity.) However, the reduction of e-p luminosity resulting from the increased electron beam height can be compensated for by going to small crossing angles. The bending magnet arrangement used for the high luminosity p-p interaction area can also be used for e-p collisions, and, in principle, the whole range of crossing angles of 0 - 11.4 mrad can be used. Figure 5 shows the proton and electron beam trajectories for a 3.4 mrad crossing angle which is the minimum value obtained by a maximum permissible electron tune shift of 0.06. The effect of synchrotron radiation on the superconducting magnets as well as on the experimental equipment will have to be looked into.

PERFORMANCE

Table II gives the performance parameters for collisions between 200 GeV and 15 GeV electrons. The electron ring can be operated with a variable number of bunches. Assuming a rf frequency of 400 MHz, the maximum number of bunches is 3921 leading to an extremely low proton tune shift of $\sim 10^{-5}$. Going to the

TABLE II

Performance Parameters for e-p Collisions at Top Energy

	Proton	Electron
Energy	200 GeV	15 GeV
Beam Current	10 A	0.2 A
Number of bunches (N_B)	nonbunched	8-3921
Transverse rms emittances		
Horizontal	0.015×10^{-6} π m·rad	0.124×10^{-6} π m·rad
Vertical	0.015×10^{-6} π m·rad	0.008×10^{-6} π m·rad
Crossing angle (horizontal)	3.4 mrad	
Free Drift Space	± 13 m	
Dispersion Function		
Horizontal	0.0 m	0.0 m
Vertical	0.0 m	0.25 m
Beta Function at Crossing point		
Horizontal	20 m	20 m
Vertical	1 m	1 m
rms momentum spread	1×10^{-3}	1×10^{-3}
rms beam sizes at crossing point		
Horizontal	0.055 cm	0.157 cm
Vertical	0.017 cm	0.027 cm
Longitudinal		1.75 cm
Luminosity at 200 GeV × 15 GeV	$0.35 \times 10^{32} cm^{-2} sec^{-1}$	
	5×10^{-3} ($N_B^e = 8$)	
$\Delta\nu_v$	1×10^{-5} ($N_B^e = 3925$)	0.06

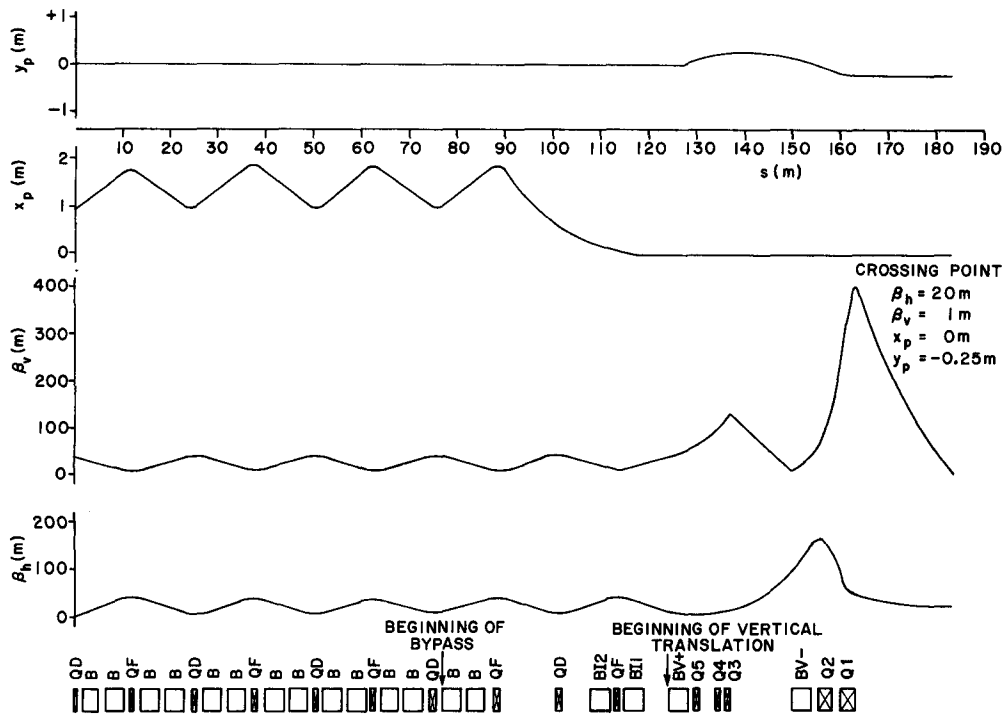

Fig. 3. Beta and dispersion functions in ½ octant of electron ring with bypass for e-p collisions (other half is nearly mirrow image).

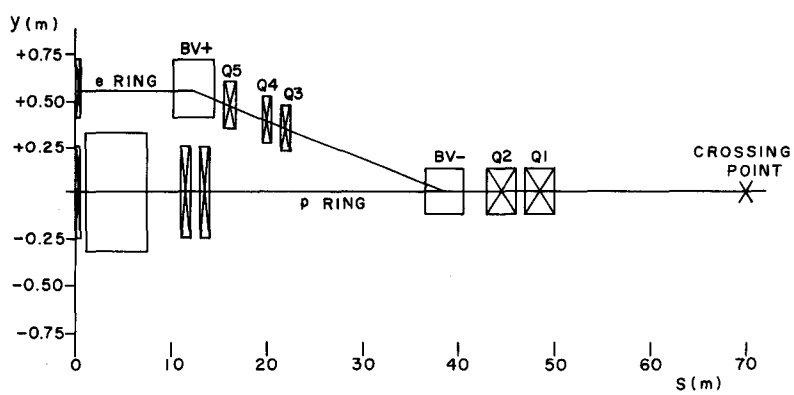

Fig. 4. Electron ring with vertical translation.

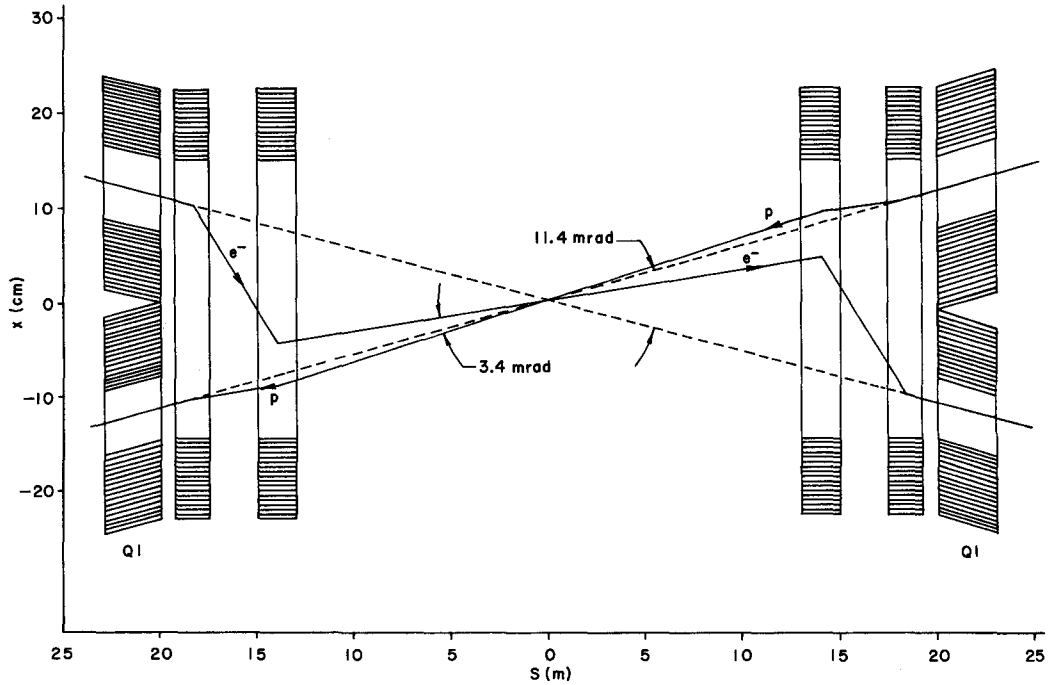

Fig. 5. Variable angle horizontal crossing geometry for e-p collisions (maximum crossing angle 11.4 mrad).

other extreme, the minimum number of electron bunches is determined by the maximum permissible proton tune shift. Assuming $\Delta\nu_p$ = 0.005, one could operate the electron ring with as few as 8 bunches. More work is required to determine the optimum working conditions which most certainly will be arrived at by considering the effects of collective bunch-bunch instabilities, filling time, etc.

Going to lower electron energies, higher luminosities can be reached. RF power limitations lead to electron currents of many amperes at electron energies around 5 GeV. Because there is no experience in storing such high intensity electron beams, a maximum current of 1 A will be assumed here. From rf power considerations 1 A can be reached at an electron energy of 10 GeV leading to maximum luminosity of 1.7×10^{32} $cm^{-2}sec^{-1}$. It should be noted that the crossing angle will have to be varied inversely with electron energy to maintain an electron tune shift of 0.06. Also the minimum number of electron bunches determined by $\Delta\nu_p$ = 0.005 will go up with electron beam current.

RF SYSTEM

The described electron ring requires an rf system similar to that of the original ISABELLE e-p option. Maintaining a frequency of 400 MHz the changed ring geometry leads to a higher harmonic number and a slightly larger peak voltage. The rf parameters are summarized in Table III.

TABLE III

ISABELLE e-Ring RF System

Frequency	400 MHz
Harmonic number	3921
Power dissipated in cavities	1.2 MW
Power radiated by beam	5.3 MW
Peak rf voltage	43 MV
Total shunt impedance	1250 MΩ
Total accelerating cavity length	50 m

REVIEW OF e-p COLLISION GEOMETRIES

K. Steffen
Deutsches Elektronen Synchrotron
J. Maidment
Rutherford High Energy Laboratory
Y. Cho
Argonne National Laboratory

In colliding a bunched electron beam with a continuous proton beam, the luminosity is inversely proportional to the crossing angle times the effective transverse beam size perpendicular to the crossing plane. These two quantities, then, must be made as small as compatible with the beam-beam effect, the required free space around the interaction region and the space restrictions of a particular crossing geometry.

Assuming that a separate 15 GeV electron ring would be added to ISABELLE, the options group looked at various possible e-p crossing schemes that have no magnets in a region of at least ± 10 m around the interaction point. The class of e-p interaction schemes that involves a transverse bending field at the interaction point have been worked out at the CERN and FNAL summer studies and have not been further pursued here.

Regarding the placement of the electron ring with respect to the proton rings in the ISABELLE tunnel, we may distinguish the following possible arrangements:

Horizontal - All three rings lie side by side in the same vertical plane. No extra bending is required; no vertical dispersion will be introduced.

Vertical (up/up)-The electron ring is placed on top of one of the proton rings in all eight ISABELLE octants, and the vertical dispersion function will have a nonzero value at the interaction point, increasing the beam height there. The vertical dispersion must be matched.

Vertical(up/down) - The electron ring is placed alternately above and below one of the proton rings. The vertical dispersion must be matched but can be made zero at the interaction point.

For a vertically displaced electron ring the electrons are assumed to follow the beam line of one of the proton rings. Calling this proton ring "No. 1" and the other proton ring "No. 2", the electrons may either collide with the protons in No. 1 by vertical crossing or with the protons in No. 2 by horizontal crossing.

These two cases are characterized by the following features:

When crossing with ring No. 1, the electron, having a much lower momentum than the protons, are bent onto the proton beam line or near to it by a common bending magnet. Thus, the crossing angle can be made as small as wanted. However, the low-β proton quadrupoles must then be further removed from the interaction point, so that the electrons can clear them. This results in an increased proton beam size.

When crossing with ring No. 2, on the other hand, the position of the proton quadrupoles as well as horizontal crossing angle equal those of the p-p interaction geometry (2α = 11.4 mrad).

In both cases, the luminosity may be somewhat increased by applying one of the following schemes:

In the case of vertical crossing the electron beam size can be reduced by installing additional low-β electron focusing quadrupoles closer to the interaction point. Because of the small separation of the two proton beam lines in that region, these quadrupoles, being centered about the electron beam, must be specially designed to let the other proton beam line (No.2) pass through their aperture off-center.

In the case of horizontal crossing one can reduce the crossing angle by bending the protons closer to the electron beam by the use of septum magnets:

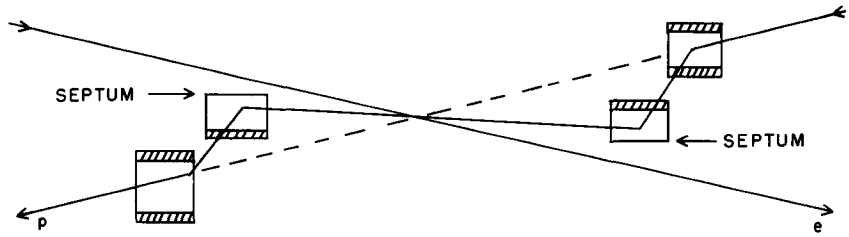

Fig. 1. Reduction of Crossing Angle with Septum Magnets

The possibility of reducing the crossing angle by using common magnets for bending both beams closer together is not considered practicable since it would generate too much synchrotron radiation in the interaction region.

Putting together the various ring placements and the two options of colliding with either ring No. 1 or No. 2, we will number the different e-p crossing geometries in the following way:

	Crossing with p-ring	
	"No. 1"	"No. 2"
Horizontal	(1)	(2)
Vertical (up/up)	---	(3)
Vertical (up/down)	(4)	(5)

We shall briefly describe and comment on these alternatives, concluding with detailed design examples for alternatives (4) and (5):

(1) Horizontal, No. 1 Crossing:

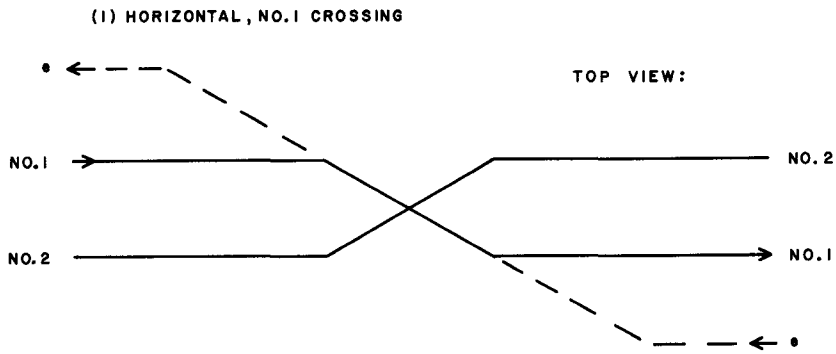

Fig. 2. Horizontal, No. 1 Crossing.

(2) Horizontal, No. 2 Crossing:

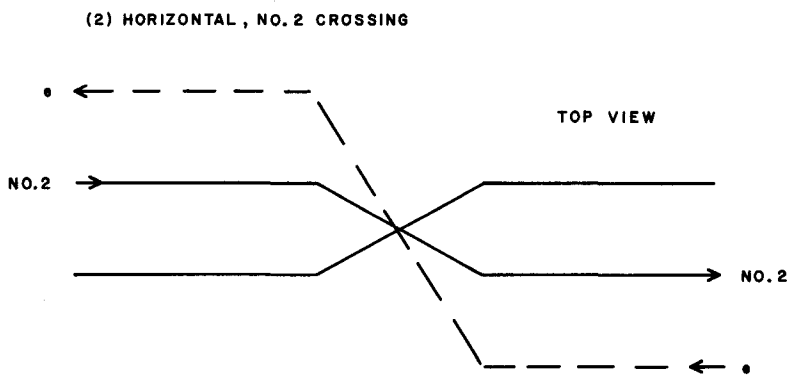

Fig. 3. Horizontal, No. 2 Crossing.

Both horizontal arrangements, although basically the simplest, have the disadvantage that they require a larger tunnel and introduce additional beam lines in the interaction areas.

(3) Vertical (up/up), No. 2 Crossing:

A solution of this type is described in detail in Ref. 1.

(4) Vertical (up/down), No. 1 Crossing:

A design example for this arrangement is shown schematically in Fig. 4. The electron quadrupoles (Fig. 5) are placed at a distance of 13 m from the interaction point and are designed so that the beam pipe of proton ring No. 2 (which is not used during e-p physics) can be led through it. The proton quadrupoles are pulled back to 36 m from the interaction point for clearing the vertically approaching electron beam. The vertical crossing angle between the colliding beams is 1 mrad. The e-ring is 54 cm above the proton ring on the other side. This has implications on the initial design of the superconducting magnet support system to allow the later inclusion of such an option.

The vertical dispersion in the electron ring is matched to be zero at the interaction points and throughout the arcs. The maximum amplitude functions are moderate ($\beta_{max} < 300$ m) and do not much contribute to the chromaticity ($\Delta\xi_V = 1.4$ per insertion). They are shown together with the vertical dispersion, in Fig. 6.

The relevant interaction point parameters are:

	Protons (m)	Electrons (m)
β^*_H	13	0.64
β^*_V	3.24	24
	Luminosity, $L = 0.7 \times 10^{32}$ cm^{-2} sec^{-1}	
	Interaction Length $\approx$ 22 cm	

1. R. Chasman, Status of ISABELLE e-p Option at time of summer study, 1975, these Proc.

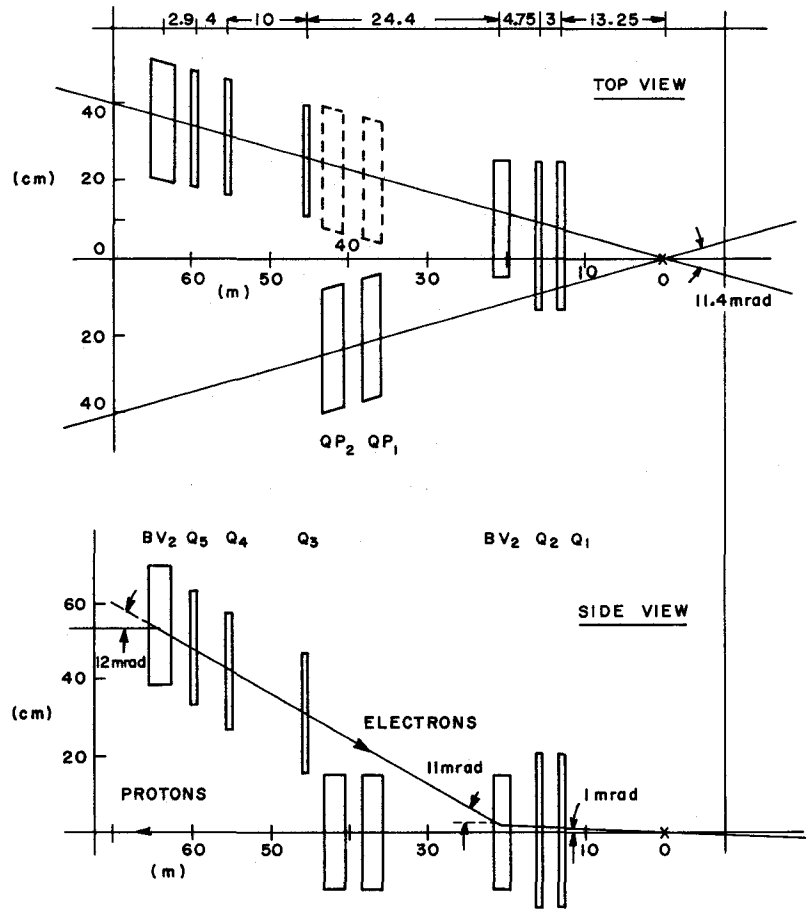

Fig. 4. Vertical (up/down), No. 1 Crossing.

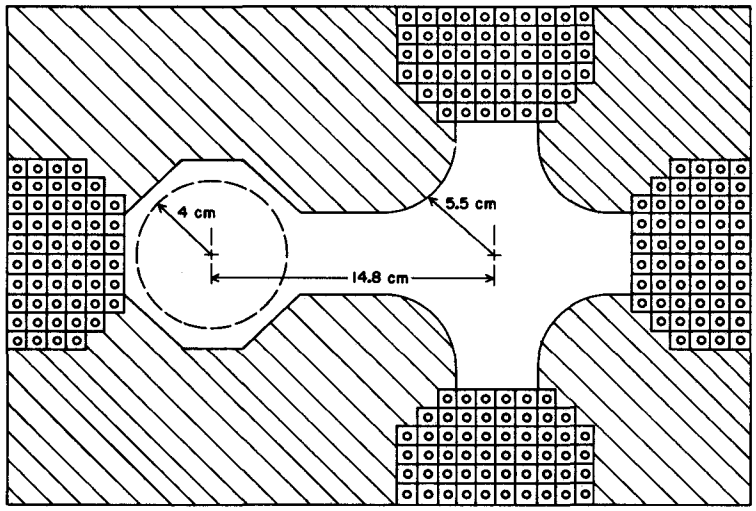

Fig. 5. Electron quadrupole, No. 1 Crossing.

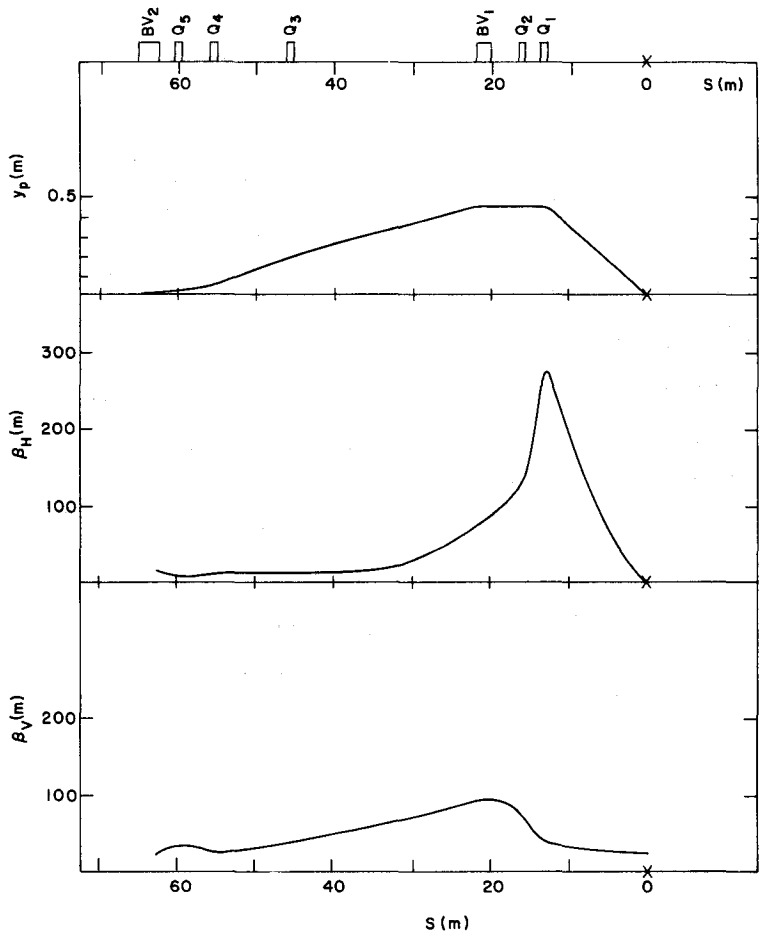

Fig. 6. Betatron and Vertical Dispersion function, No. 1 crossing.

(5) Vertical (up/down), No. 2 Crossing:

Figure 7 shows a design example for this arrangement. The electron quadrupoles start at 10 m from the interaction point and are designed to let the protons in ring No. 2 pass through a nearly homogeneous field region at the edge of the aperture (see Fig. 8). Beam crossing is horizontal at an angle of 11.4 mrad, and the proton quadrupoles remain at 20 m from the interaction point.

The overall ring geometry is similar to the preceding example and has the same implication on the superconducting magnet support system. The vertical translation section in the electron ring is steeper, requiring higher field and thus generating more synchrotron radiation. The vertical dispersion is matched again; it is shown, together with the amplitude functions, in Fig. 9. The design calls for improvement to achieve greater luminosity.

The interaction point parameters are:

	Protons (m)	Electrons (m)
β^*_H	20	30
β^*_V	1	0.33
	Luminosity, $L = 0.2 \times 10^{32}\ cm^{-2} sec^{-1}$	
	Interaction Length $\approx$ 4.8 cm	

All e-p interaction geometries have in common that the nearby bending of the electrons will send an intolerable amount of synchrotron radiation into the interaction region if no precautions are taken. A remedy consists in strongly reducing the field in those parts of the bending magnets that are closest to the interaction point. This will result in much longer magnets and, due to the restricted length of the insertion, in a stronger overall bending which must be taken into account in a final design.

Having dealt with the e-p interaction regions, the question of how to design the other straight sections remains to be looked

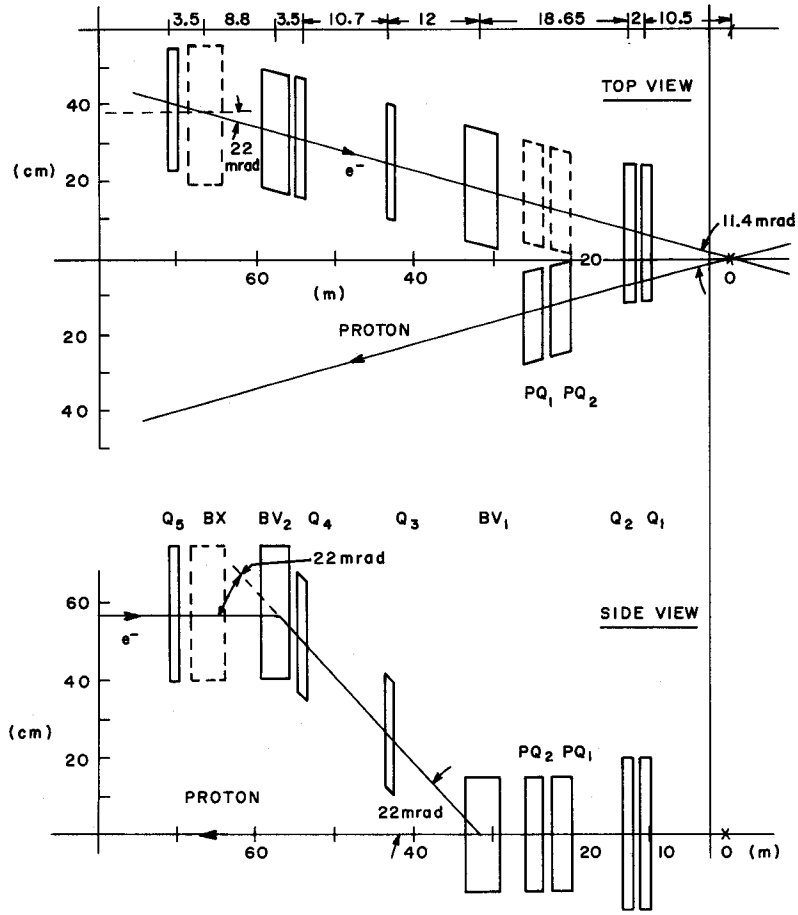

Fig. 7. Vertical (up/down), No. 2 Crossing.

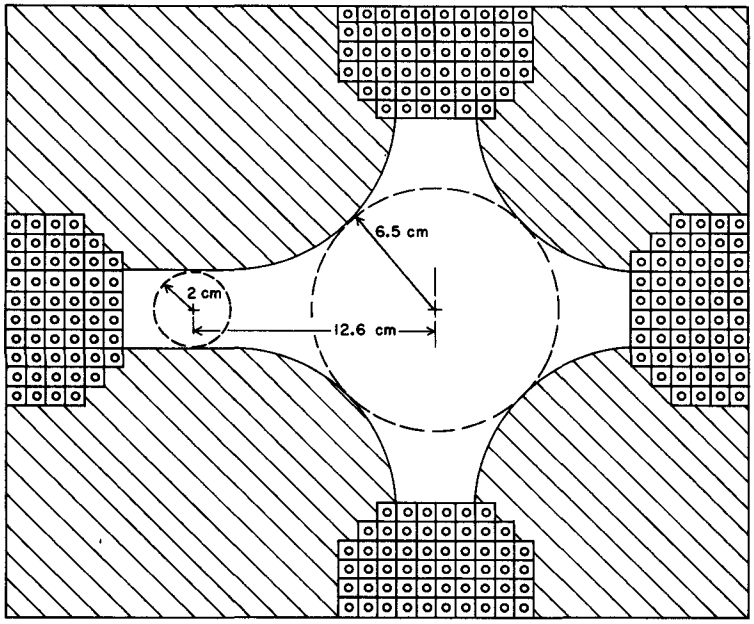

Fig. 8. Electron quadrupole, No. 2 crossing.

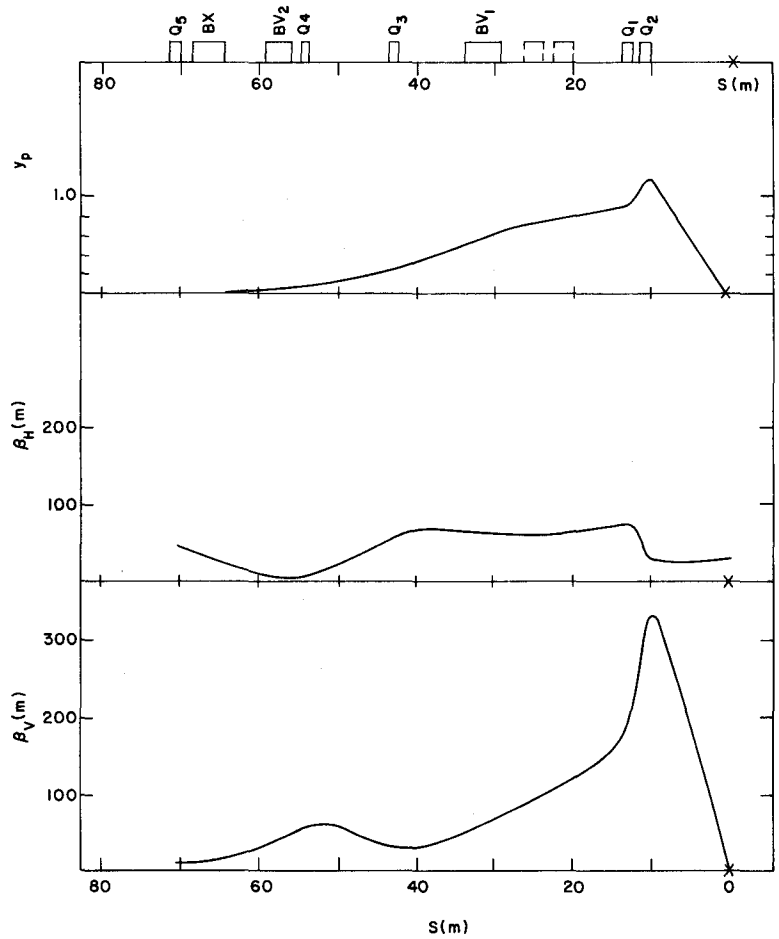

Fig. 9. Betatron and Vertical Dispersion function, No. 2 crossing.

into. It was agreed in the study that two e-p interaction regions appear adequate, in principle leaving the other six for p-p experiments. Three possibilities have been thought of for getting the electrons around or through the p-p interaction regions.

(1) A horizontal bulge that carries the electrons to a distance of about 6 m around the p-p interaction region. The design of this bulge is described in Ref. 1. It gives the least interference with the proton rings and allows to run the electron ring while carrying on p-p experiments. The buildings must be designed to accept these bulges, and some interference with moving or mounting large experimental equipment might still arise.

(2) A straight pipe carried parallel to the p-p straight section at a distance of the order of 0.5 m from the proton beam pipes. This will probably interfere with the p-p experimental setup, and prohibit simultaneous e-p and p-p experiments. However, it is by far the cheapest solution and may be quite practical.

(3) The electrons can be introduced into the proton beam pipe at the interaction region as shown in Fig. 7. Depending on the p-p detector system used, the electrons may or may not interfere with the p-p experiment.

COMMENTS ON INJECTION INTO ISABELLE ELECTRON RING

J.R. Maidment

Rutherford High Energy Laboratory

1. Assumptions[1]

Injector: 200 MeV electron linac.

Output emittance: $\sim 5\pi$ mm mrad (95%)

Booster: AGS, cycled at 10 pulses/sec for 4 GeV acceleration. Emittance at 4 GeV (taking into account radial anti-damping): $\sim 8\pi$ mm mrad (95%).

2. Injection Hardware

Using the distorted closed orbit method of injection two kickers and one septum magnet are required. The kickers should be located ¼ betatron wavelength on each side of the septum magnet. Adapting the electron ring lattice described in Ref. 2, the injection could easily be done in the bulge situated near one of the proton ring insertions, used for injection. In this way full advantage can be taken of the AGS-ISABELLE transport system. The quadrupole (QFE,QDE), kicker (K_1,K_2) and septum magnet arrangement in the bulge section is shown in Fig. 1.

In this design $\beta_s = \beta_{K_1} = \beta_{K_2} = 35$ m. Ignoring dispersion, the required orbit bump can easily be derived from Fig. 2.

With an injected beam width of $2\sqrt{35 \times 8 \text{ mm}} = 33.5$ mm and a septum width of 2.5 mm the orbit bump has to be 36 mm. Assuming a half-aperture of 40 mm, the injected beam then has to damp to 4 mm before applying the next orbit bump. This will take about two damping times or ~ 1.5 sec.

---

1. "A Proposal for Construction of a Proton-Proton Storage Accelerator Facility ISABELLE", BNL 20161 (June 1975).
2. R. Chasman, Status of the ISABELLE e-p Option at Time of Summer Study, 1975 , these Proc.

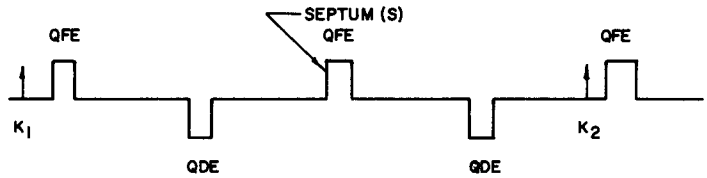

Fig. 1. ISABELLE Injection Arrangement.

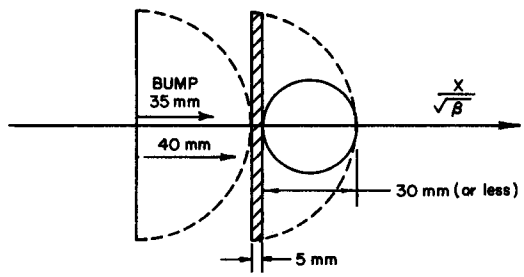

Fig. 2. Beam Displacement at Injection Septum Magnet.

3. Filling Time

The filling time will depend on how many of the rf buckets will be occupied. Going to the two extremes in Ref. 2 of 3921 and 8 electron bunches the situation is as follows:

a. 3921 Bunches:

Even with a moderate linac performance good filling rates can be obtained. In principle, four AGS pulses can be stacked side by side around the main ring circumference. Assuming a linac current such that the AGS traps and accelerates 10 mA it would take 20×1.5 sec = 30 sec to accumulate 200 mA. If one wants to avoid gaps in the string of electron bunches due to the finite rise and fall time of the kickers one would have to wait 1.5 sec between each AGS pulse increasing the filling time by a factor of 4 or to 120 sec.

b. 8 Bunches:

With the same linac performance as assumed in (a), the filling time would be of the order of 4 hours. To reduce this time, one needs to go to a high intensity electron linac injector. Peak currents of several amperes have been achieved in such machines and it seems feasible to trap 1×10^8 particles in a 400 MHz bucket in the AGS. It will then take 1.5 sec to stack this intensity in each of the 8 bunches (either by one or four AGS pulses) resulting in a total filling time of $\sim$ 4 min. The high peak intensity may be achieved by linac gun modulation possibly coupled with some pre-bunching. Although the higher spacecharge forces may somewhat degrade the emittances, the beam into the AGS should still be contained within the very conservative assumption of 5π mm mrad.

It would take much longer to fill the electron ring with positrons, especially in the 8 bunch mode, because of lower linac output currents. To avoid excessive injection times one could

think of a scheme proposed by Tigner[3] in which all the rf buckets in the electron ring are first filled and damped in betatron phase space, whereafter their content is compressed into 8 bunches by single bunch transfer to the AGS and back.

---

3. M. Tigner, CLNS 299, Laboratory of Nuclear Studies, Cornell University, Ithaca, N.Y.

STORING AND ACCELERATING ELECTRONS IN ONE OF THE p-RINGS OF ISABELLE

M. Tigner
Cornell University

Introduction

It is difficult, but not impossible, to use one of the p-rings for electrons. The engineering problems involved become significantly easier to solve if the electron energy is lowered from 15 GeV to 7.5 GeV. Thus, one should consider the possibility of a 2-stage e-p option in which one of the p-rings is used for the initial stage of e-p work during which one learns how to do e-p physics and to handle the machine problems. In the second stage one could add an optimized e-ring for 15 GeV based on the experience with the initial stage. The available cm energy in the first stage would be 77.5 GeV or contrasted with 109.5 GeV for the second stage. The theoretical luminosity for stage 1 would be the same as that quoted for 15 GeV electrons in the yellow book, i.e. 2×10^{31} $cm^{-2}sec^{-1}$.

Design Considerations

While there is no fundamental reason so far discovered why electrons cannot be stored and accelerated in one of the superconducting p-rings, there are four engineering considerations which add significant constraints to the p-ring design. These are:

1. The synchrotron radiation from the electrons must be substantially attenuated before reaching the cold parts of the magnet. In all cases, water cooling must be added to the warm bore. In the 15 GeV case, a heavy metal tube must be added to the warm inner tube to absorb the high energy part of the synchrotron light spectrum. If this tube were of tantalum, a minimum weight of 31 tons would be required at a material cost of 3×10^6 \$. Due to the materials

constraints to be discussed, the required amount could well be twice the quoted figures.

2. A large number of chamber enlargements (approximately 264) with clearing electrodes and beam pick-ups are required for the p rings. In tentative ISABELLE designs the typical dimensions of these boxes and the devices they contain are $\sim$ 12 cm. To electron bunches of a few cm length, these insertions will appear as complicated microwave cavities with rather substantial shunt impedances. These cavities can be harmful in two ways. First, the beam can lose substantial amounts of energy into the cavities which represents an extra load on the rf system, and a thermal protection problem for the "cavities" and their contents. Second, the fields engendered in the boxes can act back on the beam causing instabilities in the beam. While it is very difficult to quantify this argument, especially before the ISABELLE design is complete, experience at SPEAR and DORIS show that this kind of equipment in the vacuum system can cause serious troubles at even low currents.

3. Magnetic field errors at low field due to persistent currents in the superconductor are likely to be quite large and require correction, perhaps even on an individual basis, thus adding to the complexity of control and magnet power systems. This is a tentative conclusion and must be checked experimentally.

4. At 15 GeV, at least 50 m of rf cavity length will be required to replenish the beam energy lost through synchrotron radiation. This means that electron rf equipment will have to be installed in each of at least two and probably four of the straights. Because of the high interaction impedance of these devices they will have to be removed each time the ring is changed over from e to p operation, thus causing a delay of some days before the required vacuum can be reestablished. There is no known technique by which these cavities can be effectively short circuited without breaking the vacuum.

Further Details

A. Synchrotron Radiation Protection - 15 GeV

The 2 mm wall thickness of the proposed ISA vacuum chamber is not nearly thick enough to absorb the synchrotron light even though it strikes at a small angle giving an equivalent thickness of 8 cm. That this is so, arises from two sources:

(i) Mode of the power is in the x-ray region above the 100 keV. This energy is far above the K edge of aluminum so that photoelectric absorption is very weak.

(ii) In Al, Compton scattering of large angles is made more probable than absorption, so that the x-rays tend to be scattered and exist through the thin dimension of the Al rather than be absorbed. In a heavy element such as tantalum, the situation is substantially improved. The absorption is made stronger in the wavelength region of interest and the absorption length is made shorter than the interaction length for Compton scattering.

Using all the criterion that 1 to 2 kW of the power emitted by synchrotron radiation (out of the 5.3 MW total emission) may be permitted to enter the cold region of the magnet (total refrigeration capacity 13 kW/ring). We find that a 1 cm thick Ta tube surrounding the Al bore tube will suffice.[1,2]

Because Compton scattering in a heavy metal such as Ta is relatively weak compared to absorption, a heavy metal tube used as vacuum chamber as well as shield would allow a smaller shield thickness and thus a saving of material. It is this case for which the material cost was quoted. The wall thickness (total both tubes) may be of the order of ½ cm although a detailed Monte Carlo calculation will be necessary to make this precise. An obvious problem with the use of a heavy metal bore tube is its conductivity and consequent

1. M. Tigner, "Shielding the Cold Region of the ISA Magnets from Synchrotron Radiation", these Proc.

2. Note that the power that reaches the cold region will be quite diffuse due to the Compton scattering so there should be no radiation damage or heating problem in cryostat.

lowering of the threshold for the resistive wall instability. It would be difficult to deposit a high conductivity coating of the requisite thickness (several mils) on the interior of the bore tube without compromising its vacuum properties.

B. Synchrotron Radiation - 7.5 GeV

The situation at 7.5 GeV is materially different. For the same beam current the synchrotron power is only 330 kW and the critical energy of the x-rays is only 5.3 keV. A warm chamber consisting of an inner envelope of 2 mm Al surrounded by a second 2 mm wall Al tube with water flowing between, would be adequate to keep the synchrotron power escaping to a few hundred watts.[1]

C. Vacuum Chamber Boxes

If it were felt attractive to use the p-ring for electrons, great attention would need to be paid to designing the clearing electrodes, pick-up electrodes and their housings as far as impedance properties are concerned. An advance in experimental methods for assessing the microwave properties of some complicated structures will be required.

D. Magnet Field Errors

The only information existing which is directly relevant to this subject is the first tests of the 4¼ m model.[3] At 700 G excitation (the field required for ejection of 4 GeV electrons is ~ 800 G) the contribution to the dipole field of the persistent currents is about 1%. This is expected to vary from magnet to magnet in sign, but to be stable from pulse to pulse so that it can be corrected. More magnets will need to be tested to make the estimates precise. A random fluctuation of $\Delta B/B$ of rms value 1% would produce an rms closed orbit distortion of 3 - 4 cm. If one decides to take this course then the

3. A.McInturff, private communication.

magnets will all need to be measured at the appropriate field level. Once their field errors are known then they can be arranged to be partially compensating for the dipole error.

There are also multipole components which are relatively large at injection, e.g., at 5 cm radius the 6-pole components (700 G dipole) at the first 4¼ m magnet is ~ 5 G. Again, this will need correction, but that can be done. Detailed measurements will be needed to clarify the picture.

Two suggestions have been made concerning alternate solutions to the low field error problems arising from the persistent currents.

(i) By raising the operating temperature close to transition, one could make the time constant for the currents to die away small. This would entail alterations in the refrigeration system and require the addition of a control system to maintain the correct operating point during acceleration. The difficulty of this cannot be assessed until a first cryogenic design is made.

(ii) If the magnets were operated above transition or "warm", then there would be no persistent currents and close control of the operating point would not be necessary. The normal state resistance of the magnets is 320×10^{-3} Ω/magnet. The magnets give 12.43 G/A. At 15 GeV the magnetic field would be about 3×10^{3} G, requiring 241.4 A. Thus,

$$\text{Power (each magnet)} = 241.4^2 \times 0.32\ \Omega = 18.6\ \text{kW}$$

or

$$P_{tot} = 18.6 \times 264 = 4.9\ \text{MW} \quad .$$

At 7.5 GeV the power would be 1.2 MW.

These power levels look, at first sight, to be impractically high for the type of magnet and cooling system envisioned.

SHIELDING THE COLD REGION OF THE ISA MAGNETS FROM SYNCHROTRON RADIATION

M. Tigner
Cornell University

If the ISA superconducting ring is to be used for electron acceleration, one of the most severe problems is the enormous power (5.3 MW) given off by the electron beam.

The refrigeration capacity available per ring is 13 kW, thus the loading of the refrigerator by synchrotron radiation should not be more than 1 to 2 kW so that effectively the synchrotron radiation power must be reduced by a factor of 5×10^3 before it enters the cold part of the magnet.

To do this, an additional warm bore tube of heavy metal and a means of water cooling must be added. If the heavy metal tube is placed outside of the present Al tube it will need to be somewhat thicker than if the heavy metal tube is placed outside of the Al tube. If the tube is of Ta then it will need to be from ½ to 1 cm in wall thickness, depending upon whether it is inside or outside. The most serious problem in absorbing the synchrotron light comes from the high end of the spectrum. Figure 1 is a copy of p. 64 of the PEP proposal which describes the situation in the ISA adequately. As one can see from the plot, the spectral power per eV is falling by an order of magnitude per 100 keV interval at the high energy end of the spectrum. This means, for example, that photons in the 300 - 400 keV bunch carry approximately:

$$\tfrac{1}{2} \times 10^{-3}\ \text{W/eV-mA} \times 10^5\ \text{eV} \times 200\ \text{mA} = 10^4\ \text{W}.$$

If this was the only energy band responsible, then x-rays in this band would have to be attenuated in the shield by a factor of 10. It will turn out that if this condition is met, all other energy bands will suffer sufficient absorption.

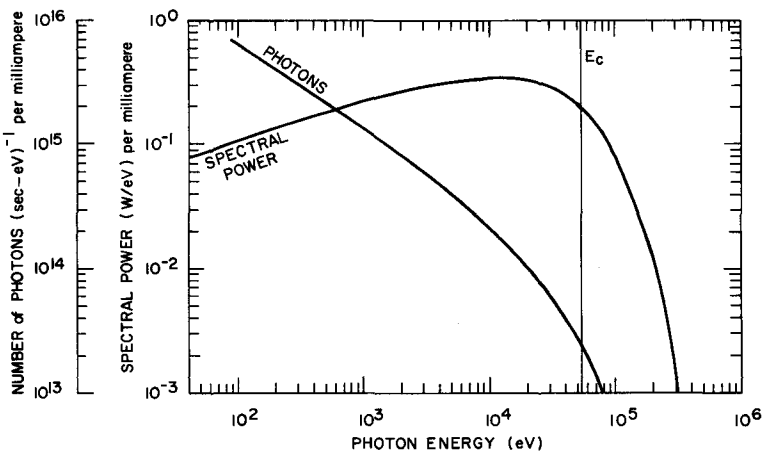

Fig. 1. Spectral Power and Number of Photons per mA vs Photon Energy.

Case A

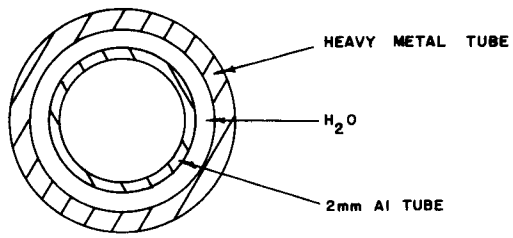

Fig. 2. Shielded Beam Chamber.

The x-rays impinge on the Al tube at a small angle. This angle is given approximately by the magnet bending angle because the vacuum chamber forms a polygon whose edges meet at this angle or 24 mrad. This next figure shows the trajectory of the γ-rays in the event that they are not deflected. In the aluminum wall then, the x-rays traverse $\sim$ 8 cm.

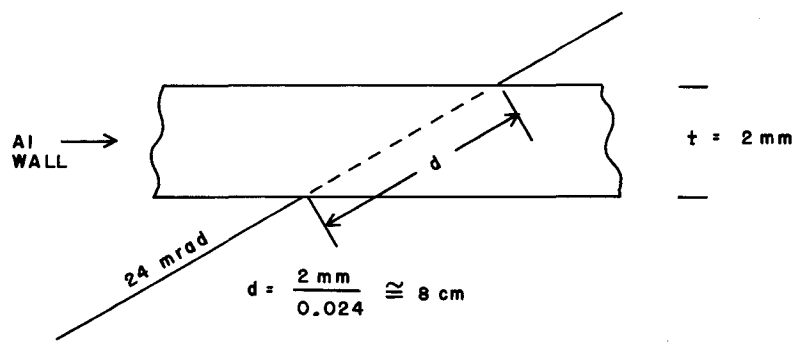

Fig. 3. γ-ray Path in Al Wall.

However, in Al x-rays of 300 - 400 GeV are Compton scattered more strongly than they are absorbed. The scattered intensity compared to the incident intensity is

$$I_s = I_o e^{-\alpha d}$$

at 400 GeV $\alpha = 0.06 \times 2.7\ cm^{-1} = 0.16\ cm^{-1}$

$$\alpha \sim 1.3 \quad .$$

The absorption (photoelectric) coefficient is $\alpha_{abs} = 0.0002$ at 400 keV so very few of these photons are absorbed but most of them are scattered. The Compton cross section at this energy is peaked[2] around 45°, but the cross section is ½ the maximum at 90° so a substantial fraction of the photons are redirected along the thin dimension of the vacuum chamber. The wall thickness of the Ta outer chamber will not then be enough to cut the intensity of the primary beam (in the 300 - 400 keV band) by a factor of 10 or

$$\alpha d_{Ta}(\text{absorption}) \simeq 2.3$$

$\alpha_{abs}(T_a - 300 - 400 \text{ keV}) \simeq 0.15 \times 16.5 \text{ cm}^{-1} = 2.49 \text{ cm}^{-1}$ and $d_{Ta} \sim 1$ cm. Now we've got sufficient absorption for the 300 - 400 keV band, what about lower and high energy bands? In the 400 - 500 keV band the spectral power has dropped another order of magnitude so the power in this band is ~ 1 kW and thus the contribution from this band could be 1 kW without attenuation and with all photons Compton scattered at 90°. In fact, $\alpha_{abs} d_{Ta}(400 - 500 \text{ keV}) = 0.08 \times 16.7 = 1.33$. So in the 4 - 500 keV band the power is reduced by a factor of 3.8. In the next higher band (500 - 600) the power has dropped another order of magnitude and the Compton cross section is smaller and more peaked in the forward direction. Thus, the effect of the x-rays of energy greater than 500 keV is completely negligible.

Now consider the band 200 - 300 keV. In this band

$$P_{\gamma}(200 - 300 \text{ keV}) \simeq \tfrac{1}{2} \times 1.5 \times 10^{2} \times 100 \times 10^{3} \times 200 = 1.5 \times 10^{5} \text{ W}$$

$$\alpha_{abs} d_{Ta} = 0.42 \times 16.7 \simeq 7.01 \times 1 \quad .$$

So attenuation in this band is a factor of 10^3 and only 150 W from this band gets through even if all γ's are Compton scattered at 90°:

In the band 100 - 200 keV

$$P_{\gamma} \cong \tfrac{1}{2}(0.080 - 0.015) \times 10^{5} \times 200 = 6.5 \times 10^{5}$$

but $\alpha_{abs} T(100 - 200 \text{ keV}) \cong 32$, so attenuation here is overwhelming.

These results are plotted in Figure 4. The rather sharp transmission about a narrow band of wavelength is the result of the

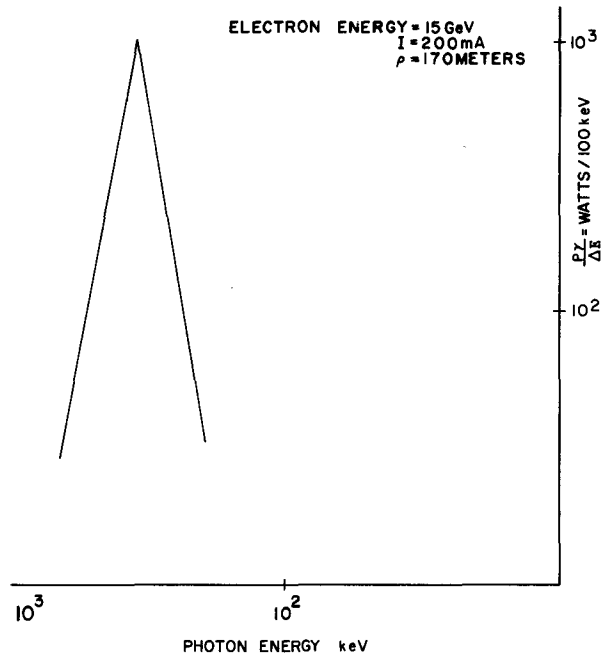

Fig. 4. Synchrotron Power Penetrating 1 cm of Ta Assuming Normal Incidence and Other Parameters Listed.

rapid decrease in spectral power on the high photon energy side and and a rapid increase in photoelectric absorption coefficient on the low photon energy side.

Case B

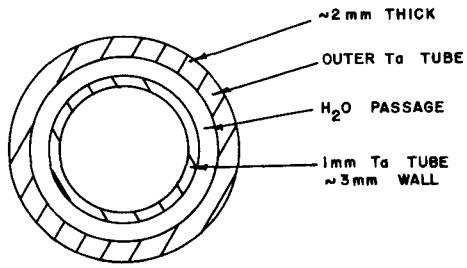

Fig. 5. Shielded Beam Chamber with Double Ta Wall.

If Ta were used for both tubes then the interaction length for Compton scattering would be a factor of two less than for photoelectric absorption in the 300-400 keV band. Thus in this band, photons traversing one absorption length have ~ 30% of their number scattered out by Compton scattering and if these that are scattered must traverse one absorption length their number is reduced by another factor of 3 so that only 1/10 of the original number emerge. This means that ~ ½ cm total wall thickness should be ample if both tubes are of Ta. The inner tube should be thicker as the water will absorb little, but will scatter the x-rays to some extent.

If one decides to put e's in the p-ring then this computation should be done using the Monte Carlo method to get the real minimum possible wall thickness.

Shielding Against the Synchrotron Light at a Beam Energy of 7.5 GeV.

At 200 mA beam current, the synchrotron radiation power at 15 GeV was 5.3 MW. Thus, $P_\gamma(7.5\ \text{GeV}) = (7.5/15)^4 \times 331$ kW and $\epsilon_c(7.5\ \text{GeV}) = (7.5/15)^3 \times 43$ keV = 5.4 keV.

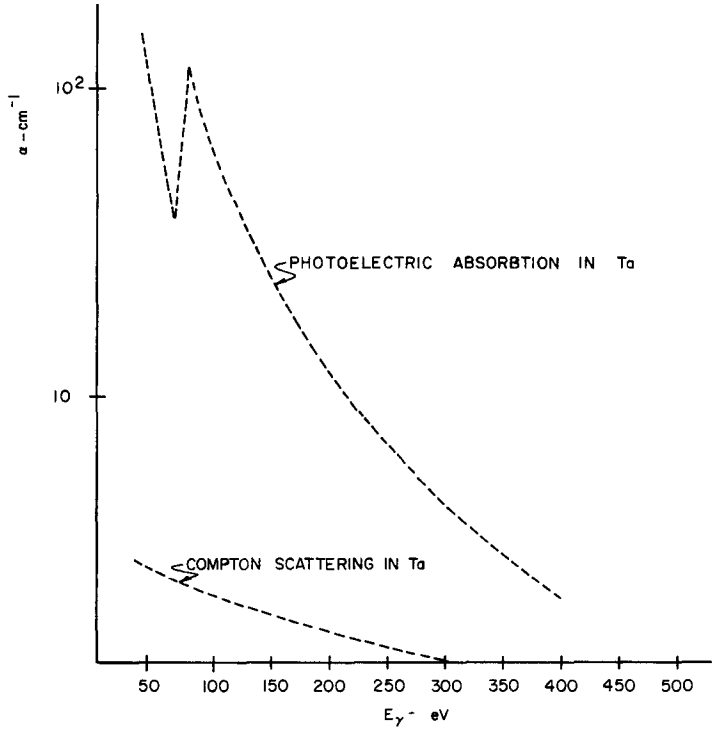

Fig. 6. Photoabsorption and Compton Scattering in Tantalum.

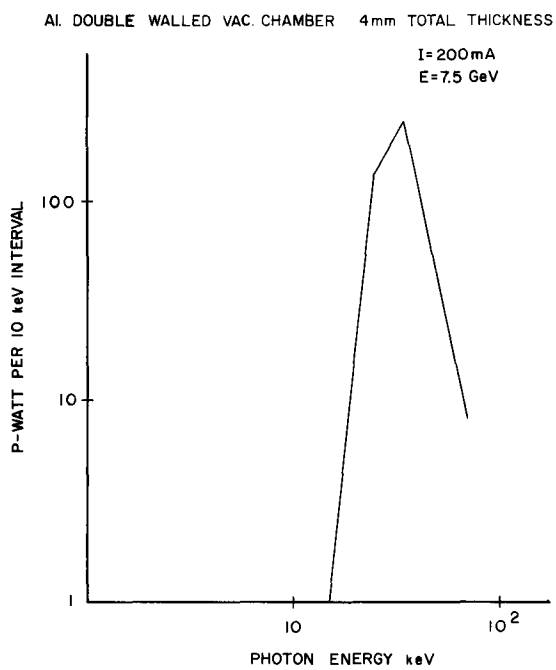

Fig. 7. Synchrotron Radiation Power which Reaches the Cold Part of the Magnet in ISABELLE.

Figure 6 is the result of a rough computation of the power that escapes into the cold part of the magnet taking into account that at the photon energies encountered the absorption in aluminum is substantial when compared to the Compton scattering. The very conservative description is made that all Compton scattered x-rays are scattered at 90° and all of these then pass through the thinnest dimension of the chamber. A few hundred watts at most escape into the cold region.

Thus, shielding the cold region from the synchrotron radiation is not difficult.

DOES THE PROTON BEAM IN AN e-p COLLIDING DEVICE DETERIORATE BY INDIVIDUAL e-p COULOMB INTERACTIONS ?

H. Bruck

Saclay

I. INTRODUCTION

In the 1974 CERN Autumn Study on Storage Rings at several hundred GeV/c, reservations had been expressed,[1] concerning the long-term proton beam evolution in a proton-electron colliding ring.

We consider here the deterioration of the proton beam by individual proton-electron Coulomb interactions. Rough order of magnitude evaluations show that effects of this nature should be negligible. The present more precise calculations will confirm these appraisals, showing that e-p Coulomb interactions fortunately do not interfere with the proton beam behavior in an e-p storage device.

One finds in the literature[2,3] formulae of the differential cross section $d\phi/d\Delta E'$ of energy transfer $\Delta E'$ in proton-electron collisions, considered in the rest frame K' of the electron, the proton energy in this frame being E'. This cross section is:*

$$\frac{d\phi/d(E',\Delta E')}{d\Delta E'} = \frac{2\pi r_e^2 mc^2}{B'^2}\,\frac{1}{(\Delta E')^2}\left[1 - B'^2 \times \frac{\Delta E'}{\Delta E'_m} + \frac{1}{2}\left(\frac{\Delta E'}{E' + Mc^2}\right)^2\right] \quad (1.1)$$

$$\approx 2\pi r_e^2 mc^2\,\frac{1}{(\Delta E')^2} \quad (1.1a)$$

---

* For the meaning of the symbols, see appendix A.

1. Possible options in a LSR, CERN/ISR-AS/74-66, October 1974.
2. Y. Cauchois, Y. Héno, Introduction à l'emploi de rayonnements en chimiephysique, vol. 1, Paris, 1964.
3. B. Rossi, High Energy Particles, Prentice Hall, 1956.

In (1.1) the second and third terms inside the brackets express the spin interaction and are not essential in this case. Formula (1.1a) is the Rutherford formula in the extreme relativistic approximation of $B' \approx 1$.

Yet, in a proton-electron colliding ring the electrons are not at rest, but both particle species move in the laboratory frame K, wherein the cross sections have to be considered.

Obviously this can be taken into account with the help of Lorentz transformations.

II. DEFINITION OF SYMBOLS AND GUIDELINE OF SUBSEQUENT TEST

The transformation law of various entities will be needed from or into the electron rest frame K′, the laboratory frame K and the center-of-mass frame K_c of the e-p collisions.

Required entities are for instance the ratios $\Delta E/\Delta E'$ of the transferred energy or θ/θ' of the deflection angle. All these relations can be derived from Lorentz transformations of the momentum-energy vector $\vec{Q}$.

Combining the two transverse space components Q_x and Q_z of the momentum-energy vector, the latter has three components:

$$\vec{Q} = (Q_\perp = \frac{1}{c} P_\perp \; ; \; Q_\parallel = \frac{1}{c} P_\parallel \; ; \; Q_4 = \frac{i}{c^2} E) \qquad (2.1)$$

The following notations will be used:

$$\vec{Q} = \text{vector before collision}$$
$$\underline{\vec{Q}} = \text{vector } \underline{\text{after}} \text{ collision}$$
$$\Delta\vec{Q} = \underline{\vec{Q}} - \vec{Q} \qquad (2.2)$$

The proton-electron interactions will be expressed first in the c.m. frame K_c, where collisions deflect protons and electrons oppositely by the same angle $\theta_c = \Theta_c$ with energy transfer $\Delta E_c = 0$, maintaining energy and momentum of each of the interacting particles.

Transformed into frames K and K′, the $\vec{Q}$-vector will then reveal the transferred energy in these frames, as a function of θ_c:

$$\Delta E = \frac{c^2}{i} Q_4(\theta_c) \tag{2.3a}$$

$$\Delta E' = \frac{c^2}{i} Q_4'(\theta_c). \tag{2.3b}$$

The deflection angles in K and K′ are given by

$$\tan\theta = \underline{Q}_\perp (\theta_c)/\underline{Q}_\parallel(\theta_c) \tag{2.4a}$$

$$\tan\theta' = \underline{Q}_\perp' (\theta_c)/\underline{Q}_\parallel(\theta_c). \tag{2.4b}$$

Finally, with the help of the ratios $\Delta E/\Delta E'$ and θ/θ' it is also possible to express the <u>cross sections</u> of energy transfer and deflection angle in the laboratory frame.

III. CENTER-OF-MASS PROPERTIES AND TRANSFORMATION MATRIX ELEMENTS

Under extreme relativistic conditions, energy and momentum in the c.m. are related to the same entities in the laboratory frame by:

$$\Gamma_c = \Gamma\sqrt{\frac{m\gamma}{M\Gamma}} = \sqrt{\frac{1}{2}\frac{m}{M}\gamma_{ep}} \tag{3.1}$$

$$\gamma_c = \gamma\sqrt{\frac{M\Gamma}{m\gamma}} = \sqrt{\frac{1}{2}\frac{M}{m}\gamma_{ep}} \tag{3.2}$$

$$P_c = \frac{1}{c} E_c = \frac{1}{c}\sqrt{Mc^2\Gamma \times mc^2\gamma} \tag{3.3}$$

with

$$\gamma_{ep} = \Gamma\gamma + \sqrt{(\Gamma^2 - 1)(\gamma^2-1)} \approx 2\Gamma\gamma\ . \tag{3.4}$$

The transformation $\vec{Q} = L(K_c \rightarrow K) \times \vec{Q}_c$ is performed with the help of the 3 × 3 matrix

$$L(K_c \to K) = \begin{bmatrix} 1 & 0 & 0 \\ 0 & \gamma_o & -i(\beta\gamma)_o \\ 0 & +i(\beta\gamma)_o & \gamma_o \end{bmatrix}, \qquad (3.5)$$

where $\beta_o c$ is the velocity of K_c in K (see figure) and $\gamma_o = (1 - \beta_o^2)^{-\frac{1}{2}}$.

It is necessary to express β_o and $(\beta\gamma)_o$ analytically: the figure shows, that the velocity B of the proton in K can be considered as resulting from the addition of two velocities in the frame K_c: the proton velocity B_c in K_c and the velocity $-\beta_o$ of the frame K in K_c. Therefore the energy Γ of the proton in K can be expressed by Γ_c and γ_o by:

$$\Gamma = \Gamma_c\gamma_o + \sqrt{(\Gamma_c^2 - 1)(\gamma_c^2 - 1)} \qquad (3.6)$$

Here generally $\Gamma_c \gg 1$, whereas γ_o is of the order of some units (the laboratory and the c.m. frames are generally not very different). Then γ_o can be found by solving the equation

$$\gamma_o + \sqrt{\gamma_o^2 - 1} = \Gamma/\Gamma_c \qquad (3.7)$$

with

$$\Gamma/\Gamma_c = \gamma_c/\gamma = \sqrt{M\Gamma/m\gamma} \qquad [\text{cf. } (3.1), (3.2)]$$

Neglecting 1 beside γ_o^2 in (3.6) one has very roughly

$$\gamma_o \approx \frac{1}{2}\sqrt{\frac{M\Gamma}{m\gamma}}. \qquad (3.7a)$$

The matrix elements of the transformation $K_c \to K'$ are obtained by substituting in (3.5):

$$\begin{aligned} \gamma_o &\to \gamma_c \\ \beta_o &\to \beta_c \end{aligned} \qquad (3.8)$$

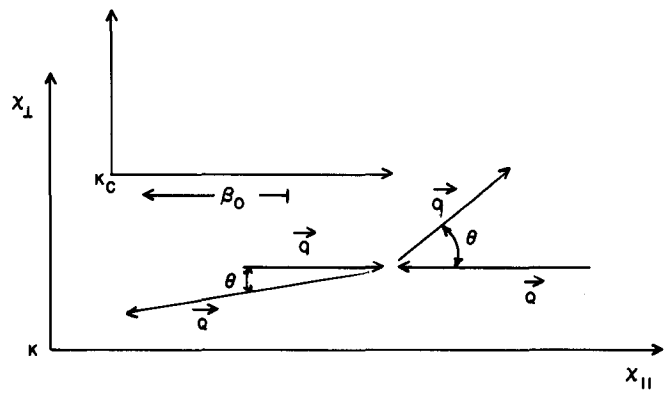

Fig. 1. Velocity Transformations, K_c and K Systems.

with

$$\gamma_c = \gamma\sqrt{\frac{M\Gamma}{m\gamma}} \quad ; \; \beta_c \approx 1 \qquad [\text{cf. } (3.2)\,]$$

IV. LORENTZ TRANSFORMATIONS RESULTS

Having formulated in Section III the momentum-energy vector in the c.m. frame K_c, and also the matrix elements of transformation to the frames K of the laboratory and K′ of the electron at rest, it is now possible to express in accordance with Section II various entities in K and K′. It is easy to ascertain, that one finds by Lorentz transformation:

A. Angle transformations:

In the K frame, and using (2.4):

$$\tan\theta = \frac{B_c \sin\theta_c}{\gamma_o(\beta_o + B_c \cos\theta_c)} \; ; \; B_c \approx -1; \; \beta_o < 0. \qquad (4.1)$$

If $\beta_o \approx -1$: $\tan\theta \approx \frac{1}{\gamma_o} \tan(\theta_c/2)$ (4.1a)

If β_o not ≈ -1, but θ, $\theta_c \ll 1$, formula (4.1) yields:

$$\theta \approx \frac{\theta_c}{\gamma_o[(-\beta_o) + 1]} \qquad (4.1b)$$

In the K′ frame:

$$\tan\theta' = \frac{B_c \sin\theta_c}{\gamma_c(-\beta_c + B_c \cos\theta_c)} \; ; \; B_c \approx -1; \; \beta_c \approx 1. \qquad (4.2)$$

If furthermore θ', $\theta_c \ll 1$:

$$\theta' \approx \frac{\theta_c}{\gamma_c(\beta_c + 1)} \approx \frac{\theta_c}{2\gamma_c} \qquad (4.2a)$$

and

$$\frac{\theta}{\theta'} \approx \frac{\gamma_c(\beta_c + 1)}{\gamma_o[(-\beta_o) + 1]} \approx \frac{2\gamma_c}{\gamma_o[(-\beta_o) + 1]} \tag{4.3}$$

B. Energy transfer transformations:

The energy transfer in K, associated with a given deflection angle θ_c in K_c is, according to (2.3a):

$$\Delta E = -Mc^2(B\Gamma)_c(\beta\gamma)_o \frac{2}{1 + \mathrm{ctn}^2(\theta_c/2)} \tag{4.4}$$

If $\theta_c \ll 1$,

$$\Delta E \approx \frac{1}{2} Mc^2(B\Gamma)_c(\beta\gamma)_o\theta_c^2 \tag{4.4a}$$

In the electron rest frame K′, one has:

$$\Delta E' = Mc^2(B\Gamma)_c(\beta\gamma)_c \frac{2}{1 + \mathrm{ctn}^2(\theta_c/2)} \tag{4.5}$$

$$\Delta E' \approx \frac{E'}{1 + \mathrm{ctn}^2(\theta_c/2)} \approx Mc^2\gamma_{ep}\left(\frac{\theta_c}{2}\right)^2 \tag{4.5a}$$

Comparing (4.4) and (4.5):

$$\Delta E/\Delta E' = (-\beta\gamma)_o/(\beta\gamma)_c \tag{4.6}$$

For $(-\beta\gamma)_o$ see (3.7); $(\beta\gamma)_c \approx \gamma_c \approx \gamma\sqrt{\frac{M\Gamma}{m\gamma}}$ [cf/ (3.2)].

V. EXTREME VALUES OF θ AND ΔE

Protons crossing an electron cloud interact mostly with the collective electron space-charge field. They interact individually with an electron only inside a limited domain around this electron, domain of about spherical dimensions in the electron rest frame K′, with radius $\rho_e \approx \frac{1}{2}(D_e^{*\prime})^{-1/3}$.

$D_e^{*\prime}$ is the electron density in the frame K′. The meaning of

the star is that $D_e^{*\prime}$ is the electron density in the low-β^* interaction regions of the storage ring. Expressed by the density D^* in the laboratory frame K:

$$D^* = \frac{\sigma_e^*}{(4\pi)^{\frac{1}{2}}\,\delta\ell_e} \quad : \tag{5.1}$$

$$\rho_e \approx \frac{1}{2}\,(D_e^*/\gamma)^{-1/3} \,. \tag{5.2}$$

The extreme values of angular deflection of a proton, crossing an electron cloud, have to be evaluated in the c.m. frame K_c, because there the interaction takes place without energy transfer, and can be represented as diffraction of the proton de Broglie wave with wavelength λ_c on the effective electron interaction domain which is in K_c a flat disk of radius ρ_e.

$$\lambda_c = \frac{h}{P_c} \tag{5.3}$$

For P_c see (3.3).

The minimum proton deflection angle is then

$$(\theta_c^*)_m \approx \sin(\theta_c^*)_m = 0.61\,\frac{\lambda_c}{\rho_e} \tag{5.4}$$

(The meaning of the star is that the deflection happens in a low-β^* interaction region).

The maximum angle is not limited by diffraction, because the extension of the diffracting obstacle o is the transverse electron dimension as given by the Heisenberg relation, and

$$o = \hbar/\gamma_{ep}\,mc \ll \lambda_c$$

Therefore

$$(\theta_c^*)_M = \pi \tag{5.5}$$

The extreme angles and energy transfers of interest are given here below in K_c and in K:

K_c	K
$(\theta_m^*)_c = 0.61 \frac{\lambda_c}{\rho_e}$ [cf. (5.4)]	$\theta_m^* = \frac{1}{\gamma_o[(-\beta_o) + 1]} (\theta_m^*)_c$ [cf. (4.1b)]
$(\theta_m^*)_c = \pi$ [cf. (5.5)]	
$(\Delta E_m)_c = 0$	$\Delta E_m = \frac{1}{2} Mc^2 (B\Gamma)_c (-\beta\gamma)_o (\theta_m^*)_c$ [cf. 4.4a)]
$(\Delta E_M)_c = 0$	$\Delta E_M = 2Mc^2 (B\Gamma)_c (-\beta\gamma)_o$ [cf. (4.4)]

The stability domain of the protons in the ring is supposed to be limited by the (angular) θ_1-acceptance of the ring in its normal (not low-β^*) part: $\theta \leq \theta_\ell = b/\beta_{pM}$.

Then in the low-β^* part, θ^* is stable, if

$$\theta^* \leq \theta_\ell^* = \frac{b}{\sqrt{\beta_{pm} \times \beta_p^*}} \approx b\sqrt{\frac{\upsilon_p}{R \times \beta_p^*}} \tag{5.6}$$

with b = normal vacuum chamber radius.

Simultaneously, the energy transfer is limited to $\Delta E \leq \Delta E_1$, the latter satisfying:

$$\frac{\Delta E_\ell}{\Delta E_m} = \left(\frac{\theta_\ell^*}{\theta_m^*}\right)^2 . \tag{5.7}$$

VI. CROSS SECTIONS, MEAN VALUES AND BEAM DETERIORATION RATES IN THE LABORATORY FRAME

In Section IV, relations between scattering angles and transferred energies in various frames have been given. Now the probability or cross section of these angles or energies will be expressed, as well as various mean values.

A. Energy transfer:

The cross section ϕ [Ef. (1.1) or (1.1a)], because it is a surface transverse to the movement of each of the two involved particle species, is a relativistic invariant; let a given transferred energy interval be $d\Delta E$ or $d\Delta E'$, respectively in K or in K′, then

$$\frac{d\phi}{d\Delta E}\, d\Delta E = \frac{d\phi}{d\Delta E'}\, d\Delta E' \tag{6.1}$$

The probability dP of energy transfer ΔE in K or $\Delta E'$ in K′ from the protons to the electrons, after crossing an electron layer of product density × depth = S_e, is

$$dP = S_e \frac{d\phi(\Delta E)}{d\Delta E}\, d\Delta E = S_e \frac{d\phi(\Delta E')}{d\Delta E'}\, d\Delta E' \tag{6.2}$$

The <u>mean</u> transferred energy after crossing this electron layer is in the laboratory frame K:

$$\overline{dE} = \int_{\Delta E_m}^{\Delta E_\ell} \Delta E \frac{dP}{d\Delta E}\, d\Delta E = \frac{\Delta E}{\Delta E'} \times \int_{\Delta E'_m}^{\Delta E'_\ell} \Delta E' \frac{dP}{d\Delta E'}\, d\Delta E' , \tag{6.3}$$

$$\overline{\Delta E} = \frac{\Delta E}{\Delta E'}\, \overline{\Delta E'} = \frac{(-\beta\gamma)_o}{(\beta\gamma)_c}\, \overline{\Delta E'} \tag{6.4}$$

This means that the mean energy transfer in K differs from the transfer $\overline{\Delta E'}$ to the motionless electrons by the ratio of the momentum coefficients of K and of K′, both with respect to the c.m. frame K_c. If the laboratory K coincides with K_c, the energy transfer is zero.

Introducing (1.1) into (6.2) and (6.3), integrating and substituting furthermore $\Delta E'_\ell/\Delta E'_m = \Delta E_\ell/\Delta E_m$, one obtains:

$$\overline{\Delta E} = S_e\left(\frac{\Delta E}{\Delta E'}\right) 2\pi r_e^2 mc^2 \left(\ln \frac{\Delta E_\ell}{\Delta E_m} - \frac{3}{4}\right) \tag{6.5}$$

At maximum intensity, the mean surface density of a single electron rf bunch is [see Ref. 4]:

$$S_{el} = \sigma_e^* = \frac{1}{2} \frac{\Gamma \Delta \nu_p}{r_p \times \beta_p^*} \tag{6.6}$$

The total surface density, added up with time as a sum of repeatedly crossed electron bunches grows like

$$\frac{d}{dt} S_e = k f_o \sigma_e^* \tag{6.7}$$

k = number of low-β^* beam crossings per turn in the storage ring
$f_o = c/2\pi R$ = revolution frequency of the protons.

Then, with (6.5), (6.7) and (4.6), the mean proton energy diminishes like

$$\frac{d}{dt} \overline{E} = - \left(\frac{d}{dt} S_e\right) \times \frac{(-\beta\gamma)_o}{(\beta\gamma)_c} 2\pi r_e^2 mc^2 \left[\ln\left(\frac{\Delta E_\ell}{\Delta E_m}\right) - \frac{3}{4}\right] \tag{6.8}$$

B. Angular dispersion:

The m.s. scattering angle in K grows like

$$\frac{d}{dt} \overline{\theta^2} = \left(\frac{d}{dt} S_e\right) \times \int_{\theta_m}^{\theta_e} \theta^2 \frac{d\phi}{d\theta} d\theta \tag{6.9}$$

4. M. Sands, "The Physics of Electron Storage Rings", SLAC Rept. 121, November 1970.

The angular dispersion in the laboratory frame K is $\delta\theta = \sqrt{\overline{\theta^2}} = (\theta/\theta')\delta\theta'$, and with Eq. (4.3);

$$\delta\theta = \left(\frac{\theta}{\theta'}\right) \delta\theta' = \frac{\gamma_c(\beta_c + 1)}{\gamma_o[(-\beta_o) + 1]} \delta\theta' \tag{6.10}$$

The angular dispersion, $\delta\theta$, observed in the laboratory frame K differs from the angular dispersion $\delta\theta'$, observed in the electron rest frame K′ about as the inverse of the energy transfer [cf. (6.4)]. The angular dispersion $\delta\theta$ in K is <u>maximum</u>, when laboratory frame K and c.m. frame K_c coincide, (excluding $\beta_o > 0$).

We shall now evaluate $d\overline{\theta^2}/dt$, as given by Eq. (6.9). The differential cross section $d\phi/d\theta$ is

$$\frac{d\phi}{d\theta} = \frac{d\phi}{d\Delta E'} \times \frac{d\Delta E'}{d\theta_c} \times \frac{d\theta_c}{d\theta} \tag{6.11}$$

with

$$\frac{d\phi}{d\Delta E'} = 2\pi r_e^2 mc^2 \frac{1}{(\Delta E')^2} \qquad \text{[cf. (1.1a)]}$$

$$\Delta E' = Mc^2 \gamma_{ep}(\theta_c/2)^2 \qquad \text{[cf. (4.5a)]}$$

and

$$\theta_c = \gamma_o[(-\beta_o) + 1]; \ (-\beta_o) > 0 \qquad \text{[cf. (4.1b)]}$$

Introduction of these formulae into (6.11)

$$\frac{d\phi}{d\theta} = \frac{2^4\pi r_e^2}{(M/m)\gamma_{ep}\ \gamma_o^2[(-\beta_o) + 1]^2} \times \frac{1}{\theta^3}\ , \tag{6.11a}$$

$$\frac{d}{dt}\ \overline{\theta^2} = \left(\frac{d}{dt}\ S_e\right) \frac{2^4\pi r_e^2}{(M/m)\gamma_{ep}\ \gamma_o^2[1 + (-\beta_o)]^2} \ln \frac{\theta_e}{\theta_m} \tag{6.12}$$

C. Single scattering losses:

If in a collision the proton deflection is $\theta > \theta_1$, the proton is lost. The fraction of particles lost in this way grows like

$$\frac{1}{N}\frac{dN}{dt} = -\left(\frac{d}{dt} S_e\right) \int_{\theta_\ell}^{\theta_m} \frac{d\phi}{d\theta}\, d\theta$$

With the help of (6.11a):

$$\frac{1}{N}\frac{dN}{dt} = -\left(\frac{d}{dt} S_e\right) \frac{2^3 \pi r_e^2}{(M/m)\gamma_{ep}\, \gamma_o^2 [1 + (-\beta_o)]^2} \times \frac{1}{\theta_\ell^2} \qquad (6.13)$$

VII. APPLICATIONS AND CONCLUSION

In Table I numerical results are gathered for three storage ring projects 5, 6, 7, with possible e-p option and broadly different proton energies. The respective rates of proton beam deterioration are nevertheless of the same order in all three projects, and they are negligible.

Referring the results to one working hour, the total layer of electrons $(S_e)_{1h}$, crossed by the protons is equivalent to the electron layer in an aluminum sheet of some 1/10 mm of thickness. Furthermore, the cm of the collision nearly coincides with the laboratory frame in all three cases (see value of γ_o). For both these reasons the mean proton to electron energy transfer is nearly zero.

On the contrary, the angular dispersion $\delta\theta_c$ of protons by electrons in the c.m., if compared to the dispersion in the

5. Preliminary Study of a CERN 400 GeV Storage Ring Facility, R.W. Chasman et al., CERN/ISR-GS-Th/74-45.

6. ISABELLE, ed. H. Hahn, "A Proposal for Construction of a Proton-Proton Storage Accelerator Facility ISABELLE," BNL 18891 (May 1974).

7. L. Smith, "The Proton-Electron-Positron Project PEP," LBL Rept. 3032, PEP-note 86, Proc. IX Intern. Conf. on High Energy Accelerators, 1974, p. 557.

electron rest frame, is multiplied by 10^5. Nevertheless, the observed angular dispersion in the laboratory, accumulated in one hour, even so is only of the order of 10^{-6} rad. The proton losses by single scattering are also very small.

The general conclusion is that the deterioration rate of the proton beam by e-p Coulomb interaction in e-p storage devices is, by far, negligible.

<u>POST-SCRIPTUM</u>: <u>SINGLE SCATTERING ELECTRON LOSSES</u>:

The electron scattering cross section is

$$\frac{d\phi}{d\Theta^*} = \frac{d\phi}{d\Delta E'} \frac{d\Delta E'}{d\Theta_c^*} \frac{d\Theta_c^*}{d\Theta^*} \qquad \text{(PS 1)}$$

$$\frac{d\phi}{d\Delta E'} \text{ cf. (1.1a)}; \quad \frac{d\Delta E'}{d\Theta_c^*} = \frac{d\Delta E'}{d\theta_c^*}$$

because $\Theta_c^* = \theta_c^*$; $\frac{d\Delta E'}{d\theta_c^*}$ cf (4.5a).

By Lorentz transformation and in analogy to (4.1):

$$\tan\Theta^* = \frac{\beta_c \sin\Theta_c^*}{\gamma_o(\beta_o + \beta_c \cos\Theta_c^*)} \; ; \; \beta_c \approx +1; \; \beta_o < 0; \quad \Theta^*, \Theta_c^* << 1 \qquad \text{(PS 2)}$$

$$\Theta^* \approx \frac{\Theta_c^*}{\gamma_o[1 - (-\beta_o)]} \qquad \text{(PS 2a)}$$

Introduction of these relations into (PS 1) yields

$$\frac{d\phi}{d\Theta^*} = \frac{2^4 r_e^2}{(M/m)\gamma_{ep}\gamma_o^2[1 - \beta_o)]^2} \times \frac{1}{\Theta^{*3}} \; . \qquad \text{(PS 1a)}$$

The electron loss rate is

$$\left(\frac{1}{N}\frac{dN}{dt}\right)_e = -\left(\frac{d}{dt}S_p\right)\int_{\Theta_\ell^*}^{\Theta_M^*} \frac{d\phi}{d\Theta^*}\, d\Theta^*$$

$$= -\left(\frac{d}{dt}S_p\right)\frac{2^3 r_e^2}{(M/m)\gamma_{ep}\,\gamma_o^2\left[1-(-\beta)\right]^2}\frac{1}{\Theta_\ell^{*2}} \qquad \text{(PS 3)}$$

where $(d/dt)S_p = kf_o\sigma_p^*$; $\sigma_p^* = \frac{1}{2}\frac{\gamma\Delta\upsilon_e}{r_e \times \beta_e^*}$

We suppose $\beta_\ell^* \approx \beta_p^*$ and the diaphram limited angle $\Theta_1^* \approx \theta_1^*$.

Numerical values of the electron loss rate have been added in Table I.

APPENDIX A: SYMBOLS

β, γ, m	= usual electron characteristics, r_e = classical radius, Θ = scattering angle
B, Γ, M, r_p, θ	= corresponding proton characteristics
K', K, K_c	reference frames (el. at rest, laboratory, c.m.)
β_o, γ_o	speed and energy coeff. of K_c in K
$\gamma_{ep} \approx 2\gamma\Gamma$	relative electron-proton energy coeff.
R	physical ring radius
b	vacuum chamber cross section radius
k	number per turn of low-β electron-proton crossing points
f_o	$2\pi R/c$
ν_p	proton wave number
$\Delta\nu_p$	Amman-Ritson limit for protons
β^*_{ep}	β^* in interaction region
ρ_e	radius of sphere with an electron at center
λ_c	de Broglie wavelength of protons in c.m. frame
$\delta\ell$	length of electron bunch
σ^*_e	projected plane electron density per bunch, cf. (6.6)
D^*_e	electron density in low-β^* region, cf. (5.1)
S_e	total projected plane electron density in low-β^* region, cf. (6.7)

TABLE I

	Symbols	Units	[5] LSR (CERN)	[6] ISABELLE (BNL)	[7] PEP (low en.) (LBL-SLAC)	Formula
Proton energy	$E = Mc^2\Gamma$	GeV	400	100	50	
Electron energy	$mc^2\gamma$	GeV	20	15	15	
Growth of electron layer	$(d/dt)S_e$	$m^{-2}h^{-1}$	1.04×10^{26}	1.20×10^{26}	1.78×10^{26}	(6.7)
Growth of equivalent Al sheet	$(d/dt)x_{al}$	mm h^{-1}	0.128	0.148	0.315	
En. coeff. of c.m. in the lab.	γ_o		2.35	1.43	1.19	(3.7)
Transformation factors	$\Delta E/\Delta E'$		1.21×10^{-5}	1.38×10^{-5}	1.19×10^{-5}	(4.6)
	θ/θ'		7.83×10^{4}	6.04×10^{4}	5.87×10^{4}	(6.10)
Energy transfer limits	ΔE_m	eV	2.54×10^{-14}	1.15×10^{-14}	8.55×10^{-15}	(4.4a)
	ΔE_1	eV	2.71×10^{7}	1.96×10^{6}	1.75×10^{6}	(5.7)
Deflection limits	θ^*_m	rad	1.16×10^{-13}	3.15×10^{-13}	5.41×10^{-13}	table after (5.5)
	θ^*_ℓ	rad	3.78×10^{-3}	4.11×10^{-3}	7.74×10^{-3}	(5.6)
Energy loss rate	$-(d/dt)E$	$eV\times h^{-1}$	1.53	1.94	2.94	(6.8)
One hour scattering	$(\delta\theta)_{1h}$	rad	9.04×10^{-7}	4.11×10^{-6}	9.30×10^{-6}	(6.12)
Loss rate by single scattering (protons)	$-[(1/N)dN/dt]_p$	h^{-1}	1.19×10^{-9}	2.15×10^{-8}	3.08×10^{-8}	(6.13)
Loss rate by single scattering (electrons)	$-[(1/N)dN/dt]_e$	h^{-1}	5.57×10^{-7}	2.07×10^{-6}	1.43×10^{-6}	(PS 3)

APPENDIX B: ADDITIONAL MACHINE DATA

Entity	Unities	LSR 5	ISABELLE 6	PEP 7	Formula
R	m	1.30×10^{3}	428	345	
P_c	$eV \times m^{-1}s$	2.98×10^{2}	1.26×10^{2}	9.13×10^{1}	(3.3)
f_o	h^{-1}	1.32×10^{8}	4.02×10^{8}	4.98×10^{8}	
b	mm	30	40	40	
k		2	4	6	
R/ν	m	36.9	$\beta_{pM} = 43$	18.4	
β_p^*	m	1.75	2.2	1.45	
$\Delta\nu_p$		5×10^{-3}	5×10^{-3}	5×10^{-3}	
δl_e	m	0.1	0.1	0.1	
ρ_e	m	1.64×10^{-5}	2.59×10^{-5}	2.80×10^{-5}	(5.2)
λ_c	m	1.39×10^{-17}	3.28×10^{-17}	4.53×10^{-17}	(5.3)
σ_e^*	m^{-2}	3.94×10^{17}	7.46×10^{16}	5.94×10^{16}	(6.6)
D_e^*	m^{-3}	1.11×10^{18}	2.11×10^{17}	1.68×10^{17}	(5.1)
Γ		4.26×10^{2}	1.07×10^{2}	5.33×10^{1}	
γ		3.91×10^{4}	2.94×10^{4}	2.94×10^{4}	
γ_{ep}		3.33×10^{7}	5.96×10^{6}	3.13×10^{6}	(3.4)
Γ_c		9.54×10^{1}	4.03×10^{1}	2.92×10^{1}	(3.1)
γ_c		1.75×10^{5}	7.34×10^{4}	5.36×10^{4}	(3.2)

A POSSIBLE ALTERNATIVE FOR THE e-p OPTION

A. Kanofsky
Lehigh University

There has been a great deal of discussion on construction of an electron proton colliding beam facility at ISABELLE.[1] Such a facility would require an electron storage ring of 15 GeV energy. It is possible that a facility with lower energy would still provide an interesting look at e-p high energy interactions, possibly at a much reduced cost.

What I propose is a linear electron accelerator $\sim$ 4 GeV with insertion of the beam into a far end of the insertion region nearest the AGS. It is easy to match the beam size to that of the internal proton beam at ISABELLE. However, high beam currents, on the order of 0.2 A, are needed for luminosities of about 10^{32}.

The c.m. energy for an electron energy of 4 GeV would be 56.6 GeV. This should be more than adequate to produce a variety of interesting reactions and sufficiently higher than SLAC energies to produce new physics. Possibly it could also be used to produce secondary pions which would collide with one of the proton beams. It would be possible in this way to study high c.m. energy pion proton collisions. This has been first proposed by Baltay,[2] using in place of the e beam, one of the colliding p beams.

How would the new facility be built? The linear accelerator could be installed in the straight tunnel leading out to the injection intersection of the storage ring. This is shown in Fig. 1. Details of the insertion are shown in Fig. 2. In this way, building costs could be minimized. It could be designed in an expandable form so that later additional lengths, providing even higher energies, could be incorporated at later times.

1. R. Chasman, "Status of ISABELLE e-p Option at the Time of Summer Study 1975," these Proc.

2. C. Baltay, "Pion-Proton Interactions at ISABELLE," BNL 16911, BNL Informal Report, CRISP 72-22 (1972).

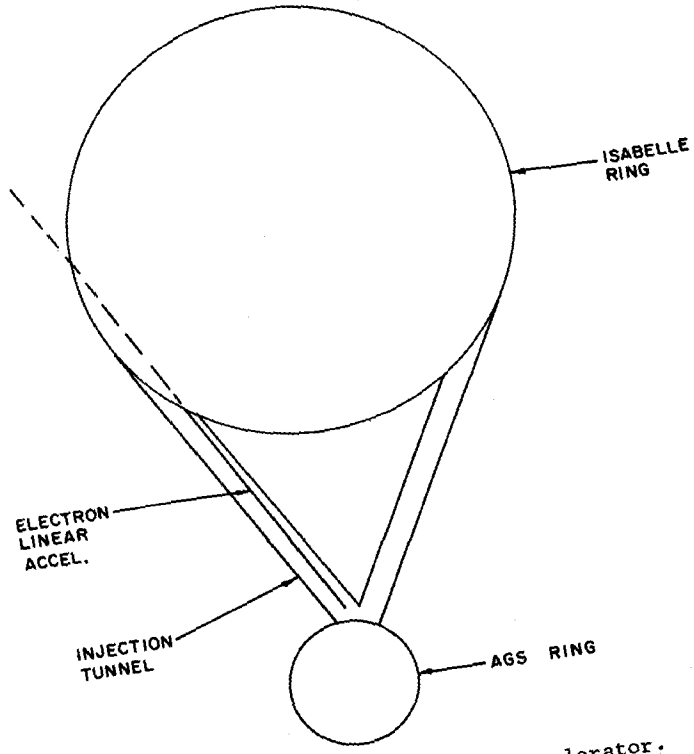

Fig. 1. Location of Electron Accelerator.

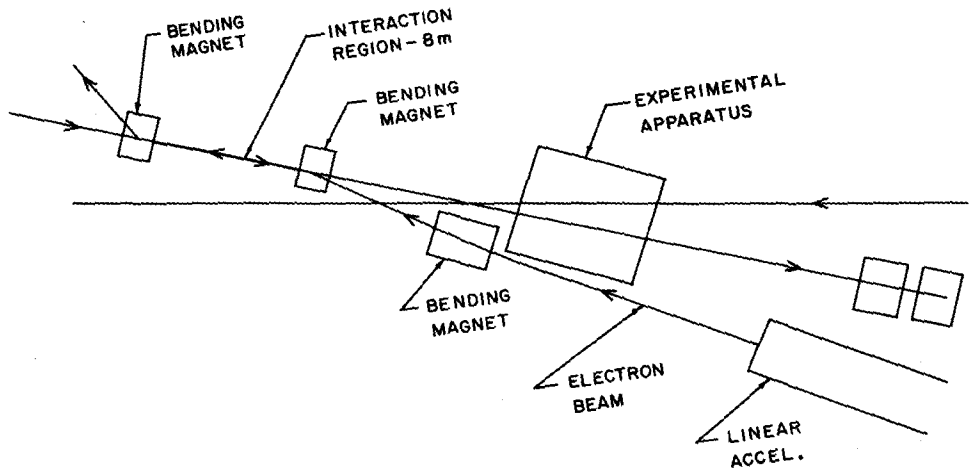

Fig. 2. Detail of Electron Insertion.

Eventually such a linear accelerator could be built up to the full 15 GeV energy or it could itself be used at low energy as an injector to a storage ring. Alternatively, the beam could be recycled through the linear accelerator several times to reach the desired energies. This is presently being done at Stanford.[3]

I now discuss the feasibility of such a facility. I consider questions of comparative costs, beam stability and operating parameters. I take the 20 GeV SLAC accelerator operating parameters for comparison. At SLAC the beam is of 1.5 μsec duration for 360 times a second. Peak current is 40 mA. Thus, the average current is ~ 0.02 mA. The machine length is two miles. Since the energy increases linearly with length, for an energy of 4 GeV, we would need a length of 2/5 of a mile for the accelerator. Supposedly, modern klystrons and cavities could reduce that length by ½ or more. We may now ask how we may increase the intensity and luminosity. There are two bunches in the ISABELLE storage ring, each 500 meters long. The total circumference of the ring is 3000 meters. Thus we can get a duty factor of 3 at the present bunching. Tighter bunching might be possible, but questions of stability must be answered as to whether this is possible. It should be possible to increase the 0.02 mA average current by factors of 10 - 100 by higher current sources, better cavities (possibly superconducting) higher power klystrons, and duty factor increases by ISA beam bunching, etc.

We can expect another factor of 20 increase in luminosity by expansion of the beam-beam intersection region to 8 meters. This would be possible because electron beam stability is no longer a problem.

In the case of electron proton colliding beams, the proton electron interactions at the intersection cause instabilities in the electron beam while only slightly affecting the proton beam. This is, of course, no longer a problem with a linear accelerator and

3. Alan Schwettman, private communication.

the interaction region can be quite long. The long interaction region should present no problems to experimenters because all the interaction products will be moving at a small angle relative to the proton beam direction, and such products need only small aperture "downstream" detectors for detection. Thus, the luminosity we could expect would be 0.02 - 0.2 the luminosity of 10^{32} with 0.2 A. This is not as bad as it looks if the electrons are delivered in small time bunches well separated in time. The actual "livetime" for many experiments could be the same as for continuous beams because the time between bunches could be used to read in event data without loss of actual sensitivity during beam interaction time.

I may mention one more unique way to increase the event rate. If we turn off the electron beam while data from the detecting chambers and counters are being read in, we could have much higher peak currents in the time interval when the apparatus is set to trigger on or detect the occurrence of an event than if we ran the beam continuously. This is because we are mainly limited in average current. We could turn the internal electron beam off with a signal from the experimental apparatus occurring with an event trigger. We could then turn the beam back on with a signal from the experimental apparatus when the event has been read in. This method could also be used to reduce the power consumption involved in accelerating electrons to the high energies involved.

As an example, suppose we have an event rate of 20 events/second and it takes 20 millisec to read in the data for a single event. The total read-in time per second is 0.4 seconds. If we shut off the beam during the read-in time, power consumption drops to 60% of its value with the beam on continuously. Alternatively, we could have run the beam at almost double the original current in the sensitive time period to further increase the event rate.

The energy cost savings and instantaneous luminosity increase further as the event rate increases.

By making the accelerator an integral part of the apparatus,

such performance improvements are possible.

As far as costs, detailed studies will have to be made. I present here a very rough estimate. High current 20 MeV electron accelerators are available from commercial manufacturers for $300K. If the price scales linearly with energy, a 4 GeV machine would cost $40M. However, it is unlikely that it scales this way. Probably half or a quarter of the cost is more reasonable giving $10M - $20M for the cost. Much of the construction costs could be saved by putting the accelerator in an existing tunnel and by sharing cooling facilities, controls, etc.

As to operating costs, the SLAC accelerator operating budget is about $10M per year. Probably $2M of this is spent on machine power and replacement parts. This would be an upper limit to what we could expect on the 4 GeV machine. Power costs could be cut more if it used superconducting cavities. The Stanford superconducting accelerator people failed to achieve their objectives in power savings and volt/meter increase but possibly their achieved results are more than adequate at the ISA, especially since the superconducting facilities will exist.

Detailed cost estimates should be made on all of the above-mentioned items. Clearly, there has to be some cross-over point in at least power costs for a synchrotron as compared to a linear accelerator since synchrotron radiation beam energy losses go as the fourth power of the electron energy and there are no radiation losses for a linear accelerator.

In conclusion, it seems that the ISABELLE facility provides an excellent opportunity for low cost construction and operation of a linear accelerator for use in e-p colliding beams.

VERTICAL DISPERSION MATCHING IN THE ISA ELECTRON OPTION

A. Garren
Lawrence Berkeley Laboratory

Schemes are discussed by Steffen et al [1] in which the circular octants of the electron ring are placed alternately above and below the proton ring. With such a ring topology electron vertical dispersion can be brought to zero at the crossing points and in the machine octants, by using a method previously designed by the author for the e-p option of PEP. This scheme is shown schematically in Fig. 1.

Starting at the interaction point (IP), where the proton and electron beams cross vertically at a very small angle, the beams next pass through the quadrupole doublet Q1, Q2 centered on the electron beam. This doublet focuses the electron beam envelopes at the IP. At the same time it causes the electron vertical dispersion to cross the midplane at the IP. Due to the higher energy of the protons, it has little effect on the proton beam.

Following the doublet, both beams pass through a vertical low field (about 200 G) magnet BVL. The small deflection of the electrons there permits one to install masks in the interaction region to shield the detectors from synchrotron radiation emitted in the following common vertical bending magnet, BV1. Magnet BV1 separates the proton and electron beams. The electrons are deflected vertically to BV2, which restores them to the horizontal direction with the vertical beam separation required in the octants. At the end of BV2 the electron vertical dispersion and its slope are zero. The following doublet, Q3, Q4, acts together with Q1, Q2 to produce the low-β focus at the IP. Since the whole figure is inverted through the IP, the dispersion is corrected in the same way on both sides.

The proton beam after leaving BV1, passes through the conventional vertical magnet BV2, and then through the superconducting

1. K. Steffen, J. Maidment and Y. Cho, "Review of e-p Collision Geometries", these Proc.

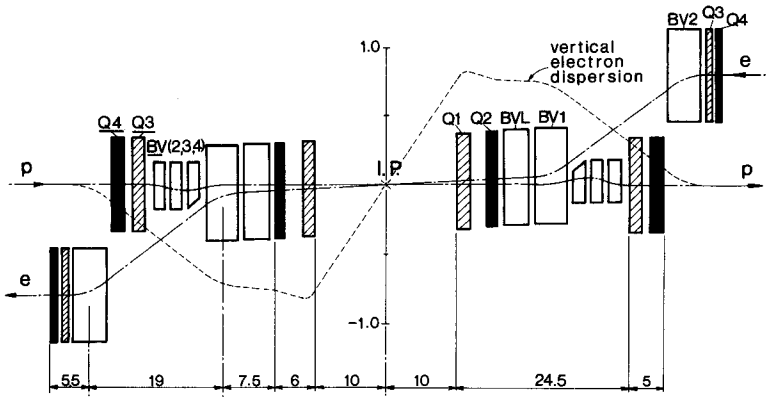

Fig. 1. Side view of p-e insertion geometry for ISA, based on a modification of the PEP p-e design. (Dimensions in meters.)

magnets BV3, BV4. These three magnets restore the protons to the median plane. The following doublet, Q3, Q4, provides the low-β focus of the proton beam at the IP.

The advantages of this scheme are that by elimintating the need for quadrupoles between BV1 and BV2 on the electron-line, the whole insertion can be shortened and the chromaticity reduced. The latter effect can be substantial, since to produce zero dispersion, not only at the IP but throughout the interaction region, a complete vertical oscillation in the BV1 - BV2 region is required.

AUTHOR INDEX

Volumes I and II

Baynham, D.A., 565
Berley, D., 739
Blechschmidt, D., 665, 680
Blumberg, L., 452
Brown, H., 442
Bruck, H., 791
Burnstein, R., 9
Carithers, W.C., 9
Carroll, A., 739
Chang, C.Y., 244, 356
Chao, A.W., 386, 418
Chasman, R., 751
Cheng, D., 319
Chien, C.Y., 255
Cho, Y., 761
Chung, Suh-Urk, 183
Claus, J., 515
Dahl, P., 583
Danby, G., 149, 631
Dimmler, G., 701
Duong-Van, M., 9
Edelstein, R.M., 234
Edwards, D., 382
Engels, E., 244
Faltens, A., 476, 486
Fitch, V., 723
Foley, K.J., 292
Gareyte, J., 395
Garren, A., 372, 814
Giacomelli, G., 301
Giordano, S., 500, 508
Good, M.L., 1, 289
Gordon, H., 255
Goulianos, K., 319
Gourber, J.P., 395
Grannis, P., 183, 277
Green, D., 183, 277
Gröbner, O., 661
Halama, H.J., 640, 688
Halzen, F., 715
Hereward, H.G., 555
Herrera, J.C., 418, 640, 658
Hobson, J.P., 151, 652, 690
Hübner, K., 562, 729
Imlay, R., 9
Kanofsky, A., 255, 273, 316, 351, 363, 365, 809
Keil, E., 133, 531
Kirz, J., 269
Knapp, B., 319
Kramer, M.A., 244, 255
Kreisler, M., 9
Kycia, T.F., 70
Lanou, R., 244
Laslett, L.J., 486, 587
Lederman, L.M., 84
Li, K.K., 707
Lindenbaum, S.J., 52, 624
Louttit, R., 52
Love, W., 52
Lowenstein, D., 710
Maidment, J., 761, 774
Majka, R.D., 204
Mallory, K.B., 160, 712

Mann, A., 739
Marx, J.N., 204
McInturff, A.D., 567
Meadows, B.T., 292
Messerschmid, E., 520
Mikaelian, K.O., 340
Month, M., 418, 520
Nauenberg, U., 9
Nawrocky, R.J., 703
Ozaki, S., 52
Paige, Frank E., 52, 333
Parzen, G., 573, 583
Paschos, E., 9, 715
Peierls, R., 327, 715
Pellegrini, C., 552
Perot, J., 585
Peterson, J., 447, 470
Platner, E., 52
Pondrom, L., 244
Protopopescu, S., 52
Ranft, J., 452
Remsbottom, R.H., 567
Rosen, J., 319
Rosenson, L., 52
Rubbia, C., 9
Ruggiero, A.G., 531, 539, 545
Russ, J., 255
Russell, J., 52
Sakitt, M., 9
Samios, N.P., 356
Sandweiss, J., 70
Sanger, P., 149, 626
Schlein, P., 319
Schnell, W., 126
Selove, W., 52, 348
Sidhu, D.P., 715
Smith, L., 111
Snow, G., 9
Steffen, K., 761
Stevens, A., 452
Strauss, B.P., 567
Sulak, L., 9
Teng, L.C., 117, 423, 447, 470
Thomas, D.B., 140
Thorndike, A.M., 301
Tigner, M., 163, 778, 783
Ting, S., 52
Trueman, T.L., 715
van Steenbergen, A., 117, 423, 430, 447, 452, 463
Wang, C.L., 9
Wang, L.L., 9
Williams, H.H., 9
Willis, W.J., 170
Wolgast, R.C., 694
Yu, M.L., 672
Zeller, M., 234